CENTRAL RESEARCH LIBRARY

ORNL-5107

Cy 1

Mechanical Properties Test Data for Structural Materials Quarterly Progress Report for Period Ending October 31, 1975

[redacted]

OAK RIDGE NATIONAL LABORATORY
CENTRAL RESEARCH LIBRARY
DOCUMENT COLLECTION
LIBRARY LOAN COPY
DO NOT TRANSFER TO ANOTHER PERSON
If you wish someone else to see this document, send in name with document and the library will arrange a loan.
UCN-7969
(3 3-67)

OAK RIDGE NATIONAL LABORATORY
OPERATED BY UNION CARBIDE CORPORATION • FOR THE U.S. ATOMIC ENERGY COMMISSION

Printed in the United States of America. Available from
the Energy Research and Development Administration,
Technical Information Center
P.O. Box 62, Oak Ridge, Tennessee 37830
Price: Printed Copy $11.75 ; Microfiche $2.25

This report was prepared as an account of work sponsored by the United States Government. Neither the United States nor the Energy Research and Development Administration, nor any of their employees, nor any of their contractors, subcontractors, or their employees, makes any warranty, express or implied, or assumes any legal liability or responsibility for the accuracy, completeness or usefulness of any information, apparatus, product or process disclosed, or represents that its use would not infringe privately owned rights.

ORNL-5107
UC-79b, -h, -k
(Liquid Metal Fast
Breeder Reactors)

Contract No. W-7405-eng-26

METALS AND CERAMICS DIVISION

MECHANICAL PROPERTIES TEST DATA FOR STRUCTURAL MATERIALS QUARTERLY PROGRESS REPORT FOR PERIOD ENDING OCTOBER 31, 1975

Aerojet Nuclear Company
Argonne National Laboratory
Oak Ridge National Laboratory
Naval Research Laboratory
Hanford Engineering Development Laboratory
Westinghouse Advanced Reactors Division
University of Cincinnati
University of California at Los Angeles
General Electric Company

Compiled by M. R. Hill

DECEMBER 1975

OAK RIDGE NATIONAL LABORATORY
Oak Ridge, Tennessee 37830
operated by
UNION CARBIDE CORPORATION
for the
U.S. ENERGY RESEARCH AND DEVELOPMENT ADMINISTRATION

FOREWORD

This is the ninth in a series of progress reports, the purpose of which is to record and distribute quarterly the collected results of all structural materials mechanical properties test programs sponsored by the Reactor Research and Development Division of the USERDA.

To be useful as resource documents, the reports in this series must be published and distributed in a timely manner to those in the reactor design and materials technology community who have a need of mechanical property test data for nuclear reactor and power plant applications. A test and material index is included to increase the effectiveness of the report.

Reports previously issued in this series are as follows: ORNL-4936, period ending October 31, 1973; ORNL-4948, period ending January 31, 1974; ORNL-4963, period ending April 30, 1974; ORNL-4998, period ending July 31, 1974; ORNL-5103, period ending October 31, 1974; ORNL-5104, period ending January 31, 1975; ORNL-5105 for period ending April 30, 1975; and ORNL-5106 for period ending October 31, 1975. The next quarterly report will be for the period ending January 31, 1976, and contributions are due at ORNL by February 15, 1976.

W. R. Martin
Metals and Ceramics Division
Oak Ridge National Laboratory

CONTENTS

SUMMARY ix

1. AEROJET NUCLEAR COMPANY (No report) 1

2. ARGONNE NATIONAL LABORATORY 3

2.1 INTRODUCTION 3

2.2 FRACTURE AND FATIGUE STUDIES ON STAINLESS STEEL 3

2.2.1 Correlation Between Geometrical Parameters of Surface Roughness and Fatigue Crack Initiation . . 3

2.3 SODIUM EFFECTS ON LFMBR MATERIALS 12

2.3.1 Influence of Sodium Environment on the Low-Cycle Fatigue Behavior of Austenitic Stainless Steels . . 12

2.4 REFERENCES 15

3. OAK RIDGE NATIONAL LABORATORY 17

3.1 INTRODUCTION 17

3.2 MECHANICAL PROPERTIES AND BEHAVIOR FOR STRUCTURAL MATERIALS 17

3.2.1 Mechanical Property Characterization of Type 304 Stainless Steel Reference Heat 17

3.2.1.1 Creep and Rupture Properties of the 51-mm (2-in.) Plate of Reference Heat . . 17

3.2.1.2 Tensile Tests Following Periods of Creep . 18

3.2.2 Mechanical Property Characterization of Type 316 Stainless Steel Reference Heat 34

3.2.2.1 Tensile Data 34

3.2.2.2 Product Form Characterization 42

3.2.2.3 Creep Properties 45

3.2.3 Heat-to-Heat Variation of Mechanical Properties of Types 304 and 316 Stainless Steel 47

3.2.3.1 Time-Independent Design Stress Intensity for Type 304 Stainless Steel 47

3.2.3.2 Creep Properties 61

3.2.4 Materials Behavior in Support of Development and Evaluation of Failure Criteria for Materials . . . 65

3.2.4.1 Methods for Analysis of Creep and Creep-Rupture Data 65

3.2.4.2 Development of Creep Equation for Type 316 Stainless Steel 81

3.2.5 Material Data Processing 94

3.2.6 Elastic Properties of Engineering Construction Materials 94

3.2.6.1 Elastic Properties Determined by Static Tests 95

3.2.6.2 Correlation of Elastic Constants 97

3.3 MECHANICAL AND METALLURGICAL BEHAVIOR OF WELDMENTS FOR LMFBR 101

3.3.1 Studies of Strain Distribution in Weldments and Room-Temperature Elastic Constants 101

3.3.1.1 Test Procedure 102

3.3.1.2 Directional Variation of Apparent Elastic Modulus 107

3.3.1.3 Directional Variation of Yield Strength . 109

3.3.2 General Stainless Steel Welding Development 110

3.3.3 Creep-Rupture Behavior of Gas Tungsten-Arc Types 308, 316, and 16-8-2 Stainless Steel Welds Made with Special Filler Materials 111

3.3.4 Characterization Tests of Type 308 CRE Stainless Steel Welds in Type 304 Reference Heat Base Metal . 112

3.3.5 Characterization of a Type 308 SA Stainless Steel Weld in 0.76-m-diam by 9.5-mm-wall (30 by 3/8 in.) Type 304 Stainless Steel Pipe: Progress Report . . 127

3.3.6 Observation of Substructural Separation During Creep Rupture of Type 16-8-2 Reference Heat at 593°C (1100°F) and 482°C (900°F) 134

3.3.7 Observations of Intergranular Failures in the Heat-Affected Zone of Austenitic Stainless Steel Weldments 135

3.4 MECHANICAL PROPERTIES OF STEAM GENERATOR MATERIALS 141

3.4.1 Creep-Rupture Properties of 2 1/4 Cr-1 Mo Steel . . 141

3.4.2 Fatigue Behavior of 2 1/4 Cr-1 Mo Steel 154

3.4.2.1 Creep-Fatigue Data Analysis 154

3.4.2.2 Bilinear Cyclic Stress-Strain Constants . 158

3.5 HIGH-TEMPERATURE DESIGN 171

3.5.1 Exploratory Studies in Support of Structural Design Methods 171

3.5.1.1 Characterization of the Product Forms of the Reference Heat of Type 304 Stainless Steel 171

3.5.1.2 Exploratory Testing to Identify Behavioral Features 171

3.5.1.3 Exploratory Testing of 2 1/4 Cr-1 Mo Steel 182

3.5.2 Investigations of Creep Failure Under Uniaxial and Multiaxial Conditions 185

3.5.2.1 Topical Report 185

3.5.2.2 Constant-Load Uniaxial Tests 185

3.5.2.3 Interrupted-Load Uniaxial Tests 185

3.5.2.4 Modified Reanneal 188

3.5.2.5 Tubular Tests 190

3.6 MECHANICAL PROPERTIES OF HTGR STEAM GENERATOR AND PRIMARY CIRCUIT MATERIALS 194

3.6.1 Tensile Testing 194

3.6.2 Environmental Creep Testing 194

3.6.3 Subcritical Crack Growth Studies 196

3.6.3.1 Tests in Air 197

3.6.3.2 Tests in Steam 201

3.6.3.3 Tests in HTGR Helium 201

3.6.4 Fatigue-Life Testing 201

3.7 REFERENCES 204

4. NAVAL RESEARCH LABORATORY (No report) 213

5. HANFORD ENGINEERING DEVELOPMENT LABORATORY 215

5.1 INTRODUCTION 215

5.2 MATERIALS INFORMATION DOCUMENTATION FATIGUE AND FRACTURE . 215

5.2.1 Objectives 215

5.2.2 Significant Accomplishments 215

6. WESTINGHOUSE ADVANCED REACTORS DIVISION 225

6.1 INTRODUCTION 225

6.2 BASIC SPECIMEN TESTING 226

6.2.1 Plate Specimens Under Tension and Bending 226

6.2.2 Notched Weld Specimens 236

6.2.3 Specimens with Transverse Welds, Types B and G . . 236

6.2.4 Specimens with Central Axial Welds 236

6.2.5 Central Axial Weld with Hole in Weld 238

6.3 TUBULAR SPECIMEN TESTING 238
6.3.1 Test Piece Description 238
6.3.2 Type 304 Stainless Steel Testing 240
6.3.3 Type 304 Stainless Steel Topical Report 240
6.3.4 Type 316 Stainless Steel Testing 241
6.3.5 Data Reduction 243
6.4 SODIUM EFFECTS ON MECHANICAL PROPERTIES OF STRUCTURAL MATERIALS 246
6.4.1 Type 316 Stainless Steel 246
6.4.2 Inconel 718 256
6.5 REFERENCES 259
7. UNIVERSITIES 263
7.1 UNIVERSITY OF CINCINNATI 263
7.1.1 Introduction 263
7.1.2 Experimental Program 263
7.1.2.1 Analysis of Relationships of Deformation Rate, Stress and Temperature for 304 Stainless Steel 264
7.1.2.2 Change in Stress Experiments on 304 Stainless Steel, Reference Heat 9T2796 . . 269
7.1.2.3 Critical Dislocation Density for Subboundary Formation in Fatigue of Incoloy 800 275
7.1.2.4 Some Aspects of Dislocation Mechanisms During High Temperature Fatigue of Incoloy 800 280
7.1.3 References 286
7.2 UNIVERSITY OF CALIFORNIA, LOS ANGELES 289
7.2.1 Mechanical Properties Evaluation of Carburized Type 304 Stainless Steel 289
8. GENERAL ELECTRIC COMPANY 295
8.1 INTRODUCTION 295
8.2 MECHANICAL PROPERTIES OF STAINLESS STEEL IN CARBURIZING SODIUM 296
8.2.1 Background 296
8.2.2 Current Progress 303

8.2.2.1 Creep/Fatigue of Carburized Stainless Steel 303

8.2.2.2 Fatigue Crack Growth Studies of Carburized Stainless Steel 312

8.3 DECARBURIZATION KINETICS AND DESIGN METHODS VERIFICATION TESTING 313

8.3.1 Background 313

8.3.2 Current Progress 316

8.4 METALLURGICAL CHARACTERIZATION OF VAR AND ESR 2 1/4 Cr-1 Mo ALLOY STEEL 320

8.4.1 Background 320

8.4.2 Current Progress 322

8.4.2.1 Chemical Composition 323

8.4.2.2 Heat Treatment 323

8.4.2.3 Tensile Tests 323

8.4.2.4 Charpy Impact Tests and Drop-Weight Tests 333

8.4.2.5 Creep-Rupture Tests 337

8.5 FRACTURE TOUGHNESS OF LMFBR STEAM GENERATOR MATERIALS . . 337

8.5.1 Background 337

8.5.2 Current Progress 342

8.6 REFERENCES 353

INDEX 357

SUMMARY

1. AEROJET NUCLEAR COMPANY

(No report)

2. ARGONNE NATIONAL LABORATORY

A direct mathematical method to determine the important geometrical parameters relative to surface roughness has been discussed. The surface-roughness characteristics that were produced on low-cycle fatigue specimens of Type 304 stainless steel by a silicon carbide grinding technique have been evaluated. An attempt has been made to establish a correlation between the shape and depth of the surface grooves and the fatigue crack-initiation life determined from Type 304 stainless steel fatigue specimens at 1100°F (593°C).

Low-cycle fatigue data have been obtained on annealed Type 316 stainless steel tested in sodium at 600 and 700°C. The fatigue life at both temperatures is substantially greater when tested in sodium than when tested in air. For low strain ranges ($\Delta\varepsilon_t \sim 0.7\%$), the fatigue life of specimens tested in sodium at 600°C was enhanced by a 1500-hr sodium exposure. This effect is partially attributed to the surface carburization of the steel during the long-term exposure. The carbon concentration of the steel is not significantly altered by the 700°C sodium exposure, and enhanced fatigue life is not observed at this temperature. Differences in the cyclic stress-strain response at the two temperatures were also observed.

3. OAK RIDGE NATIONAL LABORATORY

Elevated-temperature creep testing of the ORNL reference heat of type 304 stainless steel is continuing.

The intragranular hardening due to precipitates, dislocation substructure, precipitates on dislocations and grain boundaries, and intergranular creep cavities are suggested to be responsible for loss in tensile strength and ductility due to prior creep deformation.

Tensile data on 15.9-mm (5/8-in.) as-received plate of the reference heat of type 316 stainless steel are reported for test temperatures in the range from room temperature to 760°C (1400°F). True stress-strain curves for the as-received and reannealed material have been compared with the tensile equation in the *Nuclear Systems Materials Handbook*. The present tensile equation in the Handbook describes the tensile data very well.

Room-temperature hardness data on specimens machined from various product forms of the reference heat of type 316 stainless steel are presented. The present status of creep tests on the reference heat of type 316 stainless is described.

Temperature dependences of tensile data for 20 heats of type 304 stainless steel were analyzed in terms of the property itself and in the ratio form. Reannealing significantly decreased yield strength and the yield strength ratio. The methods of calculating minimum tensile properties are compared. The tensile results on 20 heats of type 304 stainless steel were used to examine the time-independent stresses reported in ASME Code Case 1592. Time-independent stresses in the code were shown to be too underconservative for the reannealed material.

Long-term creep tests on several heats of type 304 stainless steel were updated. Several test times have exceeded 30,000 hr. The heat-to-heat variation was shown to exist for long-term data and also for aged material: weak and strong heats remained weak and strong even after long-term aging. Increasing niobium content increased long-term time to rupture and decreased minimum creep rate. Niobium was shown to be an effective strengthener even for test times exceeding 31,000 hr.

A method was developed for estimating trends in the creep strain to tertiary creep as a function of rupture life and minimum creep rate. Application of the method to data for four elevated-temperature structural materials has yielded good results in general, although the results contain a large amount of scatter.

The existing double-exponential thermal creep equation for type 316 stainless steel is observed to suffer a number of deficiencies, some of which are delineated. In searching for an improved or simplied substitute a nonlinear least squares fit is obtained for the minimum creep rate, with somewhat disappointing results. Additional effort in this direction, with respect to the primary creep strain parameters, is demonstrated to be impractical.

Linearized least squares fits are obtained for the logarithms of the equation, using presently available data, with promising results. More test results are being modelled by several equation forms to obtain specific creep equations. A single rational polynomial form may prove adequate to describe the observed creep.

Operation of a mechanical properties data storage and retrieval system is continuing. In conjunction with this system, a new computer program for analysis of fatigue and creep-fatigue data is being developed.

A new method for determining accurate static elastic constants (E, G, and ν) as functions of temperature by repeatedly employing a single test specimen for gathering the bulk of the test data was developed. Key features of the method include (1) confining test runs to strain levels well within the elastic range ($\varepsilon < 1.2 \times 10^{-4}$), and (2) correcting

for "softening" or "hardening" resulting from repetitive use of the test piece should the effect prove significant. Preliminary tests showed repetitive use of the specimen to produce modest softening. The amount of reduction in Young's modulus was about 0.6% at 482°C (900°F) for isothermally annealed 2 1/4 Cr-1 Mo steel and 0.9% at 538°C (1000°F) for mill-annealed type 304 stainless steel.

A correlation of existing elastic constant data on 2 1/4 Cr-1 Mo steel was completed. The results are reviewed.

Creep-rupture testing at 649°C (1200°F) has been used to determine the effects of residual elements on the ductility of types 308, 316, and 16-8-2 stainless steel weld metal deposited by the gas tungsten-arc process. Types 308 and 316 weld metal containing 0.006% B, 0.04% P, and 0.5% Ti had good strength and significantly improved ductility. However, the compositional variants of 16-8-2 that have been explored to date have not yielded improvement.

The local stress-strain behavior of weldments can have significant impact on engineering design codes when it is understood. Room-temperature data for a type 308 electroslag weld show systematic variations in elastic modulus of about a factor of 2.3 with specimen orientation relative to substructure. Yield strength varies by about 1.3 with direction.

Much of the 593°C (1100°F) mechanical properties characterization of type 308 CRE stainless steel welds that are now being tested at the Westinghouse Research Laboratory is complete. The behavior is similar to that of FFTF vessel test welds. Transverse specimens fail in the heat-affected zone (HAZ) in an intergranular mode; the behavior is consistent with the generalization of a base metal relatively weaker and less ductile than the weld metal. Evidence for intergranular failures at low total strains in type 304 HAZ regions has been found at 593 and 649°C (1100 and 1200°F).

Unannealed type 308 double submerged-arc stainless steel seam welds in pipe have low creep ductility at 649°C (1200°F) and fracture surfaces consistent with sigma phase embrittlement. Evidence of interphase separation has been found in a GTA 16-8-2 weld (Bechtel reference heat, Arcos 2367R) creep tested for 11,896 hr at 593°C (1100°F) with *no* extensometer damage.

The effect of heat treatment on the creep-rupture properties of annealed 2 1/4 Cr-1 Mo steel was investigated at 454, 510, and 566°C (850, 950, and 1050°F). Three different heat treatments were used on plates taken from heat 20017: two different full anneals (different furnace cooling rates) and an isothermal anneal. The cooling rate affected creep-rupture properties. The properties for the slower cooling rate (for the full anneals) and the isothermal anneal were quite similar. The slower cooling rate is the anneal on which most of the mechanical properties were determined on heat 20017.

Data from fatigue tests with hold times for annealed and isothermally annealed 2 1/4 Cr-1 Mo steel have been analyzed by the method of strain range partitioning, and preliminary results are reported. Life predictions appear accurate within a factor of 2.

Interim curves have been constructed showing the bilinear stress-strain constants κ_0, κ_1, κ_2, E_m, and C as functions of maximum strain, ε_{max}, of 2 1/4 Cr-1 Mo steel at various temperatures from room temperature to 538°C (1000°F). Heat-to-heat, heat treatment, and strain rate effects appear to be significant, but the proposed interim curves apply to a single isothermally annealed heat at a ramp strain rate of 4×10^{-3}/sec.

Creep characterization tests on the reference heat of type 304 stainless steel were completed, and results are compared with curves recommended for use in inelastic analysis at 593°C (1100°F). Data showing the cyclic hardening behavior for type 304 stainless steel are provided for temperatures in the range 427 to 649°C (800–1200°F). Data are represented by a model and the parameter values of the model are represented in terms of temperature and strain range. Relaxation data are provided for 2 1/4 Cr-1 Mo steel at 482, 510, and 538°C (900, 950, and 1000°F). Creep rupture results under uniaxial and multiaxial stresses are presented for type 304 stainless steel to beyond 20,000 hr.

The results of stress rupture tests in simulated HTGR helium environment are reported for single heats of Hastelloy X and 2 1/4 Cr-1 Mo steel. Rupture lives and elongations were consistent with literature values.

Subcritical crack growth tests on 2 1/4 Cr-1 Mo steel are discussed. Crack growth rates in air are given as a function of temperature [204 to 593°C (400–1100°F)], frequency (40 to 6000 cpm), and mean stress level. Comparative effects in steam and helium are also reported.

An environmental chamber has been designed for low-cycle strain-controlled fatigue testing in vacuum or simulated HTGR helium. Continuous-cycling strain-controlled fatigue tests on Hastelloy X in air have begun.

4. NAVAL RESEARCH LABORATORY

(No report)

5. HANFORD ENGINEERNG DEVELOPMENT LABORATORY

The summary, major conclusions and some data of a recently completed comprehensive document on the fatigue crack propagation of Inconel 718 and its weldments are presented. Two important points from HEDL work are: limited data indicates the fatigue crack growth rate of Inconel 718 in sodium at 800°F (427°C) is approximately an order of magnitude lower than

that in air under similar conditions; and, the ANC developed heat treatment results in lower crack growth rates relative to the "conventional" heat treatment at test temperatures below the final aging temperatures of 1150°F (621°C). Crack propagation information on A-286 steel is also given.

6. WESTINGHOUSE ADVANCED REACTORS DIVISION

Creep testing of bar, plate, and tube specimens was continued using material from the ORNL Type 304 stainless steel reference heat (9T2796).

A plate test under combined tension and bending has accumulated 12.2 percent permanent strain with the creep rate continuing to decrease. Test results for welded plates and bars have been compared to unwelded specimens. The rupture strength of the transverse weld plate specimens is slightly less than that for base metal under plane stress. Similar specimens with axial welds indicate that the rupture life at comparable stress is about three times that of the base metal but less than that of all-weld-metal specimens under plane stress. Results for notched bar specimens with transverse welds indicate notch insensitivity in the weld metal and notch weakening in the heat affected zone.

Data reduction on results obtained from the tubular specimens continued. The CREEP-FIT data reduction program was updated to allow for a least-square fit to a two exponential term creep equation. This has resulted in a better fit with the test data in the transient creep range. Automatic plotting capability has also been expanded for better comparison of test data. Reference heat Type 316 stainless steel material has been received and heat treatment procedures are being established.

Fatigue tests of Type 316 stainless steel in flowing sodium at 1100°F (593°C) are reported. Results are presented for as-fabricated samples, as well as samples pre-treated in flowing sodium or argon at temperatures of 1200°F or 1325°F for 5000 hours. At a total strain range of $\sim$1 percent, in-sodium data are essentially the same as in-air data reported in the literature. Samples pre-treated at 1200°F for 5000 hours and tested at 1100°F in sodium show a factor of two increase in fatigue life when compared to as-fabricated data. Samples pre-treated at 1325°F for 5000 hours show a factor of four increase in the fatigue life. A strain hardening exponent of 0.32 is obtained from the data for the pre-treated samples.

Low-cycle fatigue data for Inconel 718 tested in air at 1000°F (538°C) are presented. The material was heat treated per AMS-5596C and tested in the as-fabricated condition. The results will be used as baseline data for future in-sodium tests of the same material.

7. UNIVERSITIES

UNIVERSITY OF CINCINNATI

Work on the preliminary evaluation of the dislocation substructure of the creep and tensile specimens from the reference heat 9T2796 (1 inch plate) of AISI 304 stainless steel was completed. The deformation behavior of these specimens which were tested at temperatures ranging from 538 to 816°C and strain rates from 9.7×10^{-9} sec^{-1} to 8.3×10^{-2} sec^{-1} has been analyzed in terms of the influence of dislocation substructure. The existing relationships of the deformation rate, stress and temperature were viewed and a modified version in which a substructure parameter is explicitly included is shown to adequately describe the deformation behavior. More work is still required and being done to elucidate the influence of second phase carbides on the deformation characteristics.

The dislocation substructure of a set of specimens from the reference heat of 304 stainless steel in which the stress levels were changed during steady state creep were evaluated and the results are presented. The subsequent creep behavior obtained from these tests is being understood in the light of the substructure and the results will be reported later.

TEM evaluation and preliminary analysis of substructure data observed in Incoloy 800 push-pull fatigue specimens are presented and discussed in terms of several existing theories. The critical dislocation density for subboundary formation was experimentally confirmed to exist and found to be inversely proportional to the square of absolute temperature. Misorientation angle between adjacent cells or subgrains for specimens tested to failure was found to be independent of any of those parameters employed in this study. The density of dislocations associated with subboundaries, ρ_{SB}, was estimated from the misorientation angle and the ratio of ρ_{SB} to free dislocation density, ρ, was found to be approximately one and a half. This fraction was independent of strain, stress range and temperature for the test conditions of this experiment.

Saturation shear stress was calculated on the basis of the free mesh length of dislocation networks in the subboundaries by using the density of dislocations forming the subboundary and found to be consistent with the observed stress.

UNIVERSITY OF CALIFORNIA, LOS ANGELES

Calibration experiment on crack propagation study in Type 304 stainless steel is described. Using compliance measurements, the length of a part-through crack can be determined to be an accuracy of better than 0.002 in.

8. GENERAL ELECTRIC COMPANY

Programs designed to study the effects of high temperature sodium environments on the mechanical properties of stainless steels and 2¼Cr-1Mo are continuing. The results of a program evaluating the effect of heat treatment and melting practice on the mechanical behavior of 2¼Cr-1Mo are reported for the first time.

Type 316 stainless steel has been tested at 510°C in carbon saturated sodium after 1,000 hr. pre-exposure. Creep, creep/fatigue and fracture mechanics bend tests are being performed to assess the effect of carburization on the mechancial behavior of this alloy. Creep rupture data are not yet avilable from control tests, however, the minimum creep rates of the carburized samples in sodium are about twice those of the control tests. Initial control tests run in the crack growth rate apparatus are in agreement with results of the investigations.

Creep/fatigue (unaxial and biaxial) testing of 2¼Cr-1Mo at 510°C in decarburizing sodium continued. Results of these tests fall only marginally above the minimum values required by Code Case 1592 of the ASME B&PV Code.

The mechanical properties of vacuum arc and electroslag remelted 2¼Cr-1Mo are being determined for several different heat treatments in-order-to assess the effect of consumable remelting on the mechanical behavior of this alloy. Both short term tensile properties and creep rupture properties fall within the tolerances limits specified for the respective properties in the Nuclear Systems Materials Handbook.

Charpy impact and drop-weight tests have also been performed. The electroslag remelted steel has considerably better impact strength and a lower ductile/brittle transition temperature than the vacuum arc remelted steel. However, this may be due to the inherently fine ferritic grain size of electroslag remelted steels.

The fracture toughness of 2¼Cr-1Mo, both air melted and vacuum arc remelted is being evaluated by elastic-plastic fracture toughness testing methods employing thick compact tension specimens. J integral theory has been employed to compute K_{Ic} values for room temperature tests on annealed steel; a multiple specimen analysis gave a K_{Ic} value of 214 $MPa\sqrt{m}$(194 $ksi\sqrt{in}$).

1. AEROJET NUCLEAR COMPANY

(Contribution not received in time for inclusion in this issue.)

2. ARGONNE NATIONAL LABORATORY

R. W. Weeks

2.1 INTRODUCTION

Argonne National Laboratory (ANL) is conducting extensive programs to provide elevated-temperature, low-cycle fatigue data on Types 304 and 316 stainless steel and to study the effects of sodium environment on the elevated-temperature mechanical properties of these materials. Both programs are in support of LMFBR component design. The report describes a mathematical method developed to correlate the shape and depth of the surface grooves on Type 304 stainless steel fatigue specimens with the number of cycles to initiate a crack and presents the results of low-cycle fatigue tests conducted on Type 316 stainless steel in sodium at 600 and 700°C.

2.2 FRACTURE AND FATIGUE STUDIES ON STAINLESS STEEL -- D. R. Diercks

2.2.1 Correlation Between Geometrical Parameters of Surface Roughness and Fatigue Crack Initiation -- P. S. Maiya

A straightforward mathematical analysis of surface-roughness profiles produced on the low-cycle fatigue specimens (hourglass shape) of Type 304 stainless steel is presented. The surface roughness was produced circumferentially by grinding with silicon carbide paper of different grit sizes. A Talysurf instrument was used to trace the surface profile. The vertical and horizontal resolutions of the Talysurf instrument used in the present work are better than 0.01 and 4 μm, respectively. The profiles were then analyzed to obtain numerical values for the several surface-roughness parameters related to the shape of surface grooves. The geometrical parameters were then used to determine the possible correlation with fatigue life.

Consider the appearance of a typical surface profile recorded for a ground surface, using a Talysurf instrument, as shown schematically in Fig. 2.1. In general, the profile is described by a Fourier series

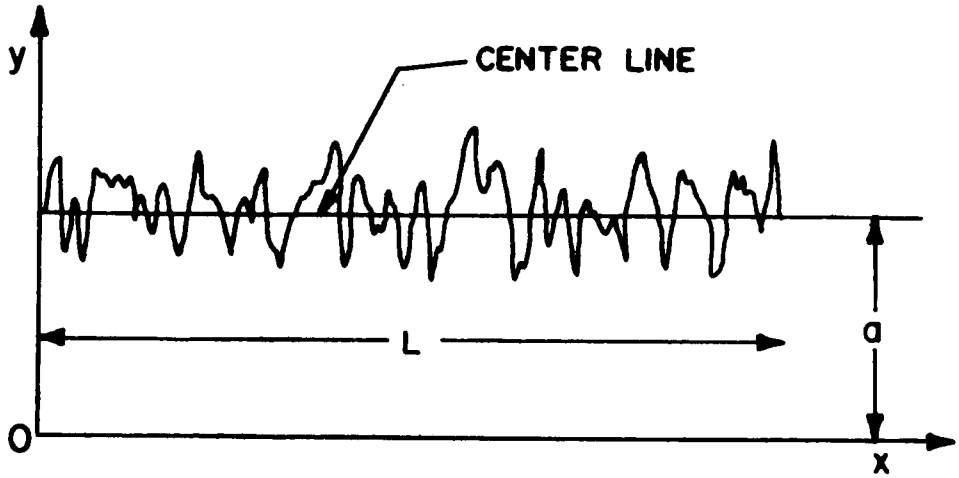

Fig. 2.1. Surface-roughness Profile. Neg. No. MSD-60691.

$$y = \frac{A_o}{2} + \sum_{k=1}^{N-1} \left(A_k \cos \frac{2\pi\ k\ x}{L} + B_k \sin \frac{2\pi\ k\ x}{L}\right) + A_N \cos \frac{2\pi\ N\ x}{L} \quad , \tag{1}$$

where A_o, A_k, B_k ($k = 1, 2, \ldots N-1$), and A_N are the Fourier coefficients. The Fourier coefficients are given by

$$A_o = \frac{2}{L} \int_0^L y\ dx, \tag{2}$$

$$A_k = \frac{2}{L} \int_0^L y \cos \frac{2\pi\ k\ x}{L}\ dx, \tag{3}$$

and

$$B_k = \frac{2}{L} \int_0^L y \sin \frac{2\pi\ k\ x}{L}\ dx. \tag{4}$$

The 2N amplitude measurements were made on a profile of length L at 2N points along the x-axis, starting from origin 0, either at equal intervals or at the locations of peaks and valleys. From the amplitude data, the 2N Fourier coefficients were evaluated from Eqs. (2)-(4). The integration was carried out numerically using the trapezoidal rule.

The various surface-roughness parameters are defined as follows: The average depth of surface grooves is

$$R_{av} = \frac{1}{L} \int_0^L |f(x)| dx. \tag{5}$$

The root-mean-square (rms) value* for the profile is

$$R_{rms} = \left\{ \frac{1}{L} \int_0^L [f(x)]^2 \, dx \right\}^{1/2} . \tag{6}$$

The average wavelength[1] is

$$\lambda_{av} = 2\pi \frac{\int_0^L |f(x)| dx}{\int_0^L |f'(x)| dx} , \tag{7}$$

and the rms wavelength is

$$\lambda_{rms} = 2\pi \frac{\left\{ \frac{1}{L} \int_0^L [f(x)]^2 \, dx \right\}^{1/2}}{\left\{ \frac{1}{L} \int_0^L [f'(x)]^2 \, dx \right\}^{1/2}} , \tag{8}$$

---

*The distinction between the average and rms values is not of practical importance in the present paper.

where $f(x) = y - a$, $a = \frac{1}{L}\int_0^L y\,dx$, and the prime denotes differentiation. Physically, a is the distance between the center line and the 0x axis (Fig. 2.1). From Eqs. (6) and (8), it follows that

$$R_{rms}/\lambda_{rms} = \frac{1}{2\pi}\left\{\frac{1}{L}\int_0^L [f'(x)]^2\,dx\right\}^{1/2} = \frac{Z_1}{2\pi}, \tag{9}$$

where Z_1 is the rms of the first derivative (slope) of the profile. The quantities given by Eqs. (5)-(7) have been determined by using the standard techniques of numerical integration.

Another useful geometrical parameter that indicates the sharpness or degree of curvature of the "hills" and "valleys" is the rms of the second derivative of the profile defined by

$$Z_2 = \left\{\frac{1}{L}\int_0^L [f''(x)]^2\,dx\right\}^{1/2}. \tag{10}$$

The parameters Z_1 and Z_2 may be of importance in fatigue and in friction and wear properties.

A determination of which parameter is the most important may depend upon a particular application. For example, the Z_1 characteristics have been found to be more useful than Z_2 in predicting the frictional behavior of cold-worked disks.[2]

The Fourier representation of a surface profile also provides a convenient method of determining analytically the rms properties of the profile, namely, R_{rms}, λ_{rms}, and Z_2. For example, using orthogonality relations such as

$$\int_0^L \cos\frac{2\pi k x}{L}\cos\frac{2\pi k' x}{L}\,dx = \begin{cases} 0, & k \neq k' \\ L/2, & k = k' \end{cases}, \tag{11}$$

we find that R_{rms}, γ_{rms}, and Z_2 can be expressed in terms of the Fourier coefficients as follows:

$$R_{rms} = \sqrt{1/2}\left[\frac{A_o^2}{2} + \sum_{k=1}^{N-1} (A_k^2 + B_k^2) + A_N^2\right]^{1/2}, \tag{12}$$

$$\lambda_{rms} = 2\pi \frac{\left[\frac{A_o^2}{2} + \sum_{k=1}^{N-1} (A_k^2 + B_k^2) + A_N^2\right]^{1/2}}{\left\{\left[\sum_{k=1}^{N-1} \left(\frac{2\pi\ k\ A_k}{L}\right)^2 + \left(\frac{2\pi\ k\ B_k}{L}\right)^2\right] + \left(\frac{2\pi\ N\ A_N}{L}\right)^2\right\}^{1/2}}, \tag{13}$$

and

$$Z_2 = \sqrt{1/2}\left\{\left[\sum_{k=1}^{N-1} \left(\frac{2\pi\ k}{L}\right)^4 A_k^2 + \left(\frac{2\pi\ k}{L}\right)^4 B_k^2\right] + \left(\frac{2\pi\ N}{L}\right)^4 A_N^2\right\}. \tag{14}$$

The rms values can thus be determined from Eqs. (12)-(14), which involve the summation of the Fourier coefficients. The cutoff length L was chosen such that $L >> \lambda$, for better representation of surface profile. The maximum depth of surface roughness (R_{max}) was also determined from the profile amplitude measurements.

The variation of the surface-roughness parameters with the grit size of the silicon carbide paper for the fatigue specimens containing circumferential grooves is summarized in Table 2.1. The low-cycle fatigue tests have been performed under axial push-pull strain-cycling conditions at 593°C at a strain rate of 4×10^{-3} sec^{-1}. From the fatigue-striation spacing measurements, the crack-initiation life N_o (number of cycles to initiate a crack length equal to 0.1 mm) has been determined. The technique for producing surface roughness, the fatigue test results, and the details concerning the determination of N_o can be found elsewhere.[3-5] Because surface roughness affects only N_o, it is meaningful to

Table 2.1. Values for Geometrical Parameters Related to Surface Roughness for Type 304 Stainless Steel

Surface Preparation	R_{av}, μm	R_{rms}, μm	R_{max}, μm	λ_{av}, μm	λ_{rms}, μm	R_{rms}/λ_{rms}	Z_2, μm^{-1}
Mechanically Polished[a]	-	0.0075	<0.027	-	∿6	0.00125	-
Ground on Silicon Carbide Paper							
600 grit	0.032	0.0386	0.18	19.0	18.5	0.0021	0.00611
240 grit	0.393	0.482	1.8	23.2	22.8	0.021	0.0434
50 grit	2.758	3.736	8.9	83.0	89.5	0.042	0.023

[a]The values for this case were determined by interferometric techniques.

obtain a correlation between the parameter related to surface roughness and N_o. When the strain range is held constant and only the surface roughness is varied in fatigue tests, the relation between N_o and the geometrical parameter (which enhances the strain at the root of surface notches produced by grinding) is assumed to be of the following form:

$$N_o = A \text{ (surface-roughness parameter)}^{-\alpha}, \tag{15}$$

where A and α are constants. Equation (15) is based on the Coffin-Manson relation for crack initiation, i.e., $N_o = A\ (\Delta\varepsilon_p)^{-\alpha}$, where $\Delta\varepsilon_p$ is the plastic strain range. When $\Delta\varepsilon_p$ is held constant and only surface roughness increases, the effect of surface roughness may be considered to enhance the strain concentration[6] that depends on the surface-roughness characteristics, as suggested in Eq. (15). Figures 2.2-2.4 show the correlation between R_{rms}/λ_{rms} and N_o, R_{max} and N_o, and R_{rms} and N_o,

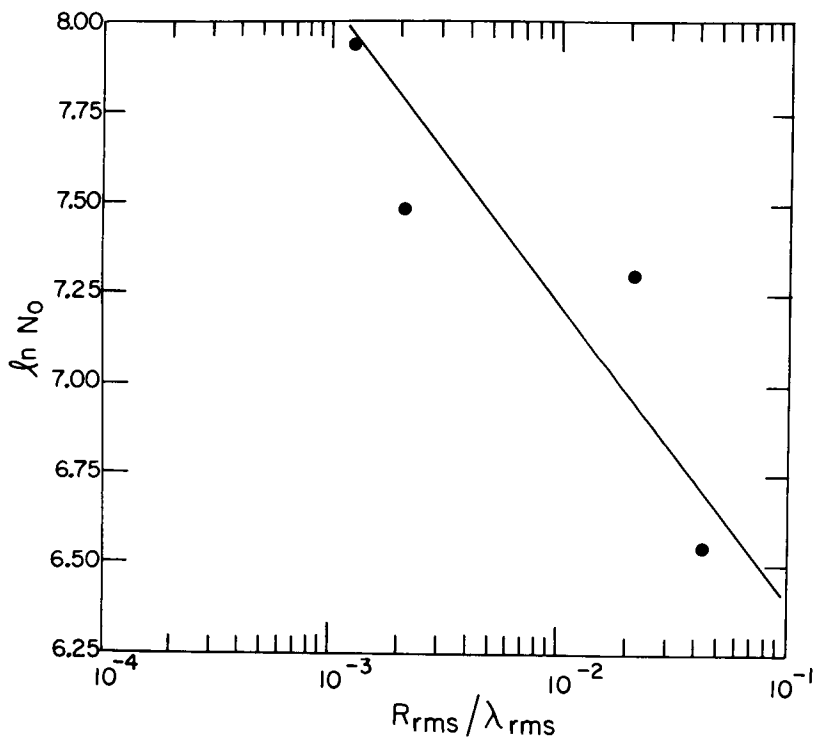

Fig. 2.2. Fatigue Crack-initiation Life vs rms of the First Derivative of Surface Profile. Neg. No. MSD-60693.

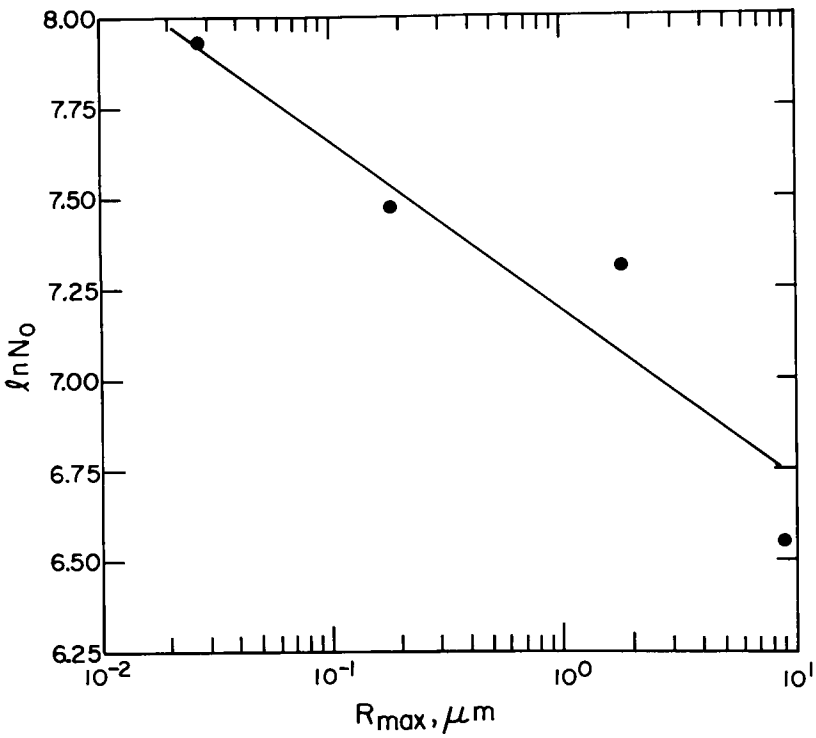

Fig. 2.3. Fatigue Crack-initiation Life vs Maximum Depth of Surface Roughness. Neg. No. MSD-60694.

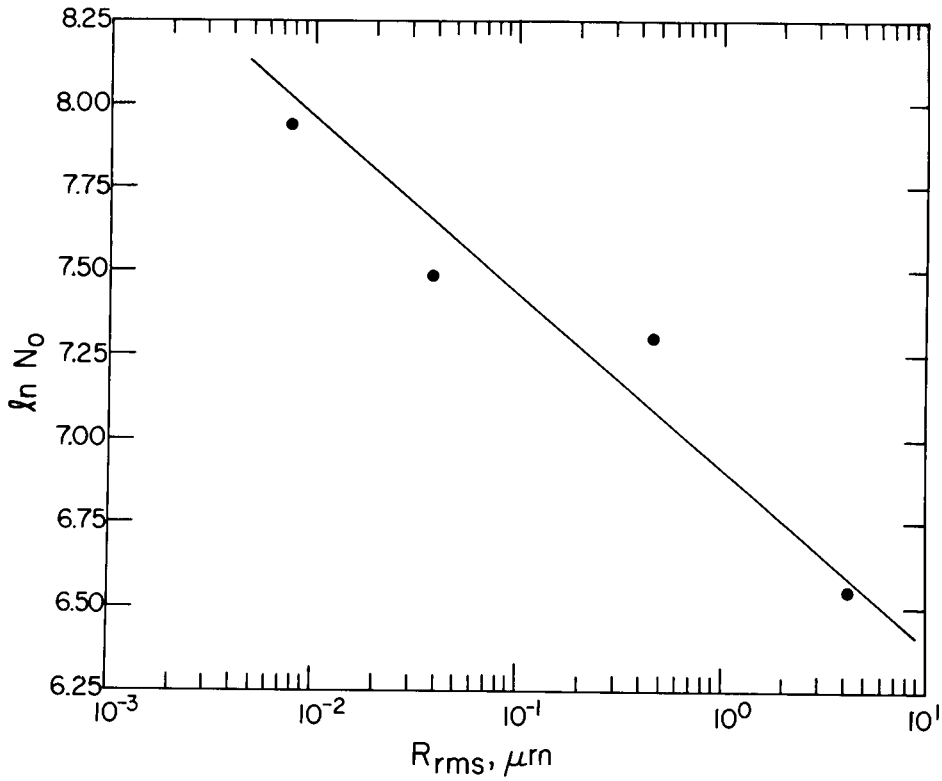

Fig. 2.4. Fatigue Crack-initiation Life vs rms of Surface Profile. Neg. No. MSD-60692.

respectively, on log-log plots. Based on the correlation factor of linear regression for limited data, the amplitude, particularly the rms value (R_{rms}) of the surface profile, gives better correlation with N_o (Fig. 2.4, correlation factor = 0.96) than the rms of the first derivative of the profile (Fig. 2.2, correlation factor = -0.89). However, more extensive data are needed to firmly establish this point of view and the importance of parameters such as Z_2. It is also important to note that the present analysis is also applicable to the analysis of surface topography that develops in initially smooth specimens subjected to fatigue.[6]

2.3 SODIUM EFFECTS ON LMFBR MATERIALS -- T. F. Kassner

2.3.1 Influence of Sodium Environment on the Low-cycle Fatigue Behavior of Austenitic Stainless Steels -- D. L. Smith and G. J. Zeman

Fatigue tests in sodium are being conducted to investigate the influence of a high-temperature sodium environment on the low-cycle fatigue behavior of Types 304 and 316 stainless steel. The effect of testing in a sodium environment and the effect of long-term sodium exposure are being investigated. The fatigue tests are conducted in sodium of controlled purity, viz., ∿1 ppm oxygen and ∿0.4 ppm carbon, at a strain rate of 4×10^{-3} sec^{-1}. Data reported previously[7] indicate that the fatigue life (for $\Delta\varepsilon_t$ ∿1%) of annealed Type 316 stainless steel tested in sodium is about a factor of four greater than when tested in air at a temperature of 600°C.

Figure 2.5 shows the fatigue data for both the annealed and sodium-exposed Type 316 stainless steel tested in sodium at 600°C. The carbon concentration in sodium during the 1512-hr exposure was maintained at ∿0.4 ppm. Additional data have been obtained at both higher and lower strain ranges during the present report period. Data at the lower strain ranges ($\Delta\varepsilon_t$ ∿ 0.7%) indicate a slightly longer fatigue life for the sodium-exposed specimens. This difference has tentatively been attributed to slower crack initiation that results from carburization

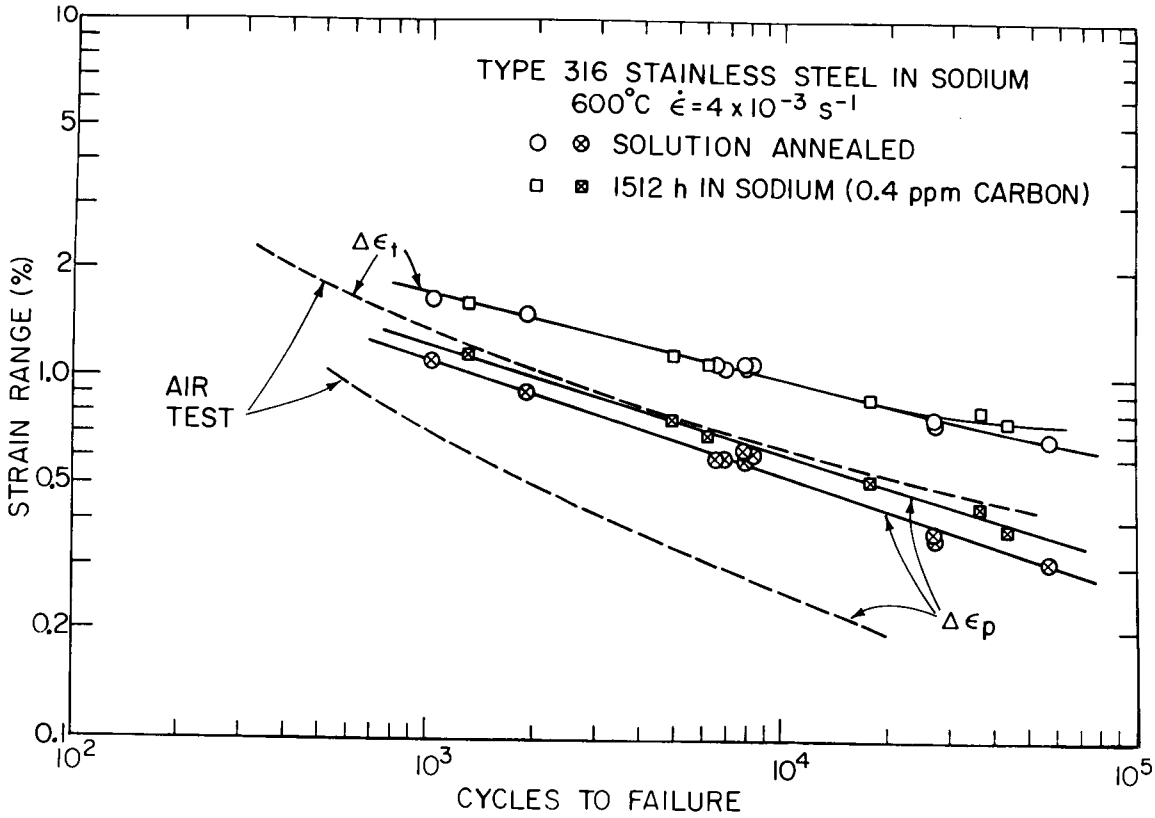

Fig. 2.5. Strain Range vs Cycles to Failure for Type 316 Stainless Steel Tested at 600°C in the Annealed and Sodium-exposed Conditions. Neg. No. MSD-61867.

of the sodium-exposed steel. The recent data for annealed material also indicate that the ratio of fatigue life in sodium to that in air increases from ∿2 to 6 as the total strain range decreases from 1.5 to 0.7%.

Fatigue data obtained at 700°C for Type 316 stainless steel are shown in Fig. 2.6. The fatigue life at 700°C is nearly a factor of two lower than that at 600°C. However, the fatigue life in sodium at 700°C is substantially better than that reported for aged material tested in air at the same temperature.[8] Little difference is found between the data for the annealed material and the sodium-exposed samples. In contrast to the 600°C data, the annealed material at 700°C appears to have a slightly longer fatigue life at the lower strain ranges ($\Delta\varepsilon_t$ ∿0.7%). It should be pointed out that, during the 1512-hr exposure to sodium

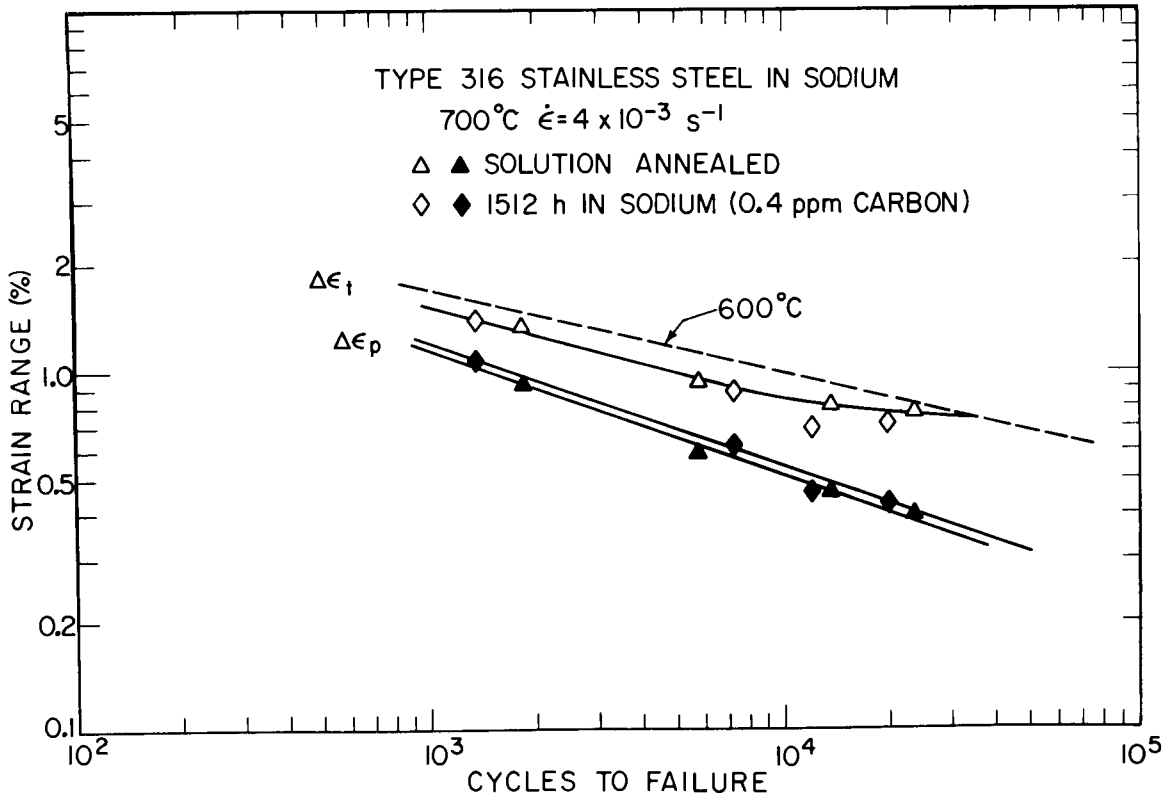

Fig. 2.6. Strain Range vs Cycles to Failure for Type 316 Stainless Steel Tested at 700°C in the Annealed and Sodium-exposed Conditions. Neg. No. MSD-61868.

(∿0.4 ppm carbon), the carbon concentration at the surface of the 600°C specimens increases to ∿0.3 wt%, whereas the carbon concentration at the surface of the 700°C specimens changes very little from the initial concentration of ∿0.06 wt%. The cyclic stress-strain response is shown in Fig. 2.7 for both temperatures. The stress range for the sodium-exposed samples is significantly less than that for the annealed material at 600°C; however, little difference is observed at 700°C. Apparently substantial thermal aging occurs at 700°C during exposure to sodium for the thermal equilibration period just before fatigue testing. This conclusion is also supported by the much lower strain-hardening exponent (∿0.15) at 700°C compared with a value of ∿0.31 at 600°C for the annealed material. Additional tests are being conducted on aged samples to ascertain which effects are due only to aging in sodium and which are due to sodium effects, primarily carburization.

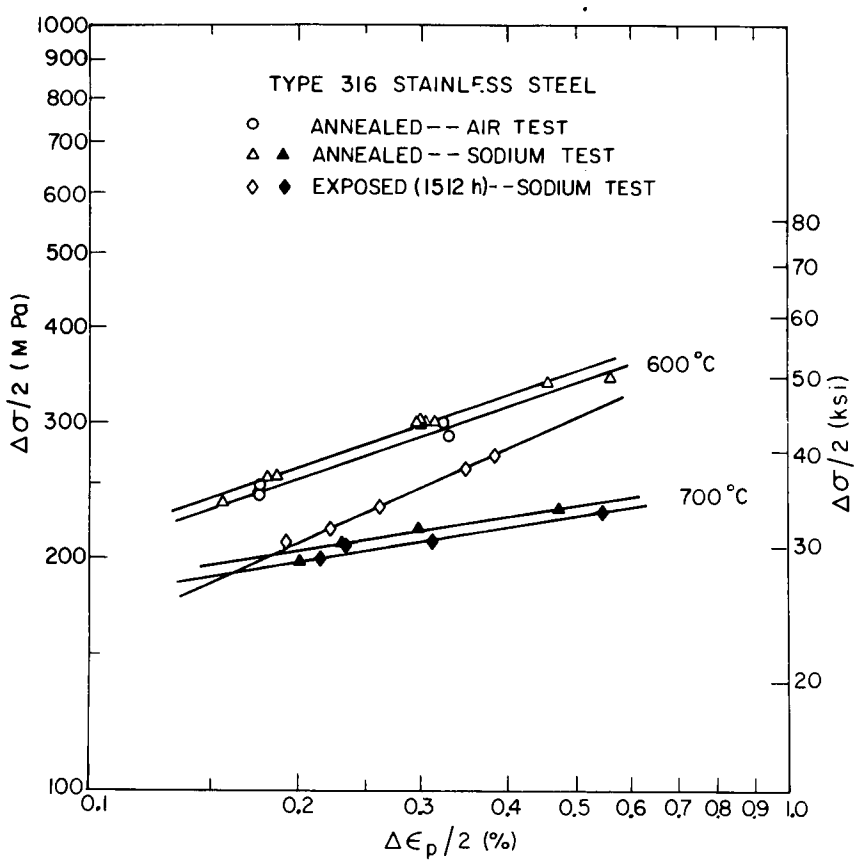

Fig. 2.7. Cyclic Stress-Strain Response for Type 316 Stainless Steel Tested at 600 and 700°C in the Annealed and Sodium-exposed Conditions. Neg. No. MSD-61869.

2.4 REFERENCES

1. R. C. Spragg and D. J. Whitehouse, "An Average Wavelength Parameter for Surface Metrology," Measurement and Control 5, 95 (1972).

2. N. O. Myers, "Characterization of Surface Roughness," Wear 5, 182 (1962).

3. P. S. Maiya and D. E. Busch, "Effect of Surface Roughness on Low-Cycle Fatigue Behavior of Type 304 Stainless Steel," Met. Trans. 6A, 1761 (1975).

4. P. S. Maiya, "Considerations of Crack Initiation and Crack Propagation in Low-cycle Fatigue," to be published in Scripta Met.

5. P. S. Maiya, "Effects of Surface Roughness and Strain Range on the Low-cycle Fatigue Behavior of Type 304 Stainless Steel," to be published in Scripta Met.

6. P. S. Maiya, "Geometrical Characterization of Surface Roughness and Its Application to Fatigue Crack Initiation," to be published in Materials Science and Engineering.

7. Mechanical Properties Test Data for Structural Materials Quarterly Progress Report for Period Ending June 30, 1975, Oak Ridge National Laboratory, ORNL-5106, pp. 36-40.

8. C. R. Brinkman, G. E. Korth, and J. M. Beeston, "Effects of Radiation on Substructure and Mechanical Properties of Metals and Alloys," ASTM STP 529 (1973), pp. 473-492.

3. OAK RIDGE NATIONAL LABORATORY

W. R. Martin

3.1 INTRODUCTION

The ORNL mechanical properties effort comprises several programs. The program Mechanical Properties and Behavior for Structural Materials deals with materials of general applicability to the LMFBR program. Other programs are concerned with the mechanical properties of weldments in LMFBR components, the specific materials of interest for LMFBR steam generators, collection and correlation of mechanical data needed for design on high-temperature LMFBR systems, and materials for the primary circuit and steam generators of HTGR systems.

3.2 MECHANICAL PROPERTIES AND BEHAVIOR FOR STRUCTURAL MATERIALS — C. R. Brinkman

The objective of this program is to collect mechanical property data and material behavior for LMFBR structural and component materials. Included in the scope of this effort are the following: (1) basic tensile, creep, creep-rupture, and relaxation base-line data that are directly applicable to design criteria and methods for types 304 and 316 stainless steel reference heats and cyclic stress-strain tests performed with emphasis on loading and aging history effects, (2) variations in properties for several heats of types 304 and 316 stainless steel determined to allow establishment of minimum and average values of specific properties and the equation parameters required for design purposes. This work will include determination of property variation of samples from different mill products within a given heat of stainless steel.

3.2.1 Mechanical Property Characterization of Type 304 Stainless Steel Reference Heat — V. K. Sikka, R. H. Baldwin, and E. B. Patton

3.2.1.1 Creep and Rupture Properties of the 51-mm (2-in.) Plate of Reference Heat

Several creep tests on 51-mm (2-in.) plate of the reference heat of type 304 stainless steel (9T2796) continued. The test times and strains

for all tests have been updated and are summarized in Table 3.1. Several tests have approached a test time of 25,000 hr. Creep curves on all tests were updated and showed them to be progressing smoothly.

3.2.1.2 Tensile Tests Following Periods of Creep

Data on tensile tests following periods of creep were reported previously.[1] In this section we present possible reasons for the loss in tensile ductility due to prior creep.

The possible reasons for loss in tensile ductility due to thermal aging and prior creep deformation have been summarized in Table 3.2 along with several postulated microstructural changes due to thermal aging and prior creep. Examples of microstructural changes and hardness data are described here. The influence of thermal aging for 10,000 hr at 482, 593, and 649°C (900, 1100, and 1200°F) on microstructural changes for types 304 and 316 stainless steels are shown in Figs. 3.1 and 3.2, respectively. Electron microstructures for thermally aged and precrept specimens are compared in Figs. 3.3 and 3.4. Note that the creep stress for thermal aging conditions has produced dislocations and a uniform distribution of fine precipitate (carbides) on dislocations. Precipitates at the grain boundaries can be observed for both thermally aged and precrept specimens. Several other examples of the influence of prior creep on microstructure of several heats of type 304 stainless steel are shown in Figs. 3.5 through 3.8. Note that heat 807, which is one of the weakest heats out of the 20 being studied[3] at ORNL, showed even on loading a well defined dislocation cell structure, Fig. 3.5, as compared with only a dislocation tangled and slipband structure produced, as shown in Fig. 3.6, in a relatively strong heat (414). The increase in room-temperature hardness due to prior creep deformation (plastic and creep) is compared in Fig. 3.9 for the weak and relatively strong heat. Note that for the same strain, hardness increased much more for heat 807, which developed a well defined dislocation cell or subgrain structure, as compared to heat 414, which developed no such structure.

Increase in room-temperature hardness due to thermal aging and to prior creep deformation is presented in Fig. 3.10. Note that for the

Table 3.1. Creep Tests on Type 304 Stainless Steel Reference Heat 9T2796 51-mm-Thick (2-in.) Plate[a]

Test	Temperature		Stress		Time in Test	Strain, %		Ratio of Creep Stress to Yield Stress[b]	Comments[c]
	(°C)	(°F)	(MPa)	(ksi)	(hr)	Loading	Creep		
11595	427	800	138	20.0	19,940	2.67	0.081	1.57	
12368	427	800	124	18.0	16,908	1.91	0.0138	1.42	
12472	427	800	110	16.0	16,086	1.17	0.064	1.26	
12570	427	800	97	14.0	15,759	0.83	0.048	1.10	
15319	482	900	207	30.0	3,666	7.86	0.102	2.54	
15268	482	900	138	20.0	4,241	3.38	0.043	1.70	
11569	482	900	138	20.0	15,455	3.27	0.141	1.70	Discontinued
12375	482	900	124	18.0	12,376	2.40	0.072	1.53	Discontinued
11675	482	900	110	16.0	2,451	1.48	0.032	1.36	Discontinued
11693	482	900	97	14.0	97	0.92	0.14	1.19	Discontinued
11830	482	900	83	12.0	83	0.35	0.04	1.02	Discontinued
13152	482	900	69	10.0	13,768	0.089	0.0134	0.85	
13020	482	900	69	10.0	14,624	0.085	0.029	0.85	
10489	538	1000	138	20.0	24,992	3.80	0.73	1.80	
12250	538	1000	124	18.0	17,410	2.62	0.291	1.62	
11625	538	1000	110	16.0	19,656	1.79	0.262	1.44	Discontinued
10491	538	1000	97	14.0	25,014	1.16	0.277	1.26	
12444	538	1000	97	14.0	16,453	1.18	0.263	1.26	
12445	538	1000	97	14.0	4,498	1.17	0.090	1.26	Discontinued
11568	538	1000	83	12.0	20,052	0.53	0.111	1.08	
11626	538	1000	69	10.0	19,813	0.071	0.107	0.90	
11641	538	1000	55	8.0	3,170	0.040	0.027	0.72	Discontinued
10853	593	1100	124	18.0	4,547	2.84	5.94	1.65	Ruptured
10852	593	1100	110	16.0	14,647	2.29	3.55	1.47	Ruptured
13947	593	1100	110	16.0	9,801	2.13	1.51	1.47	
10554	593	1100	97	14.0	8,710	1.40	0.65	1.28	Discontinued
11596	593	1100	83	12.0	19,908	0.52	0.47	1.10	
10490	593	1100	69	10.0	24,992	0.22	0.389	0.92	
13710	593	1100	69	10.0	2,010	0.096	0.204	0.92	Discontinued
14163	593	1100	69	10.0	8,971	0.228	0.288	0.92	
11227	593	1100	55	8.0	6,103	0.041	0.080	0.73	Discontinued
12459	593	1100	34	5.0	16,195	0.024	0.116	0.46	
10855	649	1200	110	16.0	304	2.41	12.0	1.57	Ruptured
13764	649	1200	110	16.0	245	2.42	14.53	1.57	Ruptured
10854	649	1200	97	14.0	761	1.60	13.0	1.37	Ruptured
11563	649	1200	83	12.0	2,674	0.59	13.0	1.18	Ruptured
11226	649	1200	69	10.0	7,278	0.18	7.0	0.98	Ruptured
10851	649	1200	55	8.0	20,059	0.044	5.03	0.78	Ruptured
12255	649	1200	34	5.0	992	0.030	0.08	0.49	Discontinued
12443	649	1200	34	5.0	16,151	0.024	0.188	0.49	
12460	649	1200	21	3.0	16,168	0.020	0.240	0.29	
10856	704	1300	69	10.0	568	0.067	15.60	0.90	Ruptured
11562	704	1300	69	10.0	653	0.12	22.50	0.90	Ruptured
11222	704	1300	55	8.0	2,760	0.031	16.40	0.72	Ruptured
12254	704	1300	34	5.0	17,345	0.030	3.12	0.45	
12461	704	1300	21	3.0	16,167	0.018	0.378	0.27	
12462	704	1300	14	2.0	15,980	0.010	0.236	0.18	

[a]Annealed 0.5 hr at 1093°C before testing. All tests loaded at a strain rate of 0.004/min.

[b]Yield stresses used in this ratio were 12,700 psi (88 MPa) at 427°C (800°F), 11,800 psi (81 MPa) at 482°C (900°F), 11,100 psi (77 MPa) at 538°C (1000°F), 10,900 psi (75 MPa) at 593°C (1100°F), 10,200 psi (70 MPa) at 649°C (1200°F). 11,000 psi (77 MPa) at 704°C (1300°F).

[c]Unless otherwise noted, tests in progress.

Table 3.2. Summary of Possible Microstructural Changes Due to Thermal Aging and Prior Creep Deformation in the Range 482–649°C (900–1200°F) and Their Influence on Tensile Properties

Possible Microstructural Changes	Influence of Microstructural Changes on Tensile Properties
A. Thermal Aging	
Results in precipitates (carbides and intermetallic compounds) at any or all of following locations: 1. grain boundaries, 2. incoherent twin boundaries, 3. coherent twin boundaries, 4. matrix (homogeneous nucleation, at dislocations and inclusion-matrix interfaces). Formation of precipitates depletes the matrix of interstitial atoms carbon and nitrogen. Transformation of prior δ-ferrite into sigma phase.	Flow stress, S, is given by $$S = S_0 + k_y d^{-1/2} ,$$ where S_0 = frictional stress and k_y measures the extent to which the dislocations are piled at the boundary. Precipitate formation in matrix and at grain boundaries increases S_0 and k_y, respectively, and thus the flow stress.[2] Depending on the particle size and distribution of precipitates, the matrix can become stronger than the grain boundaries. Formation of precipitate-denuded zones at grain boundaries can make deformation more localized. A stronger matrix with respect to grain boundaries results in preferential deformation along the grain boundaries, which can cause a loss in tensile ductility. The depletion of interstitial atoms from the matrix decreases the amount of dynamic strain aging and thus can again cause a decrease in ultimate tensile strength and ductility (uniform, total elongation, and reduction of area). The transformation of δ-ferrite into sigma phase can cause a possible nucleation and propagation of cracks along the sigma-austenite interface.
B. Prior Creep Deformation (Stresses Greater than Proportional Limit)	
The applied stress (greater than proportional limit) produces a large number of dislocations. These dislocations under proper stress and temperature conditions can produce a dislocation cell or subgrain structure. Precipitate formation can occur at following locations: 1. grain boundaries, 2. dislocation cell or subgrain boundaries, 3. incoherent twin boundaries, 4. coherent twin boundaries, 5. intra sub- and grain boundaries. The creep stress may enhance the precipitation process. In addition to precipitation processes mentioned above, and intragranular deformation, stress concentration at the grain boundaries causes intergranular cavitation. Under certain conditions of temperature and stress, cavitiation can also occur along the annealing twin boundaries. At the highest temperature 649°C (1200°F), grain boundary migration may also occur, which results in some transformation of carbides into sigma phase.	Dislocation generation and cell and subgrain formation produce a fine distribution of precipitates, which stabilizes the boundaries. The matrix is strengthened much more during prior creep by dislocations and subboundaries, as opposed to strengthening produced by plain thermal aging. The matrix strengthening causes the tensile deformation to concentrate along the grain boundaries, which generally have creep cavities. The creep cavities and change in morphology of grain boundaries due to precipitates reduce the load-carrying capacity and thereby reduce both the ultimate tensile strength and uniform elongation. The greater loss in tensile ductility for prior creep specimen is probably due greater matrix strengthening and creep cavities.

Table 3.2. (Continued)

Possible Microstructural Changes	Influence of Microstructural Changes on Tensile Properties
C. Prior Creep Deformation (Stresses Less than Proportional Limit)	
The applied stress (less than proportional limit) produces only elastic strain on loading. The dislocation density is only slightly increased due to local stress concentration. The precipitates are formed at locations described in A. For short times (times of the order required to reach the onset of second stage or including a part of second stage) the influence of prior creep is expected to be essentially similar to that for thermal aging. For longer creep times, stress concentration at the grain boundaries and triple points causes grain boundary sliding, giving rise to intergranular cracks. At the highest test temperature 649°C (1200°F), grain boundary migration may also occur, which results in some transformation of carbides into sigma phase.	For prior creep periods in which no intergranular cracks form the loss in tensile ductility due to prior creep deformation is expected to be similar to that for thermal aging. For periods in which intergranular cavitation occurs due to prior creep damage the loss in ultimate tensile strength and ductility is expected to be quite significant. The reasons for loss in tensile strength and ductility have been discussed in A and B.

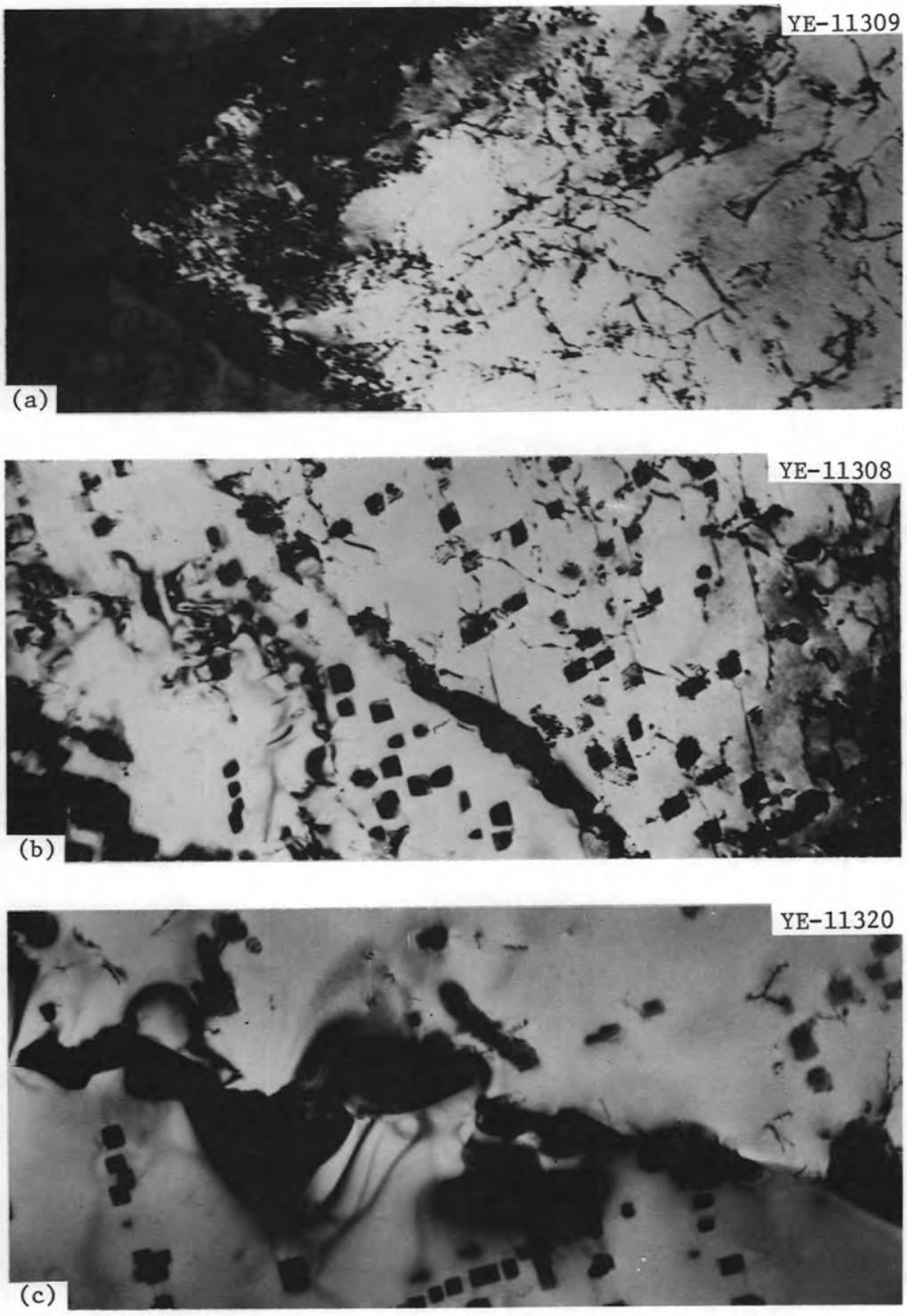

Fig. 3.1. Typical Transmission Electron Micrographs Showing Microstructural Changes Produced in Heat 926 of Type 304 Stainless Steel by Aging for 10,000 hr at (a) 482°C (900°F), (b) 593°C (1100°F), and (c) 649°C (1200°F). 30,000×.

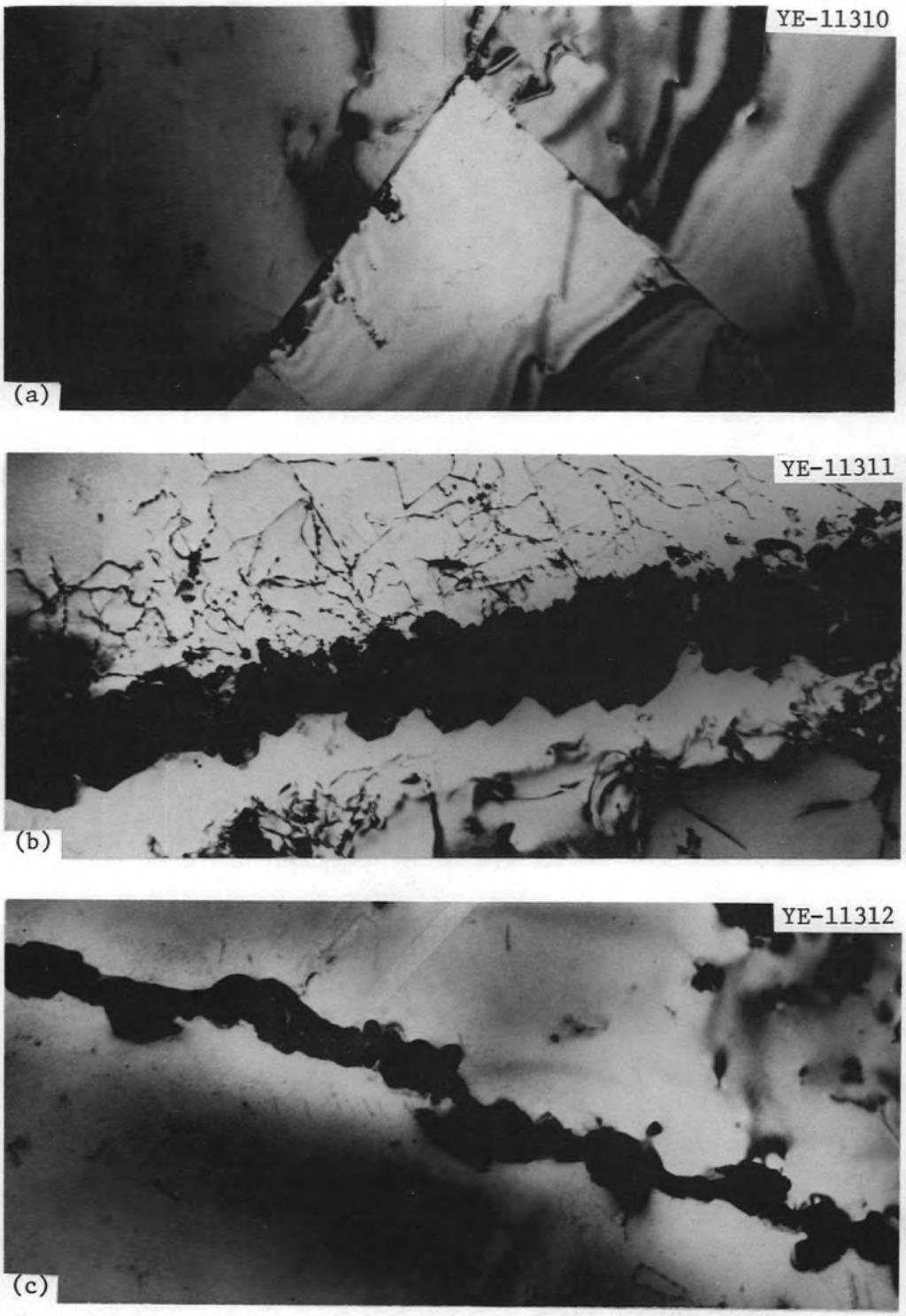

Fig. 3.2. Typical Transmission Electron Micrographs Showing Microstructural Changes Produced in Heat 212 of Type 304 Stainless Steel by Aging for 10,000 hr at (a) 482°C (900°F), (b) 593°C (1100°F), and (c) 649°C (1200°F). 30,000×.

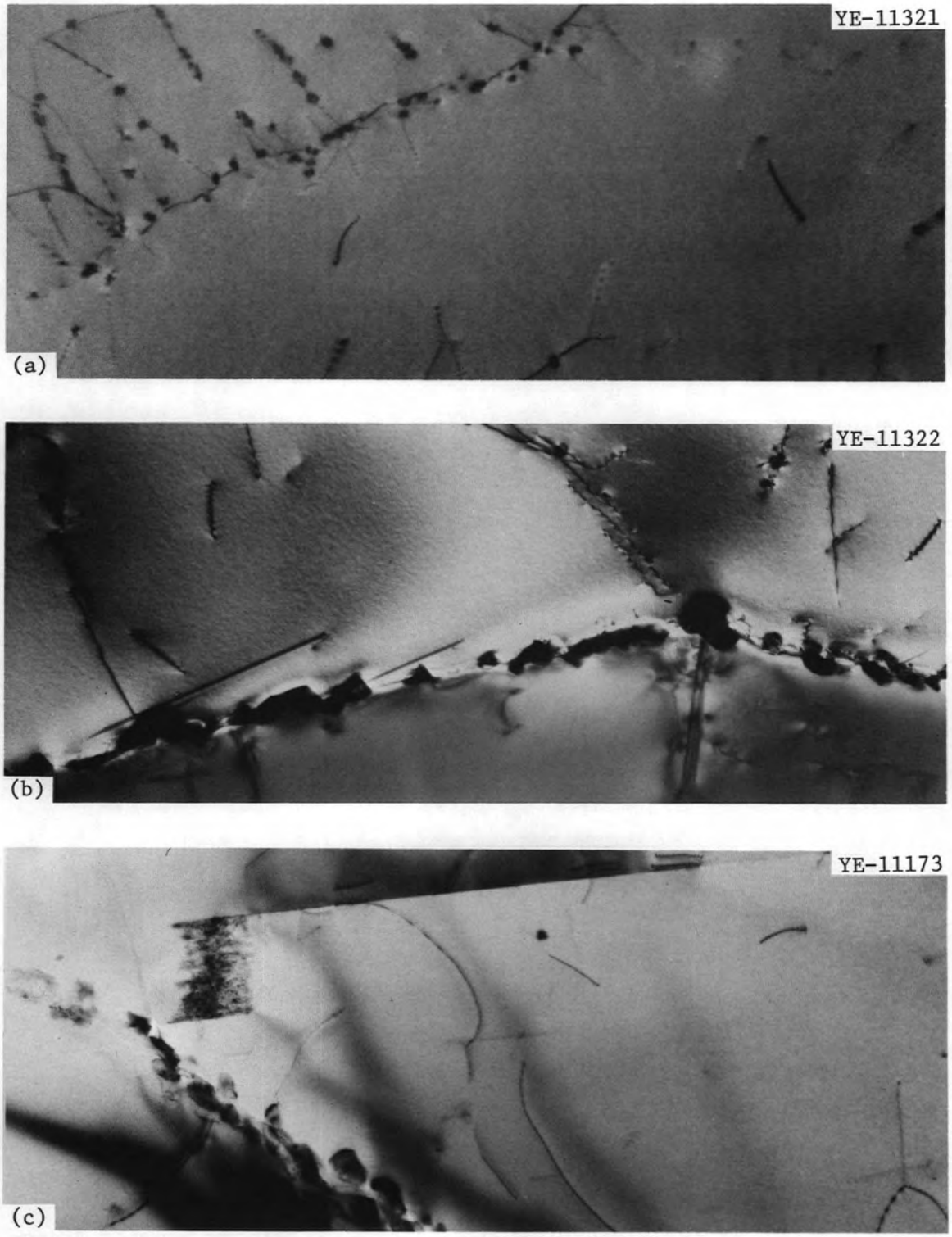

Fig. 3.3. Typical Electron Micrographs Showing the Microstructure Produced on Thermal Aging Heat 926 of Type 304 Stainless Steel for 2580 hr at 593°C (1100°F). 30,000×. Precipitates are shown in (a) matrix, (b) matrix and grain boundary, and (c) twin and grain boundaries.

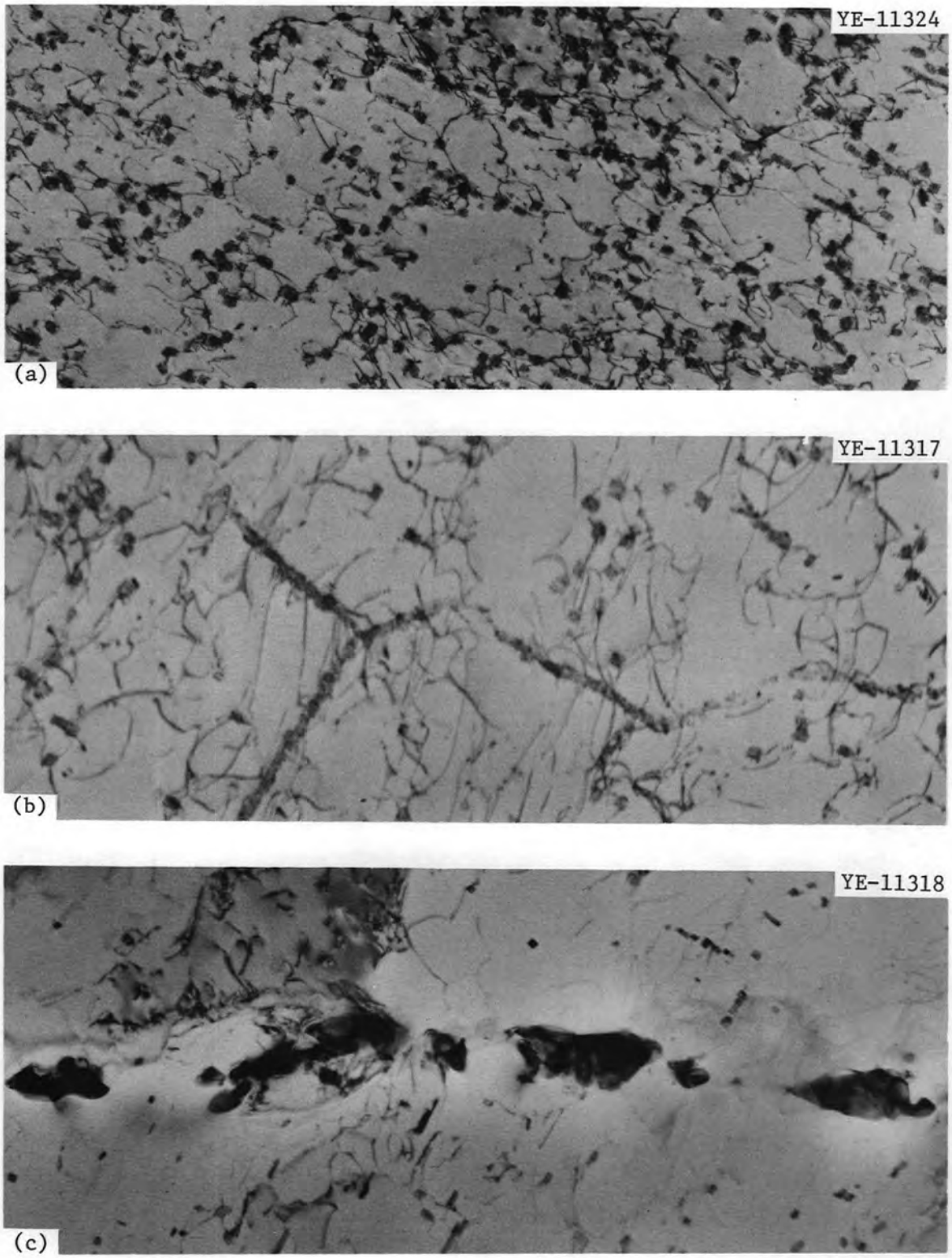

Fig. 3.4. Typical Electron Micrographs Showing the Microstructure Produced in a Creep Deformed Specimen of the Reference Heat (796K) of Type 304 Stainless Steel. The Creep test was performed at 593°C (1100°F) and 138 MPa (20 ksi) for 2200 hr to a total strain of 8.2%. 30,000×. Precipitates are shown (a) in matrix, (b) segregated on slip planes, and (c) at grain boundary.

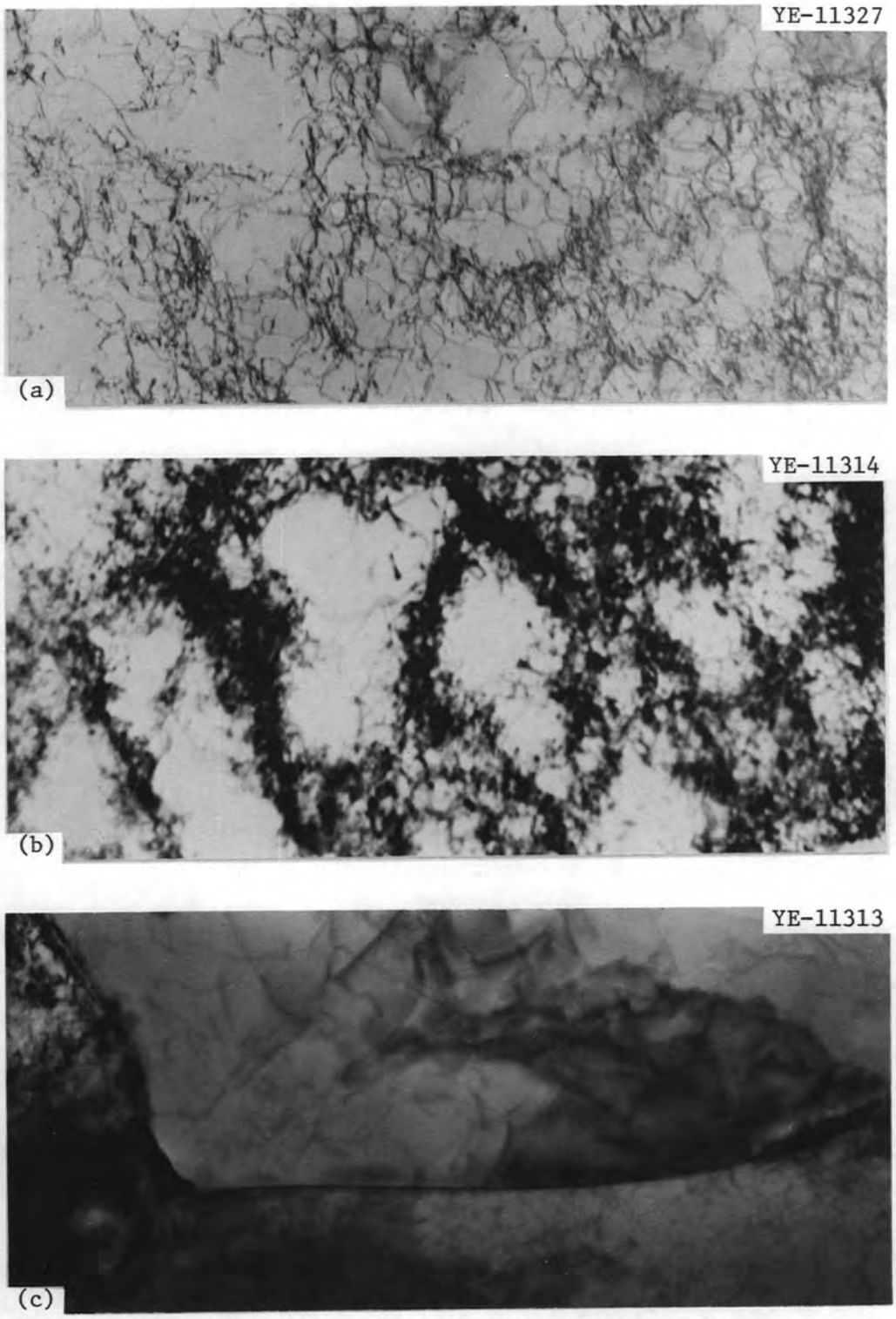

Fig. 3.5. Typical Transmission Electron Micrographs Showing Microstructural Changes Produced on Loading a Creep Specimen of Heat 807 (Weakest) of Type 304 Stainless Steel. The creep test was performed at 593°C (1100°F) and 172 MPa (25 ksi) and discontinued after loading. 30,000×. (a) Dislocation tangling. (b) Well defined subgrain boundaries. (c) Precipitates at triple points and grain boundaries.

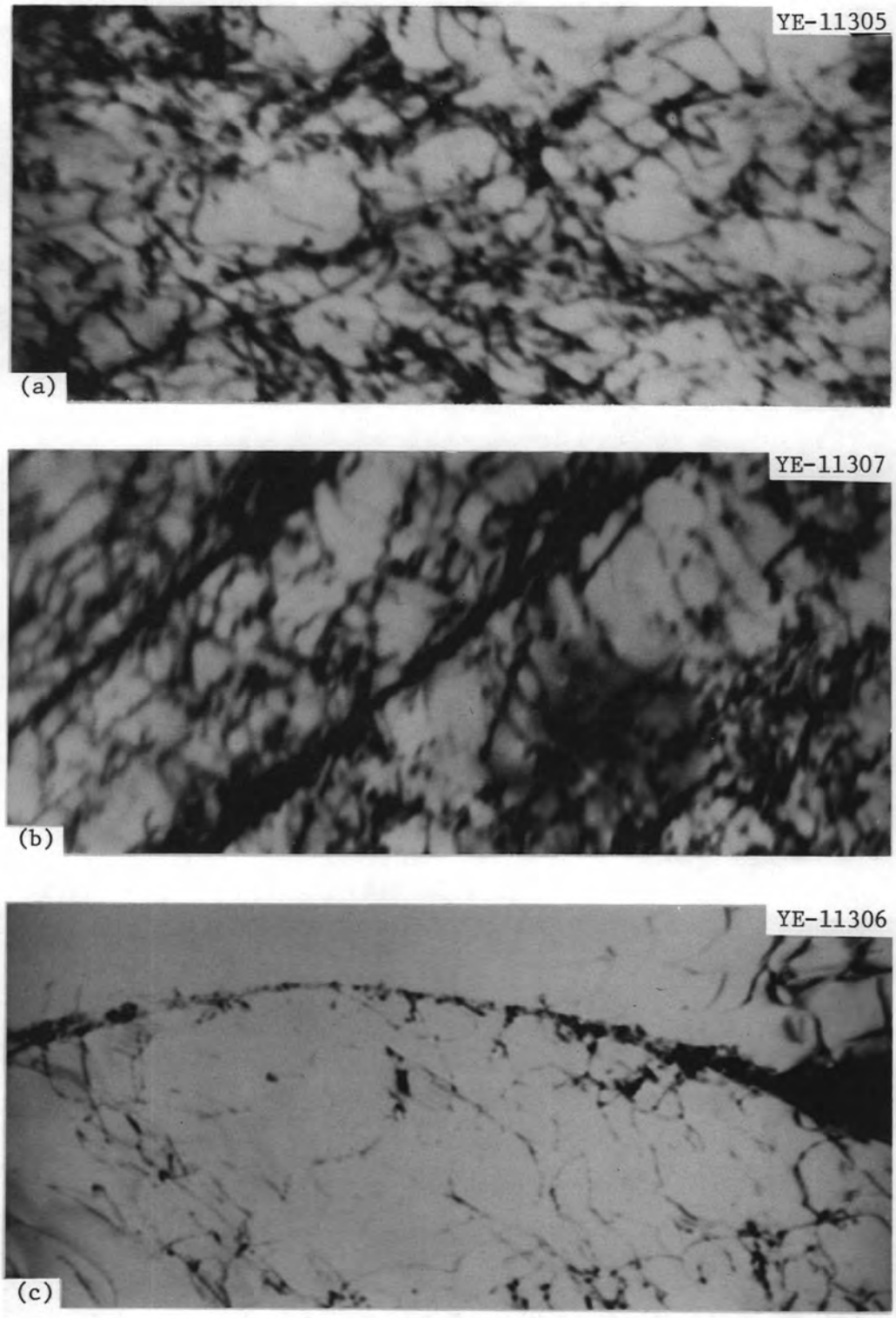

Fig. 3.6. Typical Transmission Electron Micrographs Showing Microstructural Changes Produced on Loading a Creep Specimen of Heat 414 (Strong) of Type 304 Stainless Steel. The creep test was performed at 593°C (1100°F) and 172 MPa (25 ksi) and discontinued after loading. 30,000×. (a) Dislocation tangling. (b) Dislocation slip bands. (c) No precipitation at grain boundaries. Compare with Fig. 3.5 for the weak heat.

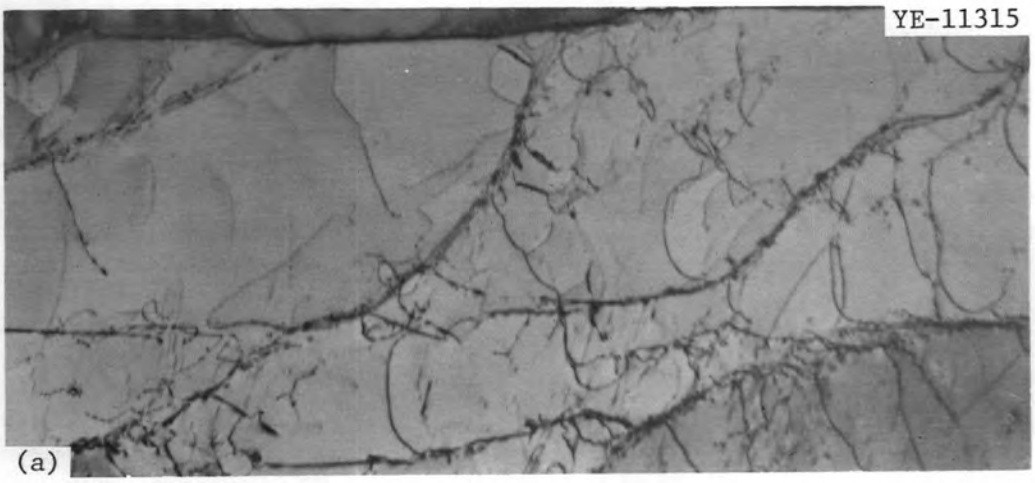

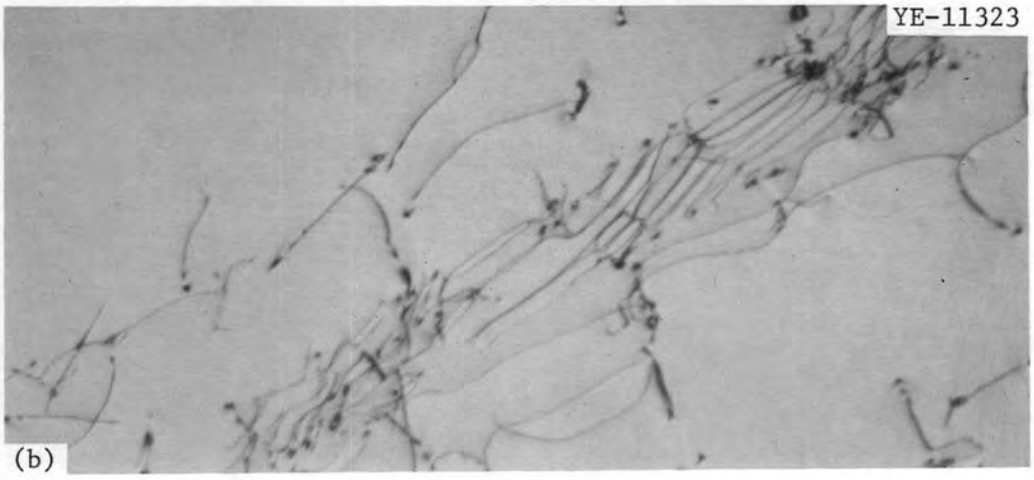

Fig. 3.7. Typical Transmission Electron Micrographs Showing Microstructural Changes Produced in a Creep Deformed Specimen of Heat 414 of Type 304 Stainless Steel. The creep test was performed at 593°C (1100°F) and 138 MPa (20 ksi) for 500 hr to a total strain of 2.43%. 30,000×. (a) Dislocation substructure fromation. (b) Precipitates on dislocations. (c) Precipitates at the grain boundaries.

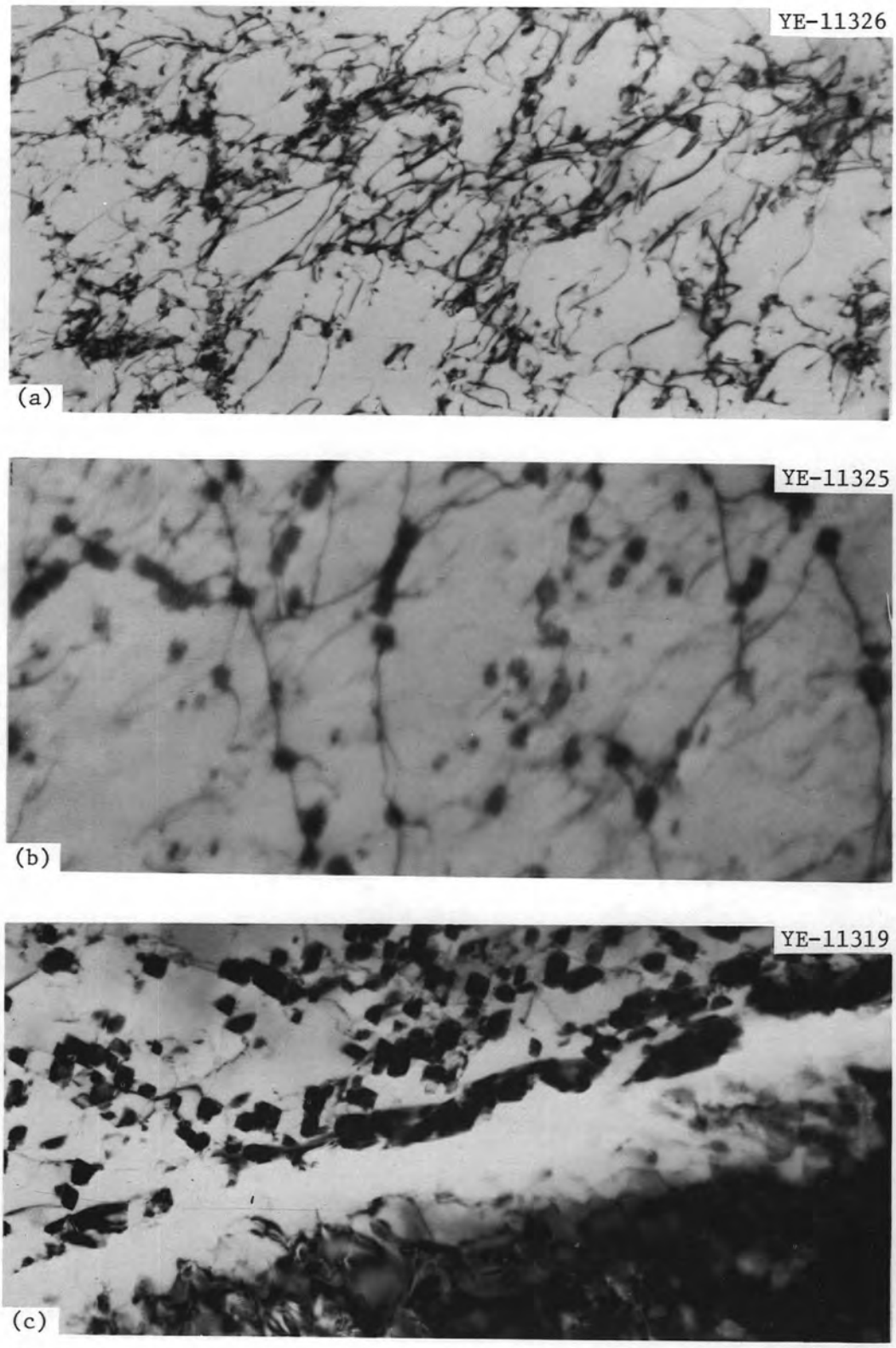

Fig. 3.8. Typical Transmission Electron Micrographs Showing Microstructural Changes Produced in a Creep Deformed Specimen of Heat 414 of Type 304 Stainless Steel. The creep test was performed at 593°C (1100°F) and 172 MPa (25 ksi) for 2425 hr to a total strain of 5.8%. 30,000×. (a) Dislocation tangling. (b) Precipitate on dislocations. (c) Precipitates near and at the grain boundary.

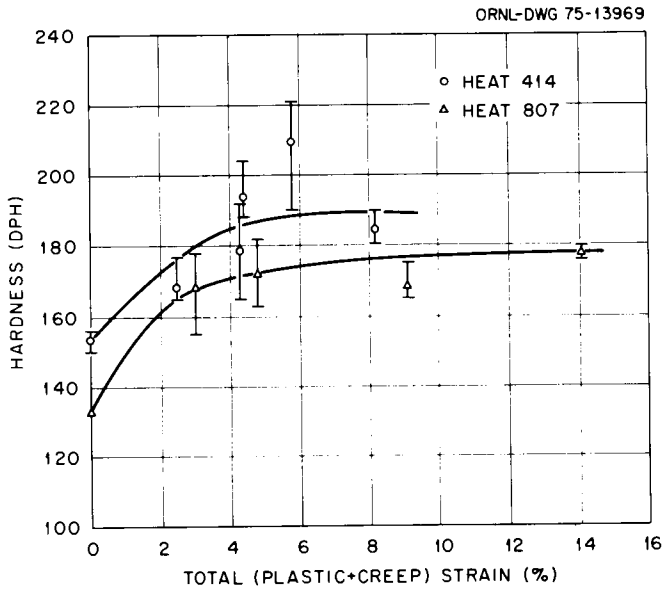

Fig. 3.9. Increase in Room-Temperature Microhardness for Prior Creep Specimens of Two Heats of Type 304 Stainless Steels. These specimens were tested at 172 MPa (25 ksi) and 593°C (1100°F). Discontinued specimens were cooled under load. The error bands show the scatter in four determinations made on each specimen.

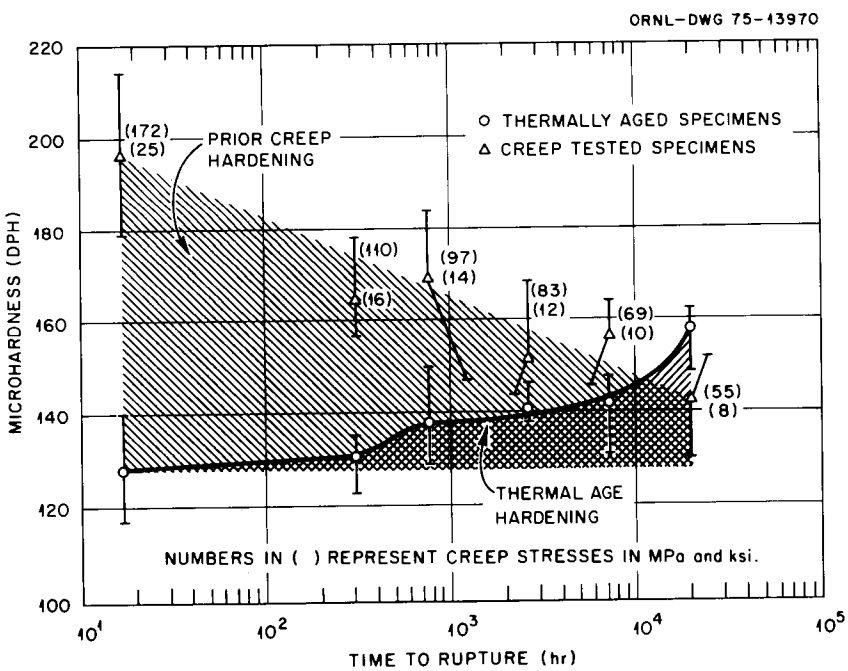

Fig. 3.10. Increase in Room-Temperature Microhardness Due to Thermal Aging and Prior Creep Deformation for the Reference Heat of Type 304 Stainless Steel. Specimens were creep tested at several stresses and at 649°C (1200°F). The error bands show the scatter in 12 determinations made on each specimen.

same period and stresses greater than the proportional limit the increase in hardness due to prior creep deformation is much more significant than that due to thermal aging without stress. For stresses less than the proportional limit the influence of thermal aging and prior creep deformation are essentially the same. The greater loss of tensile ductility due to prior creep deformation than to thermal aging in Fig. 3.11 is quite consistent with the increase in hardness produced due to these two

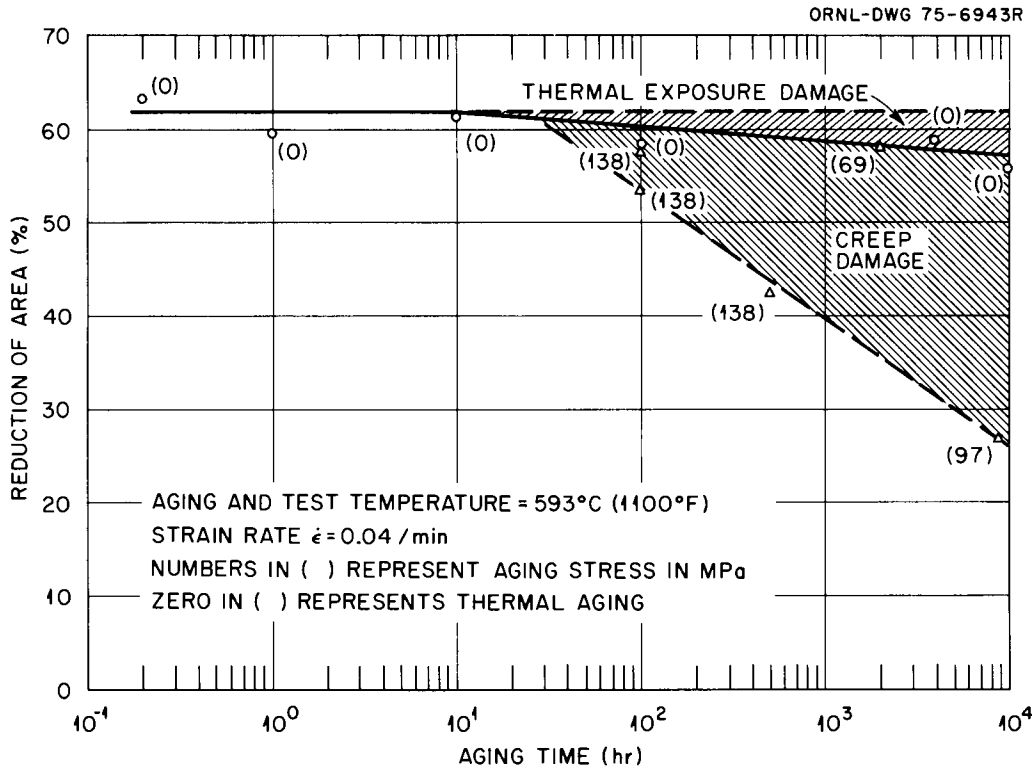

Fig. 3.11. Comparison Between Aging With and Without Stress on Reduction of Area of the Reference Heat of Type 304 Stainless Steel.

processes in Fig. 3.10 and the mechanisms suggested in Table 3.2. The additional factor in loss of tensile ductility due to prior creep deformation is the nucleation of intergranular cracks. A set of micrographs showing prior creep cracks in uniform sections of specimens tested at 649°C (1200°F) and various stresses is presented in Figs. 3.12 and 3.13. Note that the higher creep stresses not only produce a significant intragranular deformation but also a high density of intergranular cracks.

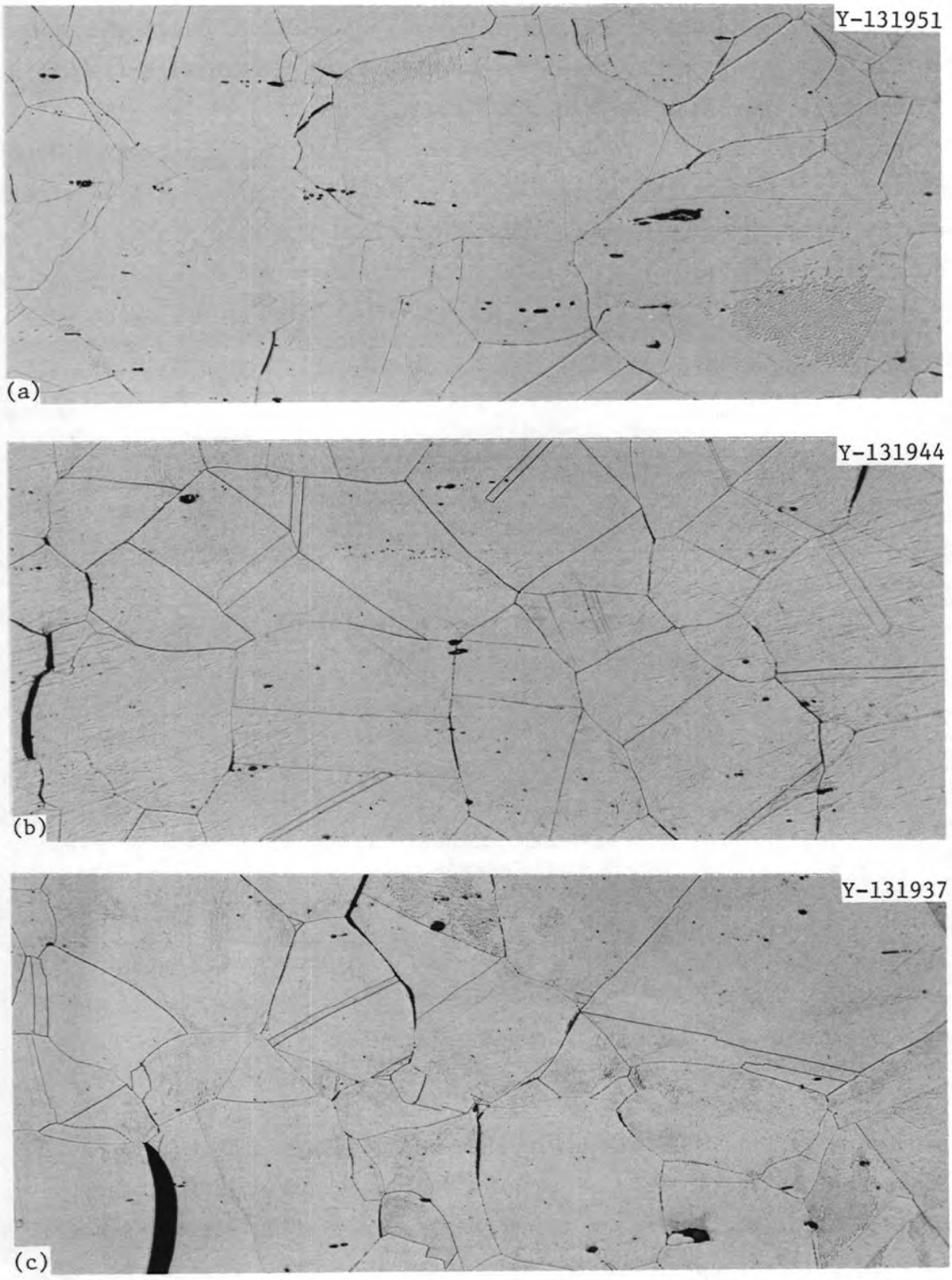

Fig. 3.12. Optical Micrographs Showing Creep Cracks in the Reference Heat of Type 314 Stainless Steel Tested at 649°C (1200°F) and Various Stresses. 100×. (a) 172 MPa (25 ksi). (b) 110 MPa (16 ksi). (c) 97 MPa (14 ksi).

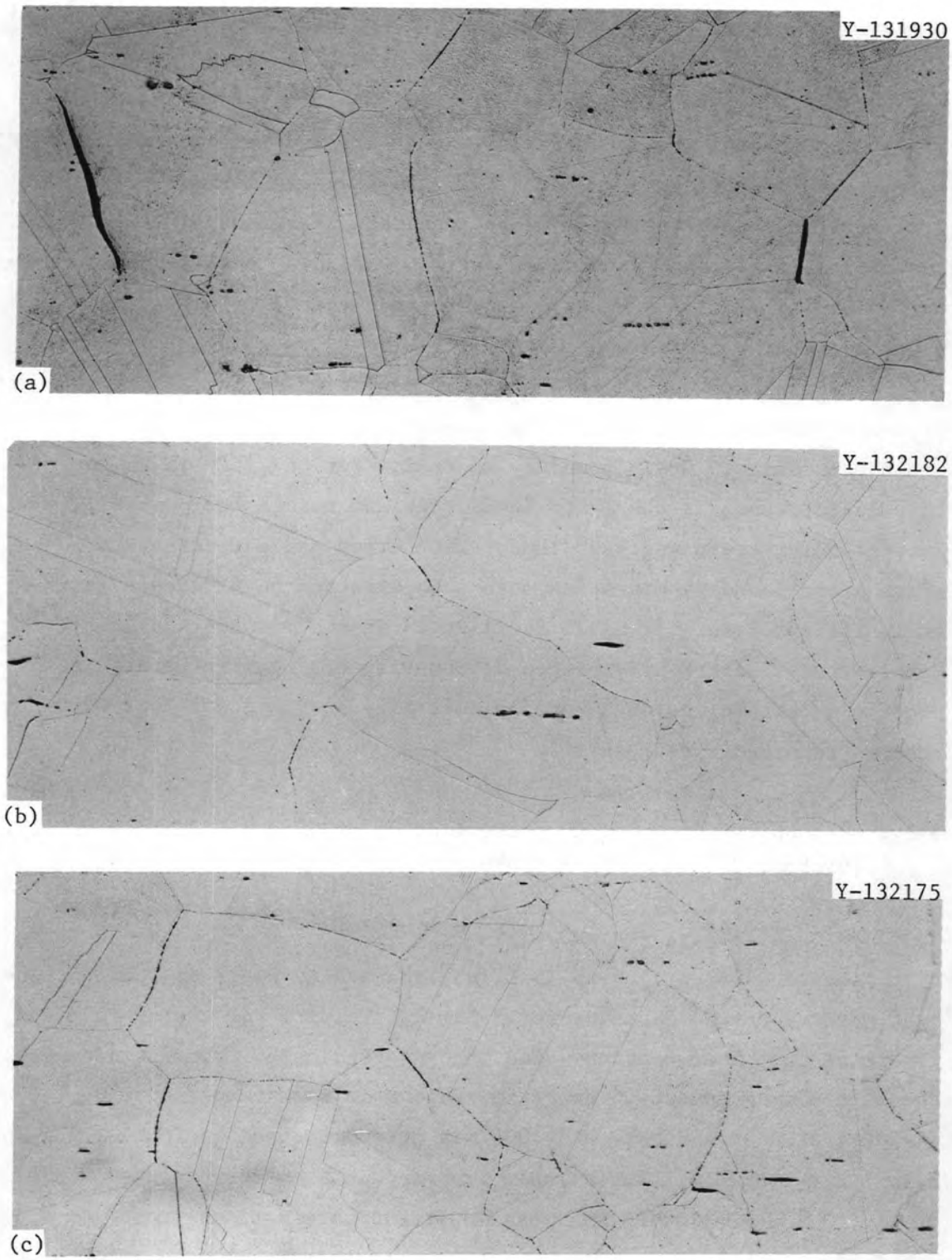

Fig. 3.13. Optical Micrographs Showing Creep Cracks in the Reference Heat of Type 314 Stainless Steel Tested at 649°C (1200°F) and Various Stresses. 100×. (a) 83 MPa (12 ksi). (b) 69 MPa (10 ksi). (c) 55 MPa (8 ksi).

A specimen tested at stress below the proportional limit [Fig. 3.13(c)] shows essentially no intragranular deformation, but only intergranular cracks. Furthermore, cracks for this specimen are few but have been linked for several grain boundaries. Such cracks are expected to be relatively easy to propagate compared with small cracks formed during high stresses. Although the prior creep specimens tested as stresses below the proportional limit contain relatively unstable cracks, their matrix hardening (Fig. 3.10, same as due to thermal aging) is much less than produced in high stress specimens.

Micrographs showing grain boundary migration during prior creep are presented in Fig. 3.14. They also show the precipitate denuding at the grain boundaries. Grain boundary migration during creep is suggested[4] to relax stresses at the grain boundaries and reduce the possibility of intergranular creep cracks. Thus, prior creep at test temperatures where grain boundary migration occurs is expected to produce relatively insignificant loss in tensile ductility. In other words, at such test temperatures, larger prior creep deformation can be incorporated to produce a certain residual tensile ductility and is consistent with the results reported[1] previously.

3.2.2 Mechanical Property Characterization of Type 316 Stainless Steel Reference Heat — V. K. Sikka

3.2.2.1 Tensile Data — V. K. Sikka

Tensile data on 15.9-mm (5/8-in.) reannealed plate of the reference heat were reported[5] last quarter. Similar results for the as-received condition have been completed and are reported here. Tensile data for the as-received condition over the range from room temperature to 760°C (1400°F) at a strain rate of 0.004/min are summarized in Table 3.3. These data are compared with previously reported data on reannealed material in Fig. 3.15. Following are some important observations from Fig. 3.15 and Table 3.3.

1. *Proportional Limit* — The proportional limit for as-received material was lower than for the reannealed material for the whole temperature range investigated. The difference in proportional limit was

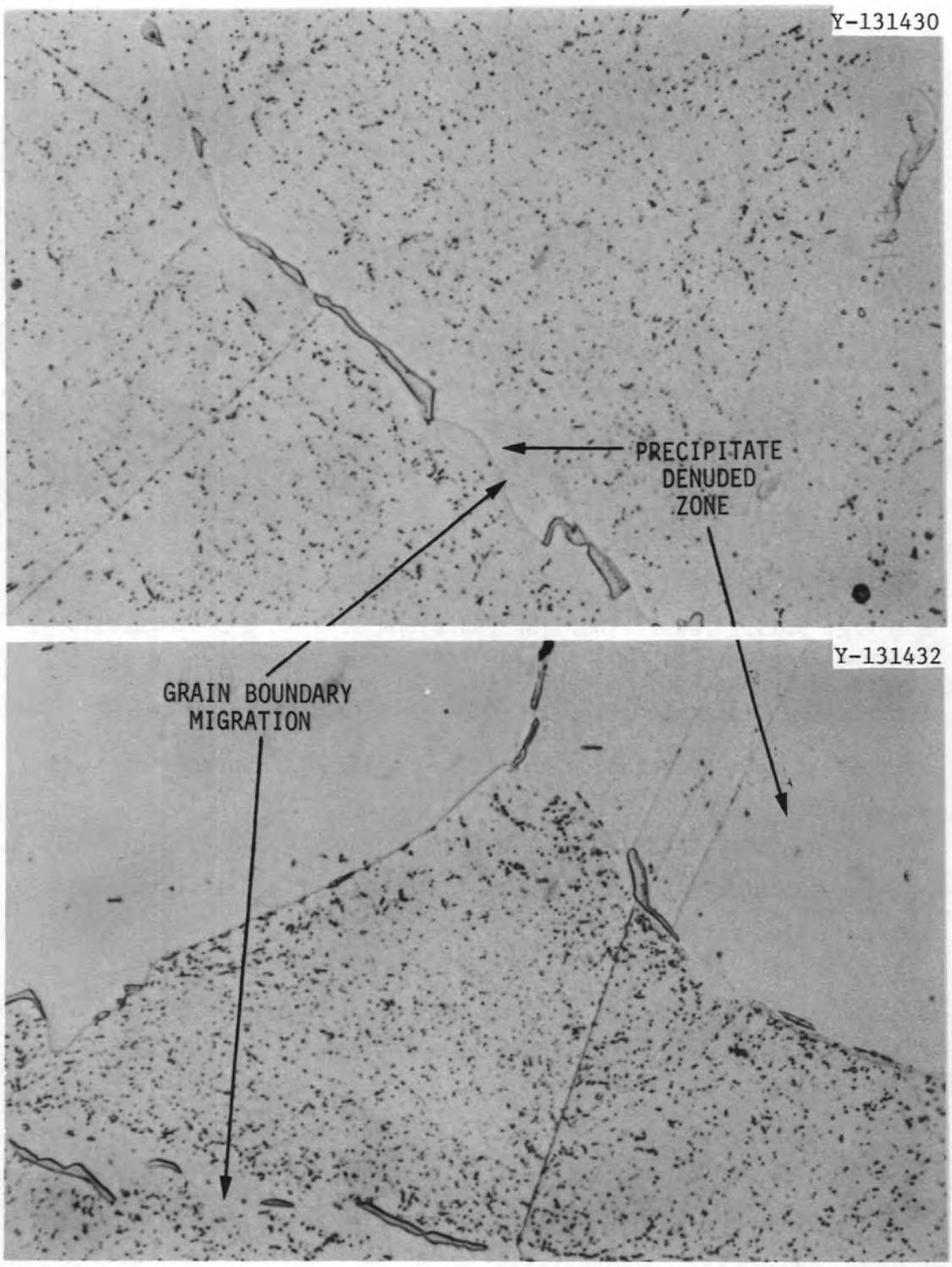

Fig. 3.14. Optical Micrographs Showing Grain Boundary Migration and Precipitate Denuding in a Creep Specimen of the Reference Heat of Type 304 Stainless Steel, Tested at 649°C (1200°F) and 55 MPa (8 ksi). 1500×.

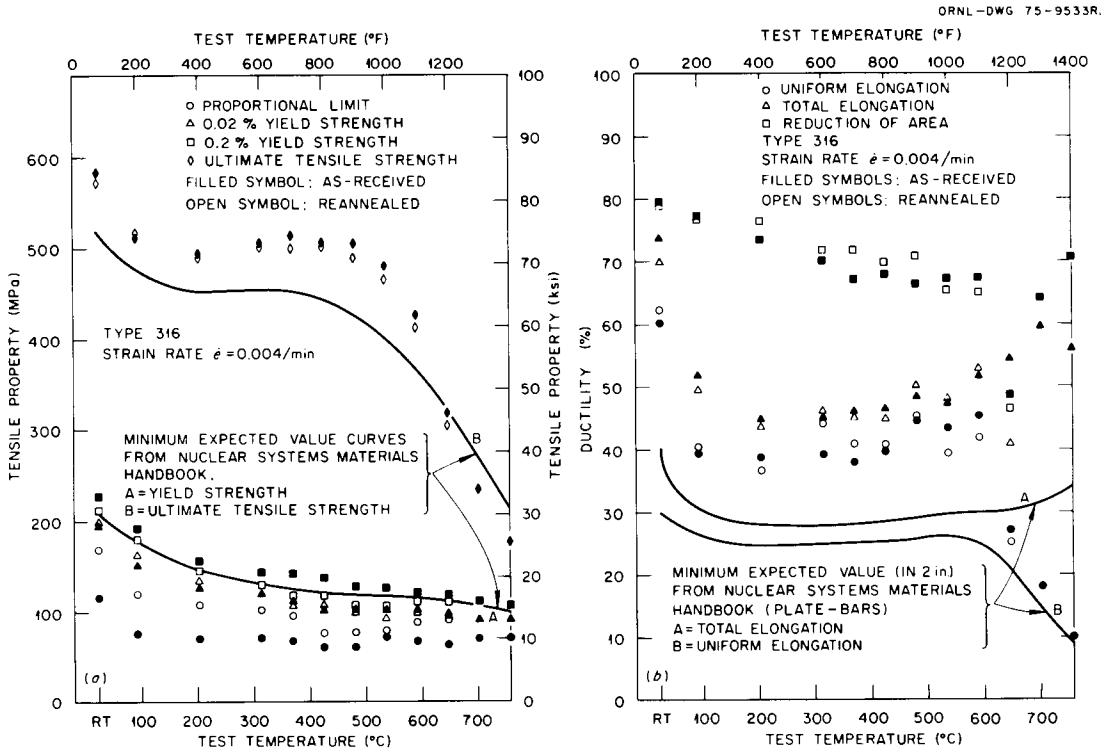

Fig. 3.15. Tensile Data as Functions of Test Temperature for 15.9-mm (5/8-in.) Plate of the Reference Heat of Type 316 Stainless Steel at a Strain Rate of 0.004/min.

greatest at room temperature and it decreased with increasing test temperature.

2. *0.02% Yield Strength* — Values of 0.02% yield strength for the as-received material were slightly lower than or equal to the values for the reannealed material.

3. *0.2% Yield Strength* — Values of 0.2% yield strength for as-received material were higher than for the reannealed material over the whole temperature range, and they also fell above the minimum expected value curve from the *Nuclear Systems Materials Handbook.*[6]

4. *Ultimate Tensile Strength* — Values of Ultimate tensile strength for the as-received material were higher than for the reannealed material for the whole temperature range.

5. *Ductility* — All ductility measures — uniform and total elongation and reduction of area — were 1 to 5% lower for the as-received than the reannealed material. Such differences in ductility are quite consistent

Table 3.3. Tensile Properties of 15.9-mm (5/8-in.) Plate of Reference Heat 297 of Type 316 Stainless Steel, Tested in Mill-Annealed (As-Received) Condition at a Strain Rate of 0.004/min

Test Temperature		Stress, MPa (ksi)				Elongation, %			Reduction of Area (%)
		Proportional Limit	Yield		Tensile	Uniform	Total		
(°C)	(°F)		0.02%	0.2%			1 in.	2 in.	
25	77	115 (16.7)	194 (28.1)	227 (33.0)	583 (84.5)	60.1		73.9[a]	79.6
93	200	76 (11.0)	150 (21.8)	191 (27.7)	513 (74.4)	39.5		51.6[a]	77.2
204	400	70 (10.2)	125 (18.2)	155 (22.5)	493 (71.5)	38.8		44.7[b]	73.5
316	600	70 (10.2)	117 (17.0)	143 (20.8)	505 (73.3)	39.0		44.9[a]	70.0
371	700	68 (9.9)	111 (16.1)	142 (20.6)	513 (74.4)	37.7		46.0[a]	67.0
427	800	62 (9.0)	102 (14.7)	137 (19.9)	504 (73.1)	39.9		46.4[a]	68.0
482	900	62 (9.0)	101 (14.6)	127 (18.4)	505 (73.2)	44.3		48.3[b]	66.4
538	1000	73 (10.6)	104 (15.1)	125 (18.1)	478 (69.3)	38.6	54.9	47.1[a]	67.4
593	1100	67 (9.8)	101 (14.7)	120 (17.4)	425 (61.6)	40.2	61.0	51.6[a]	67.5
649	1200	63 (9.2)	95 (13.8)	117 (16.9)	316 (45.8)	27.0	51.7	54.4[b]	48.7
704	1300	70 (10.2)	90 (13.1)	111 (16.1)	234 (34.0)	17.9	75.9	59.5[a]	63.9
760	1400	70 (10.2)	90 (13.0)	105 (15.3)	174 (25.3)	9.9	55.4	55.9[b]	70.6

[a]Specimen broke at center and thus contained the neck.

[b]Specimen broke off-center and therefore did not contain the neck.

with previously[7,8] estimated values of 3 to 4% residual cold work associated with the plate product of several heats of type 316 stainless steel.

The true stress-strain behavior of the reference heat in both as-received and reannealed conditions was compared with the predicted stress-strain curves from the present tensile equation in the *Nuclear Systems Materials Handbook.*[6] Figure 3.16 shows the comparison for temperatures in the range from 371 to 538°C (700–1000°F), whereas

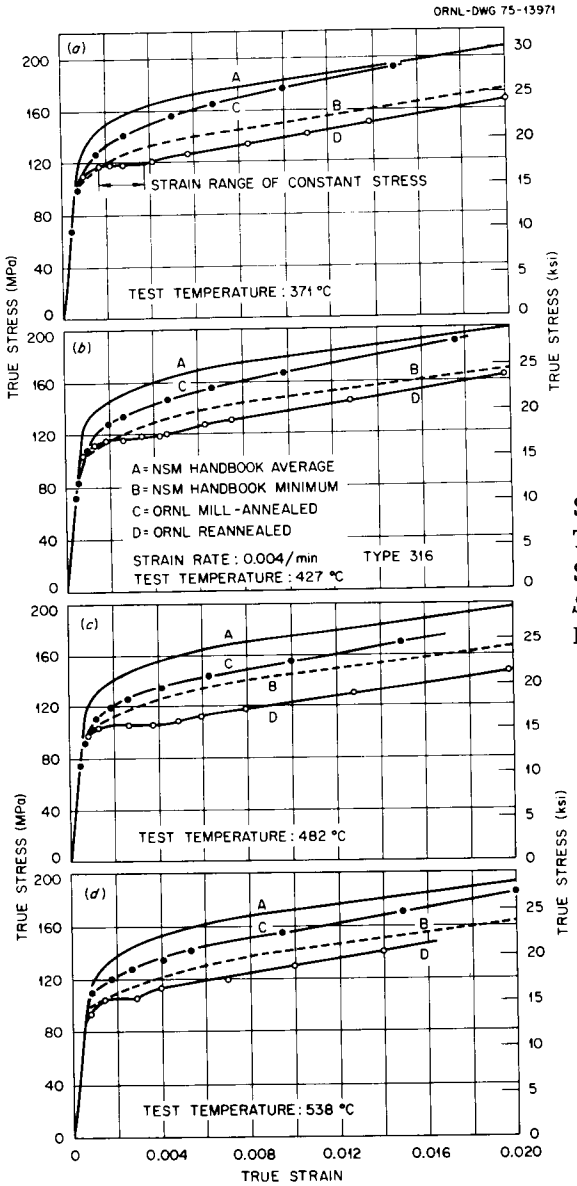

Fig. 3.16. Comparison of Stress-Strain Behavior of Reference Heat of Type 316 Stainless Steel with Predicted Stress-Strain Curves Using *Nuclear Systems Materials Handbook* Tensile Equation. Test temperatures: (a) 371°C (700°F), (b) 427°C (800°F), (c) 482°C (900°F), (d) 538°C (1000°F).

Fig. 3.17 shows the same comparison for the range 593 to 760°C (1100–1400°F). The stress-strain comparisons have been made only for up to 2% strain.

The stress-strain curves of the reference heat in the as-received condition fell in between the predicted average and minimum curves for test temperatures in the range 371 to 704°C (700–1300°F), but fell below the minimum curve for 760°C (1400°F). Furthermore, the Handbook equation

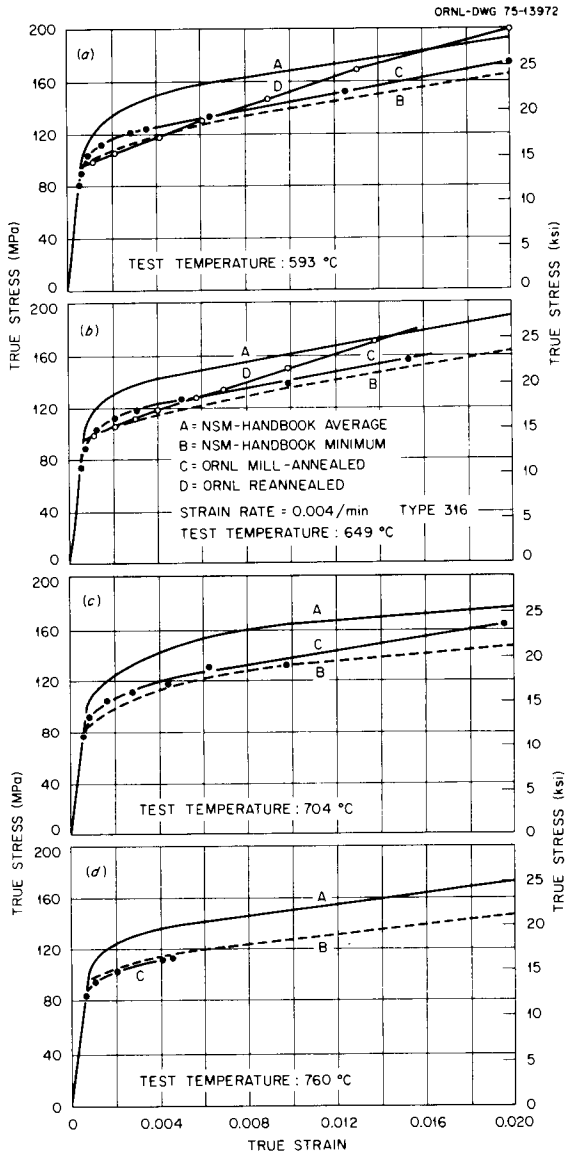

Fig. 3.17. Comparison of Stress-Strain Behavior of Reference Heat with Predicted Stress-Strain Curves Using *Nuclear Systems Materials Handbook* Tensile Equation. Test temperature: (a) 593°C (1100°F), (b) 649°C (1200°F), (c) 704°C (1300°F), (d) 760°C (1400°F).

in general describes reasonably well the stress-strain behavior of the reference heat in the as-received condition.

The stress-strain curves for the reannealed condition fell below those for the as-received condition in the range from 371 to 538°C (700—1000°F). For same temperature range stress-strain curves for the reannealed condition also fell below the mininum predicted[6] curves. Furthermore, the stress-strain curves for the reannealed condition also showed a strain range, between 0.1 and 0.4%, for which stress remained constant. Reasons for such a behavior of the reannealed material are not clear.

For test temperatures of 593 and 649°C (1100 and 1200°F) the stress-strain curves for the reannealed condition showed the following unusual behavior.

1. The stress-strain curves were below the curves for as-received condition up to a strain of 0.6% and then showed a crossover.

2. These curves did not fall below the minimum predicted curves in contrast with those in the range from 371 to 538°C (700—1000°F), shown in Fig. 3.16.

3. These curves also did not show any strain range of constant stress, such as was observed in the temperature range from 371 to 538°C (700—1000°F).

Tensile properties of the reference heat presented so far showed that as-received plate contained approximately 3% residual cold work. The result of the residual cold work was to increase 0.2% yield and ultimate tensile strengths and decrease ductility of the reannealed material. Two properties that showed the opposite behavior were proportional limit and 0.02% yield strength. These two properties were much higher for the reannealed than for the as-received material. It is suggested that the opposite behavior of proportional limit and 0.02% yield strength for as-received material is probably associated with Bauschinger effect,[9] Fig. 3.18. This effect describes the directionality of strain hardening and can be explained as follows:

The initial yield stress of the material in tension is *A*. If the same ductile material were tested in compression, the yield strength

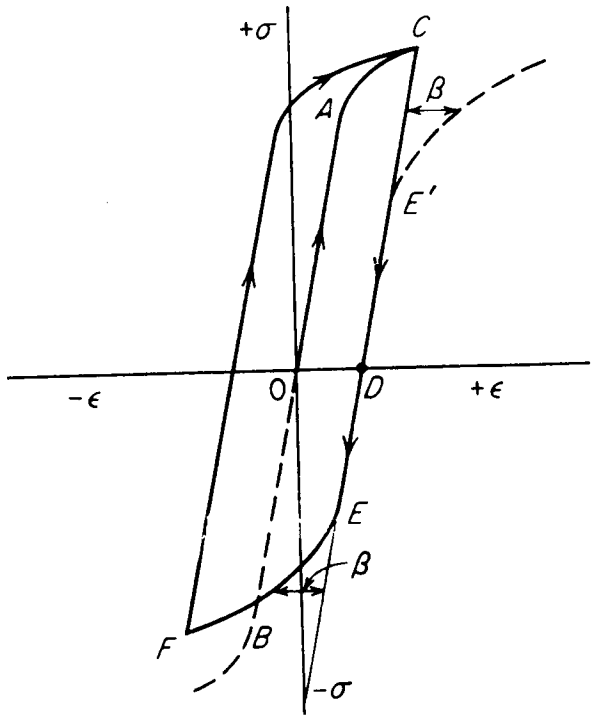

Fig. 3.18. Bauschinger Effect and Hysteresis Loop. From G. E. Dieter, Jr., *Mechanical Metallurgy*, McGraw-Hill, New York, 1961. Reproduced with permission.

would be approximately the same, point *B* on the dashed curves. Now, consider that a new specimen is loaded in tensile yield stress to *C* along the path *OAC*. If the specimen is then unloaded, it will follow the path *CD*, small elastic hysteresis effects being neglected. If now a compressive stress is applied, plastic flow will being at the stress corresponding to point *E*, which is appreciably lower than the original compressive yield stress of the material. While the yield stress in tension was increased by strain hardening from *A* to *C*, the yield stress in compression was decreased. Such an effect is called the Bauschinger effect. The phenomenon is reversible, for had the specimen originally been stressed plastically in compression, the yield stress in tension would have decreased.

In the present case, the proportional limit and 0.02% yield strength were lower in tension for the as-received material than for reannealed material. Based on Bauschinger effect, the processing and straightening stresses associated with the as-received reference heat must be com-

pressive. Thus, we can conclude that the as-received plate of reference heat type 316 stainless steel not only contains about 3% residual cold work, but it is compressive.

3.2.2.2 Product Form Characterization

A set of 24 specimens was machined from each product form of the reference heat except 15.9-mm (5/8-in.) plate, from which 150 specimens were machined. To determine the uniformity of each product form, Rockwell hardness was measured on both ends of each specimen. The hardness data so obtained were plotted as hardness distribution histograms for each product and are shown in Figs. 3.19 through 3.22. The

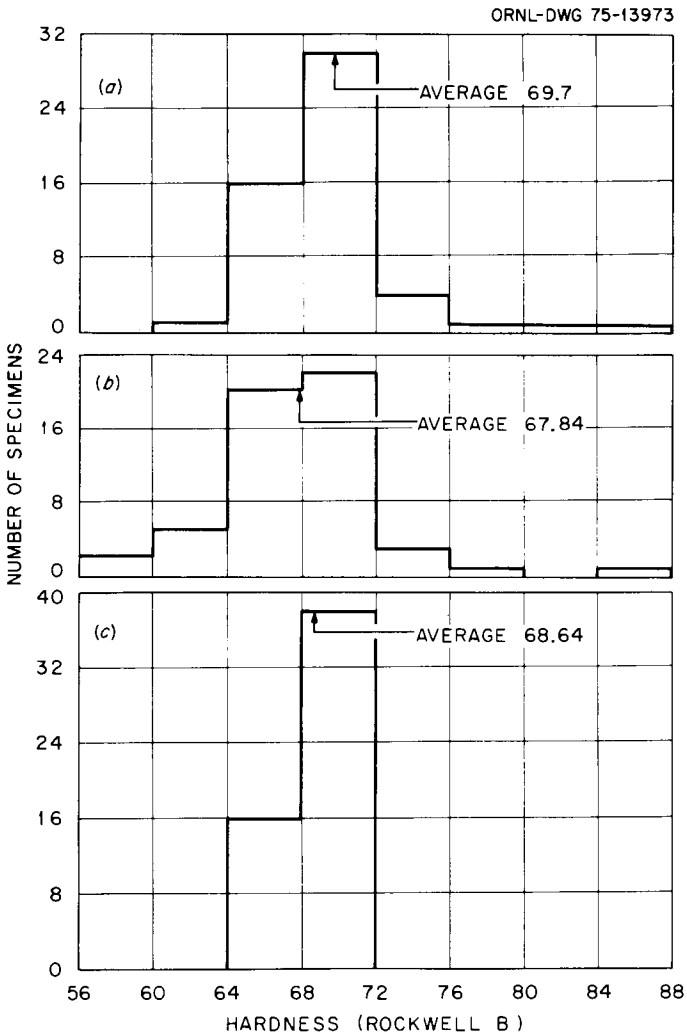

Fig. 3.19. Hardness Distribution of Specimens Machined from Three Different Sections of 15.9-mm (5/8-in.) Plate of the Reference Heat of Type 316 Stainless Steel.

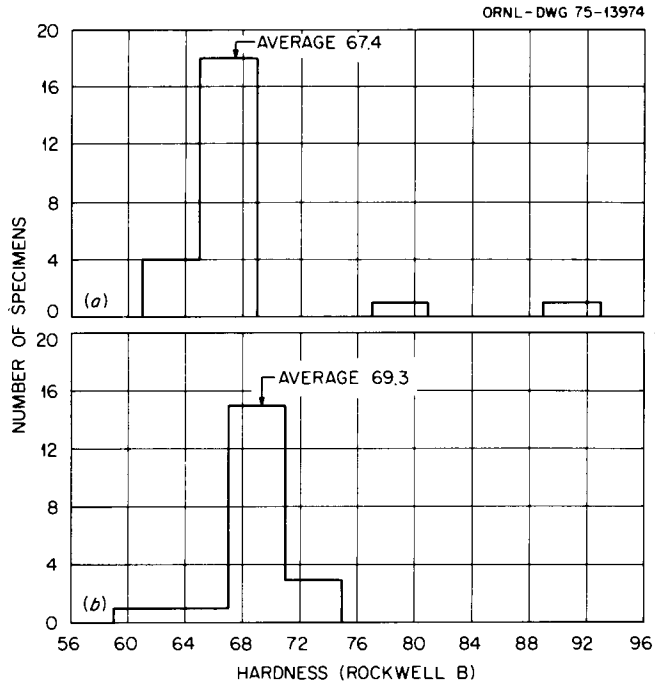

Fig. 3.20. Hardness Distribution of Specimens Machined from (a) 25-mm (1-in.) and (b) 51-mm (2-in.) Plate of the Reference Heat of Type 316 Stainless Steel.

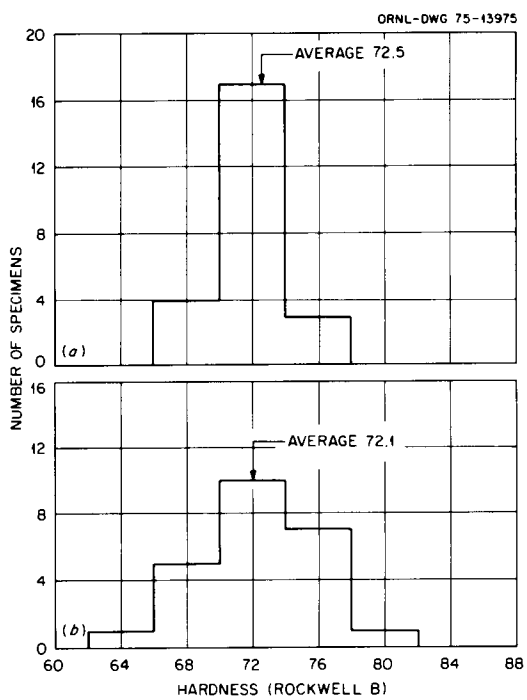

Fig. 3.21. Hardness Distribution of Specimens Machined from (a) 0.114-m-diam (4 1/2-in.) and (b) 0.219-m-diam (8 5/8-in.) Pipe of the Reference Heat of Type 316 Stainless Steel.

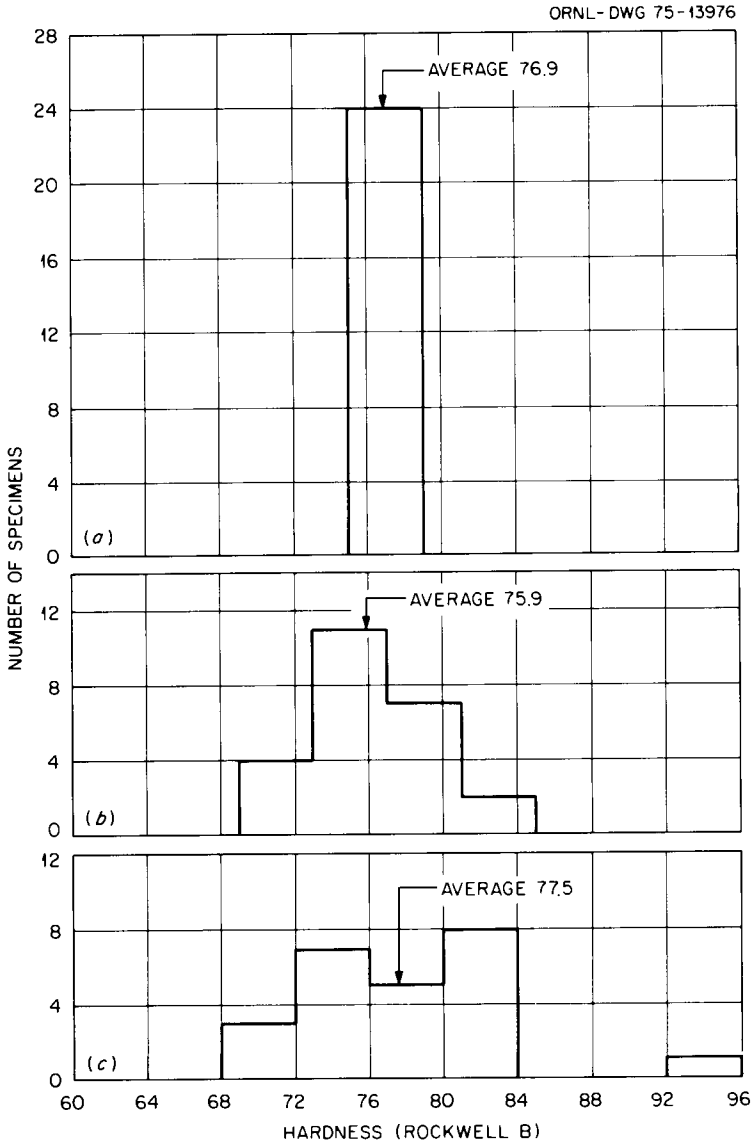

Fig. 3.22. Hardness Distribution of Specimens Machined from (a) 25-mm-(1-in.-), (b) 51-mm-(2-in.-), and (c) 64-mm-(2 1/2-in.-) Diam Bars of the Reference Heat of Type 316 Stainless Steel.

average hardness values for each product are summarized in Table 3.4. It should be noted that the most uniform set, Fig. 3.22(a), of specimens was obtained only from the 25-mm (1-in.) bar product. All other products showed variation in hardness among specimens. These variations were most widely spread for various plate products of the reference heat. The specimens made from the edge of the plates had the greatest hardness, whereas those machined from the center of the plates showed average behavior. It is also interesting to note that in general pipe products were slightly stronger than plate, and bars of all sizes were stronger than plate and pipe. The higher hardness values observed for bar product

Table 3.4. Summary of Room-Temperature Hardness of Various Products of Reference Heat of Type 316 Stainless Steel

Product Form	Dimensions		Hardness, R_B	
	(mm)	(in.)	Round	Flat[a]
Plate	15.9	5/8	68.7	71.8
Plate	25.4	1	67.4	70.5
Plate	50.8	2	69.3	72.3
Bar	25.4	1	76.9	79.8
Bar	50.8	2	75.9	78.8
Bar	63.5	2 1/2	77.5	80.3
Pipe	12.7 × 114	0.5 × 4 1/2 OD	72.5	75.6
Pipe	12.7 × 219	0.5 × 8 5/8 OD	72.1	75.2

[a]Hardness of flat surface = round hardness plus correction from hardness conversion tables.

of the reference heat are consistent with approximately 10% residual cold work estimated[7,8] for the bar product, as opposed to 3 to 4% for the plate and pipe products.

The hardness values of each specimen will be used in selecting specimens for testing. We expect that the specimens of similar hardness will produce a more consistent and reproducible data set.

3.2.2.3 Creep Properties

Creep testing of 15.9-mm (5/8-in.) plate of the reference heat of type 316 stainless continued. Four of the tests have ruptured thus far and one was discontinued during the last quarter. Four more new creep tests were started and their status is summarized in Table 3.5.

Table 3.5. Summary of Creep Tests on Type 316 Stainless Steel Reference Heat 8092297 15.9-mm-Thick (5/8-in.) Plate[a]

Test	Temperature		Stress		Time in Test[b] (hr)	Strain (%)		Comments
	(°C)	(°F)	(MPa)	(ksi)		Loading	Creep	
15891	538	1000	110	16	90.0	0.126	0.031	
15791	538	1000	179	26	976.8	2.200	0.042	
15607	593	1100	207	30	831.1	3.93	34.28	Ruptured
15842	649	1200	97	14	762.5	0.139	1.235	
15594	649	1200	124	18	1983.0	0.54	16.78	Discontinued
15538	649	1200	138	20	1884.2	0.79	44.42	Ruptured
15460	649	1200	207	30	110.2	4.27	40.17	Ruptured
15889	704	1300	83	12	234.0	0.0303	3.20	
15593	760	1400	97	14	100.0	0.083	90.6	Ruptured

[a]All tests are being performed for plate in the as-received (mill-annealed) condition.

[b]Unless otherwise noted tests are in progress.

3.2.3 Heat-to-Heat Variation of Mechanical Properties of Types 304 and 316 Stainless Steel — V. K. Sikka

3.2.3.1 Time-Independent Design Stress Intensity for Type 304 Stainless Steel — V. K. Sikka and T. L. Hebble

Elevated-temperature design is controlled by the following stress intensity limits. S_0 = the maximum allowable value of general primary membrane stress intensity to be used as a reference for stress calculations under design condition. S_{mt} = the allowable limit of general primary membrane stress intensity to be used as a reference for stress calculations for the actual service life and under the normal upset conditions. The S_{mt} value is the lower of two stress intensity values, S_m (time-independent) and S_t (time-dependent).

Values of S_m are based on tensile and yield strengths of the material. The criteria employed in determining S_m values for austenitic stainless steels call for the lowest of the following four values:

1. 1/3 of the specified minimum tensile strength at room temperature,
2. 1/3 of the tensile strength at the operating temperature,
3. 2/3 of the specified minimum yield strength at room temperature,
4. 90% of the yield strength at the operating temperature.

In this section we present the tensile data for 20 heats of type 304 stainless steel in both mill-annealed (as-received) and laboratory-annealed (reannealed) conditions and checked the results so obtained against the time-independent design stresses included in ASME Code Case 1592. The summary of vendor, product form and grain size of 20 heats of type 304 stainless is presented in Table 3.6. Several product forms of the reference heat of type 304 stainless steel were also included in this analysis. They are listed in Table 3.7. The tensile data for 20 heats of type 304 stainless steel have been reported in other reports.[10–12] The tensile data for various products of the reference heat were reported[13] last quarter. Most of the tensile data were obtained at a strain rate of 0.04/min, but some specimens were also tested at other strain rates in the range 4 to 0.0004/min. The present analysis has examined the yield and ultimate tensile strengths as functions of temperature for a data base

Table 3.6. Summary of Vendors and Product Forms of 20 Heats of Type 304 Stainless Steel

Heat	Heat Symbol	Vendor	As-Received Form	Dimensions	
				(mm)	(in.)
9T2796	796	USS	Plate	50.8	2.00
X22807	807	USS	Plate	63.5	2.50
9T2797	797	USS	Plate	25.4	1.00
R23283	283	USS	Plate	19.0	0.75
R22926	926	USS	Plate	50.8	2.00
337187	187	Allegheny Ludlum	Plate	38.1	1.50
55697	697	Allegheny Ludlum	Bar	15.9	0.63
345866	866	Allegheny Ludlum	Plate	76.2	3.00
346544	544	Allegheny Ludlum	Plate	50.8	2.00
337330	330	Allegheny Ludlum	Plate	28.6	1.13
346845	845	Allegheny Ludlum	Plate	69.9	2.75
346779	779	Allegheny Ludlum	Plate	63.5	2.50
310390	390	Carlson	Plate	50.8	2.00
600414	414	Carlson	Plate	60.3	2.38
60551	551	Carlson	Bar	127 × 178	5 × 7
616737	737	Carlson	Plate	66.7	2.63
300380	380	Carlson	Plate	60.3	2.38
544086	086	Carlson	Plate	25.4	1.00
8043813	813	Republic	Plate	25.4	1.00
3121	121	Cameron	Pipe	710 × 9.5	28 OD × 3/8 wall

Table 3.7. Product Forms of the Reference Heat of Type 304 Stainless Steel

Product Form	Size (mm)	Size (in.)	Specification
Plate	9.5	5/8	RDT M5-1T(A 240)
Plate	12.7	1/2	RDT M5-1T(A 240)
Plate	19	3/4	RDT M5-1T(A 240)
Plate	25	1	RDT MT-1T(A 240)
Plate	51	2	RDT M5-1T(A 240)
Bar	44	1 3/4	RDT M7-3T(A 479)
Bar	48	1 7/8	RDT M7-3T(A 479)
Bar	114	4 1/2	RDT M7-3T(A 479)
Pipe	102 sched 160	4	ASTM A 376
Pipe	203 sched 40	8	ASTM A 376
Tube (hot reduced)	64 OD 16 wall	2 1/2 5/8	RDT M7-3T(A 479)
Tube (cold drawn)	64 OD 16 wall	2 1/2 5/8	RDT M3-3T(A 376)

using a single strain rate, 0.04/min, and one using all strain rates, 4 to 0.0004/min.

Figure 3.23 shows the plots of 0.2% yield strength as a function of test temperature for several heats in the as-received condition. The plot in Fig. 3.23(a) is for tensile data at a single strain rate, whereas that in Fig. 3.23(b) is for several strain rates. Figure 3.24 shows similar plots of ultimate tensile strength. Plots of 0.2% yield and ultimate tensile strength data for heats in the reannealed condition are shown in Figs. 3.25 and 3.26. The 0.2% yield and ultimate tensile strength data are expressed by third-degree polynomials of the form:

$$S = \alpha_0 + \alpha_1 T + \alpha_2 T^2 + \alpha_3 T^3 \ ,$$

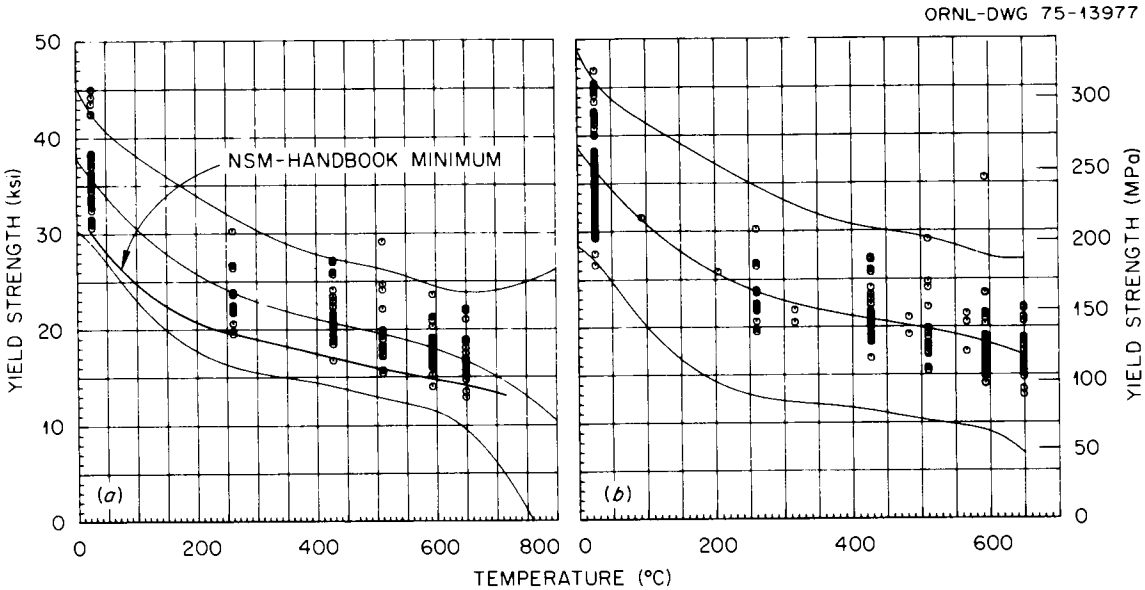

Fig. 3.23. Plot of 0.2% Yield Strength as a Function of Test Temperature for 20 Heats of Type 304 Stainless Steel in the As-Received Condition. (a) Data for a strain rate of 0.04/min, compared with *Nuclear Systems Materials Handbook* minimum curve. (b) Data for several strain rates in the range 4 to 0.0004/min.

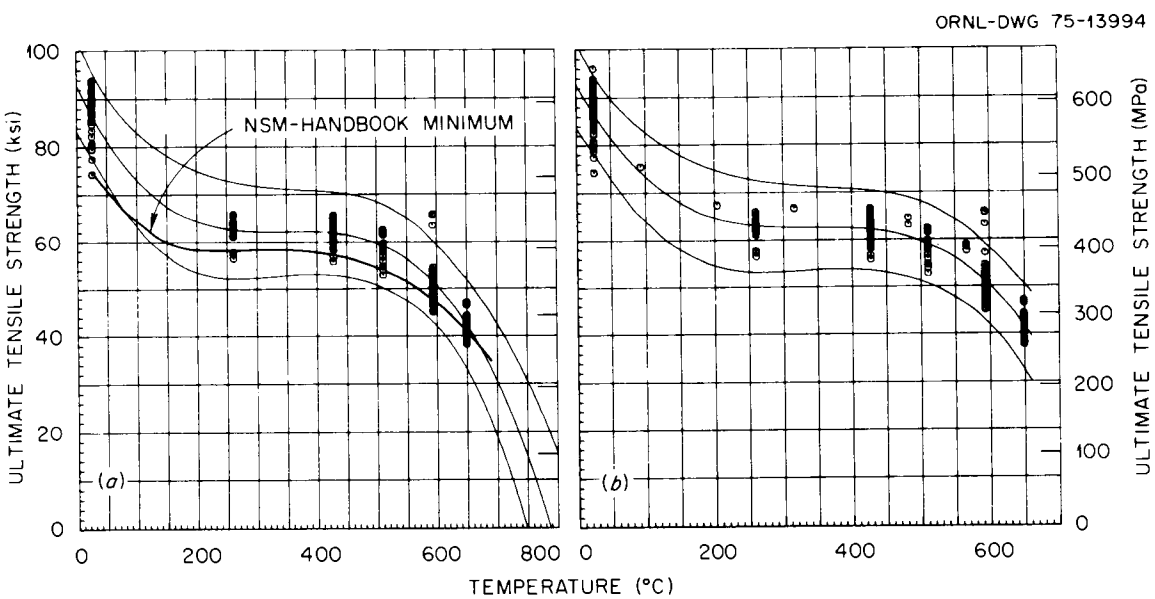

Fig. 3.24. Ultimate Tensile Strength as a Function of Test Temperature for 20 Heats of Type 304 Stainless Steel in the As-Received Condition. (a) Data for a strain rate of 0.04/min, compared with *Nuclear Systems Materials Handbook* minimum curve. (b) Data for several strain rates in the range 4 to 0.0004/min.

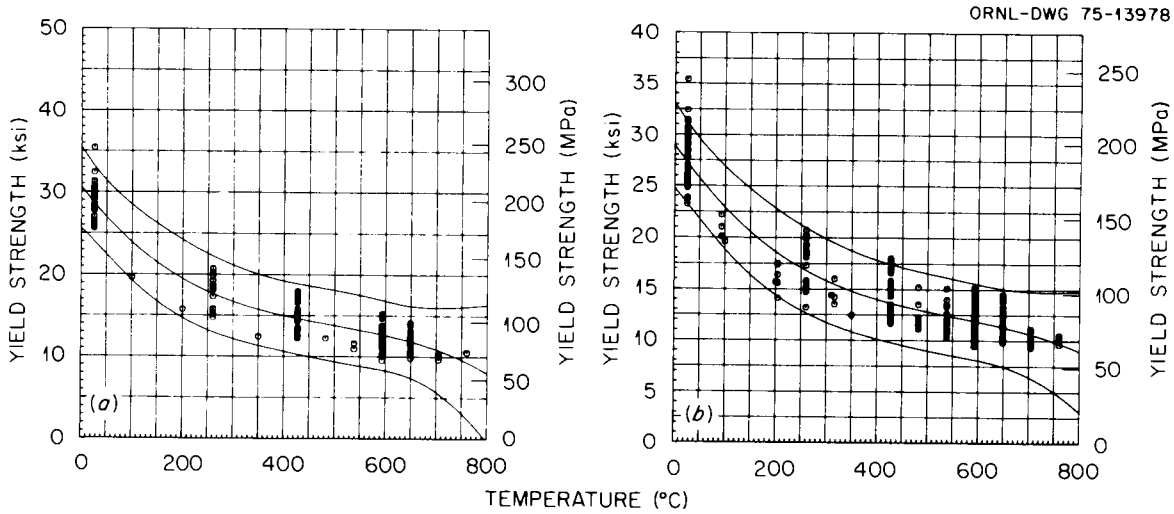

Fig. 3.25. Plot of 0.2% Yield Strength as a Function of Test Temperature for 20 Heats of Type 304 Stainless Steel in the Reannealed Condition. (a) Data for a strain rate of 0.04/min. (b) Data for several rates in the range 4 to 0.0004/min.

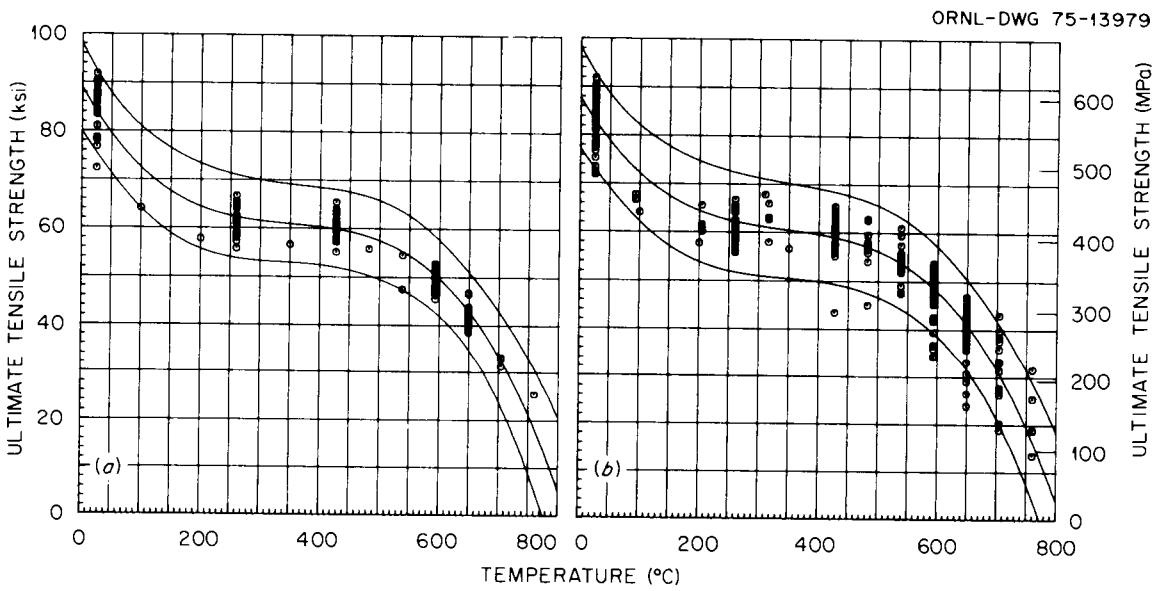

Fig. 3.26. Ultimate Tensile Strength as a Function of Test Temperature for 20 Heats of Type 304 Stainless Steel in the Reannealed Condition. (a) Data for a strain rate of 0.04/min. (b) Data for several strain rates in the range 4 to 0.0004/min.

where S = 0.2% yield or ultimate tensile strength, T = test temperature (°C), and the α_i are constants.

The method of least squares was used to estimate the constants in the equation. The lower and upper bounds shown in Figs. 3.23 through 3.26 are lower and upper central tolerance limits (λ = 0.95, P = 0.90) about the expected value obtained from the polynomial model. Thus, with a confidence level of 0.95%, 95% of the observed values are expected to be greater than the lower limit and 95% of the observed values are expected to be below the upper limit. It should be noted from the figures that reannealing reduced the data spread. The data spread observed for the as-received material is expected to result from the different amount of processing and straightening stresses[14] present in different product forms.

Smith[15,16] used a ratioing technique to establish the trends of variation of yield and ultimate tensile strengths with temperature of several austenitic stainless steels. His method involves normalizing the data available for a specific material by dividing the elevated-temperature strength values for individual lots by the room-temperature strengths of the same lots, and then establishing by the method of least squares the trend curve of best fit for these ratios. The trends expressed as ratios were multiplied by the specified minimum values of the purchase specification (for example a minimum 0.2% yield strength of 30 ksi is specified[17] for plate products of various austenitic stainless steels) to obtain the minimum 0.2% yield and ultimate tensile strength values reported in *Nuclear Systems Materials (NSM) Handbook*. The ORNL tensile data on 20 heats of type 304 stainless steel were subjected to the ratioing technique and the results are presented here.

Figures 3.27 and 3.28 show the yield and tensile strength ratios and best fit curves for 20 heats of type 304 stainless steel in the as-received condition. Similar plots for the reannealed condition are shown in Figs. 3.29 and 3.30. The expected yield and ultimate tensile strength ratios for both as-received and reannealed conditions are summarized in Table 3.8. The comparison of Fig. 3.30(a) and (b) clearly shows the influence of strain rate on ultimate tensile strength ratios for test temperatures of at least 538°C (1000°F). The ultimate tensile

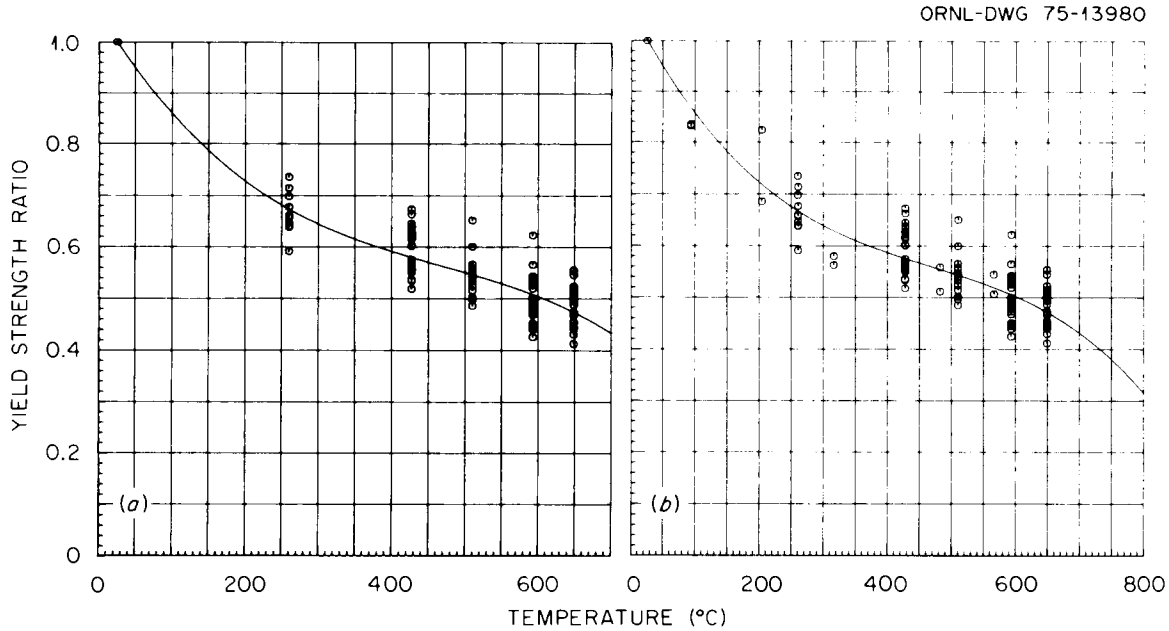

Fig. 3.27. Plot of 0.2% Yield Strength Ratio as a Function of Test Temperature for 20 Heats of Type 304 Stainless Steel in the As-Received Condition. (a) Data for a strain rate of 0.04/min. (b) Data for several strain rates in the range 4 to 0.0004/min.

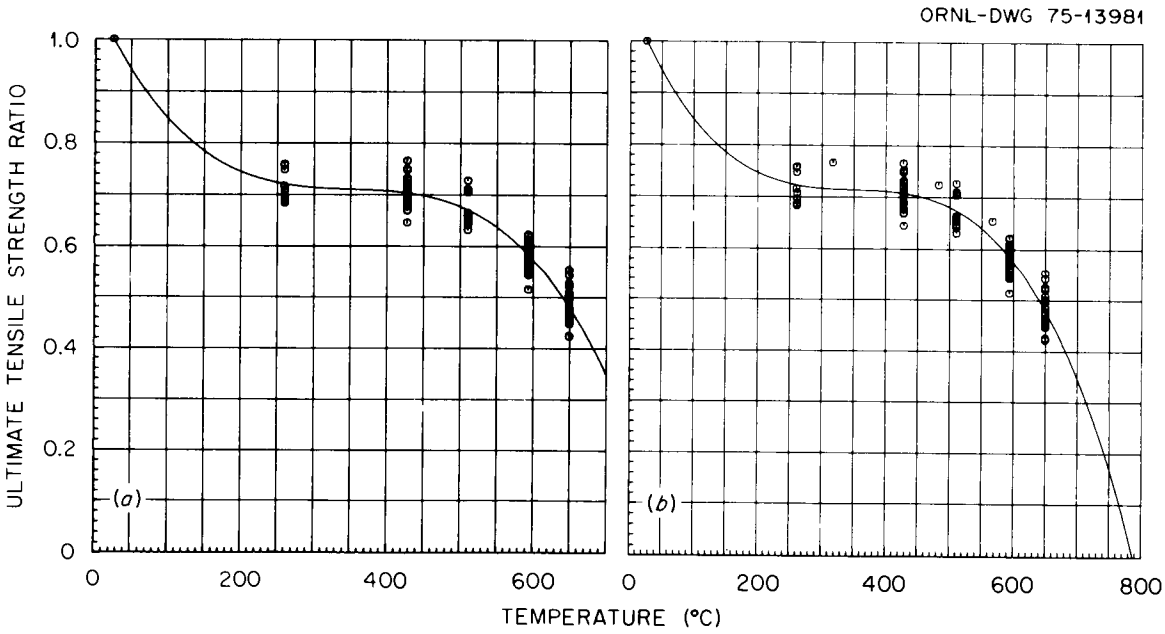

Fig. 3.28. Plot of Ultimate Tensile Strength Ratio as a Function of Test Temperature for 20 Heats of Type 304 Stainless Steel in the As-Received Condition. (a) Data for a strain rate of 0.04/min. (b) Data for several strain rates in the range 4 to 0.0004/min.

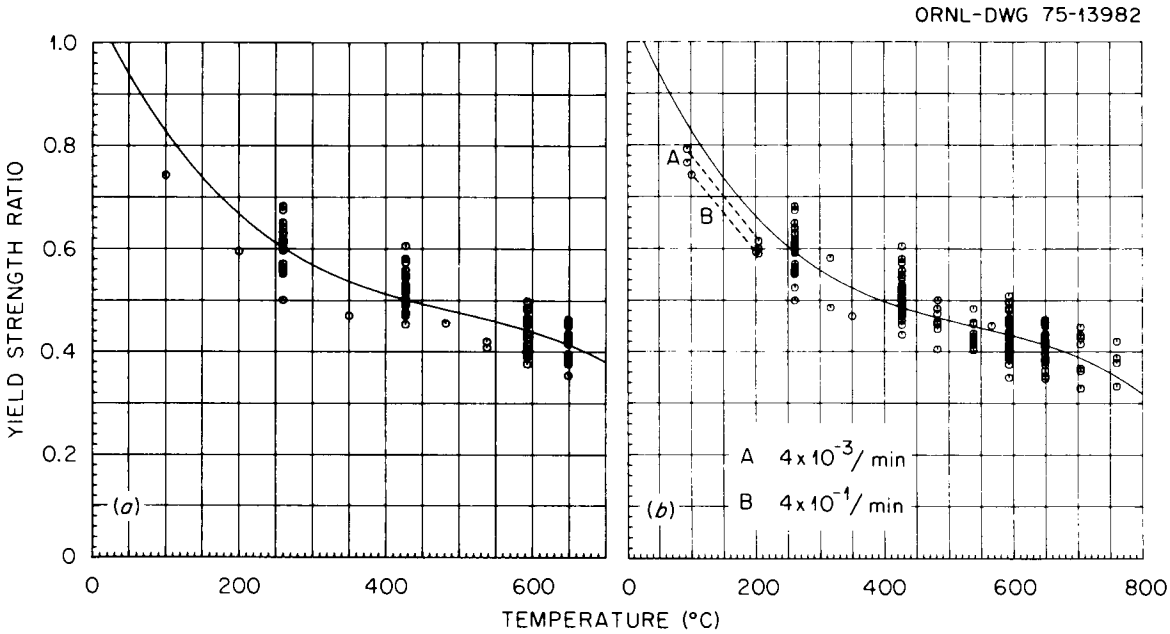

Fig. 3.29. Plot of 0.2% Yield Strength Ratio as a Function of Test Temperature for 20 Heats of Type 304 Stainless Steel in the Reannealed Condition. (a) Data for a strain rate of 0.04/min. (b) Data for several strain rates in the range 4 to 0.0004/min.

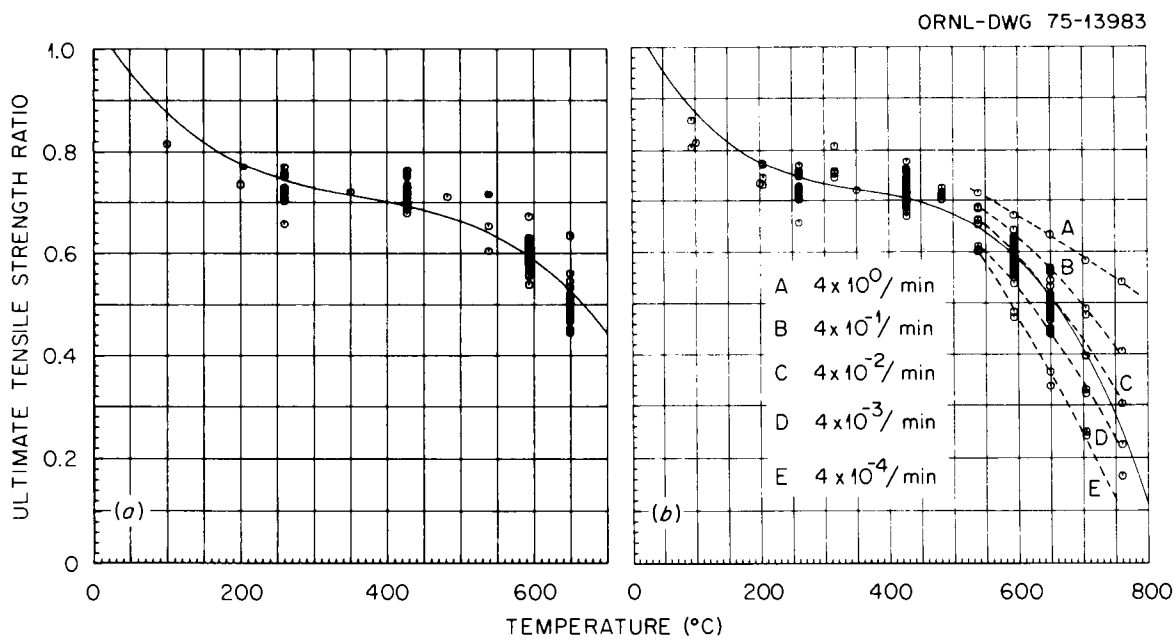

Fig. 3.30. Plot of Ultimate Tensile Strength Ratio as a Function of Test Temperature for 20 Heats of Type 304 Stainless Steel in the Reannealed Condition. (a) Data for a strain rate of 0.04/min. (b) Data for several strain rates in the range 4 to 0.0004/min.

Table 3.8. Summary of Yield and Ultimate Tensile Strength Ratios[a] for 20 Heats of Type 304 Stainless Steel

Test Temperature		Yield Strength Ratio		Ultimate Tensile Strength Ratio	
(°C)	(°F)	As Received	Reannealed	As Received	Reannealed
25	77	1.000	1.000	1.000	1.000
50	122	0.948	0.936	0.940	0.953
100	212	0.859	0.827	0.847	0.876
150	302	0.786	0.737	0.784	0.819
200	392	0.727	0.666	0.744	0.778
250	482	0.681	0.611	0.723	0.749
300	572	0.644	0.569	0.714	0.729
350	662	0.615	0.536	0.711	0.714
400	752	0.591	0.512	0.707	0.701
450	842	0.570	0.493	0.698	0.685
500	932	0.550	0.476	0.676	0.663
550	1022	0.529	0.458	0.636	0.632
600	1112	0.503	0.439	0.572	0.587
650	1202	0.472	0.413	0.478	0.525
700	1292	0.433	0.380	0.348	0.442

[a]Ratios are based on data for a single strain rate of 0.04/min.

strength at room temperature is not strain-rate sensitive. Thus, when it is used in determining ratios for tensile data produced over a strain rate range, a spread will result in the ratios, with highest strain rate ratios lying above the average strain rate and lowest strain rate lying below, as in Fig. 3.30(b). Thus, room-temperature ultimate tensile strength and ratio trend curve can only be used to produce the elevated-temperature tensile data for a single strain rate. At any other strain rate, a new ratio trend curve would be required. The yield strength values are strain rate sensitive for test temperatures in the range from room temperature to 204°C (400°F), as seen in Fig. 3.29(b).

The strain rate sensitivity was such that yield strength decreased with decreasing strain rate. Thus, yield ratios for high strain rates will be smaller than the ratios for the small strain rates. Such an effect of strain rate on yield ratio is opposite to that observed for ultimate tensile strength ratio. It should be noted that one of the limitations of the ratioing technique (not specified by Smith[15,16]) is the strain rate sensitivity of both the yield and ultimate tensile strength.

The 0.2% yield strength average and minimum curves for as-received and reannealed conditions are compared with the *Nuclear Systems Materials Handbook* minimum curve in Fig. 3.31. It should be noted that the reannealed

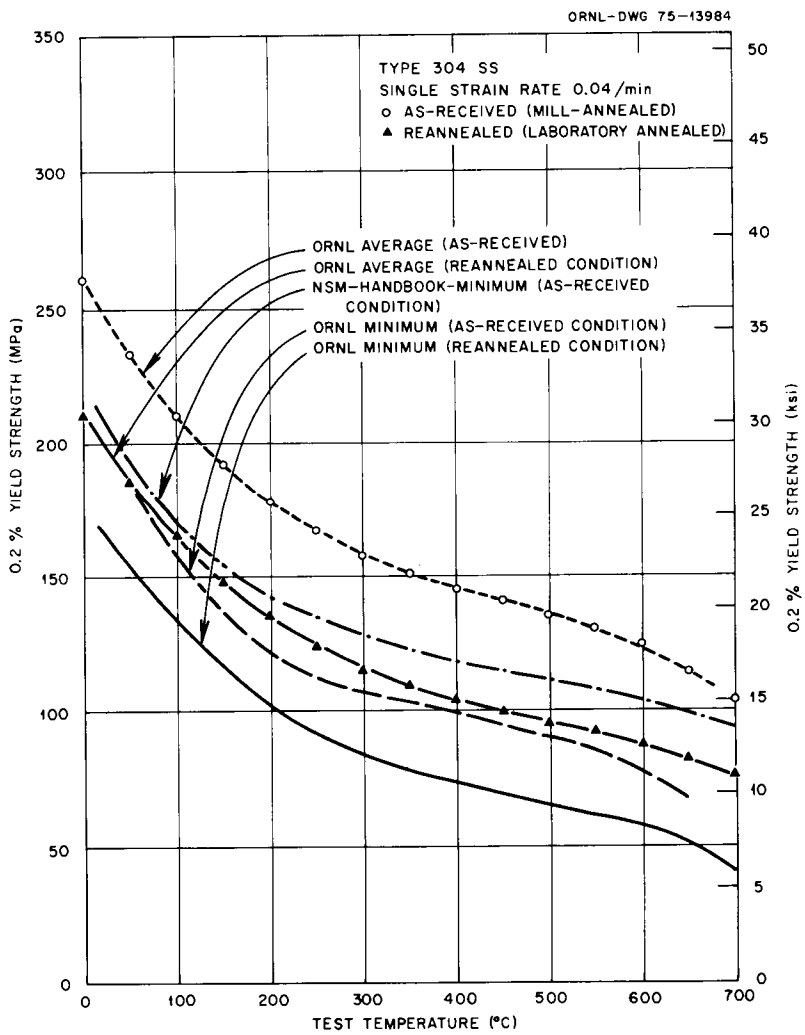

Fig. 3.31. Comparison of ORNL 0.2% Yield Strength Average and Minimum Curves for As-Received and Reannealed Conditions with *Nuclear Systems Materials Handbook* Minimum Curve.

curve is approximately 41 MPa (6 ksi) lower than the as-received curve for the range of test temperatures investigated thus far. The ORNL minimum curve for the as-received condition is slightly below the average curve for the reannealed condition. The *NSM Handbook* minimum curve is above the ORNL minimum for the as-received condition and average curve for the reannealed condition. Figure 3.32 shows the similar comparison for ultimate tensile strength. Note again that the *NSM Handbook* minimum curve is significantly above the ORNL minimum curve.

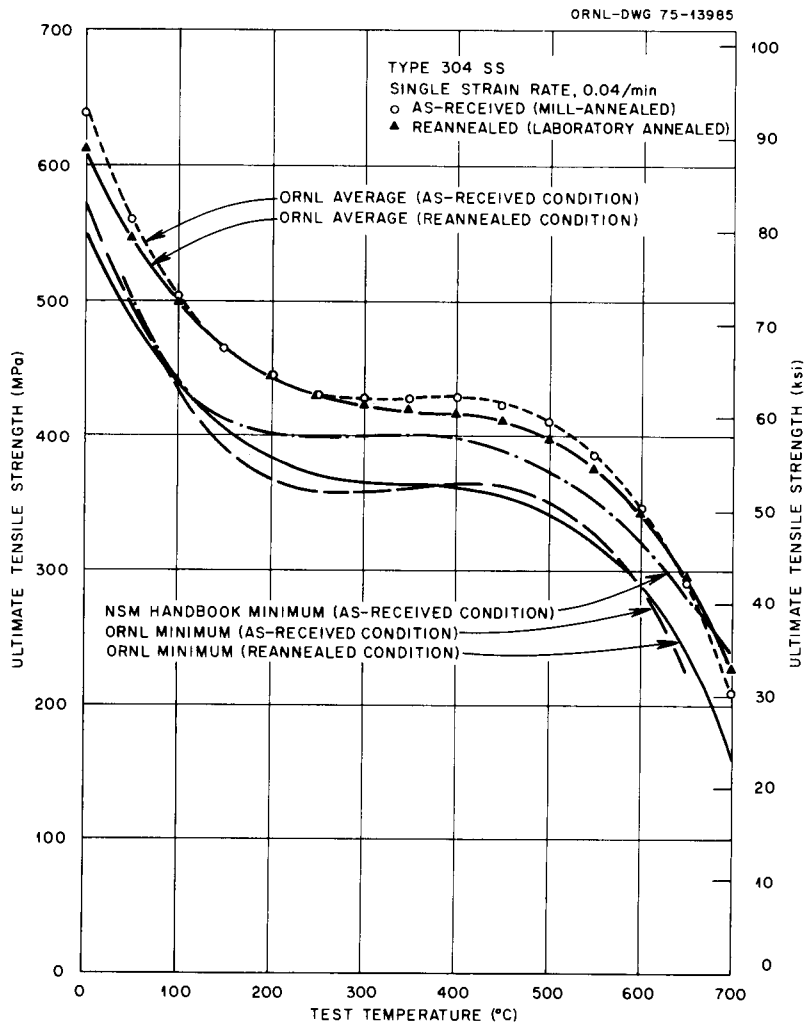

Fig. 3.32. Comparison of ORNL Ultimate Tensile Strength Average and Minimum Curves for As-Received and Reannealed Conditions with *Nuclear Systems Materials Handbook* Minimum Curve.

Figures 3.33 and 3.34 compare the 0.2% yield and ultimate tensile strength ratios for the ORNL data with those reported by Smith.[15,16] Smith's yield strength ratio trend curve is below the ORNL curve, but his ultimate tensile strength curve is significantly higher than the ORNL curve. The differences between the ORNL and Smith trend curves are probably due to the data base used in two investigations. The ORNL data were mostly on thick plates, whereas Smith used data mostly from the bar and pipe-tube and some from the plate product. Furthermore, Smith's data are from several sources, while ORNL data represent a single source. It should also be noted from Fig. 3.33 that reannealing significantly lowers the yield strength ratio trend curve but has only a small influence on the ultimate tensile strength ratio curve.

The *NSM Handbook* minimum values for yield and ultimate tensile strength as functions of temperature were obtained by multiplying the

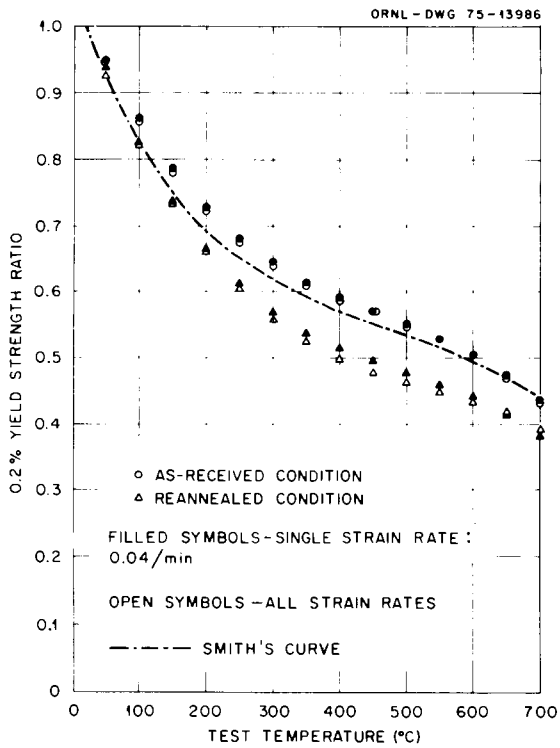

Fig. 3.33. Comparison of ORNL 0.2% Yield Strength Ratios for As-Received and Reannealed Conditions with Smith's Curve.

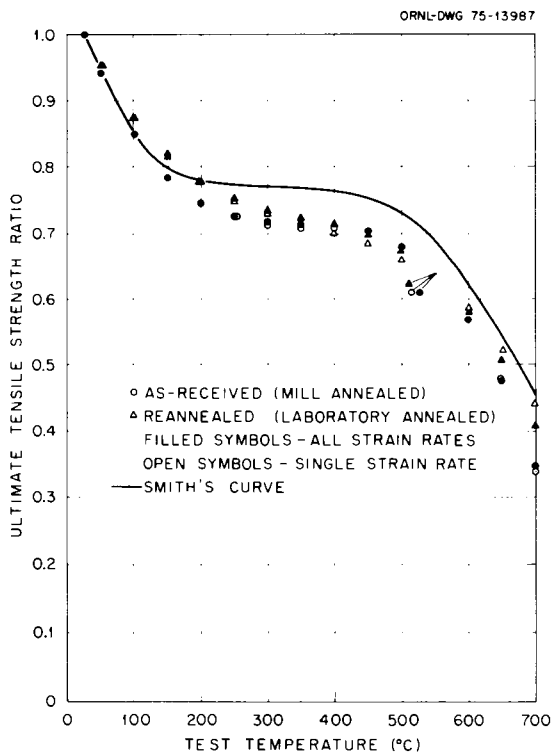

Fig. 3.34. Comparison of ORNL Ultimate Tensile Strength Ratios for As-Received and Reannealed Conditions with Smith's Curve.

ratio trend values by the specified minimum values of the purchase specification. For example, the minimum curve for yield strength was obtained by multiplying the Smith ratios by 207 MPa (30 ksi). Similarly the ultimate tensile strength minimum was obtained by multiplying the Smith ratio by 517 MPa (75 ksi). We have used the Handbook procedure and our ratios to obtain the minimum curves for yield and ultimate tensile strength. The minimum values obtained by using ORNL ratios are compared with those obtained by using Smith ratios in Figs. 3.35 and 3.36. These minimum curves are also compared with the 95% lower bound obtained for the ORNL data. The minimum values of yield strength obtained from ORNL and Smith ratios compare very well, but are significantly higher than the 95% lower bound. The statistical 95% lower bound indicates that 95% of the observed values are expected to be greater than the lower limit. On the other hand, the method used in the Handbook suggests that all materials purchased according to ASTM specifications should meet the minimum room-temperature mechanical properties requirement. Furthermore, the Handbook method of obtaining the minimum from the ratios suggests that the material purchased to room-temperature specification will have elevated-temperature data above the minimum. Handbook minimums are compared with the ORNL data in Figs. 3.23(a) and 3.24(a). It should

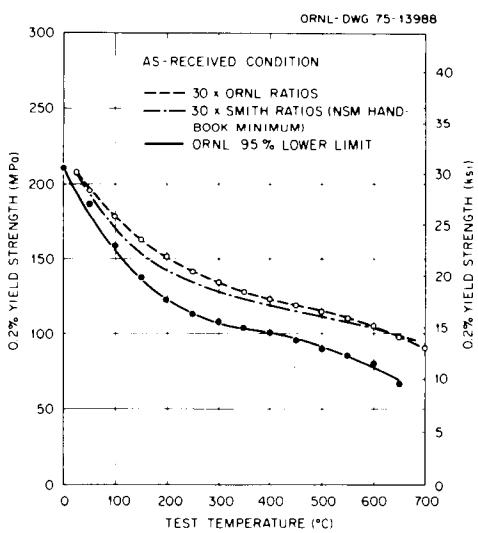

Fig. 3.35. Comparison of 0.2% Yield Strength Minimum Curves Calculated by Different Methods.

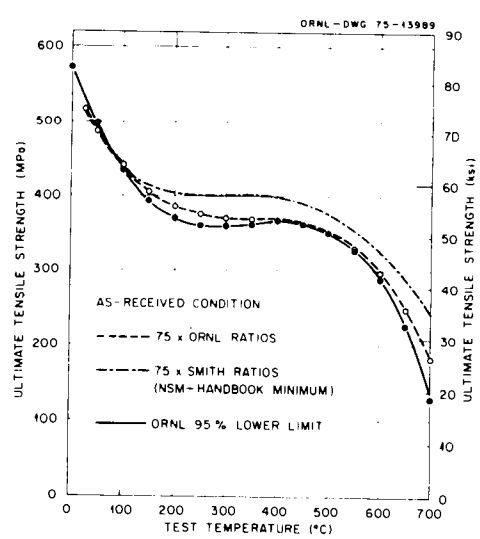

Fig. 3.36. Comparison of Ultimate Tensile Strength Minimum Curves Calculated by Different Methods.

be noted that although all 20 heats are above the minimum at room temperature (meet the purchase specifications), data on several heats at elevated temperatures fall below the minimum. Thus, the Handbook method used for calculating the minimum tensile properties appears to be rather less conservative. On the other hand the 95% lower bound appears to be a little overconservative. It almost appears that more work is needed in finding better methods to define the minimum properties.

The ORNL data on 20 heats of type 304 stainless steel in both as-received and reannealed conditions have been used in Fig. 3.37 to examine the time-independent stresses and compare them with those reported in the code. For the as-received condition S_m values in the code are below the limits on yield and ultimate tensile strengths for test temperatures

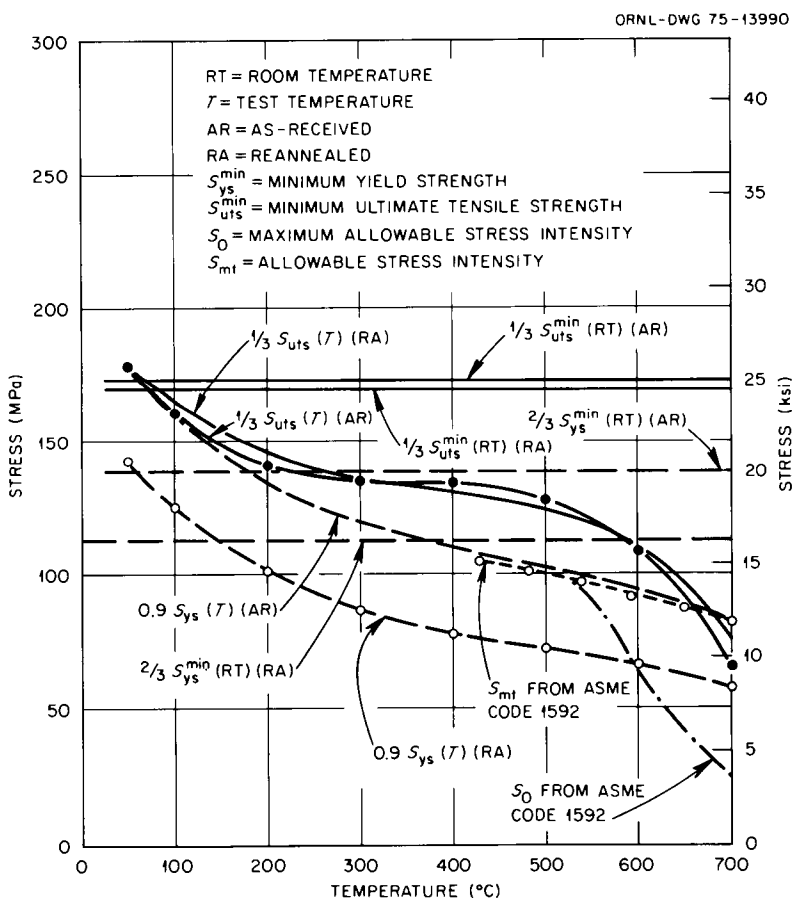

Fig. 3.37. Comparison of ORNL Tensile Data with Time-Independent Stresses Reported in ASME Code Case 1592.

below 660°C (1220°F). The S_0 values are below the yield and ultimate tensile limits for all test temperatures. Thus, for material to be used in the as-received condition, S_m values in code are conservative for test temperatures below 660°C (1220°F) and appear to become less conservative for higher temperatures. For the reannealed material, S_m values are above the $0.9S_{ys}$ curve for test temperatures of interest, 427–704°C (800–1300°F). Not only the S_m but also S_0 values for test temperatures below the 590°C (1094°F) are above the $0.9S_{ys}$ curve. Thus, if type 304 stainless steel is used in the reannealed condition, the S_m and S_0 values in the code would need to be revised if the criteria used to calculate S_m remain the same.

3.2.3.2 Creep Properties — V. K. Sikka, E. B. Patton, and R. H. Baldwin

Several long-term creep tests are in progress on several heats of type 304 stainless steel. Their status is summarized in Tables 3.9 and 3.10. All continuing tests listed in Table 3.9 have reached test periods greater than 30,000 hr. The creep curve on one long-term test is shown in Fig. 3.38. Note that this test is progressing smoothly and has reached a creep strain of only 1.0%. Tests listed in Table 3.10 are those which were started about a year to a year and a half ago. These tests are a part of long-term testing program on the weak, medium, and strong heats. Note that for approximately same test time and test conditions creep strain is greater for heat 807 than for heat 544 and greater for heat 544 than for heat 845. From the results presented in Tables 3.9 and 3.10 and those reported[3] before, heats 807, 544, and 845 still show the weak, medium, and strong heat behavior. Furthermore, the real long-term data presented in Table 3.9 show that the heat-to-heat variation observed for short-term creep tests is also observed in long-term tests.

Heat-to-heat variation was also examined for the aged material. The purpose of such a test was to check if weak and strong heats remain weak and strong even after aging. Creep-rupture data for several heats in unaged and aged conditions are shown in Fig. 3.39: (a), (b), and (c) represents the results for different aging conditions. Note that the weak and strong heats in the unaged condition remained weak and strong

Table 3.9. Status of Several Long-Term Creep Tests of Type 304 Stainless Steel at 593°C (1100°F)

Test	Heat	Condition[a]	Stress (MPa)	Stress (ksi)	Test Time[b] (hr)	Strain, % Loading	Strain, % Creep	Minimum Creep Rate (%/hr)	Time to Rupture (hr)
10396	551	A 479	172	25.0	Ruptured	1.81	6.31	1.4×10^{-4}	19,180
10395	845	A 240	172	25.0	Ruptured	1.37	11.35	1.4×10^{-4}	14,077
9499	380	Reannealed	117	17.0	31,790	0.72	1.08	~0	
9483	414	Reannealed	117	17.0	31,875	1.49	1.02	1.1×10^{-5}	
9464	330	A 240	117	17.0	32,124	0.20	0.28	5.5×10^{-6}	
9446	796	A 479	117	17.0	Ruptured	0.13	6.32	2.1×10^{-5}	29,253
9443	187	A 240	117	17.0	Ruptured	0.47	10.18	9.7×10^{-5}	22,622
9371	697	A 479	117	17.0	Ruptured	0.62	8.27	1.4×10^{-4}	25,823
9221	414	A 240	117	17.0	34,264	0.18	0.86	1.0×10^{-5}	
9508	544	A 240	117	17.0	Ruptured	0.22	9.04	4.5×10^{-5}	26,875

[a]As received per indicated specification or reannealed 0.5 hr at 1065°C (1950°F).

[b]Unless otherwise noted tests are in progress.

Table 3.10. Summary of Creep Data for Several Heats[a] of Type 304 Stainless Steel

Test	Heat	Temperature		Stress		Time in Test	Strain (%)	
		(°C)	(°F)	(MPa)	(ksi)	(hr)	Loading	Creep
13160	807	593	1100	69	10	14105	0.061	0.431
13157	807	593	1100	69	10	14166	0.078	0.441
13159	544	593	1100	69	10	14227	0.059	0.246
13151	845	593	1100	69	10	13973	0.051	0.181
14259	845	593	1100	97	14	8682	0.578	0.396
14042	807	593	1100	110	16	9254	0.938	2.409
14423	807	649	1200	69	10	8322	0.073	2.332
15422	845	649	1200	97	14	3138.2	0.495	0.993

[a]Reannealed for 0.5 hr at 1065°C (1950°F).

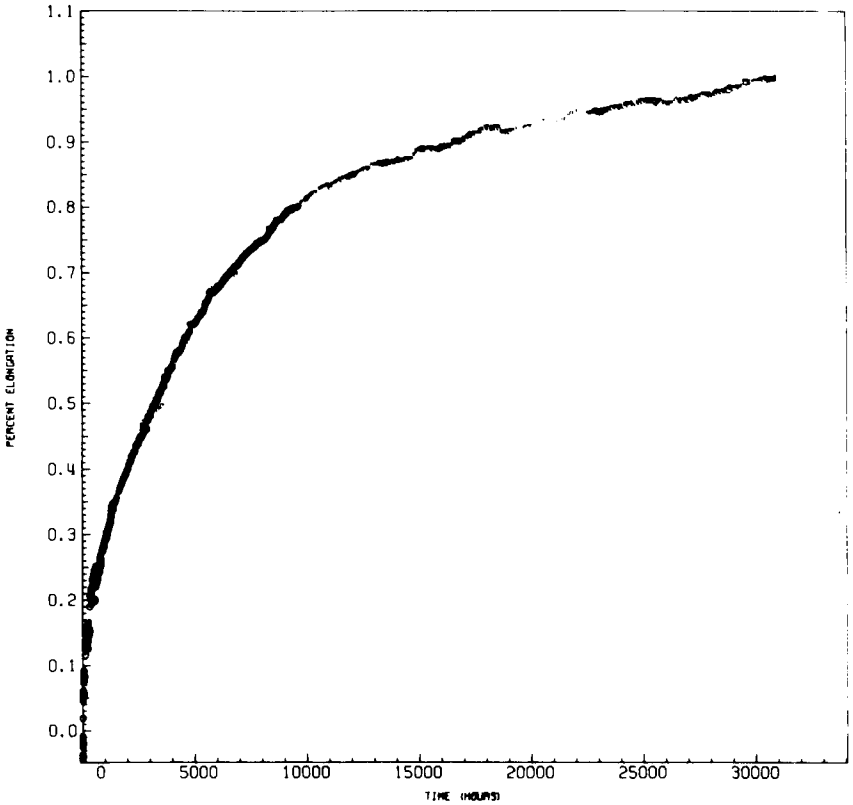

Fig. 3.38. Creep Curve for a Long-Term Test in Progress on Heat 414 of Type 304 Stainless Steel at 117 MP (17 ksi) and 593°C (1100°F).

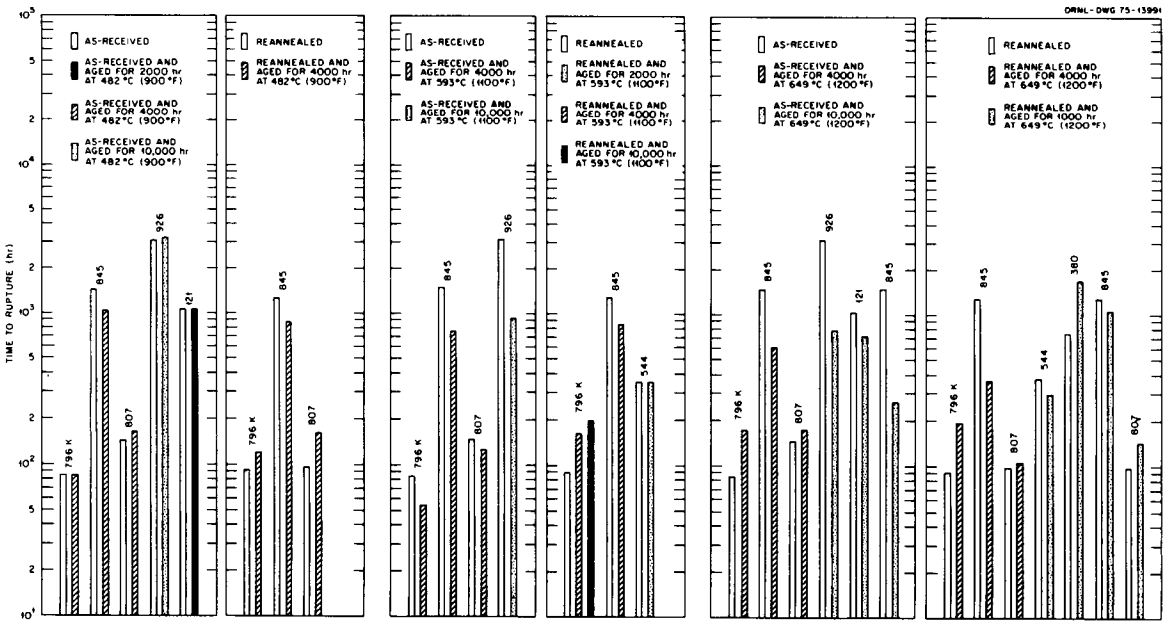

Fig. 3.39. Bar Charts Showing Heat-To-Heat Variation Observed in Unaged and Aged Conditions of Several Heats of Type 304 Stainless Steel. All tests were performed at 207 MPa (30 ksi) and 593°C (1100°F).

even on aging. Additional tests on aged heats are in progress to check the validity of what has been said above and will be reported later.

In a previous report[18] we showed that increasing niobium content increased the creep-rupture strength and decreased minimum creep rate. We have plotted the long-term creep rupture and minimum creep rate data as functions of niobium content in Figs. 3.40 and 3.41, respectively. It should be noted from these figures that long-term time to rupture increased and minimum creep rate decreased with increasing niobium content. Thus, it can be stated that niobium at a content of a few parts per million is an effective strengthening element not only for short-term data but also for long-term data past 31,000 hr.

3.2.4 Materials Behavior in Support of Development and Evaluation of Failure Criteria for Materials

3.2.4.1 Methods for Analysis of Creep and Creep-Rupture Data — M. K. Booker

The amount of inelastic strain that a component can endure at elevated temperatures without developing plastic instabilities or excessive cracking and voidage can be a useful design limit. Current design rules[19] specify a fixed 1% limit on total inelastic membrane strain for elevated-temperature components. Moreover, the minimum stress required to cause 1% inelastic strain at a given temperature in a time, t, is one of the criteria to be used in establishing time-dependent allowable stress intensities. Clearly, though, a strain limit that could be directly related to material ductility under the temperature and loading conditions of interest would be more fundamentally meaningful. One indicator of such a limit might be the amount of creep strain that a material can withstand before the onset of tertiary creep. Unfortunately, creep ductility data are difficult to analyze quantitatively because of their inherent large amount of scatter. Also data for the strain (or time) to tertiary creep are often scarce. Methods have been presented[20] for predicting the time to tertiary creep, t_3, including the use of a relationship between t_3 and the rupture life, t_r. The technique presented here allows the prediction of the strain to tertiary creep using rupture

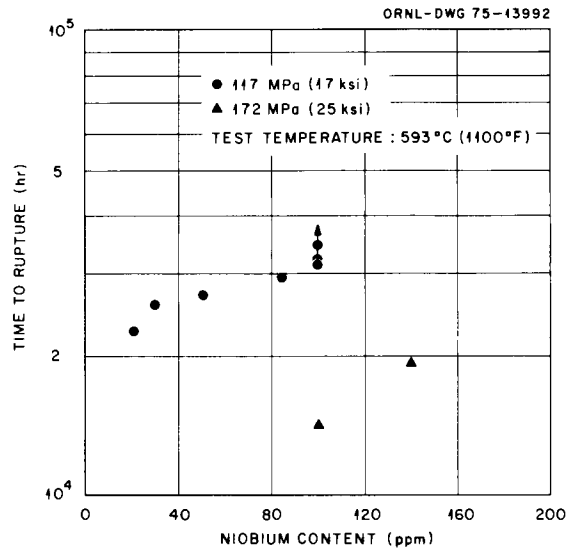

Fig. 3.40. Time to Rupture at 117 MPa (17 ksi) and 172 MPa (25 ksi) at 593°C (1100°F) as a Function of Niobium Content for Several Heats of Type 304 Stainless Steel.

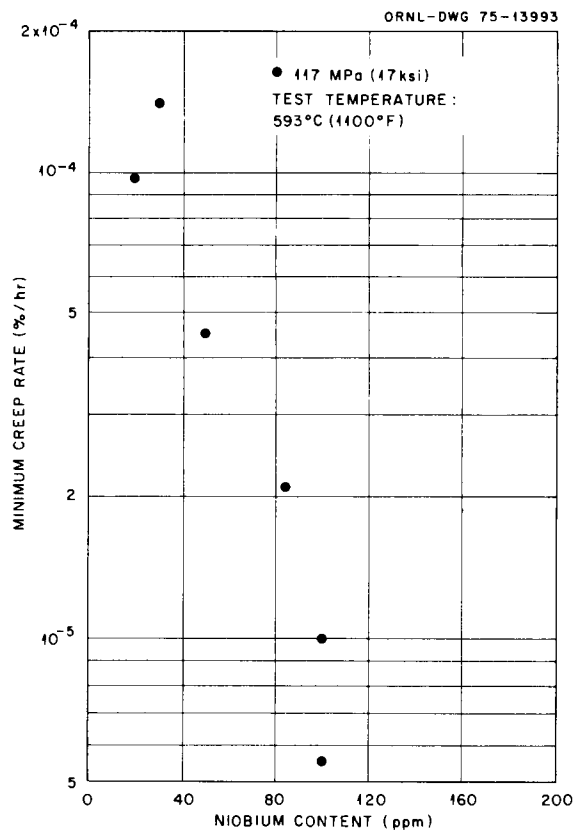

Fig. 3.41. Minimum Creep Rate at 117 MPa (17 ksi) and 593°C (1100°F) as a Function of Niobium Content for Several Heats of Type 304 Stainless Steel.

life and minimum creep rate ($\dot{e}_m$) data only, both of which are widely available. The method has been applied to data for types 304 and 316 austenitic stainless steel, ferritic 2 1/4 Cr-1 Mo steel, and nickel-base Inconel Alloy 718 — all important elevated-temperature structural alloys. Results obtained compare well with previously reported[21] parametric predictions.

The current method for analysis of data for the strain to tertiary creep is based on the approach suggested by Smith,[22] who defined an "average strain rate to failure," $\dot{e}_r$ by

$$\dot{e}_r = e_t/t_r \ , \tag{1}$$

where e_t is the total strain at rupture. In the present case, the average creep rate to tertiary creep, $\dot{e}_3$ is defined by

$$\dot{e}_3 = e_3/t_3 \ , \tag{2}$$

where e_3 is the creep strain to the onset of tertiary creep. Analysis of available data for the above four materials reveals that excellent results can be obtained with the following equations:

$$\dot{e}_3 = B\dot{e}_m^{\ \alpha} \ , \tag{3}$$

and

$$\dot{e}_3 = D t_r^{-\gamma} \ , \tag{4}$$

where the constants B, α, D, and γ may be functions of temperature, although B and α will be shown below to be relatively insensitive to temperature. In Ref. 20, the relationship $t_3 = At_r^{\ \beta}$ was proposed, where A and β were again relatively independent of temperature. Thus, since $e_3 = \dot{e}_3 t_3$, e_3 may be given by

$$e_3 = ABt_r^{\ \beta}\dot{e}_m^{\ \alpha} \ , \tag{5}$$

or by

$$e_3 = ADt_r^{\beta-\gamma} . \tag{6}$$

Thus, values of e_3 can be predicted from data for t_r and $\dot{e}_m$.

Tables 3.11 and 3.12 describe the data sets used to demonstrate the applicability of Eqs. (5) and (6), these data being the same as those analyzed in Ref. 21. No discernible effects due to specimen geometry were found in Ref. 21, while effects due to heat-to-heat and heat treatment variations will be discussed below. Data for the Garofalo et al.[26] heat and for Inconel Alloy 718 heat Y8509 include total strain (i.e. both instantaneous loading strain and creep strain) since separate measurements of loading strain were not available. Also, for heats 9T2796 and 8043813 of type 304 stainless steel, both heats of Inconel Alloy 718, and 2 1/4 Cr-1 Mo steel, onset of tertiary creep was determined by the 0.2% offset method. For the other heats, onset of tertiary creep was determined by the first deviation from linear secondary creep (see Fig. 3.42). Thus, the data used provided an opportunity to assess the effects of a fairly broad range of conditions and possibilities.

Unlike the method presented in Ref. 21, Eqs. (3) through (6) were found to be simultaneously applicable to material from various heats with various heat treatments. This applicability was probably due to the fact the current approach is really a normalization procedure. In fact, this normalization even makes it possible to treat data determined by the two different definitions of onset of tertiary creep together. Thus, the constants in Eqs. (5) and (6) for a given material have been evaluated by use of all data for that material, as long as e_3 for a given heat in a given material condition is predicted from the appropriate rupture life and minimum creep rate data for that heat.

Tables 3.13 and 3.14 display the results obtained by analyzing the current data according to Eqs. (3) and (4), while Table 3.15 shows the results obtained in Ref. 20 for the constants A and β. Again, it should be noted that A, β, B, and α are considered in these tables to be temperature independent, while D and γ are functions of temperature.

Table 3.11. Compositions and Product Forms of Materials Investigated

Heat	Reference	Product Form	Content, wt %[a]												
			C	Mn	P	S	Si	Cr	Ni	Co	Mo	Cu	N	Nb+Ta	Ti
						Type 304 Stainless Steel									
9T2796	23	25.4-mm plate	0.051	1.37	0.041	a	0.4	18.5	9.87	0.1	0.3	0.24	0.031	b	b
9T2796	3	50.8-mm plate	0.047	1.22	0.029	0.012	0.47	18.5	9.58	0.05	0.10	0.10	0.031	b	b
55697	24	7-mm rod	0.052	1.1	0.011	0.01	0.52	18.92	9.52	0.035	0.12	0.10	0.052	b	b
8043813	25	25.2-mm plate	0.062	1.87	0.04	0.0043	0.48	17.8	8.95	0.20	0.32	0.20	0.033	b	b
ASTM A 240, 479		Plate, rod	0.08[c]	2.0[c]	0.045[c]	0.03[c]	1.0[c]	17–19	8–10						
						Type 316 Stainless Steel									
332990	24	7-mm rod	0.052	1.72	0.012	0.02	0.38	17.8	13.55	0.14	2.33	0.20	0.041	b	b
Garofalo et al.	26	12.7-mm bar	0.07	1.94	0.01	0.021	0.38	18.0	11.4	b	2.15	b	0.043	b	b
ASTM A 240, 479		Plate, rod	0.08[c]	2.0[c]	0.045[c]	0.03[c]	1.0[c]	16–18	10–14		2–3				
						Inconel Alloy 718									
C56445	27,28	25.2-mm pancake	0.05	0.21		0.006	0.05	18.18	52.16	0.06	3.03	b	b	5.31	0.76
GE Spec C50T79			0.10[c]	0.35[c]		0.03[c]	0.4[c]	17.0–21.0	50.0–55.0	0.75[c]	2.80–3.30			5.0–5.5	0.65–1.15

[a]All analyses include balance iron. No analysis available on Inconel alloy 718 heat Y8509 (ref. 27), 2 1/4 Cr-1 Mo data used included bar and pipe forms conforming to the following specifications: 2.00–2.50% Cr; 0.9–1.1% Mo; room temperature 0.2% offset yield strength ≥207 MPa (30 ksi); room-temperature ultimate tensile strength ≥414 MPa (60 ksi).

[b]Not reported.

[c]Maximum allowed.

Table 3.12. Heat Treatments and Specimen Gage Lengths of Materials Studied

Heat, Description	Initial Gage Length (mm)	Treatment	Time (hr)	Temperature (°C)	Cooling Method
			Type 304 Stainless Steel		
9T2796, 25-mm plate	57.2[a]	Anneal	0.5	1093	Air cool
9T2796, 51-mm plate	57.2	Anneal	0.5	1093	Air cool
8043813	57.2[a]	Anneal	0.5	1065	Air cool
55697	31.8	Anneal	1.0	1066	Rapid air cool
			Type 316 Stainless Steel		
332990	31.8	Anneal	1.0	1066	Rapid air cool
Garofalo et al.	38.1	Anneal	0.5	1093	Water quench
			2 1/4 Cr-1 Mo Steel		
Annealed[b]	50.8[c]	Austenitize	1	927	Furnace cool 28°C/hr to 450°C Air cool to room temperature
Isothermally annealed[b]	50.8[c]	Austenitize	1	927	Furnace cool 83°C/hr to 704°C
		Hold	2	704	Furnace cool 333°C/hr to room temperature
			Inconel Alloy 718		
C56445	50.8	Anneal	2.0	982	Air cool
		Age	8.0	718	Furnace cool 55°C/hr to 621°C
		Age	8.0	621	Air cool
Y8509	Unknown	Anneal	1.0	982	Water quench
		Age	8.0	718	Furnace cool 11–56°C/hr to 621°C, air cool

[a]Some high-stress and/or low-temperature tests were run on 31.8-mm-gage-length specimens.

[b]Typical heat treatment.

[c]Some tests were run on 76.2-mm-gage-length specimens.

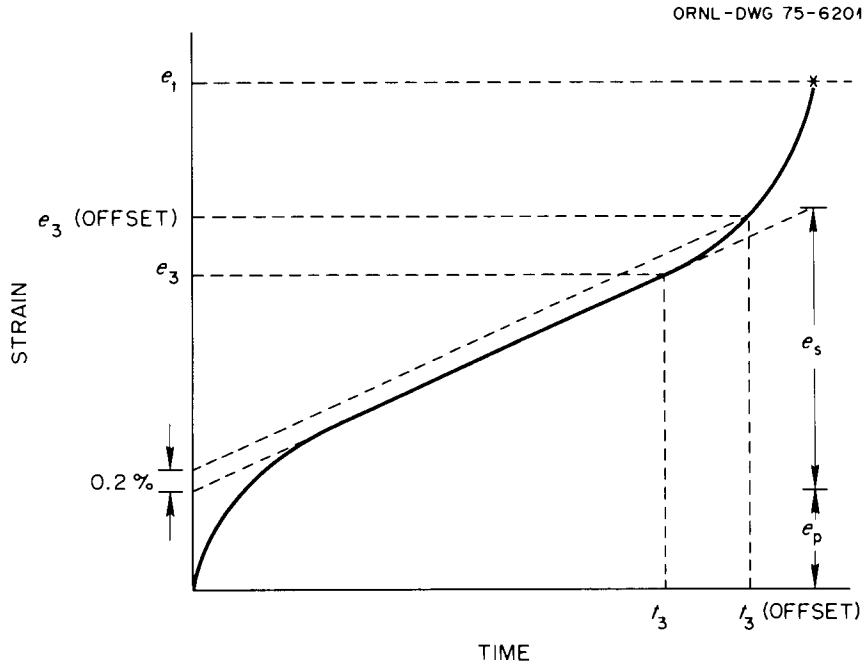

Fig. 3.42. Definitions of Quantities Examined.

Table 3.13. Results of Correlation Between Minimum Creep Rate and Average Creep Rate to Tertiary Creep[a]

Data Set	Number of Points	B	α	RMS[b]	R^2[c]	Temperature Range of Data (°C)
304 Stainless	138	1.110	0.974	0.050	99.3	482–816
316 Stainless G[d]	120	1.602	0.995	0.269	95.6	593–816
316 Stainless H[e]	38	1.092	0.991	0.0235	99.6	538–760
Inconel 718 T[f]	18	3.723	1.183	0.254	92.2	538–760
Inconel 718 C[g]	26	4.000	1.174	0.322	96.2	538–704
2 1/4 Cr-1 Mo	117	0.637	0.854	0.241	90.2	482–677

[a]Minimum creep rate, $\dot{e}_m$, and average creep rate to tertiary creep, $\dot{e}_3$, have been related by $\dot{e}_3 = B\dot{e}_m^{\alpha}$.

[b]RMS = $\Sigma Y^2/(n - \nu)$, where n = number of data points and ν = number of coefficients in the model (here $\nu = 2$); ΣY^2 = sum of squared residuals, $\Sigma Y^2 = \Sigma(\ln \dot{e}_{3pred} - \ln \dot{e}_{3exp})^2$ where $\ln \dot{e}_{3pred}$ = ln [predicted rate (%/hr)] and $\ln \dot{e}_{3exp}$ = ln [experimentally observed rate (%/hr)].

[c]R^2 = coefficient of determination; R^2 describes how well a regression model describes variations in the data. R^2 = 100 signifies complete description, R^2 = 0.0 signifies no description. $\sqrt{R^2/100} = r$, the linear correlation coefficient.

[d]Data for total strain, from Ref. 26.

[e]Data for creep strain only, from Ref. 24.

[f]Data for total strain, from Ref. 27.

[g]Data for creep strain only, from Ref. 28.

Table 3.14. Results of Correlation Between Rupture Life and Average Creep Rate to Tertiary Creep[a]

Data Set	Temperature (°C)	Number of Points	D	γ	RMS[b]	R^2[c]
304 Stainless	538	24	4.899	1.030	0.174	94.4
	593	37	22.571	1.198	0.202	96.2
	649	44	25.091	1.089	0.172	97.3
	704	14	33.882	1.099	0.124	98.5
	760	11	33.115	1.034	0.048	99.3
316 Stainless G[d]	593	36	30.265	1.078	0.020	99.6
	704	48	49.383	1.081	0.030	99.6
	816	36	42.921	1.103	0.023	99.6
316 Stainless H[e]	538	7	7.131	1.154	0.174	93.5
	593	12	12.783	1.038	0.171	96.5
	649	12	23.220	1.005	0.027	99.6
	760	7	31.690	1.004	0.014	99.6
Inconel 718 T[f]	593	4	2.044	1.048	0.339	94.4
	649	6	27.859	1.442	0.121	97.4
	704	4	0.081	0.710	0.00406	99.5
	760	3	2.545	1.125	0.0566	97.0
Inconel 718 C[g]	538	6	32.394	1.429	0.491	97.0
	593	6	3.968	1.218	0.0636	99.3
	649	8	1.212	1.020	0.0259	99.7
	704	6	6.640	1.232	0.103	98.8
2 1/4 Cr-1 Mo	538	23	3.531	0.903	0.422	73.1
	593	41	51.761	1.280	0.699	77.2
	649	26	18.168	1.185	0.411	83.8

[a]Rupture life, t_r, and average creep rate to tertiary creep, $\dot{e}_3$, are related by $\dot{e}_3 = Dt_r^{-\gamma}$.

[b]RMS = $\Sigma Y^2/(n - \nu)$, where n = number of data points and ν = number of coefficients in the model (here $\nu = 2$); ΣY^2 = sum of squared residuals, $\Sigma Y^2 = \Sigma(\ln \dot{e}_{3pred} - \ln \dot{e}_{3exp})^2$ where $\ln \dot{e}_{3pred}$ = ln [predicted rate (%/hr)] and $\ln \dot{e}_{3exp}$ = ln [experimentally observed rate (%/hr)].

[c]R^2 = coefficent of determination; R^2 describes how well a regression model describes variations in the data. R^2 = 100 signifies complete description, R^2 = 0.0 signifies no description. $\sqrt{R^2/100} = r$, the linear correlation coefficient.

[d]Data for total strain, from Ref. 26.

[e]Data for creep strain only, from Ref. 24.

[f]Data for total strain, from Ref. 27.

[g]Data for creep strain only, from Ref. 28.

Table 3.15. Results of Correlation Between Rupture Life and Time to Tertiary Creep[a]

Data Set	Number of Points	A	β	RMS[b]	R^2[c]	Temperature Range of Data (°C)
304 Stainless, t_{ss}	277	0.752	0.977	0.090	96.6	482–816
304 Stainless, t_2	233	0.685	0.968	0.117	93.6	538–649
316 Stainless, t_2	183	0.526	1.004	0.071	93.5	538–816
2 1/4 Cr-1 Mo, t_{ss}	126	0.334	1.046	0.067	96.1	482–677
Inconel 718, t_{ss}	63	0.424	1.045	0.080	98.2	538–704
Inconel 718, t_2	52	0.285	1.049	0.142	94.3	538–704

[a]Time to tertiary creep, t_3, and rupture life, t_r, have been related by $t_3 = At_r^{\beta}$; t_3 may be t_{ss} (0.2% offset time to tertiary creep) or t_2 (time to first deviation from linear secondary creep).

[b]RMS = $\Sigma Y^2/(n - \nu)$ where n = number of data points and ν = number of coefficients in the model (here $\nu = 2$); ΣY^2 is as in Table 3.13 but refers to $\ln(t_3)$.

[c]R^2 is defined in Table 3.13.

Figures 3.43 and 3.44 illustrate the fit of Eqs. (3) and (4); the fit of $t_3 = At_r^{\beta}$ is discussed in Ref. 20.

In Table 3.14, the constant D clearly varies with temperature, while the variations in γ are somewhat minor. To obtain a clearer view of the constant D as a function of temperature, a standard γ value can be obtained for each data set from data at all temperatures, and the D values recalculated at each temperature with γ fixed at this value. Also, the proximity of the values of α, β, and γ to unity suggest that these parameters might all be replaced by values of one to simplify the models. However, it must be remembered that the values given here for the various regression constants all represent only estimates of the true values of these constants. Different data sets might yield different estimates. Still, based on the data used here, the values in Tables 3.13 through 3.15 are the best available estimates, and these values are used in the following calculations. The use of any other values for the constants (such as unity for α, β, γ) introduces an unnecessary bias. If desired,

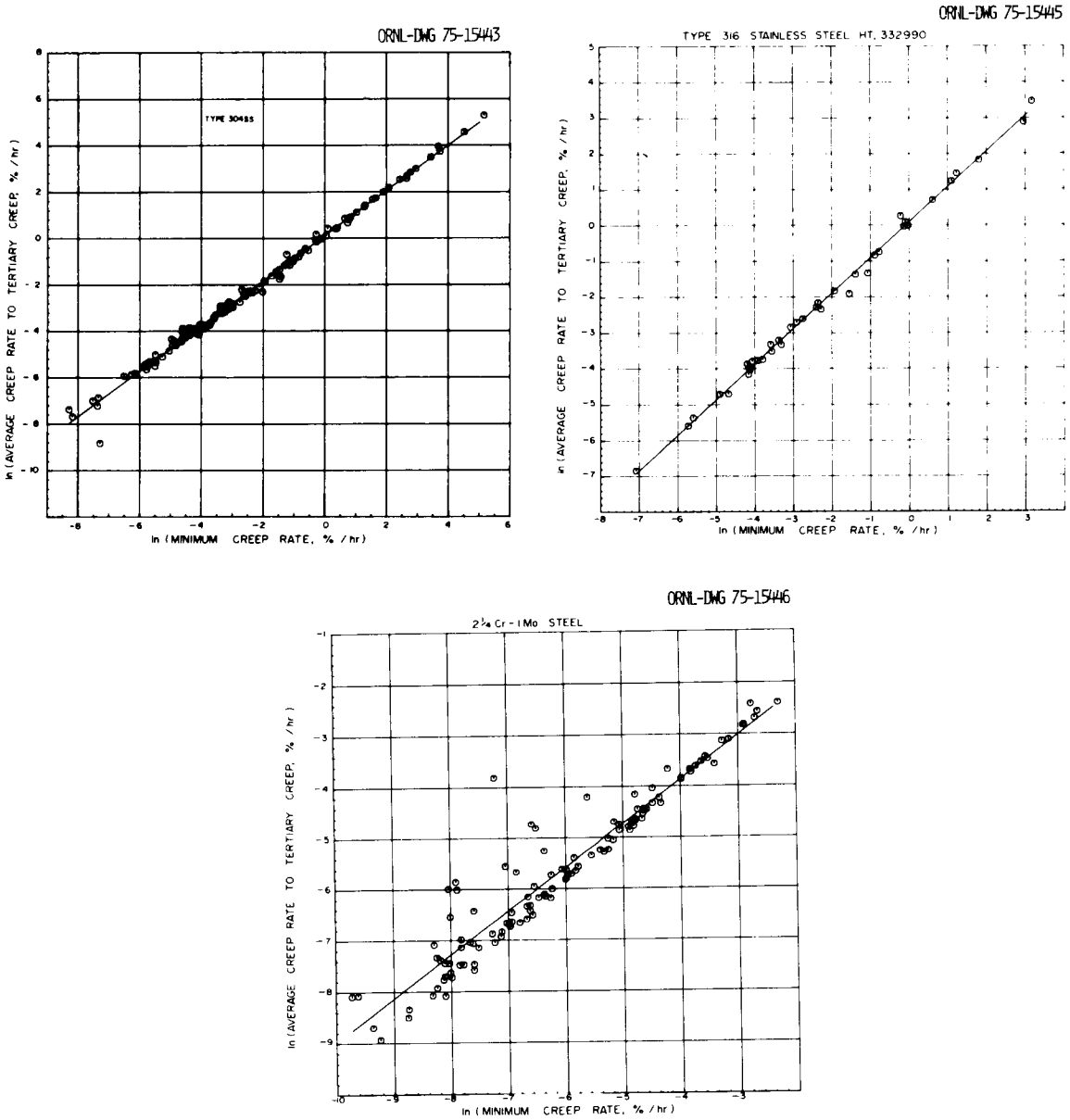

Fig. 3.43. Relationship Between Minimum Creep Rate and Average Creep Rate to Tertiary Creep for (a) Type 304 Stainless Steel, (b) Type 316 Stainless Steel Heat 332990, and (c) 2 1/4 Cr-1 Mo Steel.

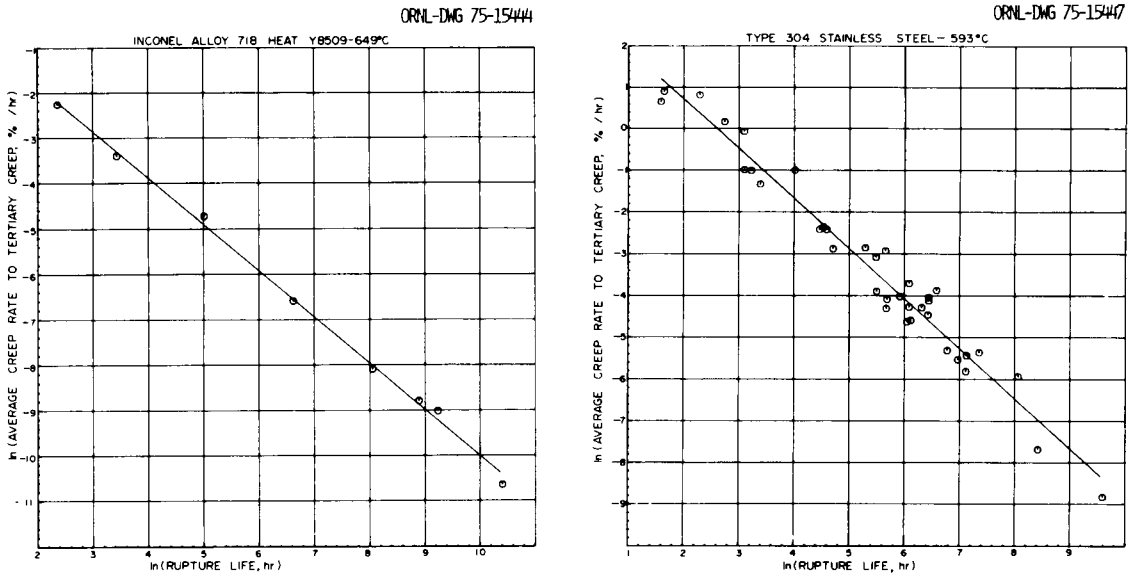

Fig. 3.44. Relationship Between Rupture Life and Average Creep Rate to Tertiary Creep for (a) Inconel Alloy 718 Heat Y8509 and (b) Type 304 Stainless Steel.

the uncertainty in the values of these constants can be analyzed by standard statistical techniques. Additional statistical analysis of these constants is reported elsewhere,[29] where many of the values for α, β, and γ are indeed shown to be significantly different from unity.

Since D (and perhaps γ) from Eq. (6) is a function of temperature, that equation clearly indicates that at a given value for t_r e_3 is a function of temperature. All constants in Eq. (5), however, are independent of temperature, indicating that at a given value for t_r e_3 is a function of $\dot{e}_m$ only. Monkman and Grant[30] found that t_r and $\dot{e}_m$ were related by

$$\dot{e}_m = F t_r^{-\lambda} , \tag{7}$$

where λ was about equal to unity and F was a constant independent of temperature. Results of analysis of current data are shown in Table 3.16. (Note that in this table data sets* 316 stainless G and H and Inconel 718 T and C have been combined since both t_r and $\dot{e}_m$ are independent of whether reported strains are total strains or creep strains only.) Clearly in

*These separate data sets are defined in Table 3.13.

Table 3.16. Results of Correlation Between Rupture Life and Minimum Creep Rate

Data Set	Temperature (°C)	Number of Points	F	λ	RMS	R^2
304 Stainless	538	24	8.604	−1.115	0.237	94.0
	593	41	15.991	−1.180	0.214	96.4
	649	45	24.522	−1.119	0.160	97.7
	704	14	28.633	−1.086	0.140	98.2
	760	11	31.416	−1.042	0.0339	99.5
316 Stainless	538	8	10.452	−1.232	0.159	94.6
	593	48	6.410	−0.982	0.0949	97.8
	649	12	21.574	−1.000	0.0591	99.2
	704	48	32.259	−1.038	0.0476	99.3
	760	7	29.207	−1.003	0.0183	99.5
	816	36	35.696	−1.082	0.0318	99.4
Inconel 718	538	8	13.296	−1.378	0.162	98.5
	593	11	2.791	−1.211	0.897	90.9
	649	13	1.393	−1.142	0.362	95.5
	704	11	2.405	−1.165	1.022	81.4
	760					
2 1/4 Cr-1 Mo	538	26	7.030	−1.075	0.795	65.4
	593	45	97.820	−1.414	0.751	81.5
	649	28	36.122	−1.316	0.536	84.0

the present case F (and possibly λ) is a function of temperature, agreeing with the results presented in Ref. 21. Thus, Eq. (5) also predicts that e_3 is a function of temperature, since this equation may be rewritten as

$$e_3 = ABF^{\alpha} t_r^{\beta-\alpha\lambda} , \tag{8}$$

which is equivalent in form to Eq. (6), showing that the two equations are indeed consistent. Equation (6), being more direct, is preferred to Eq. (8).

Predictions from Eqs. (5) and (6) can be compared with experimental data in several ways. Figure 3.45 illustrates comparisons between experimentally measured values for e_3 and values of e_3 calculated by the above equations for type 304 stainless steel.

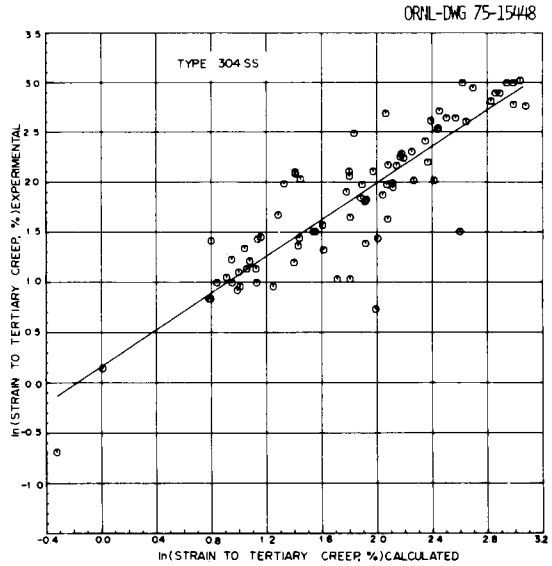

Fig. 3.45. Comparison of Experimentally Measured Strain to Tertiary Creep with Calculations from Eq. (5) for Type 304 Stainless Steel.

Considering the large amount of scatter inherent in the data, the agreement in this figure is good. To assess the trends in the data and the calculated values with time, stress, and temperature, several approaches can be taken. For a plot of e_3 vs t_r (as in Fig. 3.46) Eqs. (6) and (8) can be evaluated easily by simply substituting any desired value for t_r into them. These equations will yield average predictions for a material with no measure of variations due to heat differences, heat treatment, etc. To evaluate Eq. (5), one must have a means for choosing the appropriate value of $\dot{e}_m$ for a given value of t_r. If this choice is made by Eq. (7), then Eq. (8) results. For a given heat of material, however, more accurate results might be obtained as follows (if enough data are available). First, fit both the rupture life and minimum creep rate data by some mathematical model, such as a time-temperature parameter,[31] yielding equations of the form

$$t_r = F(\sigma,T) \ , \tag{9}$$

$$\dot{e}_m = G(\sigma,T) \ , \tag{10}$$

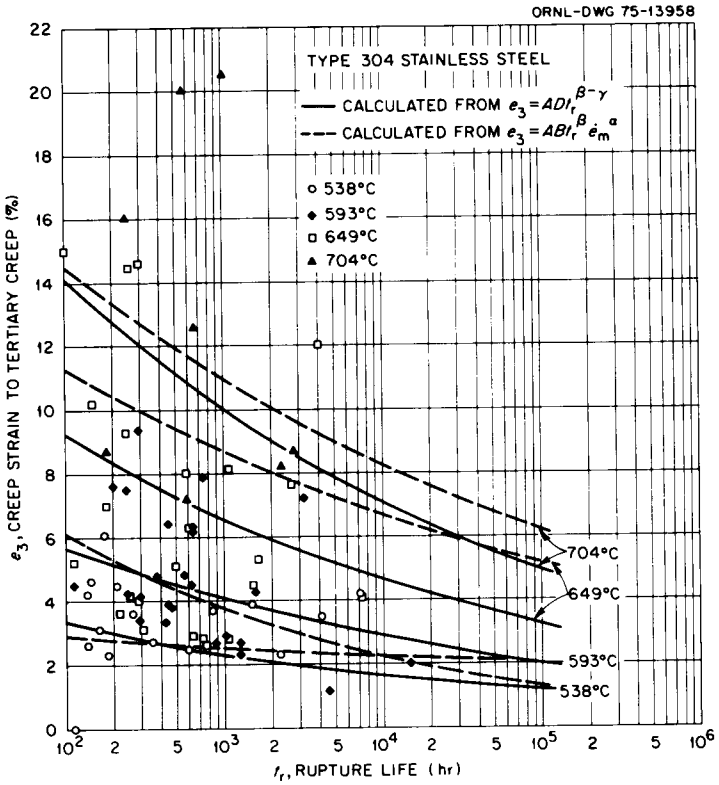

Fig. 3.46. Comparison of Calculated and Experimental Values of Creep Strain to Tertiary Creep for Type 304 Stainless Steel as a Function of Rupture Life.

where σ = stress,

T = temperature, and

F, G = functions.

At the chosen values for T and t_r, Eq. (9) can be solved for σ; substituting these values for T and σ into Eq. (10) yields a value for $\dot{e}_m$. The dashed lines in Fig. 3.46 were calculated by this method, using the Orr-Sherby-Dorn[32] parametric results from Ref. 21 from a simultaneous fit to all four data sets of type 304 stainless steel. However, as discussed in Ref. (21), it might be more meaningful to plot e_3 vs σ at various temperatures. Figures 3.47 through 3.49 illustrate results obtained from such plots for individual heats of material. The abscissa in these plots is the σ value obtained above in solving Eq. (9). The results agree reasonably well with the data and indicate general trends reasonably well. Also, as shown in Fig. 3.47, the results are quite

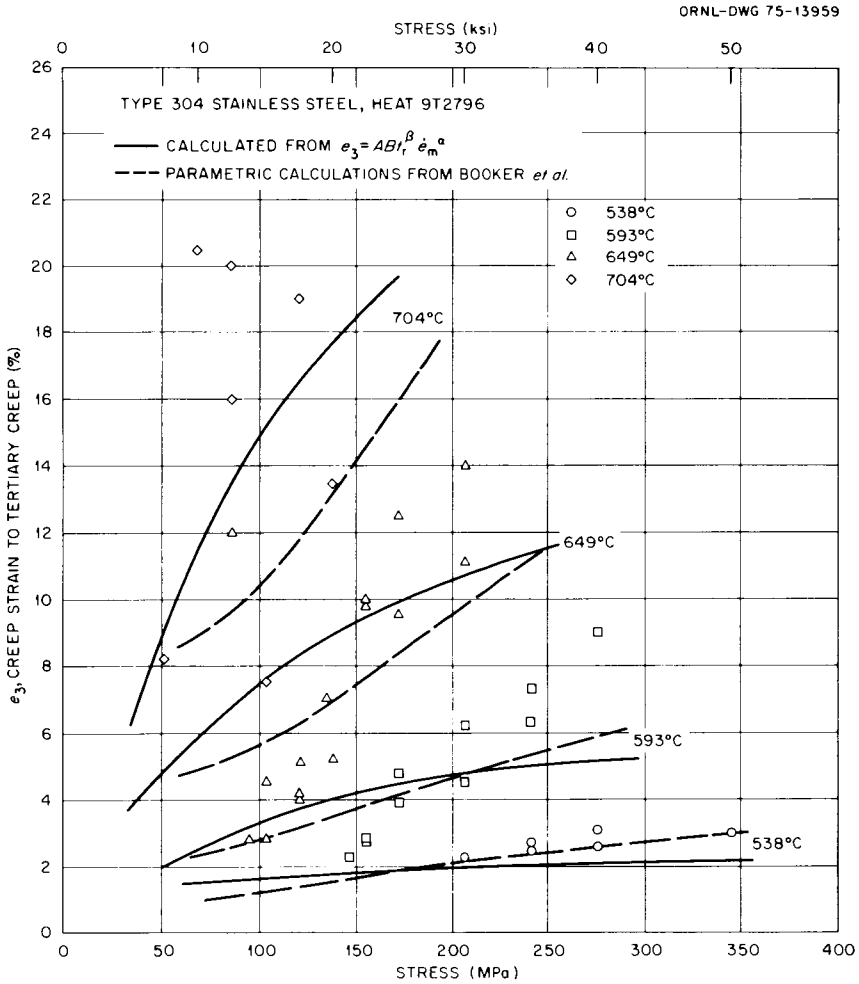

Fig. 3.47. Variation of Strain to Tertiary Creep with Stress for Heat 9T2796 (25-mm Plate) of Type 304 Stainless Steel. Solid lines were calculated by Eq. (5); dashed lines from Ref. 21.

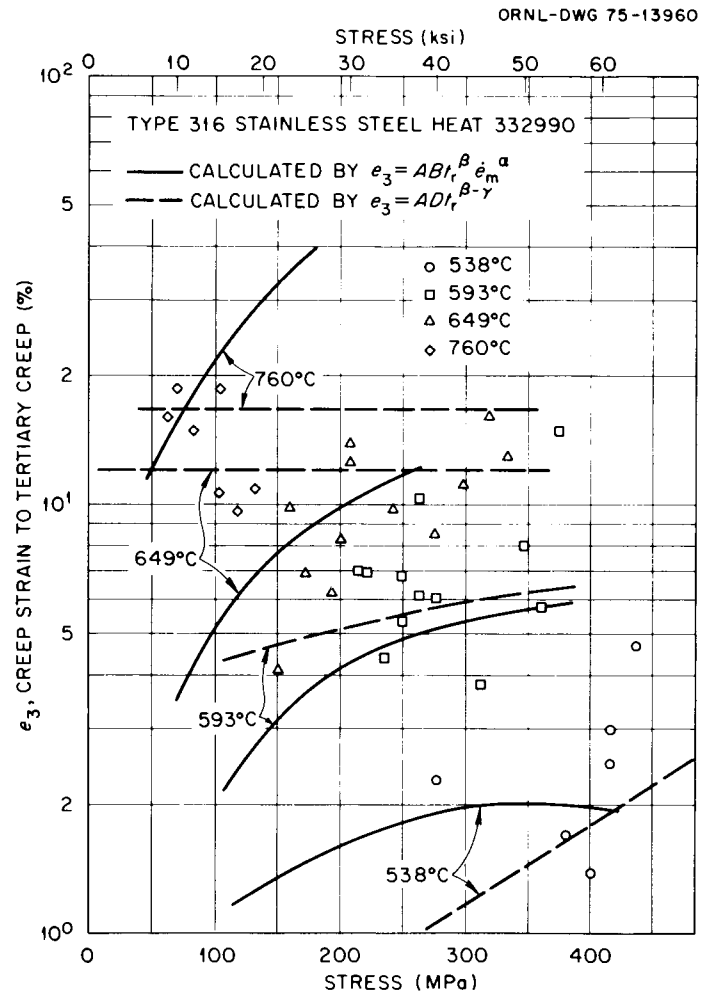

Fig. 3.48. Variation of Strain to Tertiary Creep with Stress for Heat 332990 of Type 316 Stainless Steel. Lines calculated by Eqs. (5) and (6).

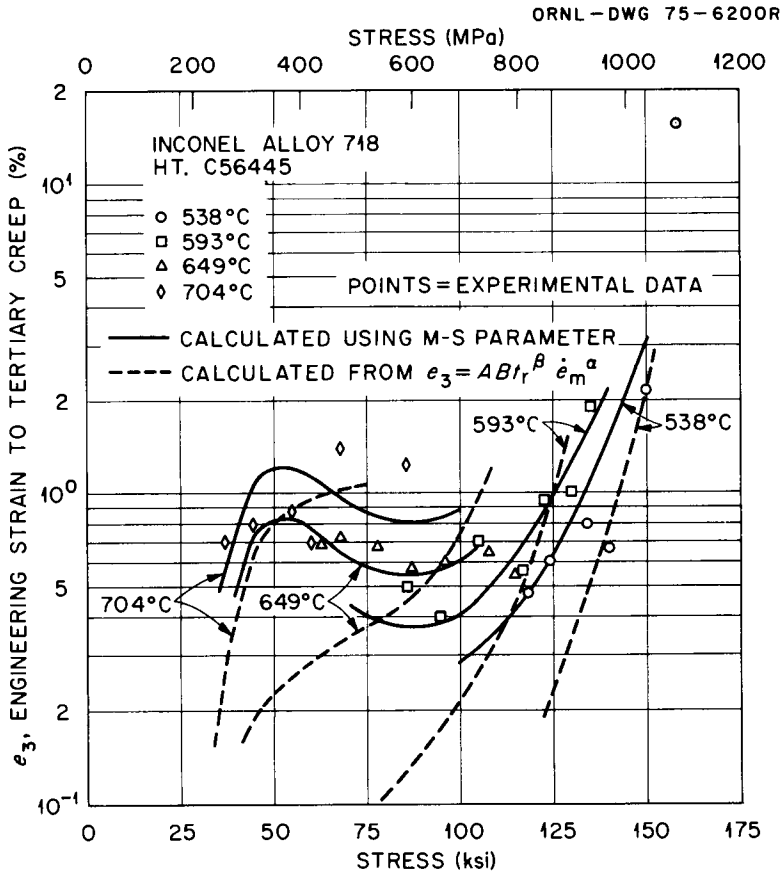

Fig. 3.49. Variation of Strain to Tertiary Creep with Stress for Heat C56445 of Inconel Alloy 718. Solid lines from Ref. 21; dashed lines calculated by Eq. (5).

comparable to the parametric results from Ref. 21. It should be noted that, although Eqs. (6) and (8) do not yield different predictions for different heats for e_3 as a function of t_r, they can yield different predictions for e_3 as a function of σ, since different heats have different rupture strengths.[3]

Use of ductility or strain limits in design is briefly reviewed in Ref. 21. Obviously, predictions cannot yield a precise value for e_3 (or any other ductility index) because of scatter in the data. The current method does, however, allow one to discern trends that might otherwise be hidden by the scatter. Thus, a designer might use such predictions to get some feel for how some changes in operating conditions might affect material ductility or to aid in materials selection. Also,

the current predictions provide a basis for examining the current 1% strain limits[19] in ASME Code Case 1592. Tables 3.17 and 3.18 show predictions for strain to tertiary creep for the materials examined here at various values of rupture life. The minimum values in these tables were calculated by the method outlined in Ref. 21, which yielded the "safety factors" on Eqs. (3) and (4) and from Ref. 20 [and thus on Eqs. (5) and (6)], as tabulated in Table 3.19.

From Figs. 3.47 through 3.49 and from Table 3.18, the trends that emerge are similar to those discussed in Ref. 21, except that Eqs. (6) and (8) restrict the trends in e_3 to being monotonic (either increasing or decreasing) with t_r. For the austenitic stainless steels, at a given stress, e_3 increases with temperature from 538 to 704°C. Also, these materials exhibit a decrease in e_3 at constant temperature as the stress is decreased (or rupture life increased). Trends in the data for Inconel Alloy 718 are more complicated, although again in general the predicted values of e_3 increased with both stress and temperature. As in Ref. 21, no clear trends were apparent in the data for 2 1/4 Cr-1 Mo steel. The data and their implications are discussed further in Ref. 21.

3.2.4.2 Development of Creep Equation for Type 316 Stainless Steel — W. E. Stillman*

A detailed analysis was made of the derivation, accuracy, and applicability of the current NSMH creep equation[6] for 316 stainless steel:

$$\varepsilon_c = \varepsilon_x(1 - e^{-st}) + \varepsilon_t(1 - e^{-rt}) + \dot{\varepsilon}_m t \ , \tag{11}$$

$$\varepsilon_x = \begin{cases} 0 & \text{for } \sigma \leqslant 28 \text{ MPa (4000 psi)} \\ G + H\sigma & \text{for } \sigma > 28 \text{ MPa (4000 psi)} \end{cases} , \tag{12}$$

$$s = D[\sinh(\beta\sigma/n)]^n \exp(-Q/RT) \text{ or}$$
$$s = 2.5 \times 10^{-2}, \text{ whichever is larger} \ , \tag{13}$$

*Consultant from The University of Tennessee.

Table 3.17. Predicted Values for Creep Strain to Tertiary Creep from Eq. (5)

Temperature		Predicted Strain, %, for Rupture Time[a]			
(°C)	(°F)	10^2 hr	10^3 hr	10^4 hr	10^5 hr
		Heat 9T2796 25-mm Plate 304 Stainless			
538	1000	2.13(0.83)	2.03(0.79)	1.85(0.72)	1.61(0.63)
593	1100	4.75(1.85)	4.25(1.66)	3.60(1.40)	2.85(1.11)
649	1200	9.01(3.51)	7.47(2.91)	5.81(2.26)	4.30(1.68)
704	1300	14.46(5.64)	11.16(4.35)	8.22(3.20)	5.98(2.33)
		Heat 9T2796 51-mm Plate 304 Stainless			
538	1000	1.24(0.48)	1.25(0.49)	1.07(0.42)	0.80(0.31)
593	1100	3.82(1.49)	3.02(1.18)	2.14(0.83)	1.56(0.61)
649	1200	7.64(2.98)	5.36(2.09)	4.18(1.63)	3.99(1.56)
704	1300	12.60(4.91)	10.26(4.00)	10.28(4.01)	11.37(4.43)
		Heat 55697 7.0-mm Rod 304 Stainless			
538	1000	3.30(1.29)	2.41(0.94)	2.00(0.78)	1.70(0.66)
593	1100	6.33(2.47)	5.39(2.10)	4.41(1.72)	2.56(1.00)
649	1200	13.28(5.18)	10.45(4.08)	5.33(2.08)	1.11(0.43)
		Heat 8043813 25-mm Plate 304 Stainless			
538	1000	7.08(2.76)	5.20(2.03)	3.64(1.42)	2.20(0.86)
593	1100	9.92(3.87)	6.54(2.55)	4.08(1.59)	2.96(1.15)
649	1200	11.00(4.29)	6.66(2.60)	4.06(1.58)	3.19(1.24)
704	1300	10.88(4.24)	6.90(2.69)	4.88(1.90)	4.72(1.84)
		Heat 332990 7.0-mm Rod 316 Stainless			
538	1000	1.57(0.71)	1.73(0.78)	1.50(0.68)	1.10(0.50)
593	1100	3.52(1.58)	2.71(1.22)	1.88(0.85)	1.33(0.60)
649	1200	4.62(2.08)	3.17(1.43)	2.44(1.10)	2.74(1.23)
704	1300	5.30(2.38)	4.39(1.98)	5.77(2.60)	18.08(8.14)
		Garofalo et al. 12.7-mm Bar Type 316			
593	1100	6.68(1.60)	8.62(2.07)	10.32(2.48)	10.81(2.59)
649	1200	13.28(3.19)	15.35(3.68)	15.05(3.61)	11.22(2.69)
704	1300	21.26(5.10)	20.10(4.82)	14.26(3.42)	7.87(1.89)
		2 1/4 Cr-1 Mo Various Heats			
482	900	0.44(0.10)	1.72(0.41)	4.43(1.06)	8.35(2.00)
538	1000	1.19(0.28)	2.69(0.64)	4.56(1.09)	6.14(1.47)
593	1100	1.56(0.37)	2.52(0.60)	3.26(0.78)	3.63(0.87)
649	1200	1.42(0.34)	1.82(0.44)	2.01(0.48)	
		Inconel Alloy 718 Heat C56445 25.4-mm Pancake			
538	1000	2.34(0.40)	0.65(0.11)	0.20(0.03)	0.08(0.01)
593	1100	1.00(0.17)	0.36(0.06)	0.17(0.03)	0.10(0.02)
649	1200	0.76(0.13)	0.42(0.07)	0.31(0.05)	0.16(0.03)
704	1300	1.09(0.18)	0.86(0.15)	0.15(0.02)	0.00(0.00)
		Inconel Alloy 718 Heat Y8509 15.9-mm Bar			
538	1000	3.62(0.62)	1.12(0.19)	0.36(0.06)	0.12(0.02)
593	1100	1.74(0.30)	0.58(0.10)	0.20(0.03)	0.08(0.01)
649	1200	0.20(0.03)	0.38(0.06)	0.17(0.03)	0.11(0.02)
704	1300	0.77(0.13)	0.39(0.07)	0.22(0.04)	0.06(0.01)

[a]Values in parentheses are lower limits.

Table 3.18. Predicted Values for Creep Strain to Tertiary Creep from Eq. (6)

Temperature		Predicted Strain, %, for Rupture Time[a]			
(°C)	(°F)	10^2 hr	10^3 hr	10^4 hr	10^5 hr
		Type 304 Stainless Steel			
583	1000	2.88(0.69)	2.55(0.61)	2.26(0.54)	2.00(0.48)
593	1100	6.13(1.41)	3.69(0.85)	2.22(0.51)	1.33(0.30)
649	1200	11.26(2.82)	8.70(2.18)	6.72(1.68)	5.20(1.30)
704	1300	14.25(3.42)	10.97(2.63)	8.28(1.99)	6.25(1.50)
760	1400	19.15(6.13)	16.80	14.73(5.38)	12.92(4.13)
		Type 316 Stainless Steel — G			
593	1100	11.32(5.21)	9.55(4.39)	8.05(3.70)	6.79(3.12)
704	1300	18.22(8.02)	15.26(6.71)	12.78(5.62)	10.70(4.71)
816	1500	14.31(6.44)	11.39(5.12)	9.07(4.08)	7.22(3.25)
		Type 316 Stainless Steel — H			
538	1000	1.88(0.28)	1.33(0.20)	0.94(0.14)	0.67(0.10)
593	1100	5.75(1.15)	5.32(1.06)	4.92(0.98)	4.54(0.91)
649	1200	12.16(4.86)	12.13(4.85)	12.10(4.84)	12.07(4.83)
760	1400	16.67(7.00)	16.67(7.00)	16.67(7.00)	16.67(7.00)
		Inconel 718 — T			
593	1100	0.85(0.02)	0.85(0.02)	0.84(0.02)	0.84(0.02)
649	1200	1.90(0.30)	0.76(0.12)	0.30(0.05)	0.12(0.02)
704	1300	0.16(0.06)	0.35(0.14)	0.75(0.31)	1.62(0.66)
760	1400	0.75(0.06)	0.62(0.05)	0.52(0.04)	0.43(0.03)
		Inconel 718 — C			
538	1000	2.34(0.09)	0.97(0.04)	0.40(0.02)	0.16(0.01)
593	1100	0.76(0.17)	0.51(0.12)	0.34(0.08)	0.23(0.05)
649	1200	0.58(0.20)	0.61(0.21)	0.65(0.23)	0.68(0.24)
704	1300	1.19(0.20)	0.77(0.13)	0.50(0.08)	0.33(0.06)
		2 1/4 Cr-1 Mo Steel			
538	1000	2.28(0.32)	3.17(0.44)	4.40(0.62)	6.12(0.86)
593	1100	5.88(0.65)	3.43(0.38)	2.00(0.22)	1.17(0.13)
649	1200	3.20(0.35)	2.32(0.26)	1.69(0.18)	1.22(0.13)

[a]Values in parentheses are lower limits.

Table 3.19. Safety Factor for Calculation of Minimum Values[a]

Data Set	Temperature (°C)	Safety Factors on Dependent Variable in				
		Eq. (3)	Eq. (4)	Ref. 20	Eq. (5)[b]	Eq. (6)[c]
304 Stainless	538	0.66	0.40	0.59	0.39	0.24
	593	0.66	0.39	0.59	0.39	0.23
	649	0.66	0.43	0.59	0.39	0.25
	704	0.66	0.41	0.59	0.39	0.24
	760	0.66	0.55	0.59	0.39	0.32
316 Stainless — G	593	0.38	0.74	0.62	0.24	0.46
	704	0.38	0.71	0.62	0.24	0.44
	816	0.38	0.73	0.62	0.24	0.45
316 Stainless — H	538	0.73	0.24	0.62	0.45	0.15
	593	0.73	0.33	0.62	0.45	0.20
	649	0.73	0.65	0.62	0.45	0.40
	760	0.73	0.67	0.62	0.45	0.42
Inconel 718 — T	593	0.30	0.04	0.58	0.17	0.02
	649	0.30	0.27	0.58	0.17	0.16
	704	0.30	0.71	0.58	0.17	0.41
	760	0.30	0.14	0.58	0.17	0.08
Inconel 718 — C	538	0.29	0.07	0.58	0.17	0.04
	593	0.29	0.39	0.58	0.17	0.23
	649	0.29	0.60	0.58	0.17	0.35
	704	0.29	0.30	0.58	0.17	0.17
2 1/4 Cr-1 Mo	538	0.40	0.23	0.62	0.25	0.14
	593	0.40	0.18	0.62	0.25	0.11
	649	0.40	0.24	0.62	0.25	0.15

[a]Minimum value of e_3, $\dot{e}_3$, or t_3 is given by the product of the expected value and the safety factor.

[b]Safety factor on Eq. (5) is the product of the factors from Eq. (3) and Ref. 20. This factor does not include a measure of the uncertainty in the value of $\dot{e}_m$ for a given t_r, but is felt to be adequately conservative.

[c]Safety factor on Eq. (6) is the product of the factors from Eq. (4) and Ref. 20.

$$r = B[\sinh(\beta\sigma/n)]^n \exp(-Q/RT) \text{ or}$$

$$r = L\sigma^{n-3.6}, \text{ whichever is larger ,} \tag{14}$$

$$\dot{\varepsilon}_m = A[\sinh(\beta\sigma/n)]^n \exp(-Q/RT) \tag{15}$$

$$\dot{\varepsilon}_t = C\dot{\varepsilon}_m/r \ . \tag{16}$$

Several severe objections to the continued use of this equation are set forth below. Additional details are reported elsewhere.[33]

1. The equation parameters (ε_t, r, ε_x, s, $\dot{\varepsilon}_m$), when varied through the temperature range of 427 to 760°C (800–1400°F), demonstrate highly unusual variation between discrete temperature levels [56°C (100°F) increments], with no supporting evidence to justify these irregularities.

2. Several of the parametric coefficents (A, B, etc.) show serious misfits at their temperature interfaces. Also the precision used in their computation is quite inconsistent.

3. The overall complexity of the equation produces unnecessarily high computational costs in structural problems.

4. Primary strain factors do not demonstrate a decrease at higher stress levels, although the data so indicate.[34]

5. The initial strain rate $\dot{\varepsilon}_i$ is shown not to vary linearly with minimum creep rate $\dot{\varepsilon}_m$ except at 760°C (1400°F). The equation postulates a linear dependence, while, in general, $\dot{\varepsilon}_i/\dot{\varepsilon}_m$ is a function of stress for a given temperature.

An effort was made to derive a single nonlinear equation to describe the minimum creep rate of a form similar to Eq. (15):

$$\dot{\varepsilon}_m = A[\sinh(\beta\sigma)]^n \exp(-Q/RT) \ . \tag{17}$$

First n was assumed to be constant with an approximate value of 6. Plots indicated that β had a form $\beta = a + bT$ and that A could be modeled $A = c \exp(-dT)$. Several combinations were used in an effort to obtain a best fit to the data obtained[35] at Hanford Engineering Development Laboratory (HEDL). A nonlinear least squares curve fitting package was used to obtain the following equations:

$$\dot{\varepsilon}_m = 5.416 \times 10^{45} \exp(-0.000242T)$$
$$\times [\sinh(-3.48 + 0.0006458T)\sigma/1000]^{10.61} \exp(-55730/RT) \ , \tag{18}$$

$$\dot{\varepsilon}_m = 2.993 \times 10^{39}[\sinh(-0.1347 + 0.000255T)\sigma/1000]^{10.714}$$
$$\times \exp(-56010/RT) \ , \tag{19}$$

$$\dot{\varepsilon}_m = 4.094 \times 10^{45} \exp(-6.132 \times 10^{-9}T)$$
$$\times [\sinh(-3.591 + 6.224 \times 10^{-4}T)\sigma/1000]^{10.034} \exp(-60180/RT) \ , \qquad (20)$$

where R = gas constant,

T = temperature, K, and

σ = stress, ksi (1 ksi = 6.89 MPa).

The computed rms errors of these forms are 0.6158, 0.4304, and 0.4220, respectively. Equation (20) was obtained from (18) by assigning weights of 1.7 to the 760°C (1400°F) data and 2.0 to the 538°C (1000°F) data, the others being weighted at 1. An effort to model n as a linear function in T failed. Other modifications were deemed fruitless. The best nonlinear fit, Eq. (20), is plotted in Fig. 3.50, together with measured data. Agreement is disappointing.

Further effort along this line can best be appraised by reference to Fig. 3.51 and 3.52. In Fig. 3.51 the natural logarithm of the Zener-Hollomon parameter ($Z = \dot{\varepsilon}_m e^{Q/RT}$) is plotted against stress for an activation energy of $Q = 60{,}000R$ [≈ 120,000 cal/mole (0.5 MJ/mole)], with the scatter from a double straight line fit fairly small. The apparent activation energy for primary creep is found to approximate $45{,}000R$ [≈ 90,000 cal/mole (0.38 MJ/mole)]. With this value a similar plot is made in Fig. 3.52 with $re^{Q/RT}$ replacing Z. Note the substantially greater amount of scatter from a double straight line fit.

In view of the difficulties already elucidated in obtaining an acceptable fit to $\dot{\varepsilon}_m$ with a single nonlinear equation, one concludes from Fig. 3.52 that a similar effort with respect to primary creep time factor, r, would be unreasonable. This leads to a decision to abandon further consideration of this method of attack, in favor of linear statistical fitting.

A series of linear equations was fitted to the HEDL data by means of a least squares numerical technique. The resulting best fits found for each parameter are shown, together with corresponding rms errors.

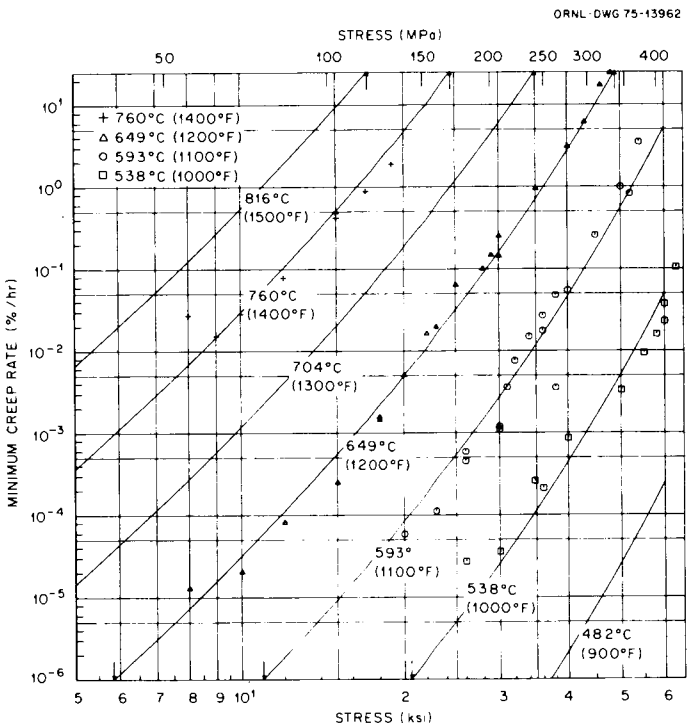

Fig. 3.50. Nonlinear Best Fit for Minimum Creep Rate of Type 316 Stainless Steel, HEDL Data.

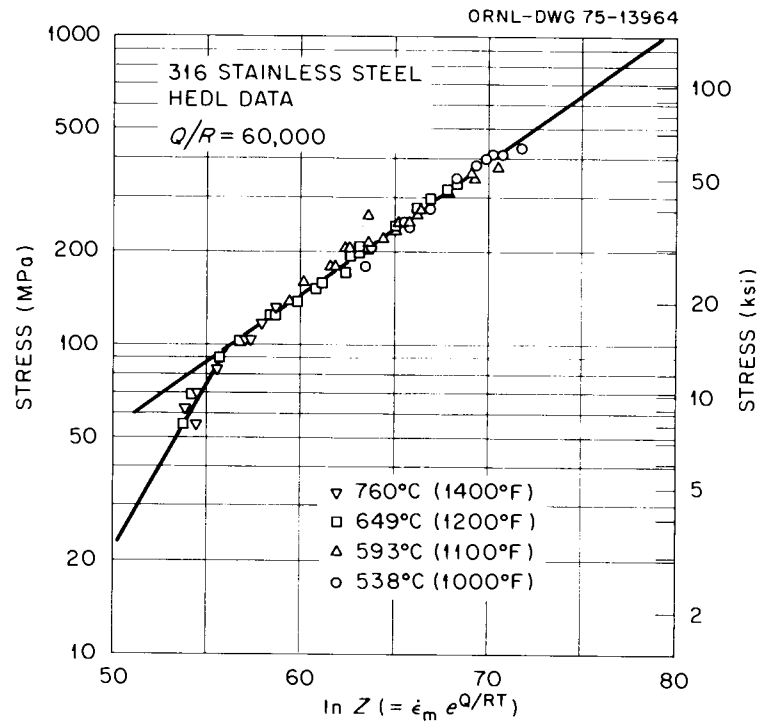

Fig. 3.51. Stress for an Activation Energy of 60,000R as a Function of the Zener-Hollomon Parameter for HEDL Data on Type 316 Stainless Steel.

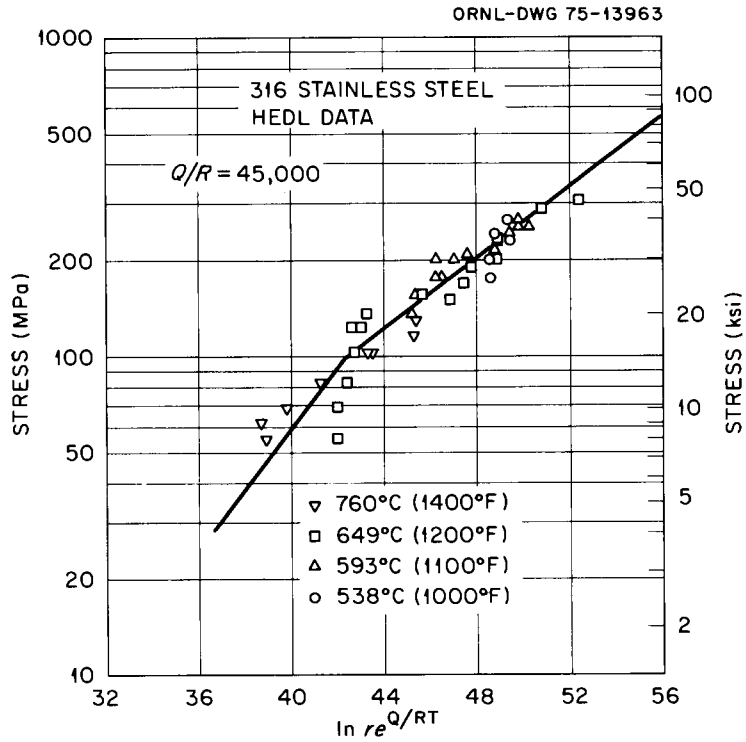

Fig. 3.52. Stress for an Activation Energy of 45,000R as a Function of re exp(Q/RT) for HEDL Data on Type 316 Stainless Steel.

$$\ln \dot{\varepsilon}_m = 39.37 - 58{,}580/T + 0.1257\sigma + 5.457 \ln \sigma,$$

$$\text{rms error} = 0.3745 \; ; \tag{21}$$

$$\ln \varepsilon_t = 2.293 - 3050/T + 0.05263\sigma - 0.00249\sigma^2,$$

$$\text{rms error} = 0.2112 \; ; \tag{22}$$

$$\ln r = 36.167 - 45{,}090/T + 0.5190\sigma - 0.004096\sigma^2,$$

$$\text{rms error} = 0.9739 \; ; \tag{23}$$

$$\ln \varepsilon_x = -13.58 + 11{,}135/T - 0.06442\sigma + 0.006094\sigma^2 - 0.0001393\sigma^3,$$

$$\text{rms error} = 0.2652 \; ; \tag{24}$$

$$\ln s = 59.16 - 60{,}270/T + 0.4008\sigma - 0.003985\sigma^2,$$

$$\text{rms error} - 0.6243 \; . \tag{25}$$

These equations are plotted, together with experimental data, on Figs. 3.53 through 3.57.

Several observations can be made about these results. The minimum creep rate enjoys a much better fit in Fig. 3.53 than in Fig. 3.50. It is evident that extrapolation to the low-stress low-temperature regime is unlikely to cause any difficulty. The combination of σ and $\ln \sigma$ in the equation seems consistent with the observations of Garofalo,[36] and the constant 5.457 pertains to the value of n in a resulting hyperbolic sine relationship. Garofalo also noted that the primary strain appears to decrease with increasing stress beyond a certain critical point. This behavior is apparent in Fig. 3.54 with the stress at which ε_t peaks approximately 262 MPa (38 ksi). It is hoped that the use of more data will ameliorate the problem of scatter for this parameter.

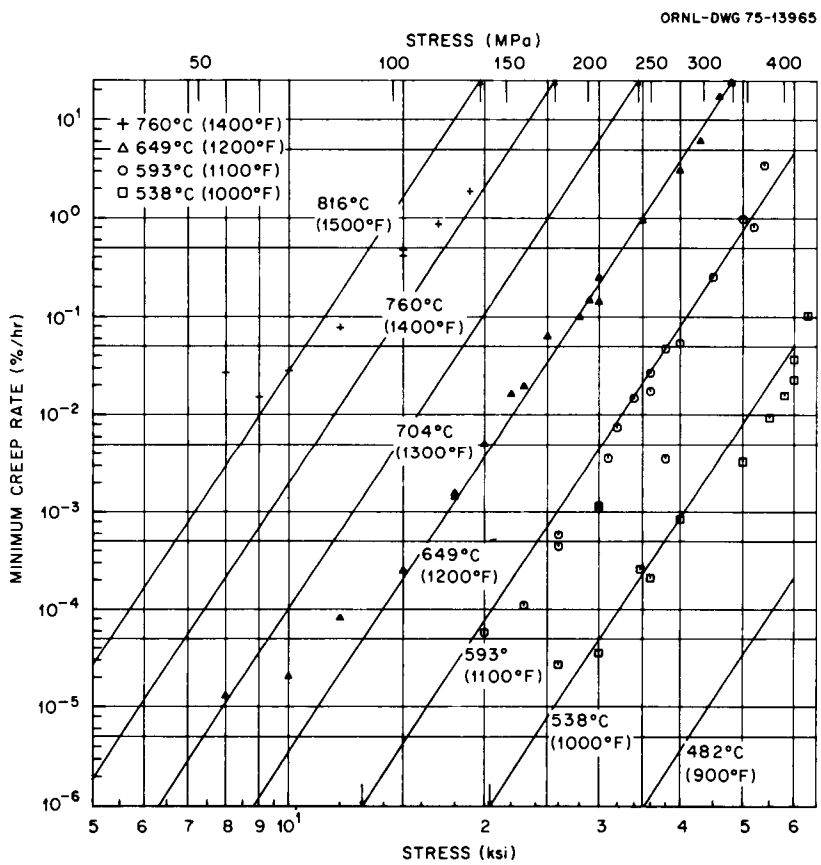

Fig. 3.53. Minimum Creep Rate, $\dot{\varepsilon}_m$, Isotherms for Type 316 Stainless Steel, HEDL Data.

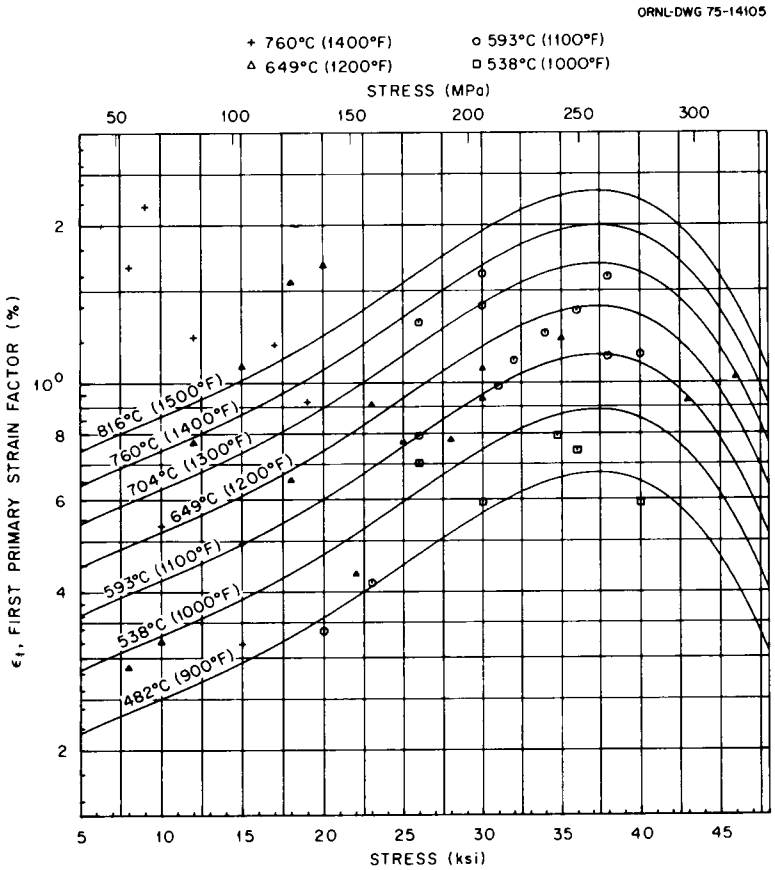

Fig. 3.54. First Primary Creep Strain Factor, ε_t, Isotherms for Type 316 Stainless Steel, HEDL Data.

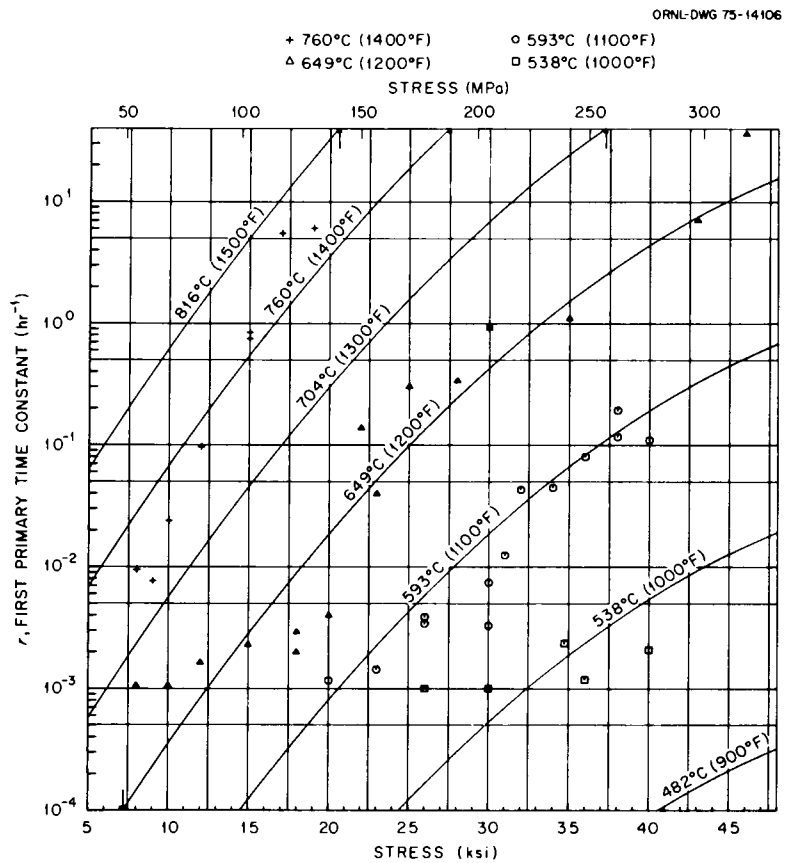

Fig. 3.55. First Primary Creep Strain Time Constant, r, Isotherms for Type 316 Stainless Steel, HEDL Data.

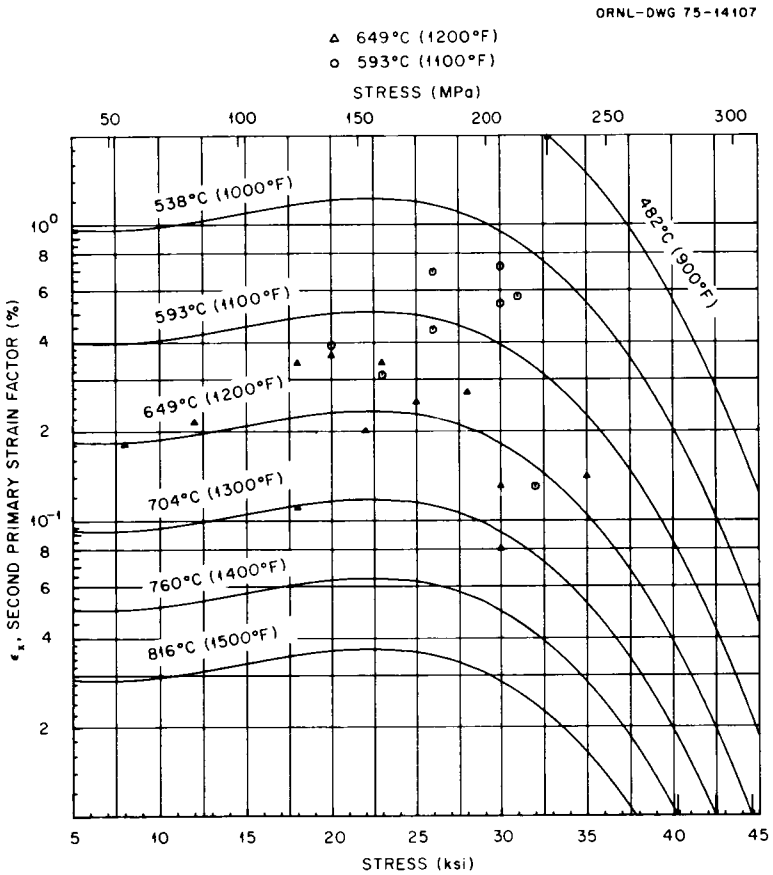

Fig. 3.56. Second Primary Creep Strain Factor, ε_x, Isotherms for Type 316 Stainless Steel, HEDL Data.

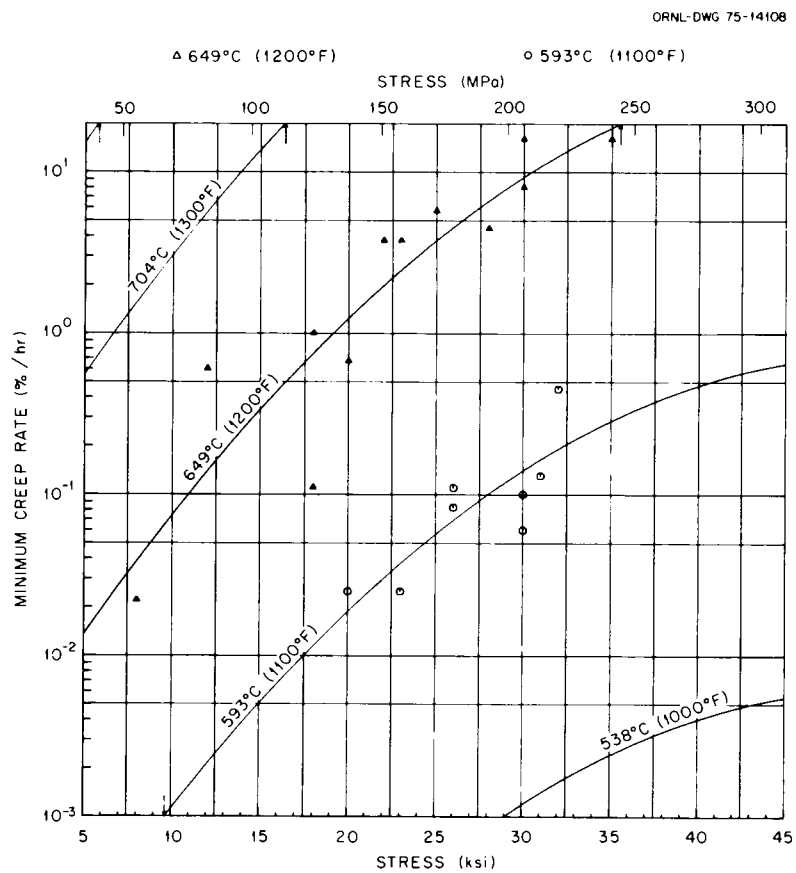

Fig. 3.57. Second Primary Creep Strain Time Constant, s, Isotherms for Type 316 Stainless Steel, HEDL Data.

A further consideration is the best form of the final recommended creep equation. Equation (11) superseded an earlier single-exponential version:

$$\varepsilon_c = \varepsilon_t(1 - e^{-rt}) + \dot{\varepsilon}_m t \ . \tag{26}$$

Suggested alternate forms include single and double rational polynomial terms of the type proposed[37] for 2 1/4 Cr-1 Mo steel:

$$\varepsilon_c = \frac{t}{a + bt} + \dot{\varepsilon}_m t \ , \tag{27}$$

$$\varepsilon_c = \frac{t}{a + bt} + \frac{t}{c + dt} + \dot{\varepsilon}_m t \ , \tag{28}$$

with the second term intended to be parallel to the second exponential term.

At present an operation is under way to fit curves of the form (11), (26), (27), (28) to all available measured creep-time data. The information in hand includes 56 tests from HEDL, 45 tests from ORNL, and 79 proprietary tests.

The early indications are that the form of the equation (of the four suggested) is not of overriding importance. This is consistent with some of the observations of Pugh.[38] To illustrate, consider a test at 117 MPa (17 ksi) and 649°C (1200°F). The equations derived are

$$\varepsilon_c = \frac{t}{223.32 + 0.67727t} + 5.7367 \times 10^{-4} t \ , \tag{29}$$

$$\varepsilon_c = 0.8484 \ (1 - e^{-0.004494t}) + 8.432 \times 10^{-4} t \ , \tag{30}$$

$$\varepsilon_c = \frac{t}{521.85 + 1.6084t} + \frac{t}{390.26 + 1.1699t} + 5.7366 \times 10^{-4} t \ , \tag{31}$$

$$\varepsilon_c = 0.80865 \ (1 - e^{-0.00456t}) + 0.5187 \ (1 - e^{-5.492 \times 10^{-4} t}) + 6.620 \times 10^{-4} t \ . \tag{32}$$

The rms errors are, respectively, 0.035266, 0.033727, 0.036462, 0.035217. Note that the single exponential and rational forms fit better than the double forms of each. In addition the single rational form is comparable in accuracy with the double exponential. The corresponding plots are shown in Fig. 3.58. Further evaluation of test data may reveal the acceptability of the single rational polynomial form.

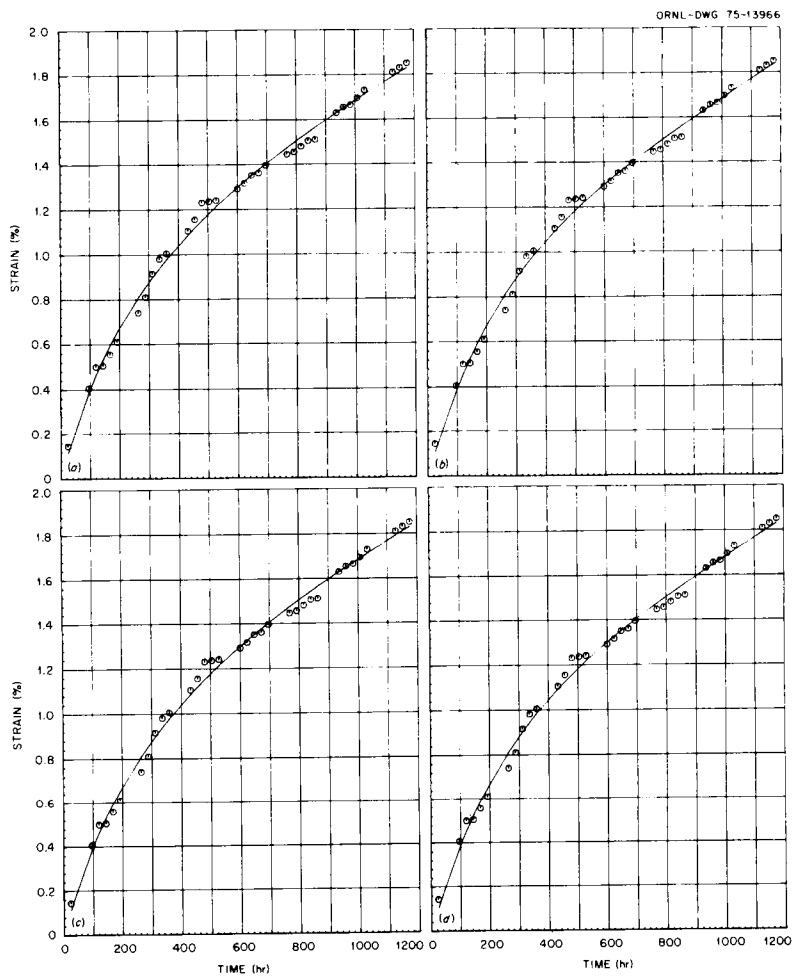

Fig. 3.58. Comparison of Analytical Creep Curves with the Same Experimental Measurements. (a) Single rational form. (b) Single exponential form. (c) Double rational form. (d) Double exponential form. Note that the four curves are almost indistinguishable.

3.2.5 Material Data Processing — M. K. Booker, B.L.P. Booker,* and C. O. Stevens

The computerized mechanical properties data processing system continues to function, expand, and develop. During the past quarter, efforts have been made to store all available tensile and creep data being used in the ORNL program[39] of mechanical properties correlations for annealed 2 1/4 Cr-1 Mo steel in support of the *Nuclear Systems Materials Handbook*. Total tests stored in DSRS now number 6918, of which 1088 contain data for 2 1/4 Cr-1 Mo steel.

In addition, a new version of the FATIGUE computer program[40] is being developed. This new program,[41] to be called ØRFAN (Oak Ridge Fatigue Analysis Program) will include substantially increased capability and flexibility. The basic program provides the same services as FATIGUE; however, in ØRFAN, the user will be able to specify a wide variety of options including increased plotting capabilities. Also, additional computational subroutines will allow analysis of hold-time fatigue data by the methods of strain range partitioning and linear summation of creep and fatigue damage. Thus, in one program raw strip chart and hysteresis loop readings will be ingested and converted into tabular and graphical output for analysis of cyclic stress-strain behavior, relaxation behavior, etc. Then, the same program will be able to use this information to produce completed analyses of the data.

3.2.6 Elastic Properties of Engineering Construction Materials — J. P. Hammond

Precise measurements show that for metals the "elastic" stress-strain relationships are not perfectly linear, even at low stresses and strain levels, and they become progressively more nonlinear as stress increases. Discrepancies thus often occur between elastic constants determined at different strain levels and rates of strain (for example, constants determined by dynamic and static techniques).

The purpose of this program is to correlate the two separate categories of elastic constants (dynamic and static) for reactor materials

---

*Consultant.

of interest, giving specific attention to temperature and other significant test variables. In addition to elastic constants (Young's modulus, E; shear modulus, G; and Poisson's ratio, ν), elastic and proportional limits (E.L. and P.L.) will be determined. This information is needed to enable more exact and enlightened use of this class of information in engineering design and structural verification work.

3.2.6.1 Elastic Properties Determined by Static Tests

Whereas in the dynamic (sonic) method of determining elastic constants, by convention, a single test specimen is used repetitively for obtaining a complete set of data points that may extend over a considerable temperature range, in the case of static testing a separate sample generally is used for each data point. The reason for this difference in practice is that with dynamic tests the stress levels are very low [7—70 kPa (1—10 psi)], and time of testing at elevated temperature is comparatively short. Therefore use history may have little effect on elastic behavior. However, in static tests, the stress levels ordinarily are quite high, and for elevated-temperature testing the time to acquire a complete set of data is substantial. Under these conditions, thermal-mechanical history may have a significant effect on properties, and for this reason a separate specimen is generally employed for each data point. This has the disadvantage of considerable expense in specimen preparation and mounting. Further, specimen-to-specimen effects and their associated effect on stress alignment in the specimen is a problem.

In our determinations of static elastic constants (with LVDT strain sensors), we are taking a different approach in that a single specimen is used repetitively for determining a complete set of data points over the entire temperature test range, much as is done in dynamic testing. To minimize effects from inelastic strain, test runs are confined to strains no higher than 1.2 to 1.5 $\times 10^{-4}$, which are well within the elastic range for the materials being tested. Whether or not the material's elastic limit is exceeded is assessed by whether strain is completely recoverable with removal of stress. By employing a single specimen throughout a data set and allowing the specimen to remain undisturbed

within the load train for the series so as to assure an identical distribution of stress within the specimen between individual tests, excellent resolution between data points is assured. However, because the principal stress nonetheless may not be perfectly aligned in the specimen, accuracy may be compromised. To lend accuracy to a mathematical equation representing the elastic property as a function of temperature, the elevated-temperature data are normalized to an accurately determined room-temperature data base. The latter is established as a statistical average of data taken on numerous specimens. The final model is our usual third-degree polynomial incorporating the $(T - T_0)$ expression, where T is test temperature and T_0 room temperature.

Notwithstanding these advantages, the resulting mathematical expression still may be somewhat in error as a result of a "softening" or "hardening" of the test material that could result from thermally activated processes such as recovery or aging. We are presently evaluating this effect for 2 1/4 Cr-1 Mo steel and type 304 stainless steel. Where the effect is appreciable, conceivably a correction could be applied.

A factor that weighed heavily in taking the single-specimen approach in our elastic property studies was the fact that costs would be prohibitively high for determining elastic constants by the resistance strain gage method, where the gages and their attendant procedures are so costly. Moreover, the strain gage method is our best approach to obtaining static Poisson's ratios and, in turn, shear moduli. Our plan, therefore, has been to qualify a procedure of conducting a complete series of tests on a single specimen by the LVDT method in terms of strain levels and thermal history, and subsequently apply it to the resistance strain gage method. Such procedures have been qualified for both 2 1/4 Cr-1 Mo steel and type 304 stainless steel. In the process, additional modulus data were obtained by the LVDT method. These are being processed to develop more accurate models for Young's modulus by this method.

In evaluating the effects of repetitive use of a single specimen on Young's modulus some "softening" occurred in the upper region of the test temperature range for both 2 1/4 Cr-1 Mo steel and type 304 stainless.

The amounts expressed in terms of percent of lowering of Young's modulus at two separate check temperatures are listed below:

2 1/4 Cr-1 Mo steel, heat 20017, isothermally annealed condition:
0.6% at 482°C (900°F); 1.4% at 704°C (1300°F).

Type 304 stainless steel, heat 9T2796, mill-annealed condition:
0.9% at 538°C (1000°F); 2.6% at 704°C (1300°F).

In the temperature ranges ordinarily prescribed for use of these materials the effects are hardly appreciable. However, at inordinately high temperatures the effects are possibly significant, and a correction for softening may be appropriate.

The following technique was used for evaluating the softening effect. A fresh specimen is used to determine the elastic property at the check temperature. Before the test, a modulus determination is made at room temperature and compared with the room-temperature normalization base (statistical average of data determined on numerous specimens) to establish a bias correction factor to apply to the check value. This factor corrects for stress misalignment in the check specimen. After this correction is applied, the degree of depression or elevation attributable to repetitive use is assessed by comparing the "fresh" value with a "repetitive" value calculated by the mathematical model for the property.

3.2.6.2 Correlation of Elastic Constants

A correlation was completed on the static and dynamic elastic constants of 2 1/4 Cr-1 Mo steel. The data base used for this correlation consisted of our early data[42] on the dynamic elastic constants (E, G, and ν) of this material; parallel information of Timken Roller Bearing Company[43] on dynamic E, G, and ν; recent unpublished ORNL data on static E (ε = 0.01/hr), and data of Garofalo[44] on static ν. Values of the static G were calculated from the ORNL static E values and the Garofalo ν by the relationship $G = E/2(1 + \nu)$.

A comparison of the ORNL dynamic data with Timken's gave remarkably good agreement for E and G but differences as large as 10% were noted for the dynamic Poisson's ratio. Because the conditions of test were

better documented for the ORNL data, our dynamic E and G data were used, but averages between the ORNL and Timken data were employed for dynamic ν. A significant difference was cited between the ORNL static E data and the long-employed ASME Pressure Vessel Code (Case 1592) values[19] at high temperatures. The ORNL data were favored again because of better documentation of the significant test conditions.

Interpretations of the ORNL dynamic data[42] and our static E data[45] were reported previously. Because treatment of the Garofalo static ν data and our calculated static G values (determined from Garofalo's ν and our E) had not been previously reported, estimates of these properties as a function of temperature are given in Table 3.20. The derived polynomial equations from which the results were calculated are given below:

Poisson's ratio:

$$\nu = 0.2588 + 2.627 \times 10^{-4}T - 4.082 \times 10^{-7}T^2, \quad 24 \leqslant T \leqslant 649°\text{C}$$

$$= 0.254 + 1.54 \times 10^{-4}T - 1.26 \times 10^{-7}T^2, \quad 75 \leqslant T \leqslant 1200°\text{F} .$$

Shear modulus:

$$G = 82.8 - 0.03882T + 3.994 \times 10^{-5}T^2 - 5.621 \times 10^{-8}T^3 \text{ GPa}, \quad 24 \leqslant T \leqslant 649°\text{C}$$

$$= (12.12 - 3.245 \times 10^{-3}T + 1.891 \times 10^{-6}T^2 - 1.398 \times 10^{-9}T^3) \times 10^6 \text{ psi}, \quad 75 \leqslant T \leqslant 1200°\text{F} .$$

The derived model for the static ν (Garofalo) is compared with the dynamic ν (average of ORNL and Timken) in Fig. 3.59. The relatively high value for the dynamic ν at highest temperature resulted from characteristically high values in the Timken data at highest temperatures for a variety of steel materials. The derived model for the static G (calculated) values are compared with dynamic G (ORNL) in Fig. 3.60. Characteristically, the static values fall somewhat below the dynamic.

Table 3.20. Static Shear Moduli and Poisson's Ratios of 2 1/4 Cr-1 Mo Steel, Heat 20017

Temperature		Static Poisson's Ratio, ν	Static Shear Modulus, G	
(°C)	(°F)		(GPa)	(psi)
24	75	0.265	81.9	11.88×10^6
38	100	0.268	81.4	11.81
66	150	0.274	80.4	11.67
93	200	0.280	79.5	11.53
121	250	0.285	78.6	11.40
149	300	0.289	77.7	11.27
177	350	0.292	76.9	11.15
204	400	0.295	76.1	11.03
232	450	0.298	75.2	10.91
260	500	0.300	74.4	10.79
288	550	0.301	73.6	10.67
316	600	0.301	72.7	10.55
343	650	0.301	71.9	10.42
371	700	0.300	71.0	10.29
399	750	0.299	70.0	10.16
427	800	0.297	69.0	10.01
454	850	0.294	68.0	9.87
482	900	0.291	66.9	9.71
510	950	0.287	65.8	9.54
538	1000	0.282	64.6	9.36
566	1050	0.277	63.3	9.18
593	1100	0.271	61.9	8.97
621	1150	0.264	60.4	8.76
649	1200	0.257	58.5	8.53

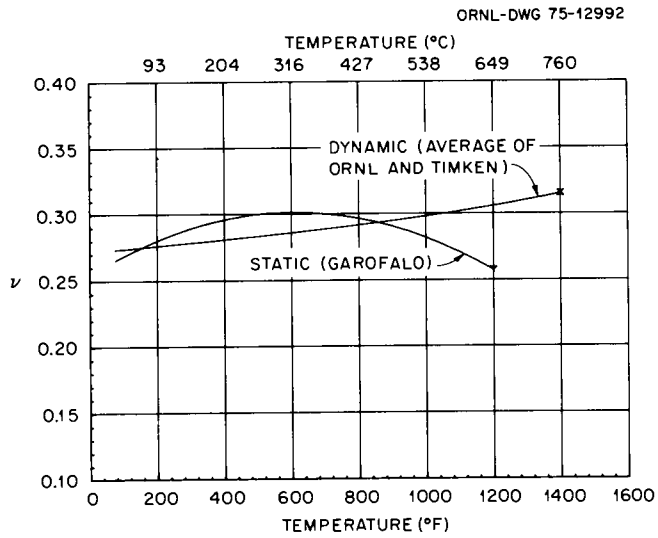

Fig. 3.59. Comparison of Poisson's Ratios on 2 1/4 Cr-1 Mo Steel

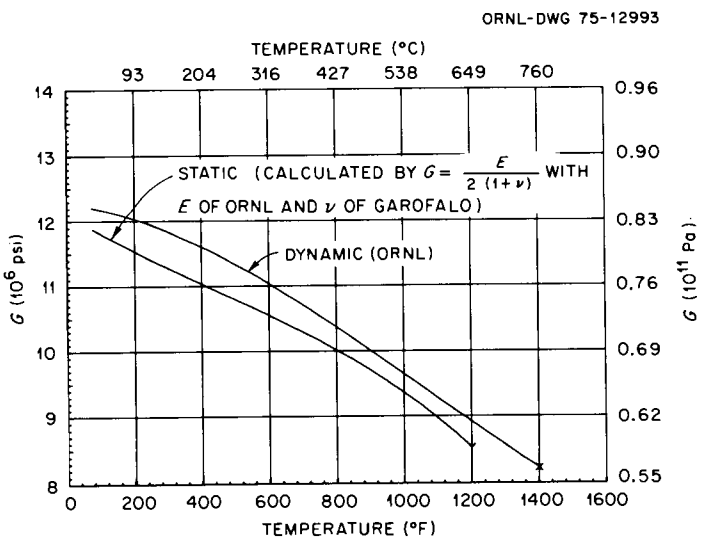

Fig. 3.60. Comparison of Shear Moduli on 2 1/4 Cr-1 Mo Steel.

3.3 MECHANICAL AND METALLURGICAL BEHAVIOR OF WELDMENTS FOR LMFBR — P. Patriarca, G. M. Slaughter, W. R. Martin, and C. R. Brinkman

3.3.1 Studies of Strain Distribution in Weldments and Room-Temperature Elastic Constants — B. R. Dewey* and R. T. King

In previous work,[46] we obtained very limited data for the elastic modulus and for Poisson's ratio from surface strain measurements on a whole weld cross section. It contained a multipass weld of type 308 CRE stainless steel in type 304 base metal. Since this work involved only surface strain measurement, only two of the nine compliance components assumed for orthotropic symmetry could be found. To find the complete set of compliances, we have commenced a series of tests of variously oriented tensile specimens. The weld metal for the test is also type 308 CRE, but made by the electroslag process. The advantage here is that the elongated subgrains are not interrupted by the interpass boundaries. This permits fabrication of reasonably sized specimens with more-or-less a unique orientation of the substructure relative to the specimen axis.

The selection of coordinate axes in the weldment is given in Fig. 3.61. The 2-axis is perpendicular to the surface of the two plates

*Subcontractor from Department of Engineering Science and Mechanics, University of Tennessee, Knoxville.

ORNL-DWG 75-13166

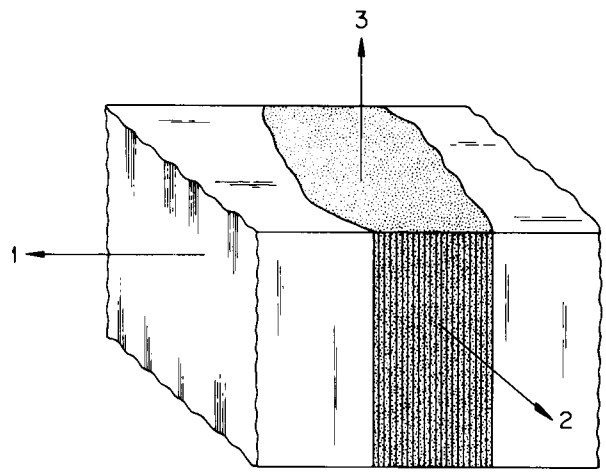

Fig. 3.61. Orientation of Axes in Weldment.

joined, and the 3-axis is in the general direction of the weld solidification. Several plates were cut from the weld section, polished, and etched to reveal the macrostructure. A section normal to the 1-axis, Fig. 3.62, shows the elongated substructure and the effect of the shoes used in fabrication extending about 2.5 mm in from the left and right sides. A very similar structure is shown in the section normal to the 2-axis, Fig. 3.63, as well as the fine-grained heat-affected zone (HAZ) (about 5 mm wide) and the base metal grains. The structure in a section normal to the 3-axis, Fig. 3.64, shows the nearly equiaxed sections normal to the elongated subgrains. The preferred growth directions shown here are very analogous to those in wood and lead to the hypothesis that the same type of elastic symmetry may exist. Orthotropic symmetry (nine independent elastic constants) has therefore been used as a working hypothesis, and we further suspect that the 1-2 plane might be a plane of isotropy.

3.3.1.1 Test Procedure

A series of tensile test specimens was fabricated from weld metal, base metal, and HAZ. Specimens were oriented with respect to the solidification direction of the subgrains. From blanks such as those shown in Fig. 3.65, specimens were fabricated with a 3.2-mm (0.125-in.) nominal diameter and a 25-mm (1-in.) reduced section. It should be noted that elongations of specimens in nonprincipal directions will be used for calculation of the shear and Poisson terms in the compliance matrix.

Writing out the relations between the strain tensor $\{\varepsilon\}$, the compliance tensor $[S]$, and the stress tensor $\{\sigma\}$ partially illustrates the method we use in determining elastic compliances,

$$\begin{Bmatrix} \varepsilon_1 \\ \varepsilon_2 \\ \varepsilon_3 \\ \varepsilon_4 \\ \varepsilon_5 \\ \varepsilon_6 \end{Bmatrix} = \begin{bmatrix} S_{11} & S_{12} & S_{13} & S_{14} & S_{15} & S_{16} \\ & S_{22} & S_{23} & S_{24} & S_{25} & S_{26} \\ & & S_{33} & S_{34} & S_{35} & S_{36} \\ & & & S_{44} & S_{45} & S_{46} \\ (\text{sym}) & & & & S_{55} & S_{56} \\ & & & & & S_{66} \end{bmatrix} \begin{Bmatrix} \sigma_1 \\ \sigma_2 \\ \sigma_3 \\ \sigma_4 \\ \sigma_5 \\ \sigma_6 \end{Bmatrix}, \qquad (33)$$

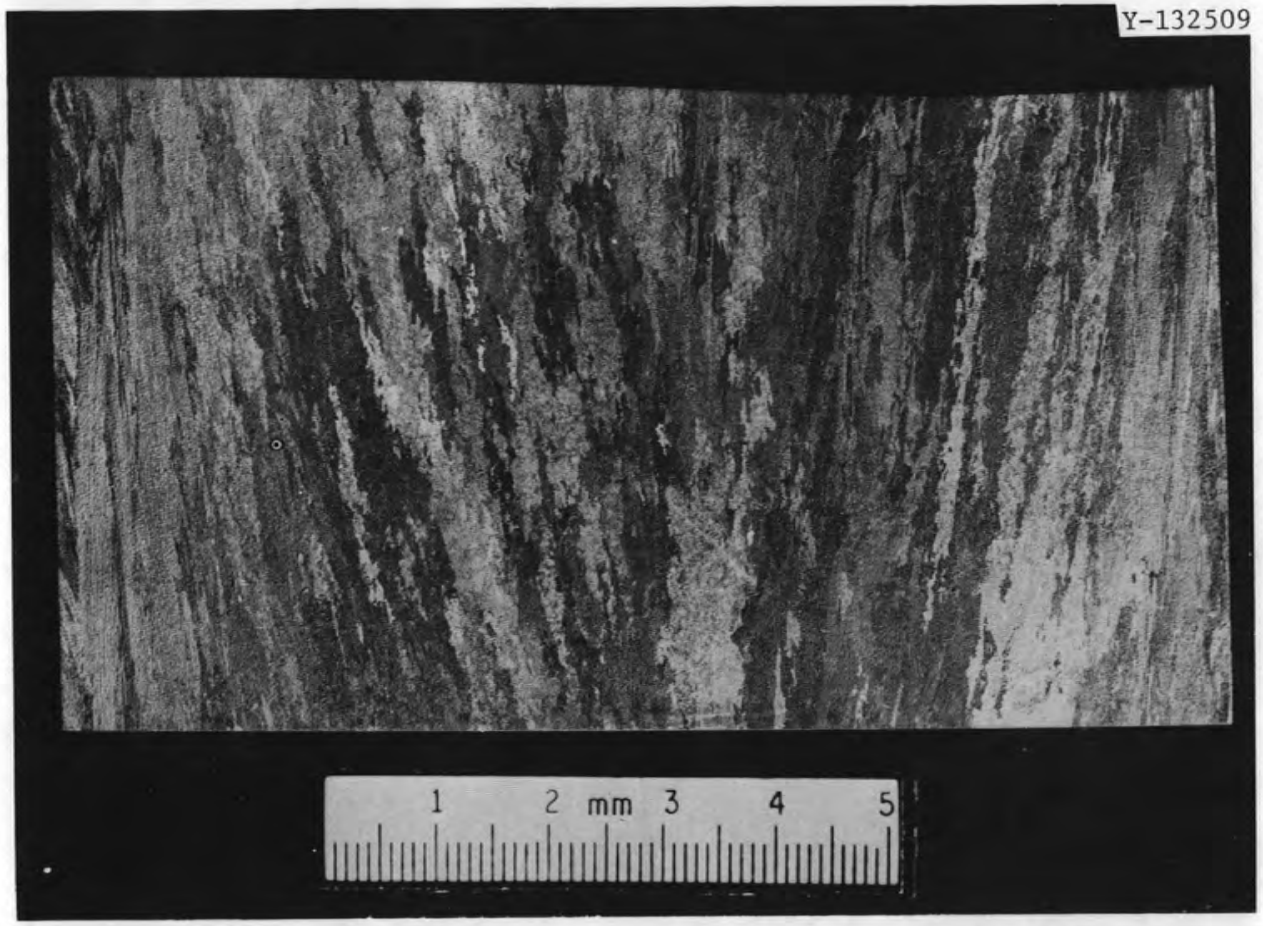

Fig. 3.62. Weld Metal Structure Normal to the 1-Axis.

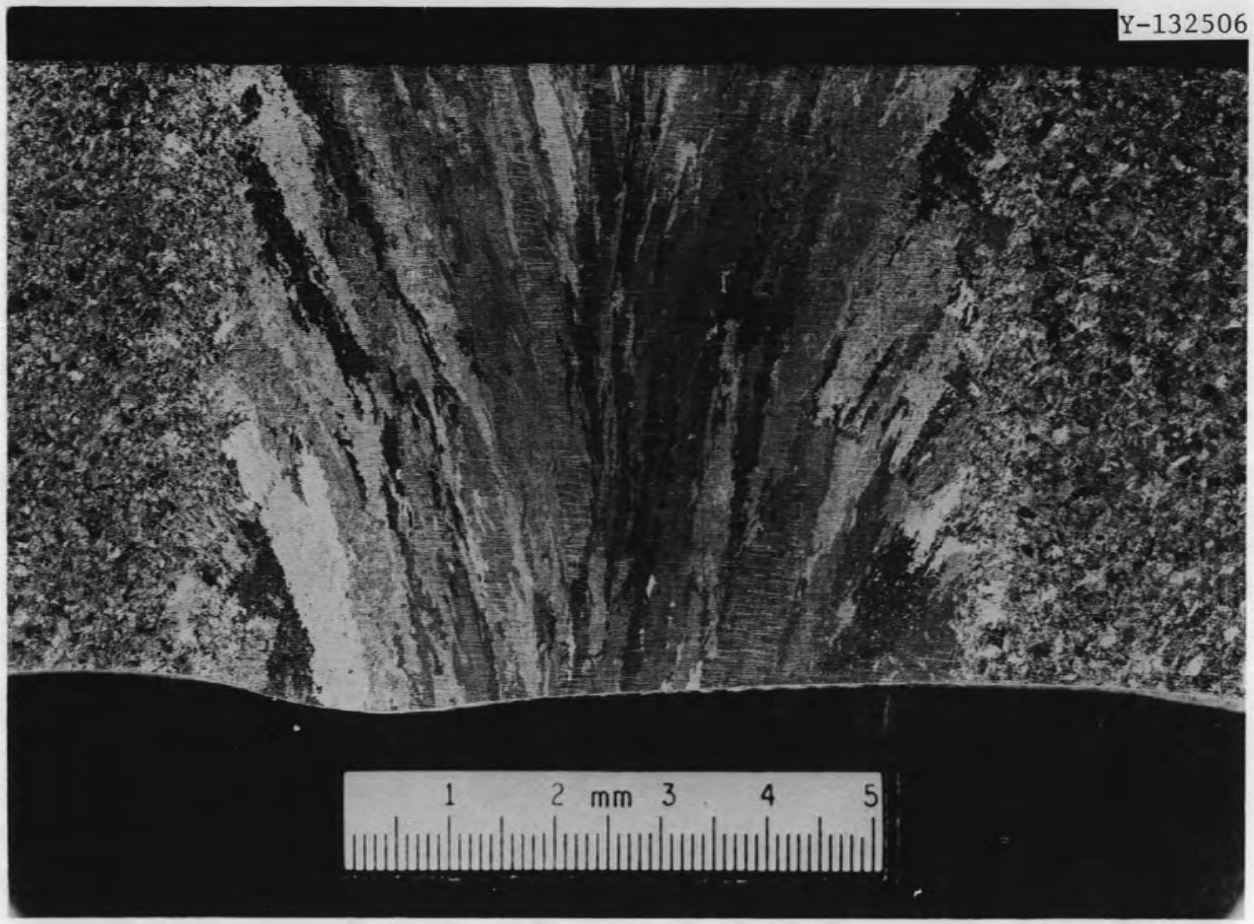

Fig. 3.63. Weld Metal Structure Normal to the 2-Axis.

Fig. 3.64. Weld Metal Structure Normal to the 3-Axis.

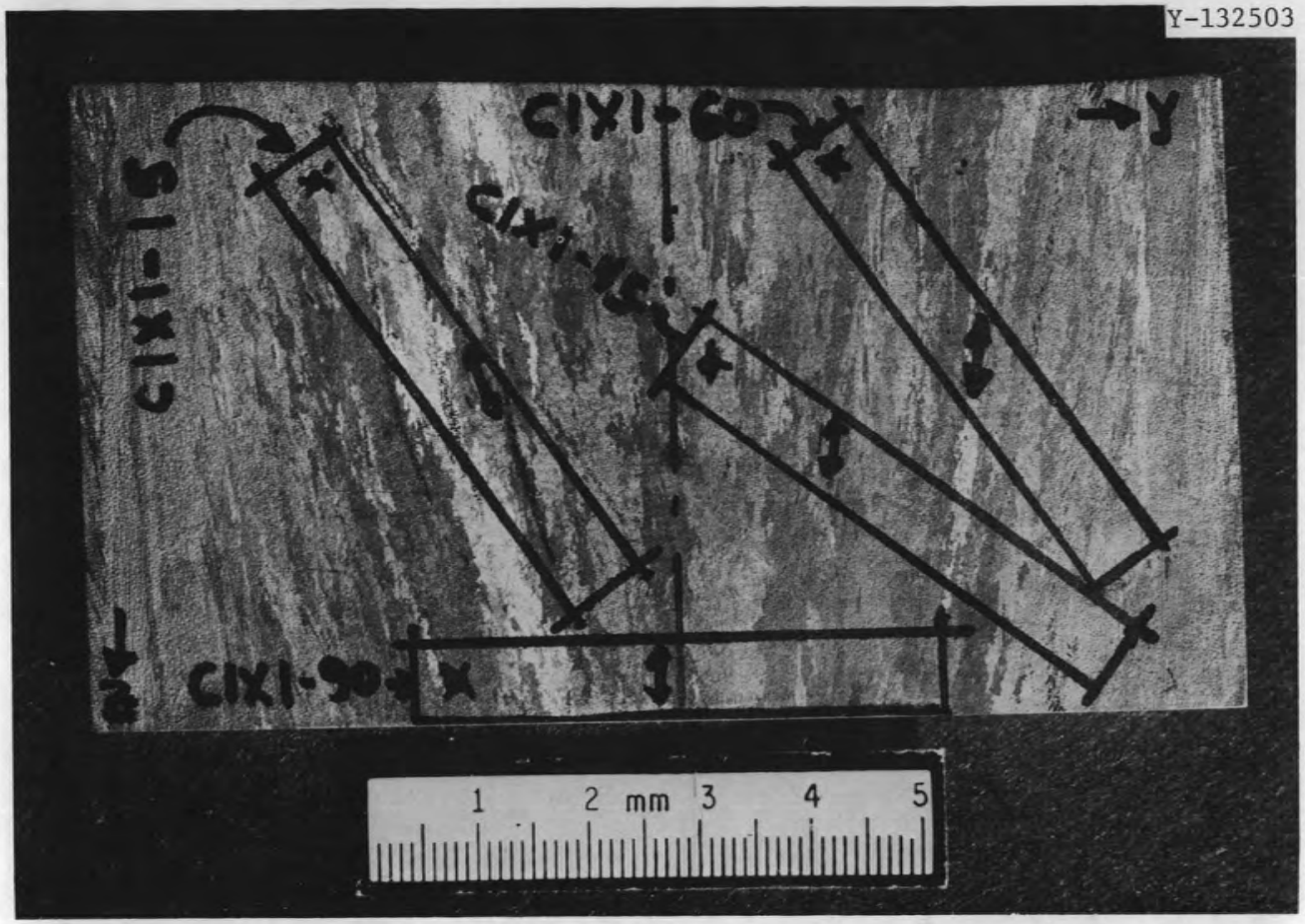

Fig. 3.65. Typical Specimen Blanking from Etched Plate.

where the 1, 2, and 3 directions are not necessarily principal directions. In a tensile test of a specimen oriented in, say, the 1-direction, if we neglect the effect of end constraint, we have only one nonzero component of stress,

$$\sigma_1 = P/A \ , \tag{34}$$

where P is the axial load and A is the cross-sectional area. Then we may write

$$\begin{aligned} \varepsilon_1 &= S_{11}\sigma_1 \ , \\ \varepsilon_2 &= S_{12}\sigma_1 \ , \\ \varepsilon_3 &= S_{13}\sigma_1 \ , \end{aligned} \tag{35}$$

where ε_1 is the longitudinal strain and ε_2 and ε_3 are the two diametral strains. Thus, if 1, 2, and 3 are principal directions, or, more precisely, if the specimen is located with its geometrical axis parallel or normal to the subgrain orientation, the slopes of the longitudinal and two diametral stress-strain curves lead to three of the compliances. The other three in the upper left-hand submatrix of $[S]$ in Eq. (33) may be found by orienting specimens in the 2 and 3 principal directions. Doing this gives checks for the symmetry relation $S_{ij} = S_{ji}$.

To date, we have measured the longitudinal stress-strain response on some 28 specimens. The diametral measurements are in progress, pending improvement in instrumentation.

3.3.1.2 Directional Variation of Apparent Elastic Modulus

The reciprocals of the compliance components S_{11}, S_{22}, and S_{33} are the elastic moduli in the 1, 2, and 3 directions respectively. We denote S_{11}' as the component associated with the $1'$ direction, where $1'$ makes an angle of θ with respect to 1, according to the sign convention of the right-hand rule. Also, we must note the axis about which the rotation takes place.

In Fig. 3.66 are plotted the results from rotations around the three principal axes. These curves are similar to those obtained by

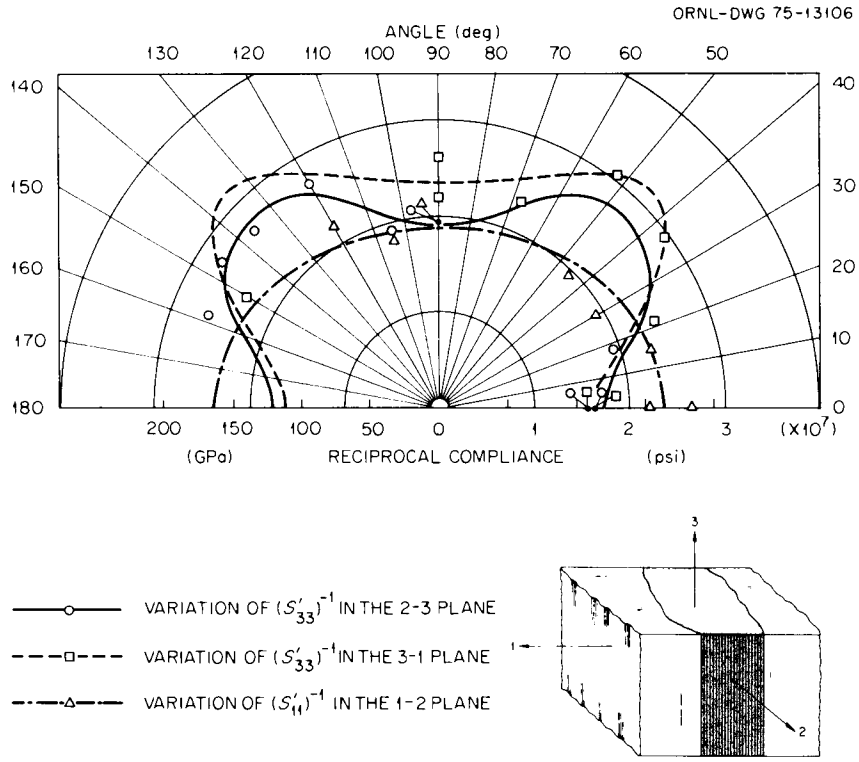

Fig. 3.66. Variation of Apparent Elastic Modulus with Orientation.

Zemzin and Chekhover,[47] who used ultrasonic techniques. The assumption of orthotropic symmetry has been forced by drawing the curves with fourfold symmetry. If a plane of isotropy were to be assumed for purposes of analysis, the two curves for $(S_{33}')^{-1}$ would be coincident, and the curve for $(S_{11}')^{-1}$ would be a circle.

The [100] crystallographic direction has previously been reported to be a preferred growth direction in fcc metals.[48] The elastic modulus of fcc material should be relatively low in the [100] direction, and this is consistent with the observation that specimens from the (2,3) plane and (1,3) plane with gage sections oriented in the 3 direction have relatively low moduli. The assumption that the plane normal to the (3) direction may be a plane of elastic isotropy is not completely borne out by the curve shown in Fig. 3.66, unfortunately.

From a continuum mechanics viewpoint, the low values of the modulus in the principal directions with the maxima at 45° to principal directions indicate that the shear modulus is greatly different from that expected

in isotropic elasticity. Hence in mechanics computations involving other than simple stress states, use of the proper anisotropic elastic constants will make a significant difference in the results.

3.3.1.3 Directional Variation of Yield Strength

From the longitudinal stress-strain curves, the yield strength at 0.1% offset was also computed. The resultant yield loci are plotted in Fig. 3.67, and show trends similar to those of the elastic moduli.

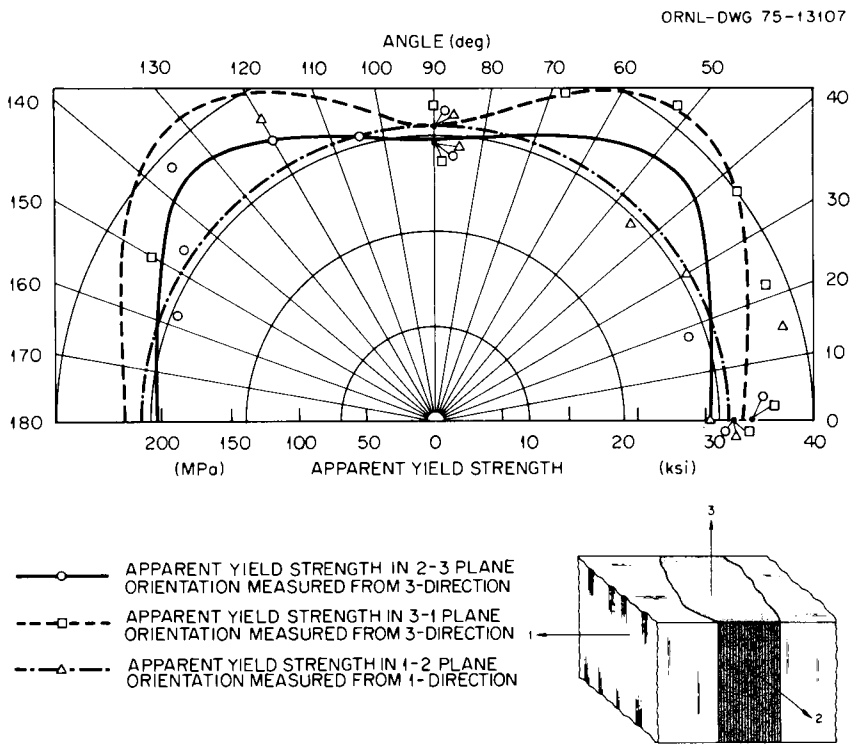

Fig. 3.67. Yield Loci for Rotations in Principal Planes.

This result opens another new area of investigation, that of developing an anisotropic yield criterion for weld metal. Such a theory would play an important role, say, in the study of nonlinear fracture mechanics of weld metal.

3.3.2 General Stainless Steel Welding Development — D. P. Edmonds, R. T. King, and E. Bolling

We are continuing to investigate and characterize experimental and commercial heats of types 308, 316, and 16-8-2 stainless steel filler metals, with and without controlled residual elements (CRE). Our primary objective at this time is to develop bare stainless steel filler wires for making submerged-arc (SA) and gas tungsten-arc (GTA) welds with improved high-temperature mechanical properties. These wires are intended for use in critical LMFBR stainless steel pressure vessel, thermal liner, and piping applications.

We are continuing to creep-rupture test at 482, 593, and 649°C (900, 1100, and 1200°F) experimental and commercial austenitic stainless steel weld deposits. We are creep-rupture testing at 649°C (1200°F) various GTA deposits made with experimental heats of type 16-8-2 CRE wires fabricated at ORNL. A test is in progress at a stress of 172 MPa (25 ksi) in excess of 9200 hr. A test at 593°C (1100°F) has been completed on a weld deposit made with the FFTF type 16-8-2 reference heat (Arcos 2367R). At a stress of 207 MPa (30 ksi), the sample ruptured after 11,896.5 hr with a total elongation of 17.9% and a total reduction of area of 28%.

In order to evaluate the creep properties of commercial vendors' iterative attempts to produce gas tungsten-arc and submerged-arc welding materials containing optimum amounts of controlled residual elements, additional creep testing equipment is being installed. The first test stand and creep machine have now been installed and checked out. The design is novel for lever-arm systems and will minimize screening test costs by allowing ten tests to be run simultaneously in a single three-zone furnace. The multiple-test creep facility has been demonstrated to provide adequate thermal characteristics for screening tests, except for a final check on the specimen-to-specimen temperature variations with ten tests in progress. The nine creep frames needed to complete the facility are on order, and the facility should be completed in early November.

On August 6, 1975, a meeting was held at ORNL comprising personnel from Babcock and Wilcox, Westinghouse Advanced Reactors Division, ERDA, and ORNL. The purposes of this conference were to discuss application

of type 16-8-2 stainless steel weld metal for fabrication of the CRBRP reactor vessel thermal liner, review the ongoing ORNL weld development program, and assess potential redirection of the ORNL welding program to support the CRBRP reactor vessel thermal liner fabrication. The CRBR thermal liner will be fabricated at B&W from type 316 stainless steel. The severe thermal environment to which the shield will be subjected requires the use of a weld filler metal with adequate elevated-temperature ductility. Commercial sources of types 316 CRE and 16-8-2 CRE welding filler wires for submerged-arc (SA), gas-tungsten-arc, and shielded metal-arc (SMA) will probably not be available when fabrication of the liner begins. Therefore, the liner will probably be fabricated with type 16-8-2 weld metal, either by SA or SMA (if acceptable SA procedures are not developed in time).

As a result of this conference, we sent B&W four 25-mm-thick (1-in.) type 316 stainless steel plates from the ORNL reference heat. They will provide welds in the plates using their production techniques, and will return them to ORNL for characterization. We have prepared and submitted to W-ARD a proposed test matrix for these welds, including metallography, δ-ferrite measurement, room-temperature hardness traverses, tensile testing, creep testing, Charpy V-notch testing, and strain-controlled cyclic fatigue testing.

ORNL personnel visited National Annealing Box Company (NABCO) in Washington, Pennsylvania, to discuss fabrication of longitudinally welded stainless steel pipe for LMFBR applications. NABCO is one of the few companies in this country known to have experience in SA welding type 316 stainless steel with type 16-8-2 filler metal. Insight into SA welding with type 16-8-2 and into possible fabrication methods for commercial and experimental welded pipe was gained.

3.3.3 Creep-Rupture Behavior of Gas Tungsten-Arc Types 308, 316, and 16-8-2 Stainless Steel Welds Made with Special Filler Materials — D. P. Edmonds, R. T. King, and E. Bolling

Previous work[49-51] has shown that minor additions of B, P, and Ti to shielded metal-arc (SMA) type 308 stainless steel weldments result in improved creep strength and long-time creep ductility. Also, we previously

reported[52] that the addition of 0.006% B, 0.042% P, and 0.5% Ti to types 308 and 316 stainless steel GTA welds produced the optimum enhancement of creep strength and ductility of the alloy combinations investigated. The techniques for welding and testing have been previously summarized.[52] The results of this work are summarized in Figs. 3.68 through 3.71. The stress required to cause rupture is plotted against the conventional Larson-Miller Parameter (C = 20) in Figs. 3.68 and 3.70 for types 316 and 308 stainless steel, respectively. The Larson-Miller Parameter is $(T + 460)\ (C + \log_{10} t_R)$, where T is temperature in °F and t_R is time to rupture in hours. Plotted on each graph for comparison are the approximate $+1.65\sigma$ (standard deviation) and -1.65σ upper and lower confidence limits[35] for rupture strength of types 316 and 304 stainless steel base metal (for rupture in 100,000 and 10,000 hr). Figures 3.69 and 3.71 are plots of total reduction of area as functions of time to rupture. Plots of total elongation are not included, but the trends in elongation are the same as those observed for reduction of area.

We are currently conducting creep-rupture tests at 649°C (1200°F) for GTA welds made with heats of type 16-8-2 stainless steel filler wire fabricated at ORNL with various additions of B, P, and Ti. Results are given in Table 3.21 together with the status and conditions of tests in progress. The effects of the residual elements being controlled on the properties of type 16-8-2 GTA welds will be analyzed when testing is complete.

3.3.4 Characterization Tests of Type 308 CRE Stainless Steel Welds in Type 304 Reference Heat Base Metal — R. T. King, G. M. Goodwin, R. S. Crouse, and E. Bolling

A series of type 308 stainless steel welds with controlled residual elements[53] (CRE) was made in reference heat 9T2796 type 304 stainless steel base metal plate. These welds were made for whole cross-section testing at the Westinghouse Research Laboratory,[54] Churchill Boro, at 593°C (1100°F), and are designated "Westinghouse Welds" for the purposes of this discussion. Concurrently, some of these welds are being tested and evaluated at ORNL to provide data for interpretation of the whole weld cross-section tests. The testing is not complete, but the creep and tensile data that are now available are presented below as a status report.

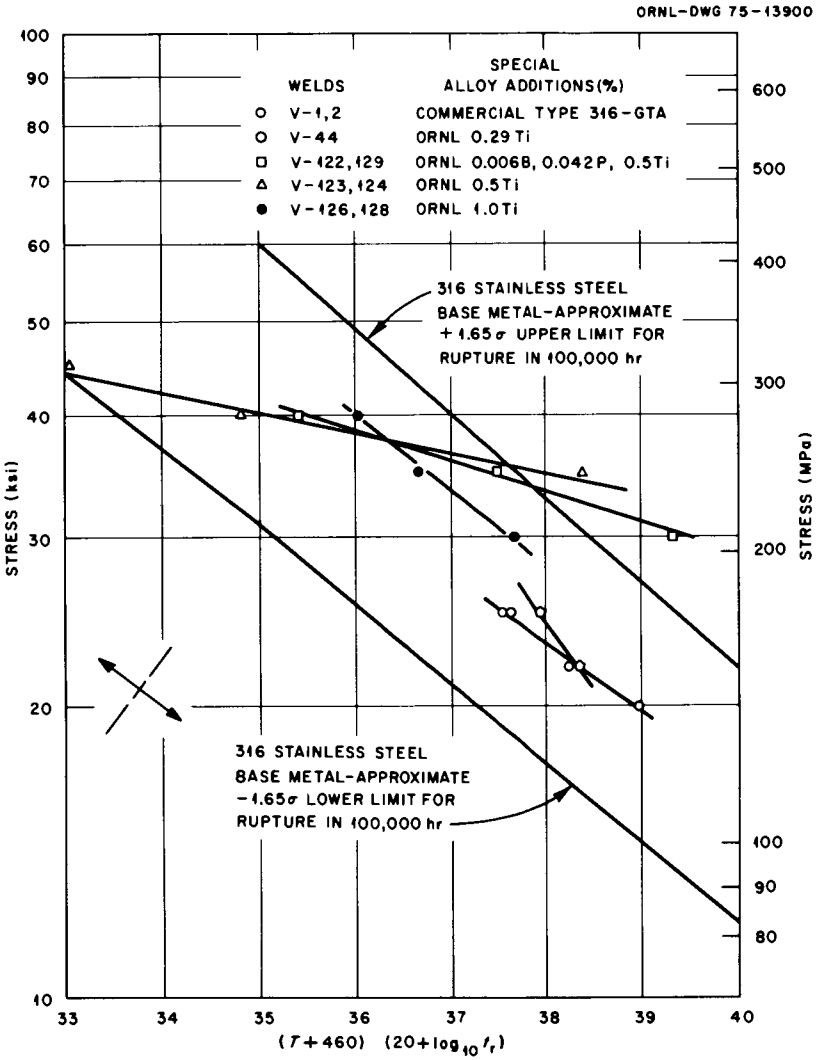

Fig. 3.68. Creep-Rupture Stress of Manual Gas Tungsten-Arc Type 316 Stainless Steel Weldments at 649°C (1200°F).

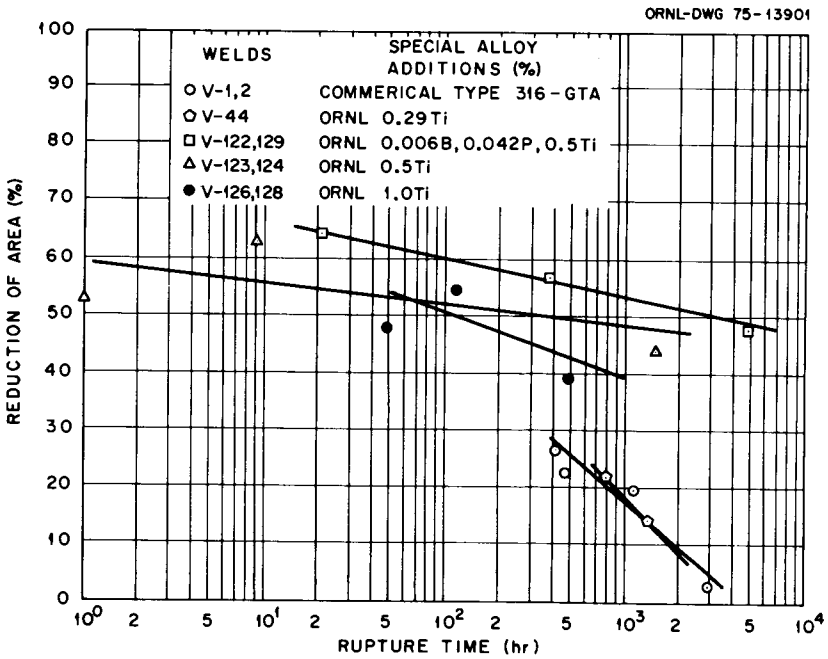

Fig. 3.69. Creep-Rupture Ductility of Manual Gas Tungsten-Arc Type 316 Stainless Steel Weldments at 649°C (1200°F).

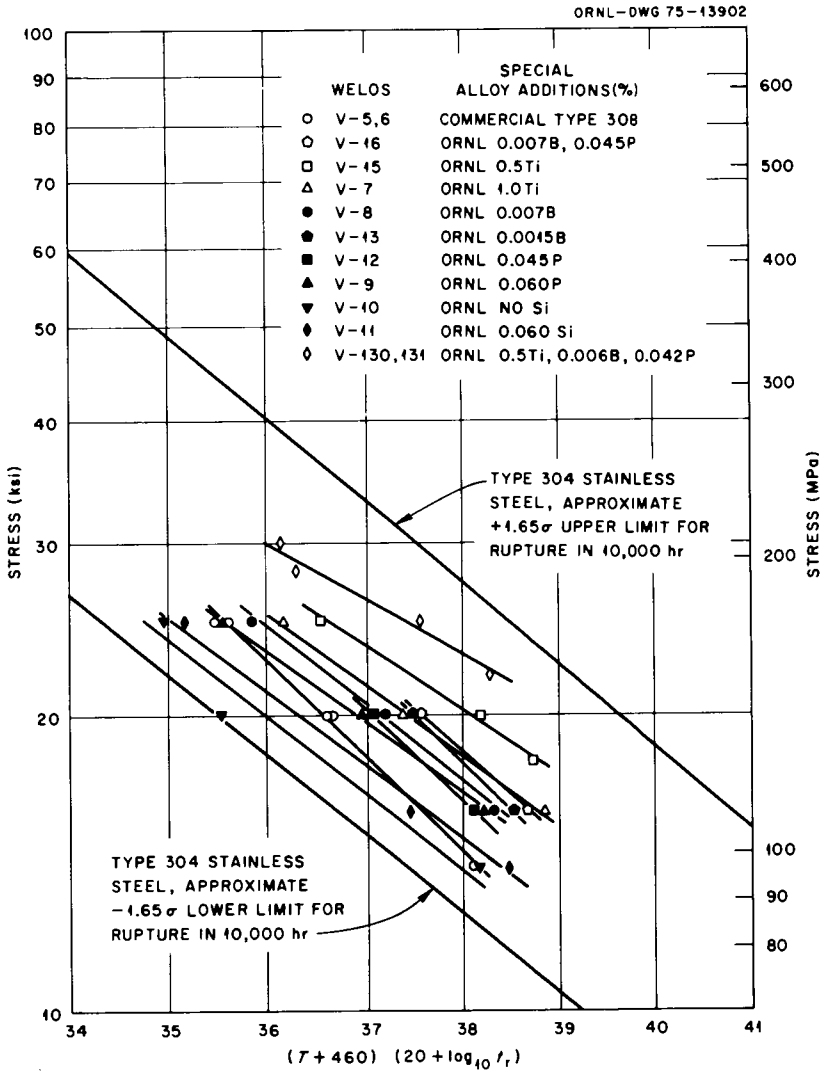

Fig. 3.70. Creep-Rupture Stress of Type 308 Stainless Steel Gas Tungsten-Arc Weldments at 649°C (1200°F).

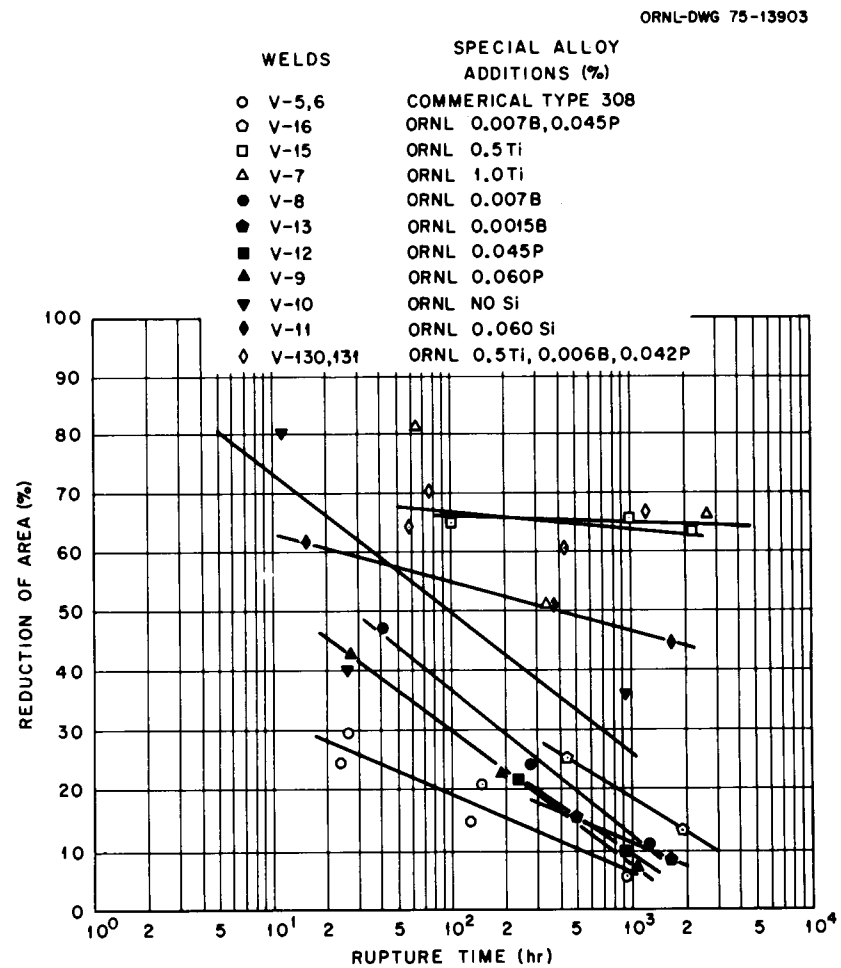

Fig. 3.71. Creep-Rupture Ductility of Manual Gas Tungsten-Arc Type 308 Stainless Steel Weldments at 649°C (1200°F).

Table 3.21. Creep-Rupture Properties of Gas Tungsten-Arc Type 16-8-2 Stainless Steel Weldments at 649°C (1200°F)

Weld	Supplier	Heat or Composition Aim	Stress (MPa)	Stress (ksi)	Time to Rupture (hr)	Total Elongation (%)	Total Reduction of Area (%)
V-55,56	Champion	45209 30-mil (0.76-mm) wire	193	28.0	358.5	12.5	50.6
			172	25.0	791.6	11.9	55.6
			152	22.0	3204.9	8.2	14.6
			207	30.0	127.2	26.5	44.5
V-57,58	Reid-Avery Armco	39048, 45-mil (114-mm) wire	193	28.0	126.9	22.0	51.6
			172	25.0	328.5	16.6	64.5
			162	23.5	843.9	27.6	47.2
			152	22.0	817.7	14.9	48.8
			145	21.0	1775.4	10.9	27.4
V-78,90, 46	Champion	56004	193	28.0	28.3	34.9	68.4
			172	25.0	74.6	18.9	45.7
			172	25.0	190.4	29.6	47.7
			172	25.0	97.1	25.6	67.8
			152	22.0	84.2	21.6	53.6
			138	20.0	1339.3	21.7	56.3
			138	20.0	431.8	34.4	73.0
			124	18.0	1204.0	43.7	54.8
V-66–74, 85, 88, 89[a]	Champion	58691	193	28.0	68.6	51.2	56.6
			172	25.0	176.8	45.7	50.2
			172	25.0	78.0	27.8	51.9
			172	25.0	104.3	62.9	52.7
			152	22.0	722.6	24.8	31.0
			138	20.0	765.6	47.6	
			124	18.0	1703.2	29.8	41.5
			110	16.0	5671.8	23.7	28.4
V-79,80	McKay	71370	207	30.0	171.9	50.8	50.8
			193	28.0	396.5	51.7	42.5
			172	25.0	1630.6	52.6	65.3
V-90	ORNL (Remelt Champion wire)	0.50% Si, 9.5% Ni	172	25.0	97.1	25.6	67.8
			138	20.0	431.8	34.4	72.9
			124	18.0	1204.0	43.7	54.8
V-86,87	Arcos	D1309T 301 Mod	207	30.0	175.3	31.2	40.3
			193	28.0	262.1	28.8	33.8
			172	25.0	767.7	27.7	47.4
V-114,115	Arcos	Reference 2367R 16-8-2	193	28.0	107.1	55.0	64.5
			172	25.0	513.0	30.1	70.0
			152	22.0	3602.4	40.1	63.3
V-118,125	ORNL	Special, 0.5% Ti	241	35.0	342.0	6.2	15.9
			207	30.0	1010.8	5.9	7.8
			193	28.0	1812.3	3.3	4.7
V-119,127	ORNL	Special, 1.0% Ti	241	35.0	128.9	12.1	42.7
			207	30.0	888.5	7.1	18.8
			193	28.0	4138.0	9.0	18.9
V-120,132	ORNL	Special, 0.5% Ti, 0.006% B, 0.042% P	207	30.0	>3160[b]		
			193	28.0	2684.2	10.5	71.7
			193	28.0	1165.0	9.3	12.8
			172	25.0	2463.1	6.2	16.0
			172	25.0	>9210[b]		
V-121,133	ORNL	Special, 0.006% B, 0.042% P	193	28.0	1717.6	13.9	65.0
			172	25.0	>4800[b]		

[a]Automatic welds, all others manual.

[b]Indicates test in progress.

The test welds that have been evaluated were made in 25-mm-thick (1-in.) type 304 stainless steel plate with 6.4-mm-diam (0.25-in.) coated electrodes from batch ABHB. The plate sections were 0.1 by 0.25 m (4 by 10 in.), with a square butt preparation. The plates were aligned with a 14-mm (0.56-in.) gap against an overlaid backing plate. Apparently five passes were used to fill the groove; the interpass temperature was below 200°C (392°F). The plates were restrained from flexing out of their plane, but motion in the plane of the plate was not completely restricted. The welding parameters were 45—48 V DCRP (direct current, reverse polarity) and 300 A.

A metallographic cross section of one weld was prepared in the plane normal to the welding direction. The specimen was polished and macroetched to reveal the substructure of the weld metal. Vickers diamond pyramid hardness (DPH) traverses were made down the weld center line, and parallel to the plate surface at a distance of 12 mm (0.5 in.) below the plate surface. The macrostructure and hardness traverse results are presented in Fig. 3.72. The hardness of the weld metal varies from about 275 DPH near the root passes to about 215 DPH near the surface, while the hardness of the base metal decreased continuously with increasing distance from the fusion line for at least 19 mm (0.75 in.). The corresponding weld metal hardnesses of the Fast Flux Test Facility vessel test welds made with similar electrodes were about 220 and 140—180 DPH, respectively.[55]

Test specimens with a 6.3-mm-diam by 31.7-mm-long (0.25 by 1.25 in.) gage section[56] have been prepared by sectioning the weld to produce blanks with center lines about 13 mm (0.5 in.) below the top plate surface. Both longitudinal all-weld-metal specimens and transverse-to-the-weld blanks (which contain base metal and weld metal) were prepared. These specimens are identical to the FFTF vessel test weld specimens, so comparisons can be made without the introduction of extraneous testing variables. Creep testing was performed at 593°C (1100°F) at stresses in the range of the stresses used in the FFTF vessel test weld matrix. The methods used in testing, including loading of specimens and monitoring of strain-time behavior, were identical, except that extensometers were not mounted directly on the gage lengths. Tensile tests were also performed on these specimens at 593°C (1100°F) and 4×10^{-3}/min nominal strain rate with an

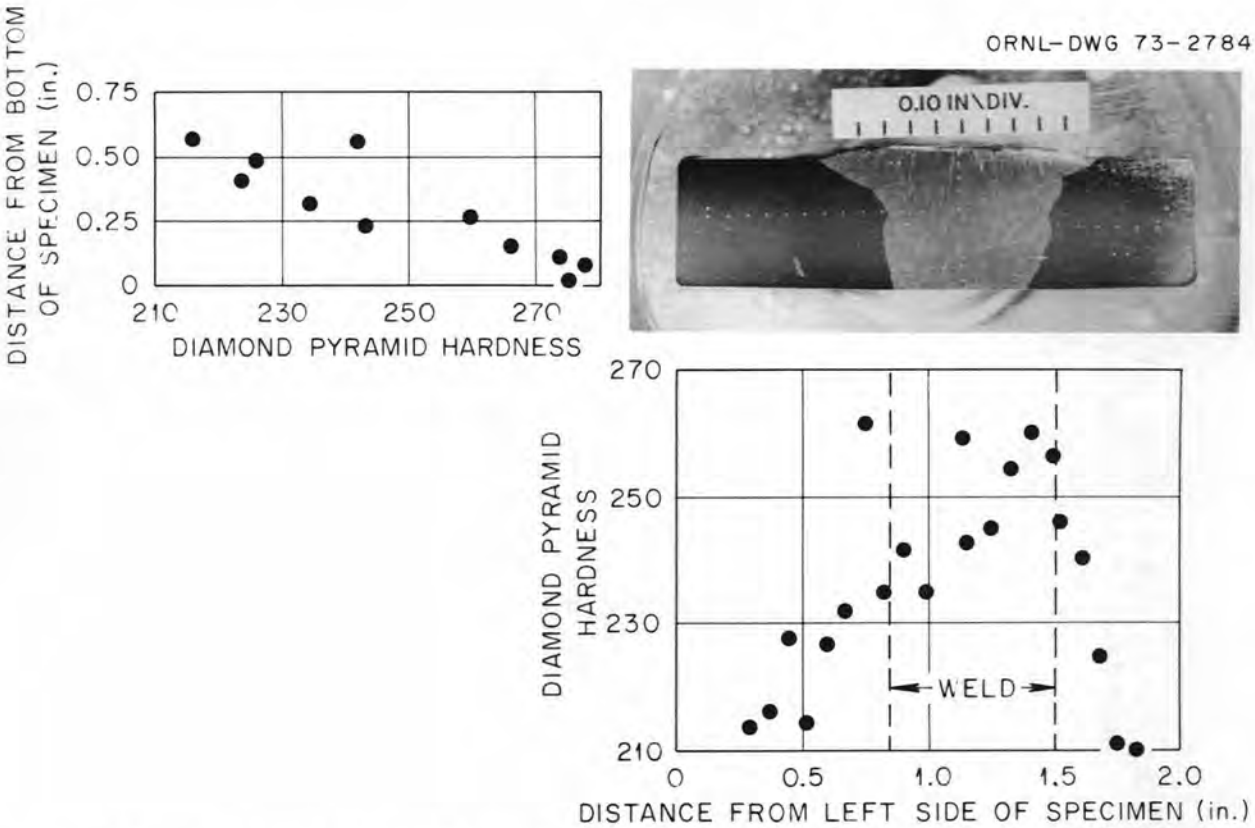

Fig. 3.72. Hardness Traverses on As-Deposited Westinghouse Welds made with 6.4-mm-diam (0.25 in.) Type 308 Stainless Steel Electrodes with Controlled Residual Elements (CRE).

Instron machine using methods that have been described before[57] and are comparable to the methods used to test the FFTF vessel test welds. Data reduction was accomplished by the same methods used previously.[57]

Additional all-weld-metal buttonhead type specimens with 3.2-mm-diam by 28.6-mm-long (0.125 by 1.125 in.) gage sections were prepared with center lines about 7.9, 13, and 17.5 mm (0.31, 0.5, and 0.69 in.) below the weld surface to explore variations in tensile properties with depth over the range for which sample preparation was feasible. These specimens were tested at 593°C (1100°F) at 4.4×10^{-3}/min nominal strain rate on an Instron machine.

The creep data for Westinghouse welds are compared with data[58] from the FFTF vessel test welds in Table 3.22. A useful (but not completely accurate) generalization is that the longitudinal all-weld-metal Westinghouse welds have properties intermediate to the L1 (surface location) and

Table 3.22. Comparison of Creep and Creep-Rupture Data for Type 308 CRE Stainless Steel Welds from FFTF Vessel Test Welds, Westinghouse Welds, and Base Metal at 593°C (1100°F)

Specimen Type	Stress (MPa)	Stress (ksi)	Strain, % Loading ε_L	Strain, % $\varepsilon_{Stage\ I}$	Strain, % $\varepsilon_{Stage\ II}$ Real	Strain, % $\varepsilon_{Stage\ II}$ Offset	Strain, % $\varepsilon_{Stage\ III}$ Real	Strain, % $\varepsilon_{Stage\ III}$ Offset	Strain, % Rupture ε_r	Strain Rate, %/hr $\dot{\varepsilon}_{Stage\ II}$ Real	Strain Rate, %/hr $\dot{\varepsilon}_{Stage\ II}$ Offset	Strain Rate, %/hr ε_r/t_r	Reduction of Area (%)	Rupture Time t_r (hr)	t_{III}/t_r [a]
							FFTF Vessel Test Welds								
Longitudinal Surface	241	35.0	3.17	1.33	31.5	32.73	19.32	18.09	55.32	2.58	2.60	2.99	65.6	18.5	0.70
	228	33.0	0.69	1.46	7.05	8.36	26.56	25.1	35.76	2.47×10^{-1}	2.53×10^{-1}	0.488	49.9	73.3	0.52
	207	30.0	2.0	8.25	3.75	4.53	12.24	11.46	26.24	5.77×10^{-2}	6.04×10^{-2}	0.111	54.6	236.4	0.59
	193	28.0	0.291	1.37	0.84	1.08	25.18	24.9	27.68	1.5×10^{-3}	1.95×10^{-3}	0.0148	58.1	1,873.9	0.40
	172	25.0	0.1	0.5	0.4	0.816	25.22	24.8	26.12	392×10^{-4}	5.20×10^{-4}	0.00829	64.0	3,152.5	0.52
	155	22.5	<0.20						>0.684					>11,104.0	
Longitudinal Intermediate	241	35.0	0.44	0.31	4.25	6.81	27.64	25.08	30.64	9.4×10^{-1}	9.7×10^{-1}	0.804	60.3	38.1	0.20
	228	33.0	0.34	1.46	2.2	2.93	19.92	19.19	23.92	8.8×10^{-3}	9.44×10^{-3}	0.0392	35.5	610.2	0.59
	207	30.0	0.249	0.28	0.69	0.91	20.48	20.26	21.7	3.7×10^{-4}	4.9×10^{-4}	0.0049	53.1	4,446.3	0.54
	193	28.0	0.251	0.219	0.695	1.11	20.9	20.5	22.08	2.8×10^{-4}	3.5×10^{-4}	0.0042	54.8	5,284.0	0.61
Longitudinal Root Pass	241	35.0	0.335	0.26	0.694	1.02	23.75	23.6	25.04	0.0191	0.024	0.291	48.1	86.0	0.55
	228	33.0	0.4	0.35	1.25	1.81	19.44	18.88	21.44	8.06×10^{-3}	9.06×10^{-3}	0.0485	52.2	441.9	0.51
	207	30.0	0.2	0.17	0.85	1.08	16.86	16.63	18.08	5.15×10^{-4}	6.35×10^{-4}	0.00648	47.9	2,791.2	0.63
	193	28.0	0.12	0.15					>0.738	$\sim 2.8 \times 10^{-5}$				>16,770.6	
							Westinghouse Welds								
Longitudinal All-Weld Metal	241	35.0	5.54	10.74	12.95	15.3	19.0	16.6	48.2	0.537	0.548	0.87	57.2	48.8	0.72
	220	32.0	2.90	10.66	7.95	11.4	25.6	22.2	47.2	0.098	0.101	0.19	55.4	237.6	0.55
	207	30.0	0.96	2.83	1.49	1.6	41.1	41.0	46.4	0.003	0.003	0.02	53.6	1,805.5	0.33
	193	28.0	1.62	3.80	1.79	1.9	27.7	27.5	34.9	0.002	0.002	0.01	52.1	3,488.3	0.30
Transverse Weldment	220	32.0	2.45	3.45	4.66		2.85		13.4	0.082		0.16	11.0	85.7	0.96
	193	28.0	0.40	0.52	1.52	1.94	7.96	7.5	10.4	0.015	0.016	0.03	5.9	317.2	0.36
	172	25.0	0.13	0.39	0.04	0.08	6.5	6.5	7.1	0.001	0.001	0.009	8.8	752.9	0.27
							Heat 9T2796 Base Metal								
Reannealed	220	32.0							22				25	45	
	193	28.0							18				20	170	
	172	25.0							15				18	550	
As Received	172	25.0							7				20	700	

[a] t_{III} = time to third-stage creep.

L2 (intermediate depth) longitudinal all-weld-metal specimens from the FFTF vessel test welds. A few graphical examples are given below. The creep-rupture comparison clearly follows the generalization (Fig. 3.73). Longitudinal, all-weld-metal type 308 CRE stainless steel specimens have shorter rupture times at high stress than the average found[60] for type 304 stainless steel base metal at 593°C (1100°F), but longer rupture times at low stress. None of the data fall below the (95, 90) tolerance limit[60] for type 304 stainless steel base metal at 593°C (1100°F). The generalization also holds for the average creep rate (Fig. 3.74). The times required to achieve 0.5%, 1%, and 2% total strain, the end of first stage creep, and the onset of tertiary creep by the 0.2% offset method are compared in Figs. 3.75 through 3.79. The scatter bands shown in the figures encompass FFTF Vessel Test Weld data at 482, 565, 593, and 649°C (900, 1050, 1100, and 1200°F). The data for both FFTF Vessel Test Welds and

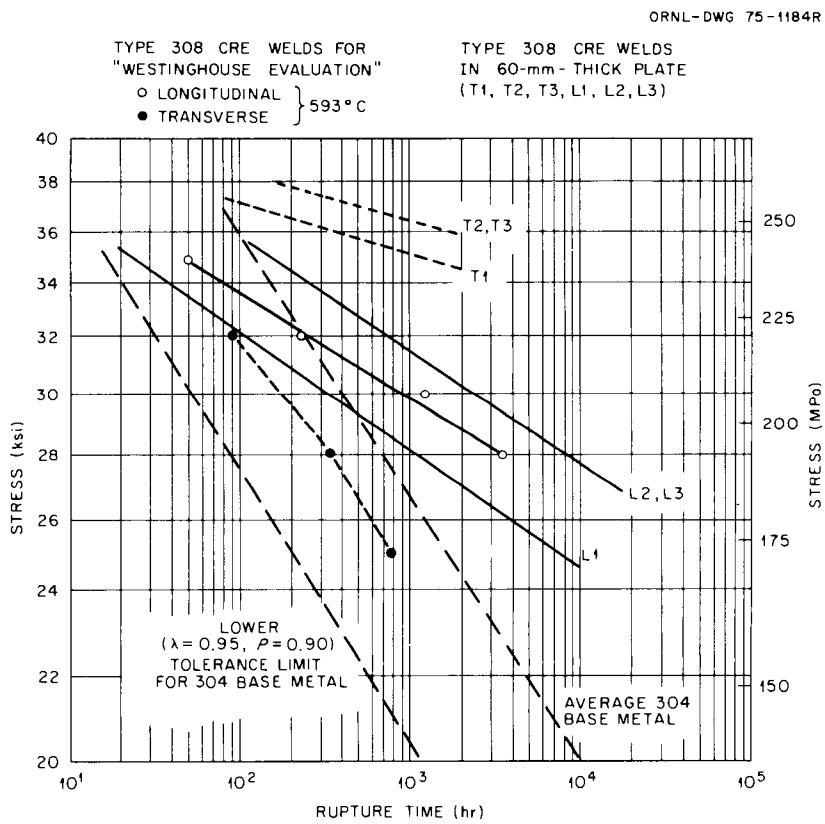

Fig. 3.73. Comparison of Creep-Rupture Behavior at 593°C (1100°F) of FFTF Vessel Test Welds and Westinghouse Welds with Behavior of Type 304 Stainless Steel Base Metal.

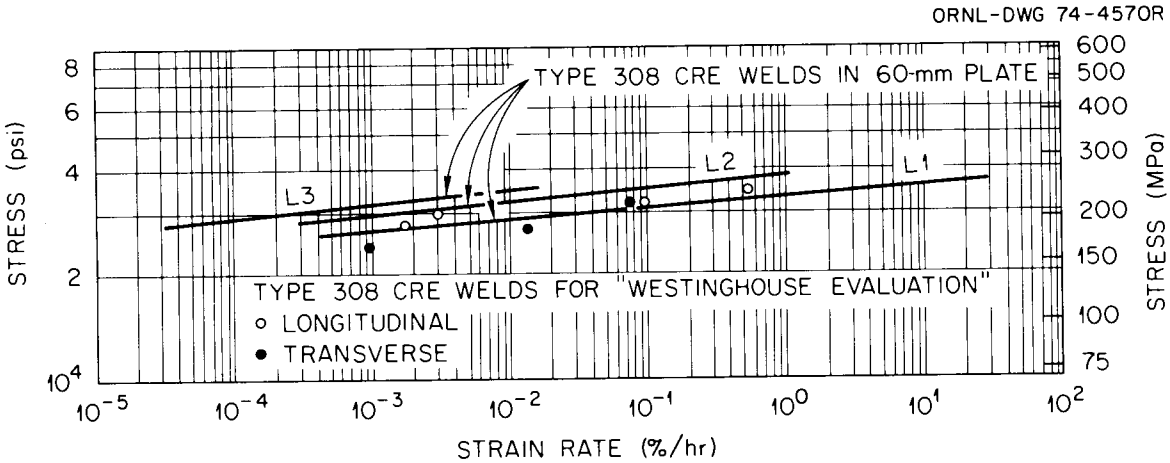

Fig. 3.74. Minimum Creep Rates for Type 308 CRE Stainless Steel Weld Metal and Weldment Specimens.

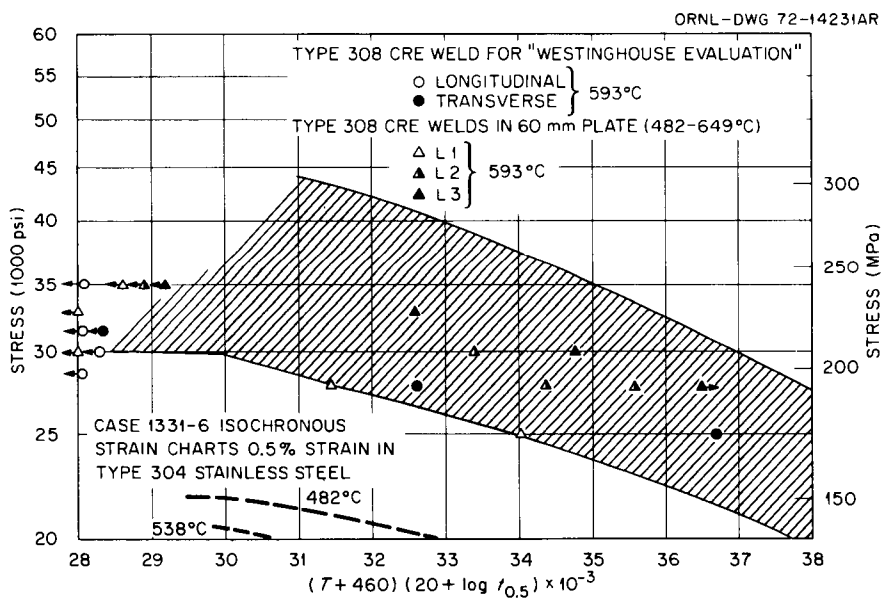

Fig. 3.75. Larson-Miller Parameter for Time to 0.5% Strain in Type 308 CRE Stainless Steel Weld Metal at 593°C (1100°F).

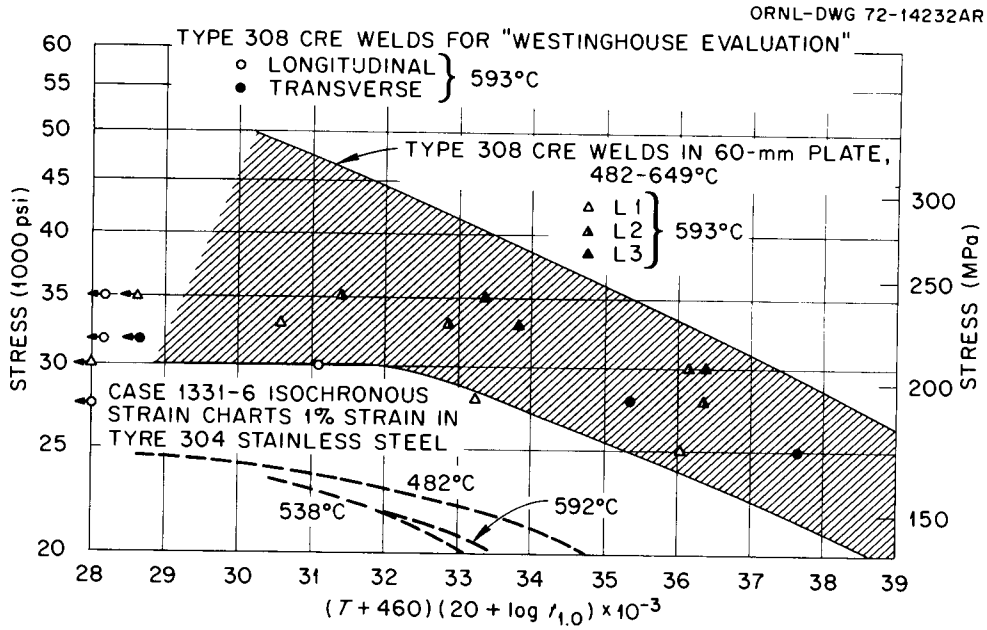

Fig. 3.76. Larson-Miller Parameter for Time to 1.0% Strain in Type 308 CRE Stainless Steel Weld Metal at 593°C (1100°F).

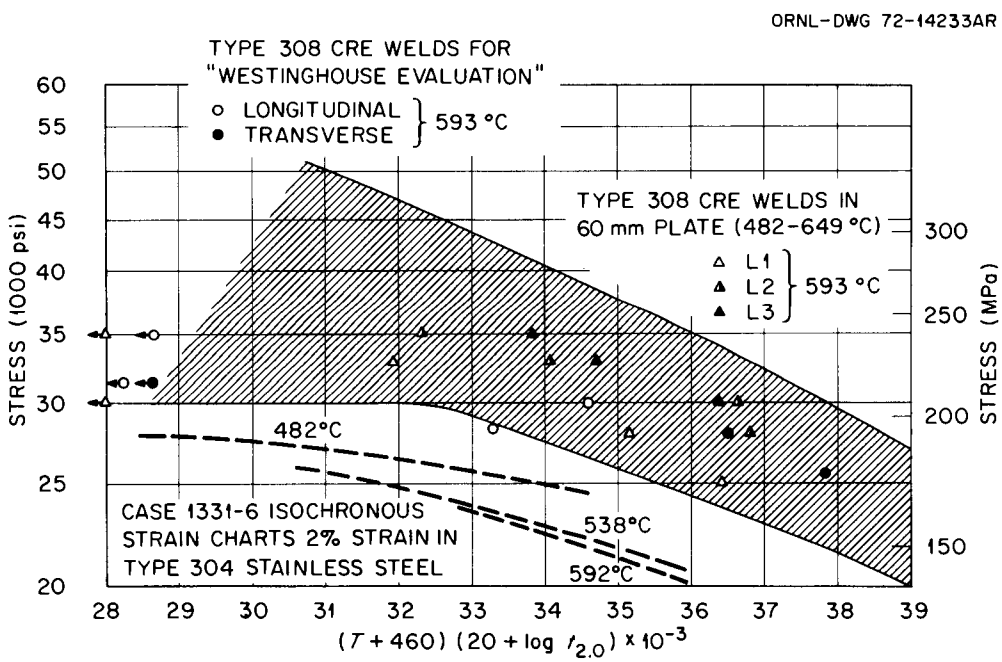

Fig. 3.77. Larson-Miller Parameter for Time to 2.0% Strain in Type 308 CRE Stainless Steel Weld Metal at 593°C (1100°F).

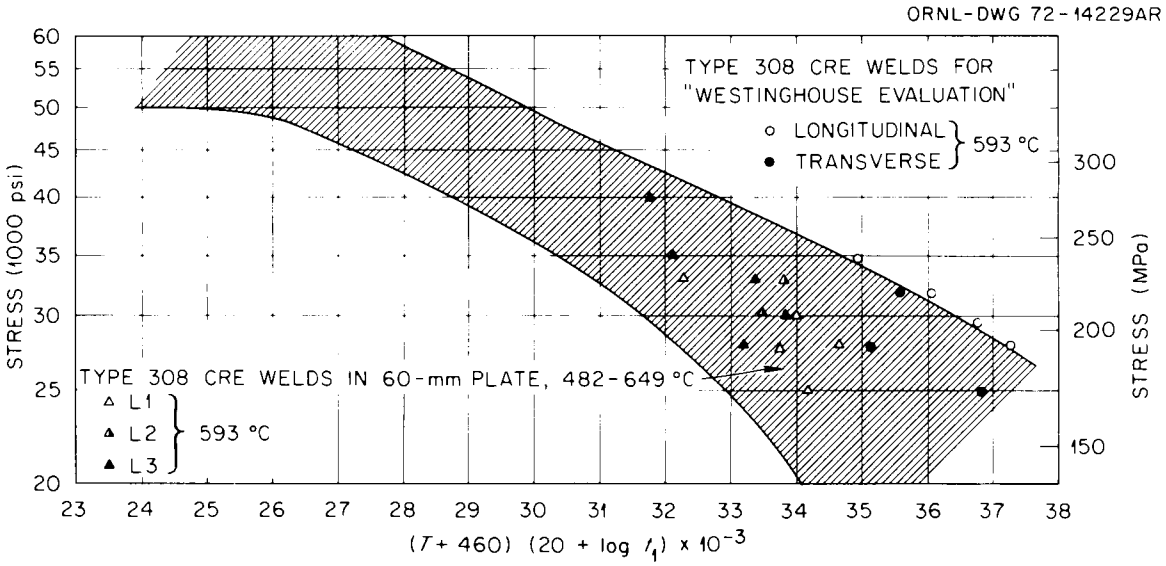

Fig. 3.78. Larson-Miller Parameter for Time to End of First-Stage Creep in Type 308 CRE Stainless Steel Weld Metal at 593°C (1100°F).

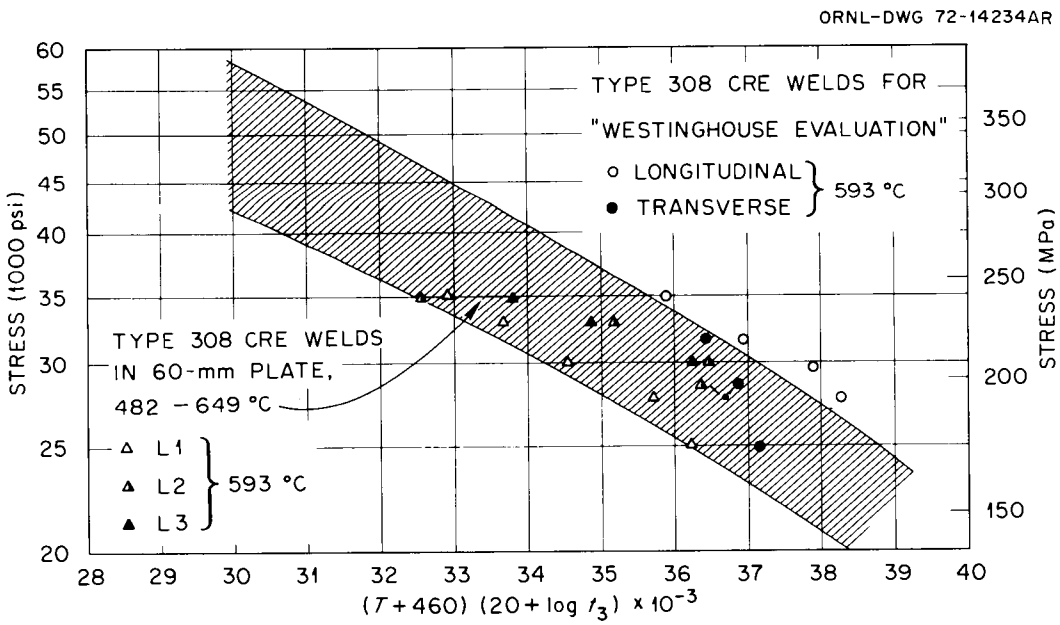

Fig. 3.79. Larson-Miller Parameter for Time to Third-Stage Creep by 0.2% Strain Offset Method in Type 308 CRE Stainless Steel Weld Metal at 593°C (1100°F).

Westinghouse welds are shown for comparison. Differences are difficult to interpret, and may not be statistically significant.

Because of their complexity, only a few comparisons will be made for transverse weldment specimens from Westinghouse welds. A fuller treatment will be made when all tests are completed. *The transverse weld specimens all failed in the heat-affected zone close to the fusion line.* A typical fracture surface is shown in Fig. 3.80.

Comparable data are available[23] for some as-received and reannealed (1093°C) heat 9T2796 specimens from 25-mm-thick (1-in.) plate that were creep tested at 593°C (1100°F), and approximate values of creep-rupture characteristics are tabulated together with the comparable results for heat-affected zone material in Table 3.22. The rupture time data are similar (even though the HAZ of the weldment specimens was constrained during testing by the weld metal and grips). The elongations and reductions of area tend to be higher for reannealed material than for HAZ material, but the as-received specimen had characteristics quite like the HAZ material. Intergranular fracture predominated for the as-received and reannealed material.

The transverse weldment specimens from Westinghouse welds exhibit shorter rupture times (Fig. 3.73), higher minimum strain rates at low stress (Fig. 3.74), longer times to 0.5, 1, and 2% total strain, (Figs. 3.75—3.77), shorter first stage creep periods (Fig. 3.75), and earlier onset of tertiary creep (Fig. 3.79) than their longitudinal all-weld-metal counterparts.

The rupture data of M. Manjoine[54] for large cross sections for GTW, BTW, BAW, and GAW specimens, taken together with extrapolations of the creep-rupture data for small longitudinal and transverse specimens (Fig. 3.73) are consistent with the behavior that might be expected for a relatively weak, low ductility base material joined by a relatively strong and ductile weld metal.

The tensile test data for Westinghouse welds are summarized in Table 3.23, together with results[60] for FFTF Vessel Test Welds. The duplicate tests LWM-6 and LWM-7 are the same within expected testing error. They may be characterized as having relatively low elastic limits,

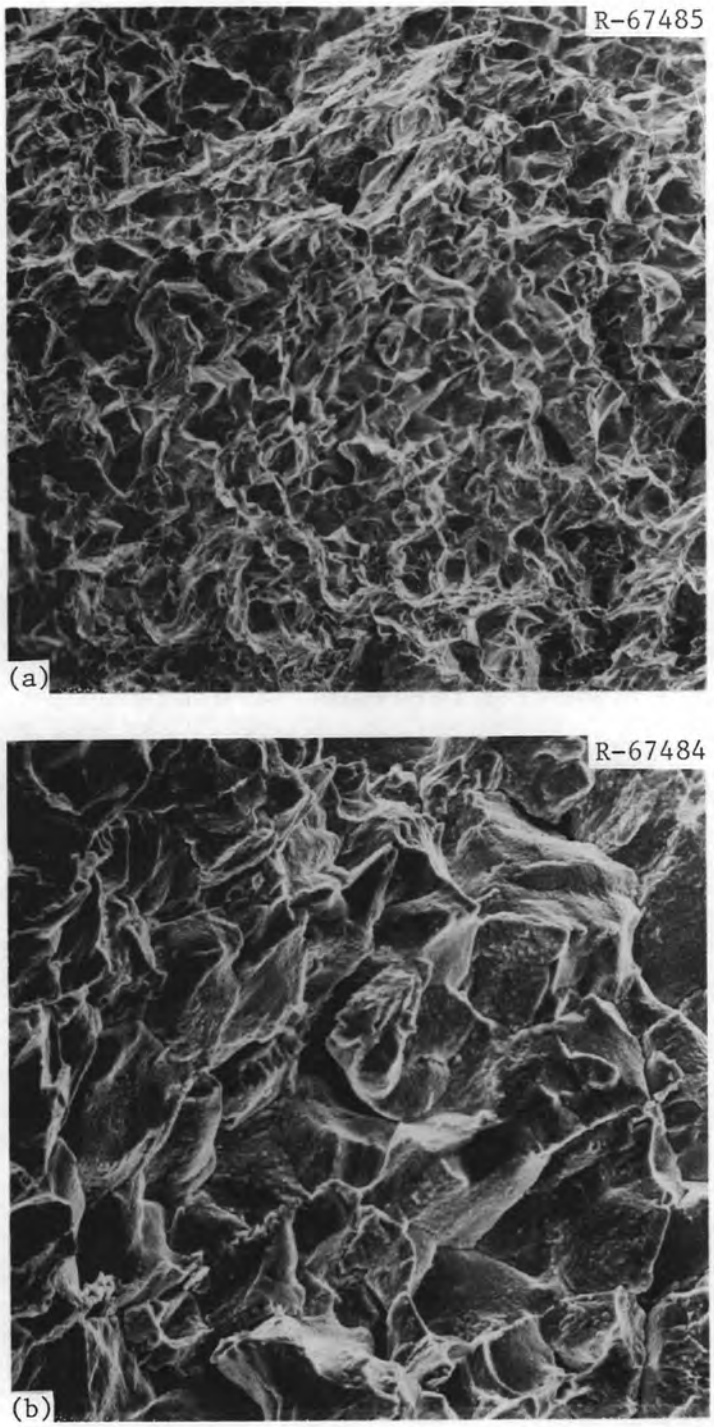

Fig. 3.80. Representative Area of Fracture Surface of Westinghouse Weld Transverse Specimen that Failed in the Heat-Affected Zone After 85.7 hr with 13.4% Average Gage Length Elongation and 11% Reduction of Area. The test was at 220 MPa (32 ksi) stress and 593°C (1100°F). Note the almost completely intergranular nature of the fracture. (a) 100×. (b) 300×.

Table 3.23. Tensile Properties of Type 308 CRE Stainless Steel FFTF Vessel Test Weld Longitudinal All-Weld-Metal Specimens and Westinghouse Weld Metal and Weldment Specimens at 593°C (1100°F) and 0.004/min Nominal Strain Rate

Specimen Type	Instron Chart Measurements					Reduction of Area (%)	Diametral Strain				Extensometer Measurements, ksi[a]	
	0.2% Offset Yield Stress (ksi)[a] (Eng/True)	Strength, ksi[a]		Strain, %			At Fracture		Away from Fracture			
		Ultimate (Eng/True)	Fracture (Eng/True)	Uniform (Eng/True)	Total (Eng/True)		(%) (max/min)	Ratio	(%) (max/min)	Ratio	Elastic Limit	0.2% Offset Yield Stress
FFTF Vessel Test Weld												
Surface	32.8/32.9	51.0/60.4	41.9/82.4	18.4/17	31.4/68	49.2	29.3/28.1	1.0	14.9/6.1	2.4	18.98	33.04
	31.3/31.4	44.2/52.7	23.6/73.6	19.4/18	35.6/114	67.8	44.6/42.2	1.1	11.6/3.2	3.6	19.00	30.80
	32.4/32.5	47.5/57.5	30.7/66.8	21.2/19	37.0/78	54.0	40.2/25.0	1.6	16.1/6.5	2.5	20.91	31.88
	32.2/32.2	49.5/59.9	33.8/63.8	21.0/19	33.1/63	47.0	32.6/22.1	1.5	12.5/5.7	2.2	16.4	31.47
	27.4/27.5	45.0/56.4	33.0/86.1	25.3/23	42.0/96	61.7	42.0/34.4	1.2	18.4/6.4	2.9	18.8	27.3
	29.2/29.2	45.3/55.0	33.1/95.3	21.4/19	37.2/106	65.2	47.2/35.5	1.3	18.1/6.5	2.8	19.1	29.0
	29.9/29.9	43.9/54.1	29.6/73.9	23.4/21	43.8/91	60.0	44.3/29.9	1.5	20.7/9.5	2.2	17.3	29.2
Intermediate	37.6/37.6	50.4/58.8	47.3/95.6	16.5/15	28.3/70	50.5	30.0/29.2	1.0	10.5/5.5	1.9	24.19	38.60
	37.4/37.5	45.7/51.9	33.9/77.0	13.5/13	31.0/82	56.0	36.5/30.9	1.2	18.2/8.1	2.2	27.77	37.02
	39.8/39.9	47.3/54.2	34.2/75.0	16.4/14	35.3/78	54.4	34.9/30.1	1.2	16.4/8.4	2.0	34.94	39.05
	37.5/37.6	50.6/59.3	41.2/72.5	17.3/16	26.0/56	43.1	30.0/19.5	1.5	10.7/7.0	1.5	17.51	37.08
	37.8/37.9	46.6/53.2	32.2/80.9	14.2/13	34.1/92	60.2	41.9/32.3	1.3	21.9/7.8	2.8	22.48	37.40
	40.9/41.0	46.4/51.9	33.7/74.7	11.7/11	29.6/80	54.9	40.4/26.1	1.5	17.1/5.5	3.1	28.6	40.6
Westinghouse Weld												
Longitudinal, 0.25 × 1.25 in. gage												
LWM-6	25.1/25.1	42.3/59.8	26.5/71.3	29.4/26	39.6/99	62.8	43.1/35.1	1.2	19.9/6.7	3.0	12.0	24.1
LWM-7	23.7/23.7	42.8/54.9	28.6/100.5	28.1/25	39.5/126	71.6	49.6/43.9	1.1	16.7/5.5	3.0	8.16	b
Transverse Weldment[c] 0.25 × 1.25 in. gage												
TWM-2	26.5/26.5	45.3/52.3	38.5/72.9	15.5/14	21.5/64	47.2	35.3/20.1	1.8			8.4	26.7
Longitudinal, 0.125 × 1.125 in. gage												
Surface LWM-1-1	25.8/25.8	41.1/50.7	26.1/65.2	23.4/21	28.8/92	60.0	44.8/29.6	1.5	10.4/2.0	5.2	6.9	24.9
Center LWM-2-1	27.2/27.2	40.9/51.2	28.0/69.3	25.2/22	34.1/92	60.0	39.0/34.2	1.1	15.7/3.8	4.2	12.6	26.7
Bottom LWM-3-1	28.8/28.9	42.1/52.2	30.2/65.0	24.0/22	34.3/76	53.5	35.9/27.9	1.3	19.1/6.2	3.1	14.3	28.2

[a] 1 ksi = 6.895 MPa.

[b] Instrumentation malfunction.

[c] Data calculated as for longitudinal specimens; diametral strain away from fracture not characterized because of extreme local variability.

0.2% offset yield strengths, and ultimate tensile strengths compared with even the weakest (L1-type) FFTF vessel test weld specimens. The longitudinal buttonhead specimens have increasing yield strengths and (extensometer) elastic limits with increasing distance from the weld surface (the same pattern observed for L1, L2, and L3 FFTF vessel test weld specimens), but the statistical significance of the observations is speculative. The Instron strain vs stress results were fit with an equation of the form:

$$\log(\text{stress}) = \log k + n \log(\text{strain}) ,$$

for the 0.2% offset yield point, the ultimate point, and six points at uniform intervals of log(strain). The results for k and n are summarized in Table 3.24. Differences between buttonhead and the larger specimens may be related to deflections arising outside the specimen gage length; results will be available soon from extensometers on the gage length.

Table 3.24. Characterization Constants for Type 308 CRE Stainless Steel Weld Metal Tensile Stress-Strain Behavior

Specimen	log k	n
LWM-6	11.050	0.1718
LWM-7	11.033	0.1594
TWM-2	11.023	0.3312
LWM-1-1	10.970	0.1328
LWM-2-1	10.982	0.1389
LWM-3-1	10.990	0.1253

The outstanding feature of the transverse weldment tensile specimen TWM-2 is its lower uniform and total strains compared with longitudinal specimens. It failed in the weld metal by transsubstructural shearing, according to preliminary visual observations (similar to behavior of FFTF Vessel Test Welds that failed in the weld metal at elevated temperatures).

3.3.5 Characterization of a Type 308 SA Stainless Steel Weld in 0.76-m-diam by 9.5-mm-wall (30 by 3/8 in.) Type 304 Stainless Steel Pipe: Progress Report — R. T. King, D. P. Edmonds, R. S. Crouse, and E. Bolling

Previous work[53,61] has demonstrated that conventional as-deposited austenitic weld metal containing some ferrite may have low creep ductility at elevated temperatures near 650°C. The ferrite transforms to sigma phase, and failure occurs by separation at austenite-sigma phase boundaries. Annealing to reduce the interphase boundary available by reducing the ferrite content or changing its morphology should, in principle, partially alleviate the ductility problem. Annealing of seam-welded austenitic steel pipe is included in SA-312 and SA-358 specifications. However, as-welded pipe has economic advantages, so we are presently characterizing some commercially made as-welded as well as welded-and-annealed pipe for high-temperature applications.

A major steelmaker produced an unfinished length of experimental type 304 stainless steel pipe 0.76 m (30 in.) OD by 9.5 mm (0.375 in.) wall thickness in a highly automated line pipe mill. The pipe is basically an A 358 product made from hot-rolled, annealed and pickled plate. The plate was formed by edge crimping, "U"-ing and "O"-ing on presses, making an inside SA type 308 stainless steel weld pass, then cold-expanding about 0.75% for sizing and straightness control. Welding parameters are proprietary. The pipe was supplied in the as-welded condition, before removal of any of the weld bead to produce a uniform wall thickness cylinder (which would be required for nuclear grades intended for elevated-temperature service). The steelmaker's analyses of the weld and base metal are given in Table 3.25.

The pipe was sectioned, polished, and etched to reveal its structure. Ferrite numbers measured on the etched surface ranged from FN 4.5 in the first pass to FN 7.8 in the second pass. Diamond pyramid hardness traverses were then made parallel to the pipe surface at distances of about 1.8, 4.3, and 6.9 mm (0.07, 0.17, and 0.27 in.) below the original plate surface. A micrograph of the area investigated is shown in Fig. 3.81. The hardness traverses are given in Fig. 3.82. The inside weld pass (made first) is harder than either the center of the weld or the outside pass.

Table 3.25. Chemical Compositions of the Weld and Base Metal of the Experimental Welded Pipe

Element	Content, %			
	Inner Weld Surface	Weld	Pipe Body	Base Metal, Ladle Analysis
C	0.063	0.061	0.059	0.054
Mn	1.84	1.69	1.39	1.58
P	0.031	0.028	0.023	0.023
S	0.013	0.012	0.016	0.013
Si	0.75	0.67	0.43	0.63
Cr	19.58	19.19	18.75	18.73
Ni	9.57	9.57	9.81	9.72
Mo	0.25	0.26	0.18	0.26
Cu	0.17	0.16	0.12	0.14
Co	0.15	0.14	0.15	0.12
Pb				0.003
B				0.0006

ORNL-DWG 75-14703

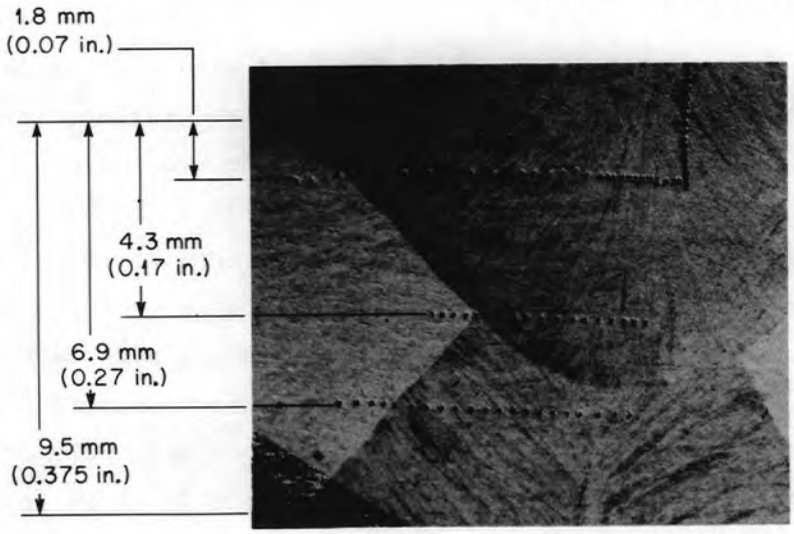

Fig. 3.81. Polished and Etched Cross-Section of Pipe Seam Weld Normal to Welding Direction, Showing Hardness Traverses at Various Depths Below the Outside Surface.

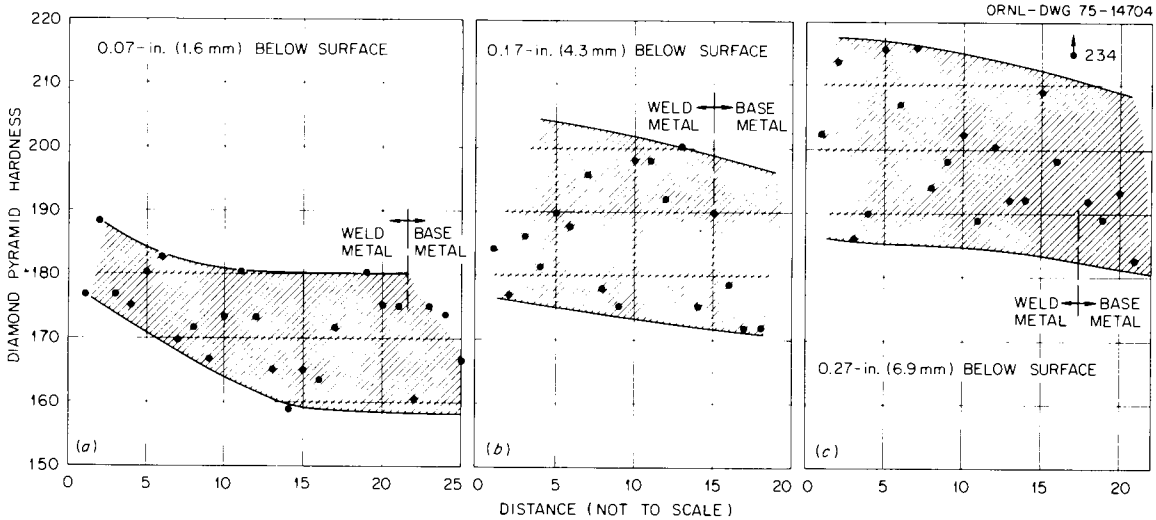

Fig. 3.82. Diamond Pyramid Hardness Traverses from Weld Center Line into Heat-Affected Zone of an As-Welded Type 308 Stainless Steel Submerged-Arc Weld in a 0.76-m-diam by 9.5-mm-wall (30 by 3/8 in.) Type 304 Stainless Steel Pipe. (a) 1.8 mm (0.7 in.) below surface. (b) 4.3 mm (0.17 in.). (c) 6.9 mm (0.27 in.).

Longitudinal all-weld-metal specimens having a 0.64-mm-diam by 31.7-mm-long (0.25 by 1.25 in.) gage section with welded-on threaded grips were prepared with their center lines about 0.8 mm (0.03 in., designated L*x*A type),* 5 mm (0.2 in., designated L*x*B), and 8.7 mm (0.34 in., designated L*x*C) below the outside pipe wall elevation. Additional transverse weldment specimens having the same specimen geometry were prepared with center lines at the 4.3-mm location. The specimen fabrication has been described previously[53] for other welds.

Tensile tests were performed on L*x*A, L*x*B, and L*x*C type specimens at room temperature, 566°C (1050°F), and 649°C (1200°F) at a nominal 0.004/min strain rate by methods that have been described previously,[56] and analyzed according to usual methods.[57] The tensile data are presented in Tables 3.26 and 3.27. No clear-cut trends could be established for differences in tensile behavior with location in the weld from these few exploratory tests. The weld metal is about as strong as the surface pass region (L1) of type 308 CRE stainless steel weld metal[62] at

*The bulge in the weld (seen in Fig. 3.81) enables this specimen location, which otherwise would be partly beyond the pipe edge.

Table 3.26. Tensile Data for As-Welded Submerged-Arc Type 308 Stainless Steel Longitudinal All-Weld-Metal Specimens from a Type 304 Stainless Steel Seam-Welded Pipe

Specimen	Test Temperature (°C)	Test Temperature (°F)	Instron Measurements							Reduction of Area (%)
			Strength, MPa (ksi)					Strain, %, Engineering (True)		
			Engineering			True				
			0.2% Offset Yield	Ultimate	Fracture	Ultimate	Fracture	Uniform	Total	
L2A	25	70	310 (44.9)	585 (84.8)	587 (85.1)	832 (120.6)	920 (133.4)	42.2 (35)	51.5 (45)	36.2
L10C	25	70	328 (47.5)	611 (88.6)	565 (82.0)	945 (137.0)	1185 (171.8)	54.7 (44)	63.0 (74)	52.3
L2B	25	70	343 (49.7)	604 (87.6)	472 (68.5)	898 (130.2)	1176 (170.5)	48.6 (40)	58.8 (91)	59.3
L5A	566	1050	198 (28.7)	347 (50.3)	283 (41.1)	451 (65.4)	439 (63.7)	29.9 (26)	39.8 (44)	35.5
L4B	566	1050	174 (25.3)	361 (52.3)	276 (40.0)	478 (69.4)	453 (65.7)	32.8 (28)	45.7 (50)	39.2
L4A	649	1200	172 (24.9)	239 (34.7)	177 (25.7)	283 (41.0)	344 (49.9)	18.2 (17)	50.9 (66)	48.5
L9C	649	1200	173 (25.1)	245 (35.6)	164 (23.8)	294 (42.6)	353 (51.2)	19.7 (18)	55.6 (77)	53.4
L3B	649	1200	149 (21.6)	226 (32.8)	167 (24.2)	274 (39.8)	338 (49.0)	21.4 (19)	45.9 (71)	50.6

Table 3.27. Additional Tensile Data for As-Welded Submerged-Arc Type 308 Stainless Steel Longitudinal All-Weld-Metal Specimens from a Type 308 Stainless Steel Seam-Welded Pipe

Specimen Number	Test Temperature		Diametral Strain						Extensometer Measurements, MPa (ksi)		Regression Analysis σ_{true} (psi) = $k\varepsilon_{true}^{n}$		
			At Fracture			Away from Fracture							
	(°C)	(°F)	(%) max	(%) (min)	Ratio	(%) max	(%) (min)	Ratio	Elastic Limit	0.2% Offset Yield Stress	n	ln k	Standard Deviation (log cycles)
L2A[a]	25	70	25.0	15.5	1.6	21.5	15.0	1.4	193 (28.0)	316 (45.8)	0.257	12.138	0.43
L10C	25	70	34.2	27.8	1.2	23.0	11.7	2.0	277 (40.2)	318 (46.1)	0.1968	11.789	0.139
L2B	25	70	40.5	33.0	1.2	24.2	12.0	2.0	211 (30.6)	314 (45.5)			
L5A	566	1050	22.2	17.3	1.3	12.4	8.0	1.5	81 (11.7)	194 (28.1)			
L4B	566	1050	27.0	17.3	1.6	19.3	7.7	2.5	88 (12.7)	171 (24.8)			
L4A	649	1200	32.0	24.7	1.3	18.7	12.1	1.5	102 (14.8)	129 (26.0)	0.1077	10.776	0.030
L9C	649	1200	39.8	24.6	1.6	20.6	18.2	1.1	104 (15.1)	172 (25.0)			
L3B	649	1200	36.0	24.0	1.5	20.0	8.0	2.5	83 (12.1)	156 (22.6)	0.1311	10.758	0.039

[a]Gage diameter had been reduced to 0.200 in. (5.08 mm) to produce a true cylinder from originally flatted, nominally 0.25 in. diam.

room temperature, but exhibits occasionally lower strength at elevated temperatures. The weld is relatively ductile in tensile tests.

Creep-rupture tests are in progress at 649°C (1200°F) to assess the susceptibility of the as-welded metal to embrittlement by sigma phase. Two transverse specimens have been annealed 1 hr at 1038°C (1900°F) for comparison tests, but they have not been tested yet. A complete analysis of the data will be performed when the testing is completed, but the available rupture data are summarized in Table 3.28.

Table 3.28. Creep-Rupture Data at 649°C (1200°F) for Type 308 Stainless Steel Submerged-Arc Seam Weld in Type 304 Stainless Steel Pipe

Specimen	Stress		Rupture Time (hr)	Total Elongation (%)	Reduction of Area (%)
	(MPa)	(ksi)			
L7B	172	25.0	35.5	a	a
L6A	138	20.0	831.4	30.8	22
L3A	124	18.0	1798.3	17.9	14.8
L6B	124	18.0	1568.5	16.7	14.8
T2	172	25.0	126.0	14.8	21.1
T5	152	22.0	547.9	9.1	8.9
T4	138	20.0	1324.3	3.9	5.0
T1	124	18.0	2169.4	3.5	3.3

[a]Data not available yet.

The creep-rupture times at a given stress for weld metal are slightly longer than those from a recent statistical analysis[59] of average rupture times for type 304 stainless steel at 649°C (1200°F) (see Fig. 3.83). There are too few data to compare longitudinal and transverse specimens meaningfully. The type L*x*A and L*x*B specimens behave quite similarly for for the available data.

The transverse weld specimens exhibit lower total elongations and reductions of area (Fig. 3.84) than the longitudinal specimens; both

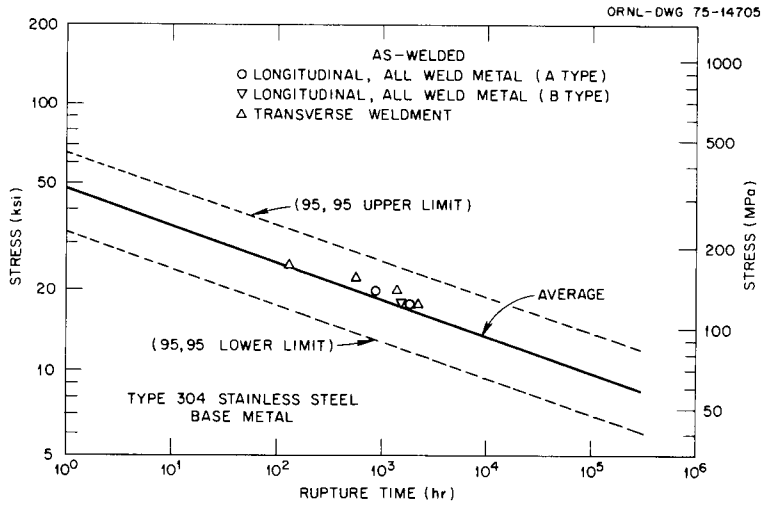

Fig. 3.83. Comparison of Creep Rupture of a Submerged Arc Type 308 Weld in a 0.76-m-diam by 9.5-mm-wall (30 by 3/8 in.) Type 304 Stainless Steel Pipe with Expected Behavior of Type 304 Base Metal as 649°C (1200°F).

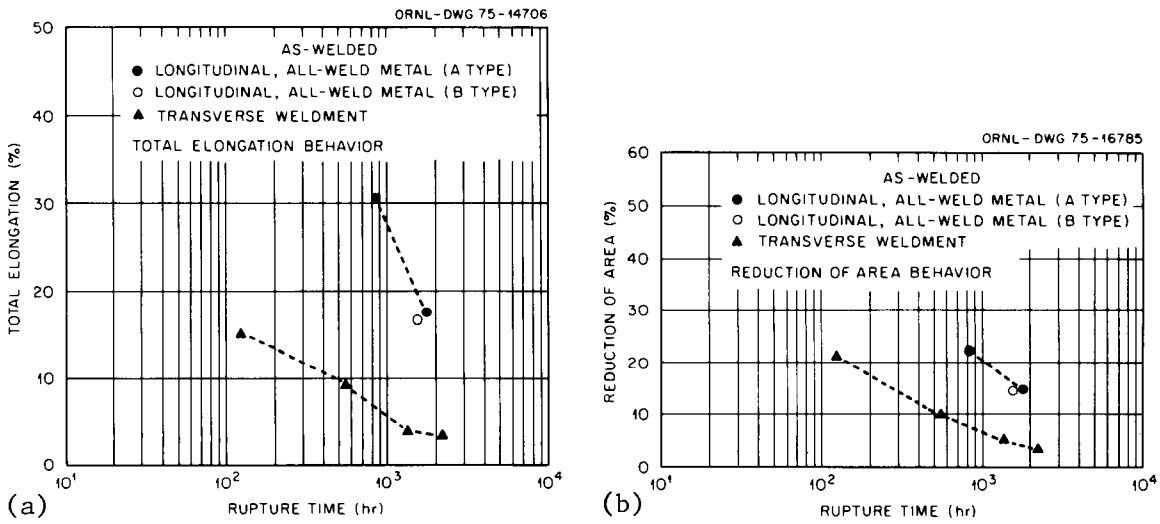

Fig. 3.84. Ductility of a Submerged-Arc Type 308 Weld in a 0.76-m-diam by 9.5-mm-wall Type 304 Stainless Steel Pipe (a) Total elongation. (b) Reduction of area.

measures of ductility decreased with increasing rupture time to about 5% after 1324 hr. The fracture surfaces (see Fig. 3.85) of all the transverse specimens were clearly of the interphase, substructurally affected type common to type 308 weld metals that have reduced elevated-temperature ductility due to sigma phase. Fractographic analyses of the longitudinal specimens remain to be performed.

Fig. 3.85. Fracture Surface of Type 308 Transverse Weldment Specimen that Failed After 547.9 hr in the Weld Metal During Creep at 649°C (1200°F) and 152 MPa (22 ksi), Showing Substructural Features Associated with Interphase Separations.

3.3.6 Observation of Substructural Separation During Creep Rupture of Type 16-8-2 Reference Heat at 593°C (1100°F) and 482°C (900°F) — R. T. King, D. P. Edmonds, G. M. Goodwin, R. S. Crouse, and E. Bolling

We have previously reported[63-65] data for a number of type 16-8-2 stainless steel welds that were creep-rupture tested at temperatures to 649°C (1200°F). The only evidence that substructural separations, probably due to interphase separation at austenite-sigma phase boundaries, might occur in this material was for automatically deposited GTA welds that

failed under an indentation punched in the gage section by the extensometer.[63] However, a long-time test at 593°C (1100°F) on a GTA weld[64] made with the Bechtel reference heat Arcos-2367R type 16-8-2 has resulted in one failure at 207 MPa (20 ksi) after 11,896.5 hr that involves fracture morphologies commonly associated with interphase separations at austenite-sigma phase boundaries (in type 308 weld metal). The fracture surface is shown in Fig. 3.86. The total elongation was 17.9%, and 28% reduction of area occurred.

The other long-time test on this material, run at 482°C (900°F) and 379 MPa (55 ksi), failed after 8261 hr with 20.5% total elongation and 19.2% reduction of area. Well-oxidized regions on the fracture surface just below the indentations made by extensometers provide indications that failure initiated in these damaged regions and propagated by shear across the remaining 80% of the gage cross section. The cracking that occurred on the side of the gage length and substructural separations in the oxidized regions are illustrated in Fig. 3.87.

3.3.7 Observations of Intergranular Failures in the Heat-Affected Zone of Austenitic Stainless Steel Weldments — R. T. King, R. S. Crouse, and E. Bolling

In Sect. 3.3.4, we showed that transverse weldment specimens made with type 308 CRE stainless steel electrodes in 25-mm (1-in.) type 304 stainless steel plate from reference heat 9T2796 failed intergranularly in the heat-affected zone (HAZ) for stresses from 124 to 152 MPa (18–22 ksi), at 593°C (1100°F). We had also reported[66] that transverse weldment specimens made with type 308 CRE stainless steel electrodes in heat 300380, 60-mm-thick (2.375 in.) plate that was used in the FFTF vessel failed in the base metal under extensometer marks during testing at 593°C (1100°F). Other tests on two transverse weldment specimens without extensometer damage and transverse specimens that contained only weld metal in the gage section led to the conclusion that the weld metal is stronger in the transverse direction for these creep conditions than the HAZ material, and that the extensometer damage is not required to cause low-ductility failures in the weld HAZ. A specimen (CE 43-33) that failed in that mode without extensometer damage had been cut from near

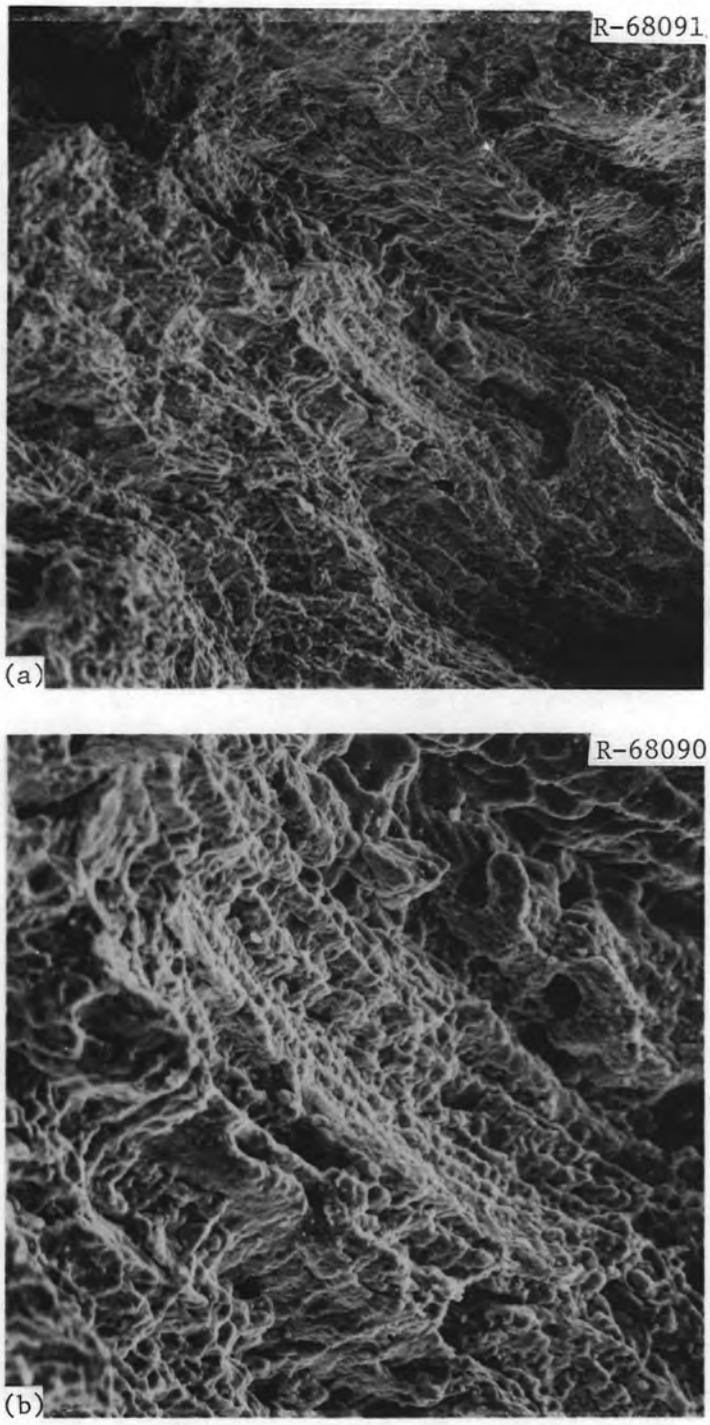

Fig. 3.86. Representative Area of Type 16-8-2 GTA Weld that Failed After 11,896.5 hr at 30 ksi (207 MPa). Fracture surface shows substructural separations commonly observed in association with low ductility failures along austenite-sigma phase boundaries. (a) 100×. (b) 300×.

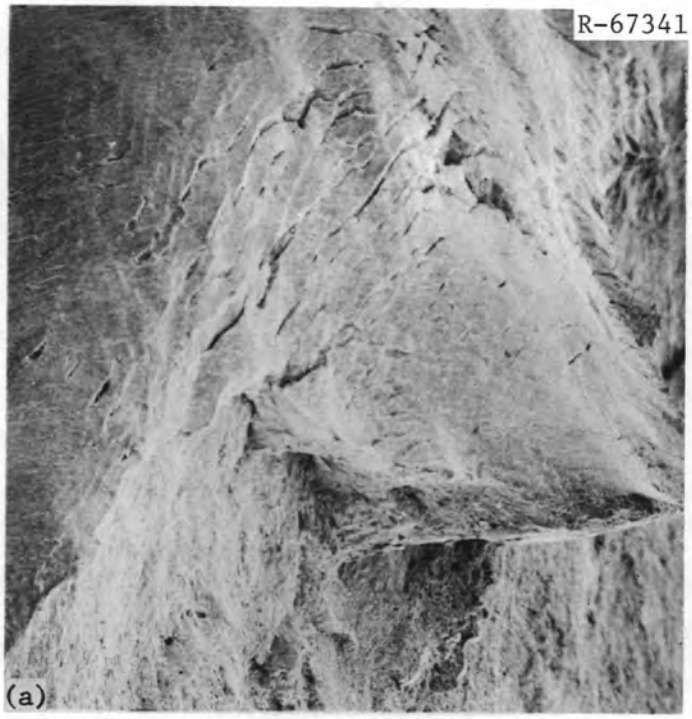

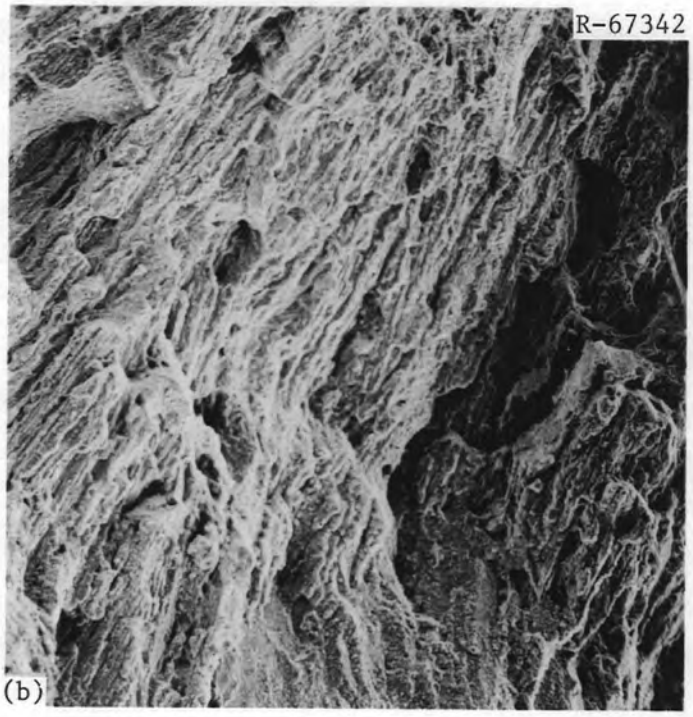

Fig. 3.87. Type 16-8-2 Specimen that Failed at 482°C (900°F) by Substructural Separation in a Region Damaged (Deformed) by Extensometer Mounting. (a) Cracking on side of specimen near damaged material. (b) Substructural separations in damaged region.

the surface (T1-type). It had been tested at 228 MPa (33 ksi) to failure in 673.8 hr and was examined by scanning electron microscopy. The predominantly intergranular fracture mode is apparent in Fig. 3.88.

A major manufacturer of thin-walled stainless steel pipe provided a relatively uncharacterized 0.13-m-long (5-in.) section of type 304 stainless steel pipe, 0.165 m (6.5-in.) OD by 6.4 mm (0.25 in.) wall thickness. The weld is likely to be autogeneous, made by the gas tungsten-arc process. We attempted to cut two longitudinal all-weld-metal specimens from the pipe, but the gage sections contained over 80% base material from the HAZ region. The specimens were creep tested at 649°C (1200°F) in air. Results are given in Table 3.29. The rupture times are slightly

Table 3.29. Creep-Rupture Behavior at 649°C (1200°F) of Type 304 Welded Pipe Specimens with Gage Sections Parallel to Welding Direction, Having About 80% Heat-Affected Zone, 20% Weld Metal

Stress		Rupture Time (hr)	Total Elongation[a] (%)	Reduction of Area (%)
(MPa)	(ksi)			
96.5	14.0	922.9	13.2	11.6
137.9	20.0	78.4	13.1	14.6

[a]Averaged over gage section.

above the (0.95, 0.95) lower limit[59] for type 304 stainless steel base metal, but the total elongations and reductions of area are relatively low. The base metal region fractured in a predominantly intergranular fashion, while the weld metal region fractured with substructural separations commonly observed for failures that involve cracking at austenite-sigma phase boundaries. Figure 3.89 shows fracture surfaces. It was not possible to ascertain which region failed first.

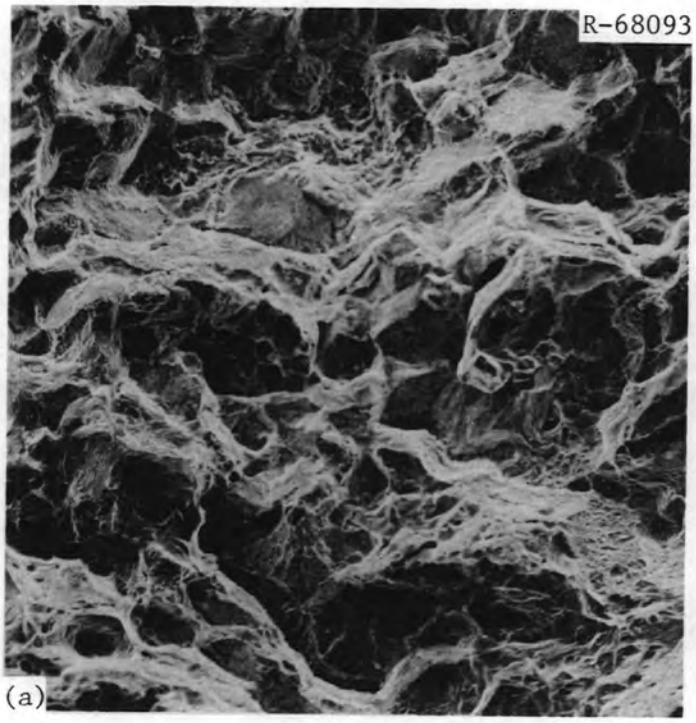

(a)

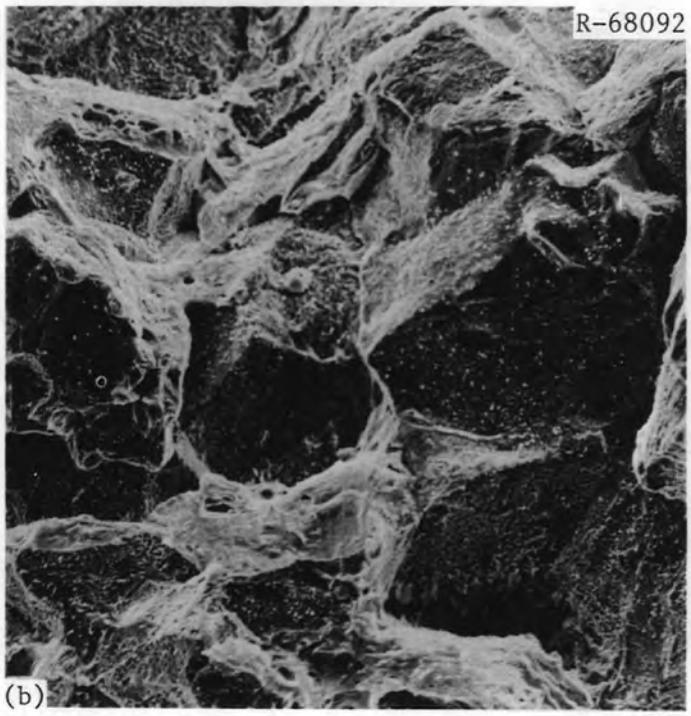

(b)

Fig. 3.88. Predominantly Intergranular Fracture Surface of a Transverse Weldment Specimen that Failed at 593°C (1100°F) in the HAZ. No extensometer damage was involved. (a) 100×. (b) 300×.

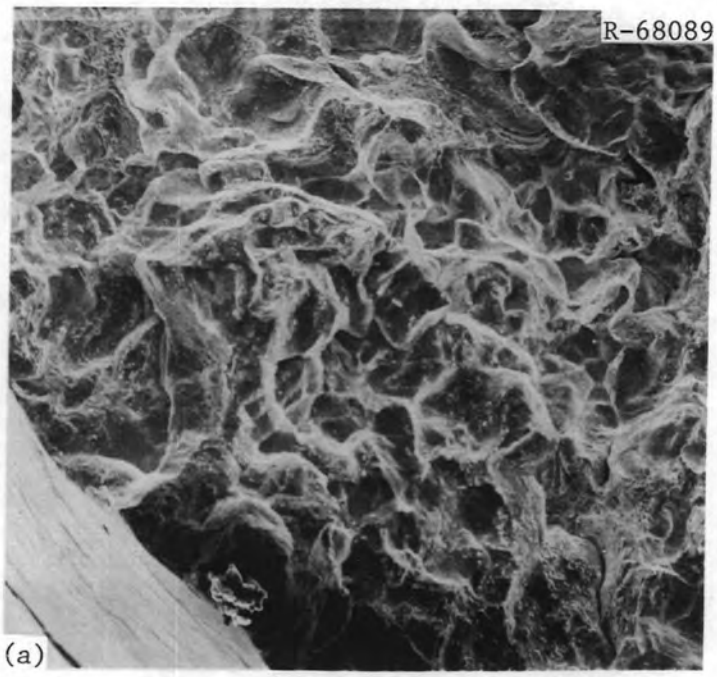

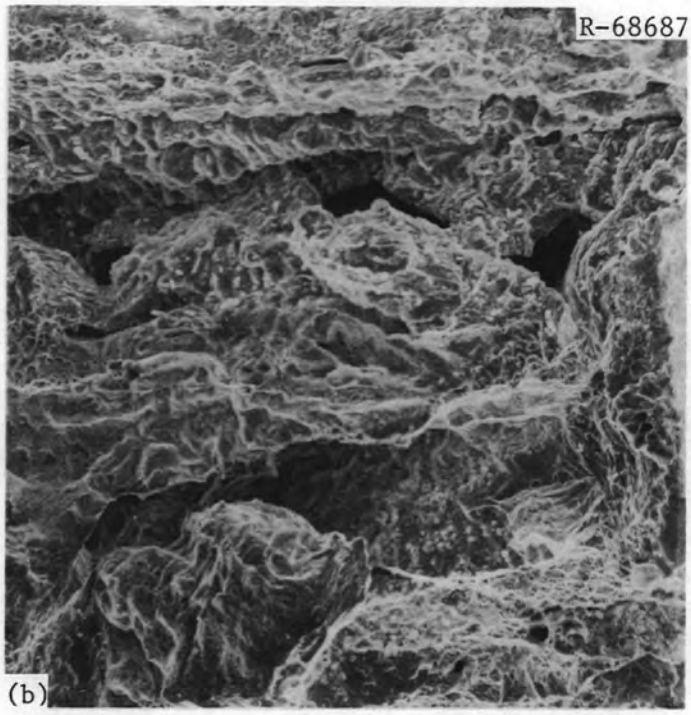

Fig. 3.89. Fracture Surface of Type 304 Stainless Steel Welded Pipe Specimens. 150×. (a) Intergranular failure in base metal region. (b) Substructural separations in weld metal.

3.4 MECHANICAL PROPERTIES OF STEAM GENERATOR MATERIALS — C. R. Brinkman

3.4.1 Creep-Rupture Properties of 2 1/4 Cr-1 Mo Steel — R. L. Klueh

Last quarter[67] we reported on the effect of heat treatment on the tensile properties of annealed 2 1/4 Cr-1 Mo steel. In this report, we discuss the effect of these same heat treatment processes on the creep-rupture properties.

A steel is given a full anneal ("annealed") by slowly cooling it from the austenitizing temperature to form a microstructure that is primarily an aggregate of proeutectoid ferrite and pearlite. Such an anneal is usually accomplished by furnace cooling. Alternatively, an isothermal anneal is often used — especially for tubing — to obtain the same microstructure. For an isothermal anneal, the steel is furnace cooled from the austenitizing temperature to some intermediate temperature, where most of the transformation to ferrite and pearlite occurs, then cooled to room temperature. For carbon steels the rate at which the tube cools to the isothermal transformation temperature and the rate at which it cools to room temperature after transformation are thought to be unimportant. We previously showed[67] that for 2 1/4 Cr-1 Mo steel, the rate at which the steel is cooled to the isothermal transformation temperature of 704°C (1300°F) and the rate at which it is cooled to room temperature after 2 hr at 704°C have a negligible effect on the room-temperature tensile properties.

Isothermally annealed 2 1/4 Cr-1 Mo steel is to be used in the steam generator of the demonstration liquid-metal fast breeder reactor. Since the decision to use that heat-treated condition was made after we had obtained a considerable amount of data on fully annealed steel (furnace cooled) and because much of the data available in the literature[68] is on fully annealed steel, it was of interest to determine the kinds of differences that can result from different annealing treatments. In the present report, steel plates given different anneals were tested. Tests were made on three steel plates (taken from the same heat of steel): two were given different full anneals (two different furnace cooling rates) and one was given an isothermal anneal. We previously reported[67] on the tensile properties of these same steels over the range 25 to 593°C (77—1100°F).

Sections of a 25-mm (1-in.) plate from a single heat (B&W heat 20017) were put in the annealed condition by austenitizing for 1 hr at 927°C and then furnace cooling. A section was also isothermally annealed by furnace cooling to 704°C (1300°F) at about 83°C/hr, held at that temperature for 2 hr, then furnace cooled. Figure 3.90 shows the cooling curves for these three heat-treated conditions. For comparison, the curve for the air-cooled plate (normalized) is also shown. Hereafter, the two annealed plates will be referred to as AN-1 and AN-2 (AN-2 was cooled faster than AN-1), and the isothermally annealed plate as IA. Most of our tests were made on AN-1 and IA.

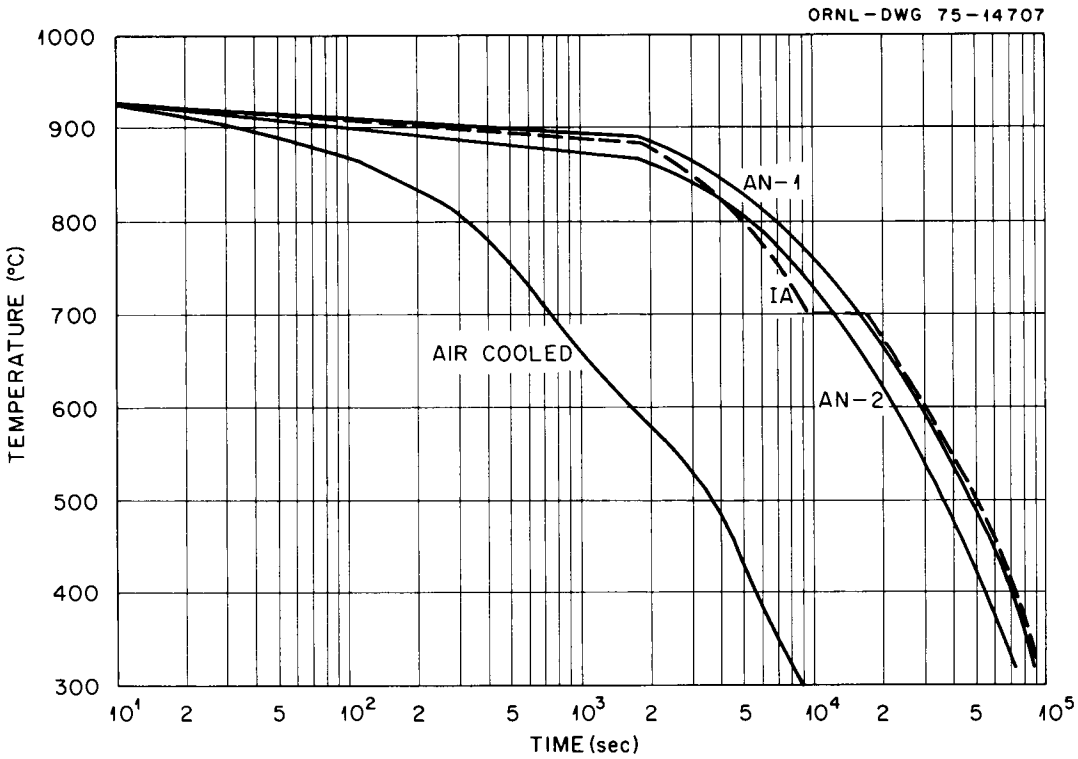

Fig. 3.90. Cooling Curves for the Three Different Heat Treatments used on the Plates. For comparison, the curve for an air-cooled plate is also shown.

The microstructures of the steel in these three heat-treated conditions were previously discussed, as was the chemical composition.[67] After all three heat treatments, the microstructures were primarily proeutectoid ferrite with some pearlite and bainite. Heat treatments

AN-1, AN-2, and IA were estimated to have respectively 1, 15, and 3—5% bainite and 5, <1, and about 1—2% pearlite.

For the creep-rupture tests at 454, 510, and 566°C (850, 950, and 1050°F), specimens with a 6.4-mm-diam × 63.5-mm-long (0.25 × 2.50 in.) reduced section were used. The tests were made in air on lever-arm creep frames with 12:1 and 20:1 ratios; the specimens were heated by a Marshall resistance furnace. During test the temperature was monitored and controlled by three Chromel vs Alumel thermocouples attached along the specimen gage section. Temperatures were controlled to ±1°C, and the temperature varied less than ±2°C along the gage section. Creep strains were measured with a mechanical extensometer attached to the specimen shoulders, and the strain was read periodically on a dial gage with a sensitivity of 10^{-5} in.

The results for the creep-rupture tests at 454, 510, and 566°C for AN-1, AN-2, and IA are given in Tables 3.30, 3.31, and 3.32, respectively. In Fig. 3.91 the creep-rupture curves are given for the three different heat treatments. Creep-rupture tests have been made over a range of stresses at all three temperatures for heat treatments AN-1 and IA, with the most detailed work being done on AN-1; considerable low-stress creep data are being obtained on AN-1 and will be reported later. For AN-2, a creep-rupture curve was obtained only at 510°C, with some comparative tests being made at the other two temperatures.

Several points are of interest from Fig. 3.91. At 510°C and low stresses, there is an obvious difference between the properties of AN-2 — the fast-cooled anneal — and the other two heat treatments. As the stress is lowered (longer rupture life), however, the properties for AN-2 appear to approach those of the other two heat treatments. At both 510 and 566°C, the properties for AN-1 are slightly above those for IA, but as the stress is decreased, the rupture times for these two steels also approach one another. Note that at 566°C the one test on AN-2 at 138 MPa (20 ksi) is stronger than the other two heat treatments, but the difference is not nearly as large as it was at 510°C. At 454°C, where only AN-1 and IA data were obtained, the curves for the two appear to deviate as the stress is decreased.

Table 3.30. Creep-Rupture Properties of Annealed (AN-1) 2 1/4 Cr-1 Mo Steel

Stress (MPa)	Stress (ksi)	Rupture Life (hr)	Elongation (%)	Reduction of Area (%)	Minimum Creep Rate (%/hr)
			454°C (850°F)		
327	47.5	a			0.000106
358	52.0	1435.3	17.2	70.8	0.00142
379	55.0	539.1	18.5	71.4	0.0056
413	60.0	233.4	19.2	64.4	0.0148
448	65.0	48.9	17.3	66.4	0.062
			510°C (950°F)		
152	22.0	9650.3	32.8	69.6	0.000125
172	25.0	b			0.0005
172	25.0	2788.0	36.4	76.1	0.00053
189	27.5	1396.4	35.6	81.4	0.00125
207	30.0	1089.3	34.7	82.3	0.0025
241	35.0	476.0	26.4	77.0	0.0043
276	40.0	135.5	28.8	76.3	0.0243
310	45.0	47.5	24.4	76.0	0.069
			566°C (1050°F)		
103	15.0	8194.8	18.6	47.0	0.00065
124	18.0	1804.6	27.9	66.1	0.0055
138	20.0	707.3	31.2	77.9	0.00187
138	20.0	885.4	32.3		
152	22.0	222.9	46.4	82.3	0.086
172	25.0	78.2	35.2	83.9	0.0375
172	25.0	136.5	34.0		0.0196
207	30.0	16.3	40.2	85.1	0.51

[a]Test in progress.

[b]Test discontinued after 1321.3 hr and 3.1% elongation.

Table 3.31. Creep-Rupture Properties of Annealed (AN-2) 2 1/4 Cr-1 Mo Steel

Stress (MPa)	Stress (ksi)	Rupture Life (hr)	Elongation (%)	Reduction of Area (%)	Minimum Creep Rate (%/hr)
			510°C (950°F)		
172	25.0	a			
207	30.0	2372.8	32.3	75.8	0.000168
207	30.0	2354.4	28.4	78.1	0.000167
276	40.0	952.9	22.8	73.4	0.00101
310	45.0	563.0	20.4	70.0	0.0029
345	50.0	308.4	19.9	61.1	0.00848
378	55.0	a			
			566°C (1050°F)		
138	20.0	982.2	33.4	73.0	0.00267

[a]Test in progress.

Table 3.32. Creep-Rupture Properties of Isothermally Annealed 2 1/4 Cr-1 Mo Steel

Stress (MPa)	Stress (ksi)	Rupture Life (hr)	Elongation (%)	Reduction of Area (%)	Minimum Creep Rate (%/hr)
			454°C (850°F)		
338	49.0	1301.9	23.2	70.3	0.00104
358	52.0	854.9	17.5	70.4	0.002
379	55.0	479.1	24.3	67.7	0.00389
413	60.0	214.6	15.7	63.2	0.00908
			510°C (950°F)		
152	22.0	6853.9	32.4	78.7	0.000165
172	25.0	1879.5	43.2	84.6	0.000462
207	30.0	526.0	39.3	81.7	0.00339
241	35.0	204.5	43.7	79.6	0.00967
276	40.0	74.2	22.4	72.9	0.0397
			566°C (1050°F)		
103	15.0				0.000605
124	18.0	1233.1	25.8	76.9	0.00723
138	20.0	400.4	47.5	80.0	0.0322
172	25.0	68.5	48.2	85.9	0.136

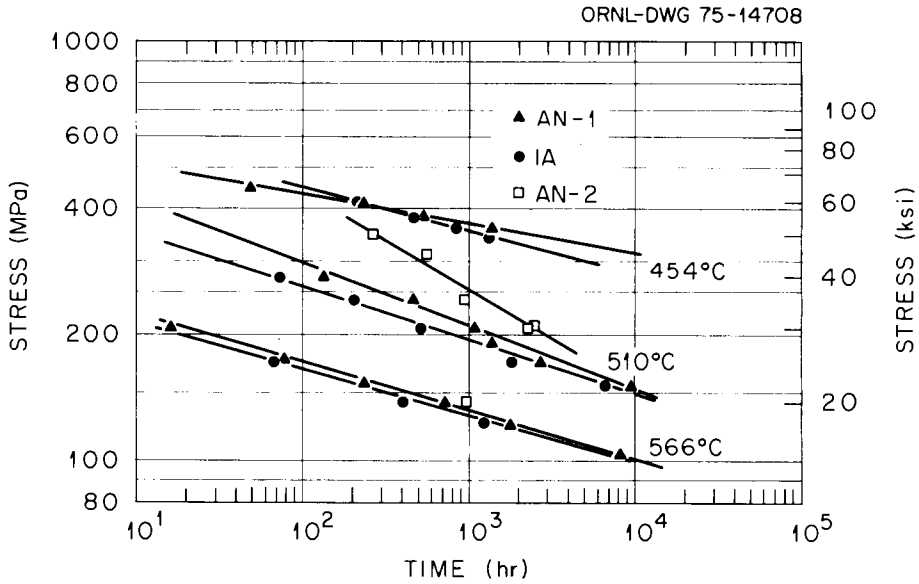

Fig. 3.91. Creep-Rupture Curves for 2 1/4 Cr-1 Mo Steel at 454, 510, and 565°C; Three Different Heat Treatments Were Tested.

In Fig. 3.92 the stress is plotted against the minimum creep rate for the tests at 454, 510, and 566°C. In general, the results parallel the rupture life results. At 454°C, Fig. 3.92(a), the AN-1 and IA creep rates again deviate with decreasing stress, while at 510°C, Fig. 3.92(b), the creep rates for these two heat treatments approach one another, especially at the low stresses. For AN-2 the creep rates are considerably greater than those for IA and AN-1, but there are again indications that the curves for AN-2 will approach those for the other two heat treatments at low stresses.

As seen in Fig. 3.92(c), the results for AN-1 and IA at 566°C are somewhat more complicated. There appears to be one curve (straight line) at low creep rates and another at high creep rates, or alternatively, a single discontinuous curve. That is, an extension of the curve through the creep rates determined for stresses of 103 and 124 MPa (15 and 18 ksi) would predict a creep rate of about 0.015 at 138 MPa (20 ksi), and with little difference between AN-1 and IA. The observed value for AN-1 is about an order of magnitude lower than this, while that for IA is half a log cycle lower. Furthermore, the observed creep rates for the 138-MPa tests are less than those for the 124-MPa tests, certainly an unexpected result.

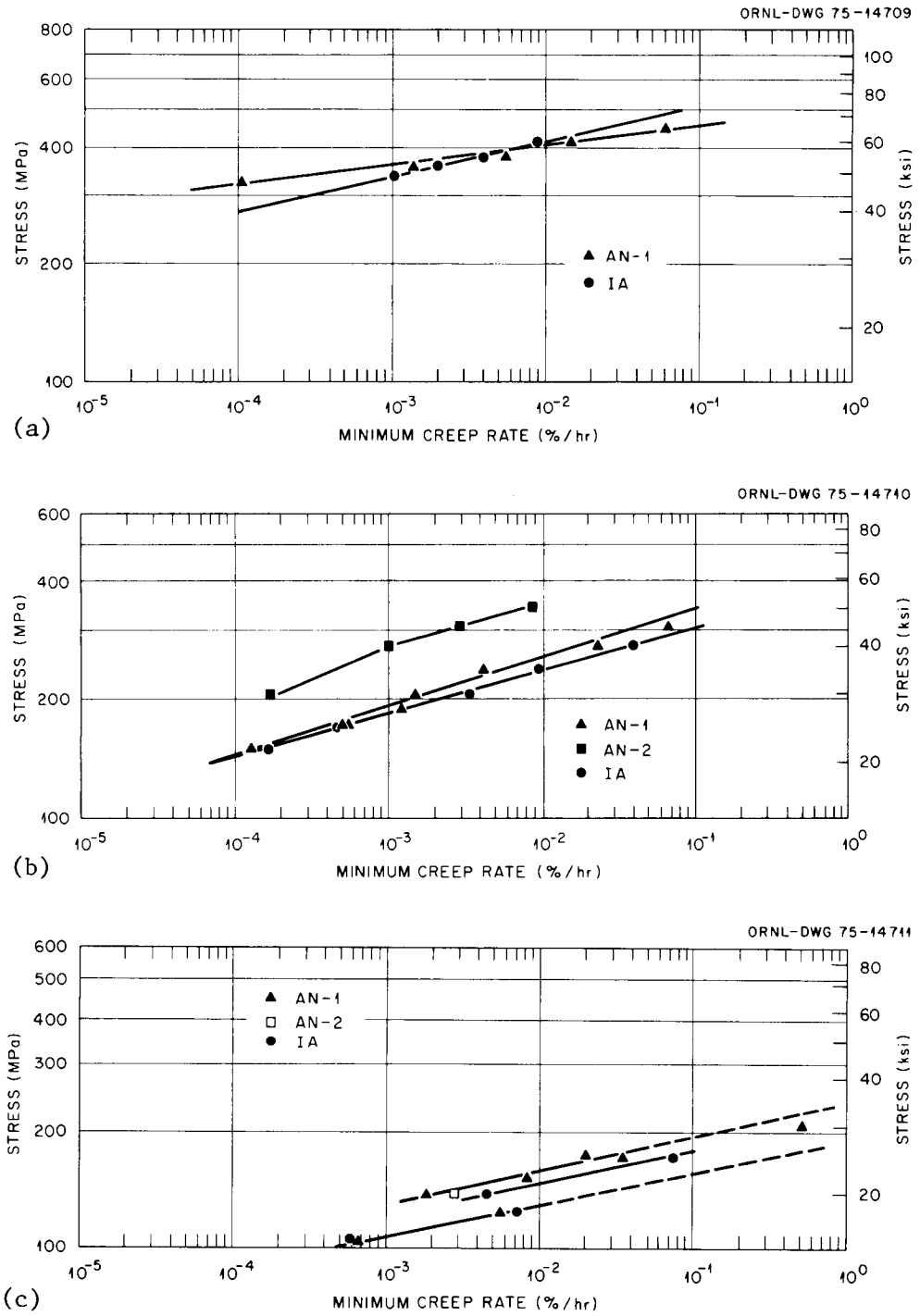

Fig. 3.92. Stress as a Function of Minimum Creep Rate for 2 1/4 Cr-1 Mo Steel. (a) Tests on annealed and isothermally annealed plates at 454°C. (b) Tests on two fully annealed and one isothermally annealed steel at 510°C. (c) Tests on two fully annealed and one isothermally annealed steel at 566°C.

To try and understand the results, we closely examined the creep curves for each of the above tests, and it was immediately obvious that there were two types of creep curves. These are shown schematically in Fig. 3.93. Curve A is the classical creep-rupture curve with primary, secondary, and tertiary creep stages. Curve B, however, is somewhat more complicated. After a period of decreasing creep rate, an apparent steady-state stage is reached, after which the creep rate beings to increase (tertiary creep?). Instead of increasing to rupture, however, the creep rate again decreases and goes into what appears to be another steady-state stage (i.e., creep rate is essentially constant). Finally, after this second steady-state region, the creep rate again increases and continues to increase until rupture. For curves that showed this nonclassical behavior, the creep rate for the first steady stage was plotted in Fig. 3.92(a) and (b).

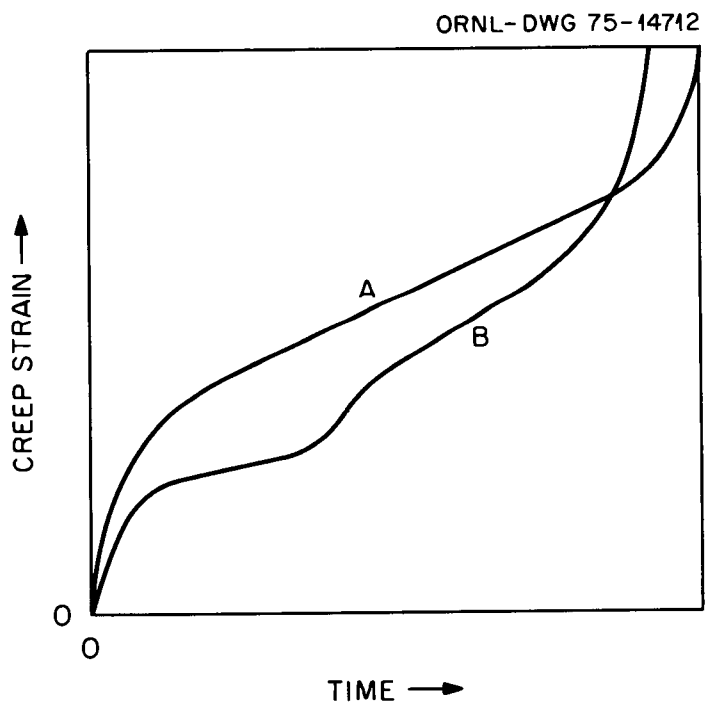

Fig. 3.93. Schematic Diagrams for Classical and Nonclassical Curves of the Type Observed for 2 1/4 Cr-1 Mo Steel.

When the creep curves were reexamined for shape, the 566°C tests at 103 and 124 MPa for both heat treatments AN-1 and IA displayed classical creep curves. At 138 MPa and above, nonclassical curves were observed. An example of a nonclassical curve is shown in Fig. 3.94. If the creep rate for the second steady-state region is plotted for the nonclassical creep curves at 566°C (stress ⩾ 138 MPa), the points appear to fall on the extension of the curve for the tests at 103 and 124 MPa — the test that displayed classical creep curves. This is shown in Fig. 3.95(a). Table 3.33 gives the data used for Fig. 3.95.

The creep rate for the second steady-state creep stage was quite easily determined for the tests up to and including 172 MPa (25 ksi). At 207 MPa (30 ksi), however, it was possible only to determine one creep rate. Whether this was because a classical strain-time relationship again existed or whether the second steady-state stage was too short to be detected cannot be stated. Note that the 207-MPa test in Fig. 3.92(c) does not appear to fall on an extension of either of the two curves for AN-1.

Classical creep curves were observed for the tests at 454°C, while at 510°C apparently only nonclassical curves are observed for AN-1 and IA. On the other hand, for AN-2 at 510°C, all classical curves were found. An example of the nonclassical behavior at 510°C is shown in Fig. 3.94 for the 152 MPa (22 ksi) test on IA. For this low-stress test, as well as the tests below about 207 MPa (30 ksi), the nonclassical shape was easily detected and a creep rate easily determined for the second steady-state creep stage. Above 207 MPa and below 310 MPa (45 ksi), however, the second steady-state stage appeared to be quite short. Although estimates were made and they fell on the extension of the low-stress curves, these estimates were often somewhat subjective. At 310 MPa we could only determine one steady-state stage. Figure 3.95(b) is a plot of the data for the second steady-state stage at 510°C; the data are given in Table 3.33.

Figure 3.96 shows the elongation and reduction of area data plotted against the rupture life at 454, 510, and 566°C. Curves, which are meant only to show data trends, have been drawn through the data points. The

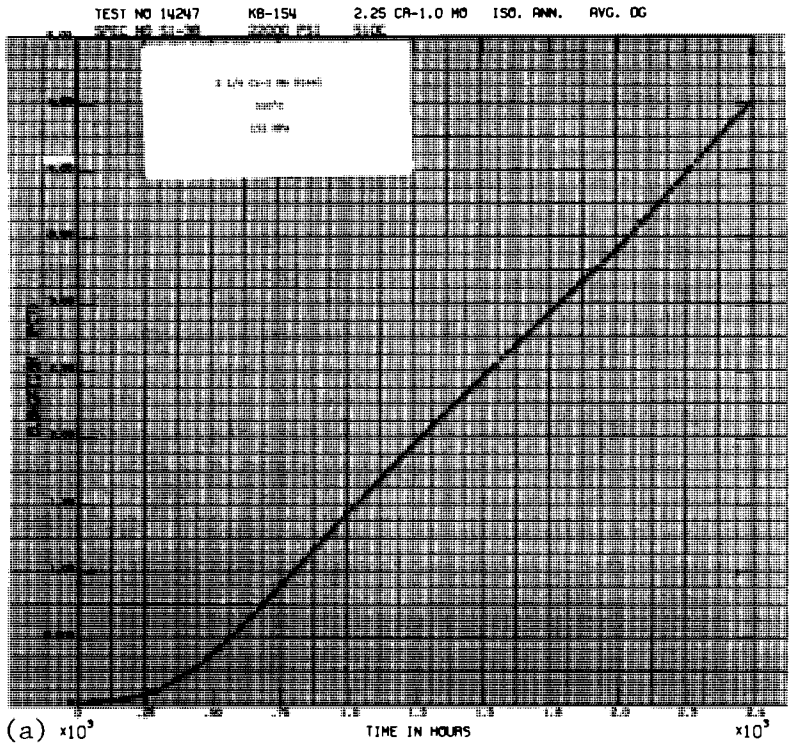

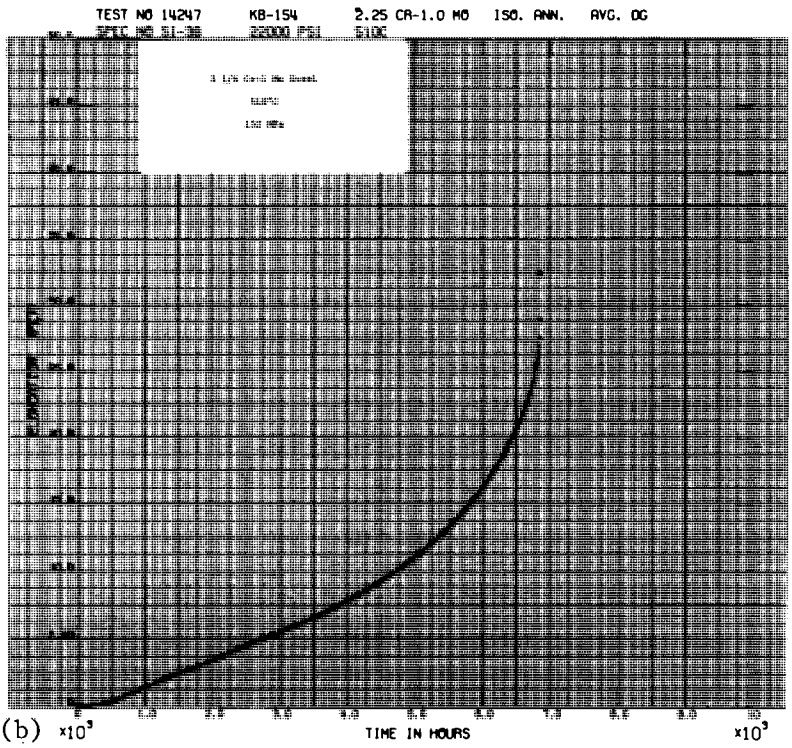

Fig. 3.94. Example of Nonclassical Creep Curve for Annealed 2 1/4 Cr-1 Mo Steel; Test at 152 MPA at 510°C. (a) To 5%. (b) To rupture.

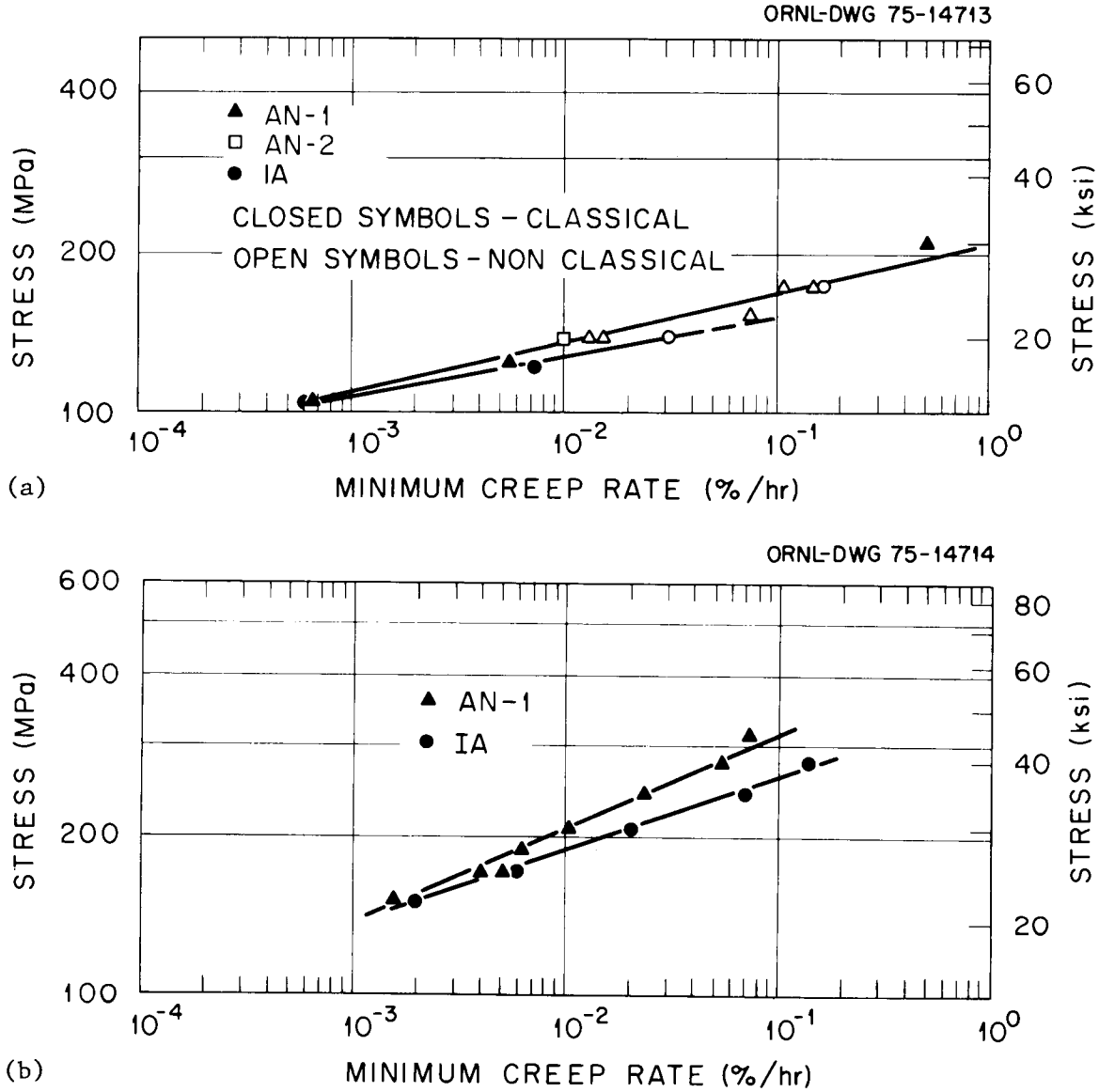

Fig. 3.95. Stress as a Function of Creep Rate for Second Steady-State Stage. (a) Heat treatments AN-1, AN-2, and IA at 566°C. (b) Heat treatments AN-1 and IA at 510°C.

Table 3.33. "Steady-State Creep Rates" for Tests at 510 and 566°C

Stress		Creep Rate, %/hr			
		AN-1		IA	
(MPa)	(ksi)	Stage 1	Stage 2	Stage 1	Stage 2
		510°C (950°F)			
152	22	0.000125	0.00153	0.000165	0.00196
172	25	0.0005	0.0042	0.000462	0.006
172	25	0.00053	0.00515		
189	27.5	0.00125	0.0061		
207	30	0.0025	0.010	0.00339	0.021
241	35	0.0043	0.0235	0.00967	0.0702
276	40	0.0285	0.0546	0.0397	0.141
310	45	0.071	a		
		566°C (1050°F)			
103	15	0.00065	a	0.000605	a
124	18	0.0055	a	0.00723	a
138[b]	20[b]	0.00187	0.0159	0.0175	0.0322
138	20	0.0033	0.013		
152	22	0.0086	0.076		
172	25	0.0375	0.150	0.075	0.17
172	25	0.0196	0.110		
207	30	0.51	c		

[a]Classical creep curve; no second steady-state creep stage was distinguished.

[b]Heat treatment AN-2 also displayed a nonclassical creep curve at 138 MPa and 566°C with creep rates of 0.00267 and 0.0099%/hr.

[c]No second steady-state stage could be delineated.

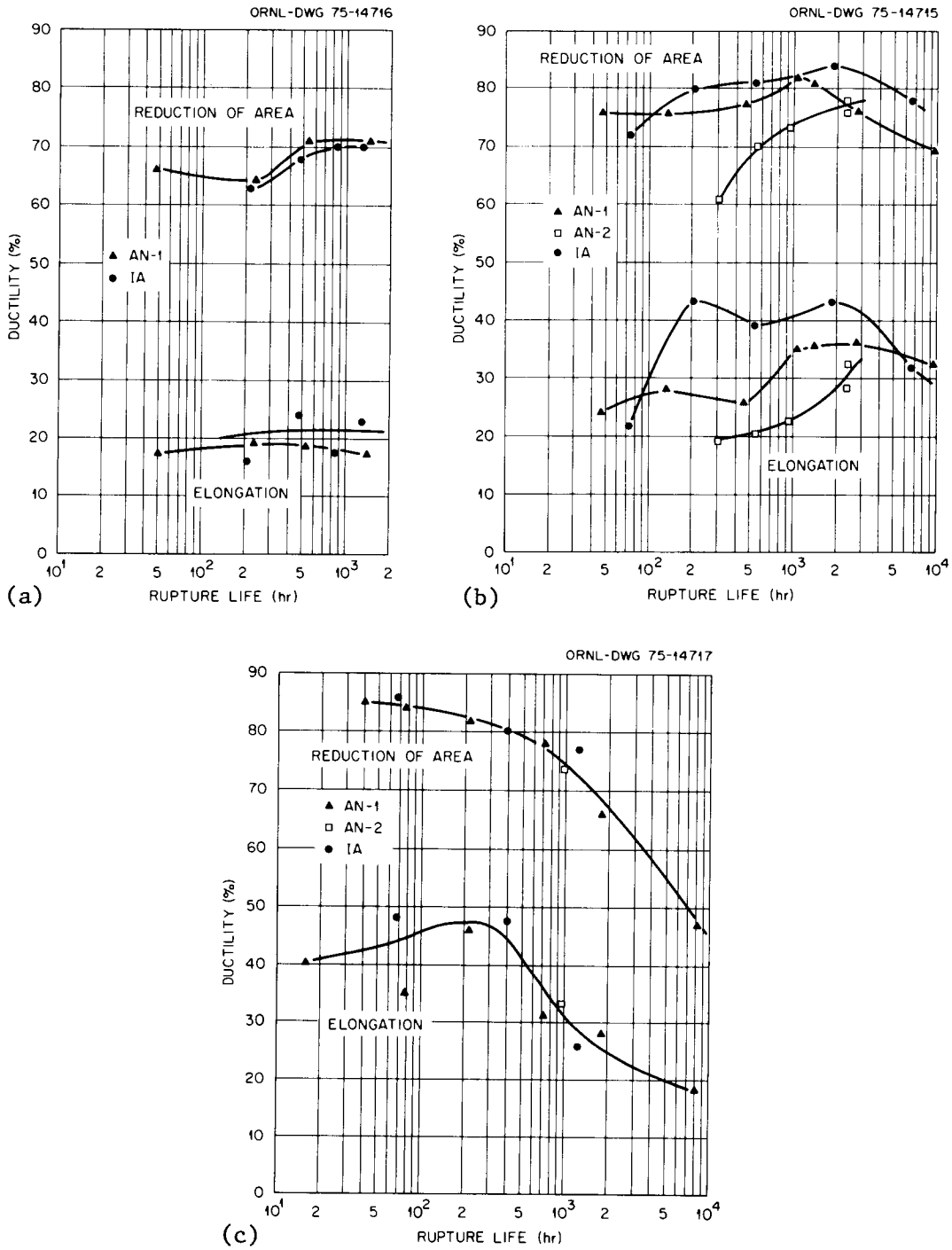

Fig. 3.96. Variation in Rupture Elongation and Reduction of Area with Rupture Time for Annealed 2 1/4 Cr-1 Mo Steel at (a) 454°C, (b) 510°C, and (c) 566°C.

ductility at 454°C [Fig. 3.96(a)] showed little change with rupture life. At 510°C [Fig. 3.96(b)], both the elongation and reduction of area appear to go through a maximum with increasing rupture life. Although heat treatment AN-2 shows the least ductility over the stress range tested, it appears that it will reach its maximum ductility at a longer rupture life than the other two heat treatments. For the 566°C ductility data, the ductility appears to rather continuously decrease with increasing rupture life, with no apparent effect of heat treatment.

Visual examination of the fractured specimens indicated that all the fractures at 454 and 510°C appeared to be of the cup-cone type. Likewise, cup-cone failures were indicated for the tests above 124 MPa (18 ksi) at 566°C. The specimens tested at 103 and 124 MPa (15 and 18 ksi) showed decreasing amounts of neck formation as the stress decreased (increased rupture life).

Metallographic examination of the fractured specimens was in general agreement with the visual observations. At 454 and 510°C, the fractures were essentially entirely transgranular. Only at 510°C was there any indication that grain boundary separation was occurring. Several grain boundaries back from the fracture surface showed separation, but the fracture itself showed considerable transgranular deformation, indicating that the fracture was transgranular. At 565°C, the only fractures that showed other than transgranular aspects were those tested at 103 and 124 MPa (15 and 18 ksi). However, even in this case, there was considerable grain deformation, and the fracture was primarily transgranular.

3.4.2 Fatigue Behavior of 2 1/4 Cr-1 Mo Steel — C. R. Brinkman

Crack growth data on 2 1/4 Cr-1 Mo steel are reported in Sect. 3.6.3 of this report.

3.4.2.1 Creep-Fatigue Data Analysis — M. K. Booker

Analysis of creep-fatigue data for 2 1/4 Cr-1 Mo steel is continuing by several methods. Current results obtained by the method of strain range partitioning[69] will be presented this quarter.

As discussed earlier,[70] the strain range partitioning approach involves partitioning the plastic strain range traversed by a cycling specimen into four types:

$\Delta\varepsilon_{pp}$ = tensile plastic strain reversed by compressive plastic strain,

$\Delta\varepsilon_{cc}$ = tensile creep strain reversed by compressive creep strain,

$\Delta\varepsilon_{cp}$ = tensile creep strain reversed by compressive plastic strain,

$\Delta\varepsilon_{pc}$ = tensile plastic strain reversed by compressive creep strain.

Here, "plastic" strain is defined as time-independent inelastic strain, while "creep" strain is defined as time-dependent inelastic strain. Figure 3.97 illustrates the "life relationships" determined for these four types of strain, whereby $\Delta\varepsilon_{pp}$, $\Delta\varepsilon_{cp}$, $\Delta\varepsilon_{pc}$, and $\Delta\varepsilon_{cc}$ are related respectively to N_{pp}, N_{cp}, N_{pc}, and N_{cc}, where N_i is the expected cycle life of a specimen cycled in pure $\Delta\varepsilon_i$ strain. Shown in the figure are the lines previously determined by Manson et al.,[69] compared with data from the current ORNL program and from the program at General Atomics Corporation.[71] The scatter in the ORNL and GA data is caused by the fact that in all cases the creep strain component ($\Delta\varepsilon_{cp}$, $\Delta\varepsilon_{pc}$, $\Delta\varepsilon_{cc}$) was small in comparison with the total plastic strain range.

It should be noted that both the lines and points in Fig. 3.97 were calculated by the linear damage rule, given by

$$\frac{1}{N_{cp}} + \frac{1}{N_{pc}} + \frac{1}{N_{cc}} + \frac{1}{N_{pp}} = \frac{1}{N} \ . \tag{36}$$

Ellis et al.[71] report somewhat similar results in the analysis of their data using the above rule, being able to predict the cylic life only

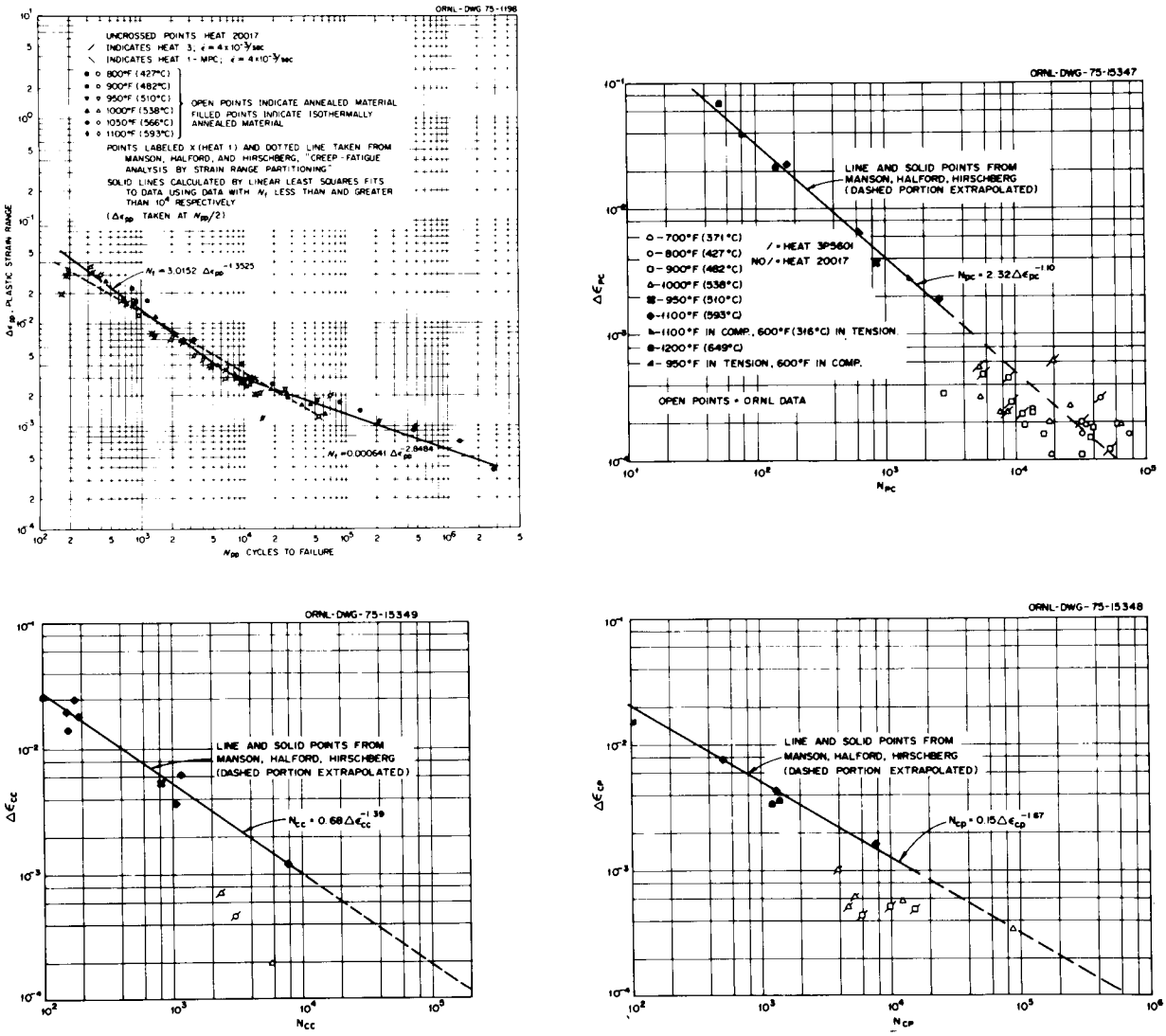

Fig. 3.97. Partitioned Life Relationship for 2 1/4 Cr-1 Mo Steel by the Method of Linear Damage Summation in the Strain Range Partitioning Approach.

within a factor of 3. Moreover, their analysis generally overestimated the cylic lines. Figures 3.98 and 3.99 show results of analysis of both the ORNL and GA data using the life relationships of Fig. 3.97 and the interaction damage rule, given by

$$\frac{F_{cp}}{N_{cp}} + \frac{F_{pc}}{N_{pc}} + \frac{F_{cc}}{N_{cc}} + \frac{F_{pp}}{N_{pp}} = \frac{1}{N} , \qquad (37)$$

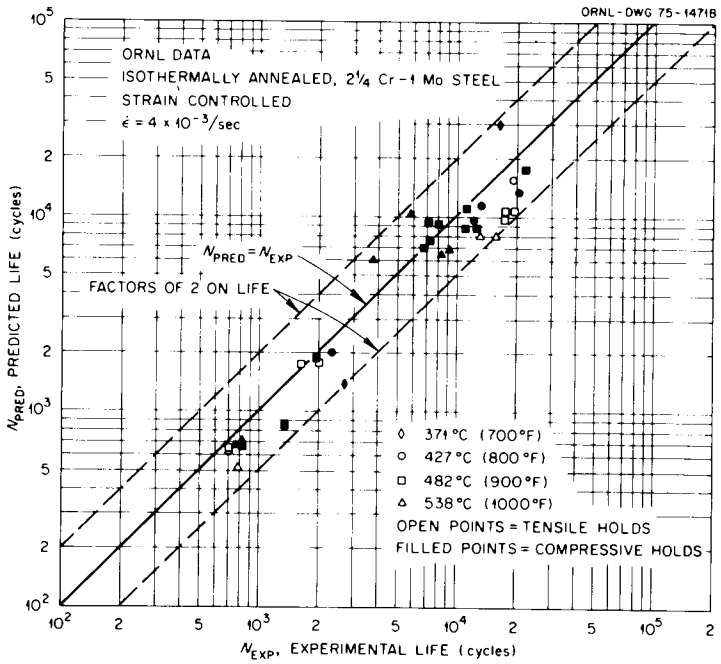

Fig. 3.98. Results of Analysis of ORNL Creep-Fatigue Data for 2 1/4 Cr-1 Mo Steel by the Method of Interaction Damage Summation in the Strain Range Partitioning Approach.

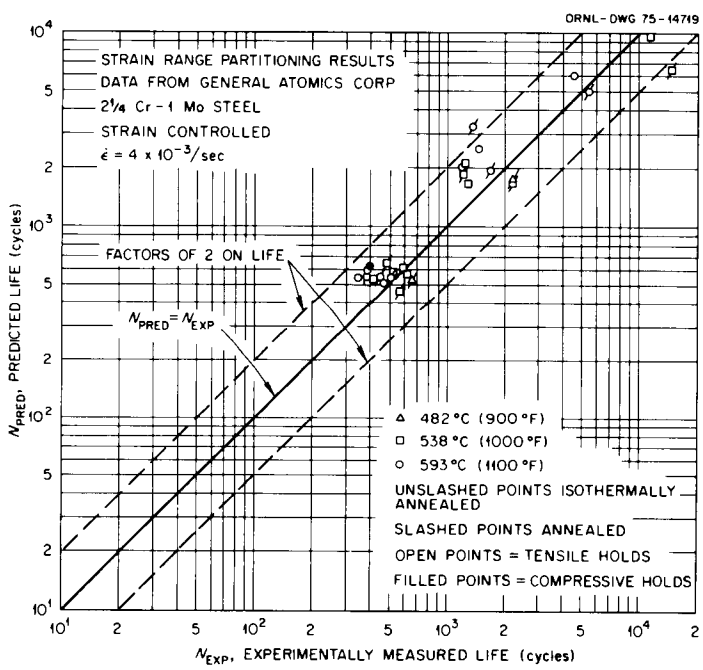

Fig. 3.99. Results of Analysis of GA Creep-Fatigue Data for 2 1/4 Cr-1 Mo Steel by the Method of Interaction Damage Summation in the Strain Range Partitioning Approach.

where, for example $F_{cp} = \Delta\varepsilon_{cp}/\Delta\varepsilon_{inel}$, $\Delta\varepsilon_{inel}$ being the total inelastic strain range. The results obtained in this manner are somewhat better than those reported in Ref. 71, the margin of error being an acceptable factor of 2.

Further results of analyses by this and other methods will be given in future reports.

3.4.2.2 Bilinear Cyclic Stress-Strain Constants — M. K. Booker

Based on the data contained herein, interim curves have been constructed showing the bilinear stress-strain constants κ_0, κ_1, κ_2, E_m, and C as functions of maximum strain, ε_{max}, at various temperatures from room temperature to 538°C (1000°F). These curves were primarily constructed to describe the behavior of cyclically strained material, although values (κ_0) obtained from monotonic tensile tests are also presented for comparison. The curves apply to isothermally annealed 2 1/4 Cr-1 Mo steel at strain rates of approximately 4×10^{-3}/sec.

Available data for the quantities κ_0, κ_1, κ_2, E_m, and C are described below. Figure 3.100 illustrates a typical bilinear stress-strain curve, which consists of a linear elastic portion whose slope is Young's modulus, E, and a linear "plastic" portion whose slope is E_m. The two portions meet at a stress value equal to the bilinear yield strength, σ_y^i, which is given by $\sqrt{3\kappa_i}$, where κ_i is κ_0, κ_1, or κ_2 depending on the type of behavior being described. The parameter C is given by

$$C = \frac{2}{3}\frac{EE_m}{E - E_m} . \tag{38}$$

Values of E_m, C, and κ_0 were obtained from monotonic tensile curves, as shown in Fig. 3.101. As shown, the plastic portion of the bilinear curve is constructed through the points on the stress-strain curve where (1) the strain is ε_{max} and (2) the plastic strain is one-half the plastic strain corresponding to ε_{max}.

For cyclic tests, we assume that E_m (and thus C) is the same as in the corresponding monotonic tensile curve. Figure 3.102 illustrates the subsequent calculation of the appropriate κ value. Here, the upper and

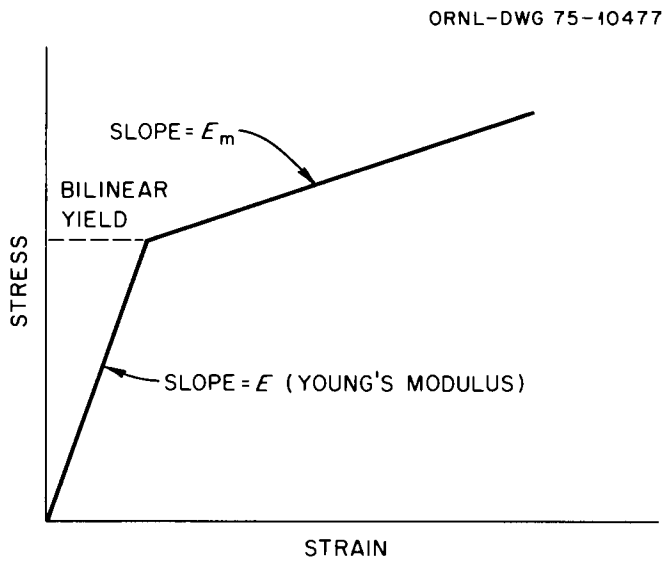

Fig. 3.100. A Typical Bilinear Stress-Strain Curve.

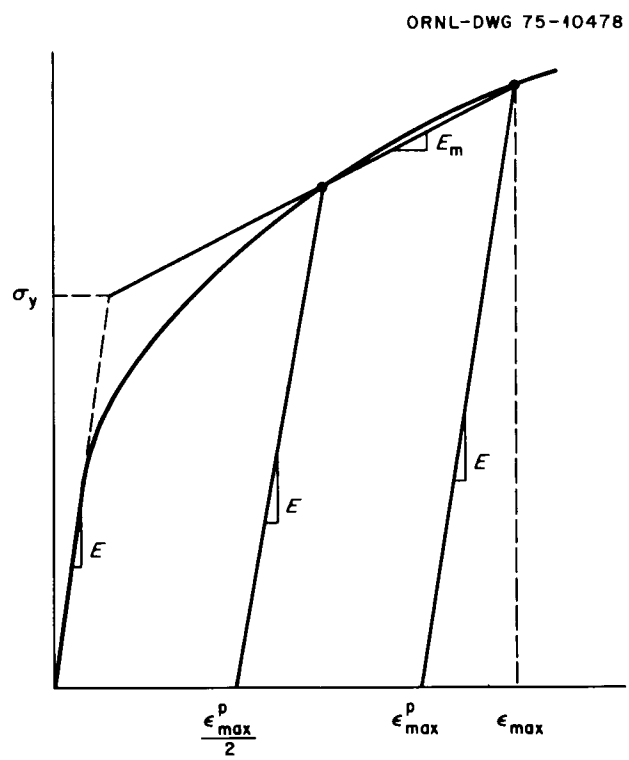

Fig. 3.101. Construction of a Binlinear Stress-Strain Curve from a Monotonic Tensile Curve.

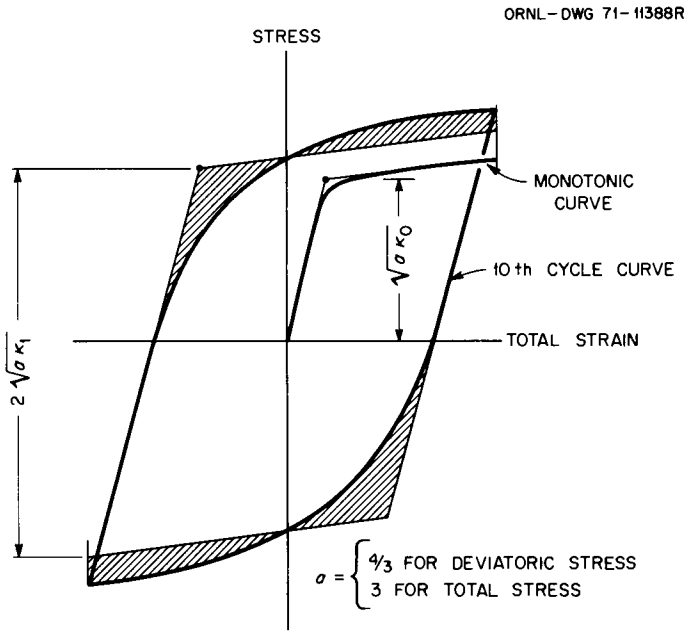

Fig. 3.102. Construction of a Bilinear Stress-Strain Curve for a Cyclic Test.

lower lines of slope E_m are placed such that for each the two shaded areas are equalized. In the present investigation, κ_1 was measured from the first recorded hysteresis loop after the tenth cycle. The actual cycles from which κ_1 was determined are listed later with the results given as N1. Meanwhile, κ_2 was measured from a cycle near the fatigue half-life, the number of this cycle being listed as $N_f/2$. The procedure for measurement of E_m, C, and κ values is summarized in Refs. 72 and 73.

The monotonic tensile tests used to calculate E_m, C, and κ_0 are shown in Table 3.34. These tests were conducted on the same heats as the cyclic tests in which their E_m values were used. Also, they were conducted as nearly as possible at the same temperatures and strain rates as the cyclic tests, within the limits of available data. However, several approximations had to be made because of limited data availability. These include: (1) for heat 3P5601, only data from tests conducted at a strain rate of 6.7×10^{-4}/sec were available; (2) for heat 3P5601, values at 482 and 538°C (900 and 1000°F) were obtained by linear interpolation between values at 454 and 510°C (850 and 950°F) and at 510 and 566°C (950 and 1050°F) respectively; (3) values at 316°C (600°F) for heat 20017

Table 3.34. Monotonic Tensile Data

Heat	Specimen	Temperature (°C)	Strain Rate (sec^{-1})	Measured Elastic Modulus		0.2% Offset Yield Strength		Source
				(GPa)	(ksi)	(MPa)	(ksi)	
20017	SI35A	25	6.7×10^{-3}	197	28,600	260	37.7	R. L. Klueh, ORNL
20017	SI4A	371	6.7×10^{-3}	196	28,500	228	33.0	R. L. Klueh, ORNL
20017	2MTL1	427	6.7×10^{-3}	190	27,600	221	32.0	J. P. Strizak, ORNL
20017	SI34A	538	6.7×10^{-3}	162	23,500	211	30.6	R. L. Klueh, ORNL
20017	KB-15	21	8.3×10^{-5}	219	31,800	281	40.8	a
20017	KB-53	21	8.3×10^{-5}	210	30,500	268	38.8	a
20017	KB-35	316	8.3×10^{-5}	165	23,900	252	36.6	a
20017	KB-27	427	8.3×10^{-5}	185	26,900	234	34.0	a
20017	KB-40	482	8.3×10^{-5}	174	25,300	233	33.8	a
20017	KB-68	482	8.3×10^{-5}	177	25,700	292	42.3	a
20017	KB-10	510	8.3×10^{-5}	175	25,400	235	34.1	a
20017	KB-4	510	8.3×10^{-5}	175	25,400	257	37.3	a
20017	KB-59	510	8.3×10^{-5}	156	22,600	232	33.7	a
20017	KB-16	538	8.3×10^{-5}	150	21,800	225	32.6	a
20017	KB-39	538	8.3×10^{-5}	158	22,900	236	34.3	a
20017	KB-64	593	8.3×10^{-5}	147	21,300	214	31.1	a
3P5601	IT-5	371	6.7×10^{-4}	172	25,000	179	26.0	J. P. Strizak, ORNL
3P5601	IT-6	427	6.7×10^{-4}	173	25,100	165	24.0	J. P. Strizak, ORNL
3P5601	IT-7	454	6.7×10^{-4}	170	24,700	176	25.5	J. P. Strizak, ORNL
3P5601	IT-8	510	6.7×10^{-4}	148	21,500	174	25.3	J. P. Strizak, ORNL
3P5601	IT-9	566	6.7×10^{-4}	143	20,700	158	23.0	J. P. Strizak, ORNL

[a]C. E. Jaske and B. N. Leis, *Final Report on Cyclic Stress-Strain of 2 1/4 Cr-1 Mo Steel*, Battelle Columbus Laboratories Report ORNL-SUB-4004-1 (October 1974).

at a strain rate of 6.7×10^{-3}/sec were assumed equal to those at 371°C (700°F); and (4) values at 482°C (900°F) for heat 20017 at 6.7×10^{-3}/sec were obtained by linear interpolation between values at 427 and 538°C (800 and 1000°F). The above approximations were necessary since some cyclic tests were available at conditions where no monotonic tests were available, but these tests still required a value for E_m. Fortunately, however, E_m is relatively insensitive to the effects of temperature and strain rate, as will be shown below.

The final curves shown in Figs. 3.103 through 3.105 were constructed from information obtained from hysteresis loops generated during continuous cycling fatigue testing of heat 20017 at ORNL and at Mar Test, Inc., on subcontract for ORNL. These tests were conducted on hourglass specimens in strain control using a triangular wave form with ramp strain rates of 4×10^{-3}/sec. Available data on other heats and/or at other strain rates indicate that heat-to-heat and strain rate variations can be significant. However, the number and diversity of these data are too

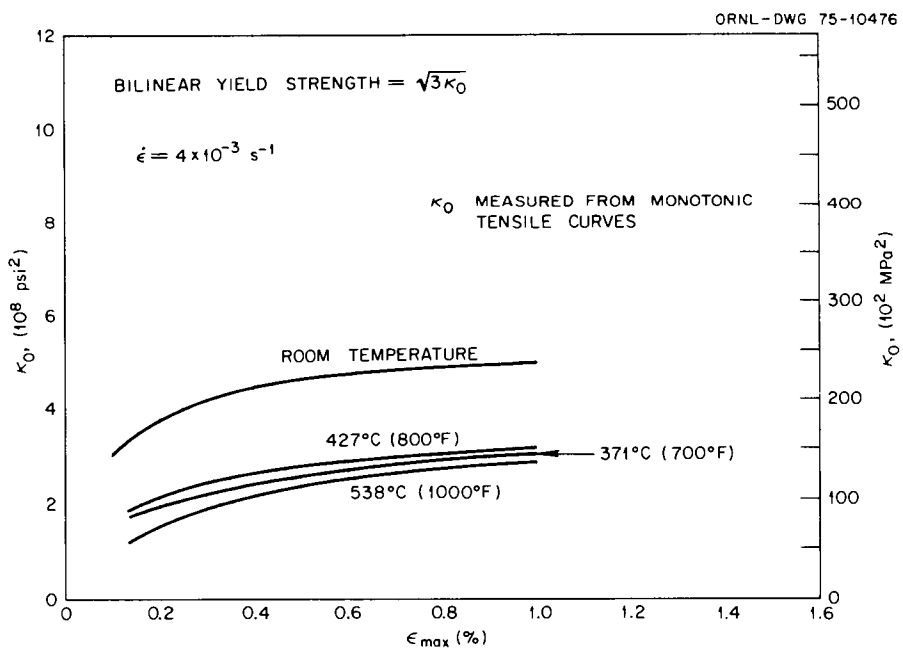

Fig. 3.103. Final Curves for κ_0 as a Function of ε_{max}.

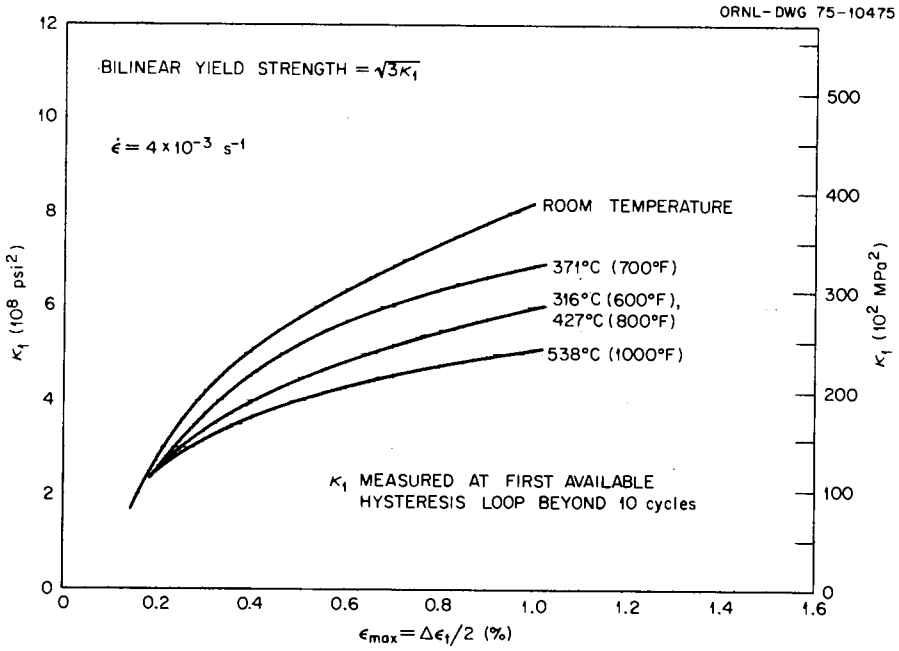

Fig. 3.104. Final Curves for κ_1 as a Function of ε_{max}.

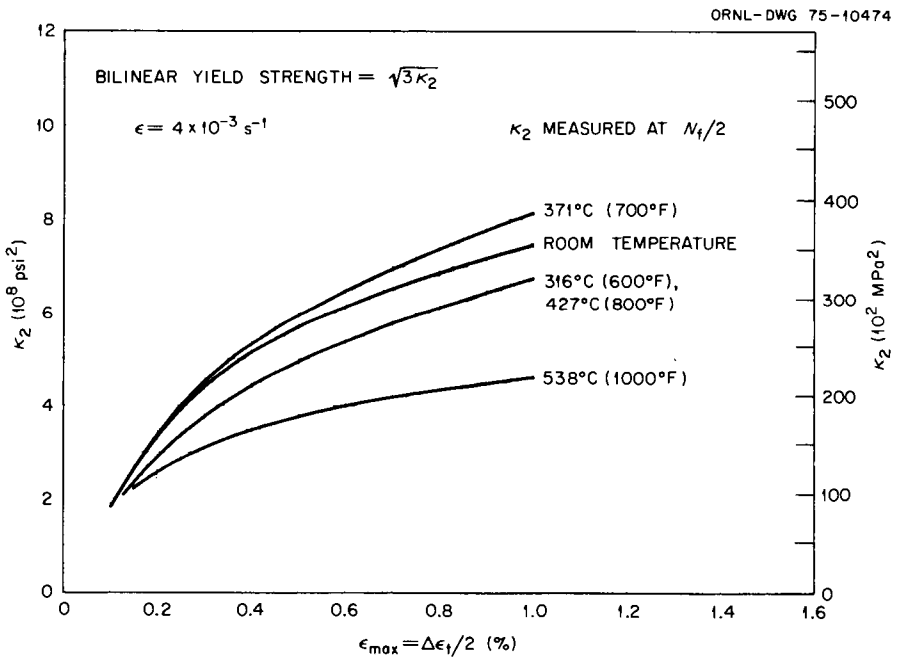

Fig. 3.105. Final Curves for κ_2 as a Function of ε_{max}.

small to allow a quantitative or statistical description of these variations. Thus the curves represent only data for a single heat of isothermally annealed plate material at a single strain rate. The available cyclic stress-strain data for 2 1/4 Cr-1 Mo steel were obtained by testing 25-mm (1-in.) plate meeting ASME specification SA-387 GR 22. The chemical analysis is given in Table 3.35. The heat treatments (isothermal anneals) of these materials follow:

ORNL data (tensile tests of Klueh and Strizak in Table 3.34, cyclic data of Brinkman et al.[74]*)*:

Austenitize at 927°C (1700°F) for 1 hr, cool to 704°C (1300°F) at a rate of 83°C/hr (150°F/hr), hold at 704°C for 2 hr, air cool to room temperature.

Data of Jaske and Leis[75] *(KB-series specimens)*:

Austenitize at 927°C (1700°F) for 0.5 hr, rapidly furnace cool to 721°C (1330°F), hold for 2 hr, air cool to room temperature.

Table 3.35. Chemical Analysis of 2 1/4 Cr-1 Mo Steel

Heat	Chemical Composition, wt %							
	C	Mn	Si	Cr	Mo	Ni	S	P
20017	0.135	0.57	0.37	2.2	0.92	0.16	0.016	0.012
3P5601	0.119	0.35	0.27	2.3	0.96	0.20	0.025	0.008

Table 3.36 lists the cyclic stress-strain data. In these cases κ_1 was measured from the first recorded hysteresis loop at N1 cycles (10 cycles or greater), while κ_2 was measured from a hysteresis loop recorded at approximately half the fatigue life. In the case of the heat 20017 8.3×10^{-5}/sec data, κ_2 was measured at approximately 100 cycles.

After all the experimental values of E_m, C, κ_0, κ_1, and κ_2 were determined, each was plotted against ε_{max} (which corresponds to $\Delta\varepsilon_t/2$ in the cyclic tests). As shown in Figs. 3.106 and 3.107, C and E_m were found to be relatively insensitive to the effects of temperature and

Table 3.36. Cyclic Stress-Strain Data

Specimen[a]	Temp (°C)	Strain Range (%)	Strain Rate (%/sec)	N_f	C	E_m	K_0	N1	K_1	$N_f/2$	K_2
29MTL	25.	2.000	0.4000	0.1273E 04	0.6591E 06	0.9556E 06	0.4483E 09	23.	0.8140E 09	0.5700E 03	0.1020E 10
29MTLA	25.	0.800	0.4000	0.1175E 05	0.8016E 06	0.1154E 07	0.4330E 09	34.	0.5070E 09	0.2100E 04	0.5420E 09
30MTL	25.	0.500	0.4000	0.4448E 05	0.1826E 07	0.2500E 07	0.3909E 09	41.	0.3520E 09	0.3406E 05	0.3950E 09
32MTL	25.	0.350	0.4000	0.1542E 06	0.2636E 07	0.4580E 07	0.3520E 09	34.	0.2250E 09	0.5893E 05	0.2950E 09
35MTL	25.	0.290	0.4000	0.6121E 06	0.8430E 07	0.8610E 07	0.3093E 09	41.	0.1700E 09	0.3068E 06	0.2650E 09
54MTL	316.	2.000	0.4000	0.1534E 04	0.8636E 06	0.1239E 07	0.2838E 09	46.	0.6040E 09	0.6900E 03	0.6630E 09
41MTL	316.	1.200	0.4000	0.4009E 04	0.1194E 07	0.1684E 07	0.2485E 09	15.	0.4630E 09	0.1090E 04	0.5450E 09
40MTL	316.	0.700	0.4000	0.1557E 05	0.1714E 07	0.2353E 07	0.2185E 09	30.	0.3150E 09	0.7259E 04	0.3500E 09
65MTL	316.	0.460	0.4000	0.2406E 05	0.2600E 07	0.3386E 07	0.1966E 09	26.	0.2610E 09	0.0	0.0
55MTL	316.	0.500	0.4000	0.3554E 05	0.2132E 07	0.2875E 07	0.2034E 09	72.	0.2890E 09	0.2573E 05	0.3030E 09
66MTL	316.	0.460	0.4000	0.4596E 05	0.2600E 07	0.3386E 07	0.1966E 09	39.	0.2390E 09	0.1232E 05	0.2030E 09
56MTL	316.	0.420	0.4000	0.2183E 06	0.3068E 07	0.3897E 07	0.1898E 09	43.	0.3070E 09	0.1128E 06	0.3130E 09
*67MTL	316.	0.370	0.4000	0.3114E 07	0.3652E 07	0.4535E 07	0.1814E 09	39.	0.1990E 09	0.1395E 07	0.2970E 09
*42MTL	316.	0.350	0.4000	0.3517E 07	0.3886E 07	0.4790E 07	0.1780E 09	34.	0.2370E 09	0.1360E 07	0.2830E 09
M-4	371.	1.000	0.4000	0.3591E 04	0.1277E 07	0.1795E 07	0.2397E 09	36.	0.5900E 09	0.0	0.0
M-5	371.	0.500	0.4000	0.4707E 05	0.2132E 07	0.2875E 07	0.2034E 09	19.	0.3900E 09	0.2417E 05	0.5370E 09
24MTL	427.	0.500	0.4000	0.2676E 05	0.1891E 07	0.2571E 07	0.2349E 09	45.	0.1930E 09	0.1745E 05	0.1960E 09
17MTL	427.	2.500	0.4000	0.8230E 03	0.7700E 06	0.1000E 07	0.3100E 09	26.	0.6190E 09	0.4770E 03	0.7060E 09
18MTL	427.	2.000	0.4000	0.1183E 04	0.8231E 06	0.1182E 07	0.3098E 09	30.	0.6040E 09	0.4740E 03	0.6300E 09
20MTL	427.	1.000	0.4000	0.3201E 04	0.1236E 07	0.1737E 07	0.2629E 09	36.	0.4380E 09	0.1428E 04	0.4630E 09
21MTL	427.	0.700	0.4000	0.9463E 04	0.1502E 07	0.2083E 07	0.2478E 09	32.	0.3470E 09	0.0	0.0
22MTL	427.	0.560	0.4000	0.1930E 05	0.1774E 07	0.2425E 07	0.2388E 09	41.	0.3200E 09	0.2140E 04	0.3610E 09
26MTL	427.	0.460	0.4000	0.8867E 05	0.2310E 07	0.3063E 07	0.2262E 09	26.	0.2930E 09	0.3595E 05	0.3110E 09
28MTL	427.	0.420	0.4000	0.1394E 06	0.2729E 07	0.3554E 07	0.2175E 09	37.	0.2750E 09	0.7428E 05	0.2930E 09
31MTL	427.	0.360	0.4000	0.4711E 06	0.3636E 07	0.4520E 07	0.2044E 09	56.	0.2140E 09	0.1995E 06	0.2270E 09
36MTL	427.	0.330	0.4000	0.1326E 07	0.4160E 07	0.5060E 07	0.1979E 09	36.	0.2460E 09	0.6670E 06	0.2650E 09
37MTL	427.	0.300	0.4000	0.2838E 07	0.4684E 07	0.5600E 07	0.1914E 09	60.	0.2410E 09	0.5008E 05	0.3070E 09
M-1	482.	1.000	0.4000	0.2164E 04	0.1254E 07	0.1751E 07	0.2454E 09	43.	0.6390E 09	0.6000E 03	0.7380E 09
38MTL	482.	0.500	0.4000	0.3515E 05	0.2350E 07	0.3071E 07	0.2018E 09	204.	0.2690E 09	0.0	0.0
M-3	482.	0.400	0.4000	0.5384E 05	0.3274E 07	0.4100E 07	0.1830E 09	30.	0.3790E 09	0.3441E 05	0.4940E 09
2MTT	538.	3.000	0.4000	0.4440E 03	0.6006E 06	0.8676E 06	0.3104E 09	26.	0.6300E 09	0.2040E 03	0.5960E 09
1MTL	538.	2.000	0.4000	0.7960E 03	0.6333E 06	0.9130E 06	0.3011E 09	24.	0.4990E 09	0.4140E 03	0.4630E 09
2MTL	538.	1.500	0.4000	0.1373E 04	0.8383E 06	0.1194E 07	0.2707E 09	16.	0.4480E 09	0.6810E 03	0.4090E 09
1MTT	538.	1.000	0.4000	0.2437E 04	0.1272E 07	0.1765E 07	0.2278E 09	35.	0.3900E 09	0.1140E 04	0.3630E 09
3MTL	538.	1.000	0.4000	0.2588E 04	0.1272E 07	0.1765E 07	0.2278E 09	33.	0.3580E 09	0.1116E 04	0.3450E 09
4MTL	538.	0.700	0.4000	0.5543E 04	0.1782E 07	0.2400E 07	0.2002E 09	46.	0.4940E 09	0.4782E 04	0.3240E 09
5MTL	538.	0.560	0.4000	0.8524E 04	0.2500E 07	0.3220E 07	0.1782E 09	43.	0.3030E 09	0.1626E 04	0.2710E 09
6MTL	538.	0.500	0.4000	0.1829E 05	0.2808E 07	0.3571E 07	0.1687E 09	43.	0.3130E 09	0.6480E 03	0.3160E 09
7MTL	538.	0.460	0.4000	0.2642E 05	0.3129E 07	0.3903E 07	0.1624E 09	55.	0.2910E 09	0.1177E 05	0.2390E 09
14MTL	538.	0.420	0.4000	0.3763E 05	0.3450E 07	0.4234E 07	0.1561E 09	60.	0.2860E 09	0.2960E 05	0.2250E 09
13MTL	538.	0.440	0.4000	0.4454E 05	0.3289E 07	0.4068E 07	0.1592E 09	54.	0.3370E 09	0.3301E 05	0.2620E 09
16MTL	538.	0.390	0.4000	0.6362E 05	0.3750E 07	0.4860E 07	0.2343E 09	55.	0.3090E 09	0.2981E 05	0.2560E 09
27MTL	538.	0.280	0.4000	0.4792E 06	0.9734E 07	0.9000E 07	0.9673E 08	81.	0.1440E 09	0.2754E 06	0.1480E 09
24BFL	25.	1.000	0.4000	0.4317E 05	0.7778E 06	0.1188E 07	0.4356E 09	159.	0.3700E 09	0.2184E 05	0.4020E 09
R65	25.	2.000	0.4000	0.5024E 04	0.6591E 06	0.9556E 06	0.4483E 09	79.	0.4850E 09	0.2500E 04	0.5600E 09
R72	25.	2.000	0.4000	0.4309E 04	0.6591E 06	0.9556E 06	0.4483E 09	48.	0.4950E 09	0.2197E 04	0.5920E 09
R73	25.	1.000	0.4000	0.3150E 05	0.7778E 06	0.1188E 07	0.4356E 09	131.	0.3620E 09	0.1412E 05	0.3800E 09
2A2	25.	2.000	0.4000	0.1111E 04	0.6591E 06	0.9556E 06	0.4483E 09	28.	0.6980E 09	0.5810E 03	0.8380E 09
4A2	25.	2.000	0.4000	0.1283E 04	0.6591E 06	0.9556E 06	0.4483E 09	32.	0.6800E 09	0.6750E 03	0.7920E 09
21BFL	25.	0.800	0.4000	0.1057E 05	0.8016E 06	0.1154E 07	0.4330E 09	72.	0.4520E 09	0.5387E 04	0.5020E 09
26BFL	25.	2.000	0.4000	0.1266E 04	0.6591E 06	0.9556E 06	0.4483E 09	29.	0.6920E 09	0.6380E 03	0.8110E 09
22BFL	371.	0.500	0.4000	0.2414E 05	0.2132E 07	0.2875E 07	0.2034E 09	92.	0.2650E 09	0.1183E 05	0.3110E 09
44BFL	371.	2.000	0.4000	0.9590E 03	0.8636E 06	0.1239E 07	0.2838E 09	87.	0.7600E 09	0.5290E 03	0.8320E 09
47BFL	371.	1.000	0.4000	0.4007E 04	0.1277E 07	0.1795E 07	0.2397E 09	100.	0.4860E 09	0.2257E 04	0.5750E 09
43BFL	371.	0.500	0.0040	0.2630E 03	0.2132E 07	0.2875E 07	0.2034E 09	18.	0.2930E 09	0.1490E 03	0.2850E 09
46BFL	371.	1.000	0.0040	0.2799E 04	0.1277E 07	0.1795E 07	0.2397E 09	12.	0.5500E 09	0.1397E 04	0.5340E 09
3BFT	371.	0.800	0.4000	0.9319E 04	0.1505E 07	0.2092E 07	0.2261E 09	102.	0.4200E 09	0.4064E 04	0.4240E 09

Table 3.36. (Continued)

Specimen[a]	Temp (°C)	Strain Range (%)	Strain Rate (%/sec)	N_f	C	E_m	K_0	N1	K_1	$N_f/2$	K_2
36BFL	371.	2.000	0.0040	0.7720E 03	0.8636E 06	0.1239E 07	0.2838E 09	14.	0.5860E 09	0.3770E 03	0.6030E 09
I2	371.	0.400	0.4000	0.4172E 06	0.1097E 08	0.1154E 08	0.6880E 08	133.	0.1980E 09	0.7949E 05	0.2440E 09
I3	371.	0.350	0.4000	0.1220E 05	0.5206E 07	0.5542E 07	0.1201E 09	0.	0.0	0.2588E 06	0.2290E 09
I4	371.	1.000	0.4000	0.4303E 04	0.1070E 07	0.1481E 07	0.1738E 09	57.	0.3770E 09	0.2131E 04	0.4220E 09
I7	371.	1.750	0.4000	0.1470E 04	0.8270E 06	0.1165E 07	0.1976E 09	32.	0.4310E 09	0.5510E 03	0.4800E 09
I9	371.	1.000	0.0040	0.0	0.1070E 07	0.1481E 07	0.1738E 09	13.	0.4300E 09	0.4450E 03	0.4490E 09
I10	371.	0.600	0.4000	0.1857E 05	0.1302E 07	0.1771E 07	0.1653E 09	269.	0.2600E 09	0.1000E 05	0.2990E 09
I11	371.	1.500	0.4000	0.2028E 04	0.8878E 06	0.1245E 07	0.1878E 09	37.	0.4490E 09	0.1100E 04	0.5040E 09
I16	371.	2.000	0.4000	0.1144E 04	0.8695E 06	0.1221E 07	0.1895E 09	27.	0.5150E 09	0.5470E 03	0.5840E 09
I17	371.	1.000	0.0400	0.3310E 04	0.1070E 07	0.1481E 07	0.1738E 09	19.	0.4040E 09	0.1722E 04	0.4510E 09
I19	371.	0.500	0.0400	0.1642E 05	0.1450E 07	0.1952E 07	0.1616E 09	20.	0.2560E 09	0.8225E 04	0.3090E 09
I20	371.	1.250	0.4000	0.2711E 04	0.9560E 06	0.1334E 07	0.1816E 09	79.	0.4220E 09	0.1909E 04	0.4860E 09
MIL-2	427.	1.000	0.4000	0.4307E 04	0.1091E 07	0.1569E 07	0.1446E 09	22.	0.3580E 09	0.0	0.0
MIL-3	427.	0.500	0.5000	0.1115E 06	0.1839E 07	0.2571E 07	0.1149E 09	27.	0.2250E 09	0.4149E 05	0.2520E 09
MIL-4	427.	0.400	0.4000	0.6052E 06	0.2725E 07	0.3688E 07	0.9567E 08	30.	0.2060E 09	0.3006E 06	0.2230E 09
MIL-5	427.	0.700	0.4000	0.9975E 04	0.1409E 02	0.2002E 07	0.1294E 09	34.	0.3150E 09	0.7200E 03	0.3300E 09
MIL-7	427.	0.550	0.4000	0.9146E 05	0.1702E 07	0.2391E 07	0.1192E 09	27.	0.2480E 09	0.4844E 05	0.2460E 09
MIL-10	538.	0.500	0.4000	0.1604E 05	0.1958E 07	0.2576E 07	0.1196E 09	29.	0.1740E 09	0.2928E 04	0.1700E 09
MIL-11	427.	0.600	0.4000	0.2505E 05	0.1604E 07	0.2261E 07	0.1226E 09	14.	0.2770E 09	0.1772E 05	0.2710E 09
MIL-18	482.	1.000	0.4000	0.3721E 04	0.1035E 07	0.1454E 07	0.1651E 09	25.	0.3090E 09	0.1500E 04	0.2930E 09
MIT-1	482.	2.000	0.4000	0.9100E 03	0.7122E 06	0.1021E 07	0.1947E 09	17.	0.4780E 09	0.4740E 03	0.4760E 09
KB-18	25.	0.410	0.0083	0.0	0.4341E 07	0.5374E 07	0.3144E 09	10.	0.2840E 09	0.1040E 03	0.2890E 09
KB-65	25.	1.020	0.0083	0.0	0.2266E 07	0.3064E 07	0.3645E 09	15.	0.5560E 09	0.9300E 02	0.5420E 09
KB-54	25.	0.980	0.0083	0.0	0.2266E 07	0.3064E 07	0.3645E 09	56.	0.5510E 09	0.0	0.0
KB-14	93.	1.010	0.0083	0.0	0.1897E 07	0.2584E 07	0.3661E 09	10.	0.5040E 09	0.0	0.0
KB-47	204.	0.400	0.0083	0.0	0.9161E 07	0.9327E 07	0.1882E 09	10.	0.3040E 09	0.1000E 03	0.5710E 09
KB-22	204.	1.010	0.0083	0.0	0.1871E 07	0.2538E 07	0.4054E 09	10.	0.5570E 09	0.0	0.0
KB-60	316.	0.400	0.0083	0.0	0.4651E 07	0.5558E 07	0.2536E 09	20.	0.4870E 09	0.0	0.0
KB-36	316.	1.020	0.0083	0.0	0.1026E 07	0.1457E 07	0.3650E 09	20.	0.7930E 09	0.0	0.0
KB-52	316.	2.000	0.0083	0.0	0.9927E 06	0.1412E 07	0.3727E 09	11.	0.1170E 10	0.0	0.0
KB-34	427.	0.420	0.0083	0.0	0.4118E 07	0.5019E 06	0.2095E 09	15.	0.4780E 09	0.0	0.0
KB-56	427.	1.020	0.0083	0.0	0.1206E 07	0.1694E 07	0.3068E 09	20.	0.9600E 09	0.0	0.0
KB-9	427.	2.000	0.0083	0.0	0.9433E 06	0.1344E 07	0.3410E 09	9.	0.1300E 10	0.1260E 03	0.1350E 10
KB-33	482.	0.400	0.0083	0.0	0.4954E 07	0.5692E 07	0.2339E 09	12.	0.4540E 09	0.0	0.0
KB-48	482.	1.060	0.0083	0.0	0.1936E 07	0.2566E 07	0.3145E 09	10.	0.7970E 09	0.0	0.0
KB-26	482.	1.980	0.0083	0.0	0.1037E 07	0.1458E 07	0.4772E 09	10.	0.1570E 10	0.0	0.0
KB-30	510.	0.390	0.0083	0.0	0.4072E 07	0.4860E 07	0.2464E 09	20.	0.3820E 09	0.1090E 03	0.3820E 09
KB-62	510.	0.600	0.0083	0.0	0.3672E 07	0.4407E 07	0.2623E 09	15.	0.5440E 09	0.0	0.0
KB-3	510.	2.050	0.0083	0.0	0.8740E 06	0.1240E 07	0.3738E 09	10.	0.8130E 09	0.0	0.0
KB-51	510.	1.020	0.0083	0.0	0.1147E 07	0.1602E 07	0.3452E 09	20.	0.1160E 10	0.0	0.0
KB-13	538.	0.410	0.0083	0.0	0.5139E 07	0.5702E 07	0.1988E 09	22.	0.3480E 09	0.1070E 03	0.3200E 09
KB-61	538.	1.040	0.0083	0.0	0.1187E 07	0.1646E 07	0.2967E 09	20.	0.4370E 09	0.0	0.0
KB-12	538.	2.040	0.0083	0.0	0.7500E 06	0.1250E 07	0.3300E 09	10.	0.8430E 09	0.0	0.0
KB-6	593.	0.410	0.0083	0.0	0.1208E 07	0.1667E 07	0.1645E 09	12.	0.1930E 09	0.0	0.0
KB-37	593.	1.030	0.0083	0.0	0.2212E 07	0.3265E 07	0.1954E 09	15.	0.2240E 09	0.0	0.0
KB-55	593.	2.110	0.0083	0.0	0.1186E 05	0.1777E 05	0.2199E 09	18.	0.1010E 10	0.0	0.0
KB-8	593.	3.060	0.0083	0.0	0.1186E 05	0.1777E 05	0.2199E 09	10.	0.3640E 09	0.1000E 03	0.2180E 09

[a]MIL, MIT, and A specimens are heat 3P5601. All others are heat 20017.

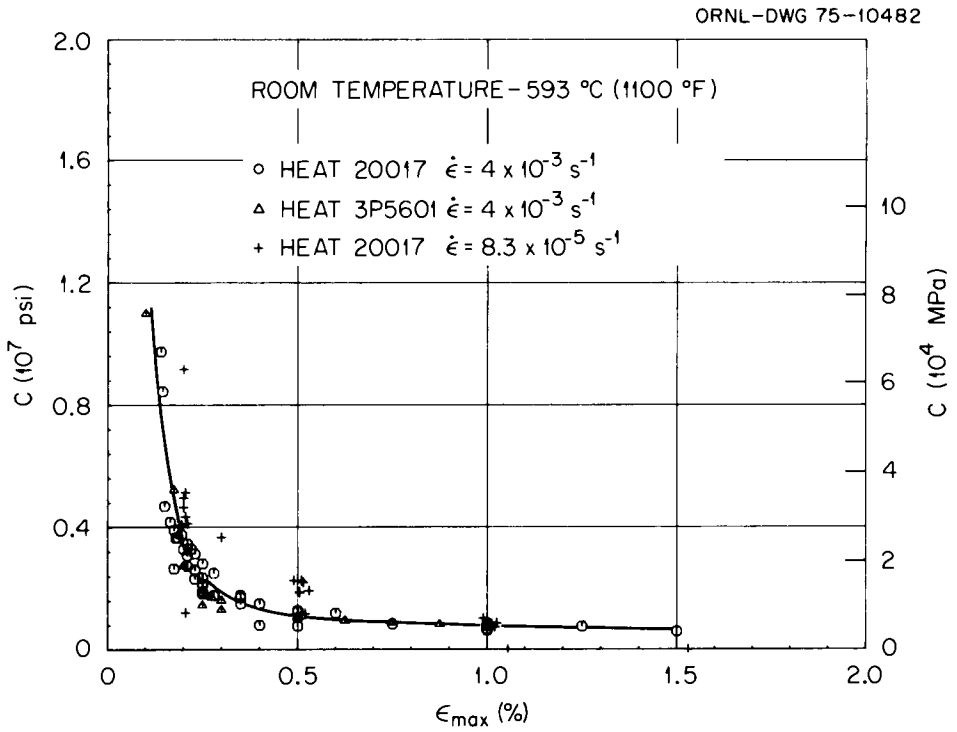

Fig. 3.106. Data and Mean Curve for C as a Function of ε_{max}.

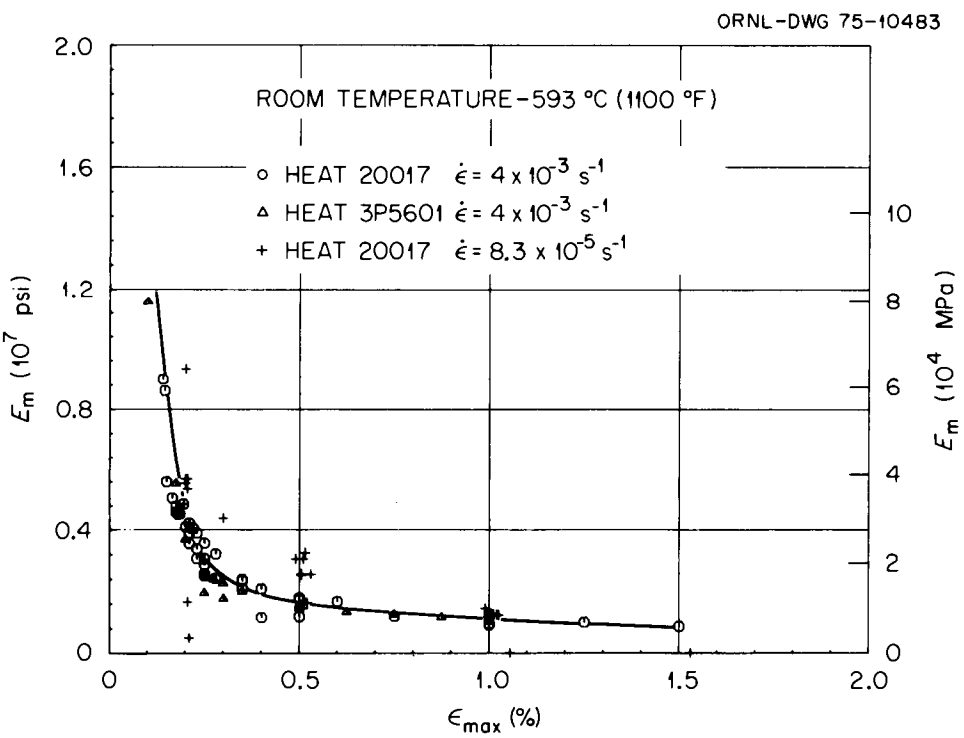

Fig. 3.107. Data and Mean Curve for E_m as a Function of ε_{max}.

strain rate, so a single mean curve was drawn through all the available data for each quantity to derive the curves shown in Fig. 3.108.

Figures 3.109 through 3.11, on the other hand, show the wide amount of scatter in the plots of κ_0, κ_1, and κ_2 against ε_{max}. Moreover, these values are temperature sensitive. Thus, as explained above, curves were drawn through the heat 20017 4×10^{-3}/sec data only to derive the curves shown in Figs. 3.103 through 3.105. These data were the most consistent of those available and tended toward average behavior for the available data. The curves in those figures illustrating the temperature dependence were constructed merely by linear interpolation between the mean values at the temperatures for which data were available [room temperature and 316, 371, 427, and 538°C (600, 700, 800, and 1000°F)].

It should be noted that the current definition of κ_2 differs from that given in Ref. 73, where κ_2 is obtained from the 100th cycle hysteresis loop. Figure 3.112 illustrates comparative κ values obtained from the first available hysteresis loop after the 100th cycle for the

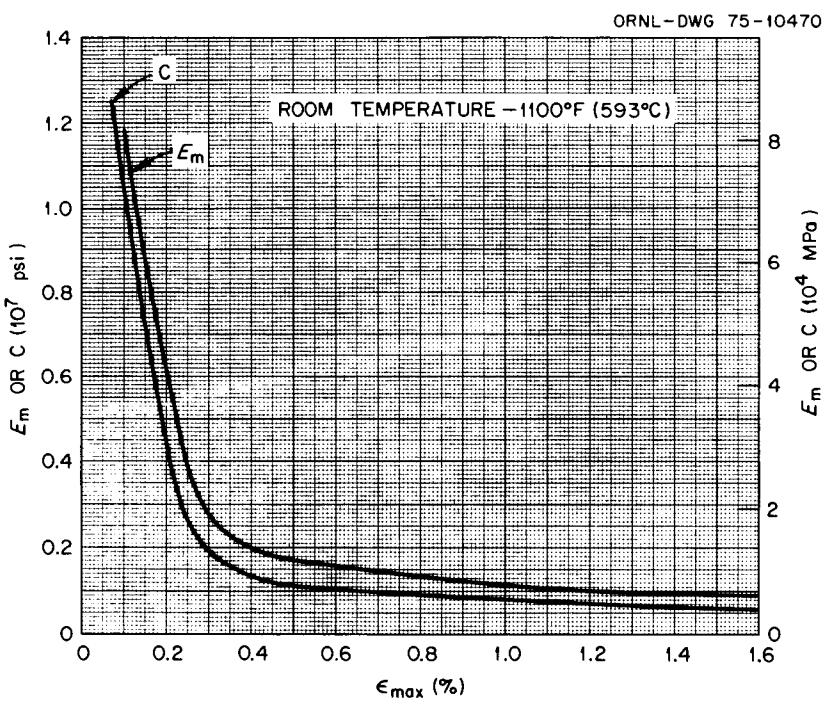

Fig. 3.108. Final Curves for C and E_m as Functions of ε_{max}.

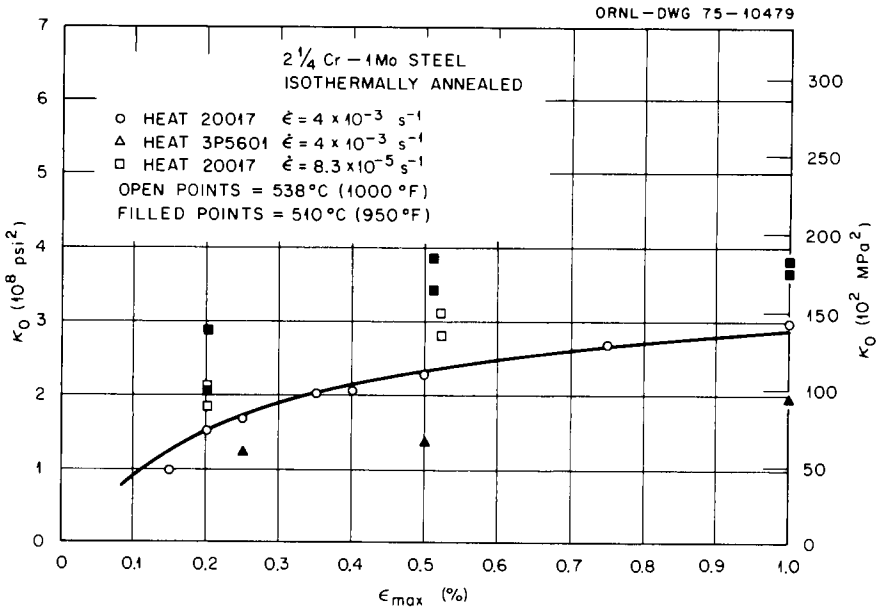

Fig. 3.109. Typical Plot of Data and Curve for κ_0 as a Function of ε_{max}.

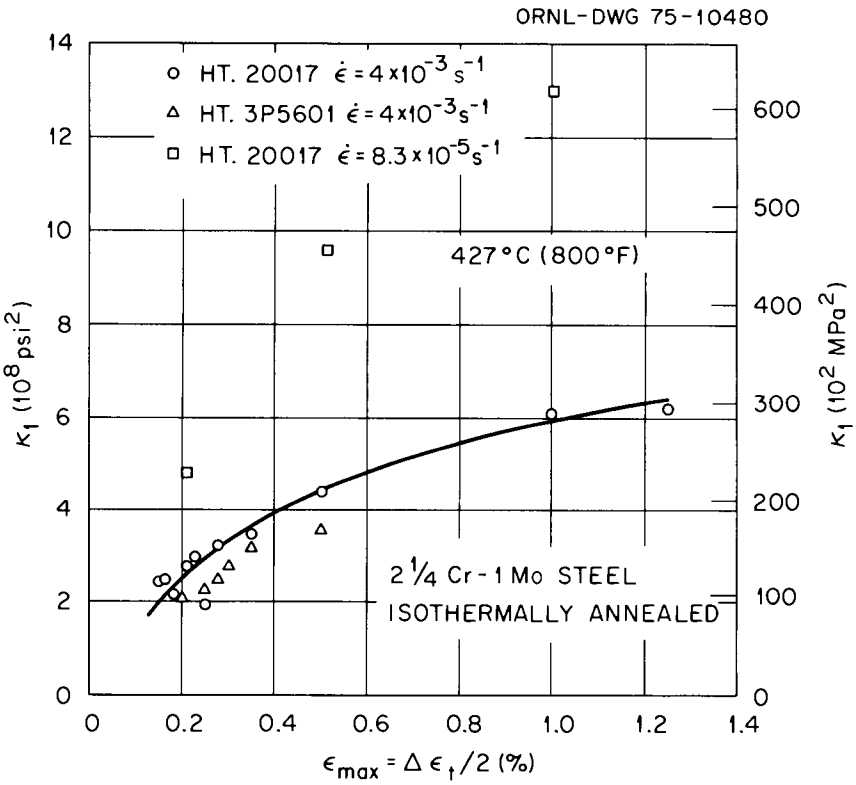

Fig. 3.110. Typical Plot of Data and Mean Curve for κ_1 as a Function of ε_{max}.

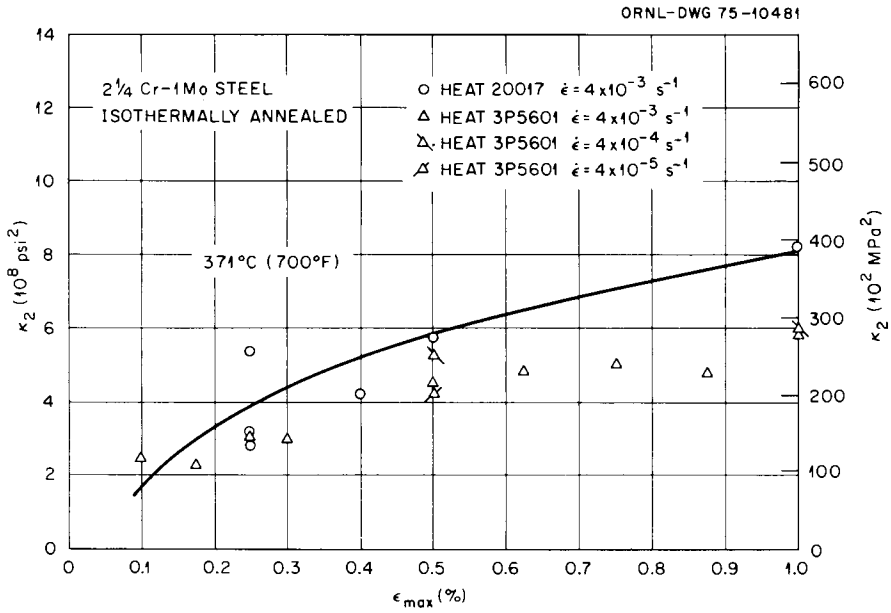

Fig. 3.111. Typical Plot of Data and Mean Curve for κ_2 as a Function of ε_{max}.

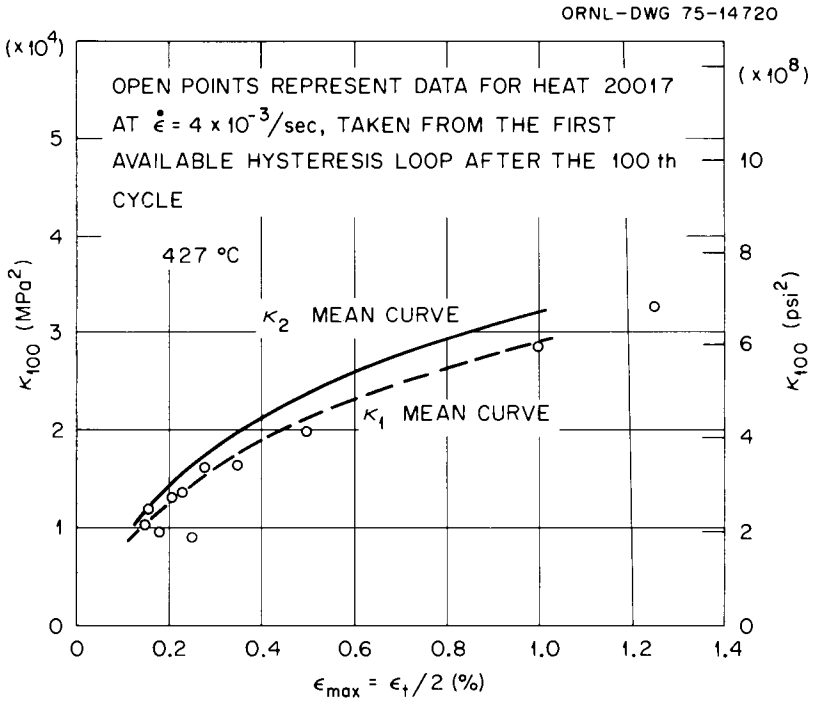

Fig. 3.112. Comparison of Mean Curves for κ_2 and κ_1 with Data for κ_{100}.

heat 20017 4×10^{-3}/sec tests with the mean curves for κ_1 and κ_2 from Figs. 3.104 and 3.105. Clearly, the 100th cycle values are comparable to the current κ_1 values. The current κ_2 values differ somewhat from the 100th cycle values, but these $N_f/2$ values are felt to be representative of the strength of cyclically strained material over a larger number of cycles. At small strain values the amount of hardening and/or softening incurred after 100 cycles is not necessarily representative of that incurred after several thousand or million cycles.

Because of the limited scope of the data from which the curves in Figs. 3.103 through 3.105 were derived, they should be regarded as interim — subject to revision upon the availability of more data.

3.5 HIGH-TEMPERATURE DESIGN — J. M. Corum* and C. E. Pugh*

3.5.1 Exploratory Studies in Support of Structural Design Methods

3.5.1.1 Characterization of the Product Forms of the Reference Heat of Type 304 Stainless Steel — R. W. Swindeman and V. K. Sikka

The creep-rupture characterization tests on the reference heat of type 304 stainless steel have been completed. Curves obtained at 593°C (1100°F) and stresses of 86 and 103 MPa (12.5 and 15 ksi) are compared with the recommended curves[76] in Fig. 3.113. At the 103 MPa (15 ksi) level 12 of 14 products exhibit strains that fall above the recommended curve, while at the 86 MPa (12.5 ksi) level, six products show higher strains at 1000 hr and seven show smaller strains than the recommended curve. Generally, the different products exhibit creep curves having the same shape as the recommended curves. More detailed studies will be undertaken before the final report on product form variability will be completed.

3.5.1.2 Exploratory Testing to Identify Behavioral Features — R. W. Swindeman

Exploratory testing is emphasizing studies that involve history effects. The influence of mechanical and thermal load histories on

---

*Reactor Division.

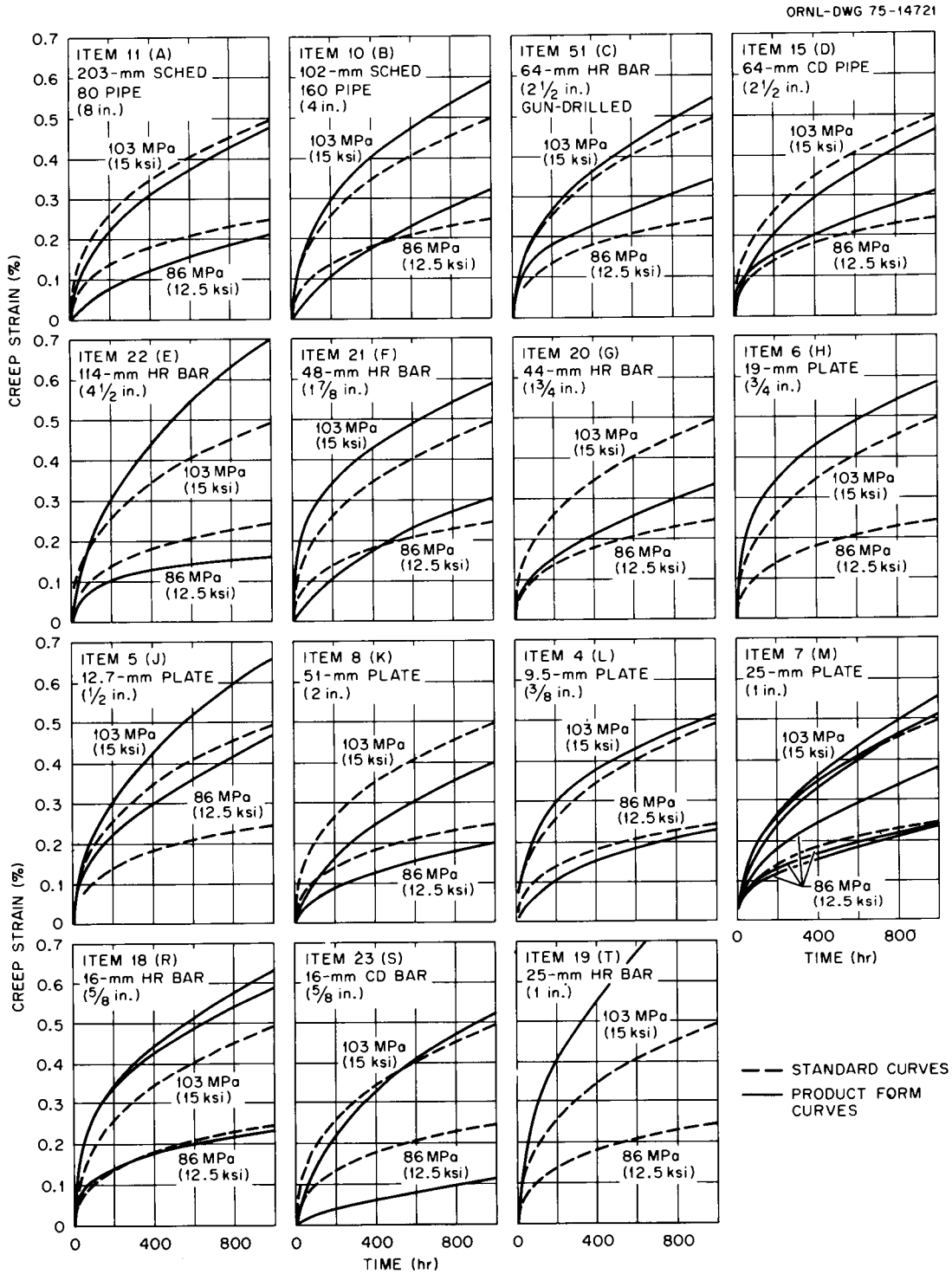

Fig. 3.113. Comparison of the Creep Curves for Different Product Forms of the Reference Heat of Type 304 Stainless Steel with Standard Curves Developed for Use in Inelastic Analysis of Test Structures. Heat 9T2796 at 593°C (1100°F).

subsequent behavior is an important consideration in the development of more sophisticated constitutive relations. With respect to both plasticity and creep, knowledge of the influence of grain size is also important. Generally, this is studied by varying the grain size for a given material. We have completed a series of tensile and creep tests using specimens machined from fined-grained material. These specimens were exposed to one of the following treatments: (1) age 24 hr at 816°C (1500°F), (2) stress relieve at 900°C (1652°F) and age 24 hr at 816°C, (3) solution anneal at 1093°C (2000°F) and age 24 hr at 816°C, (4) solution anneal at 1200°C (2200°F) and age 24 hr at 816°C, (5) solution anneal at 1093°C with no aging. The solution annealing temperature was introduced to change the grain size, while the aging was introduced to minimize the effect that carbide precipitation might have during testing. The results of tensile tests at 593°C are shown in Fig. 3.114. Here it is evident

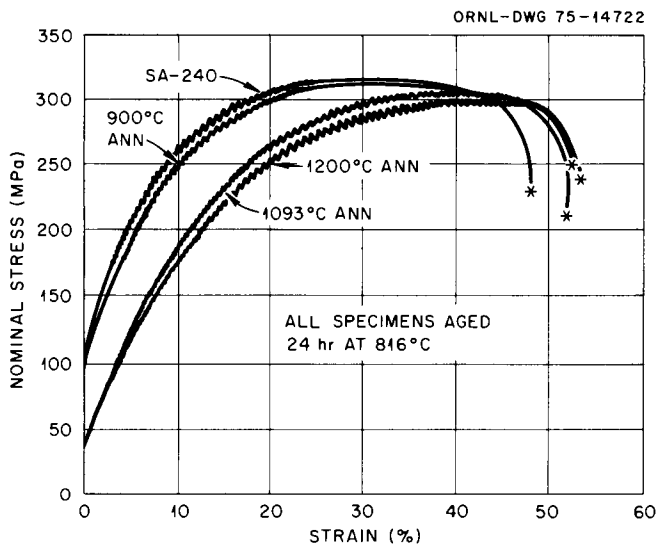

Fig. 3.114. Influence of Annealing Temperature on the Tensile Curve for Aged Type 304 Stainless Steel (Heat 9T2796).

that the high-temperature anneals, which produce coarse grain sizes, lower the yield strength and the rate of work hardening appreciably. The uniform strain, however, is extended by the higher temperature annealing. The influence on the creep curve at 593°C (1100°F) and 172 MPa (25 ksi)

is shown in Fig. 3.115. There is some evidence that the higher temperature anneal slightly reduces the creep rate. The influence on rupture life and elongation is unclear. The influence that the aging exerts on the ductility is more dramatic than the influence of annealing temperature. We have also observed that the cooling rate is important,

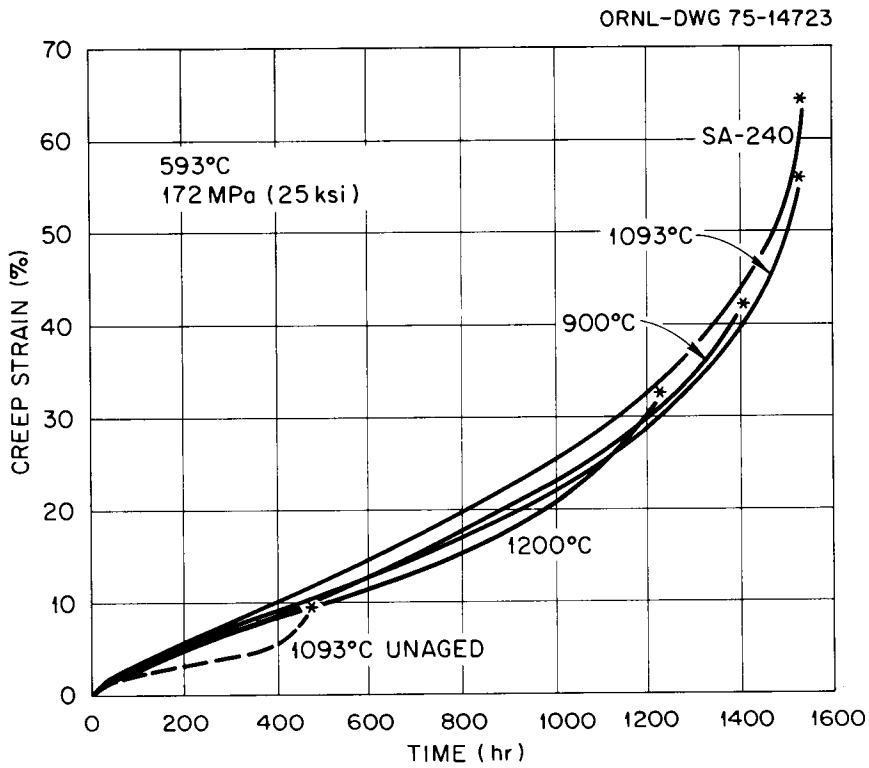

Fig. 3.115. Influence of Annealing Temperature on the Creep Curve for Aged Type 304 Stainless Steel at 593°C (1100°F).

probably for the same reason. The reason is that the precipitation of coarse globular carbide particles on the grain boundaries improves creep ductility. It is unlikely that such a carbide could form during service at temperatures below 650°C (1202°F), however, but aging is still pronounced. Strain plays an important role in the aging process. To examine the influence that strain and time exert on hardening and recovery processes at 593°C (1100°F) we have been performing cyclic load tests. The results of two tests performed with a 2-hr cycle period are shown in Figs. 3.116 and 3.117. Data are plotted twice in each figure. In Fig. 3.116, the

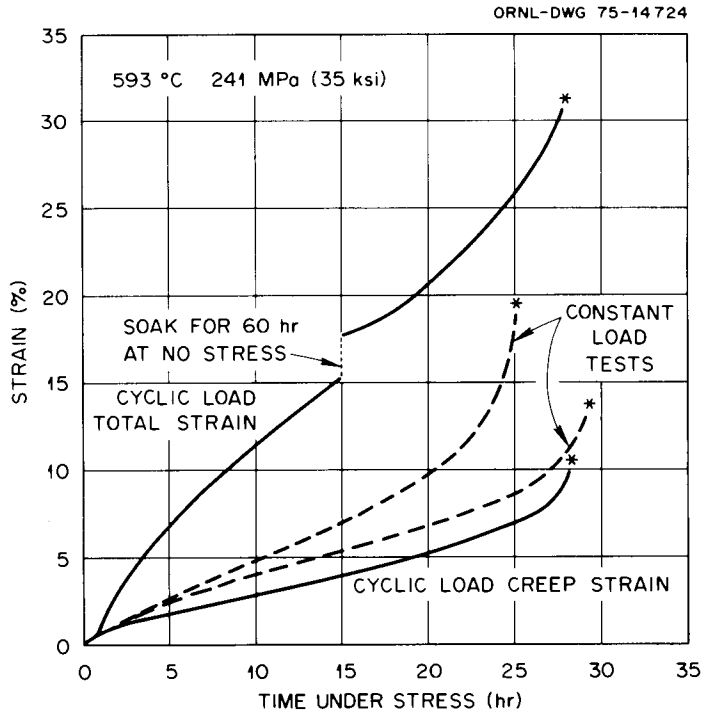

Fig. 3.116. Influence of Load Cycling on the Creep Curve of Type 304 Stainless Steel at 241 MPa (35 ksi) and 593°C (1100°F); 2-hr cycling period.

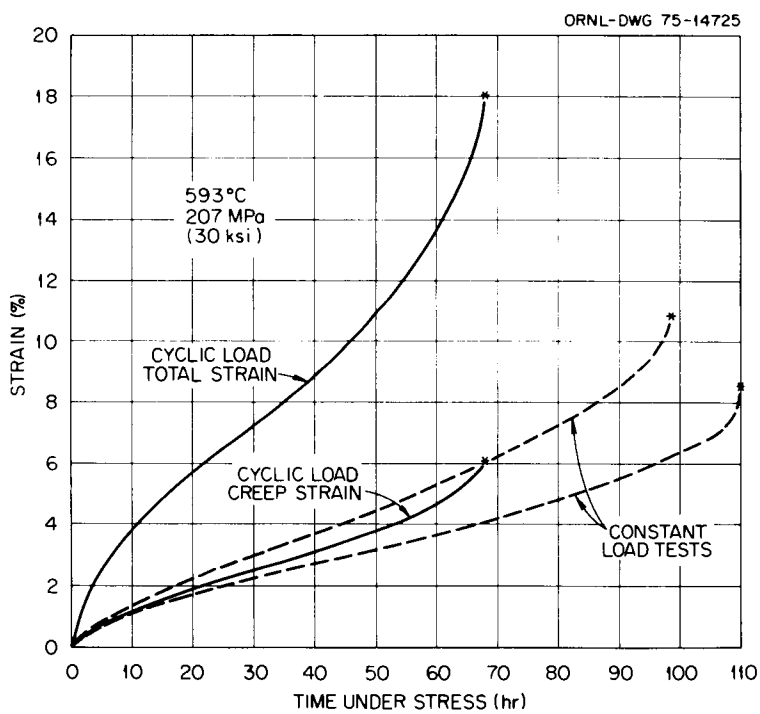

Fig. 3.117. Influence of Load Cycling on the Creep Curve of Type 304 Stainless Steel at 207 MPa (30 ksi) and 593°C (1100°F); 2-hr cycling period.

cyclic test at 241 MPa (35 ksi) exhibited plastic strains after every recovery period at 20 MPa (3 ksi). The total strain curve exhibits about 3 times the creep rate of the constant-load curve. In Fig. 3.117, the cyclic test at 207 MPa (30 ksi) showed plastic strains about half the time when the major stress was applied. The resultant total strain curve exhibits about twice the creep rate of the constant-load creep curve. For both specimens the creep curves for the cyclic tests agree with the constant-load tests when only the time under the major load is considered.

Efforts are being made to process the strain-cycling data obtained for type 304 stainless steel over the past several years. Some typical curves describing the variation of the stress range with cycle number are shown for several temperatures in Fig. 3.118 through 3.122. Data for 427°C (800°F) are summarized in Fig. 3.118, where hardening curves are shown for several strain ranges from 0.19 to 1.95%. Two important behavioral features are revealed here. First is that for strain ranges above 0.4% the material has considerable hardening capability. At the 0.6% range, for example, the cyclic strength is doubled between the first

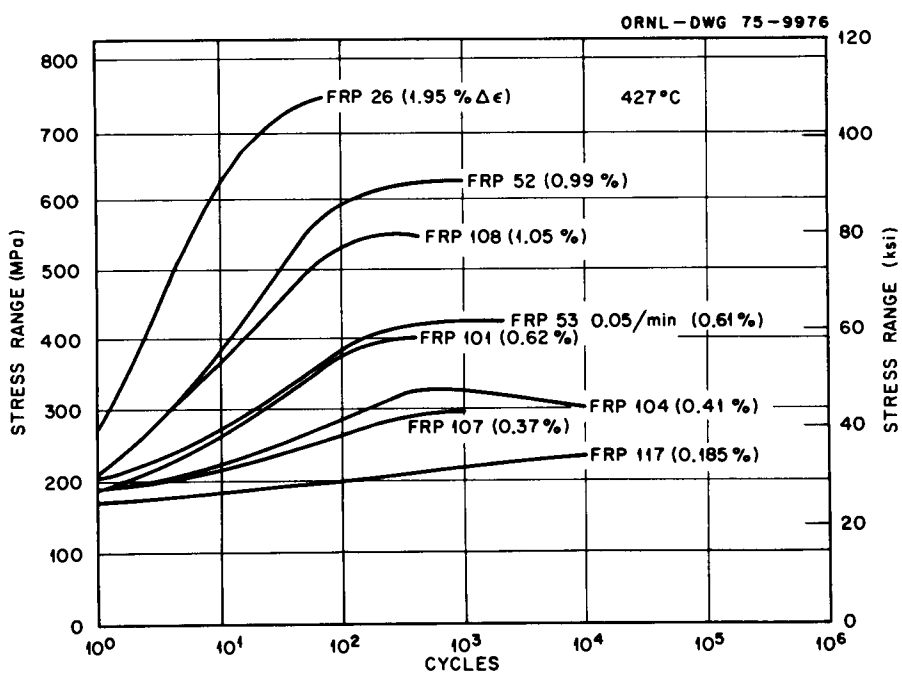

Fig. 3.118. Cyclic Hardening Curves for Type 304 Stainless Steel (Heat 9T2796) at 427°C (800°F).

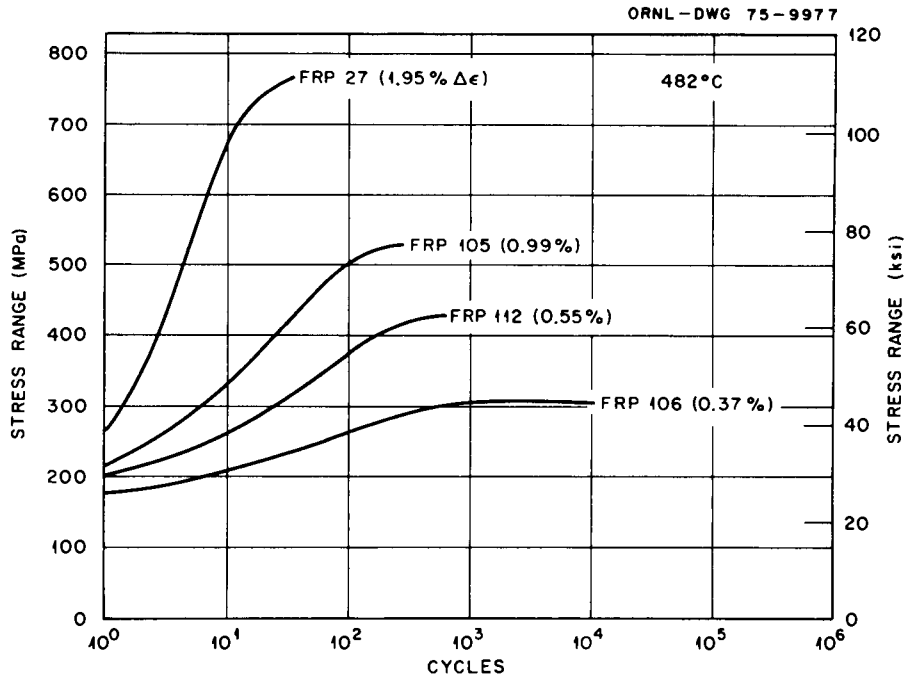

Fig. 3.119. Cyclic Hardening Curves for Type 304 Stainless Steel (Heat 9T2796) at 482°C (900°F).

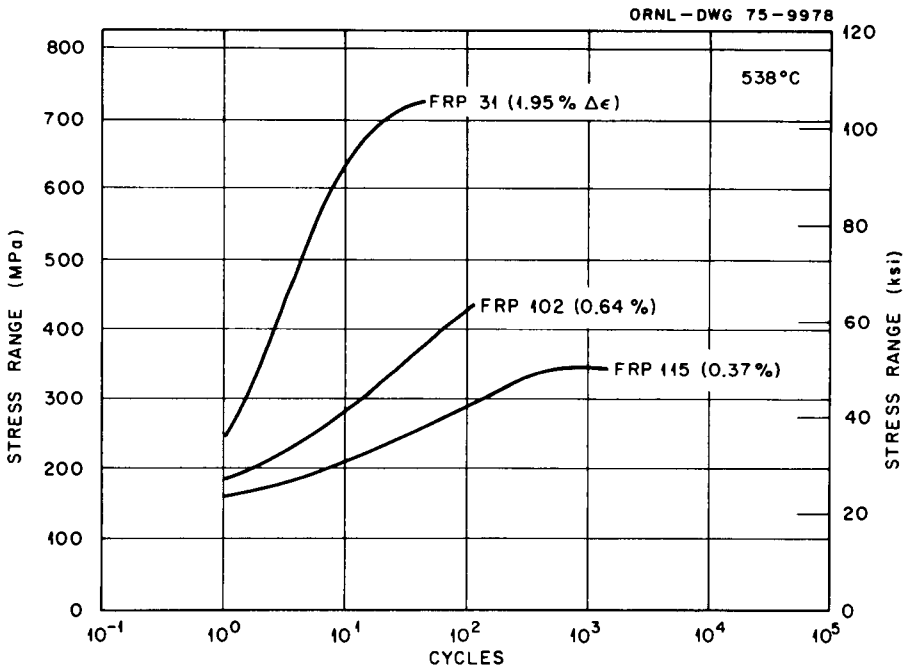

Fig. 3.120. Cyclic Hardening Curves for Type 304 Stainless Steel (Heat 9T2796) at 538°C (1000°F).

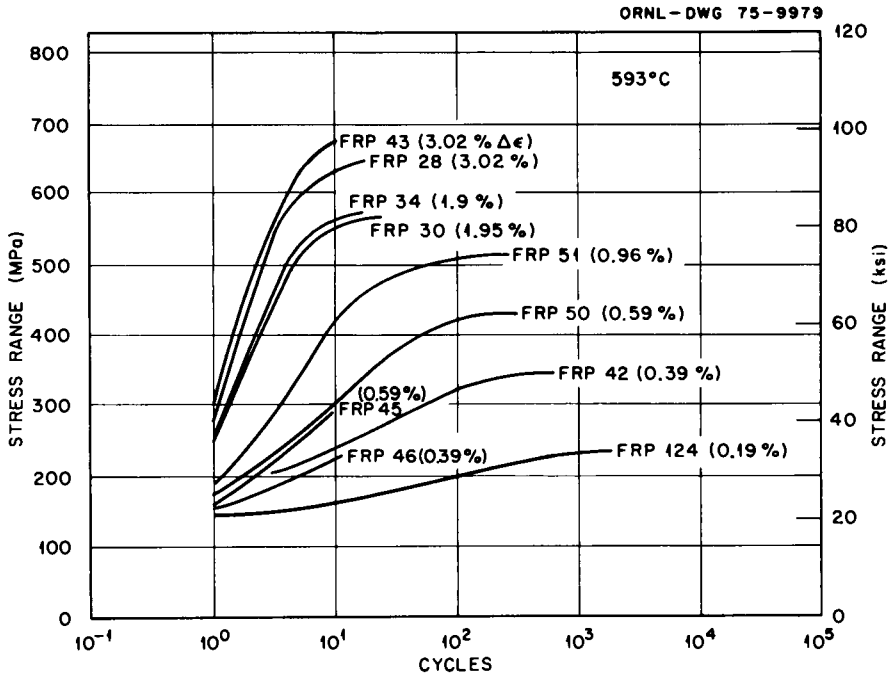

Fig. 3.121. Cyclic Hardening Curves for Type 304 Stainless Steel (Heat 9T2796) at 593°C (1100°F).

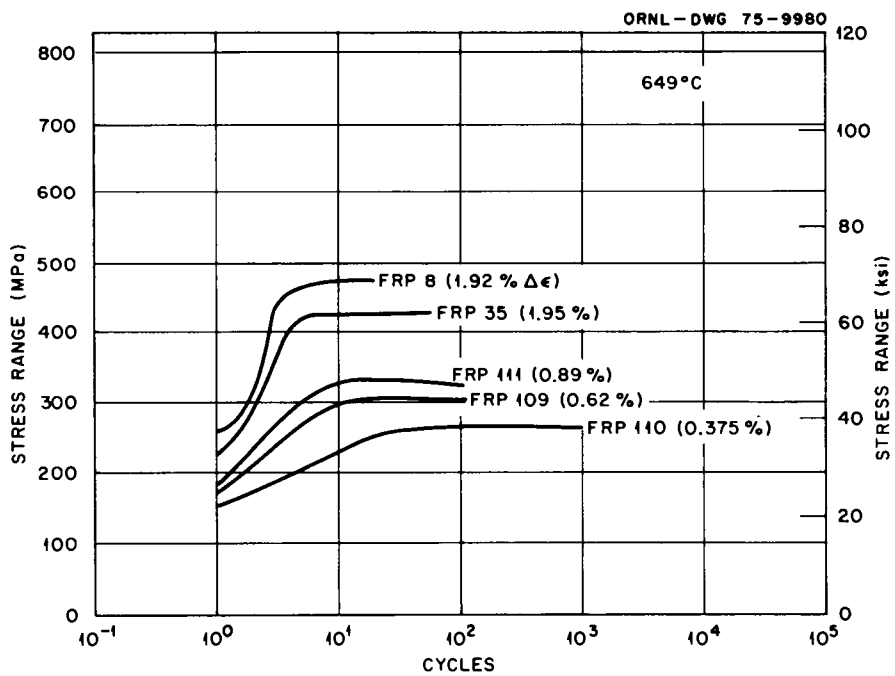

Fig. 3.122. Cyclic Hardening Curves for Type 304 Stainless Steel (Heat 9T2796) at 649°C (1200°F).

cycle and saturation, while at the 1% range the cyclic strength is nearly tripled. The second feature is that the rate of cyclic hardening is very slow, and this is particularly so at strain ranges below 1%. At the 0.4% range, for example, the strength increase at the tenth cycle is only one-third of the total hardening capability. Because of the imposition of design safety factors, the high-strain saturation stresses can never be achieved in service, and the tenth-cycle loop for design use is a good selection. At low strain ranges, however, further work involving studies of history effects is needed, particularly with reference to influence of history on the saturation strength relative to the tenth-cycle strength. The observations made for the behavior at 427°C (800°F) appear to hold for 482 and 538°C (900 and 1000°F) also, as may be seen by comparing Fig. 3.119 for 482°C (900°F) and Fig. 3.120 for 538°C (1000°F) with Fig. 3.118. The hardening behavior at 593°C (1100°F) differs somewhat from behavior at 427°C (800°F), as may be seen by comparing Fig. 3.121 (593°C) with Fig. 3.118. One noticeable difference is at high-strain levels, where it is apparent that the cyclic strength at saturation is less at 593°C (1100°F). Another difference is that hardening rate is larger at 593°C (1100°F), which means that the tenth-cycle strength is greater at 593°C (1100°F) than at lower temperatures. Data obtained at 649°C (1200°F) are shown in Fig. 3.122 and show a similar trend. By the tenth cycle the strength is near saturation for all strain levels. A plot showing the variation in the tenth-cycle strength against temperature is provided in Fig. 3.123. Data interpolated for five strain levels — 0.4, 0.6, 1, 1.5, and 2% — suggest that a peak in the strength develops and moves toward higher temperature with decreasing strain ranges. As described previously, the cyclic hardening behavior at a constant strain range can be approximated by the equation:

$$\Delta S = (\Delta S_0 - \Delta S_\infty)e^{-K\Sigma\Delta\varepsilon} + \Delta S_\infty \ , \qquad (39)$$

where ΔS is the strain range for any cycle, ΔS_0 is a constant that gives the stress range when $\Sigma\Delta\varepsilon$ is zero, ΔS_∞ is the saturation stress range, and K is a constant related to the cyclic hardening rate. For constant-strain-range tests $\Sigma\Delta\varepsilon$ can be replaced by $N\ \Delta\varepsilon$, where N is the number of

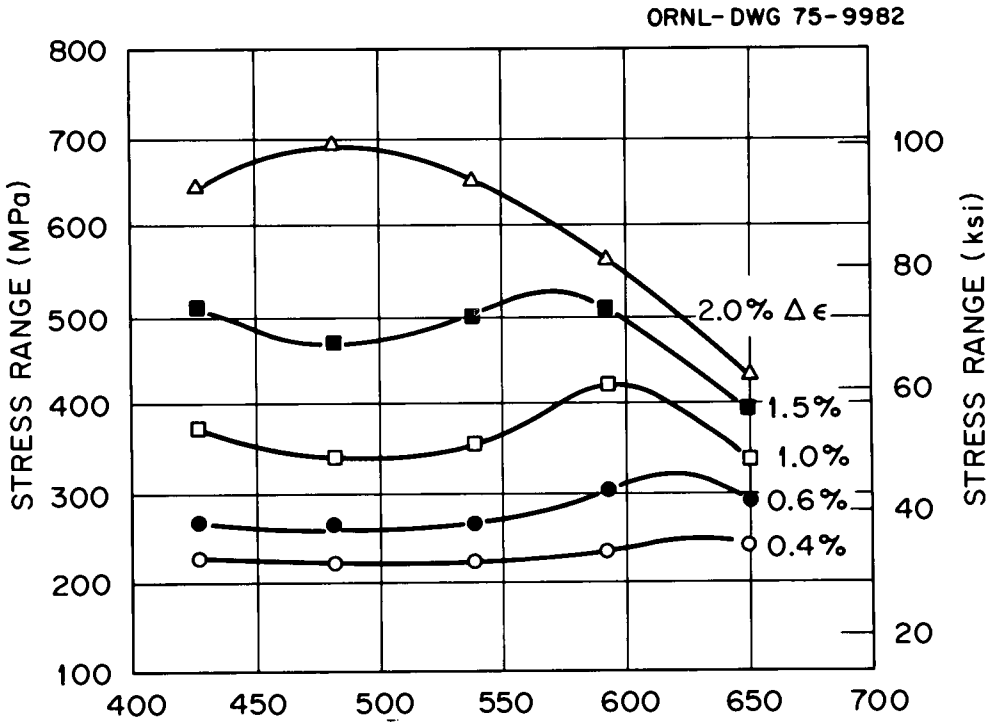

Fig. 3.123. Cyclic Strength at the Tenth Cycle for Type 304 Stainless Steel (Heat 9T2796).

cycles. For convenience the total strain range rather than the plastic strain range is used. A nonlinear least squares program was used to obtain "best fit" values for Eq. (39), but is became clear that this approach did not produce values for ΔS_0 that are consistant with the tensile flow model developed earlier. We decided to calculate the equation constants such that ΔS when N is 0.25 would agree with the tensile curve when the tensile stress and strain are doubled. Also, we chose to use to the value for ΔS from the actual hardening curve when N is 10. The values for ΔS_0, ΔS_∞, and K that we obtained using these assumptions are plotted in Figs. 3.124, 3.125, and 3.126 against the strain range. In Fig. 3.124 the value for ΔS_0 is seen to increase with increasing strain range and decreasing temperature. Values for ΔS_∞ are plotted in Fig. 3.125 against the strain range. Data for tests in the range 427 to 538°C (800–1000°F) tend to fall on a common curve. High-strain data at 593°C (1100°F) exhibit lower values, while at 649°C (1200°F) all the ΔS_∞ values are low relative to other temperatures. In Fig. 3.126, where the values for K are plotted

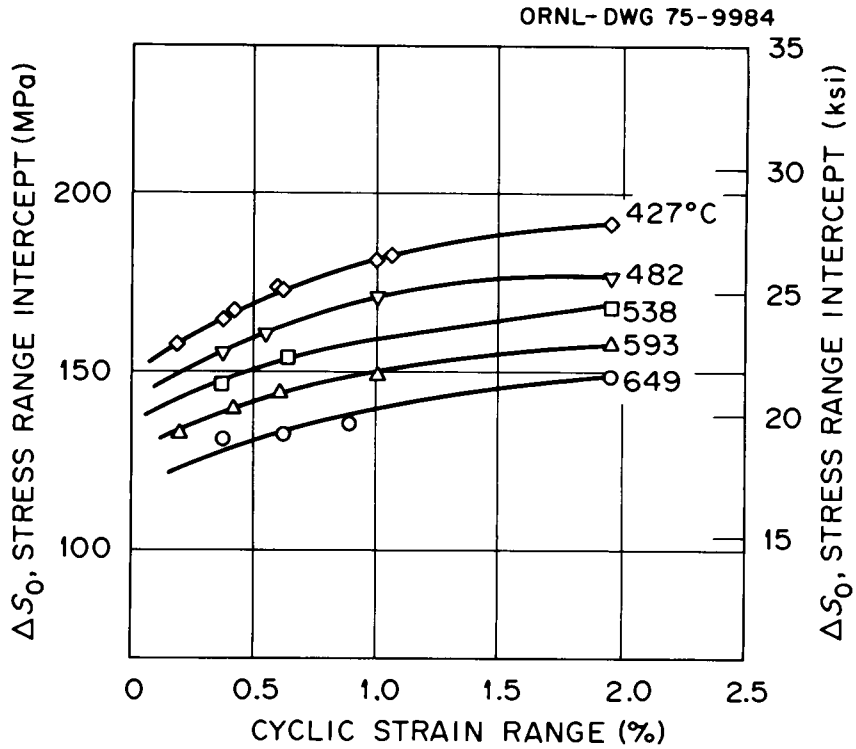

Fig. 3.124. Stress Range Intercept at Zero Cycles for Type 304 Stainless Steel (Heat 9T2796).

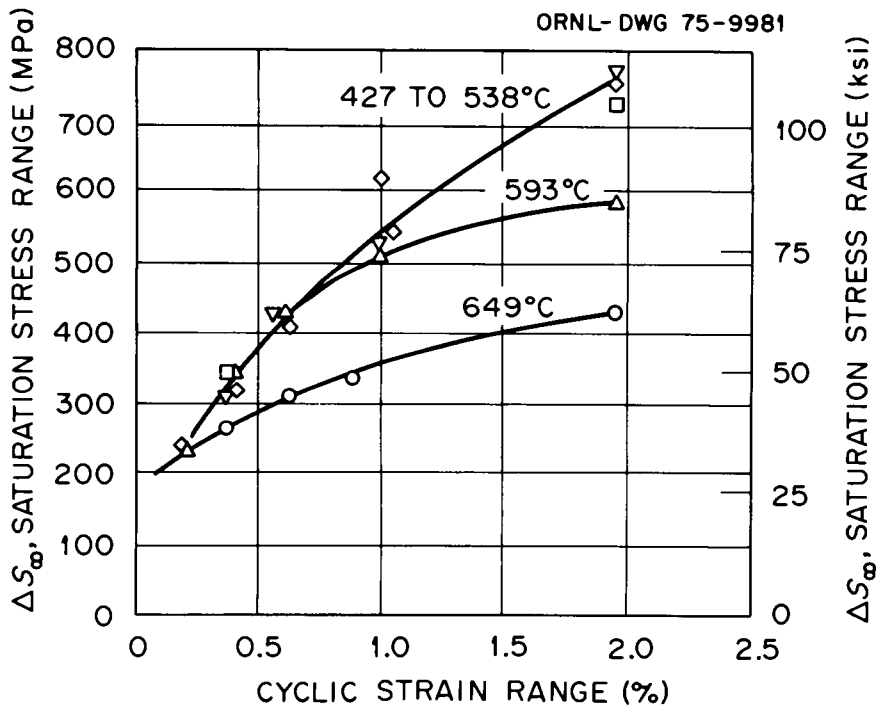

Fig. 3.125. Saturation Stress Range for Type 304 Stainless Steel (Heat 9T2796).

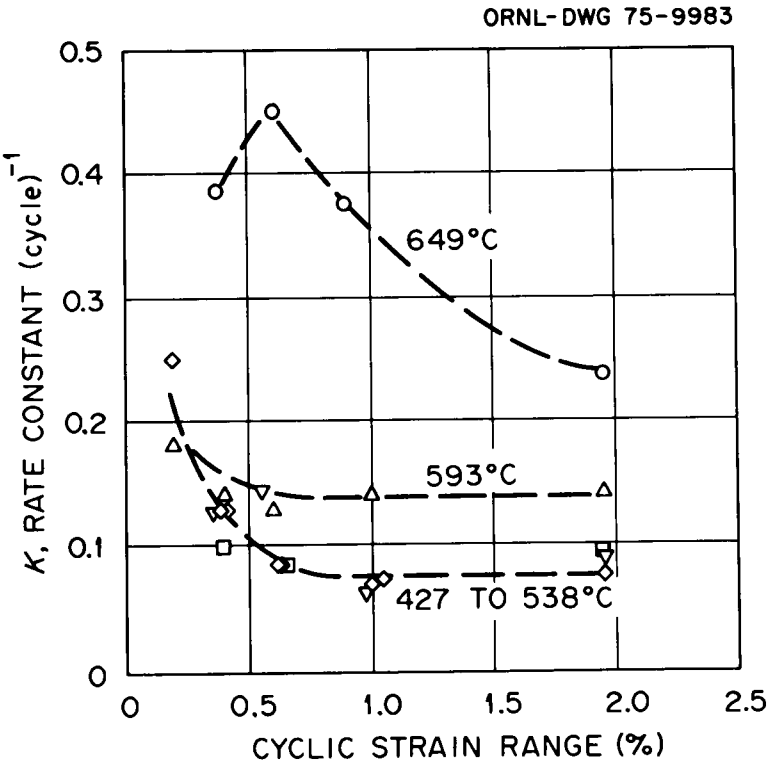

Fig. 3.126. Rate Constant, K, Describing the Rate of Approach to the Saturation Stress for Cyclic Tests on Type 304 Stainless Steel (Heat 9T2796).

against strain, it appears that at 593°C (1100°F) and below K is insensitive to the strain range at large strains. Below 0.5% strain range, however, the meager data that are available suggest that K increases with decreasing strain. The values for K are greatest at 649°C (1200°F) and tend to decrease with decreasing temperature. In the range 427 to 538°C (800–1000°F) scatter is the data obscures evidence for temperature dependence.

3.5.1.3 Exploratory Testing of 2 1/4 Cr-1 Mo Steel — R. W. Swindeman and R. L. Klueh

A limited testing program is under way on 2 1/4 Cr-1 Mo steel (heat 20017). Primarily we are studying creep-plasticity interactions and relaxation behavior. The results of the relaxation testing program are updated in Figs. 3.127, 3.128, and 3.129. Data at 482°C (900°F), shown in Fig. 3.127, reveal substantial strain hardening capability,

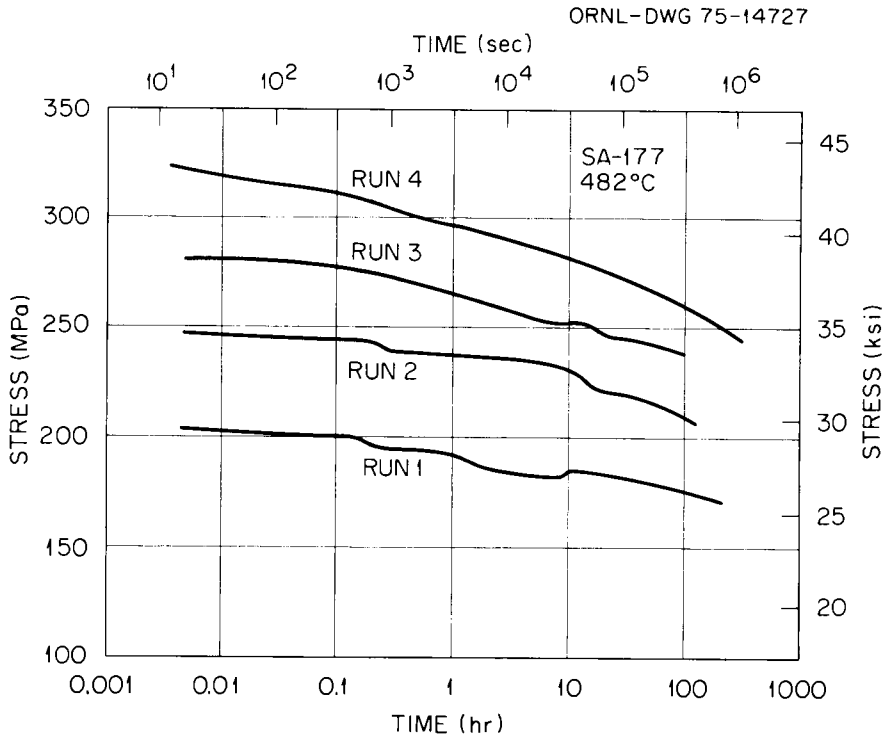

Fig. 3.127. Relaxation Curves for 2 1/4 Cr-1 Mo Steel (Heat 20017) at 482°C (900°F).

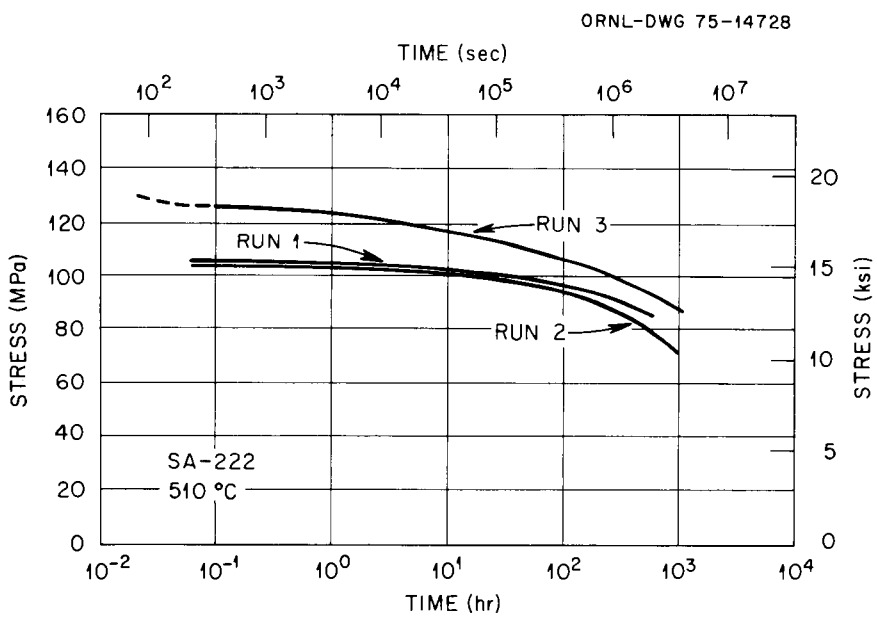

Fig. 3.128. Relaxation Curves for 2 1/4 Cr-1 Mo Steel (Heat 20017) at 510°C (950°F). Tests performed in Pneumatic-Hydraulic Machine.

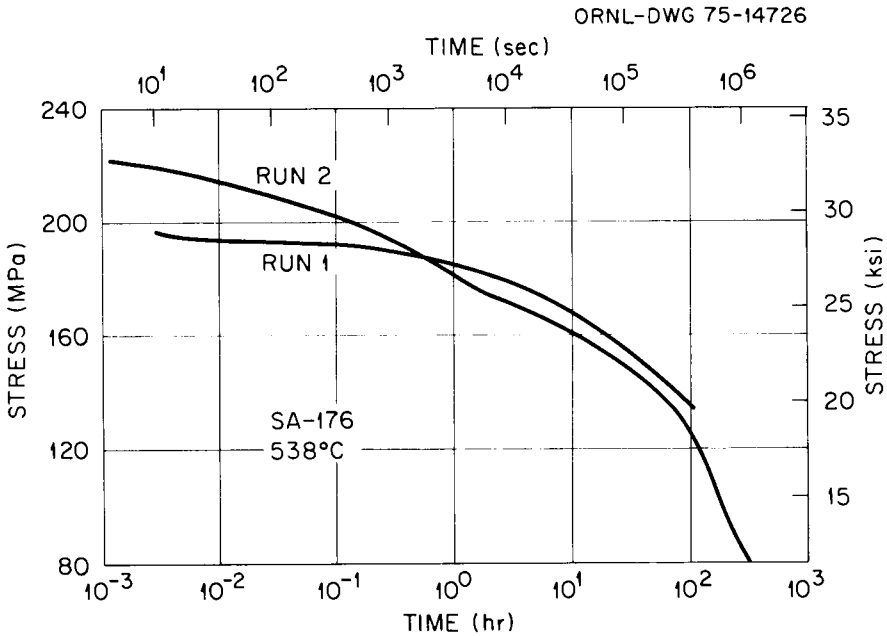

Fig. 3.129. Relaxation Curves for 2 1/4 Cr-1 Mo Steel (Heat 20017) at 538°C (1000°F).

while data at 538°C (1000°F), shown in Fig. 3.129, reveal a slight strain (or time) weakening effect. One cyclic creep test has been initiated on 2 1/4 Cr-1 Mo steel at 566°C (1050°F), and the results are summarized in Fig. 3.130. The results for a cyclic stress of ±103 MPa (±15 ksi)

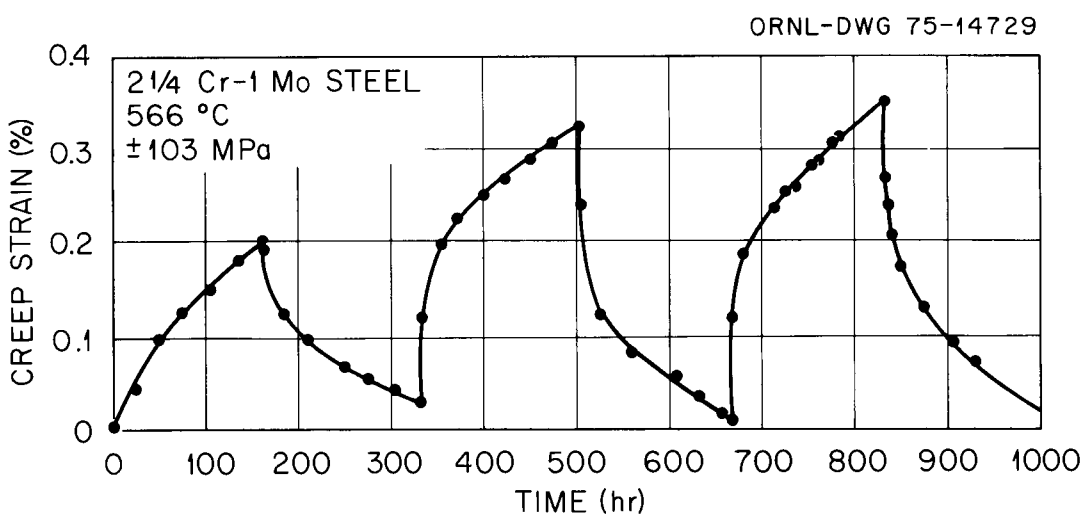

Fig. 3.130. Cyclic Creep Behavior of 2 1/4 Cr-1 Mo Steel at 566°C (1050°F) and ±103 MPa (±15 ksi).

reveal a strain (or time) induced weakening in the sense that the cyclic strains are increasing.

3.5.2 Investigations of Creep Failure Under Uniaxial and Multiaxial Conditions — C. C. Schultz (Babcock and Wilcox)

3.5.2.1 Topical Report

The primary activity during this reporting period was completion of a topical report that summarizes our findings with respect to the inconsistent microstructure observed in the 16-mm-diam (5/8-in.) hot-rolled bar product form of heat 9T2796 and the observed differences in creep response between our two types of uniaxial creep testing machines. It is anticipated that the report will be transmitted to ORNL in the near future.

3.5.2.2 Constant-Load Uniaxial Tests

Test BWR-9 [124 MPa (18 ksi)] ruptured during this reporting period. The creep strain-time data from this test are shown in Fig. 3.131. Only two uniaxial tests remain in progress at this time, test BWR-11 [117 MPa (17 ksi)] and test BWR-7 [110 MPa (16 ksi)]. As is apparent from the creep strain-time data of Fig. 3.132, test BWR-11 is very near completion. The results and status of all constant-load tests are shown in Table 3.37.

3.5.2.3 Interrupted-Load Uniaxial Tests

The original intent of this test series was to terminate pairs of tests at different life fractions for destructive testing. From each pair, one specimen was to be used for metallographic examination and one for a short-time tensile test to failure. The similar creep response of all specimens was anticipated, so that use of different specimens at different life fractions would be a reasonable approximation to the ideal of a single specimen at different points in its life. As previously reported,[77] the creep strain-time data (Fig. 3.133) suggest considering these six tests as two separate groups: BWI-1, BWI-2, BWI-4; and BWI-3, BWI-5, BWI-6. It is presently presumed that the marked differences in behavior are due to the microstructural differences that have previously

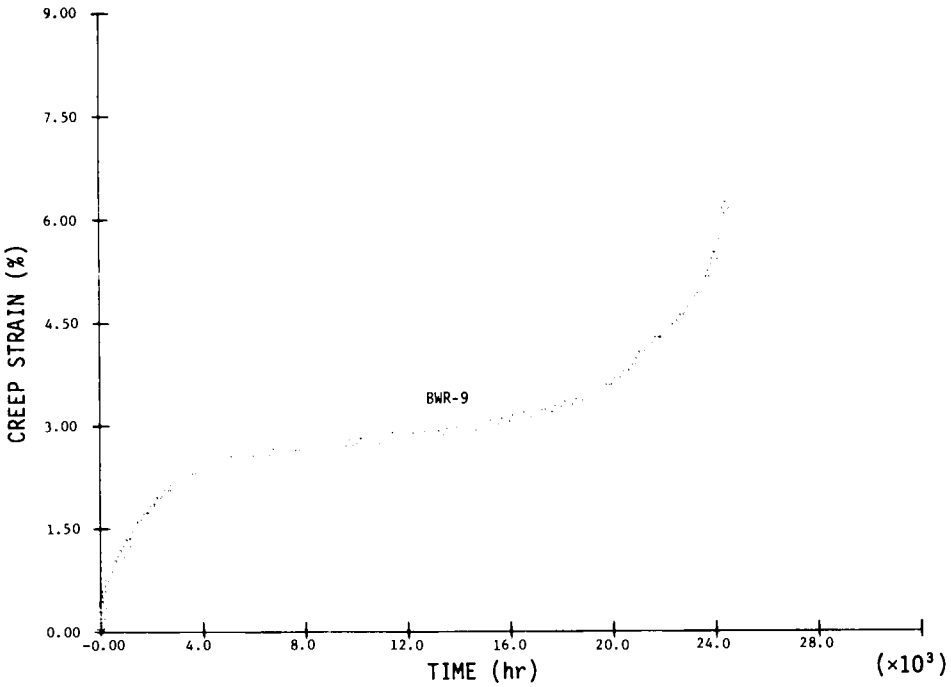

Fig. 3.131. Constant-Load Uniaxial Rupture Test at 124 MPa (18 ksi) and 593°C (1100°F). Type 304 stainless steel, heat 9T2796, 16-mm (5/8-in.) bar.

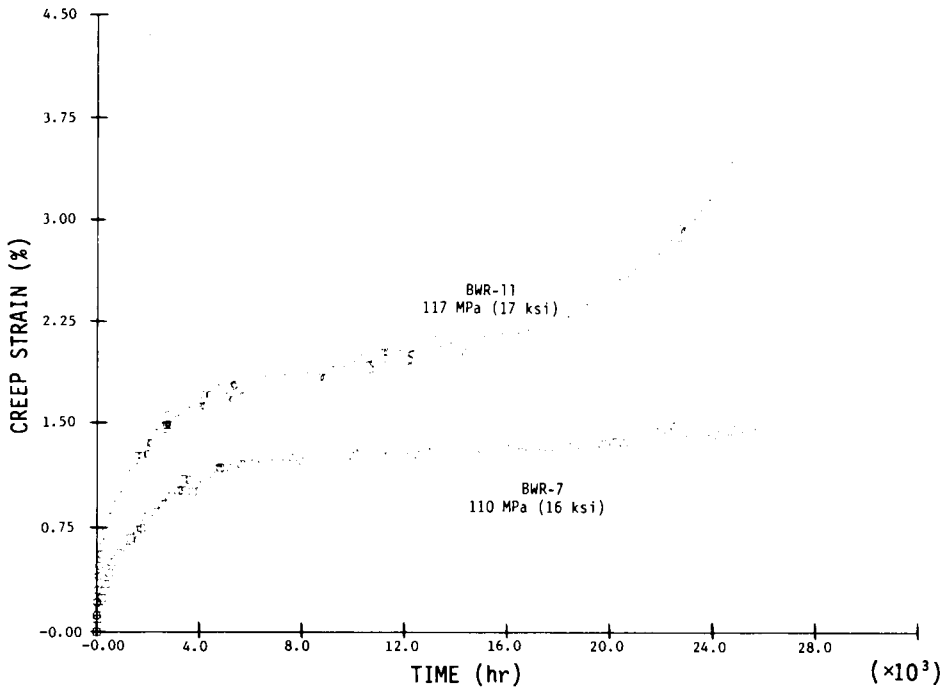

Fig. 3.132. Constant-Load Uniaxial Rupture Tests (in Progress). Loaded as shown at 593°C (1100°F). Type 304 stainless steel, heat 9T2796, 16-mm (5/8-in.) bar.

Table 3.37. Constant-Load Uniaxial Rupture Tests at 593°C (1100°F) Type 304 Stainless Steel, Heat 9T2796

Test	Specimen	Stress (MPa)	Stress (ksi)	Total Strain on Loading[a] (%)	Time to Secondary Creep (hr)	Minimum Creep Rate (%/hr)	Time to Tertiary Creep[b] (hr)	Intercept Creep Strain[c] (%)	Test Time[d] (hr)	Fracture Elongation[e] (%)	Reduction of Area (%)
BWC-1	7-15	207	30.0	5.0					187 R	19.0	30.5
BWR-1	7-1	207	30.0	7.80					138 R	21.5	32.9
BWC-2	2-22	193	28.0	6.35	40	0.016	195	0.50	227 R	13.0	20.4
BWR-2	2-1	193	28.0	5.75	40	0.022	230	0.65	368 R	16.5	18.3
BWR-13	7-13	193	28.0	6.57	60	0.023	215	0.88	276 R	16.5	18.9
BWC-9	7-25	193	28.0	4.25	85	0.021	315	1.16	415 R	18.3	25.2
BWC-3[f]	7-28	172	25.0	4.20	80	0.0065	500	0.45	667 R	12.7	12.0
BWR-3	7-8	172	25.0	3.90	100	0.0079	585	0.71	948 R	17.0	23.2
BWC-4	2-28	152	22.0	4.00	175	0.0014	1400	0.60	2130 R	10.7	13.7
BWR-4	7-7	152	22.0	3.30	160	0.0030	1170	0.72	2026 R	12.5	16.6
BWC-5[g]	2-15	138	20.0						D		
BWC-5B	2-16	138	20.0	1.83	5000	0.000165	8700	1.84	9584 R	10.5	12.0
BWR-5[h]	2-14	138	20.0	2.02					4842 D		
BWR-14	2-9	138	20.0	2.02	3200	0.00044	5800	1.88	6868 R	8.5	13.1
BWC-10	7-18	138	20.0	1.58	4000	0.00021	8000	2.30	9450 R	9.3	14.3
BWR-6	7-14	131	19.0	1.48	6000	0.000073	13500	2.90	17547 R	9.5	12.6
BWR-9	7-11	124	18.0	1.15	7500	0.000036	18000	2.40	24495 R	8.5	13.8
BWR-11[i]	2-12	117	17.0						94 D		
BWR-11B	2-10	117	17.0	1.35	6000	0.000033	20000	1.60	25000 I		
BWR-7	2-4	110	16.0	0.60	6000	0.000009		1.15	25500 I		

[a]All specimens were step loaded at 12.9-MPa (1.87-ksi) increments, except test BWC-5B, which was step loaded at 10.3-MPa (1.49-ksi) increments.

[b]Time to tertiary creep based on the 0.2% offset from the minimum rate line.

[c]Intercept creep strain does not include the elastic and initial plastic components.

[d]R = rupture; D = discontinued; I = in test.

[e]Elongation over 76.2 mm (3 in.) in BWC series; over 50.8 mm (2 in.) in BWR series.

[f]Failure occurred near end of gage length.

[g]Temperature excursion to 704°C (1300°F) before loading; replaced by test BWC-5B.

[h]Temperature excursion to 749°C (1380°F) at 4842 hr; terminated.

[i]Temperature excursion at 704°C (1300°F) at 94 hr; replaced by test BWR-11B.

been observed in this product form. As a result of these differences in behavior, one test in each group was allowed to continue to failure, and the remaining tests have been interrupted near the initiation of tertiary creep (Fig. 3.133 and Table 3.38). The planned short-time tensile testing and metallographic work has not yet been initiated.

3.5.2.4 Modified Reanneal

It was previously proposed[78] to extend the 1093°C (2000°F) reannealing time from 30 to 90 min as an attempt to eliminate the grain size variability. As discussed in our last progress report,[77] complete results from three tests and partial results from a fourth test (all using specimens reannealed for 90 min) established that the proposed modification was inadequate. The fourth test, BWC-11, has been completed

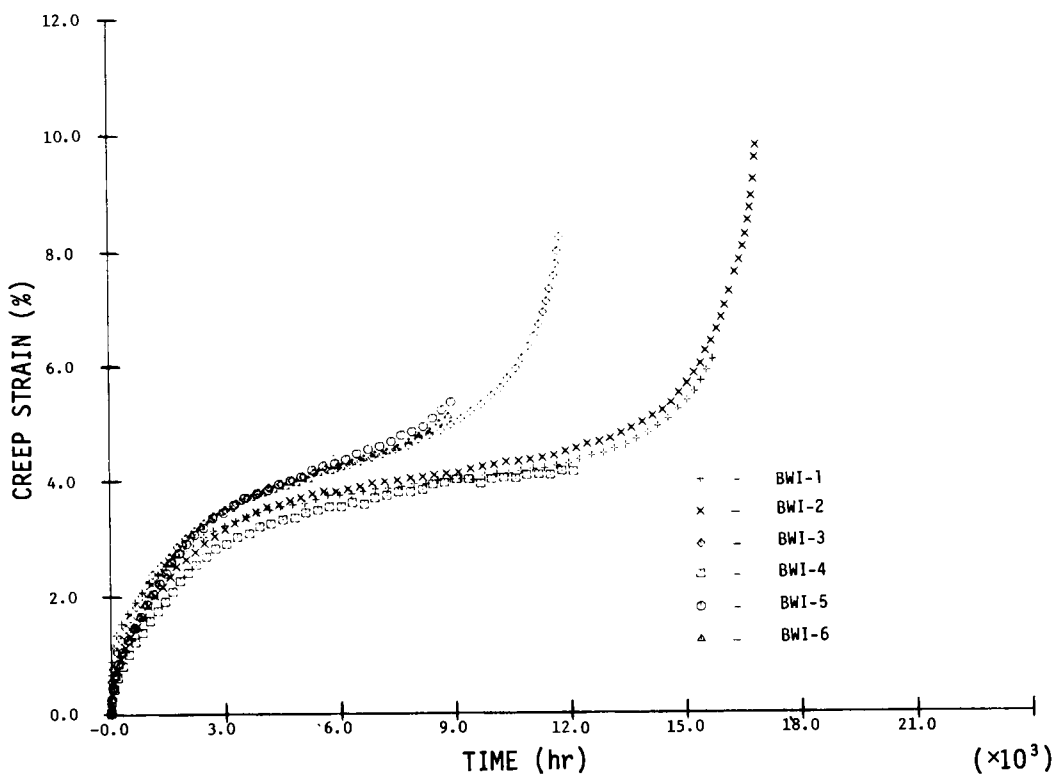

Fig. 3.133. Constant-Load Uniaxial Tests at 134 MPa (19.5 ksi) and 593°C (1100°F). Type 304 stainless steel, heat 9T2796, 16-mm (5/8-in.) bar.

Table 3.38. Interrupted Uniaxial Tests at 593°C (1100°F) and 134 MPa (19.5 ksi), Type 304 Stainless Steel, Heat 9T2796

Test	Specimen	Total Strain on Loading[a] (%)	Time to Secondary Creep (hr)	Minimum Creep Rate (%/hr)	Time to Tertiary Creep[b] (hr)	Intercept Creep Strain[c] (%)	Test Time[d] (hr)	Fracture Elongation[e] (%)	Reduction of Area (%)
BWI-1	6-4	0.98	5600	0.00008	13000	3.3	15788 D		
BWI-2	6-5	1.07	5400	0.00010	13000	3.2	16891 R	13.0	11.5
BWI-3	6-6	1.50	4800	0.00019	9000	3.2	11608 R	11.0	13.3
BWI-4	6-1	0.98	7000	0.00005		3.5	12100 D		
BWI-5	6-2	1.65	3800	0.00026	8300	2.7	9072 D		
BWI-6	6-3	1.30	3800	0.00023	7500	2.8	9049 D		

[a]All specimens were step loaded at 12.9-MPa (1.87-ksi) increments.

[b]Time to tertiary creep based on the 0.2% offset from the minimum rate line.

[c]Intercept creep strain does not include the elastic and initial plastic components.

[d]R = rupture; D = discontinued.

[e]Elongation over 50.8-mm (2-in.) gage length.

and the results are reported in Table 3.39. There are no plans for Babcock and Wilcox to evaluate any additional modifications to the reannealing procedure.

3.5.2.5 Tubular Tests

As reported earlier,[77] difficulty was experienced in maintaining internal pressure in test BWTR-3 [equal biaxial tension of 150.7 MPa (21.85 ksi)] after 585 hr under load. Since there was no conclusive visual evidence of failure, a helium leak test was performed, and a leak was detected in the pressure inlet line. After replacement of the line, no leaks were identified but pressure could not be maintained. It is now concluded that 585 hr is the valid rupture time. The creep strain-time data are thus complete as previously reported.[77]

Two unsuccessful attempts were made to initiate test BWTR-5 [axial stress of 138 MPa (20 ksi) and circumferential stress of 69 MPa (10 ksi)]. In both loading attempts, leaks developed in either the pressure inlet line or the fittings.

Test BWTR-6 [axial stress of 69 MPa (10 ksi) and circumferential stress of 138 MPa (20 ksi)] is in progress. The creep strain-time data from this test are reported in Figs. 3.134 and 3.135. In Fig. 3.134, the axial creep strain was determined by averaging the output of two extensometers measuring relative displacement over the center 12.7 cm (5 in.) of the 20.8-cm (8-in.) reduced test section. Figure 3.135 shows the circumferential strain at the midlength of the specimen. In this figure each set of data represents the average of two opposed radial DCDTs. Axial creep strain was evident in this test to the same extent as was reported[79] for an earlier test (BWTR-2), which was also loaded by internal pressure alone. After approximately 420 hr under load, it was necessary to interrupt the test for furnace repairs.

Test BWTR-7 [equal biaxial tension of 137.9 MPa (20 ksi)] was initiated. Preliminary creep strain-time results are shown in Figs. 3.136 and 3.137. The data shown in these two figures were obtained as described for test BWTR-6 (i.e., Figs. 3.134 and 3.135).

Table 3.39. Test Conditions and Results for Specimens Reannealed at 1090°C (2000°F) for 90 min and Tested at 593°C (1100°F)

Test	Specimen	Stress		Total Strain on Loading[a] (%)	Time to Secondary Creep (hr)	Minimum Creep Rate (%/hr)	Time to Tertiary Creep[b] (hr)	Intercept Creep Strain[c] (%)	Test Time[d] (hr)	Fracture Elongation[e] (%)	Reduction of Area (%)
		(MPa)	(ksi)								
BWR-15	2-3	138	20.0	2.50	225	0.00088	3000	0.50	4240	10.5	10.9
BWC-11	2-19	138	20.0	2.90	500	0.00066	3450	0.43	5008	15.0	14.8
BWC-13	7-19	172	25.0	5.30	135	0.0049	405	0.42	467	10.0	16.0
BWR-16	7-2	172	25.0	4.80	70	0.0090	250	0.50	284	11.5	21.1

[a]All specimens were step loaded at 12.9-MPa (1.87-ksi) increments.

[b]Time to tertiary creep based on the 0.2% offset from the minimum rate line.

[c]Intercept creep strain does not include the elastic and initial plastic components.

[d]All ruptured.

[e]Elongation over 76.2 mm (3 in.) in BWC series; over 50.8 mm (2 in.) in BWR series.

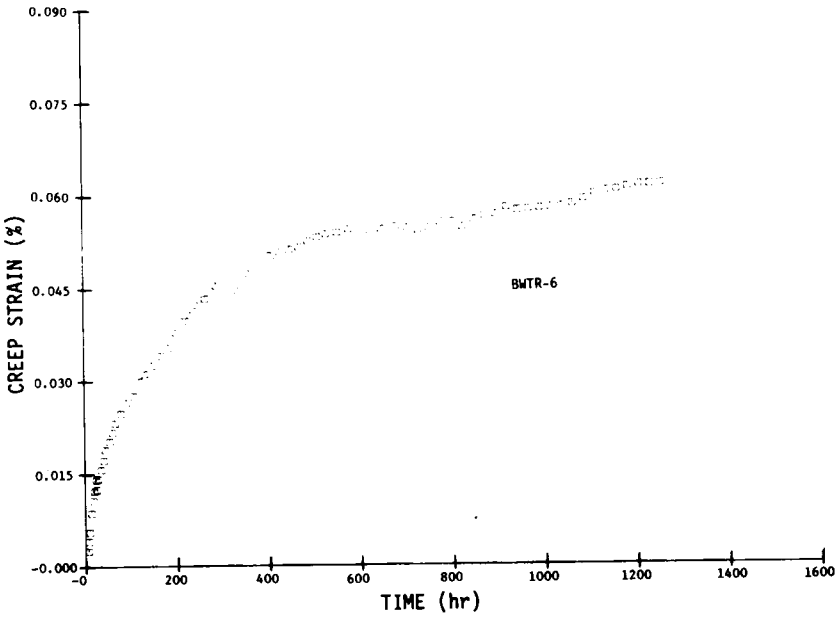

Fig. 3.134. Axial Creep Strain in Constant-Load Biaxial Rupture Test. Tubular specimen with internal pressure. Circumferential stress of 138 MPa (20 ksi) and axial stress of 69 MPa (10 ksi), tested at 593°C (1100°F). Outside diameter of 38.1 mm (1.50 in.) and wall thickness of 1.9 mm (0.075 in.). Type 304 stainless steel, heat 9T2796, 48.95-mm (1.927-in.) bar.

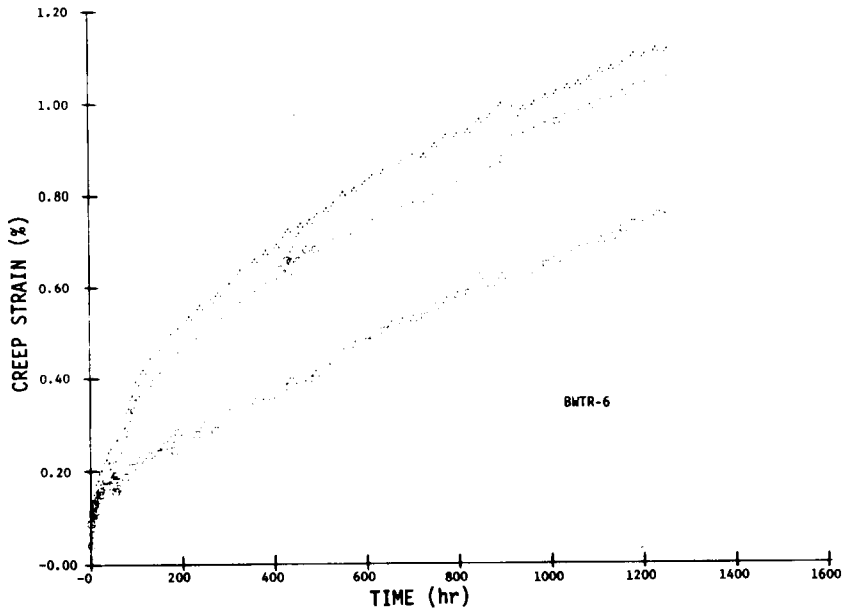

Fig. 3.135. Circumferential Creep Strain in Constant-Load Biaxial Rupture Test. Tubular specimen with internal pressure. Circumferential stress of 138 MPa (20 ksi) and axial stress of 69 MPa (10 ksi), tested at 593°C (1100°F). Outside diameter of 38.1 mm (1.50 in.) and wall thickness of 1.9 mm (0.075 in.). Type 304 stainless steel, heat 9T2796, 48.95-mm (1.927-in.) bar.

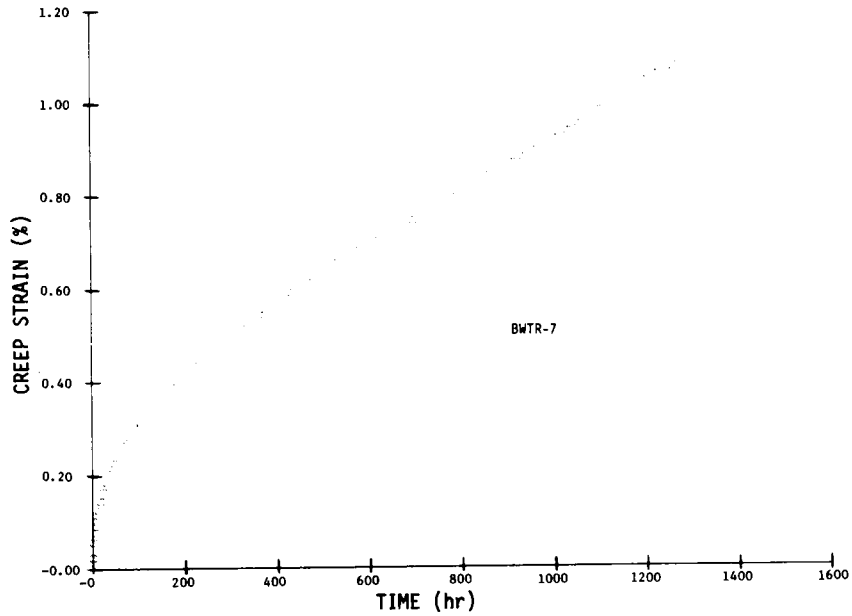

Fig. 3.136. Axial Creep Strain in Constant-Load Biaxial Rupture Test. Tubular specimen with internal pressure and additional axial load. Equal biaxial tension of 138 MPa (20 ksi), tested at 593°C (1100°F). Outside diameter of 38.1 mm (1.50 in.) and wall thickness of 1.9 mm (0.075 in.). Type 304 stainless steel, heat 9T2796, 49.95 mm (1.927-in.) bar.

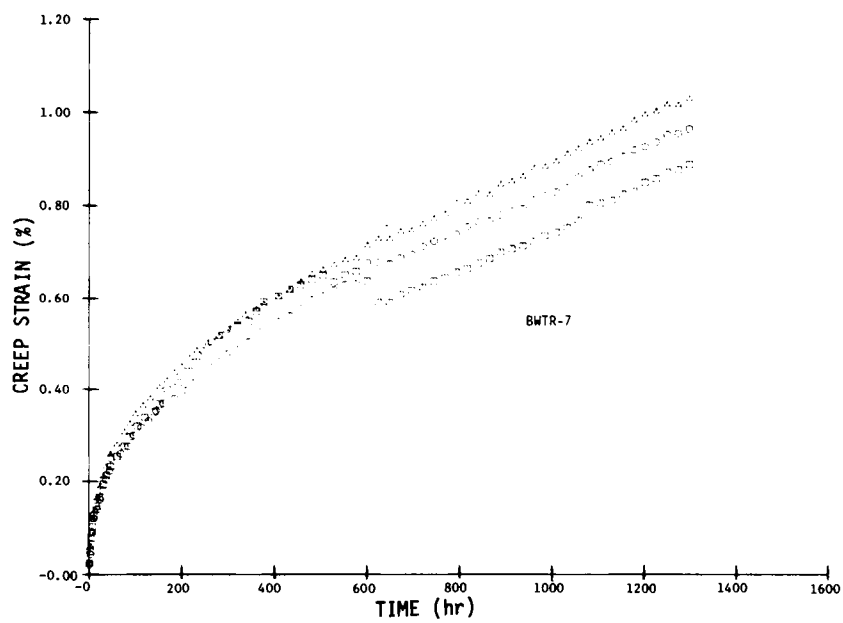

Fig. 3.137. Circumferential Creep Strain in Constant-Load Biaxial Rupture Test. Tubular specimen with internal pressure and additional axial load. Equal biaxial tension of 138 MPa (20 ksi, tested at 593°C (1100°F). Outside diameter of 38.1 mm (1.50 in.) and wall thickness of 1.9 mm (0.075 in.). Type 304 stainless steel, heat 9T2796, 48.95-mm (1.927-in.) bar.

3.6 MECHANICAL PROPERTIES OF HTGR STEAM GENERATOR AND PRIMARY CIRCUIT MATERIALS — J. R. DiStefano and P. L. Rittenhouse

The major overall objectives of this program are to (1) determine the compatibility of alloys planned for use in the HTGR steam-cycle system with their environment and (2) determine, compile, and analyze materials design data for the commercial HTGR. To achieve these objectives it is necessary to study the mechanical behavior (tensile, creep, low-cycle fatigue, and crack growth) of HTGR alloys at temperatures and in environments (helium and steam) appropriate to their service in the reactor.

3.6.1 Tensile Testing — P. L. Rittenhouse

Specimens from hot rolled, solution annealed 13-mm-thick (1/2-in.) Inconel 617 plate (heat XX01H3VS) are currently being fabricated. Tests are scheduled to be run at room temperature and at elevated temperatures through 982°C (1800°F).

3.6.2 Environmental Creep Testing — P. L. Rittenhouse

Our environmental creep tests of HTGR structural alloys in simulated primary coolant helium have continued during the quarter. The normal level of impurities in the simulated coolant during this period is shown in Table 3.40. This gas mixture is provided from premixed cylinders and is used in a once-through loop operating at about 0.15 MPa (1.5 atm). Levels of impurities are consistent with those estimated for operating gas-cooled reactor systems.

Three tests were completed during the current report period. Details and results of these are given in Table 3.41. The rupture lives and elongations shown are generally consistent with manufacturers' and literature values. The matrix of continuing tests is shown in Table 3.42. Maximum time in test is approaching 6000 hr (e.g., Tests 15023 and 15047). The Hastelloy X tests at 760 and 871°C (1400 and 1600°F) are being performed for direct comparison with identical tests at General Atomic Company.

Cross sections of specimens from two tests previously discontinued [Test 15377, 9 Cr-1 Mo, 482°C (900°F), 172 MPa (25 ksi), and Test 15045, 2 1/4 Cr-1 Mo, 593°C (1100°F), 69 MPa (10 ksi)] and Test 15058

Table 3.40. Impurity Levels in Simulated HTGR Primary Coolant Helium

Impurity	Content (μatm)[a]
H_2	380
CH_4	36
CO	24
H_2O	8
O_2	$<10^{-16}$

[a]μatm = ppm by volume × system pressure in atm; 1 μatm corresponds to a partial pressure of 0.1 Pa. Range is ±10% for all impurities except H_2O. Water vapor levels vary day-to-day and have been as high as 22 μatm and as low as 3 μatm. Normal level is 8 μatm.

Table 3.41. Details and Results of Environmental Creep Tests Completed During the Quarter

Material and Heat	Test	Temperature		Stress		Rupture Life (hr)	Elongation at Rupture (%)
		(°C)	(°F)	(MPa)	(ksi)		
Hastelloy X, 2600-3-4936	15058	704	1300	138	20	4044	21
Hastelloy X, 2600-3-4936	15771	704	1300	172	25	1007	35
2 1/4 Cr-1 Mo, 36202	15373	482	900	207	30	3494	36

Table 3.42. Current Environmental Creep Tests

Material	Heat	Test	Temperature		Stress	
			(°C)	(°F)	(MPa)	(ksi)
2 1/4 Cr-1 Mo	X-6216	15023	593	1100	69	10
2 1/4 Cr-1 Mo	X-6216	15046	593	1100	103	15
2 1/4 Cr-1 Mo	X-6216	15047	593	1100	69	10
9 Cr-1 Mo	316381-1A	15363	538	1000	103	15
2 1/4 Cr-1 Mo	36202	15369	538	1000	103	15
2 1/4 Cr-1 Mo	36202	15374	482	900	172	25
Hastelloy X	2600-3-4936	15772	649	1200	172	25
Hastelloy X	2600-3-4936	15792	704	1300	138	20
Hastelloy X	2600-3-271	Being loaded	760	1400	151	22
Hastelloy X	2600-3-271	Being loaded	871	1600	62	9

(see Table 3.41) were examined metallographically. The surface of the 9 Cr-1 Mo specimen exposed 1317 hr in simulated HTGR primary coolant at 482°C (900°F) appears to be covered by a thin (1–2 μm) continuous oxide film. After 3160 hr at 593°C (1100°F) the 2 1/4 Cr-1 Mo specimen shows evidence of what seems to be selective oxidation to a depth of about 5 μm. The Hastelloy X specimen was at 704°C (1300°F) for 4044 hr and shows little if any surface film but contains grain boundary penetrations of 15 to 50 μm. The observations and conclusions given above should be considered as preliminary until chemical etching and subsequent metallographic examination are completed.

3.6.3 Subcritical Crack Growth Studies — W. R. Corwin

All results on fatigue crack growth studies that we have obtained to date are summarized in this section. Much of the data has been published in recent quarterlies; however, it is now compiled along with the recent results and all the data have been reanalyzed.

The material used in this study is 2 1/4 Cr-1 Mo ferritic steel from Babcock and Wilcox, heat 20017. Its mechanical properties have been reported in previous quarterlies.

3.6.3.1 Tests in Air

To evaluate the temperature dependence of this material, numerous tests in air were performed at room temperature and 510°C (950°F). In addition, single comparative tests were performed at 204°C (400°F), 371°C (700°F), 454°C (850°F), and 593°C (1100°F). The data obtained at room temperature and 510°C (950°F) are shown separately in Figs. 3.138 and 3.139, respectively, along with the linear least squares best fit to the stage-two region of growth in each. These best fit lines were then assembled with results from the remaining temperatures, and these are presented in similar fashion in Fig. 3.140. The results for all temperatures except

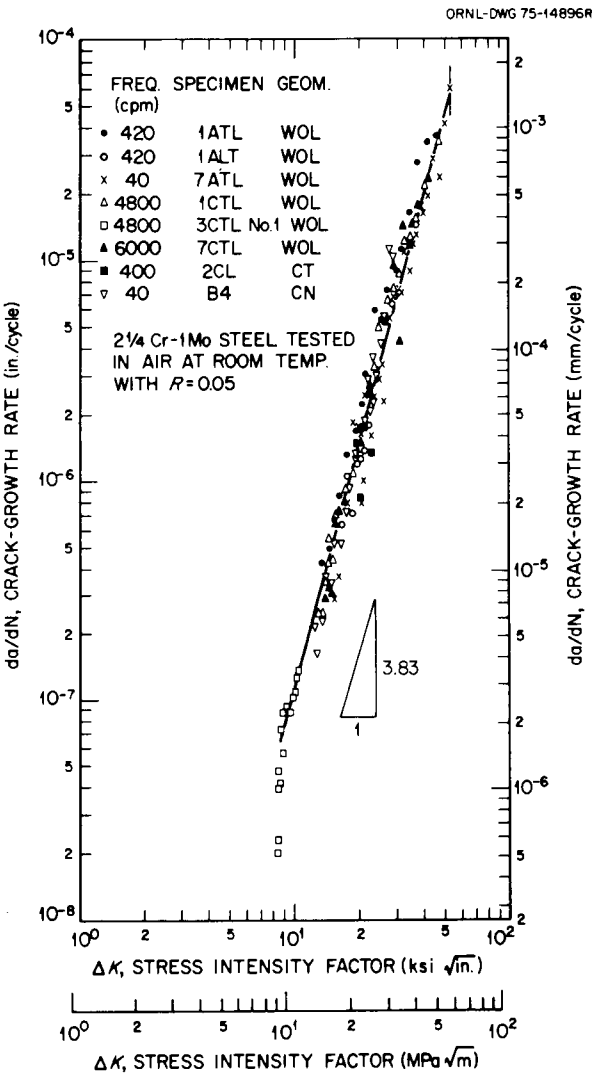

Fig. 3.138. Effects of Frequency and Specimen Geometry at Room Temperature.

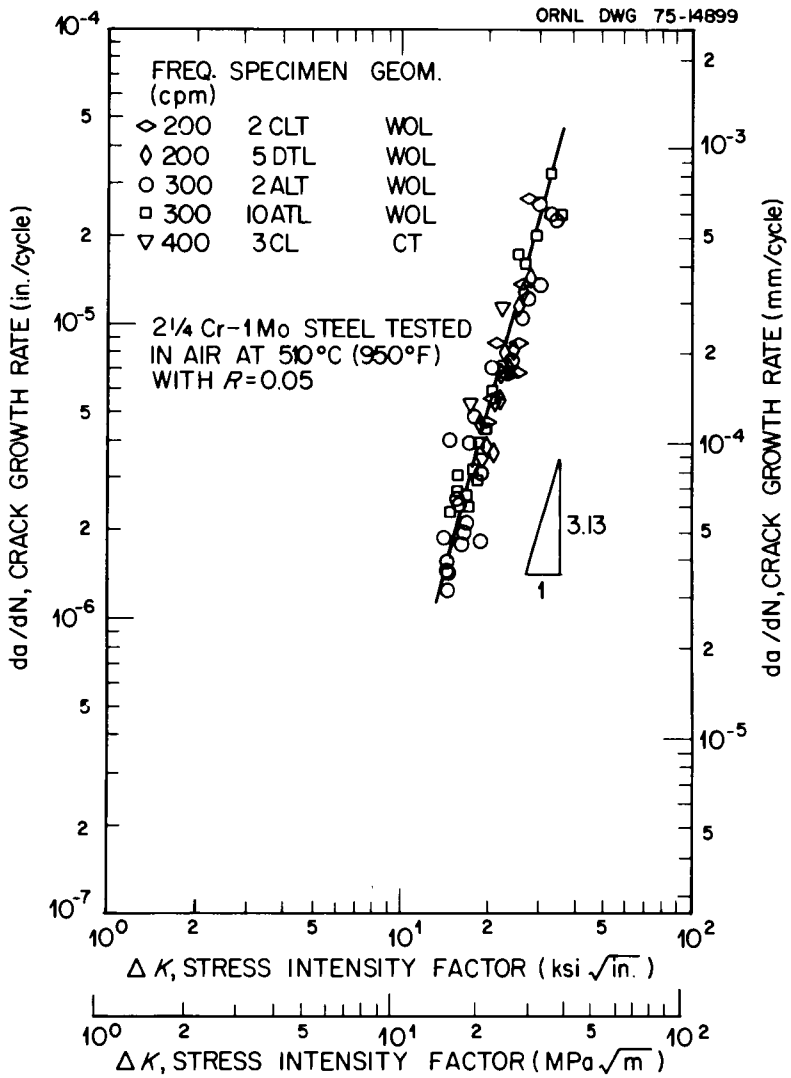

Fig. 3.139. Summary of Base-Line Crack Growth Data at 510°C (950°F).

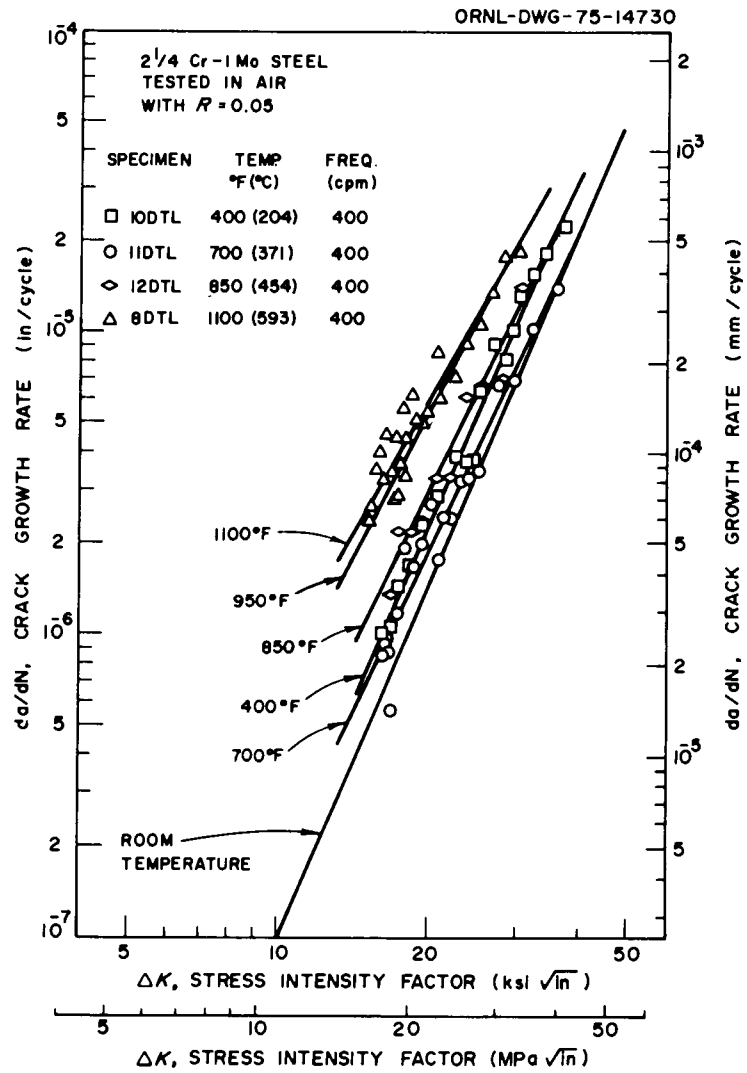

Fig. 3.140. Effects of Temperature on Crack Growth Rate.

371°C (700°F) follow the expected trend of increasing crack growth rate with increasing temperature at a constant ΔK level. The anomalous behavior at 371°C (700°F) is probably due to the effect of strain aging, which occurs in 2 1/4 Cr-1 Mo steel and peaks at roughly this temperature. An additional feature to be observed is the monotonically decreasing slope of these data sets, which occurs at all temperature evaluated including 371°C (700°F). Detailed analysis of these data leading to mathematical modeling of temperature dependence is currently under way and will be presented next quarter.

Effects of frequency have been examined at these temperatures to date: room temperature, 510°C (950°F) and 593°C (1100°F). This material exhibits no frequency dependence at room temperature over the range from 40 to 6000 cpm as shown in Fig. 3.138. Thermal processes are largely inactive at room temperature, and no effect of frequency was expected. However, at both elevated test temperatures, effects of frequency are quite marked. As seen in Fig. 3.139, there is virtually no effect of frequency at 510°C (950°F) over the range 200 to 400 cpm. However, reducing the frequency to 4 cpm significantly increased crack growth at constant ΔK level, as shown in Fig. 3.141(a). Similar behavior occurred at 593°C (1100°F), as shown in Fig. 3.141(b). Crack growth rates at 4 and 40 cpm are roughly 300% and 160%, respectively, of that at 400 cpm. The completion of a test at 510°C (950°F), ν = 40 cpm (in progress) and similar tests at additional temperatures will lead to a mathematical modeling of frequency effects.

Since few nuclear components will operate at zero mean stress, behavior at higher mean stress levels is being investigated. The index of mean stress level used in this study is the R ratio or P_{min}/P_{max}. To date R ratio effects have been examined in a few tests at room temperature and more fully at 510°C (950°F). The results of the tests at 510°C (950°F), shown in Fig. 3.142, clearly demonstrate the resultant increase in da/dN with a corresponding increase in R at a constant level of ΔK. These data have been reanalyzed by use of the concept of effective stress intensity, K_{eff}, as described previously.[80] All data at 510°C (950°F) with R from 0.033 to 0.5 were effectively normalized by the equation

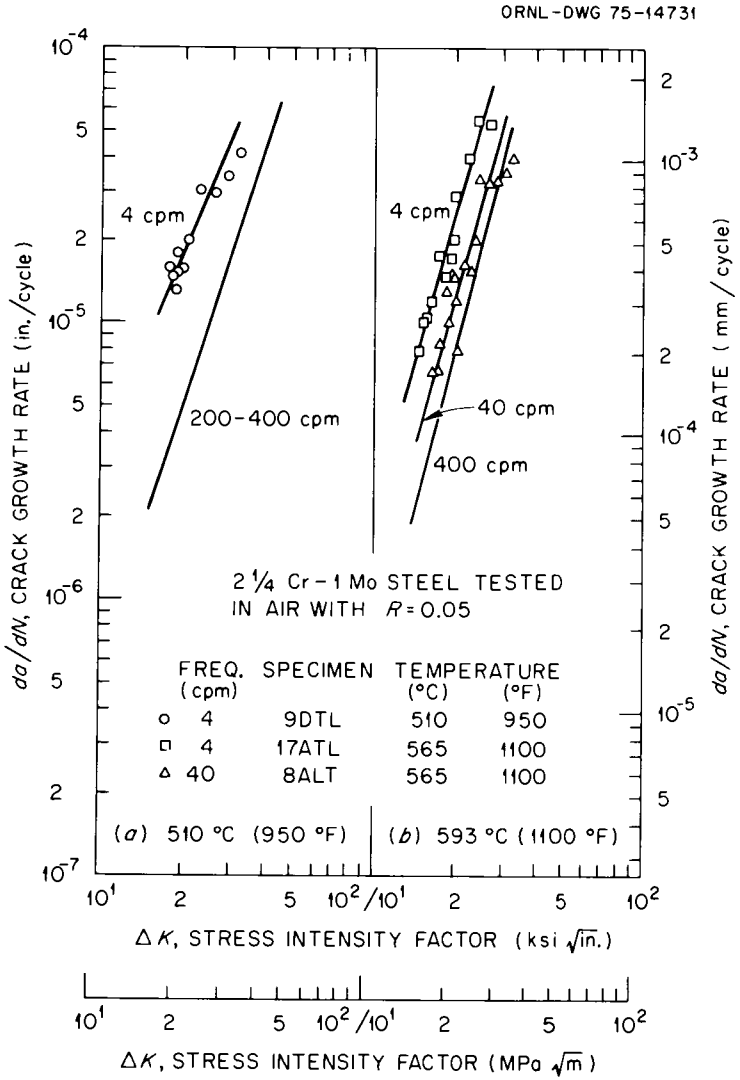

Fig. 3.141. Effects of Frequency at 510°C (950°F) and 593°C (1100°F).

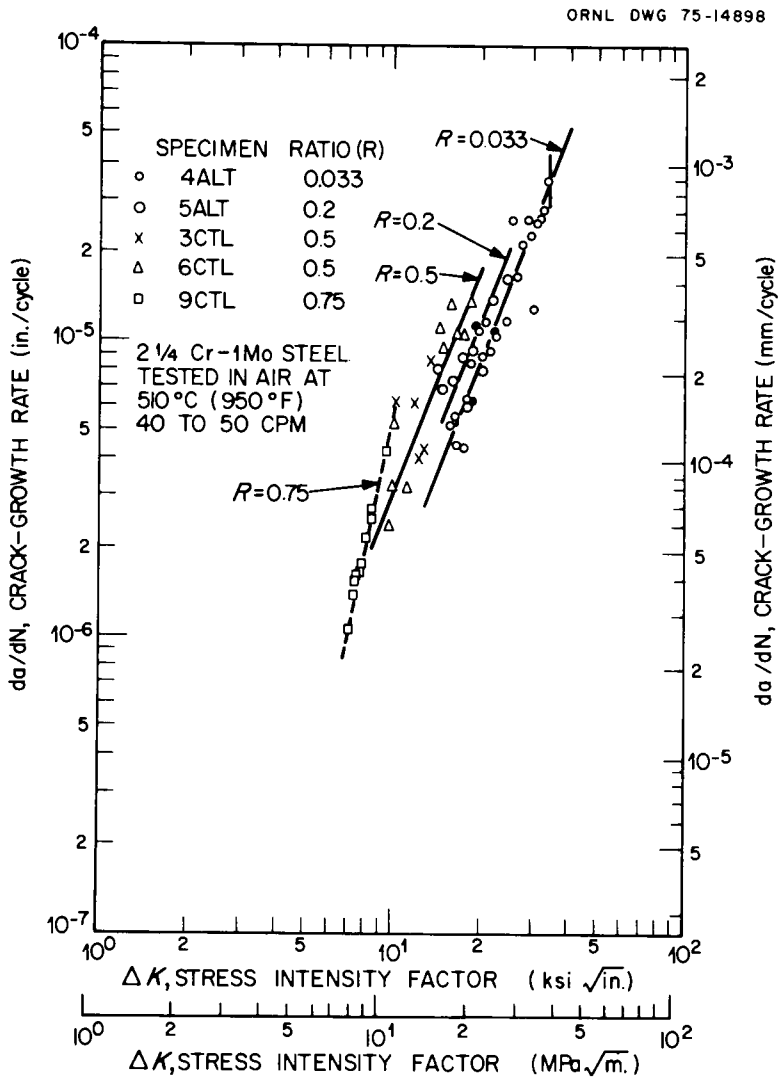

Fig. 3.142. Mean Stress Effects at 510°C (950°F).

$$K_{eff} = K_{max}(1 - R)^m ,$$

where m is in the range 0.4 to 0.6. Optimization of m is in progress. However, using K_{eff} did not normalize the data with R = 0.75. Several explanations are possible: incomplete crack closure at P_{min}, creep effects at the higher stress levels, and crack tip blunting.

The room-temperature data for R = 0.05 and 0.75 are presented in Fig. 3.143. No attempt at normalization will be made until more data are obtained.

3.6.3.2 Tests in Steam

The comparative effects of crack growth in steam and air have been examined at 510°C (950°F), with the results shown in Fig. 3.144.

At 4 cpm in steam crack growth is clearly slower than in air. Further, the effect is strongest at the lower values of stress intensity. This trend may or may not be repeated at 200 cpm. Certainly the effect is far less pronounced. A very slight reduction in crack growth rate appears at the low ΔK levels. The effect, however, becomes vanishingly small above ΔK = 27 MPa$\sqrt{m}$ (25 ksi$\sqrt{in.}$), and even below this value the shift in the data is within experimental error.

Tests are currently under way to examine this behavior at 593°C (1100°F).

3.6.3.3 Tests in HTGR Helium

Testing at 510°C (950°F), 40 cpm, R = 0.05 in simulated primary HTGR coolant is now complete, and the results are shown in Fig. 3.145. Although precise duplicate tests in air were not performed, it appears from data in air at 200–400 cpm that crack growth is slower in helium. Duplicate tests in air are currently under way. In addition, tests in helium are now under way to evaluate comparative effects at 593°C (1100°F).

3.6.4 Fatigue-Life Testing — J. P. Strizak

Aging of Hastelloy X (heat 2600-3-4936) and Inconel 617 (heat XX01A3US) has just recently been started; material will be aged at

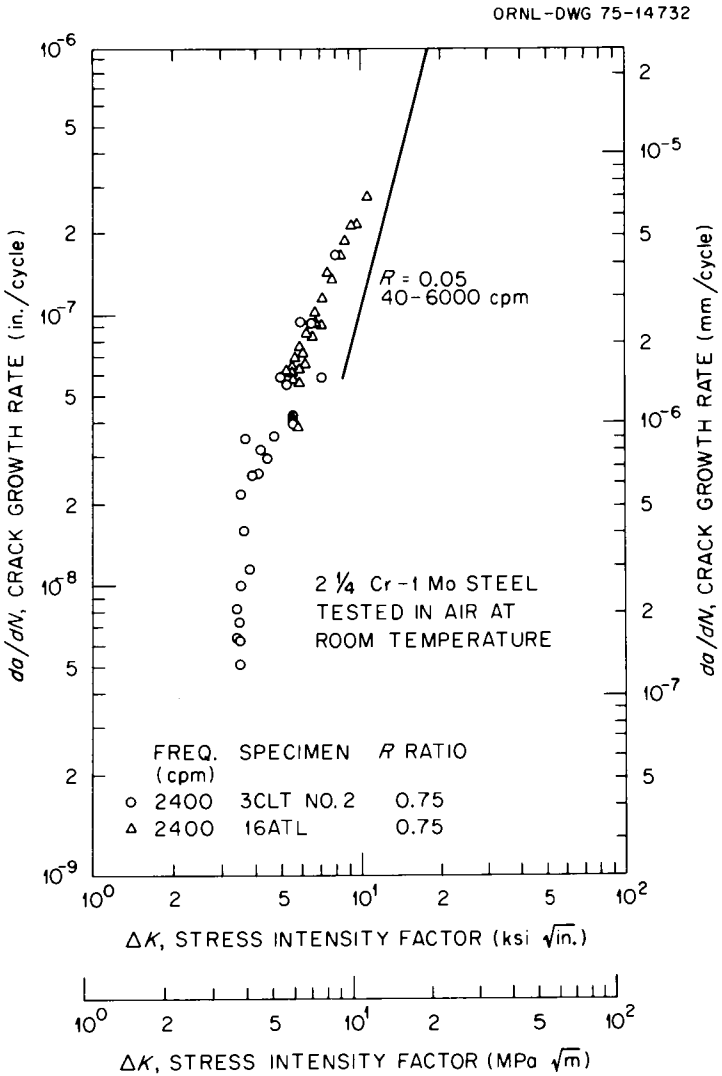

Fig. 3.143. Mean Stress Effects at Room Temperature.

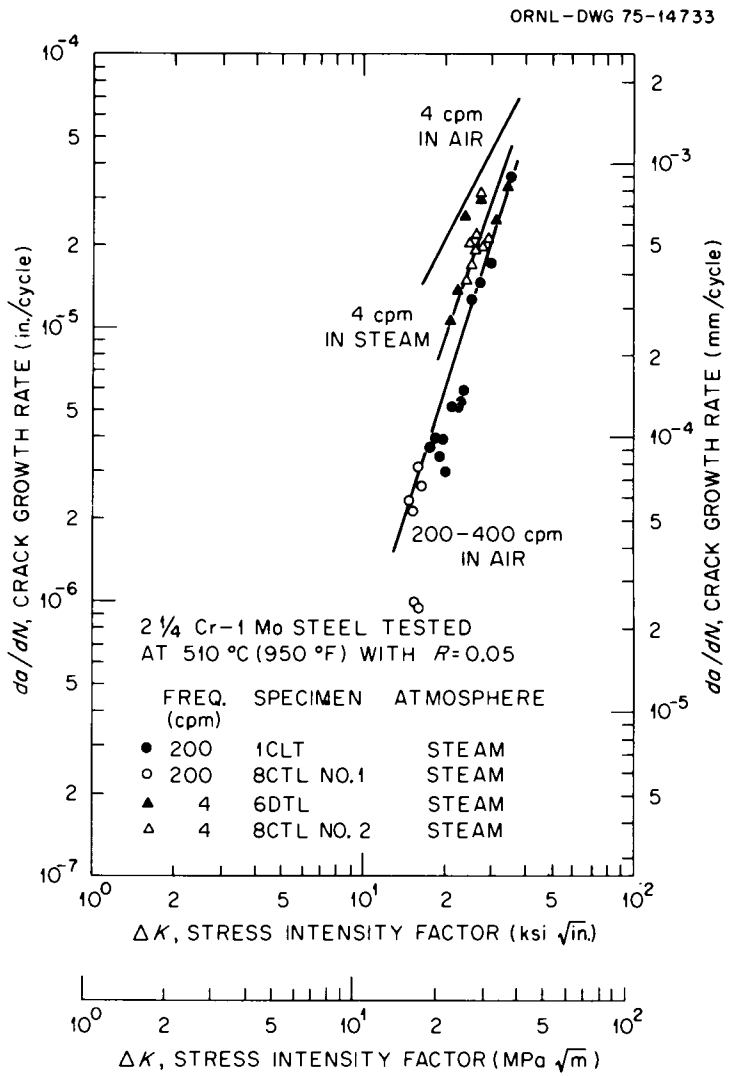

Fig. 3.144. Effects of Steam at 510°C (950°F).

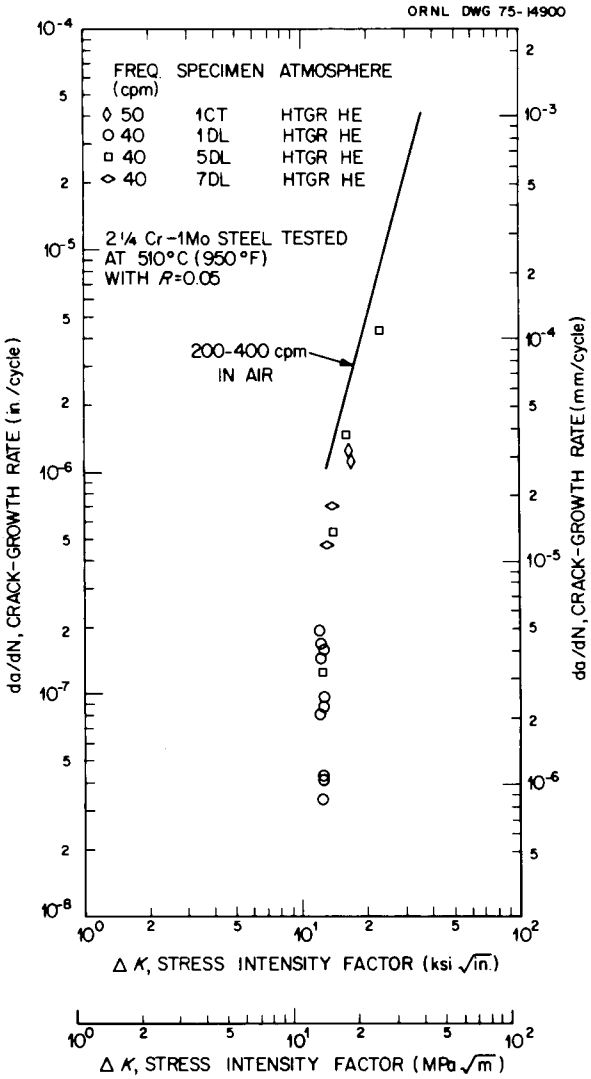

Fig. 3.145. Effects of Simulated HTGR Primary Coolant Environment at 510°C (950°F).

538, 704, and 871°C (1000, 1300, and 1600°F) for periods of 2500, 10,000, and 20,000 hr. Creep and fatigue tests will then be initiated to evaluate the thermal stability of the materials. Continuous-cycling strain-controlled fatigue tests on Hastelloy X in air at a strain rate ($\dot{\varepsilon}$) of 4×10^{-3}/sec and total strain ranges ($\Delta\varepsilon_t$) of 2% to 0.5% will be initiated at temperatures from room temperature to 871°C (1600°F). Results of these tests will appear in the next quarterly report. A completed design of an environmental chamber and specimen grip assembly is presently being reviewed. This design will facilitate low-cycle strain-controlled fatigue testing on the existing MTS machine in simulated HTGR primary coolant

helium as well as fatigue testing in vacuum to 1.3–13 μPa (10^{-8}–10^{-7} torr). Fabrication of the chamber and grip assembly and procurement of required vacuum equipment (used for purging the chamber before establishing a helium environment) are expected to start by Nov. 1, 1975.

3.7 REFERENCES

1. V. K. Sikka, "Tensile Tests Following Periods of Creep," *Mechanical Properties Test Data for Structural Materials Quart. Progr. Rep. Apr. 30, 1975,* ORNL-5105, pp. 67–91.
2. V. K. Sikka, C. R. Brinkman, and H. E. McCoy, "Effect of Thermal Aging on Tensile and Creep Properties of Types 304 and 316 Stainless Steel," to be presented at Symposium on Structural Materials for Elevated-Temperature Nuclear Power Generation Service, ASME Winter Meeting, Houston, Texas, Nov. 30–Dec. 4, 1975.
3. V. K. Sikka, H. E. McCoy, M. K. Booker, and C. R. Brinkman, " Heat-to-Heat Variation in Creep Properties of Types 304 and 316 Stainless Steels," presented at the 2nd National Congress on Pressure Vessels and Piping, 1975 ASME Summer Meeting, June 23–27, 1975.
4. F. Garofalo, *Ductility,* American Society for Metals, Metals Park, Ohio, 1968, pp. 87–129.
5. V. K. Sikka, "Mechanical Property Characterization of Type 316 Stainless Steel Reference Heat," *Mechanical Properties Test Data for Structural Materials Quart. Progr. Rep. July 31, 1975,* ORNL-5106, pp. 50–64.
6. Hanford Engineering Development Laboratory, *Nuclear Systems Materials Handbook,* TID-26666 (continually revised).
7. V. K. Sikka, R. W. Swindeman, and T. L. Hebble, "Relation Between Tensile Properties in the As-Received (Mill-Annealed) and Reannealed (Laboratory-Annealed) Conditions for Types 304 and 316 Stainless Steel," *Mechanical Properties Test Data for Structural Materials Quart. Progr. Rep. Apr. 30, 1975,* ORNL-5105, pp. 102–13.

8. V. K. Sikka and T. L. Hebble, "Relation Between Tensile and Creep Properties in the As-Received (Mill-Annealed) and Reannealed (Laboratory-Annealed) Conditions for Types 304 and 316 Stainless Steel," *Mechanical Properties Test Data for Structural Materials Quart. Progr. Rep. July 31, 1975*, ORNL-5106, pp. 64–72.

9. G. E. Dieter, Jr., *Mechanical Metallurgy*, McGraw-Hill, New York, 1961, pp. 149–50.

10. H. E. McCoy, *Tensile and Creep Properties of Several Heats of Type 304 Stainless Steel*, ORNL-TM-4709 (November 1974).

11. H. E. McCoy, *Interim Report of Tensile and Creep Data for Type 304 Stainless Steel Place (Reference Heat 9T2796, 2 in. Thick)*, ORNL-TM-4627 (October 1974).

12. R. W. Swindeman, "Representation of the High-Temperature Tensile Behavior of Reannealed Type 304 Stainless Steel by the Voce Equation," *J. Eng. Mater. Technol.* 97(2): 98–106 (April 1975).

13. R. W. Swindeman and V. K. Sikka, "Characterization of the Product Forms of the Reference Heat of Type 304 Stainless Steel," *Mechanical Properties Test Data for Structural Materials Quart. Progr. Rep. July 31, 1975*, ORNL-5106, pp. 171–74.

14. V. K. Sikka, R. W. Swindeman, T. L. Hebble, and M. K. Booker, "Residual Cold Work and Its Influence on Tensile Properties of Types 304 and 316 Stainless Steel," to be presented at 1975 Winter Meeting, American Nuclear Society, San Francisco, November 1975.

15. G. V. Smith, *An Evaluation of the Yield, Tensile, Creep, and Rupture Strengths of Wrought 304, 316, 321, and 347 Stainless Steels at Elevated Temperatures, ASTM Data Ser.* DS 5 S2, American Society for Testing and Materials, Philadelphia, February 1969.

16. G. V. Smith, "The Temperature Dependence of Yield Strength and Tensile Strength of Several Austenitic Stainless Steels," pp. 79–95 in *Symposium on Elevated Temperature Properties of Austenitic Stainless Steels*, A. O. Schaefer, ed., American Society of Mechanical Engineering, New York, 1974.

17. ASTM Designation: A 240-71, "Standard Specification for Stainless and Heat-Resisting Chromium and Chromium-Nickel Steel Plate, Sheet and Strip for Fusion Welded Unfired Pressure Vessels," *Annual Book of ASTM Standards, Part 3,* American Society for Testing and Materials, Philadelphia, April 1972.

18. V. K. Sikka, "Heat-to-Heat Variation and Its Relation with Chemical Composition," *Mechanical Properties Test Data for Structural Materials Quart. Progr. Rep. April 30, 1975,* ORNL-5105, pp. 95–101.

19. *Interpretations of the ASME Boiler and Pressure Vessel Code, Code Case 1592,* American Society of Mechanical Engineers, New York, 1974.

20. M. K. Booker and V. K. Sikka, "Interrelationships Between Creep Life Criteria for Four Nuclear Structural Materials," presented at 1975 Annual Meeting, American Nuclear Society, New Orleans (June 1975); submitted for publication.

21. M. K. Booker, C. R. Brinkman, and V. K. Sikka, "Correlation and Extrapolation of Creep Ductility Data for Four Elevated-Temperature Structural Materials," to be presented at Symposium on Structural Materials for Elevated-Temperature Nuclear Power Generation Service, ASME Winter Meeting, Houston, Texas, Nov. 30–Dec. 4, 1975.

22. G. V. Smith, *Properties of Metals at Elevated Temperatures,* McGraw-Hill, New York, 1950, p. 151.

23. R. W. Swindeman, "Creep-Rupture Correlations for Type 304 Stainless Steel (Heat 9T2796)," to be presented at Symposium on Structural Materials for Elevated-Temperature Nuclear Power Generation Service, ASME Winter Meeting, Houston, Texas, Nov. 30–Dec. 4, 1975.

24. L. D. Blackburn, Hanford Engineering Development Laboratory, private communication, November 1973.

25. R. W. Swindeman and C. E. Pugh, *Creep Studies on Type 304 Stainless Steel (Heat 8043813) Under Constant and Varying Loads,* ORNL-TM-4427 (June 1974).

26. F. Garofalo, R. W. Whitmore, and F. Von Gemmingen, "Creep and Creep-Rupture Relationships in an Austenitic Stainless Steel," *Trans. Metall. Soc. AIME* 221: 310–19 (1961).

27. J. R. Barker, E. W. Ross, and J. F. Radavich, "Long Time Stability of Inconel 718," *J. Met.* 20(1): 31–41 (January 1970).

28. C. E. Korth, Aerojet Nuclear Company, private communication, January 1975.

29. M. K. Booker and V. K. Sikka, *Empirical Relationships Among Creep Properties of Four Elevated-Temperature Structural Materials*, report in preparation.

30. F. C. Monkman and N. J. Grant, "An Empirical Relationship Between Rupture Life and Minimum Creep Rate in Creep-Rupture Tests," *Proc. Am. Soc. Test. Mater.* 56: 593–605 (1956).

31. J. B. Conway, *Stress-Rupture Parameters, Origin, Calculation, and Use*, Gordon and Breach, New York, 1969.

32. R. L. Orr, O. D. Sherby, and J. E. Dorn, "Correlations of Rupture Data for Metals at Elevated Temperatures," *Trans. Am. Soc Met.* 46: 113–28 (1954).

33. W. E. Stillman, M. K. Booker, and V. K. Sikka, *An Improved Thermal Creep Equation for Type 316 Stainless Steel*, report in preparation.

34. L. D. Blackburn, *Strain-Time Relations During Creep Deformation of Austenitic Stainless Steels*, unpublished report, Hanford Engineering Development Laboratory, August 1971.

35. L. D. Blackburn, "Isochronous Stress-Strain Curves for Austenitic Stainless Steels," pp. 15–48 in *The Generation of Isochronous Stress-Strain Curves*, ed. by A. O. Schaefer, American Society of Mechanical Engineers, New York, 1972.

36. F. Garofalo. *Fundamentals of Creep and Creep-Rupture in Metals*, Macmillan, New York, 1965.

37. M. K. Booker, T. L. Hebble, D. O. Hobson, and C. R. Brinkman, "Mechanical Property Correlations for 2 1/4 Cr-1 Mo Steel in Support of Nuclear Reactor Systems Design," paper F 8/9 in *Transactions of the 3rd International Conference on Structural Mechanics in Reactor Technology* (London, UK, 1–5 Sept. 1975), Vol 2, Part F, Commission of the European Communities, Luxembourg, 1975.

38. C. E. Pugh, "Constitutive Equations for Creep Analysis of LMFBR Components," pp. 1–15 in *Advances in Design for Elevated-Temperature Environment*, American Society of Mechanical Engineers, New York, 1975.

39. T. L. Hebble, "Mechanical Property Correlation of 2 1/4 Cr-1 Mo Steel for LMFBR Steam Generators," *Mechanical Properties Test Data for Structural Materials Quart. Progr. Rep. July 31, 1975,* ORNL-5106, pp. 155–65.

40. M. K. Booker and C. O. Stevens, "Material Data Processing," *Mechanical Properties Test Data for Structural Materials Quart. Progr. Rep. Apr. 30, 1975,* ORNL-5105, pp. 164–72.

41. B.L.P. Booker, "ORFAN," unpublished computer program.

42. J. P. Hammond and M. W. Moyer, "Measurement of Elastic Constants of 2 1/4 Cr-1 Mo Steel by the Dynamic Method," *Mechanical Properties Test Data for Structural Materials Quart. Progr. Rep. Apr. 30, 1974,* ORNL-4963, pp. 126–33.

43. *Digest of Steels for High-Temperature Service,* 6th ed., data catalogue of Timken Co., Canton, Ohio, 1957.

44. F. Garofalo, P. R. Malenock, and G. V. Smith, "The Influence of Temperature on the Elastic Constants of Some Commercial Steels," pp. 10–30 in *Symposium on Delineation of Elastic Constants* (New York, June 25, 1952), *ASTM Spec. Tech. Publ.* 129, American Society for Testing and Materials, Philadelphia, 1952.

45. J. P. Hammond, "Elastic Properties of Engineering Construction Materials," *Mechanical Properties Test Data for Structural Materials Quart. Progr. Rep. July 31, 1975,* ORNL-5106, pp. 100–11.

46. B. R. Dewey and R. T. King, "Studies of Strain Distribution in Weldments and Room Temperature Elastic Constants," *Mechanical Properties Test Data for Structural Materials Quart. Progr. Rep. July 31, 1975,* ORNL-5106, pp. 112–15.

47. V. M. Zemzin and E. A. Chekhover, "The Modulus of Elasticity of Welds in Alloy Steels," *Weld. Res. Abroad* 10(6): 68–73 (1964).

48. B. Chalmers, *Physical Metallurgy,* Wiley, New York, 1962, p. 235.

49. R. T. King, J. O. Stiegler, and G. M. Goodwin, *Creep Properties of a Type 308 Stainless Steel Pressure Vessel Weld with Controlled Residual Elements,* ORNL-TM-4131 (May 1973).

50. N. C. Binkley, R. G. Berggren, and G. M. Goodwin, "Effects of Slight Compositional Variations on Type E308 Electrode Deposits," *Weld. J. (Miami)* 53(2): 91-s–95-s (February 1974).

51. J. O. Stiegler, R. T. King, and G. M. Goodwin, "Effect of Residual Elements on Fracture Characteristics and Creep Ductility of Type 308 Stainless Steel Weld Metal," *J. Eng. Mater. Technol.* 97(3): 245–50 (July 1975).

52. D. P. Edmonds and E. Bolling, *Creep-Rupture Behavior of Gas Tungsten-Arc Types 308, 316, and 16-8-2 Stainless Steel Welds Made with Special Filler Materials,* ORNL-TM-4940 (March 1975).

53. R. T. King, J. O. Stiegler, and G. M. Goodwin, "Relation Between Mechanical Properties and Microstructure in a Thick Stainless Steel Weldment," *Weld. J. (Miami)* 53(7): 307-s–313-s (July 1974).

54. M. Manjoine, "Basic Specimen Testing," *Mechanical Properties Test Data for Structural Materials Quart. Progr. Rep. July 31, 1975,* ORNL-5106, pp. 225–40.

55. R. T. King and R. E. Gehlbach, "Characterization of FFTF Vessel-Type Weldments," *Fuels and Materials Development Program Quart. Progr. Rep. Sept. 30, 1971,* ORNL-TM-3550, pp. 187–93.

56. R. T. King and G. M. Goodwin, "Tensile Properties," *Fuels and Materials Development Program Quart. Progr. Rep. Dec. 31, 1971,* ORNL-TM-3703, pp. 209–15.

57. R. T. King, R. E. Adams, and G. M. Goodwin, "Tensile Properties of FFTF Vessel Test Weldments," *Fuels and Materials Development Program Quart. Progr. Rep. Dec. 31, 1971,* ORNL-TM-3550 pp. 210–20.

58. R. T. King and E. Bolling, "Creep and Creep-Rupture Properties of Type 308 CRE Stainless Steel Weld Metal from the FFTF Vessel Test Welds," *Mechanical Properties Test Data for Structural Materials Quart. Progr. Rep. Apr. 30, 1974,* ORNL-4963, pp. 140–43.

59. D. O. Hobson and T. L. Hebble, "Statistical Analysis of Type 304 Stainless Steel Creep-Rupture Data," *Mechanical Properties Test Data for Structural Materials Quart. Progr. Rep. Oct. 31, 1973,* ORNL-4936, pp. 111–18.

60. R. T. King, E. Bolling, and B. McNabb, Jr., "Tensile Properties of Aged SMA Type 308 CRE Stainless Steel FFTF Vessel Test Welds," *Mechanical Properties Test Data for Structural Materials Quart. Progr. Rep. Oct. 31, 1973,* ORNL-4936, pp. 145–52.

61. J. O. Stiegler, R. T. King, and G. M. Goodwin, "Effect of Residual Elements on Fracture Characteristics and Creep Ductility of Type 308 Stainless Steel Weld Metal," *J. Eng. Mater. Technol.* 97(3): 245–50 (July 1975).

62. R. T. King, J. K. Alley, and E. Bolling, "Tensile Properties of FFTF Vessel Test Welds," *Fuels and Materials Development Program Quart. Progr. Rep. Mar. 31, 1973,* ORNL-TM-4250, pp. 139–51.

63. R. T. King, N. C. Cole, R. G. Berggren, and G. M. Goodwin, "Properties and Structure of 16-8-2 Stainless Steel Weld Metal," American Society of Mechanical Engineers Paper 75-PVP-45, presented at Second National Congress on Pressure Vessels and Piping, San Francisco, Calif., June 23–27, 1975. Available through ASME, New York, until March 1, 1976.

64. R. T. King, G. M. Goodwin, and E. Bolling, "Creep-Rupture Properties of GTA Type 16-8-2 Welds," *Fuels and Materials Development Program Quart. Progr. Rep. Sept. 30, 1974,* ORNL-TM-4726, pp. 184–87.

65. D. P. Edmonds and E. Bolling, "Creep-Rupture Behavior of Gas Tungsten-Arc Types 308, 316, and 16-8-2 Stainless Steel Welds Made with Special Filler Metals," *Fuels and Materials Development Program Quart. Progr. Rep. Mar. 31, 1975,* ORNL-TM-4940, pp. 220–28.

66. R. T. King and E. Bolling, "Creep of Type 308 CRE Stainless Steel Welds in the Transverse-to-the-Weld Direction at 593°C," *Fuels and Materials Development Program Quart. Progr. Rep. Dec. 31, 1974,* ORNL-TM-4878, pp. 150–55.

67. R. L. Klueh, "Heat-to-Heat Variations of 2 1/4 Cr-1 Mo Steel," *Mechanical Properties Test Data for Structural Materials Quart. Progr. Rep. July 31, 1975,* ORNL-5106, pp. 131–44.

68. G. V. Smith, *Supplemental Report on the Elevated-Temperature Properties of Chromium-Molybdenum Steels (An Evaluation of 2 1/4 Cr-1 Mo Steel), ASTM Data Ser.* DS 6 S2, American Society for Testing and Materials, Philadelphia, March 1971.

69. S. S. Manson, G. R. Halford, and M. H. Hirschberb, *Creep-Fatigue Analysis by Strain-Range Partitioning,* NASA-TM-X-67838 (1971).

70. M. K. Booker, "Creep-Fatigue Data Analysis," *Mechanical Properties Test Data for Structural Materials Quart. Progr. Rep. Aprl 30, 1975*, ORNL-5105, pp. 215–21.

71. J. R. Ellis et al., "Elevated Temperature Fatigue and Creep-Fatigue Properties of 2 1/4 Cr-1 Mo Steel in Solution Annealed and Isothermally Annealed Conditions," to be presented at Symposium on Structural Materials for Elevated-Temperature Nuclear Power Generation Service, ASME Winter Meeting, Houston, Texas, Nov. 30–Dec. 4, 1975.

72. C. E. Pugh, K. C. Liu, J. M. Corum, and W. L. Greenstreet, *Currently Recommended Constitutive Equations for Inelastic Design Analysis of FFTF Components*, ORNL-TM-3602 (September 1972).

73. J. M. Corum, C. E. Pugh, K. C. Liu, and D. N. Robinson, "Constitutive Equation Recommendations for 2 1/4 Cr-1 Mo Steel," (proposed additional section in Chapter 4 of RDT Standard F9-5T), *High-Temperature Structural Design Program Progr. Rep. Dec. 31, 1974*, ORNL-5048, pp. 36–50.

74. C. R. Brinkman, M. K. Booker, J. P. Strizak, and W. R. Corwin, "Elevated Temperature Fatigue Behavior of 2 1/4 Cr-1 Mo Steel," presented at Second National Congress on Pressure Vessels and Piping, San Francisco, California, June 23–27, 1975. To be published in *Journal of Pressure Vessel Technology*.

75. C. E. Jaske and B. N. Leis, *Final Report on Cyclic Stress-Strain of 2 1/4 Cr-1 Mo Steel*, Battelle Columbus Laboratories report ORNL-SUB-4004-1 (October 1974).

76. J. M. Corum, "Materials Properties for Inelastic Structural Analyses," *High-Temperature Structural Design Methods for LMFBR Components Quart. Progr. Rep. Mar. 31, 1974*, ORNL-4977, October 1974, pp. 136–42.

77. C. C. Schultz, "Investigations of Creep Failure Under Uniaxial and Multiaxial Conditions," *High-Temperature Structural Design Program Progr. Rep. Dec. 1974*, ORNL-5048, pp. 117–39.

78. C. C. Schultz, "Investigations of Creep Failure Under Uniaxial and Multiaxial Conditions," *High-Temperature Structural Design Methods for LMFBR Components Quart. Progr. Rep. June 30, 1974*, ORNL-5005, pp. 52–81.

79. C. C. Schultz, "Investigations of Creep Failure Under Uniaxial and Multiaxial Conditions," *High-Temperature Structural Design Methods for LMFBR Components Quart. Progr. Rep. Mar. 31, 1974*, ORNL-4977, pp. 79–94.

80. W. R. Corwin, "Subcritical Crack Growth of 2 1/4 Cr-1 Mo Steel," *Mechanical Properties Test Data for Structural Materials Quart. Progr. Rep. July 31, 1975*, ORNL-5106, pp. 147–57.

4. NAVAL RESEARCH LABORATORY

(Contribution not received in time for inclusion in this issue.)

5. HANFORD ENGINEERING DEVELOPMENT LABORATORY

T. T. Claudson

5.1 INTRODUCTION

The objectives of the structural materials investigation conducted at the Hanford Engineering Development Laboratory are to provide control data for the in-reactor and postirradiation tests and to provide direct and timely assistance to FFTF and Demonstration plant structural design and analysis programs. The HEDL efforts involve evaluation of mechanical properties in the areas of normal and high strain rate tensile testing, creep testing and analysis, and fatigue crack growth and fracture toughness of such materials as weldments, vessel and piping, core support structures and reflectors as well as duct and cladding. Those test results and analyses appropriate to the "Structural Materials Quarterly Report" will be reported herein; however those investigations associated with irradiation effects per se will continue to be reported in the "Irradiation Damage to Reactor Structural Materials" Semi-Annual Report published at HEDL.

5.2 MATERIALS INFORMATION DOCUMENTATION, FATIGUE AND FRACTURE - R. L. Knecht, J. E. Irvin, L. A. James, R. A. Moen, M. F. Marchbanks

5.2.1 Objectives

The objectives of this program are: (1) to provide crack propagation and fracture toughness data on LMFBR component structural materials and to perform fatigue and fracture analyses; and (2) to manage, coordinate and distribute the Nuclear Systems Materials Handbook as a standard materials property reference for the nuclear community.

5.2.2 Significant Accomplishments

5.2.2.1 A comprehensive document entitled "Fatigue Crack Propagation Behavior of Inconel 718", HEDL-TME 75-80 by L. A. James has been completed and is in publication. The summary and conclusions of that report are given below and some of the recent crack propagation data of Inconel 718 welds and

base metal given a conventional heat treatment and that given the ANC developed heat treatment are shown in Figures 5.1-5.5. Heat treatments referred to in the Figures are given in Table 5.1.

- When Inconel 718 is fatigue tested in an air environment, the fatigue-crack growth rate increases with increasing test temperature.
- When Inconel 718 is fatigue tested in an air environment at elevated temperatures, the fatigue-crack growth rate increases with decreasing cyclic frequency.
- At a given value of ΔK, the fatigue-crack growth rate increases with increasing values of the stress ratio R. However, the "effective" stress intensity factor can be used to normalize the effect of stress ratio.
- Limited data indicate that the fatigue-crack growth rate in a sodium environment at 800°F (427°C) is approximately an order of magnitude lower than in air under similar conditions.
- The "modified" heat-treatment developed by Aerojet Nuclear Company produces improvements in crack growth behavior (i.e. lower crack growth rates) relative to the "conventional" treatment ranging from slight to significant at test temperatures below the final aging temperature 1150°F (621°C), and essentially the same behavior above that temperature. This is the case for both base metal specimens and weldment specimens.
- Weldment specimens given the "conventional" heat-treatment exhibited higher crack growth rates and lower apparent ductility than did specimens receiving the "modified" treatment. Since the latter treatment effectively removed most of the Laves phase, it is assumed that the Laves phase was responsible for the inferior performance of the "conventionally" treated weldments.

5.2.2.2 A document entitled "The Effect of Temperature on the Fatigue-Crack Propagation Behavior of A-286 Steel", HEDL-TME 75-82 by L. A. James, is being issued. No significant differences in crack growth behavior were noted between product forms (1/2" strip and 1-1/2" diameter bar) nor

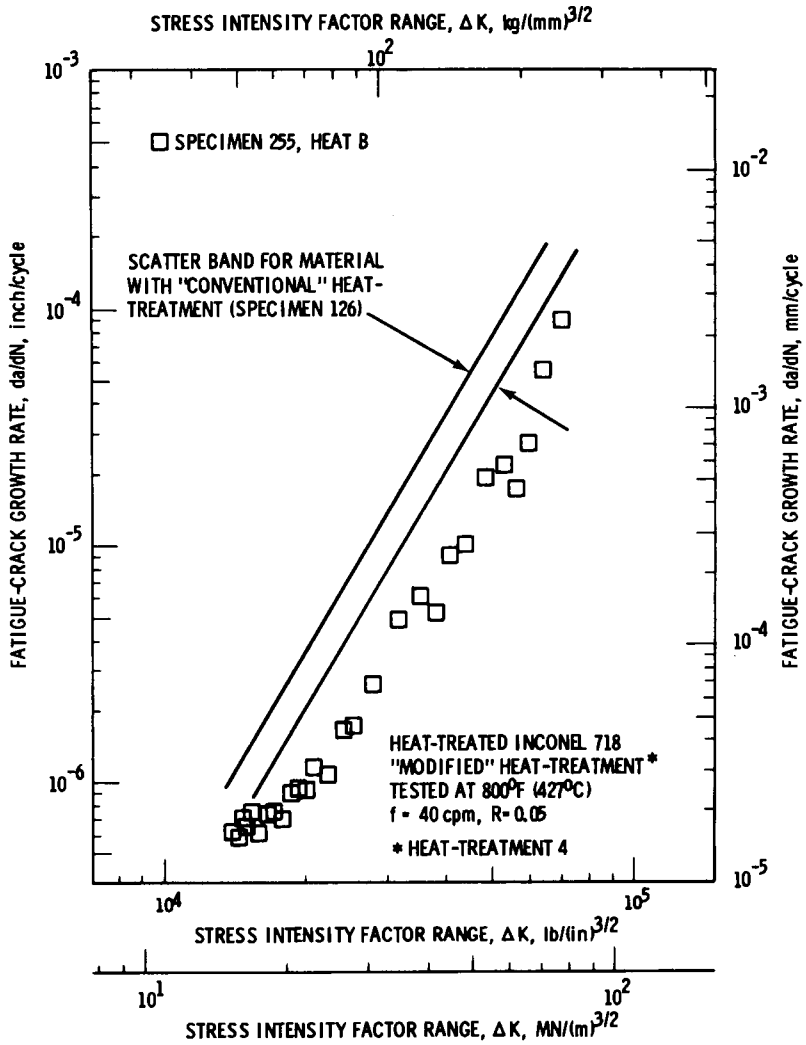

Figure 5.1. Comparison of Crack Growth Behavior at 800°F in Inconel 718 Receiving the "Conventional" and "Modified" (Aerojet Nuclear Co.) Heat-Treatments.

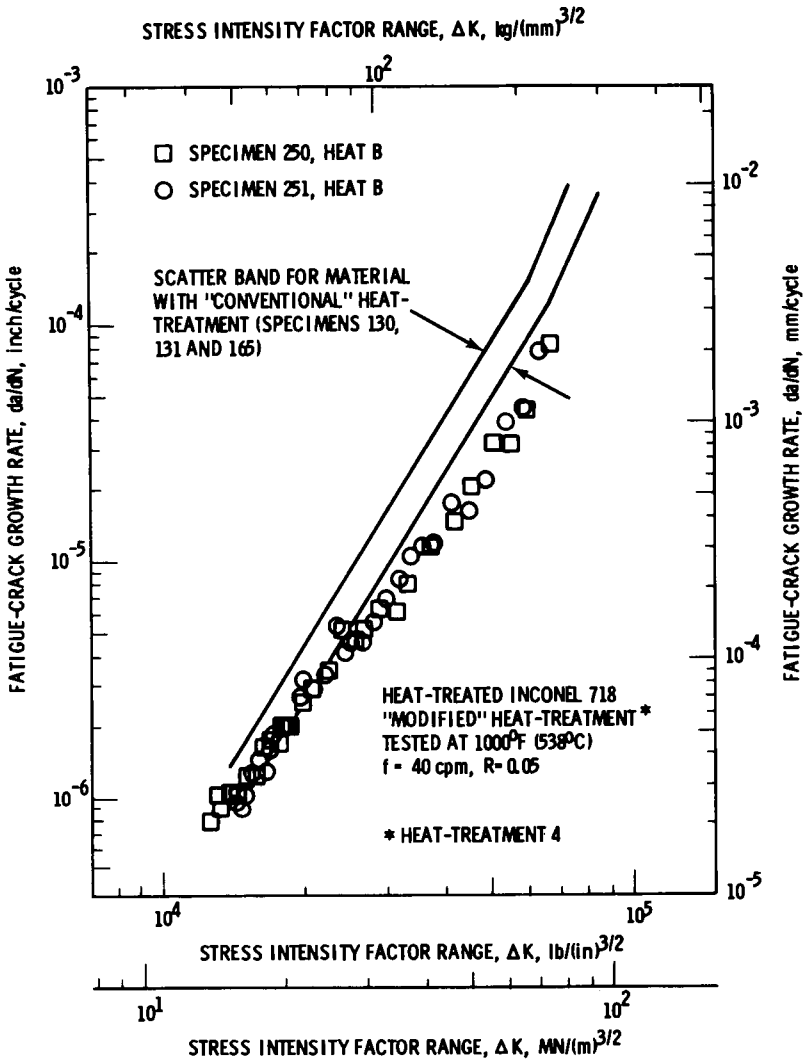

Figure 5.2. Comparison of Crack Growth Behavior at 1000°F in Inconel 718 Receiving the "Conventional" and "Modified" (Aerojet Nuclear Co.) Heat-Treatments.

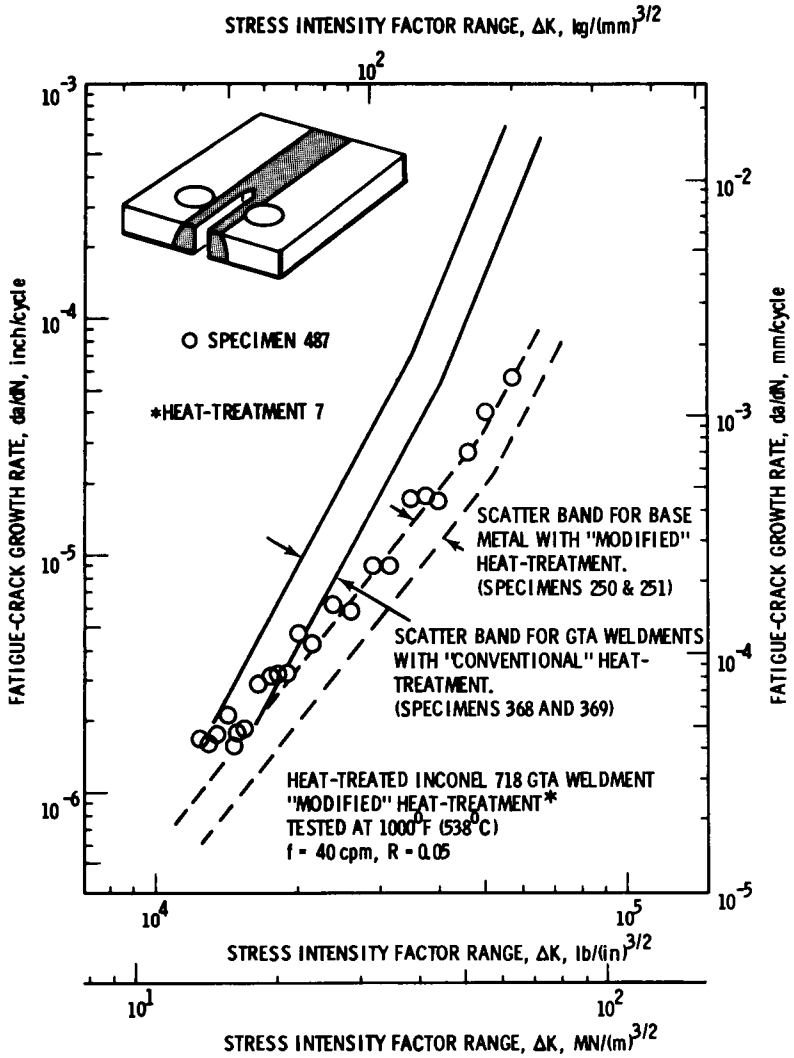

Figure 5.3. Crack Growth Behavior of Inconel 718 Weldments at 1000°F.

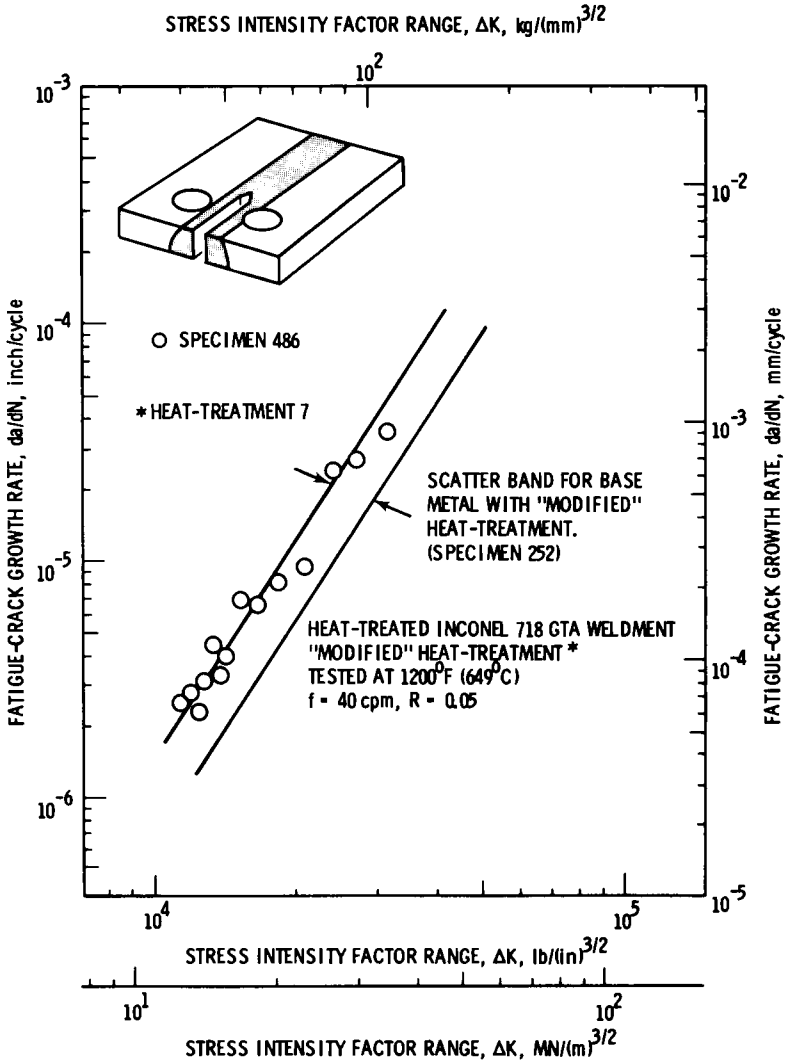

Figure 5.4. Crack Growth Behavior of Inconel 718 Weldments at 1200°F.

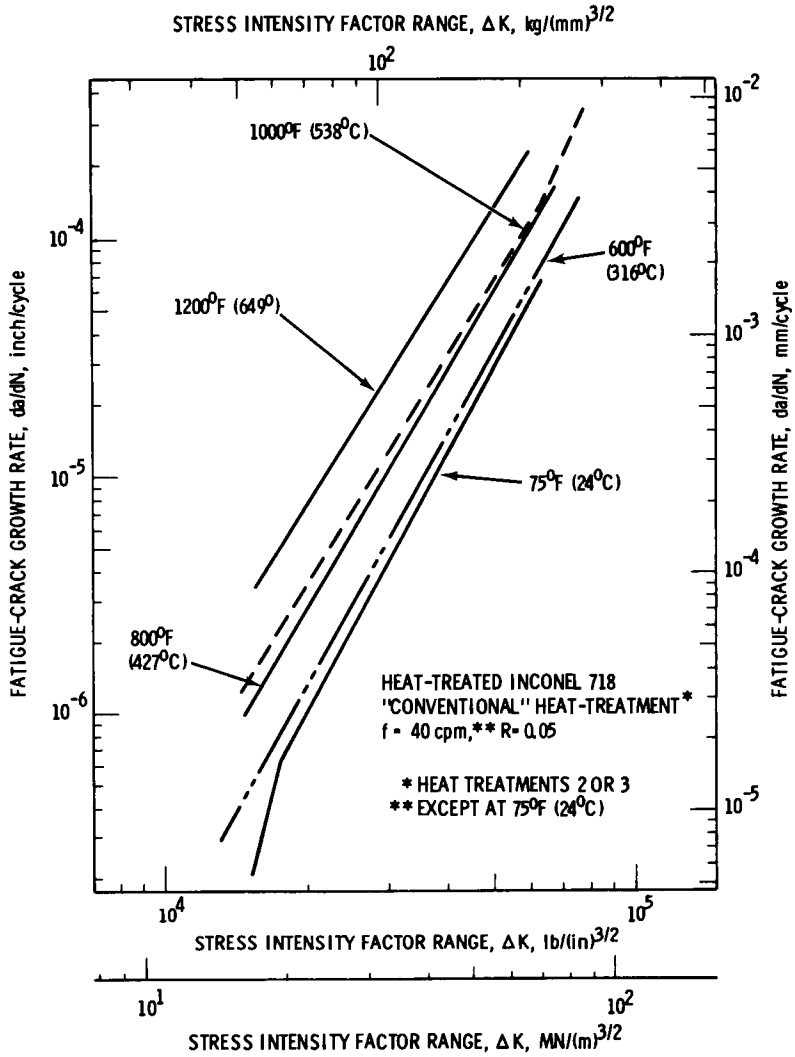

Figure 5.5. The Effect of Tenperature Upon the Crack Growth Behavior of Inconel 718 Tested in Air Environments.

between different crack orientations. The effect of temperature on the crack growth of A-286 is shown in Figure 5.6.

5.2.2.3 The Fourth meeting of the Nuclear Systems Materials Handbook Advisory Group was held at General Electric, Sunnyvale, California on October 9-10, 1975. The highlight of the meeting was the adoption of a large matrix of requirements to form the basis of most Working Group efforts over the next 18-24 months. The matrix contains approximately 2500 materials data requirements with priorities and need dates. The meeting minutes have been prepared and distributed and a summary of the requirements matrix is being prepared for issuance.

5.2.2.4 Approximately 700 data pages are now being processed in the Nuclear Systems Materials Handbook activity. Over 200 pages have been approved for publication by the NSMH Advisory Group and are scheduled for printing in November, 1975.

Table 5.1. Heat Treatments

Treatment No.	
2	Solution annealed at 1950°F, air cooled to room temperature. Aged 8 hours at 1325°F, furnace cooled to 1150°F and held at 1150°F for a total aging time of 18 hours, air cooled to room temperature.
3	"Conventional heat treatment". Annealed at 1750°F, air cooled to room temperature. Aged 8 hours at 1325°F, furnace cooled to 1150°F and held at 1150°F for a total aging time of 18 hours, air cooled to room temperature.
4	Solution annealed 1 hour at 2000°F, cooled to 1325°F at 100°F/hour, aged 4 hours at 1325°F, cooled to 1150°F at 100°F/hour, aged 16 hours at 1150°F, air cooled to room temperature.
7	Mill annealed. GTA welded. After welding given heat treatment No. 4.

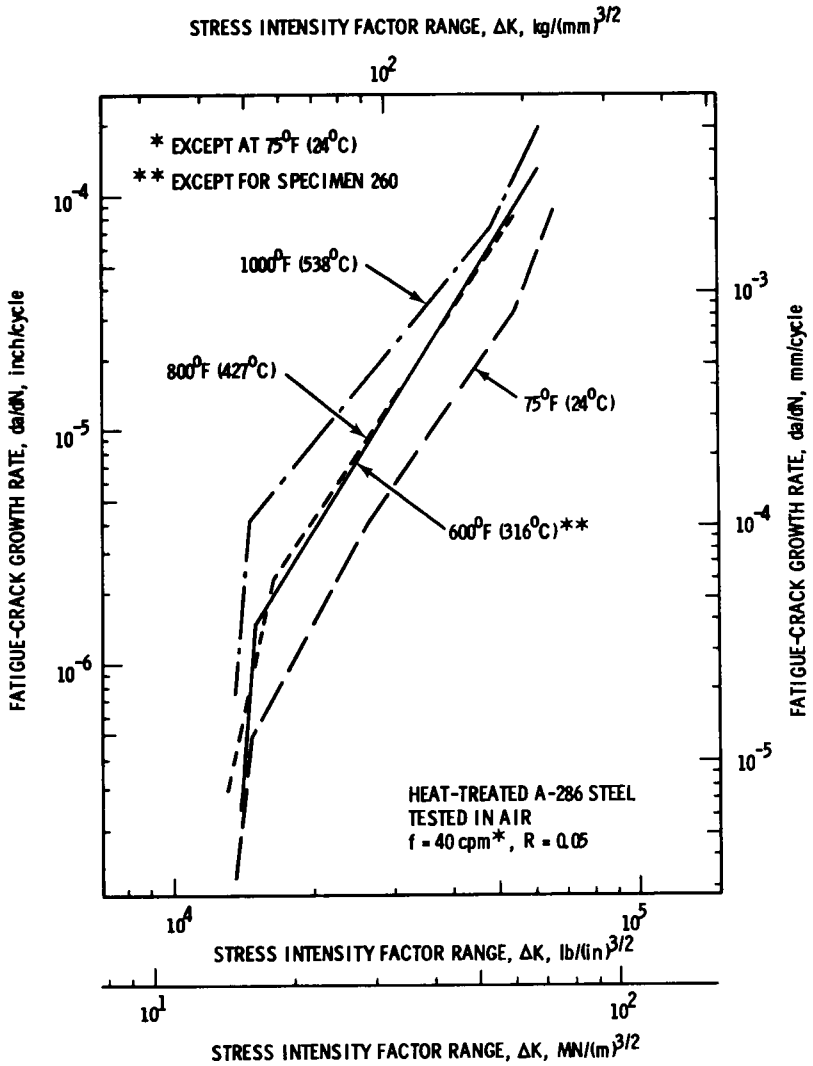

Figure 5.6. Effect of Temperature Upon the Crack Growth Behavior of A-286 Steel Tested in an Air Environment.

6. WESTINGHOUSE ADVANCED REACTORS DIVISION

E. C. Bishop, W. E. Ray

6.1 INTRODUCTION

Two programs are being performed at Westinghouse Advanced Reactors Division (ARD). The first program is "Validation of High Temperature Design Methods and Criteria" (189a CW063). Two of the tasks in this program are "Basic Specimen Testing" and "Tubular Specimen Testing." The specimen material for both tasks was supplied from the ORNL reference heat of Type 304 stainless steel and future tests will include specimens from the reference heat of Type 316 stainless steel. The second program is Component Materials Compatibility" (189a CW065). One of the tasks in this program is "Mechanical Properties."

The basic specimen tests are performed on plates and bars loaded at 1100°F (593°C). Specimen designs have been selected to provide nonuniform stress distributions (uniaxial, plane stress, and plane strain) and to determine the effects of holes, notches, and welds in various orientations. Uniform and stepped loading is applied at levels sufficient to cause significant creep strain in hundreds of hours and rupture in several thousand hours. Test data are used for: verification of constitutive equations for time-dependent material response, validation of analytical techniques for nonuniform stress states, and investigation of strain limits in base metal, welds, and at geometrical discontinuities.

The tubular specimen tests are being run at 1100°F (593°C) with various combinations of internal pressure and axial load to produce a uniform stress state with a range of biaxiality. Load levels have been selected to determine secondary creep rates in 2000 hours with both steady state and stepped loading. A limited number of tests will be continued to rupture with geometrical discontinuities. The test data are primarily used for verification of constitutive equations and validation of analytical techniques for shells under multiaxial states of stress.

Westinghouse ARD is performing experiments to identify the effects of a flowing sodium environment on the mechanical properties of LMFBR

structural components. The present scope of the program involves three materials: Type 316 stainless steel, Type 304 stainless steel, and Inconel 718. Work on these materials is in support of the CRBRP upper plenum and hot leg piping components design. Inconel 718 is also being evaluated on a limited basis, relative to the thermal transients to be experienced by the thermal baffles in the upper plenum of the FFTF reactor. More extensive evaluations of the material for the CRBRP will follow. Low-cycle fatigue, creep-fatigue, and creep-rupture experiments are being performed in flowing sodium at elevated temperatures on as-fabricated, aged, and sodium pre-exposed samples in order to identify the environmental effects. In addition, in-air experiments are being performed on the same materials to obtain baseline data.

The present report describes the results obtained to date on (1) the low-cycle fatigue of solution-annealed Type 316 stainless steel at 1100°F in flowing sodium and (2) the low-cycle fatigue of Inconel 718 at 1000°F in air. Progress on the sodium pre-exposure and vacuum aging of additional mechanical property samples is also presented.

This report covers the work performed during the period from August 1 to October 31, 1975.

6.2 BASIC SPECIMEN TESTING - M. J. Manjoine (Westinghouse Research Laboratories)

The specimen designs selected for this task are shown in Table 6.1 and Figure 6.1. Data obtained to date are presented in Table 6.2.

6.2.1 Plate Specimens Under Tension and Bending - Type E

The second test, E-2, at an average stress of 18 ksi has completed 6652 hours (see Figure 6.2). The specimen has been load cycled six times to facilitate an estimate of the retained bending strain. Since the bending stress is introduced by an eccentric load this stress will diminish with permanent strain. The creep rates will, therefore, decrease with strain, and the average creep rate will approach that of the axially loaded model B, Figure 6.3. The current average creep rate is 3.3 x 10^{-4}%h and the average overall creep strain on the peak stress side is 6 percent, Table 6.2.

TABLE 6.1

MODEL TYPES

Specimens From Base Material[a]

Code Designation	Description[b]
A.	Plane Stress Specimen 1/3 x 2/3 x 3 in. (8.5 x 17 x 76.2 mm) gage section.
B.	Plate Specimen 1/3 x 10/3 x 3 in. (8.5 x 85 x 76.2 mm) gage section.
C.	Plate Specimen with Central Hole of 1/3 in. (8.5 mm) Diameter 1/3 x 10/3 x 3 in. (8.5 x 85 x 76.2 mm) plate section.
D.	Round Circumferentially Notched Specimen Major Diameter = 0.96 in. (24.4 mm), Minor Diameter = 0.64 in. (16.2 mm), K_t = 4, Root Radius = 0.018 in. (0.46 mm), two nearly indentical notches in specimen.
E.	Plate Specimen in Bending and Tension 1/3 x 10/3 x 2 in. (8.5 x 85 x 50.8 mm) plates section, eccentric load
F.	Designation generally refers to failure or fracture; therefore, it is not used to identify a type of model.
G.	Plane Strain Specimen 1/3 x 10/3 x 1 in. (8.5 x 85 x 25.4 mm) gage section. Ends constrained in transverse direction.

Specimen With Welds

BTW - B-type plate specimen with transverse weld at mid-length of gage section.

BAW - B-type plate specimen with axial weld at center of gage section.

CTW - C-type specimen with hole through transverse weld.

CAW - C-type specimen with hole through axial weld.

DTW - D-type specimen with notch root in transverse weld.

DZTW - D-type specimen with notch root at weld fusion line of heat affected zone.

GTW - G-type specimen with transverse weld at mid-gage length.

GAW - G-type specimen with axial weld at center of gage section.

(a) Type 304 stainless steel (HT9T2796) annealed at 2000°F.

(b) Reference Figure 6-1.

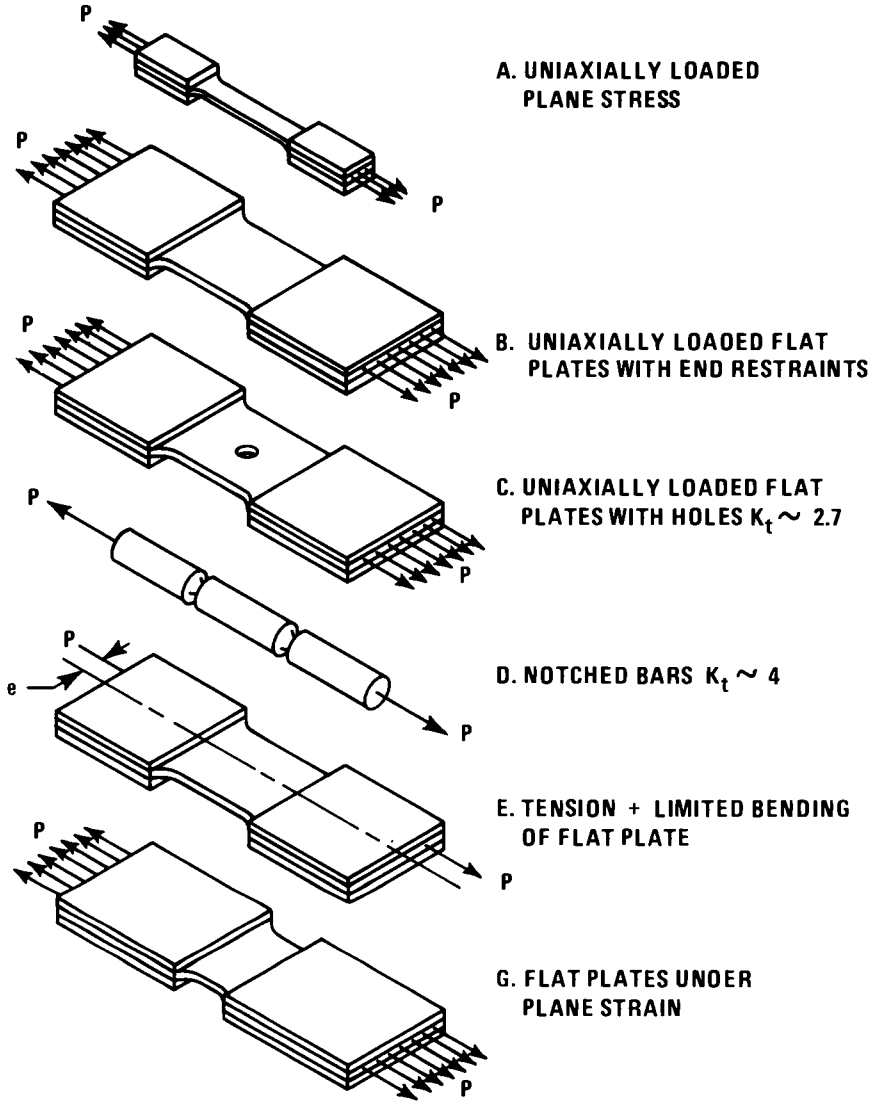

Figure 6.1. Basic Specimen Types

8043-17

TABLE 6.2

SUMMARY OF CREEP DATA FOR MODELS OF TYPE 304 STAINLESS STEEL* AT 1100°F (593°C)

Loading Data			Creep Data					
				Increment		Accumulated		
Stress (ksi)	(MPa)	Plastic Strain (%)	Creep Rate (% hr)	Strain (%)	Time (hr)	Strain (%)	Time (hr)	Permanent Strain (%)
A1, GAGE SECTION 1/3 x 2/3 x 3 in. (8.5 x 17 x 76.2 mm)								
21.0	144.8	4.66	2.2×10^{-3}	1.10	303	1.10	303[a]	5.76
			2.2×10^{-3}	0.89	403	1.99	706[a]	6.65
						3.47	1250[b]	8.13
						3.65	1270[c]	8.31
						7.34	1826[d]	12.0
A2 (STEP-LOADED TEST)								
10.0	69.95	0.215	8.5×10^{-5}	0.228	2180	0.228	2180[a]	0.443
			6.2×10^{-5}	0.028	405	0.256	2585[e]	0.471
11.0	75.84	0	8.6×10^{-5}	0.124	1349	0.380	3934[e]	0.595
12.5	86.19	0	2.0×10^{-4}	0.213	1002	0.593	4936[e]	0.808
15.0	103.4	0.014	2.5×10^{-4}	0.811	1848	1.40[a]	6784[e]	1.619
21.0	144.8	0.646	4.5×10^{-3}	14.80	2800	16.20	9584	17.07
				1.05[b]	200	17.25	9784	18.12
				12.90	1266[h]	30.15	11050	31.02
						--	4266[m]	--
B1, GAGE SECTION, 1/3 x 10/3 x 3 in. (8.5 x 85 x 76.2 mm)								
21.0	144.8	5.34	1.4×10^{-3}	1.76	666	1.76	666[a]	7.10
			7.6×10^{-4}	1.03	1005	2.79	1671[a]	8.13
			1.7×10^{-3}	--	--	--	3000[c]	--
				1.72	1587	4.51	3258[a]	9.85[g]
						5.33	3487	--
						--	3525[h]	--
B2 (STEP-LOADED TEST)								
10.0	68.95	0.273[i]	8.6×10^{-5}	0.31	1044	0.31	1644[a]	0.58
j			9.0×10^{-5}	0.17	1462	0.45	3106[e]	0.72
11.0	75.84	0	1.1×10^{-4}	0.16	1804	0.61	4910[e]	0.88
12.5	86.19	0	2.0×10^{-4}	0.33	1364	0.94	6274[e]	1.21
15.0	103.4	0.051	4.7×10^{-4}	1.00	1302[a]	1.93	7576[e]	1.98
21.0	144.8	1.880	8.4×10^{-3}	7.50	720	9.43	8296	11.64
				5.28[b]	604	14.71	8900	16.92
				3.69[h]	239	18.40	9139	20.61
				--	--	--	1563[m]	--

Loading Data			Creep Data					
				Increment		Accumulated		
Stress (ksi)	(MPa)	Plastic Strain (%)	Creep Rate (%/hr)	Strain (%)	Time (hr)	Strain (%)	Time (hr)	Permanent Strain (%)
G1, GAGE SECTION, 1/3 x 10/3 x 1 in. (8.5 x 85 x 25.4 mm)								
25.0	172.4	4.25	1.8×10^{-2}	2.1	47[a]	2.1	47	6.35
			7.2×10^{-3}	2.8	268[a]	4.9	315	9.1
			1.4×10^{-2}	--	--	6.5	420[c]	10.7
				--	170[a]	7.6	485[g]	11.8
				--	83	11.6	568[h]	--
G1, DATA FROM WELDABLE STRAIN GAGES (Middle, 5/8 in. Gage Section)								
25.0	172.4	2.00	2.6×10^{-2}	0.88	47[a]	0.88	47	2.47
			2.5×10^{-3}	1.12	268[a]	2.00	315	4.00
			7×10^{-3}	0.90	170[a]	2.90[c]	485[g]	4.90
			--	0.65	83	3.55	568[h]	5.60
G2 (STEP-LOADED TEST)								
21.0	144.8	0.43	3.9×10^{-4}	1.34	1195[a]	1.34	1195	1.77
			1×10^{-4}	0.83	5520[a]	2.17	6715[e]	2.60
25.0	172.4	0.01	2.3×10^{-3}	1.80	700	3.97	7415	4.41
			4.6×10^{-3}	2.50	450[c]	4.67	7865	6.90
				4.43	283[a]	6.60	8148	11.33
				--	404	--	8552[d]	--
							1837[m]	
C1, 1/3 x 10/3 x 3 in. (8.5 x 85 x 76.2 mm), CENTRAL HOLE, 1/3 in. (8.5 mm) Dia.								
23.3[k]	160.6	8[n]	1.2×10^{-2n}	1.7[n]	100	1.7[n]	100	8.7[n]
						2.0	125[c]	10.0
							138[d]	
C2, 1/3 x 10/3 x 3 in. (8.5 x 85 x 76.2 mm), CENTRAL HOLE, 1/3 in. (8.5 mm) Dia.								
10.0[k]	68.95	0.14[n]		0.62[n]	2808[a]	0.62	2808[e]	0.76[n]
11.0	75.84	0		0.40	1290	1.02	4098[e]	1.16
12.5	85.68	0		0.50	1300[a]	1.52	5398[e]	1.66
15.0	103.4	0.28		0.82	1148	2.34	6546[e]	2.76
18.0	124.1	0.06		3.31	1630[a]	5.65	8176	6.13
			1.1×10^{-3n}	0.89	791[a]	6.54	8967	7.02
			1.1×10^{-3n}	1.05	944[a]	7.59	9911	8.07
			9.3×10^{-4n}	1.25	1345[a]	8.84	11256	9.32
			2.2×10^{-3n}	1.54	942[c]	10.38	12198	10.86
				5.0	520	15.4	12718[d]	15.9
							6172[m]	
C3, 1/3 x 10/3 x 3 in. (8.5 x 85 x 76.2 mm), CENTRAL HOLE, 1/3 in. (8.5 mm) Dia.								
21.0[k]	144.8	4.4[n]	2.3×10^{-3n}	1.5[n]	310	1.5[n]	310[g]	5.9[n]
				0.3	28	1.8	338[c]	
				2.3	59	4.1	397[h]	8.5

Loading Data			Creep Data					
				Increment		Accumulated		
Stress (ksi)	Stress (MPa)	Plastic Strain (%)	Creep Rate (%/hr)	Strain (%)	Time (hr)	Strain (%)	Time (hr)	Permanent Strain (%)
D1-1, NOTCHED BAR D = 0.96 in. (24.4 mm) Dia., d = 0.64 in. (16.2 mm) Dia., r = 0.19 in. (0.46 mm)								
30.0	206.8	2.6[t]		0.3[t]	137	0.3[t]	137	2.9[t]
				0.2	102	0.5	239[g]	3.1[u]
D1-2								
30.0	206.8	2.2[t]		0.26[t]	137	0.26[t]	137	2.46[t]
				0.22	113	0.48	250[c]	2.68
						10.92	305[d]	13.12
D2-1 NOTCHED BAR								
25.0	172.4	0.009[r]				0.006[r]	1371[g]	0.15[r]
							1371	2.17[t]
D2-2								
25.0	172.4	0.009[r]				0.006[r]	1240[c]	
							1371[d]	5.3[t]
D3-1 and 2 NOTCHED BAR								
21.0	144.8	0.002[r]					5499[h]	1.52[t]
D4-1 and 2 NOTCHED BAR								
10.0	68.95	0			406		406[e]	
11.0	75.84				477		883[e]	
12.5	85.68				434		1317[e]	
15.0	103.4				404		1721[e]	
21.0	144.8	0.001[r]		0.004[r]	433		2154[e]	
25.0	172.4	0.003[r]		0.033[r]	1581[g]		3735[u]	1.73[t]
D4-2[u]								
25.0	172.4			0.93[t]	1323		5058	2.66
							2904[m]	
D5-1 NOTCHED BAR								
23.0	158.4				1681[g]		1681[u]	1.8[t]
D5-2[u]								
23.0	158.4				1681		1681	1.69[t]
					150		1831[d]	2.83
D6-1 NOTCHED BAR								
20.0	137.9			1.0[t]	4023[g]	1.0[t]	4023[g]	1.0[t]
D6-2								
20.0	137.9			0.94[t]	4023	0.94[t]	4023[u]	0.94[t]
					5979	0.007r	10002[x]	
							13197[x]	
							136504[f]	

Loading Data			Creep Data					
		Plastic	Creep	Increment		Accumulated		Permanent
Stress		Strain	Rate	Strain	Time	Strain	Time	Strain
(ksi)	(MPa)	(%)	(%/hr)	(%)	(hr)	(%)	(hr)	(%)
E1, TENSION PLUS BENDING, 1/3 x 10/3 x 2 in. (8.5 x 85 x 50.8 mm)								
20.0	137.9	8.17[nv]	1.2×10^{-2}	1.1[nv]	94	1.1[nv]	94[a]	8.27[nv]
±13.0[w]	± 89.64		3.5×10^{-3}	2.27	648	3.27	742[s]	11.54
				0.63	167	4.0	909[s]	12.17
				0.58	168	4.58	1077[s]	12.75
				0.57	168	5.15	1245[s]	13.32
				0.46	115	5.16	1360[a]	13.18
				0.79	262	6.40	1622[s]	14.51
			3.0×10^{-3}	0.58	190	6.98	1812[s]	15.15
				0.65	215	7.63	2027[s]	15.80
				0.90	263	8.53	2290[s]	16.70
			2.6×10^{-3}	0.49	190	9.02	2481[s]	17.19
				0.52	171	9.54	2652[s]	17.71
				0.77	237	10.31	2889[s]	18.48
				1.81	238	12.12	3127[h]	20.29
E2, TENSION PLUS BENDING								
18.0	124.1	6.25[nv]		0.47[nv]	23	0.47[nv]	23[s]	6.72[nv]
±11.7[w]	±80.7		1.9×10^{-3}	2.57	1317	3.04	1340[a]	9.29
			8.3×10^{-4}	1.51	1818	4.55	3158[a]	10.8
			4.2×10^{-4}	0.64	1515	5.19	4673[s]	11.44
			4.3×10^{-4}	0.64	1481	5.83	6154[s]	12.08
			3.3×10^{-4}	0.14	443	5.98	6587[a]	12.23
							6652[f]	
BAW-1, B-TYPE WITH CENTRAL AXIAL WELD								
25.0	172.4	0.25[n]	8.3×10^{-3}	4.35[n]	477[a]	4.35	477	4.60[g]
			1.1×10^{-2}	8.32	765	12.67	1242	12.92
			1.5×10^{-2}	3.42	216	16.09	1458	16.34
				2.35	71	18.44	1529	18.69
							1532[d]	
CAW-1, C-TYPE WITH CENTRAL AXIAL WELD								
18.0[k]	124.1	0.033[n]	3×10^{-5}	0.95[n]	7319[a]	0.95[n]	7319[g]	0.98[n]
		0.007		0.23	2955[a]	1.18	10,274	1.22
							10,750[f]	
DTW-1, D-TYPE NOTCH AT CENTER OF TRANSVERSE WELD								
29.0	200			0.005[r]	2779[f]			
DTW-2								
25.0	172.4			0.003[r]	5183		5183[e]	0.16[t]
28.0	193.0				5505		10,688	0.38[t]
							5505[m]	
DZTW-1 CIRCUMFERENTIAL NOTCH AT HAZ								
25.0	172.4						978[d]	0.39[t]
DZTW-2								
22.0	151.7						903[d]	

Loading Data			Creep Data					
				Increment		Accumulated		
Stress (ksi)	Stress (MPa)	Plastic Strain (%)	Creep Rate (%/hr)	Strain (%)	Time (hr)	Strain (%)	Time (hr)	Permanent Strain (%)
GAW-1, G-TYPE WITH CENTRAL AXIAL WELD								
23.0	158.6	0.1[n]	5.1×10^{-3}	1.56[n]	188	1.56[n]	188	1.65[n]
			4.2×10^{-3}	1.93	452[a]	3.59	640	3.69[n]
			5.3×10^{-3}	1.64	307[a]	5.13	947	5.23
			5.3×10^{-3}	2.0	379[a]	7.13	1326[g]	7.23
				2.21	456[a]	9.34	1782	9.44
				3.17	576[a]	12.54	2758	12.62
				4.69	528[a]	17.21	2886	17.31
				8.20	210	25.41	3096[d]	25.51
BTW-1, B-TYPE, CENTRAL TRANSVERSE WELD								
21.0	144.8	0.17[n]	3.2×10^{-3}	1.29[n]	339[a]	1.29[n]	339	2.47[n]
			3.2×10^{-3}	2.35	718[a]	3.64	1057[g]	3.82
				1.25	474[a]	4.89	1531	5.07
						5.67	1724	
							1734[d]	
BTW-2								
19.0	131.0	0.08[n]	2×10^{-4}	0.92[n]	2783[f]			
GTW-1, G-TYPE, CENTRAL TRANSVERSE WELD								
25.0	172.4	0.09[n]	4.7×10^{-3}	1.62[n]	240[a]	1.62[n]	240	1.71[n]
					208		448[d]	

*HT9T2796, annealed 2000°F (1094°C)

[a]Interrupted for photographic measurement

[b]Transition at 0.2% offset

[c]Transition at double minimum rate

[d]Rupture, R

[e]Stress raised (step-loaded test)

[f]Test in progress

[g]Crack initiated

[h]Test terminated, crack tearing

[i]Strain gage average, bending noted

[j]Specimen rotated 180° to investigate bending

[k]Net section stress

[m]Time at final stress

[n]Average overall strain

[p]Test in preparation

[q]Specimen to be sectioned to determine damage.

[r]Deflection of notch, inches (25.4 mm)

[s]Unloaded and reloaded to determine damage

[t]True strain = $1_n(Ao/A)$

[u]Test interrupted, 1/2 of specimen continued

[v]Peak stress side

[w]Nominal elastic bending stress

[x]Test interrupted for inspection

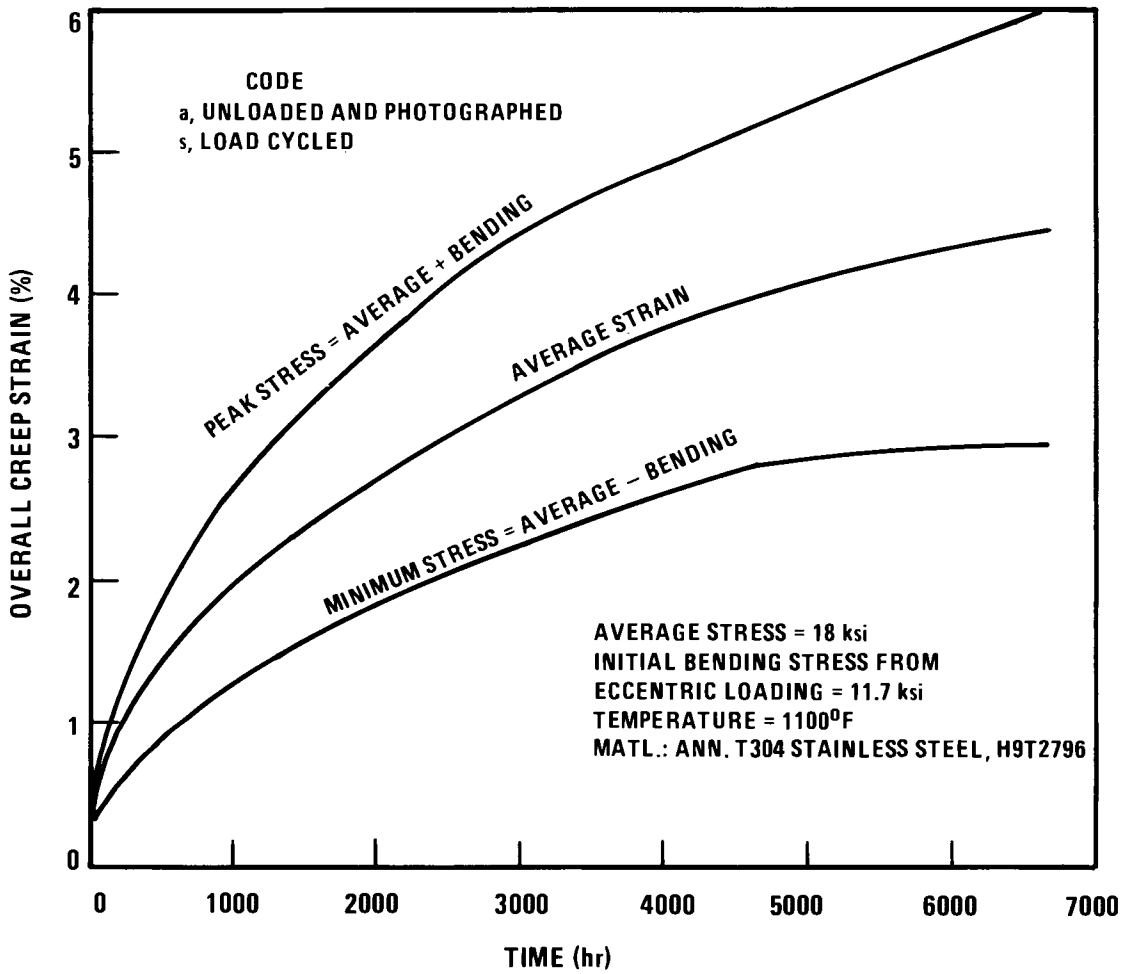

Figure 6.2. Creep Curves For Model E-2 With Tension And Bending

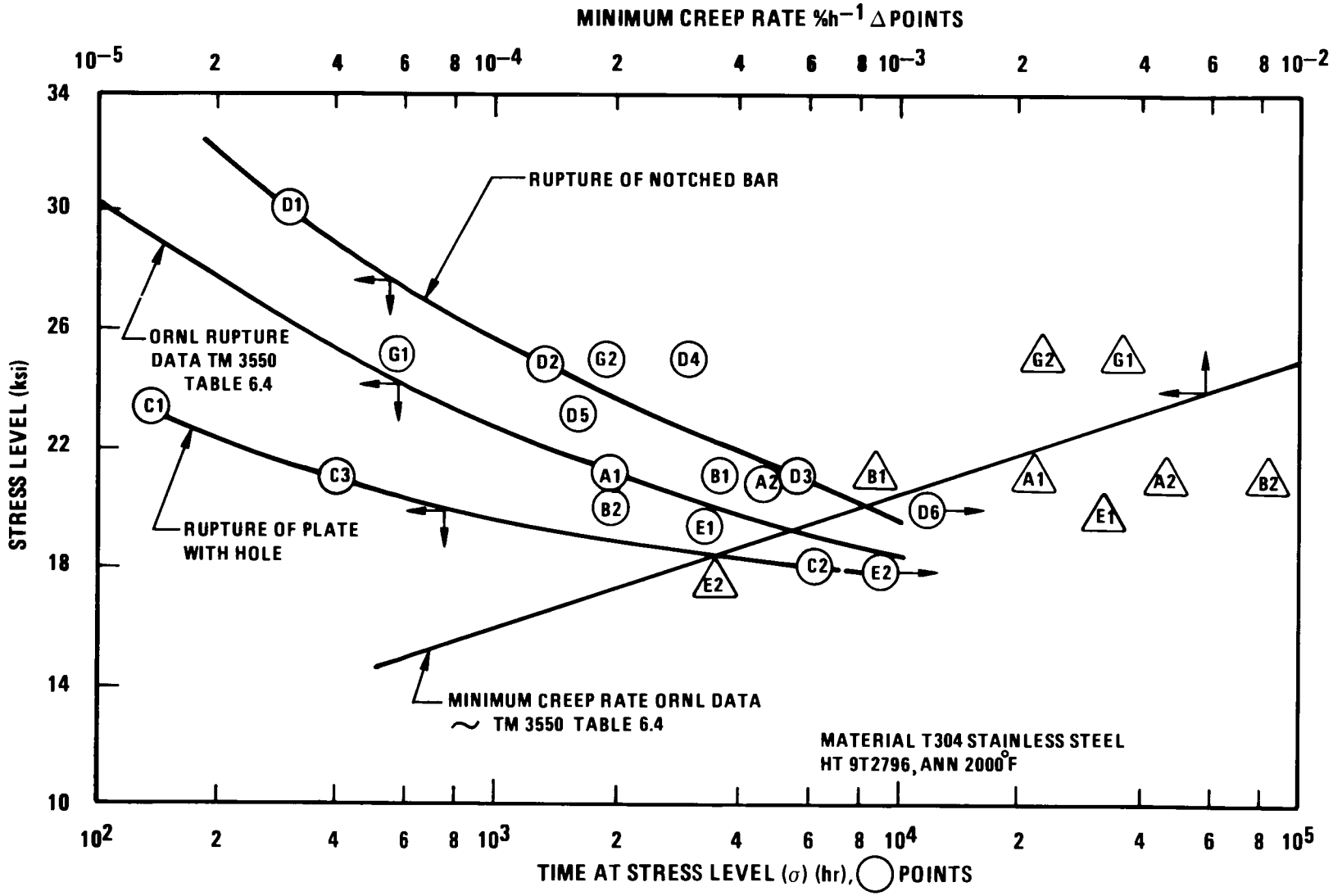

Figure 6.3. Basic Specimen Creep Data At 1100°F

6.2.2 Notched Weld Specimens

In the DTW specimens the notch is centered entirely within the weld metal which is transverse to the base metal ends. In Figure 6.4 the rupture properties of the base metal and the data band for the weld metal are shown for comparison. The wide scatterband for the weld metal is caused by the different properties across the thickness. The properties at a given distance from the surface had much lower scatter. The rupture strength of the material near the surface fell at the shorter times (bottom of the band). Only two notched weld specimens have been tested. The DTW-2 specimen, Table 6.2, was started at 25 ksi at 1100°F and after 5183 hours the stress was raised to 28 ksi. Failure occurred after 5505 additional hours. Specimen DTW-1 at 29 ksi is still in progress at 2779 hours. From a comparison in Figure 6.4 it can be stated that weld metal is notch insensitive.

In contrast, the data for the notched heat affected zone is much weaker, as shown in Figure 6.4, and showed a large scatter. The latter is attributed to the difficulty in locating the notch in the HAZ all around the specimen.

6.2.3 Specimens with Transverse Welds, Types B and G

The rupture strength of specimens with a central transverse weld is only slightly less than that of the base metal as shown by the data in Figure 6.4. Cracking initiates in the HAZ at smaller overall stresses. Measurements of the grid will be made determine the strain limit for the heat affected zone (HAZ).

Specimen BTW-2 was initiated at 19 ksi, Table 6.2, to investigate the longer time effect since rupture is estimated to be about 5000 hours.

6.2.4 Specimens with Central Axial Welds

The short time strength of these specimens is much greater than that of the annealed plate specimen and therefore, the strain on loading is much smaller. For example, BAW-1 specimen had an overall strain of only 0.25 percent at 25 ksi as compared to 4.25 percent for Specimen G-1, Table 6.2. The width of the weld metal is about 20 percent of the cross section. From the ORNL tests the rupture strength at 2000 hours of the

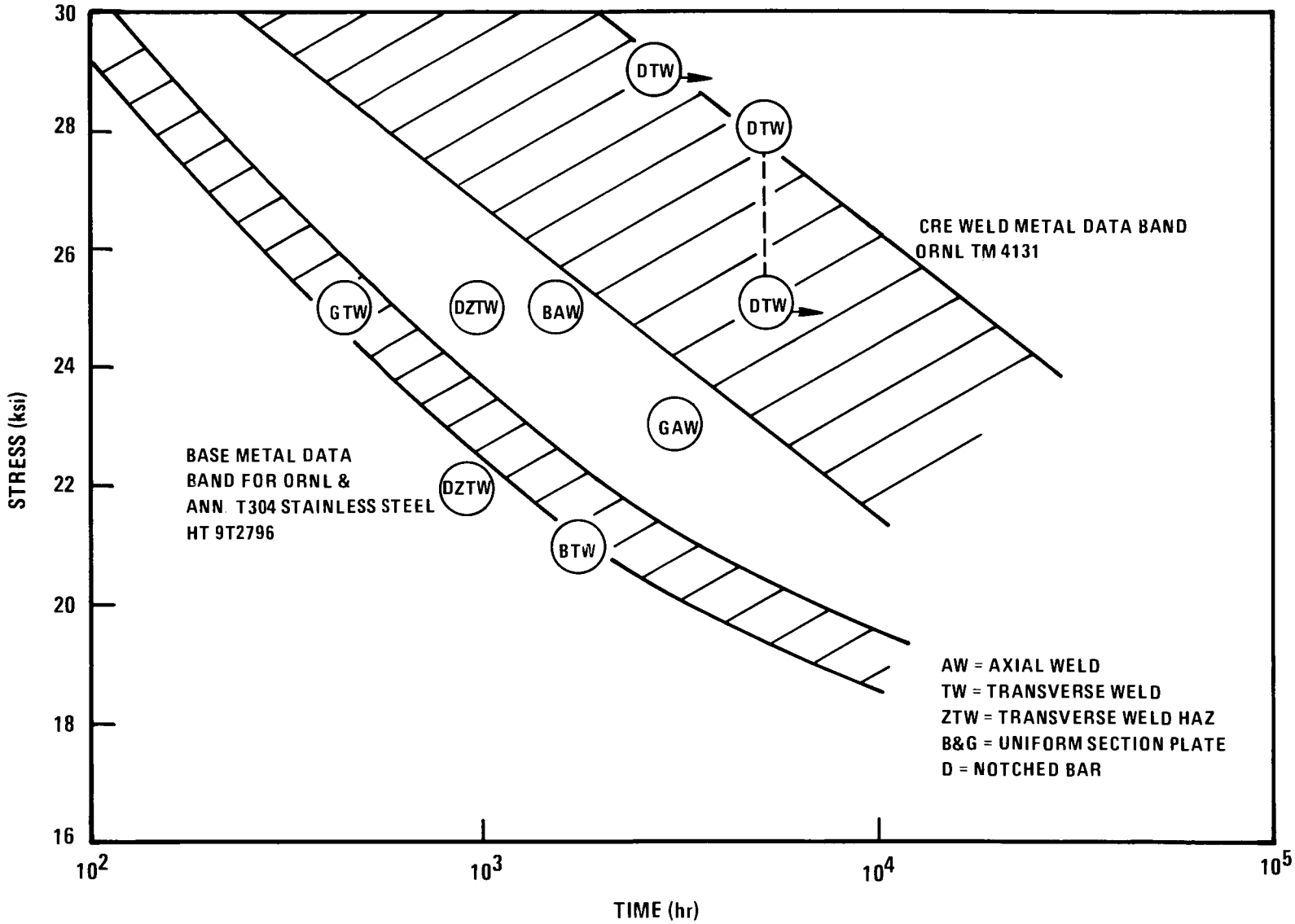

Figure 6.4. Basic Specimen Rupture Data For Welds At 1100°F

weld metal is a minimum of 25.1 ksi and a maximum of 30 ksi whereas that of the base metal is 20.9 to 22 ksi. The average strength of the weld metal is 28 percent higher than that of the base metal. The strengthening of the composite is greater than that predicted by the relative strengths. This is probably due to the gradient of plane strain which exists in the Type B and G specimens.

6.2.5 Central Axial Weld with Hole in Weld

Specimen CAW-1 has a central hole of 1/3-inch diameter entirely within the axial weld of a width of about 2/3 inch. The maximum strains will occur at the horizontal central edges of the hole and across the section at an angle of about ± 35 degrees.

Figure 6-5 shows the grid around the central hole, the location of the central axial weld and the cracks which have initiated in the HAZ. The photograph was taken after 10,274 hours at 18 ksi net section stress and 1100°F. The average overall permanent strain was 1.22 percent but the local strains are much larger. These local strains are being measured.

The cracking initiates at the HAZ along the angles where the strains are a maximum for the HAZ. Many additional cracks are present with samller growth along the HAZ. All the cracks appear to initiate and grow perpendicular to the direction of the maximum principal stress.

6.3 TUBULAR SPECIMEN TESTING - K. C. Thomas, P. C. S. Wu, A. K. Dhalla, C. Daniels

6.3.1 Test Piece Description

The tubular test pieces used in this program to date have been Type 304 stainless steel from the ORNL reference heat (9T2796). The specimens are 8.7 inches in length with a 1.6-inch internal diameter and wall thickness of either 0.1 or 0.05 inch. A detailed description of the equipment, specimen preparation, measurement and data analysis information was presented in Appendix 4-1 of Reference 1.

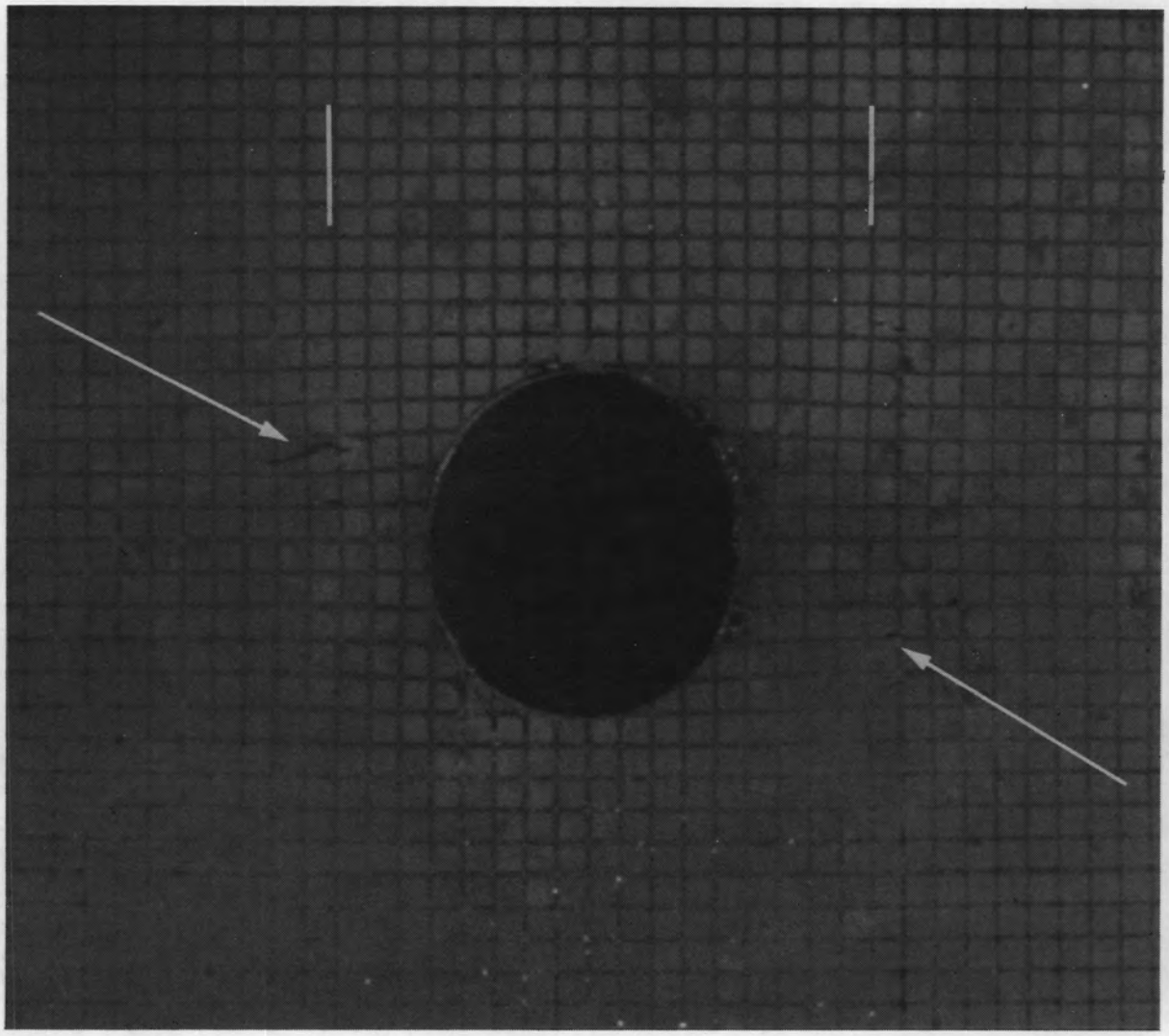

VERTICAL MARKERS – HEAT AFFECTED ZONE POSITIONS
ARROWS – INITIAL CRACKS

Figure 6.5. CAW-1 Hole Centered In Axial Weld, 10,274 Hours At 18 ksi Net Section Stress & 1100°F

6.3.2 Type 304 Stainless Steel Testing

The current test matrix for multiaxial testing of Type 304 stainless steel tubular creep specimens is shown in Table 6.3. This test matrix differs from that shown previously[2] in the following respects:

a. Tests 19 through 22 have been deleted due to non-availability of specimen material.

b. Test 17 has been changed from a 2000 hour test at 12,500 psi (stress ratio 1.5) to a step loaded test at the conditions shown in Table 6.3. The reason for this change is to obtain more information on step loading behavior. This will aid in developing a relationship between creep behavior and loading history.

Test 14 is now in the third step loading segment. Test 15 is in the second step loading. Test 17 has been initiated and Test 18 has accumulated $\sim$ 200 hours.

6.3.3 Type 304 Stainless Steel Topical Report

A topical report, prepared for the Type 304 stainless steel tubular specimen creep testing, is currently being reviewed. In this report a complete data package is provided for all tests completed or in progress for the tubular specimen test program conducted at ARD. The information includes sample history, geometry, fabrication, quality control, equipment and instrumentation, test conditions, etc., recorded for each test. The information is intended to be comprehensive and sufficient to facilitate data reduction and evaluation which will be reported in a subsequent topical report.

6.3.4 Type 316 Stainless Steel Testing

The planned test matrix for Type 316 stainless steel tubular specimens is shown in Table 6.4.

A specimen (9 inches long) of the ORNL Type 316 reference heat No. 8092297 is now being heat treated according to the recommended ORNL heat treatment schedule. ORNL also stipulated post-heat treatment grain size, hardness and tensile properties. After heat treatment, these properties will be determined to verify compliance with requirements. Provided

TABLE 6.3

TEST MATRIX FOR TYPE 304 STAINLESS STEEL TUBULAR SPECIMENS

Test Number	Effective Stress σ_e (psi)	Stress Ratio hoop/axial (σ_θ/σ_z)	Int. Pressure P (psi)	Axial Load L (lb)	Nominal Test Temperature T (°F)	Nominal Test Duration t (hr)	Wall Thickness (mils)
			I - Uniaxial Constant Load Specimens				
1A	25,000	0	0	6872.2	1100	100	50
1B	25,000	0	0	6872.2	1100	100	50
2A	10,000	0	0	5340.1	1100	2000	100
2B	10,000	0	0	5340.1	1100	2000	100
3A	20,000	0	0	10681.4	1100	2000	100 (a)
3B	20,000	0	0	10681.4	1100	2000	100
3C	7,700	0	0	4112.3	1100	2000	100
3D	5,000	0	0	2670.4	1100	2000	100
			II - Multiaxial Specimens				
4	10,000	2.0	1209.5	323.0	1100	2000	100 (b)
5	15,000	2.0	1814.3	484.0	1100	2000	100 (b)
6	20,000	2.0	2716.9	0.0	1100	2000	100 (c)
7	10,000	1.5	1180.0	1211.0	1100	2000	100 (b)
8	15,000	1.5	2000.0	1515.0	1100	2000	100 (c)
9	20,000	1.5	2668.4	2018.6	1100	2000	100 (c)
10	10,000	1.0	1049.4	2670.0	1100	2000	100 (b)
11	15,000	1.0	1574.0	4005.0	1100	2000	100 (b)
12	20,000	1.0	2353.0	5340.7	1100	2000	100 (c)
13	10,000	1.5	612.9	436.8	1100	1100	50
13 (cont.)	15,000	1.5	1030.8	734.7	1100	500	50
13 (cont.)	20,000	1.5	1374.4	979.6	1100	200	50
13 (cont.)	20,000	1.0	1212.1	2591.8	1100	200	50
14	15,000	2.0	930.3	0.0	1100	500	50 (c)
14 (cont.)	15,000	1.5	1030.8	734.7	1100	500	50
14 (cont.)	15,000	1.0	832.5	1780.0	1100	500	50
14 (cont.)	15,000	2.0	930.3	0.0	1100	500	50
15	10,000	2.0	620.2	0.0	1100	1150	50
15 (cont.)	15,000	1.5	1030.8	734.7	1100	500	50
15 (cont.)	20,000	1.0	1212.1	2591.8	1100	200	50
15 (cont.)	15,000	2.0	930.3	0.0	1100	200	50
16	12,500	1.0	757.6	1619.9	1100	2000	50
17	12,500	2.0	874.8	0.0	1100	700	50 (c)
17 (cont.)	12,500	1.0	757.6	1619.9	1100	700	50
17 (cont.)	12,500	1.0	832.5	1780.0	1100	500	50
17 (cont.)	20,000	1.0	1212.1	2591.8	1100	100	50
18	12,500	2.0	874.8	0.0	1100	2000	50

(a) Effective stress calculated by:

$$\sigma_e = \sigma_z = \frac{L}{\pi r_{av} t}$$

where: r_{av} = Average radius of the tube wall

t = Thickness of the tube

(b) Effective stress Calculated as per thick cylinder formula by:

$$\sigma_e = \frac{1}{\sqrt{2}} [(\sigma_z - \sigma_\theta)^2 + (\sigma_\theta - \sigma_r)^2 + (\sigma_r - \sigma_z)^2]^{1/2}$$

where: $\sigma_z = \sigma_{axial} = \frac{L}{A} + p \frac{a^2}{b^2 - a^2}$

$$\sigma_\theta = \sigma_{hoop} = p \frac{a^2(b^2 + r^2)}{r^2(b^2 - a^2)}$$

$$\sigma_r = \sigma_{radial} = p \frac{a^2(b^2 - r^2)}{r^2(b^2 - a^2)}$$

(c) Effective stress calculated as per thin cylinder formula by:

$$\sigma_e = [\sigma_\theta^2 + \sigma_z^2 - \sigma_\theta \sigma_z]^{1/2}$$

where: $\sigma_\theta = p \frac{r_{av}}{t}$

$$\sigma_z = \frac{p r_{av}}{2t} + \frac{L}{2\pi r_{av} t}$$

r_{av} = Average radius of the tube

t = Thickness of the tube

A = Cross-sectional area of the tube
t = Wall thickness of the tube
a = Inside radius of the tube
b = Outside radius of the tube
r = Radius at the point under consideration r = a, is used to calculate the maximum σ_e which occurs at the inside fiber of the tube
p = Internal pressure
L = Axial load

TABLE 6.4

TEST MATRIX FOR TYPE 316 STAINLESS STEEL TUBULAR SPECIMENS

Test Number	Effective Stress σ_e (psi)	Stress Ratio $\sigma_{hoop}/\sigma_{axial}$ (σ_θ/σ_z)	Int. Pressure P (psi)	Axial Load L (lb)	Nominal Test Temperature T (°F)	Nominal Test Duration t (hr)	Wall Thickness (mils)
			I - Uniaxial Constant Load Specimens				
101	25,000	0.0	0.0	6479.5	1100	2000	50
102	20,000	0.0	0.0	5183.6	1100	2000	50
103	15,000	0.0	0.0	3887.7	1100	2000	50 (a)
104	10,000	0.0	0.0	2591.8	1100	2000	50
105	7700	0.0	0.0	1995.7	1100	2000	50
			II - Multiaxial Specimens				
106	20,000	2.0	1399.6	0.0	1100	2000	50
107	20,000	1.0	1212.1	2591.8	1100	2000	50
108	15,000	2.0	1049.7	0.0	1100	2000	50
109	15,000	1.0	909.1	1943.9	1100	2000	50 (b)
110	12,500	2.0	874.8	0.0	1100	2000	50
111	12,500	1.0	757.6	1619.9	1100	2000	50
112	10,000	2.0	699.8	0.0	1100	2000	50
113	10,000	1.0	606.1	1295.9	1100	2000	50

(a) Effective Stress calculated by:

$$\sigma_e = \sigma_z = \frac{L}{2\pi r_{av} t}$$

where: R_{av} = average radius of the tube

t = thickness of the tube

(b) Effective stress calculated as per thin cylinder formula by:

$$\sigma_e = [\sigma_\theta^2 + \sigma_z^2 - \sigma_\theta \sigma_z]^{1/2}$$

where: $\sigma_\theta = p \dfrac{r_{av}}{t}$

$$\sigma_z = p \frac{r_{av}}{2t} + \frac{L}{2\pi r_{av} t}$$

r_{av} = average radius of the tube

t = wall thickness of the tube

p = internal pressure

L = axial load

these requirements are met, subsequent heat treatments will be verified by furnace temperature charts and hardness.

6.3.5 Data Reduction

The present CREEP-FIT data reduction computer program has been updated. This most recent update allows for a least-squares fit to the more complicated two exponential term creep equation:

$$\varepsilon = \sum_{n=1}^{2} \varepsilon_n \left(1 - e^{-r_n t}\right) + \dot{\varepsilon}_m t$$

where ε = creep strain (excluding loading strain)

n = integer

$\varepsilon_n = f(\sigma, T)$ = constant at fixed σ and fixed T

$r = g(\sigma, T)$ = constant at fixed σ and fixed T

$\dot{\varepsilon}_m$ = secondary creep rate

t = time

Previously the above equation was only solved for n = 1, which results in the "single exponential" equation. When n is increased to 2 the "double exponential" equation results which in many cases more accurately expresses transient creep. Several initial plots have been made. An example of the single exponential (3 parameters) versus the double exponential fit (5 parameters) is shown in Figure 6.6 and its expanded version in Figure 6.7.

In addition, capability to plot circumferential strain versus axial strain and the ratio of circumferential to axial strain versus time has been added to the data reduction routine. This will allow plots to be automatically generated, along with the existing plots, for such things as temperature and pressure error, for each test. These two additional plots will aid in evaluation of the reduced data. A program which plots up to five tests on the same chart is now being developed. When integrated with CREEP-FIT, this program will facilitate the comparison of test results which are in the data bank.

Current data analysis has included curve fitting using effective strain as a function of time and examination of data to verify the

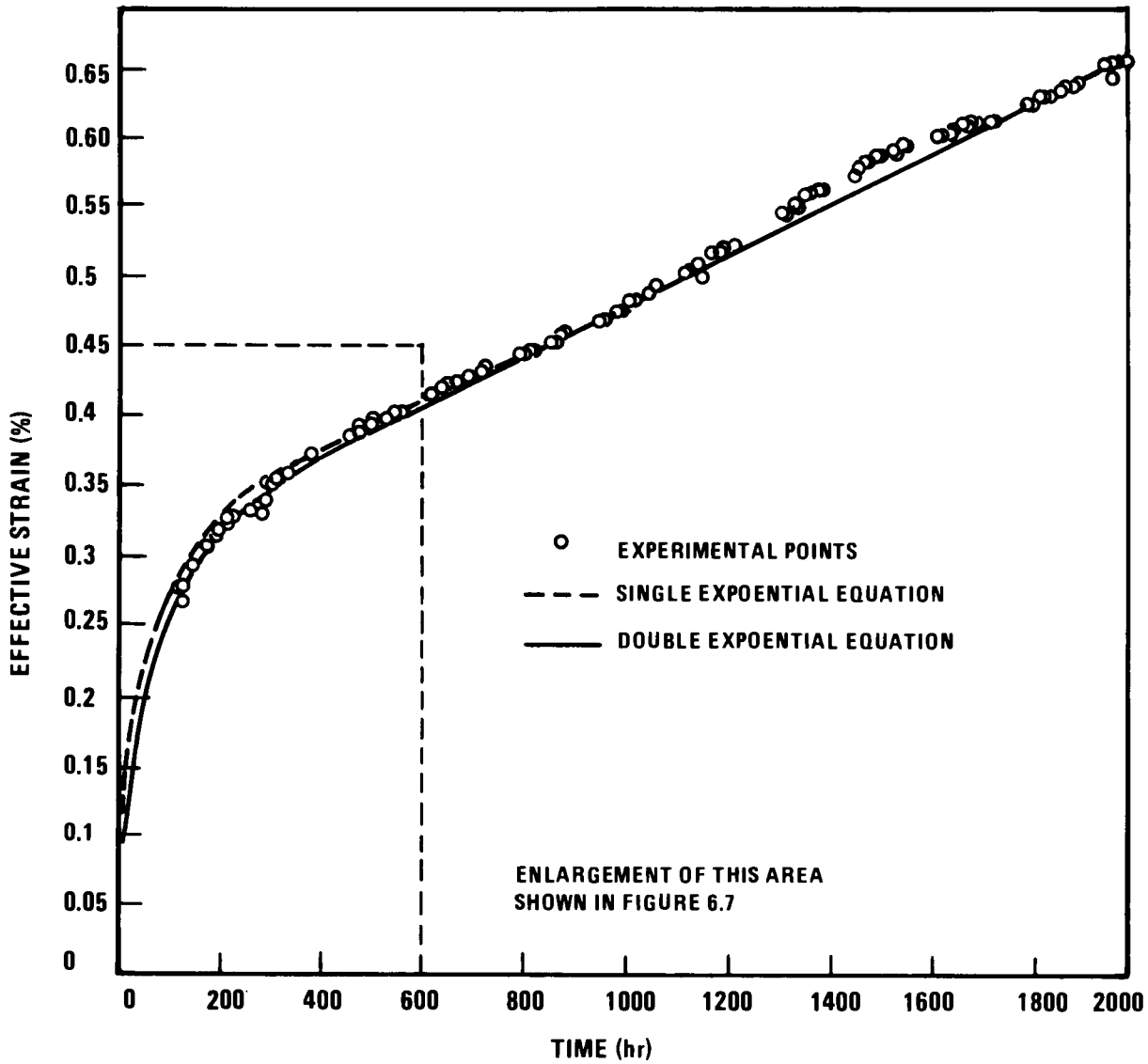

Figure 6.6. Comparison Of Creep Equation Generated Values And Experimental Values For Test 5-5

8043-3

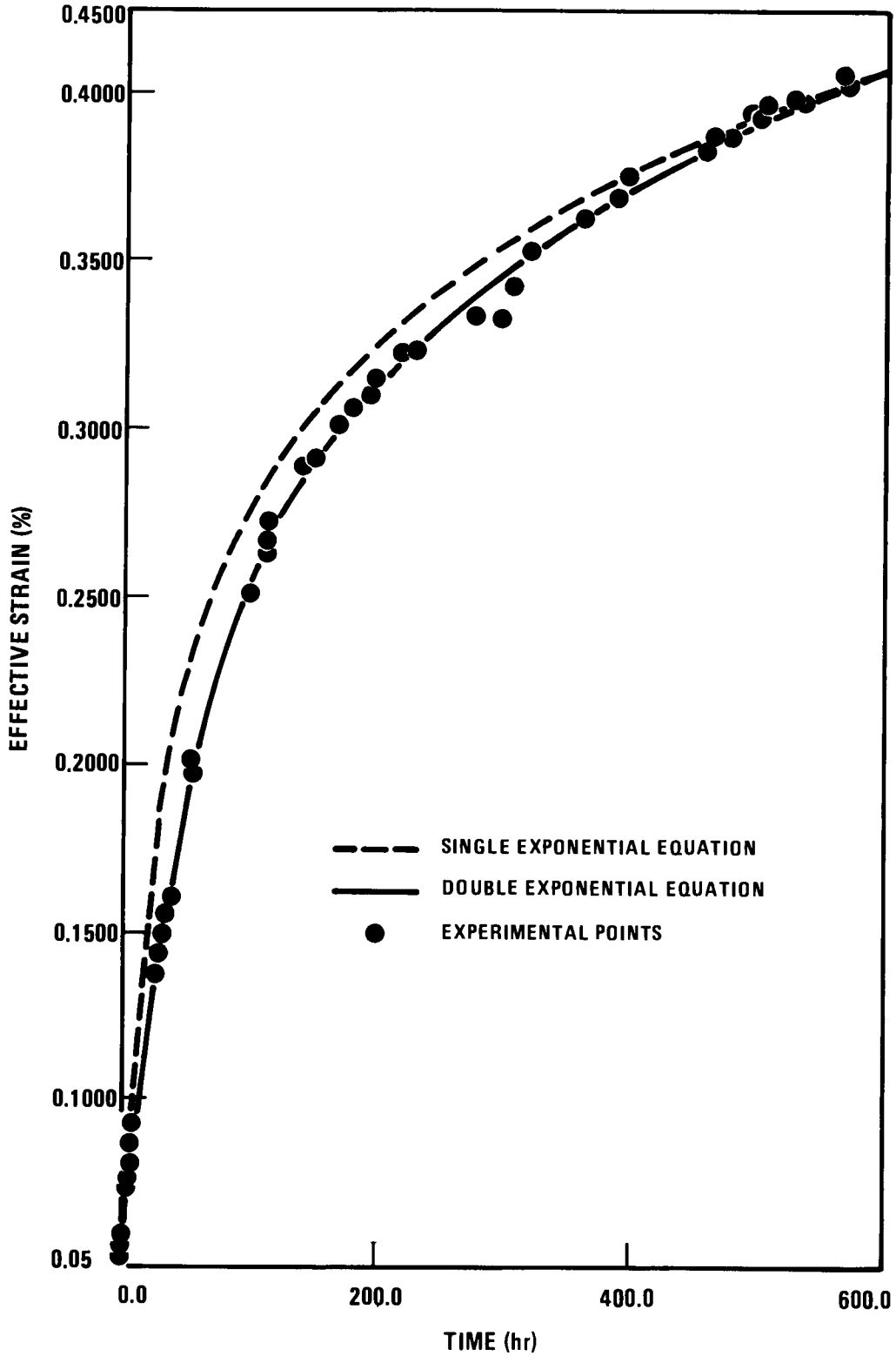

Figure 6.7. Effective Creep Strain Vs Time For Test 5-5

accuracy of data from tests done to date.

6.4 SODIUM EFFECTS ON MECHANICAL PROPERTIES OF STRUCTURAL MATERIALS - S. L. Schrock, P. N. Flagella, J. Kahrs, P. Wu

6.4.1 Type 316 Stainless Steel

Mechanical property evaluations for solution-annealed Type 316 stainless steel as affected by a flowing sodium environment involves two heats of the material. The first heat, purchased by Westinghouse ARD, involves a limited number of test samples, fabricated from bar material. Sodium exposure and thermal aging of the samples was performed previously. Mechanical property tests in sodium of these samples will provide an indication of the effect of the environment, including pre-treatment.

The second heat of solution-annealed Type 316 stainless steel plate material to be used for the evaluations was recently obtained from the HEDL stockpile (heat 65805). The larger number of mechanical property test samples from this heat will allow a more detailed study on sodium effects. Sodium exposure and thermal aging of samples at different temperatures for different amounts of time, prior to testing in sodium and air, is presently in progress.

Low-cycle strain-controlled fatigue testing of test samples from the ARD heat of material is continuing at 1100°F in flowing sodium. The samples have a 0.25-inch gage diameter and a 1.00-inch gage length. Table 6.5 presents a summary of the pre-treatment given the samples, the test conditions, and results obtained to date. The tests were performed at nominal total strain ranges of 0.5 and 1 percent for pure fatigue, with the holdtime in tension-only tests performed at 1 percent. Ramp rates in all cases were 4×10^{-3} sec^{-1}. The sodium pre-treatment was performed in the hot leg of the PEL. Velocity of the sodium past the samples was 3 fps, the loop ΔT was maintained at 300°F, and the oxygen content for the sodium >1 ppm (continuous cold trapping). The argon pre-treatment was performed by first encapsulating the test samples in argon-filled Type 304 stainless steel tubing.

TABLE 6.5

LOW CYCLE FATIGUE DATA FOR S.A. TYPE 316 SS[a] TESTED IN FLOWING SODIUM AT 1100°F[b]

Sample Number	Pre-Treatment for 5000 hr: Environment	Pre-Treatment for 5000 hr: Temp. (°F)	Strain Range, % $\Delta\varepsilon t$	Strain Range, % $\Delta\varepsilon p$	Hold Time[c] (hours)	Stress Range[d] (ksi)	Fatigue Life (N_f)
122	sodium	1325	0.51	0.25	0	47.9	56,201
114	argon	1325	0.51	0.31	0	50.3	49,753
110	argon	1200	0.51	0.24	0	50.9	43,419
118	sodium	1200	0.51	0.27	0	51.1	38,765
130	as-fabricated		0.51	0.19	0	73.8	54,670
113	argon	1325	1.03	0.69	0	68.2	9602
123	sodium	1325	1.03	0.62	0	65.0	7950
119	sodium	1200	1.01	0.66	0	70.0	5711
109	argon	1200	1.01	0.62	0	67.8	4842
128	as-fabricated		1.00	0.61	0	86.8	2356
115	argon	1325	1.01	0.69	0.1	70.0	2093
124	sodium	1325	0.99	0.68	0.1	64.3	1744
117	sodium	1200	1.02	0.67	0.1	71.0	2518

(a) ARD Heat

(b) Strain Rate: 4×10^{-3} sec^{-1}
Control Mode: Axial Strain
Wave Form: Triangular, zero mean strain

(c) Tension only

(d) At $N_f/2$ (maximum stress range for hold-time tests)

The low-cycle fatigue results obtained in sodium at 1100°F are compared to data reported in the literature[3] for solution-annealed Type 316 stainless steel tested at 1100°F in-air. Figure 6.8 compares the results for tests of as-fabricated samples. The two tests in sodium show no significant change in the fatigue life, although an increase in fatigue life at the lower strain ranges in sodium is indicated. Additional tests will be required before the effect can be established. Figure 6.9 compares the in-air and in-sodium results for test samples pre-treated 5000 hours. The in-sodium data show a significant increase in fatigue life, based on the results obtained at a total strain range of 1 percent, whereas no effect is apparent at 0.5 percent. This may be due to the fact that the fatigue curve is quite shallow in the high cycle range, and that the test results are beyond the transition fatigue life (N_{TR}). At both 0.5 and 1 percent total strain ranges, the in-sodium results show an increase in fatigue life with an increase in pre-treatment temperature for a constant time (5000 hours). Two curves are therefore shown for the in-air results in the low-cycle region ($\lesssim$ 10,000), indicating that some of the samples may have had a structure equivalent to approximately a 1200°F pre-treatment. Comparison of the plastic strain range data for the in-air and in-sodium tests involving both as-fabricated and pre-treated samples is shown in Figure 6.10. The increase in fatigue life with increased pre-treatment temperature is apparent. Effect of the sodium pre-treatment versus the thermal aging treatment (time-at-temperature) is not clear at this time.

The increase in fatigue life with the higher temperature pre-treatment is the result of the decreased strength of the material. This is shown in Figure 6.11, where the cyclic stress range (at $N_f/2$) versus plastic strain range data are correlated for both as-fabricated and pre-treated samples. At any plastic strain range, the cyclic stress range is lowest for the 1325°F pre-treatment samples and highest for the as-fabricated non-pretreated samples. The slope of the curves is approximately 0.32 and is defined as the cyclic strain-hardening exponent n in the equation

$$\Delta\sigma = K(\Delta\varepsilon p)^n$$

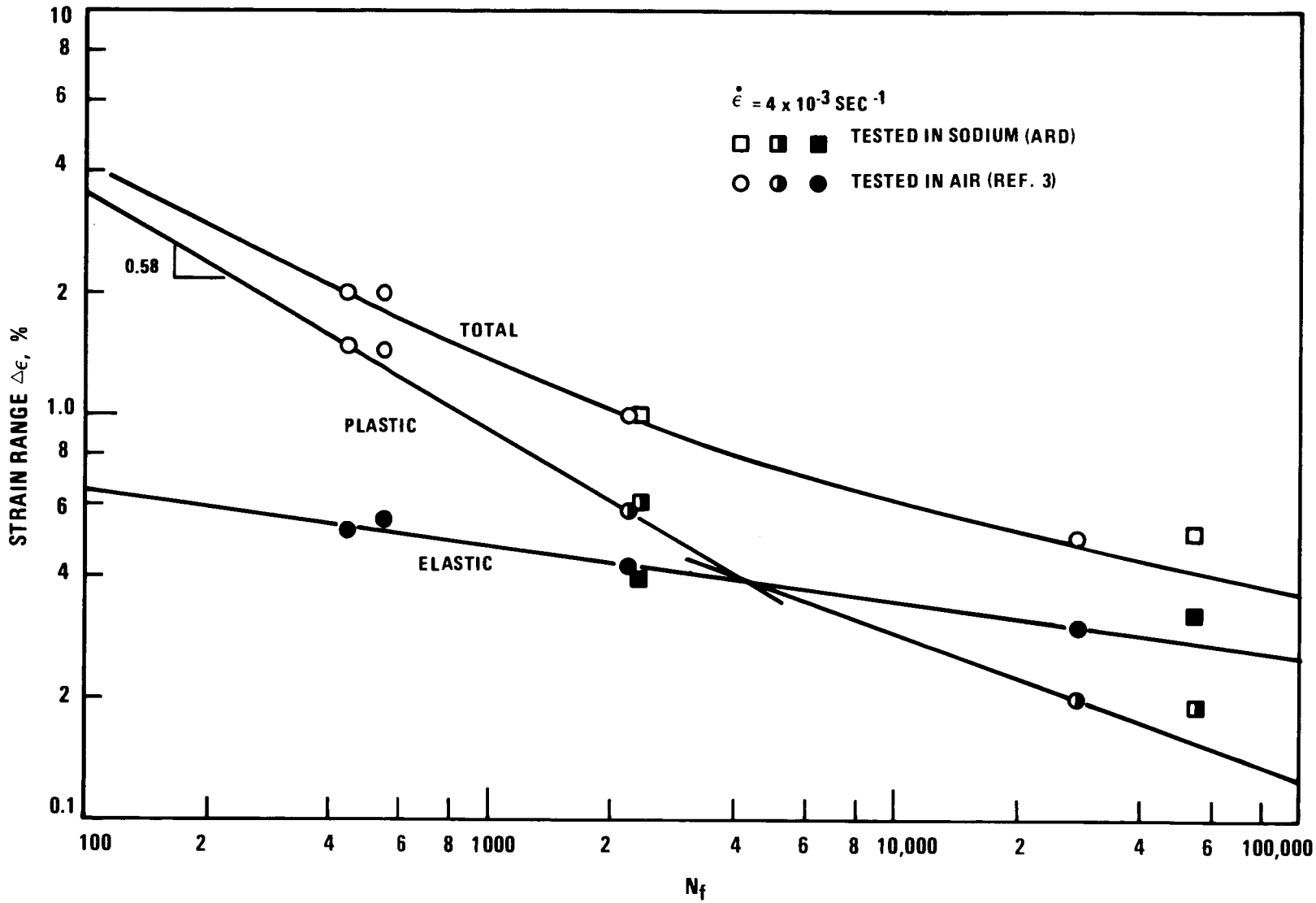

Figure 6.8. Low Cycle Fatigue Results For As-Fabricated S.A. Type 316 SS Tested At 1100°F

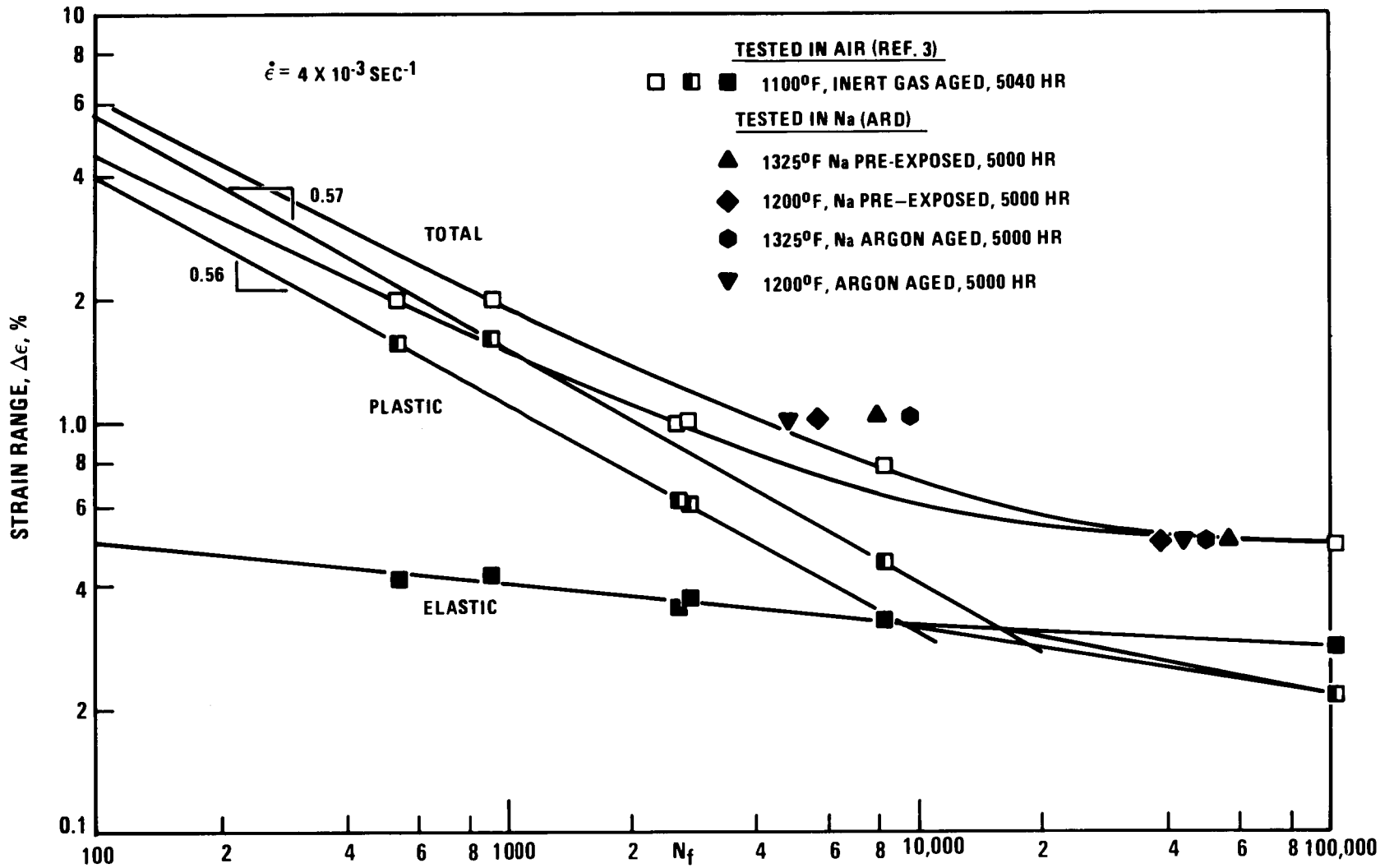

Figure 6.9. Low Cycle Fatigue Results For Pre-Treated S.A. Type 316 SS Tested At 1100°F

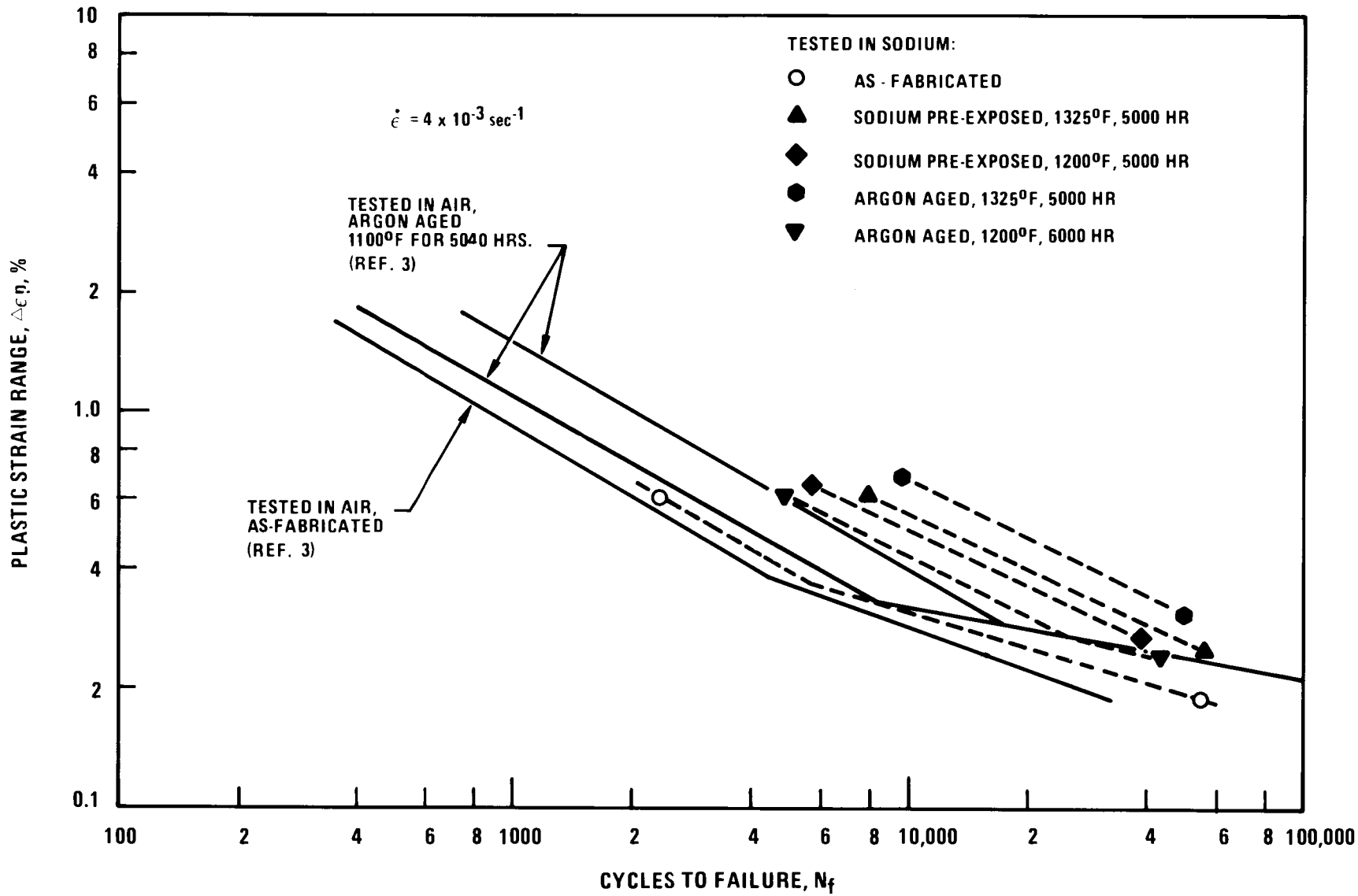

Figure 6.10. Comparisons Of Low Cycle Fatigue Data For Type 316 SS Tested At 1100°F In Air And Sodium

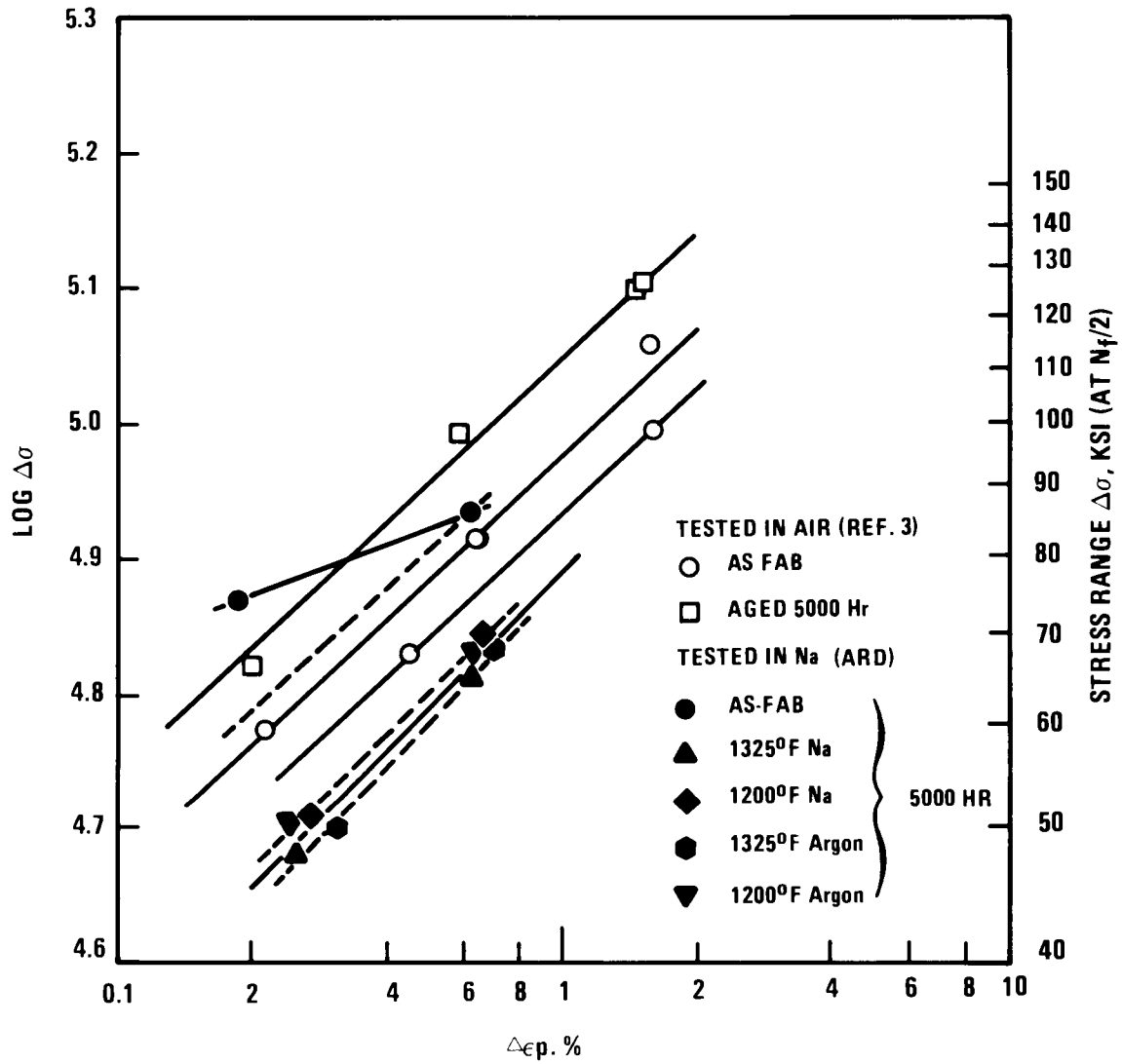

Figure 6.11. Stress Range Vs Plastic Strain Range For Strain Controlled Tests Of S.A. 316 SS At 1100°F

8043-10

Although the two as-fabricated samples tested in sodium yield a significantly different slope, examination of the test data for the 0.5 percent total strain range test showed that secondary hardening was involved. Initial stress saturation occurred at approximately 60 ksi, followed by secondary hardening to the 73.8 ksi value given in Table 6.5. The reason for the additional hardening is not known at this time. No unusual events occurred during the testing. Figure 6.12 presents the strain controlled data in terms of cyclic stress range versus fatigue life for the in-air and in-sodium tests. Variations in stress range for the same fatigue life are much greater in the high-cycle range, apparently influenced to a greater extent by microstructural differences and the larger percentage of elastic strain. Increasing the pre-treatment temperature (for 5000 hours) appears to cause the slope change for the curves in Figure 6.12 to occur at a higher fatigue life (and lower stress). This is consistent, of course, with the discussions relative to the previous figures.

The effects of test environment, pre-treatment environment, and temperature for 5000 hours on the fatigue life of solution-annealed Type 316 stainless steel tested at 1100°F are shown in Figure 6.13. The data shown for a total strain range of 1 percent appear to correlate quite well. The 2 percent data appear to be consistent if the one sample tested in air with a N_f = 910 is assumed to be aged at ∿ 1200°F rather than 1100°F. As mentioned earlier, this is strongly suggested based on the other correlations. The inconsistencies for the 0.5 percent data are apparently due to the larger variations in stress ranges involved. The data in Figure 6.13 suggest that a 5000 hour pre-treatment at 1000°F or lower will have no effect on the fatigue life, with an exponential effect as the pre-treatment temperature is increased above ∿ 1000°F. No significant effects between thermal aging and sodium pre-exposure for 5000 hours are apparent. Trends are indicated which may be real or due to material and/or experimental variations. Additional tests will be required. Comparisons of the limited test results obtained in-air and in-sodium show essentially no difference at a total strain range of 1 percent, but possibly a large difference at 0.5 percent. Further testing is required.

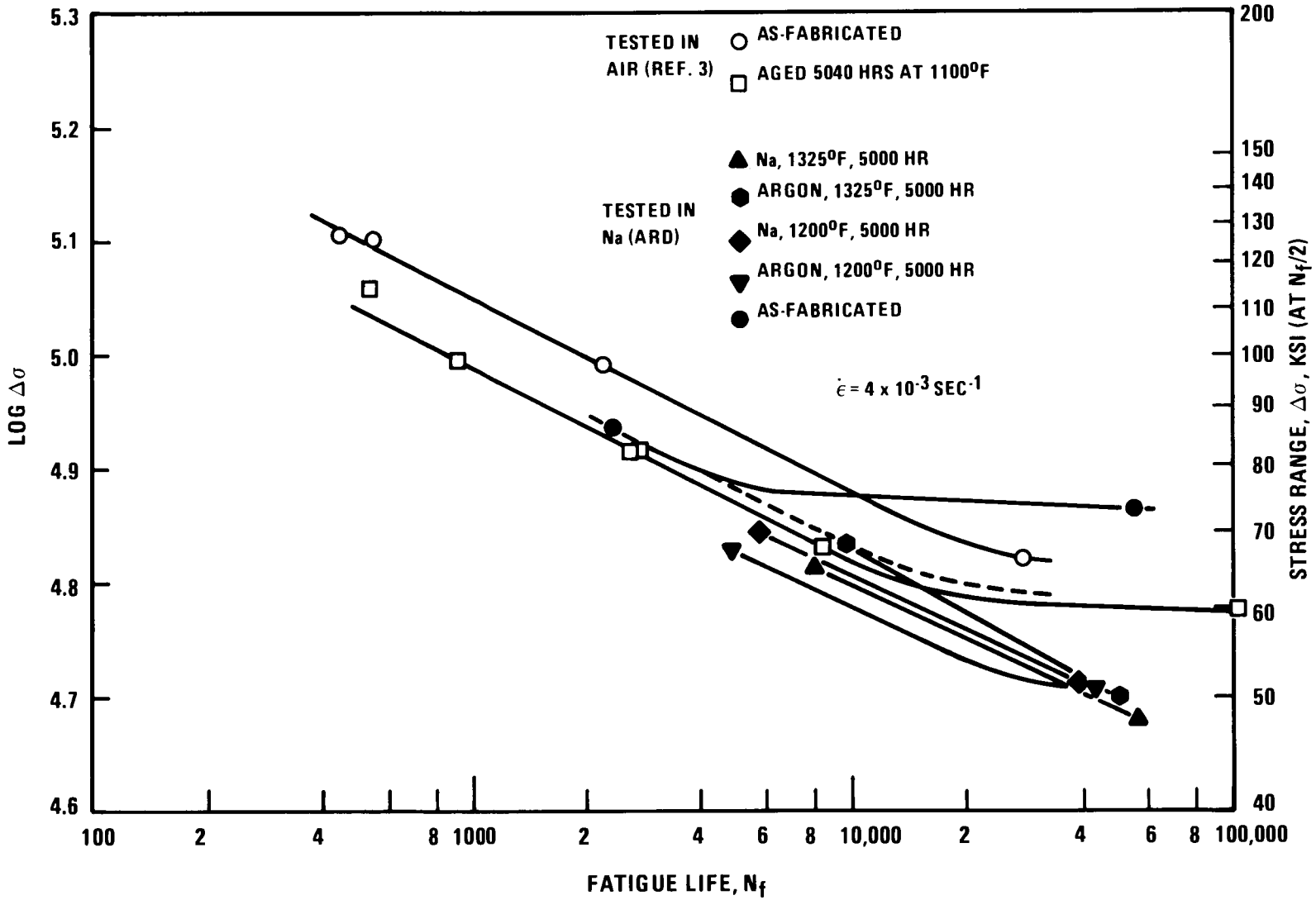

Figure 6.12. Stress Range Vs Fatigue Life For Strain Controlled Tests Of S.A. Type 316 SS At 1100°F

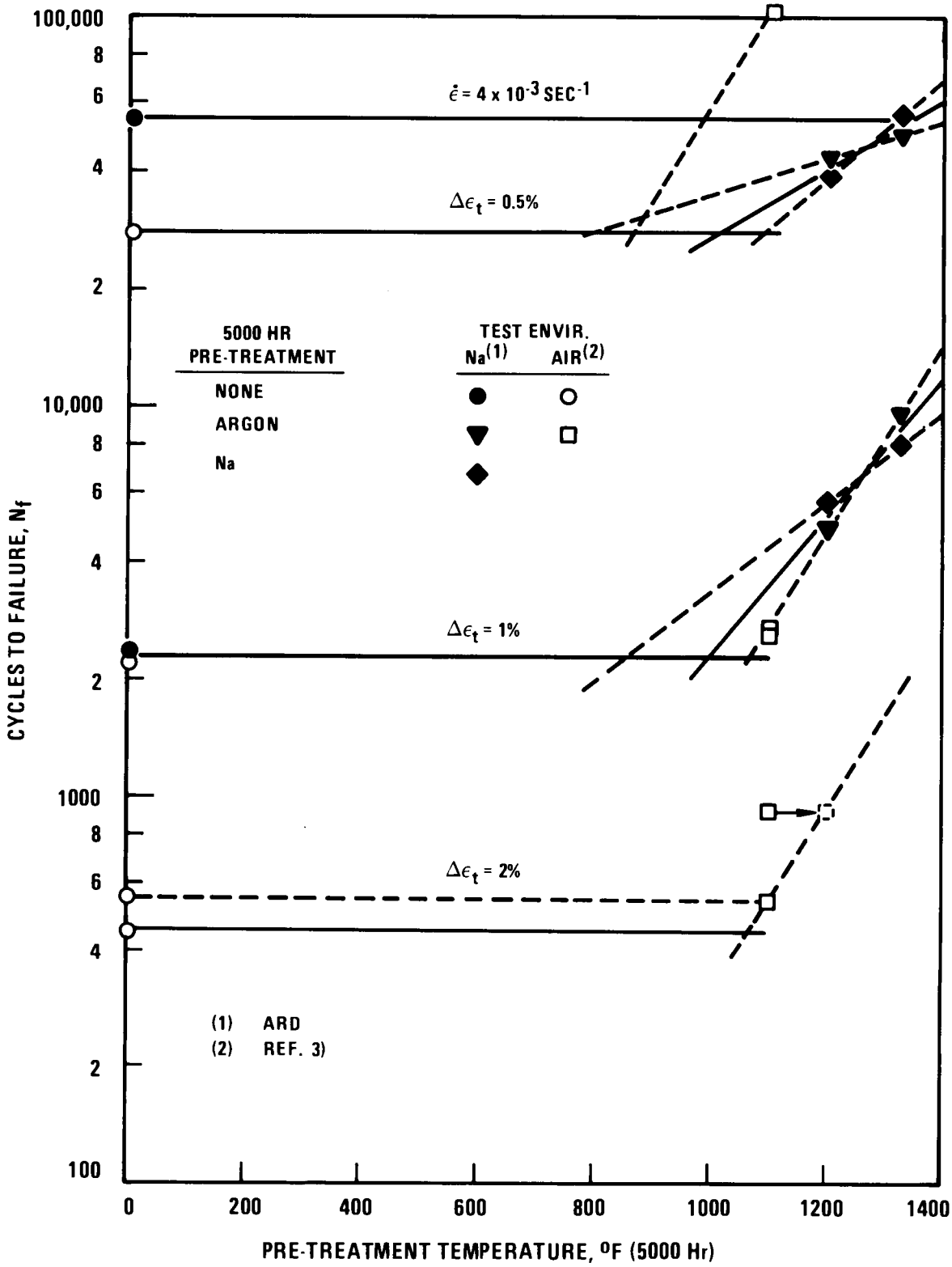

Figure 6.13. Low Cycle Fatigue Results For Type 316 SS Tested At 1100°F

8043-12

The cyclic stress-strain curves obtained from the tests performed in air and in sodium are given in Figure 6.14. The results appear to correlate quite well, and show the significant decreasing strength resulting from increasing the pre-treatment temperature. The two curves shown for the aged samples tested in air suggest possible differences in the aging temperatures. The effect of the secondary hardening observed in the as-fabricated sample tested in-sodium at 0.5 percent is again evident. The dotted line is drawn to the stress range value obtained during the initial hardening.

Three creep-fatigue tests at 1100°F in flowing sodium have been performed to date. Results for the 0.1 hour hold-time in tension-only tests are given in Table 6.5. The data show that the sample pre-exposed to sodium at 1325°F for 5000 hours had the lowest fatigue life and lowest stress range. Conversely, the sample pre-exposed to sodium at 1200°F for 5000 hours had the highest fatigue life and highest stress range. In other words, the higher pre-treatment temperature decreases the strength of the material and hence reduces the cyclic creep life. Apparently, the static creep-rupture life would be affected in the same way. The extent of the differences and the creep-fatigue interaction are being investigated.

6.4.2 Inconel 718

Low-cycle fatigue tests in-air on Inconel 718 are in progress. The results will be used as baseline data for tests of the same heat and heat treatment of material to be tested in sodium. The initial testing involves plate material with a 1725°F solution anneal plus double aging (per AMS-5596C), yielding an ASTM grain size from 8 to 10. Sample geometry, for in-air and in-sodium tests, consists of a 0.25-inch diameter x 0.50-inch long gage section. Axial strain control is obtained using an LVDT measuring the load train deflection. Calibration of the load train compliance is obtained using a zero gage length sample at test temperature, with the same test environment.

Low-cycle fatigue test results for as-fabricated Inconel 718 obtained to date in-air at 1000°F are given in Table 6.6. Included are

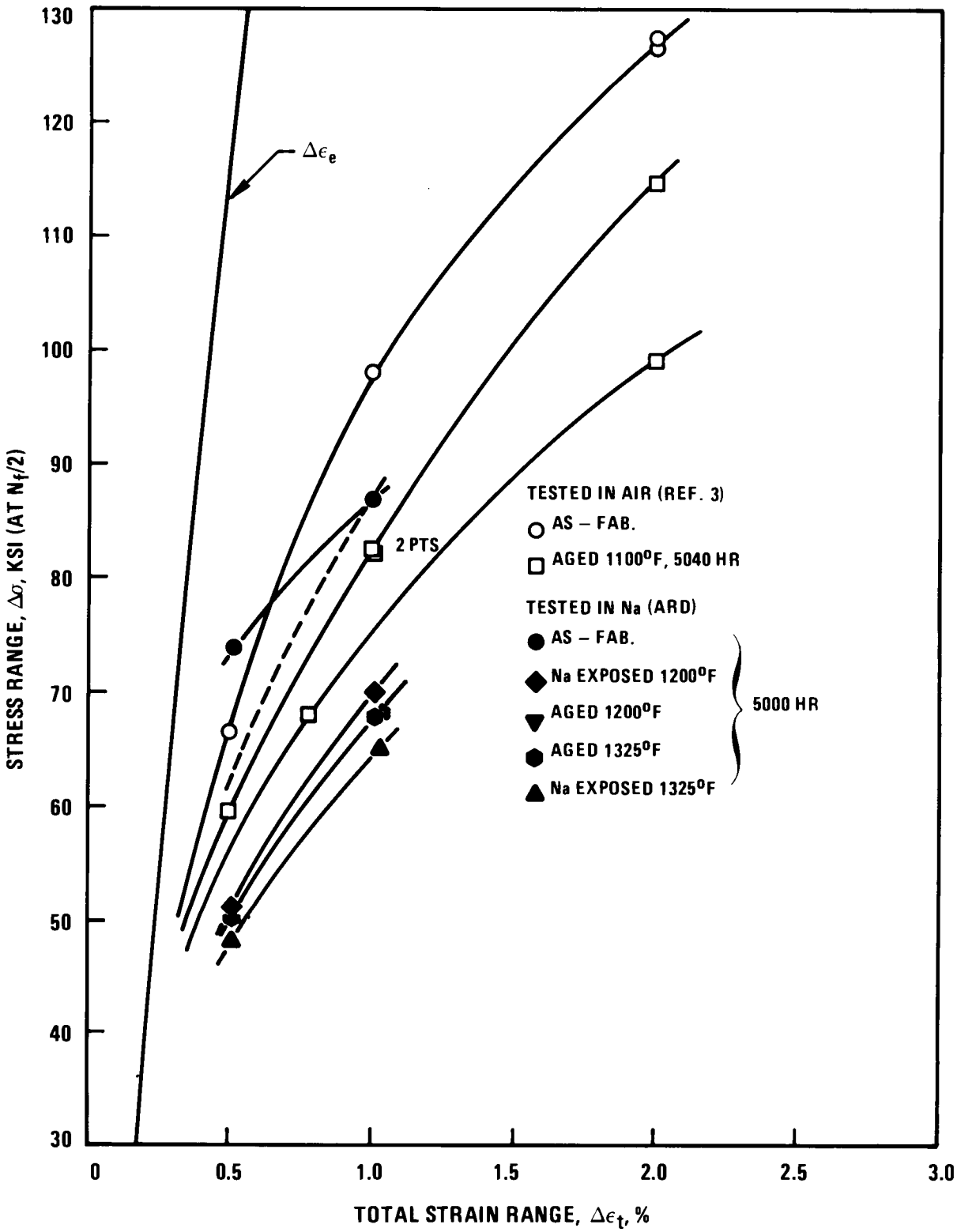

Figure 6.14. Cyclic Stress-Strain Curves For S.A. Type 316 SS At 1100°F

8043-13

TABLE 6.6

LOW-CYCLE FATIGUE DATA[a] FOR INCONEL 718[b] TESTED AT 1000°F IN AIR

Sample Number	Strain Range Total (%)	Strain Range Plastic (%)	Stress Range (ksi)	Hold Time (hours)	Fatigue Life (N_f)
9	0.96	0.22	233.6	0	2050
17	0.97	0.15	231.0	0	3340
25	1.96	0.96	286.0	0	377
1	2.04	1.09	308.0	0	400
39[d]	5.32	3.74	320.0	0	12
31	2.01	0.98	258.0	0.5[c]	357
55	2.0	0.90	266.0	1.0[c]	333

(a) Strain Rate: 4×10^{-3} sec^{-1}
Control Mode: Axial Strain
Wave Form: Triangular, zero mean strain

(b) As-fabricated, 1725°F S.A. + double age (AMS-5596C)

(c) Compression only (maximum stress range values given)

(d) Sample shows slight buckling

two creep-fatigue tests with hold-time in compression only. The data appear consistent when the total, plastic, and elastic strain ranges are plotted as a function of fatigue life in Figure 6.15. The exception is the sample (No. 39) tested at a total strain range of 5.32 percent, suggesting that buckling was involved. This will be taken into consideration in the final data analysis. The two creep-fatigue tests performed at $\Delta\varepsilon_t$ = 2 percent show no significant decrease in fatigue life when compared to the pure fatigue tests performed at the same total strain range. Figures 6.16 and 6.17 present typical hysteresis loops obtained for pure fatigue and creep-fatigue tests.

6.5 REFERENCES

1. "Validation of High Temperature Design Methods and Criteria. Quarterly Progress Report for Period Ending November 30, 1973," WARD-HT-3045-4, March 1974. (Availability: USERDA Technical Information Center).
2. Validation of High Temperature Design Methods and Criteria. Quarterly Progress Report for Period Ending May 31, 1975," WARD-HT-3045-12, November 1974. (Availability: USERDA Technical Information Center).
3. C. R. Brinkman and G. E. Korth, "Low-Cycle Fatigue and Hold-Time Comparisons of Irradiated and Unirradiated Type 316 Stainless Steel," Met. Trans. 5, pp. 792-794 (1974).

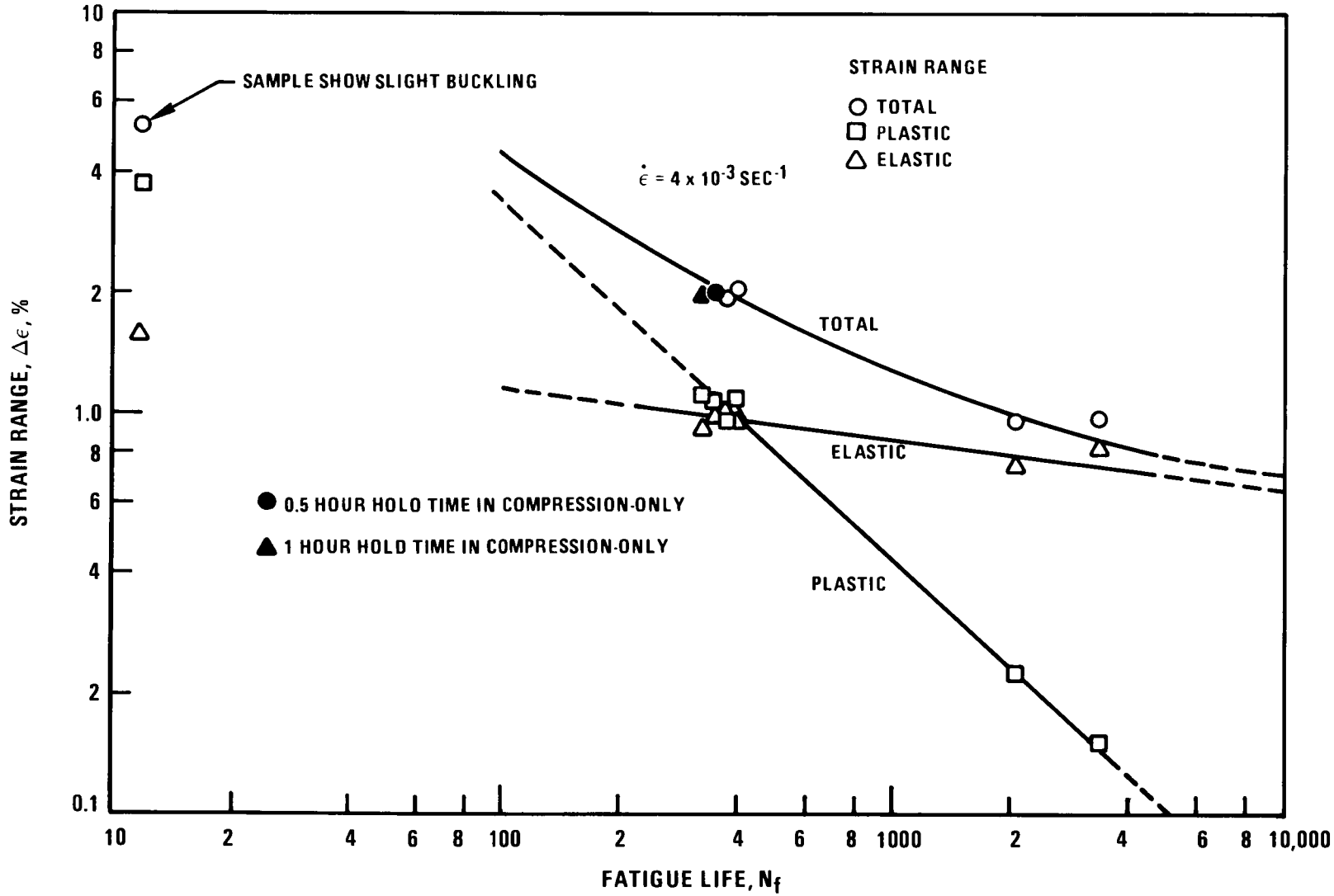

Figure 6.15. Strain Range Vs Fatigue Life For Inconel 718 At 1000°F In Air

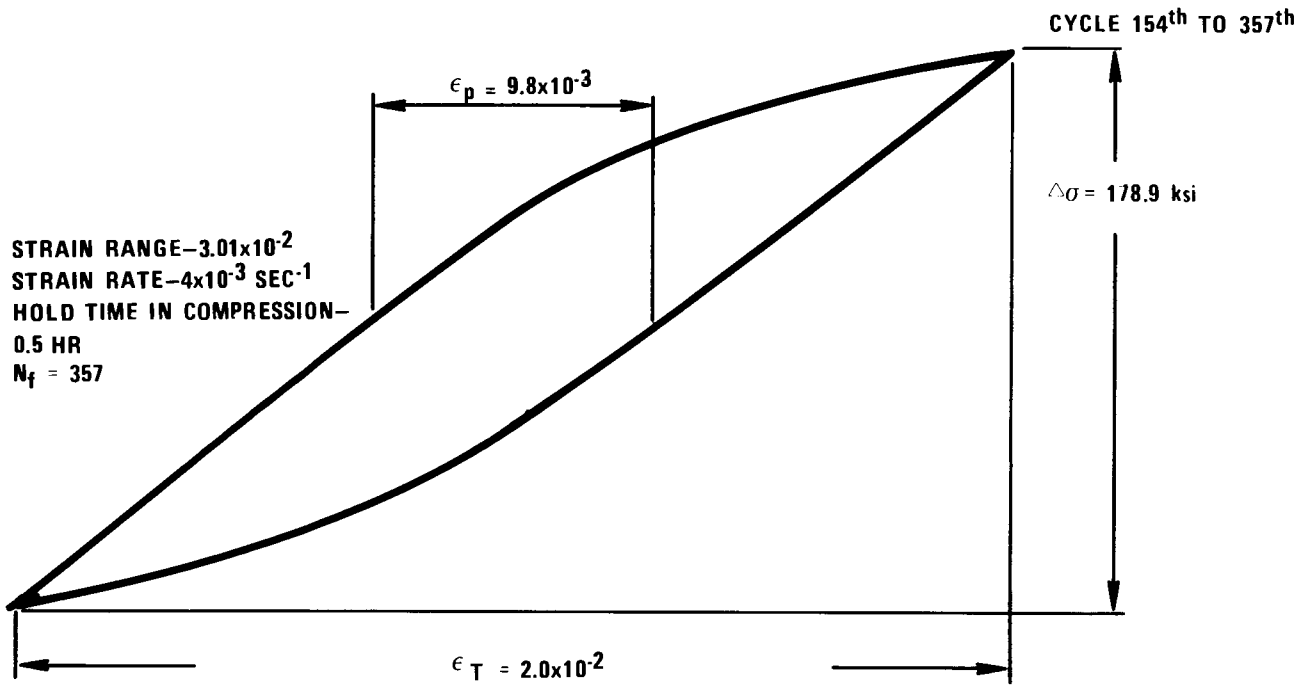

Figure 6.16. Hysteresis Loop For Inconel 718 Fatigue Test With 2.0% Strain Range At 1000°F In Air

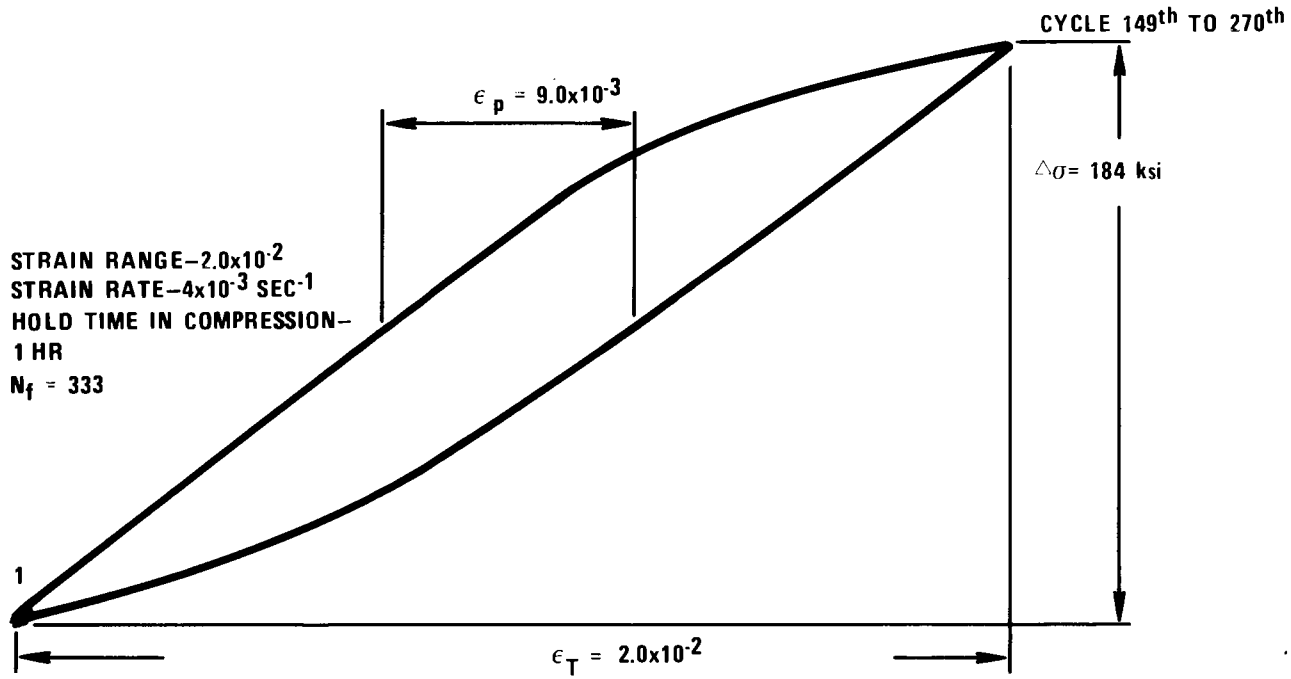

Figure 6.17. Hysteresis Loop For Inconel 718 Fatigue Test With 2.0% Strain Range At 1000°F In Air

7. UNIVERSITIES

7.1 UNIVERSITY OF CINCINNATI — J. Moteff

7.1.1 Introduction

The objective of this program is to (a) evaluate the time, temperature and stress-dependent mechanical properties of reactor structural materials, (b) determine the relationship of these properties to the microstructure and (c) show the contribution of the microstructure to the internal stress fields and the subsequent influence on microcracking and the grain boundary sliding behavior during the normal plastic deformation at elevated temperatures. New work being initiated will also include similar studies on the commercial, the developmental and the fundamental alloys being evaluated in the National Alloy Developmental Program with particular attention on the application of a hot-hardness tester as a strength microprobe. Special consideration is being given to operating conditions typical of nuclear reactor applications, including the knowledge that the radiation environment can influence the substructure of these metals, a circumstance which can lead to significant changes in the conventional mechanical property behavior.

7.1.2 Experimental Program

Transmission electron microscopy has been used to study the deformation substructure resulting from creep, fatigue and tensile deformation at elevated temperatures. The dis-

location substructure has been characterized for the creep and tensile tested specimens from the ORNL reference heat 9T2796 (1 inch plate) of AISI 304 stainless steel. The influence of the dislocation substructure along with the presence of second phase carbides on the deformation behavior is being studied. The results for the relationship of deformation rate, stress and temperature for 304 stainless steel at elevated temperature are presented. This analysis explicitly involves a substructural parameter viz., λ the cell or subgrain dimension. The dislocation substructure that is developed in a special series of specimens of 304 stainless steel (change in stress program) is also being evaluated. The results are presented. The test data is again being analyzed in the light of the substructure and the results will be reported later.

Work on the substructural evaluation in Incoloy 800 tested in the fatigue mode at elevated temperature is nearing completion. Analysis of some of the substructure data observed in Incoloy 800 push pull fatigue specimens are presented and discussed in terms of the existing theories.

7.1.2.1 Analysis of Relationships of Deformation Rate, Stress and Temperature for 304 Stainless Steel (R. K. Bhargava)

In order to understand the deformation behavior of 304 stainless steel at elevated temperatures in the light of

the substructure the tensile and creep test data (ORNL data as reported by R. W. Swindeman, ORNL Metals and Ceramics Division) have been analyzed. The dislocation substructure that is developed in the tensile and creep tested specimens has been evaluated by TEM and the results have been presented in the previous quarterly progress reports[1]. A detailed description of the dislocation substructure is also available elsewhere[2]. The analysis of the various relationships of deformation rate, stress and temperature for 304 stainless steel (reference heat 9T2796) had been initiated earlier and some of the results were also reported before[3].

In Fig. 7.1 the deformation rate, $\dot{\varepsilon}$ (minimum creep rate for creep tests and the nominal strain rates in the tensile tests), at various temperatures has been plotted versus the modulus compensated true stress parameter, σ_T/E on a ℓn-ℓn scale. Fig. 7.2 shows a plot of the temperature compensated deformation rate, Z and the modulus compensated true stress parameter, σ_T/E on a ℓn-ℓn scale. The power law

$$\dot{\varepsilon} = A(\sigma_T/E)^n \exp(-Q_c/RT) \qquad [7.1]$$

with n=7 and Q_c = 85,000 cals/mole describes the rate-stress relationship at lower stress values for all temperatures. The value of n starts to increase from 7 at σ_T/E values in the range of 1.5×10^{-3} to 2.0×10^{-3} for different temperatures. The behavior at very high strain rates and lower temperatures has been discussed before[3,4] in the light of

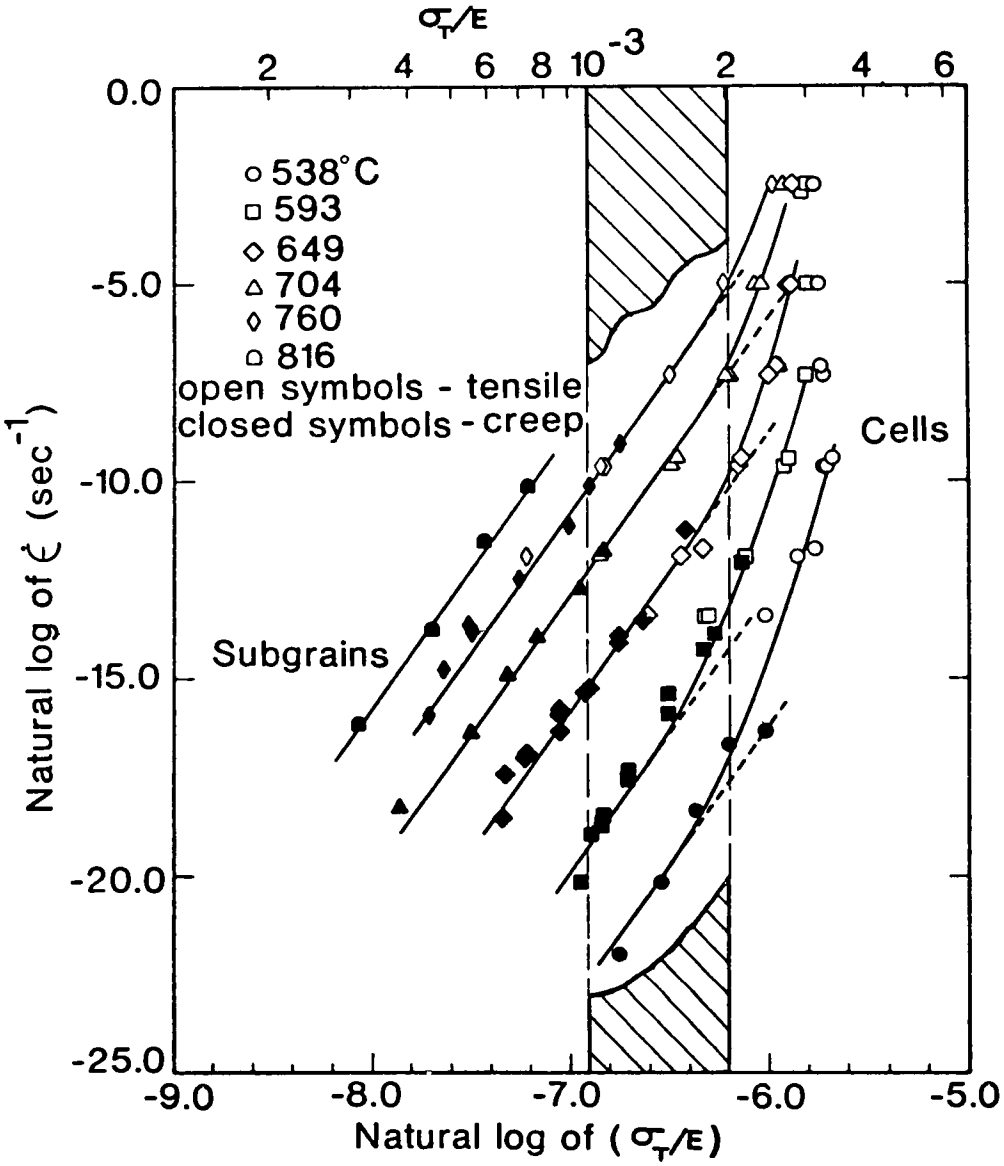

Fig. 7.1. Plot of the Natural Log of the Deformation Rate, $\dot{\varepsilon}$, vs. the Natural Log of the Modulus Compensated Stress, σ_T/E. (AISI 304 SS, Reference Heat 9T2796).

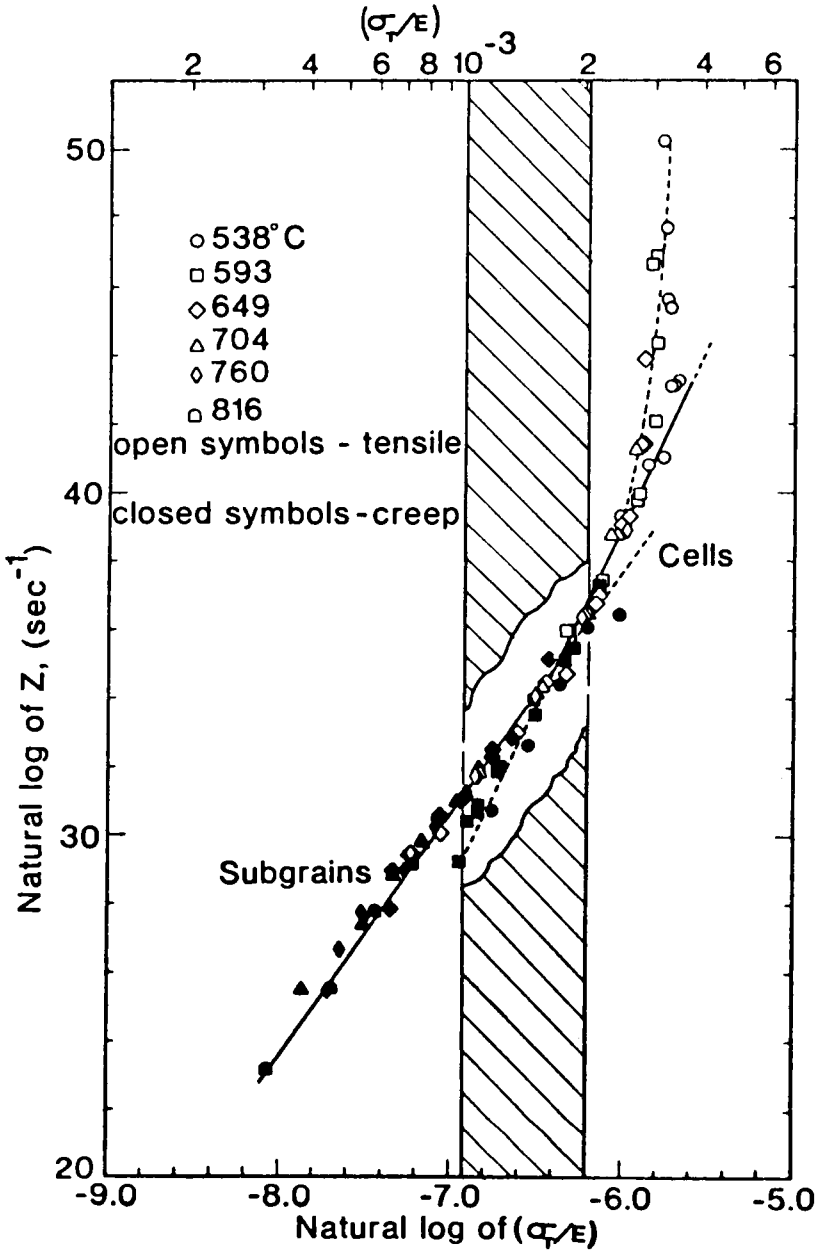

Fig. 7.2. Plot of the Temperature Compensated Deformation Rate, Z, vs. the Modulus Compensated Stress σ_T/E, on a ℓn - ℓn Scale. (AISI 304 SS, Reference Heat 9T2796).

the dislocation substructure. For most of the data, if the power law is assumed to be followed at higher stresses ($\sigma_T/E > 1.9 \times 10^{-3}$), the value of n lies between 10 and 11 (Fig. 7.2).

Cuddy[5] and Yu[6] have reported that for type 304 stainless steel the value of the stress exponent, n, ranges between 5 and 13. For pure metals and solid solution alloys where subgrains form during creep, the value of n usually lies between 4 and 5. Higher values of n have also been observed for tungsten[7] and aluminum[8,9]. Sherby and co-workers[7,9] have suggested an explanation for the high value of n by explicitly incorporating the influence of subgrains in the creep deformation equations. A similar approach is utilized in the following explanation of the results of the present study.

Creep rate at a constant temperature is given by

$$\dot{\varepsilon}_s = \text{Constant } \lambda^p \sigma^N \qquad [7.2]$$

where λ is the subgrain size, N is the stress exponent determined from differential tests where λ and T are kept constant and p is usually 2 or 3. According to a model of subgrain creep wherein pile ups of dislocations were considered to interact with subgrain boundaries, Weertman[10] arrived at the equation

$$\dot{\varepsilon}_s = \text{Constant} \cdot \lambda^3 \cdot (\sigma/G)^6 \qquad [7.3]$$

where G is the shear modulus.

In the light of the substructure that is developed, the deformation rate - stress relationship for the present result is adequately described by

$$\dot{\varepsilon}_s = \text{Constant } \lambda^3 \cdot (\sigma_T/E)^n \exp \frac{85,000}{RT} \qquad [7.4]$$

where n=7 at σ_T/E values lower than about 1.9×10^{-3} and n=10.5 for $\sigma_T/E > 1.9 \times 10^{-3}$. At lower stress levels where the subgrain size, λ, is given by

$$\lambda = 6.6b \ (\sigma_T/E)^{-1} \qquad [7.5]$$

the value of n becomes 4 and at higher stress levels where the λ - σ_T/E relation is given by

$$\lambda = 1.4 \times 10^{-2} \ b \ (\sigma_T/E)^{-2} \qquad [7.6]$$

n in Eq. [4] reduces to 4.5.

The value of n after considering the influence of subgrain or cells reduces from 7 or 11 to 4 or 4.5 and agrees very well with the usually observed values for the stress exponent during power law creep[11].

7.1.2.2 Change in Stress Experiments on 304 Stainless Steel, Reference Heat 9T2796 (R. K. Bhargava)

A set of stress change creep tests were performed at 650°C and the test matrix and the resulting creep rates were reported previously[12]. The dislocation substructure developed in the specimens during the stress change experiments

was evaluated by transmission electron microscopy. The various substructural features are shown in Figs. 7.3 thru 7.7 and the substructural data is listed in a table[2]. The specimen RP 303 which was in the test for about 110 hours showed ample evidence of carbide precipitation. The $M_{23}C_6$ type of precipitate was formed along the grain boundaries as well as within the grains. At many places, the dislocation interactions with the precipitate particles were observed (see Figs. 7.3(b) and 7.4(b)). In the rest of the specimens, there was very little evidence of the carbide phase because of the shorter durations of the tests. The test times ranged from 2 hours to 27 hours for these specimens.

The typical cell substructure developed in specimens RP 301, RP 303, RP 314 and RP 313 are shown in Fig. 7.3. Most of the dislocations within the cells as well as within the cell walls were resolved. Fig. 7.4 shows the dislocation arrangements for these specimens which were used to determine the dislocation density. Fig. 7.5 shows the cell structure developed in specimens RP 306, RP 304, RP 307 and RP 305. The cell structure of these specimens is very similar to the ones developed in the UC heat creep tests in the secondary stage[2,12]. The dislocation arrangements for these specimens are shown in Fig 7.6. The substructure developed in these specimens also showed some pile ups of dislocations. A good example of such pile ups was observed

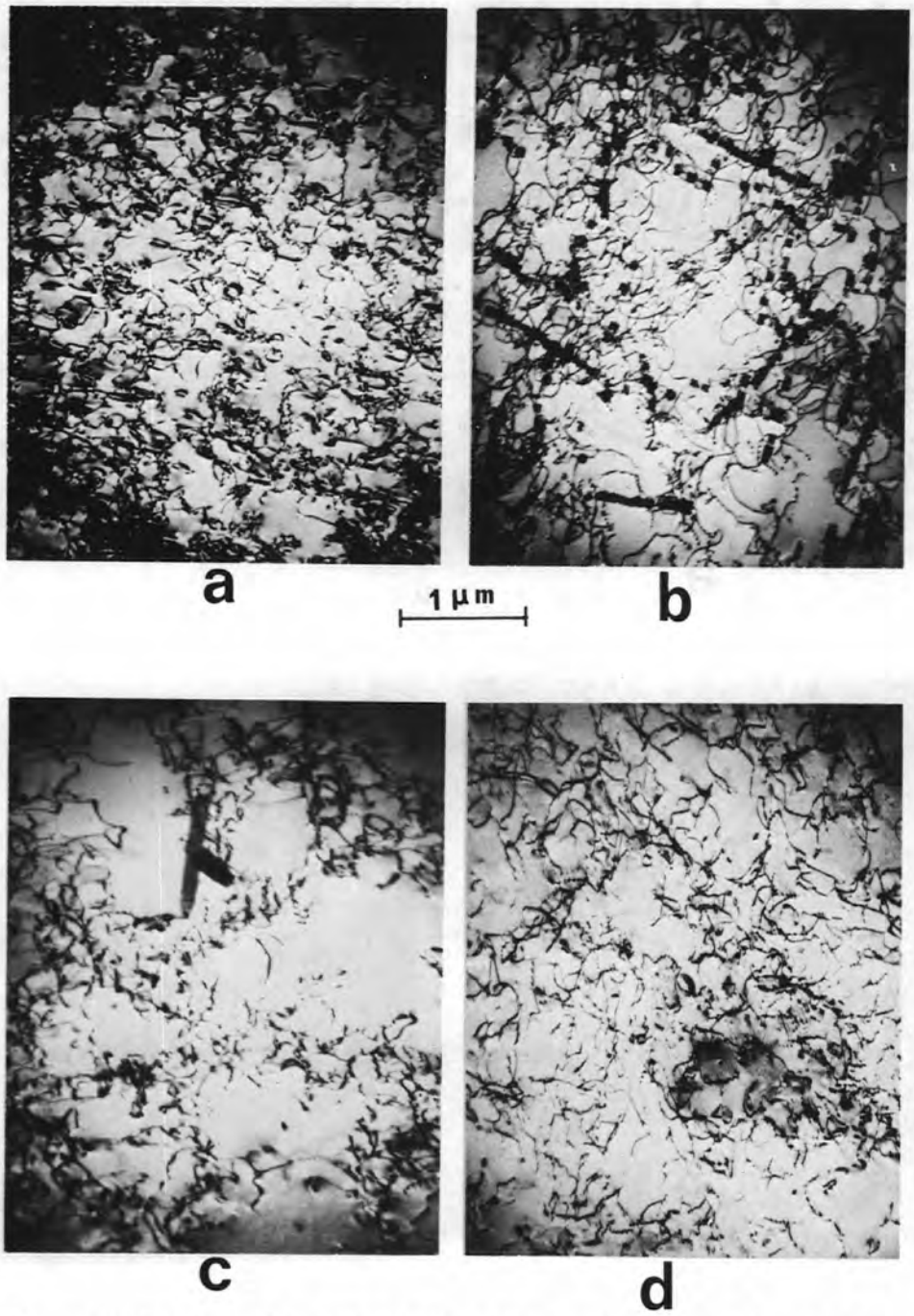

Fig. 7.3. Typical Cell Substructure Developed in Creep Tested AISI 304 SS (Heat 9T2796) at 650°C (a) 17.58 $kg \cdot mm^{-2}$; (b) 17.58→14.06 $kg \cdot mm^{-2}$; (c) 17.58→11.85 $kg \cdot mm^{-2}$; and (d) 17.58→10.42 $kg \cdot mm^{-2}$.

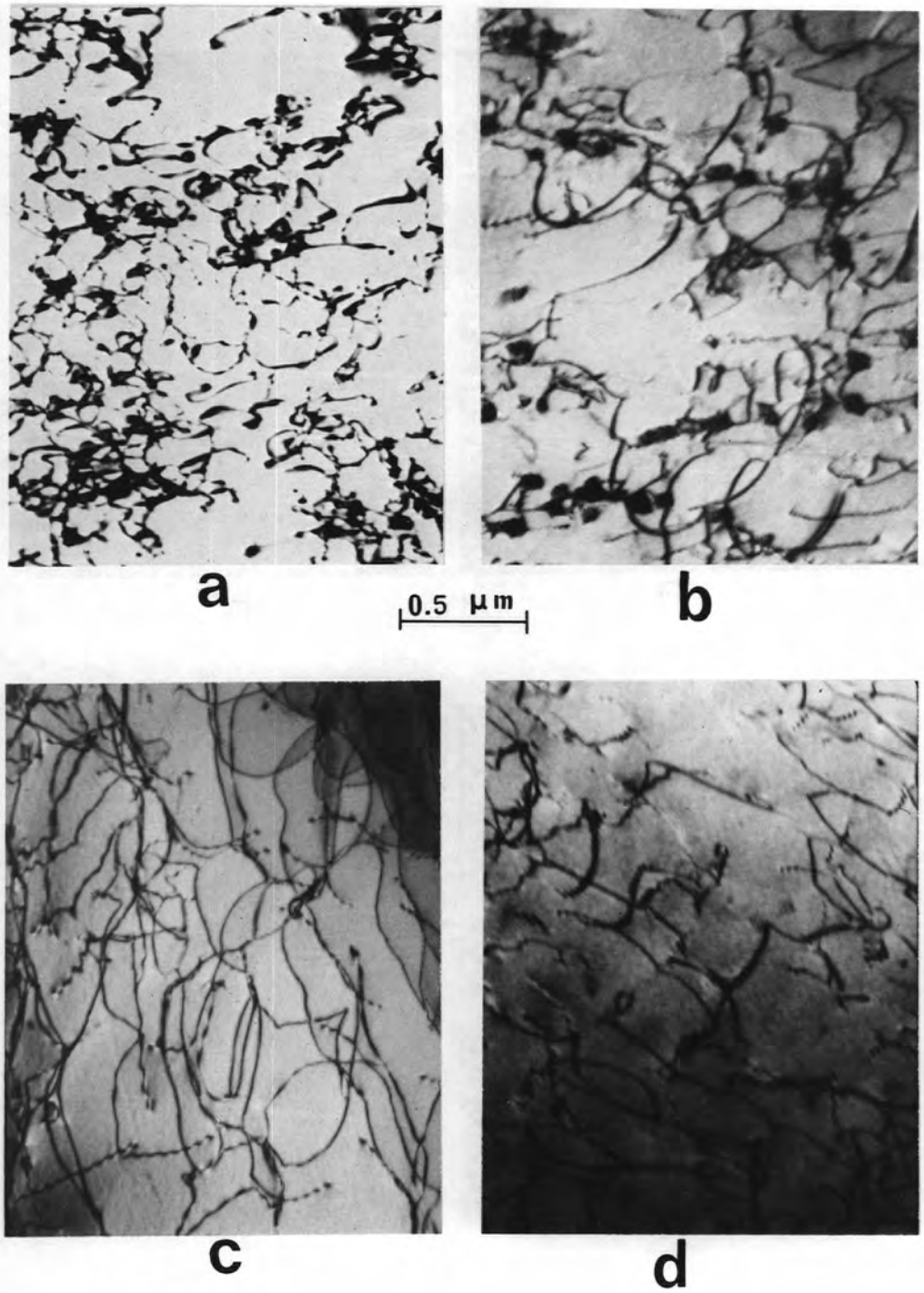

Fig. 7.4. Typical Dislocation Arrangements in AISI 304 SS (Heat 9T2796) During Creep at 650°C (a) 17.58 $kg \cdot mm^{-2}$; (b) 17.58→14.06 $kg \cdot mm^{-2}$; (c) 17.58→11.85 $kg \cdot mm^{-2}$; and (d) 17.58→10.42 $kg \cdot mm^{-2}$.

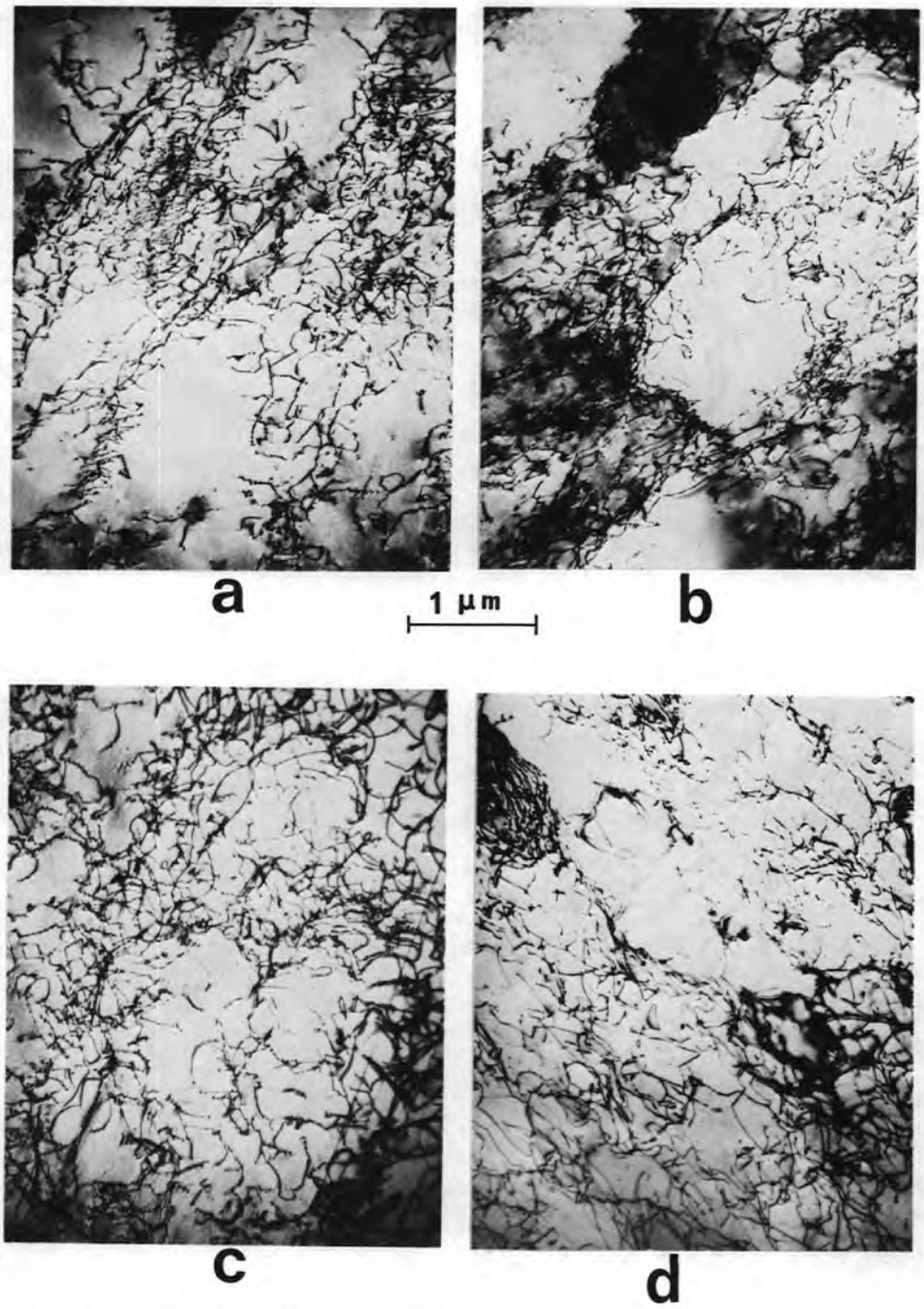

Fig. 7.5. Typical Cell Substructure Developed in Creep Tested AISI 304 SS (Heat 9T2796) at 650°C (a) 21.09→15.36 $kg \cdot mm^{-2}$; (b) 21.09→14.06 $kg \cdot mm^{-2}$; (c) 21.09→10.03 $kg \cdot mm^{-2}$; and (d) 21.09→6.88 $kg \cdot mm^{-2}$.

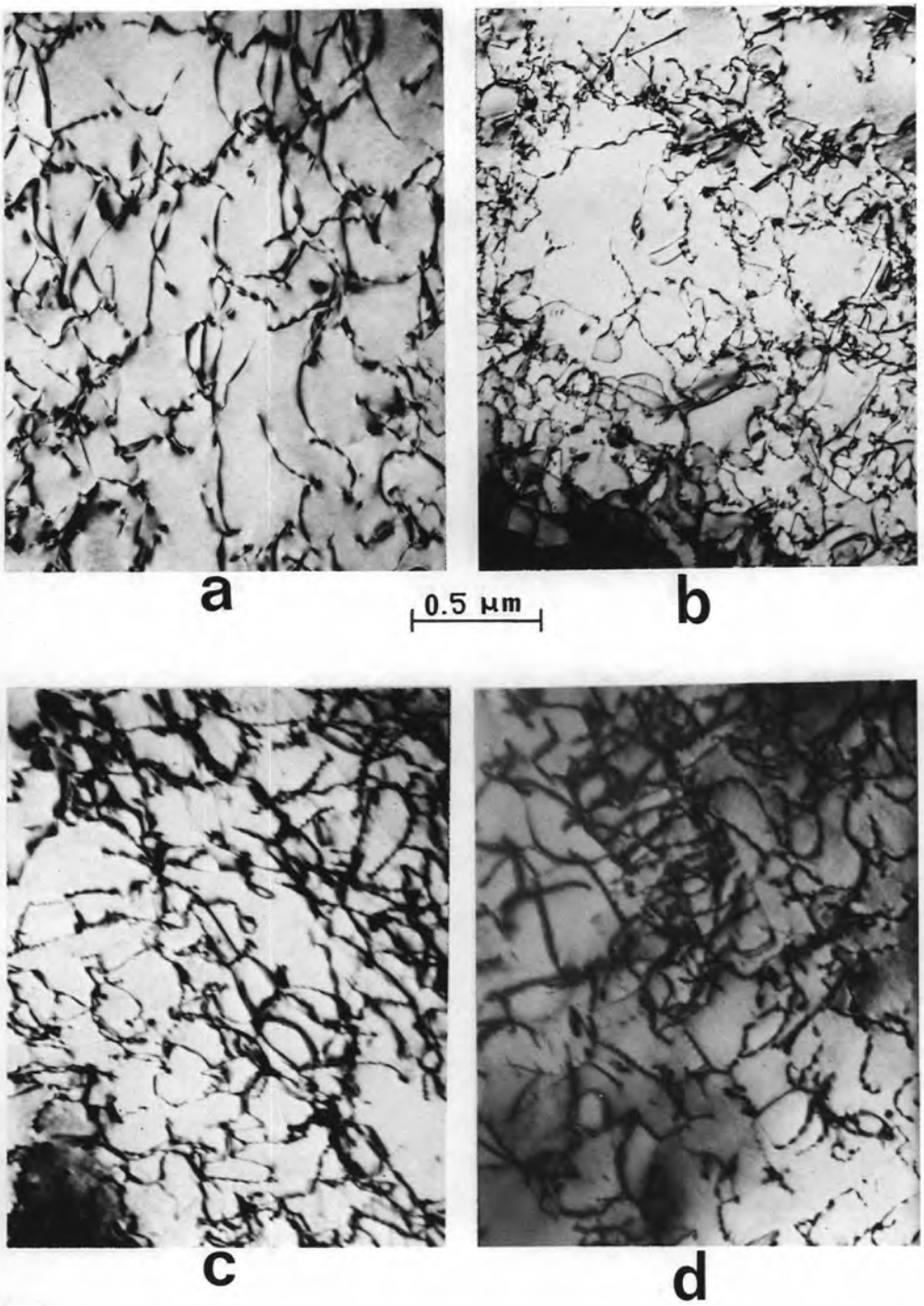

Fig. 7.6. Typical Dislocation Arrangements in AISI 304 SS (Heat 9T2796) During Creep at 650°C (a) 21.09→15.36 $kg \cdot mm^{-2}$; (b) 21.09→14.06 $kg \cdot mm^{-2}$; (c) 21.09→10.03 $kg \cdot mm^{-2}$; and (d) 21.09→6.88 $kg \cdot mm^{-2}$.

in specimen RP 314 and is shown in Fig. 7.7. Some of the dislocations lying in the pile ups are split into partials and the stacking faults are also visible. The thickness of the foil is increasing from right to left as indicated by the increasing width of the slip traces. The wavy contrast of the dislocations near the foil surfaces are also depicted in this figure. A partial pile up of dislocations is also visible in Fig. 7.6(d).

The cell intercept size, λ, the dislocation density, ρ, and the misorientation angle, θ, determined from these specimens have been reported elsewhere[2]. The cell size determined from these tests is indicative of the stress levels before the change and the dislocation density also follows a similar behavior. Such behavior shows that for the relatively short times after the changes in stress, the substructure essentially remains unchanged.

Based on the dislocation substructure, the creep behavior subsequent to the changes in stress is being further analyzed and the results will be reported in future progress reports.

7.1.2.3 Critical Dislocation Density for Subboundary Formation in Fatigue of Incoloy 800 (H. Nahm)

A concept of cell formation is that dislocations are being generated as the deformation proceeds, until the critical stage where the cell starts to form to reduce the elastic energy of dislocation[13,14]. The elastic strain energy of unit length of dislocation, E, that does not itself

Fig. 7.7. Photo Micrograph Depicting the Pile Ups of Dislocations Observed in Creep Tested AISI 304 SS at 650°C, 17.58→ 11.85 $kg \cdot mm^{-2}$.

set up any long-range stress field is approximately given by[14],

$$E = \frac{Gb^2}{4\pi(1 - 0.5\nu)} \ln \frac{R}{r_o} \qquad [7.7]$$

where G is the shear modulus, b is the Burgers vector, ν is the Poisson's ratio, R is the average distance between dislocation, r_o is the dislocation core radius. Any dislocation interaction resulting in the reduction of R will reduce E which suggests that subboundary formation is the recovery process.

Thus, the driving stress, τ_D, for subboundary formation is

$$|\tau_D| = \frac{1}{b}\frac{\delta E}{\delta R} = \frac{Gb}{4\pi(1 - 0.5\nu)R} \qquad [7.8]$$

R is a function of dislocation density, viz, $R = 1\sqrt{\rho}$. It has been shown that a critical dislocation density for cell formation exists. The only requirement is that sufficient mobility should be provided to the dislocation rearrangement process either by glide, cross-slip and/or climb. It is, therefore, expected that the critical dislcoation density for cell formation is strongly temperature dependent.

The Incoloy 800 push-pull fatigue specimens used in this investigation were tested at 538, 649, 704, and 760°C in air with the cyclic strain rates of 4×10^{-3} and 4×10^{-4} sec^{-1}. Properties determined from these tests, such as the cyclic stress-strain behavior and the fatigue life have been published

by Conway et. al.[15,16]. Thirty-two specimens were selected for TEM observations.

As expected, not all specimens showed cells or subgrains. The propensity for subboundary formation was found to be increasing with increasing test temperature and strain range. In most cases of specimens in which subboundaries were observed, the subboundary formation was found to be a local phenomenon. The proportion of the volume occupied by the subboundary appears to increase with increasing strain range, temperature and testing time. Cells or subgrains start to form near triple junctions, large angle grain boundaries, or annealing twin boundaries, and then spread toward the interior of the grain. Fig. 7.8 illustrates the variation in dislocation structure that was found in specimen #2N14 of Incoloy 800. Fig. 7.8(a) shows the distinct subgrain formation, Fig. 7.8(b) the well defined cells, Fig. 7.8(c) the planar bands of dislocations and Fig. 7.8(d) the free dislocations.

The mobile or free dislocation density in this study was evaluated from regions where the subboundaries were absent. Care should be taken in comparing these dislocation density values with those of other investigators where the mobile dislocation density often means the density inside the subgrains. The dislocation density was measured from areas with no subboundaries because: (a) the critical dislocation density for cell formation can be obtained there, and (b) the subgrain interior is almost free from dislocations in most fatigue

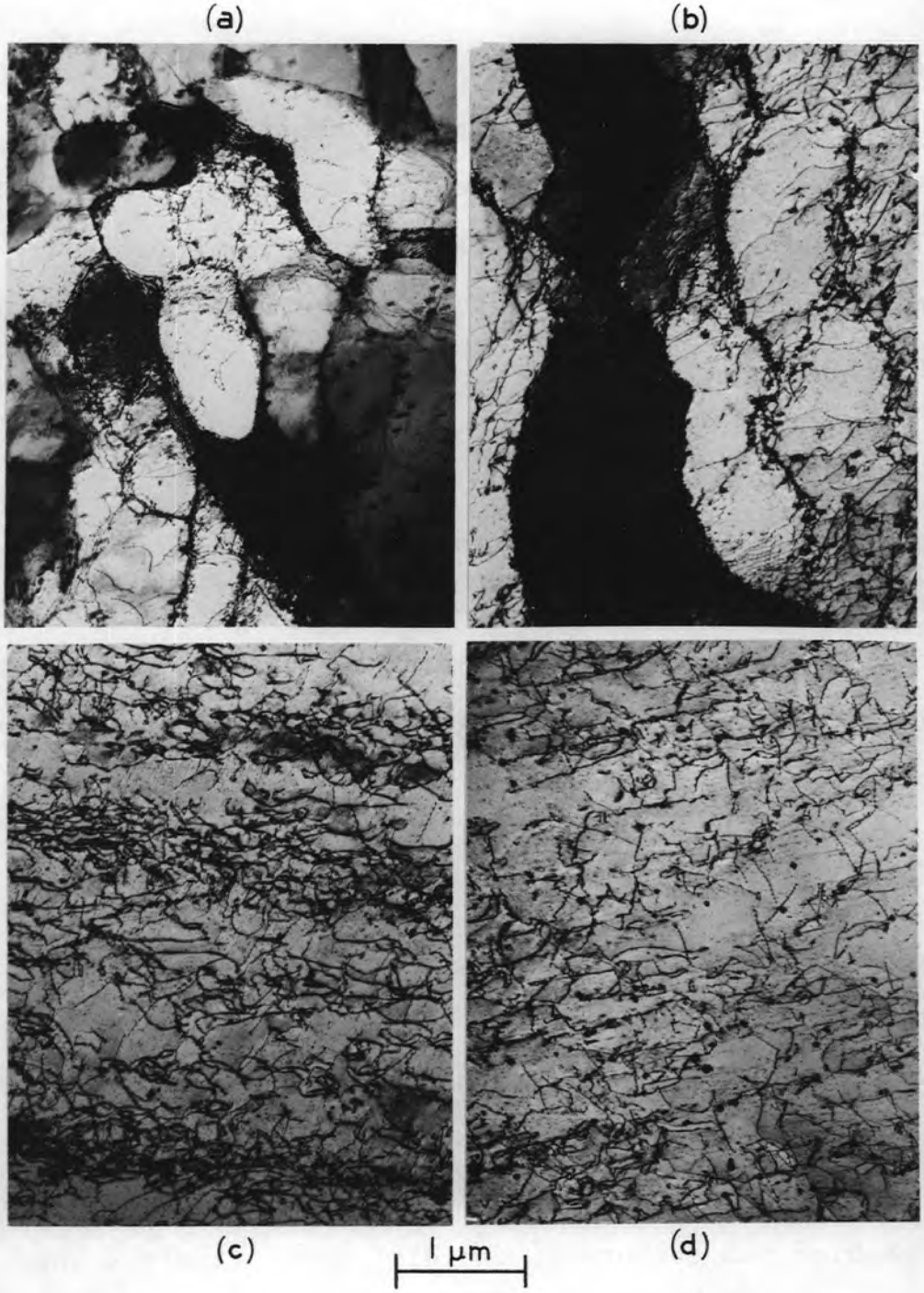

Fig. 7.8. Fatigue Substructure Variation in One Specimen 2N14 of Incoloy 800 at 649°C.

specimens.

The square root of dislocation density versus the testing temperature for Incoloy 800 is plotted in Fig. 7.9. It is evident that the critical density for subboundary formation, ρ_c, is proportional to the square of the absolute temperature,

$$\rho_c \propto 1/T^2 \qquad [7.9]$$

This strongly suggests that the subboundary formation is a thermally activated recovery process. The present result given by Equation [7.9] is consistent with the theoretical expression for creep deformation process developed by Karashima et. al.[17],

$$\rho_c = \left(\frac{\tau}{\alpha T}\right)^2 \qquad [7.10]$$

where τ is the applied stress, T is the temperature and α is a constant.

7.1.2.4 Some Aspects of Dislocation Mechanisms During High Temperature Fatigue of Incoloy 800 (H. Nahm)

In an effort to understand the deformation mechanisms in the high temperature creep, dislocation substructure was evaluated in terms of the dislocation density forming the subboundary, ρ_{SB} and the dislocation density in the subgrain, ρ_m[18,19]. It has been found that the ratio of ρ_{SB} to ρ_m is independent of applied stress and strain once steady state creep stage is reached.

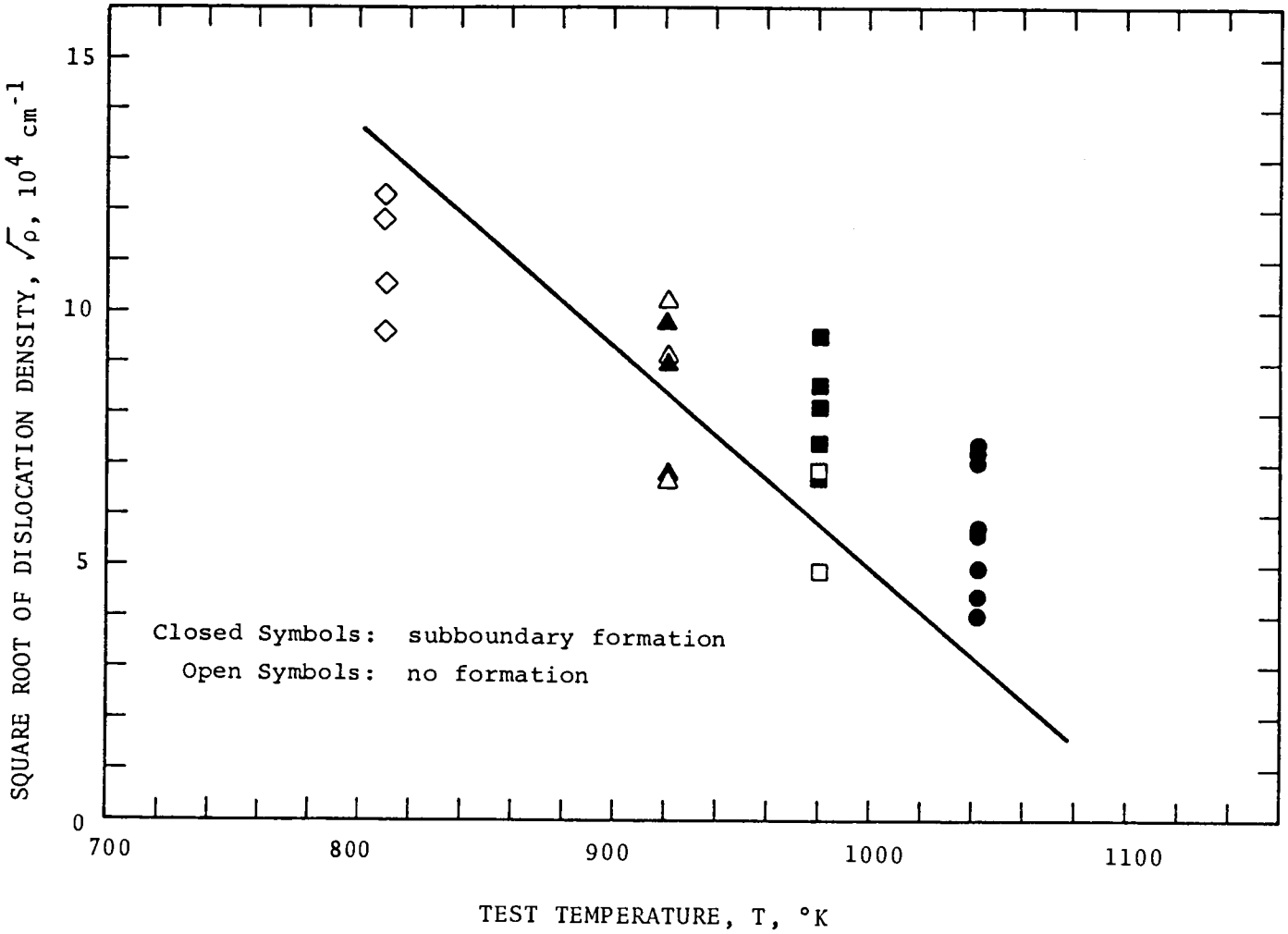

Fig. 7.9. Plot of the Square Root of Dislocation Density, $\sqrt{\rho}$, Versus the Test Temperature, T, for Incoloy 800.

Similar to the approach taken previously[18,19], the dislocation density within the subboundaries, ρ_{SB}, for Incoloy 800 can be estimated from the relation,

$$\rho_{SB} = \frac{3\theta}{b\lambda'} \qquad [7.11]$$

where b is the Burgers vector, θ is the average misorientation angle between adjacent subgrains in radians and λ' is the subgrain diameter. The experimental details and the nature of misorientation between subgrains were presented in the previous report[20].

The misorientation angle between adjacent cells or subgrains, θ, as a function of subboundary intercept size, λ, for Incoloy 800 is plotted in Fig. 7.10. As indicated in this figure, the misorientation is independent of the subgrain intercept size. It is also found that the misorientation is not a function of any of the parameters evaluated such as the stress or the strain ranges.

Fig. 7.11 shows a plot of the ratio, ρ_{SB}/ρ, versus the modulus compensated saturation shear stress τ_s/G for Incoloy 800. The ratio for AISI 316 stainless steel[18] in creep is included in this figure. The present results show that the boundary dislocation density, ρ_{SB}, is 1.5 times the free dislocation density, ρ. This is in reasonable agreement with a value of 2.1 for creep in AISI 316 stainless steel[18]. It can be concluded that the ratio, ρ_{SB}/ρ, is independent of the saturation stress and the strain range during saturation stage

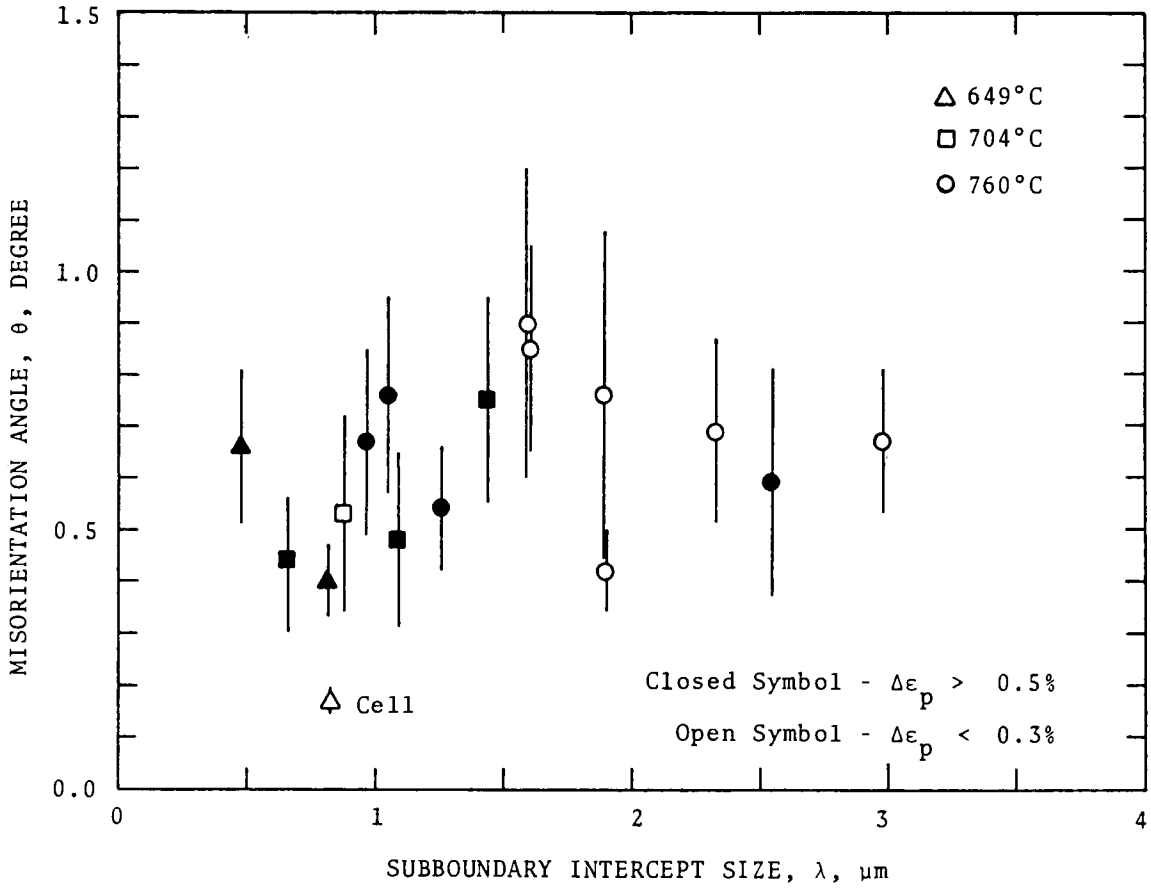

Fig. 7.10. The Misorientation Angle Between Adjacent Cells or Subgrains, θ, as a Function of the Subboundary Intercept Size for Incoloy 800.

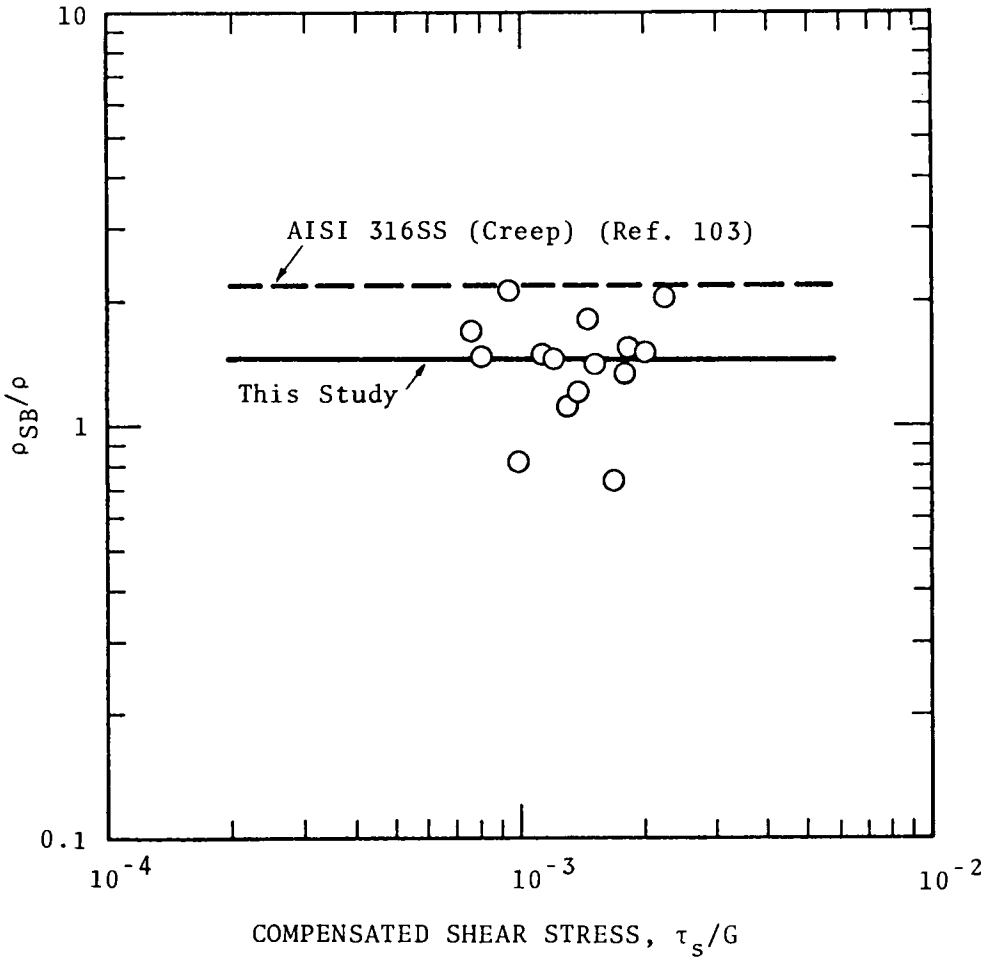

Fig. 7.11. The Ratio of the Dislocation Density of the Subboundary to the Free Dislocation Density, ρ_{SB}/ρ, as a Function of the Shear Modulus Compensated Saturation Shear Stress, τ_s/G for Incoloy 800.

of fatigue in Incoloy 800. This conclusion is consistent with the observation in unidirectional deformation where a value of five (ρ_{SB}/ρ) for copper by Bailey and Hirsh[21] and iron by Keh and Weissman[22] has been reported. Orlova and Cadek[19] observed a value of approximately 1 for α-Zirconium, approximately 8 for Aluminum and values between 8 and 12 for alpha-iron.

The fact that ρ_{SB}/ρ is independent of stress and strain during fatigue suggests that the dislocations forming the low angle boundaries might be responsible for the saturation stress. Feltner and Laird[23] proposed that the stress necessary for dislocations to bow out between the dislocation network of a cell boundary is responsible for the stress during the saturation stage, which is based on Kuhlmann-Wilsdorf's unidirectional workhardening theories for stage II[24] and III[13]. Hence, the saturation shear stress, τ_s, is given by an equation

$$\tau_s = \frac{Gb}{\alpha\ \ell_{SB}} \qquad [7.12]$$

where G is the shear modulus, b is the Burgers vector, α is a constant with a value of ∿ 3 and ℓ_{SB} is the mesh length of dislocation network in the subgrain boundary. The ℓ_{SB} was evaluated by using the relationship,

$$\ell_{SB} = \frac{1}{\sqrt{\rho_{SB}}} \qquad [7.13]$$

where ρ_{SB} was calculated from the equation [7.11]. The

modulus compensated saturation shear stress, τ_s/G, versus the mesh length in subboundary dislocation network, ℓ_{SB}, is plotted in Fig. 7.12. Reasonable agreement with the theory is obtained, considering the variance in experimental observations of the misorientation angle and the assumptions in Equation [7.11] that were needed to calculate the dislocation density necessary to form the subgrain boundary.

7.1.3 References

1. ORNL - 5106, "Mechanical Properties Test Data for Structural Materials", Quarterly Progress Report for Period Ending July 31, 1975, pp. 257-286.

2. R. K. Bhargava, Ph.D. Dissertation, 1975, University of Cincinnati.

3. ORNL - 5104, "Mechanical Properties Test Data for Structural Materials", Quarterly Progress Report for Period Ending January 31, 1975, pp. 299-322.

4. R. K. Bhargava, R. W. Swindeman, and J. Moteff, "Correlation of the Mictostructure with the Creep and Tensile Properties of AISI 304 Stainless Steel", paper to be presented at the ASME Winter Annual Meeting, Houston, Texas, December 1975.

5. L. J. Cuddy, Met. Trans., Vol. 1, 1970, pp. 640-647.

6. C. C. Yu, M.S. Thesis, 1973, University of Cincinnati.

7. S. L. Robinson and O. D. Sherby, Acta Met., Vol. 17, 1969, pp. 109-125.

8. S. K. Mitra and D. McLean, Met. Sci. J., Vol. 1, 1967, pp. 192-198.

9. S. L. Robinson, C. M. Young and O. D. Sherby, J. Mater. Sci., Vol. 9, 1974, pp. 341-343.

10. J. Weertman, "High Temperature Creep Produced by Dislocation Motion", presented at John Dorn Memorial Symposium, Cleveland, Ohio, October 1972.

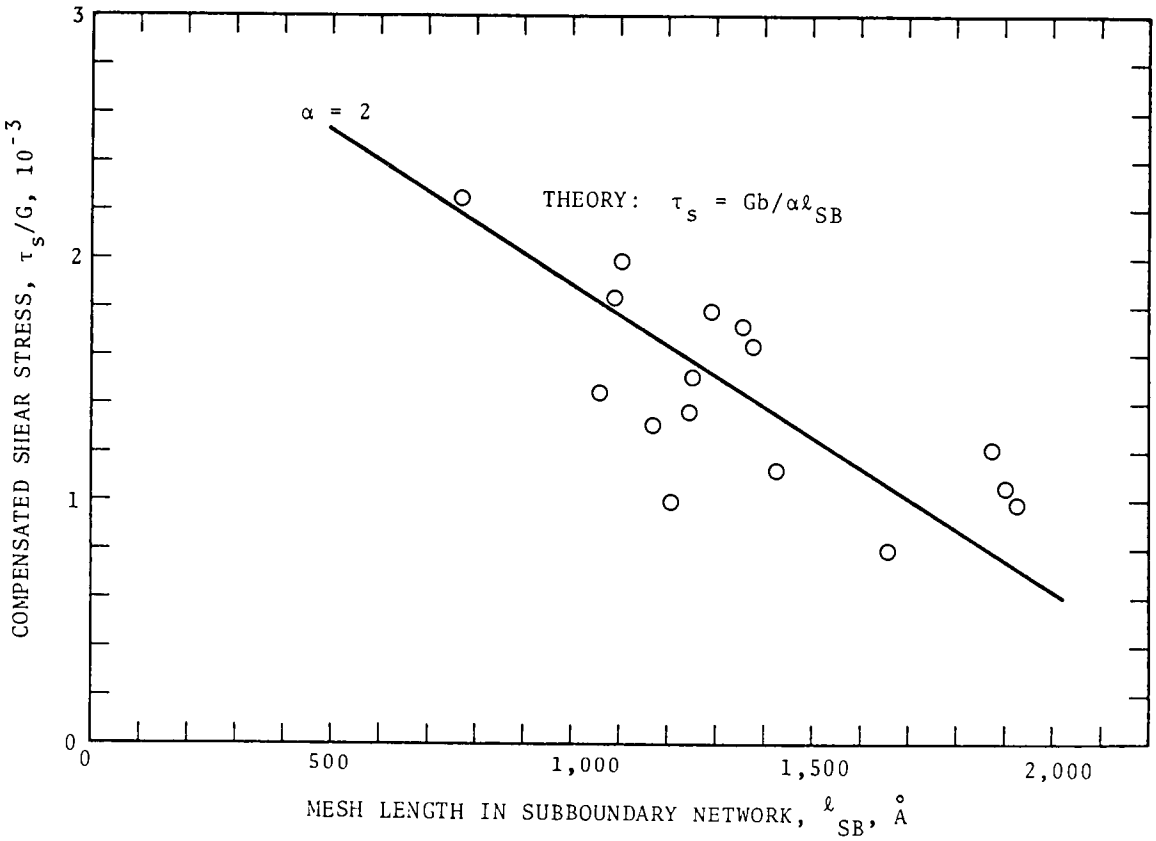

Fig. 7.12. Plot of the Modulus Compensated Saturation Stress, τ_s/G, Versus the Mesh Length of Subboundary Dislocation Network, ℓ_{SB}, for Incoloy 800.

11. O. D. Sherby and P. M. Burke, Progress in Mat. Sci., Vol. 13, 1968, pp. 235-390.

12. ORNL - 5105, "Mechanical Properties Test Data for Structural Materials," Quarterly Progress Report for Period Ending April 30, 1975, pp. 324-329.

13. D. Kuhlmann-Wilsdorf, in "Work Hardening", Gordon & Breach (1968) 97.

14. H. D. Nine and D. Kuhlmann-Wilsdorf, Can. J. Phys., 45 (1967) 865.

15. J. B. Conway, J. T. Berling and R. H. Stentz, Met. Trans., 3 (1972) 1633.

16. J. B. Conway, General Electric Company, Nuclear Systems Programs, Cincinnati, Ohio, Rep. No. GEMP-732, 1969.

17. S. Karashima, K. Murayama and N. Ono, Trans. J.I.M. 15 (1974) 265.

18. V. K. Sikka, H. Nahm, and J. Moteff, Mat. Sci. Eng., 20 (1975) 55-62.

19. A. Orlová and J. Čadek, Phil. Mag., 28 (1973) 891.

20. ORNL - 5105, "Mechanical Properties Test Data for Structural Materials", Quarterly Progress Report for Period Ending April 30, 1975, pp. 324-329.

21. J. E. Bailey and P. B. Hirsh, Phil. Mag., 5 (1960) 485.

22. A. S. Keh and S. Weissman, "Electron Microscopy and Strength of Crystals", Edited by G. Thomas and J. Washburn, Interscience, New York, (1963) 231.

23. C. E. Feltner and C. Laird, Acta Met., 15 (1967) 1633.

24. D. Kuhlmann-Wilsdorf, Trans. AIME, 224 (1962) 1047.

7.2 UNIVERSITY OF CALIFORNIA, LOS ANGELES - K. Ono, A. J. Ardell and A.S. Tetelman

7.2.1 Mechanical Properties Evaluation of Carburized Type 304 Stainless Steel (P. L. Jones and A.S. Tetelman)

This research program is designed to provide a basic understanding of the effects of surface carburization on the elevated temperature mechanical behavior of Type 304 SS. The basic research has been divided into two parts: 1) evaluation of short-term mechanical and fracture behavior; and 2) characterization of the time dependent mechanical behavior and corresponding changes in microstructure, crack growth rate and fracture behavior. Until now, work has been focussed on the first part of the research program with the results presented in previous reports. During the past quarter work has been initiated on the second portion of the research program. A clip gauge displacement technique has been successfully used to accurately determine crack depths in surface flawed Type 304 SS sheet specimens.

Sheet tensile specimens were machined from well characterized Type 304 SS obtained from Atomics International, Canoga Park, California. This steel, Reference Heat No. 72S35, was produced by the Eastern Stainless Steel Company, Baltimore, Maryland.

The as-received 0.125 in. sheet material was sheared into blanks 1.5 in. x 6 in., and machined to the final specimen geometry as

given in Fig. 1. Specimen thickness was chosen as 0.100 ± 0.005 in. in order to simulate potential crack growth in IHX piping. The part-through center notch was machined to a depth of 0.010 ± 0.001 in. using a 0.25 in. mill cutter, yielding an initial flaw aspect ratio, a/2C, of 0.10. An enlargement of the notch geometry is shown in Fig. 2.

In order to induce sharp cracks of varying lengths, a Krauss eccentric cam cantilever beam fatigue machine was modified to produce a fatigue crack. The specimens were cyclically loaded in bending using a zero-tension load cycle on the notched face. A range of crack lengths was obtained by varying the number of cycles.

An elastic compliance technique similar to that discussed by R.M. Ehret (Tech. Rep. SD71-329, Rockwell International Space Division, October 1971) was used to generate clip gauge displacement vs. load curves for each cracked specimen. Knife edges were mounted on each side of the flaw with Aron Alpha quick setting adhesive. Clip gauge displacement vs. load curves were obtained using an MTS clip gauge with a 0.150 in. gauge length in conjunction with a Sanborn amplifier and an Instron tensile testing machine. To prevent the possible effects of strain hardening, loading was confined to the elastic range. Specimens were then heat-tinted and fatigued until complete separation. Crack lengths, **a** , were then measured to the nearest 0.01 mm using a traveling microscope and the results compared to the corresponding modified slope of the clip gauge displacement vs. load curve.

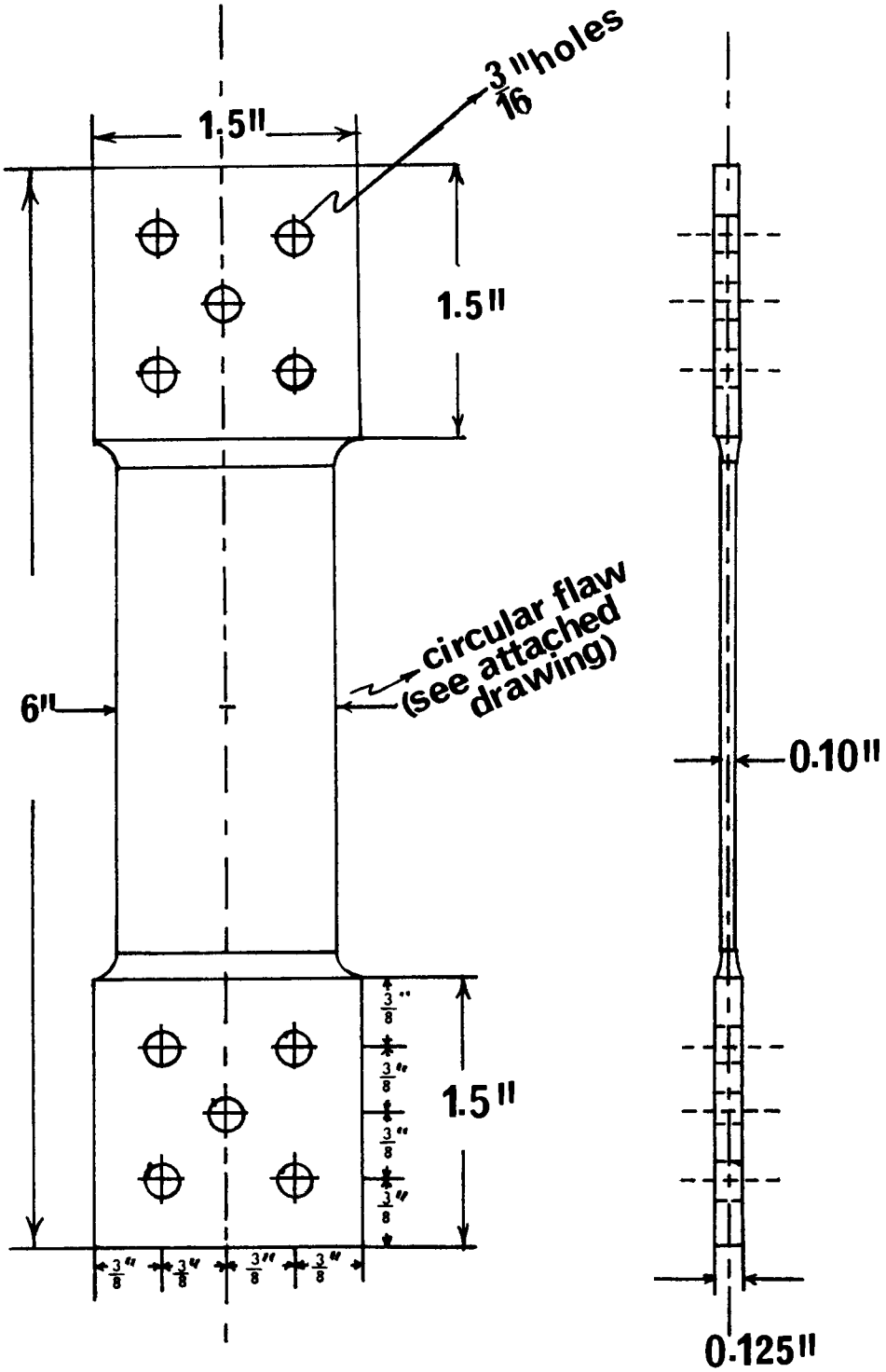

FIG. 1 SPECIMEN CONFIGURATION

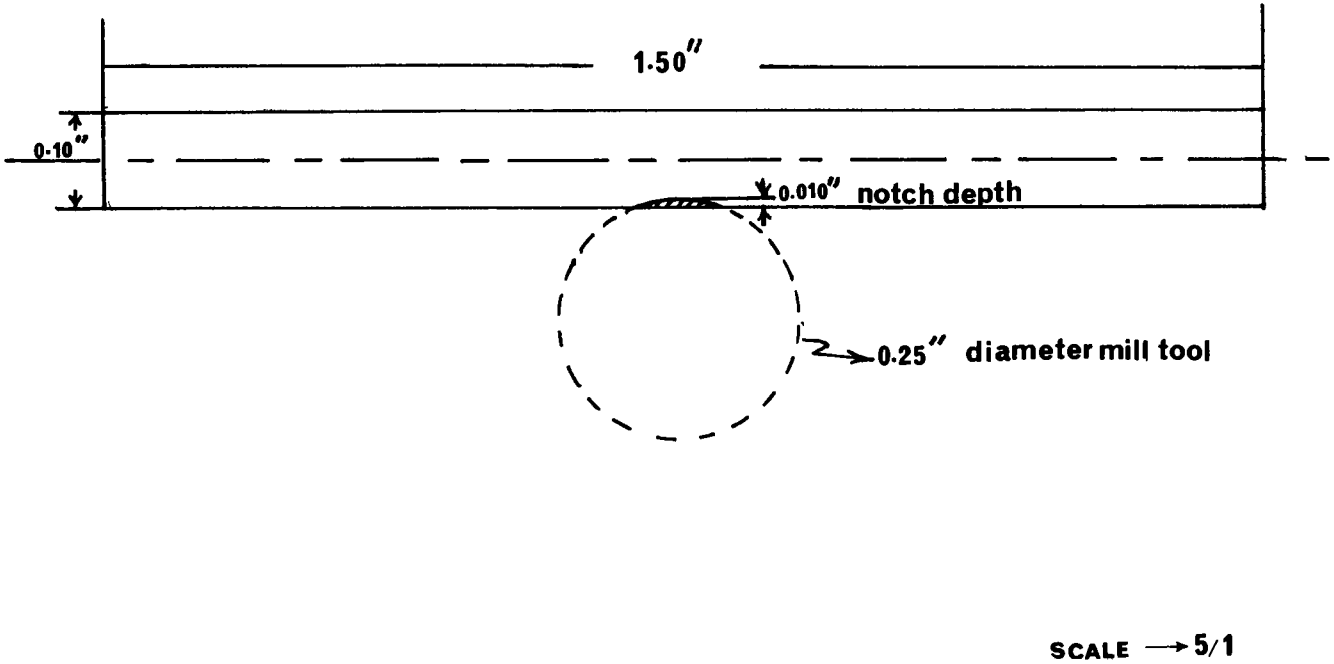

FIG. 2 NOTCH GEOMETRY

The results are shown on a semi-log plot in Fig. 3 where the modified slope of the clip gauge displacement vs. load curve, which we shall call normalized compliance, is plotted against the corresponding crack length **a**. We defined the normalized compliance, γ_{NORM}, as

$$\gamma_{NORM} = \frac{CGD}{L} \cdot E \cdot A = \frac{CGD}{\sigma} \cdot E$$

where CGD/L is the slope of the clip gauge displacement vs. load curves, E is Young's modulus, and A is the cross-sectional area of the specimen. The only purpose of multiplying by Young's modulus is to simplify the graphical presentation of the results. As can be seen, the correlation between normalized compliance and crack length is extremely good. The maximum absolute error is less than 0.002 in., which corresponds to an error of less than 5% of the crack length in question. Thus, we have demonstrated an accurate nondestructive method of obtaining the length of a part-through crack in relatively thin surface flawed specimens. This technique will be used in all subsequent crack growth experiments.

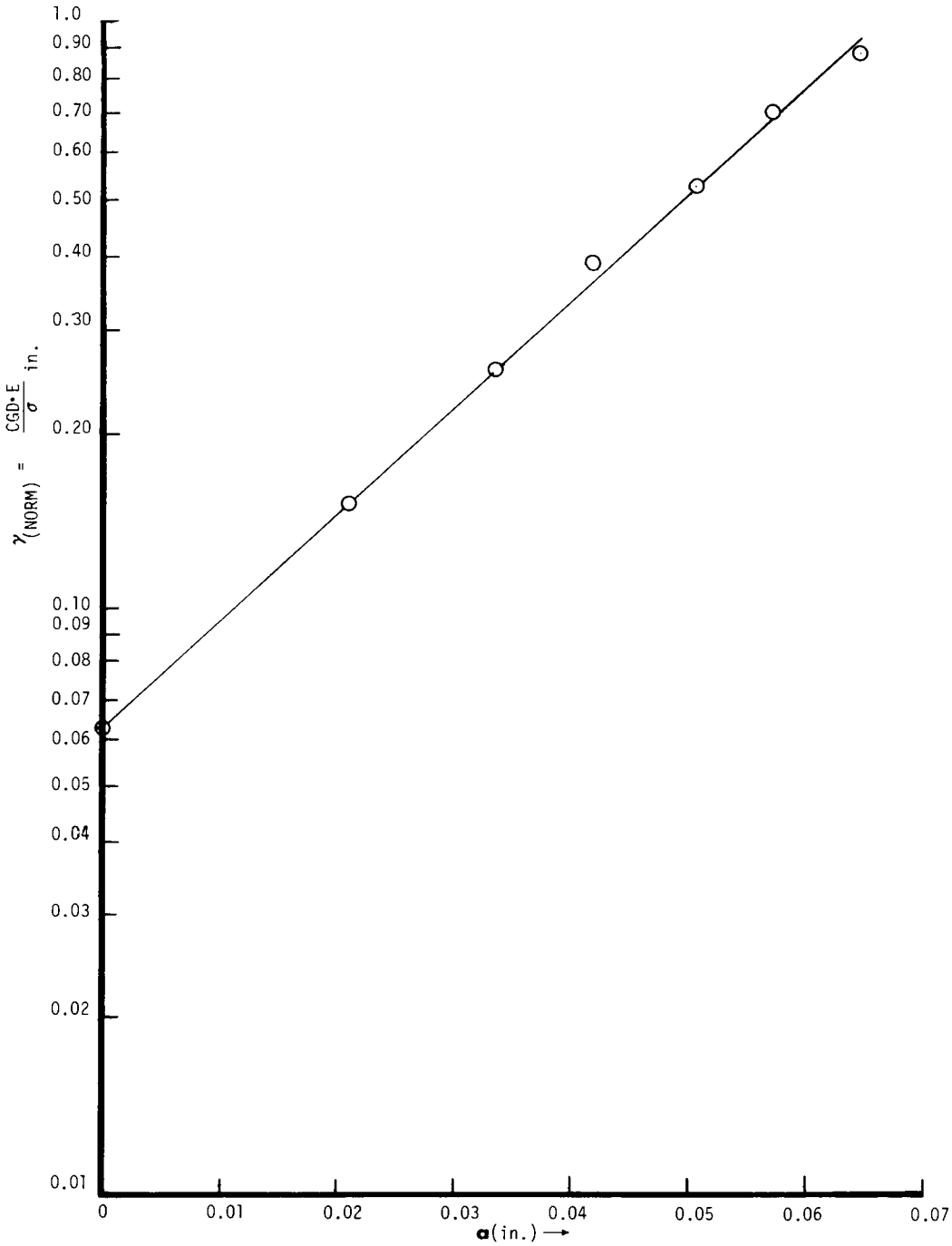

FIG. 3 Compliance Calibration Curve

8. GENERAL ELECTRIC COMPANY

K. D. Challenger

8.1 INTRODUCTION

The principal objective of mechanical properties testing at the General Electric Company is to characterize the behavior of 2¼Cr-1Mo and austenitic stainless steels in sodium environments relevent to LMFBR steam generators and intermediate heat transport systems. Under conditions predicted for the intermediate sodium system of the CRBRP, 2¼Cr-1Mo will lose carbon to the system and be weakened. The carbon will tend to carburize and embrittle stainless steel components in other portions of the system. The effects of a carburizing environment on creep rupture properties of Type 316 stainless steel will be evaluated along with an assessment of creep-fatigue interactions. In addition, studies of fatigue crack propagation rates in carburizing sodium will be performed in order to assess environmental effects under pertinent intermediate sodium loop loading conditions. The loss of carbon from 2¼Cr-1Mo steel components can result in increased creep rates of the decarburized surface layer with the possibility of ratchetting under cyclic straining. These effects will be evaluated for base metal and weld metal in a decarburizing sodium environment. Elastic-plastic fracture mechanics methods, including J-Integral and Crack Opening Displacement (COD) are being employed to determine the toughness (K_{Ic}) of 2¼Cr-1Mo steel at relevant temperatures and to compute the critical flaw sizes for the onset of rapid fracture. The effects of welding procedure, flaw location and thermal aging are being evaluated. The effect of melting practice and heat treatment on the mechanical behavior of 2¼Cr-1Mo is being evaluated to confirm that the properties of consumable remelted 2¼Cr-1Mo meet the appropriate requirements of the ASME B&PV Code for LMFBR steam generators.

8.2 MECHANICAL PROPERTIES OF STAINLESS STEEL IN CARBURIZING SODIUM

J. F. Copeland/P. P. Pizzo

8.2.1 Background

The objective of this program is to experimentally verify and supplement ASME Code design values for austenitic stainless steels to be used in LMFBR Intermediate Heat Transport Systems (IHTS). The effects of sodium carburization on creep-rupture lives and deformation rates, and the influence of creep-fatigue interaction and tension hold time at peak stresses, will be evaluated. Additionally, the effect of environment and other design-related parameters on the fatigue crack propagation rate will be determined in high carbon sodium using a fracture mechanics approach. The program includes a study of continuous carburization in sodium at a crack tip during cyclic stressing. These data will be used for assessing the integrity of LMFBR IHTS components in possible carburizing liquid sodium environments.

Type 316 stainless steel is tested at 510°C (950°F) in carbon-saturated sodium after approximately 1000 hr. specimen pre-exposures. The degree of carburization expected[1] is a case depth of about 5 mils with a surface carbon content of approximately 1-1.5 wt. %. This carburization corresponds to that expected[2] for the 30 year CRBR IHTS design life with a 2¼Cr-1Mo steel carbon source. GE analysis of bimetallic sodium test loops (Steam Generator Test Rig,[3] PA15 Loop 3,[4,5] B&W Model Steam Generator,[6] and EBR II secondary sodium system vent-line[2]) has verified that such surface carburization of stainless steel components does occur.

Testing is of two types: (a) tubular creep and creep-fatigue tests that give rupture times, deformation rates, and rupture ductilities, and (b) ASTM E399 fracture mechanics bend tests to give fatigue crack propagation rates. Under (a), specimens are filled with sodium and a carbon source and sealed prior to testing. For part (b), testing will be performed in flowing sodium (Loop A). Control tests are being performed in air. Cyclic frequency is low and includes the determination of hold-time effects.

The chemical composition and tension test characterizations of the Type 316 test material are shown in Tables 8.1 and 8.2. The ¼ schedule 80 pipe was used to fabricate test specimens, as illustrated in Figure 8.1. Twenty-four of these creep specimens were fabricated and aged for 1000 hr. at 510°C (950°F). Before aging, 15 specimens were filled with high purity sodium and a Grade 1095 steel (wire) carbon source was inserted. The remaining 9 specimens were filled with argon (atmospheric pressure at test temperature) for control testing.

Creep machines were modified to permit automatic load cycling for creep-fatigue and automatic data accumulation. The test parameters being studied are listed in Table 8.3. Again, the major emphasis in this study is to determine environmental effects (carbon-saturated sodium). Essentially, four groups of tests are represented in Table 8.3., argon creep-fatigue (control), Na/C creep-fatigue, Na/C creep-fatigue with hold time, and Na/C creep.

Chemical analysis and tensile test results for the bend test plate material are also shown in Tables 8.1 and 8.2. Fifty bend specimens were machined, and 25 of them were fatigue precracked. Thirteen of the precracked specimens were aged in carbon saturated sodium at 510°C (950°F) for 1000 hours in Loop A. The carbon source was a 20 gage sheet AISI-SAE Grade 1050 carbon steel. Type 304 0.127 mm (5 mil) foil pieces were inserted and studied before loading specimens and were loaded with the specimens to monitor the carburizing potential of the loop. The carburization of these foils indicated proper loop conditions for the required carburization. These specimens have been exposed and are now ready for testing. The remaining 12 precracked specimens were aged for 1000 hours at 510°C (950°F) in air for the control tests.

The fatigue crack growth test parameters, employing the 12.7 mm (0.5 in.) thick bend specimens, are shown in Table 8.4. Test facilities for performing these tests, both in air and in sodium, are illustrated in Figures 8.2 and 8.3. Each facility allows the simultaneous load cycling of three bend specimens.

Table 8.1 Type 316 Stainless Steel Annealed Test Material Characterization-Chemical Composition (wt. %)

	C	Mn	P	S	Si	Cu	Ni	Cr	Mo	N
					1/4 Schedule 80 pipe [(a) Tests]					
Ladle	0.056	1.63	0.029	0.015	0.56	0.08	13.32	17.24	2.40	-
Check	0.055	1.63	0.018	0.010	0.70	0.05	13.40	17.47	2.67	0.038
					15.9 mm. (5/8 in.)Plate [(b) Tests]					
Ladle	0.042	1.66	0.015	0.008	0.60	-	13.40	17.50	2.69	-
Check	0.053	1.59	0.009	0.013	0.54	0.06	13.37	17.22	2.37	0.050

Table 8.2. Type 316 Stainless Steel Annealed Test Material Characterization-Tensile Tests

	0.2% Y.S., MPa.(ksi.)	U.T.S., MPA.(ksi.)	% El. (2")	% R.A.
1/4 Schedule 80 Pipe [(a) Tests]				
Room Temperature	272(39.4)	623(90.4)	50.0	55.3
	300(43.5)	612(88.7)	44.0	48.5
510°C (950°F)	173(25.1)	479(69.4)	28.5	36.3
	166(24.0)	491(71.2)	32.5	36.6
15.9 mm. (5/8 in.) Plate [(b) Tests]				
Room Temperature	262(38.0)	612(88.7)	45.9	77.0
	271(39.3)	616(89.4)	53.6	77.4
510°C (950°F)	146(21.1)	487(70.6)	36.5	66.4
	150(21.8)	511(74.1)	41.3	61.3

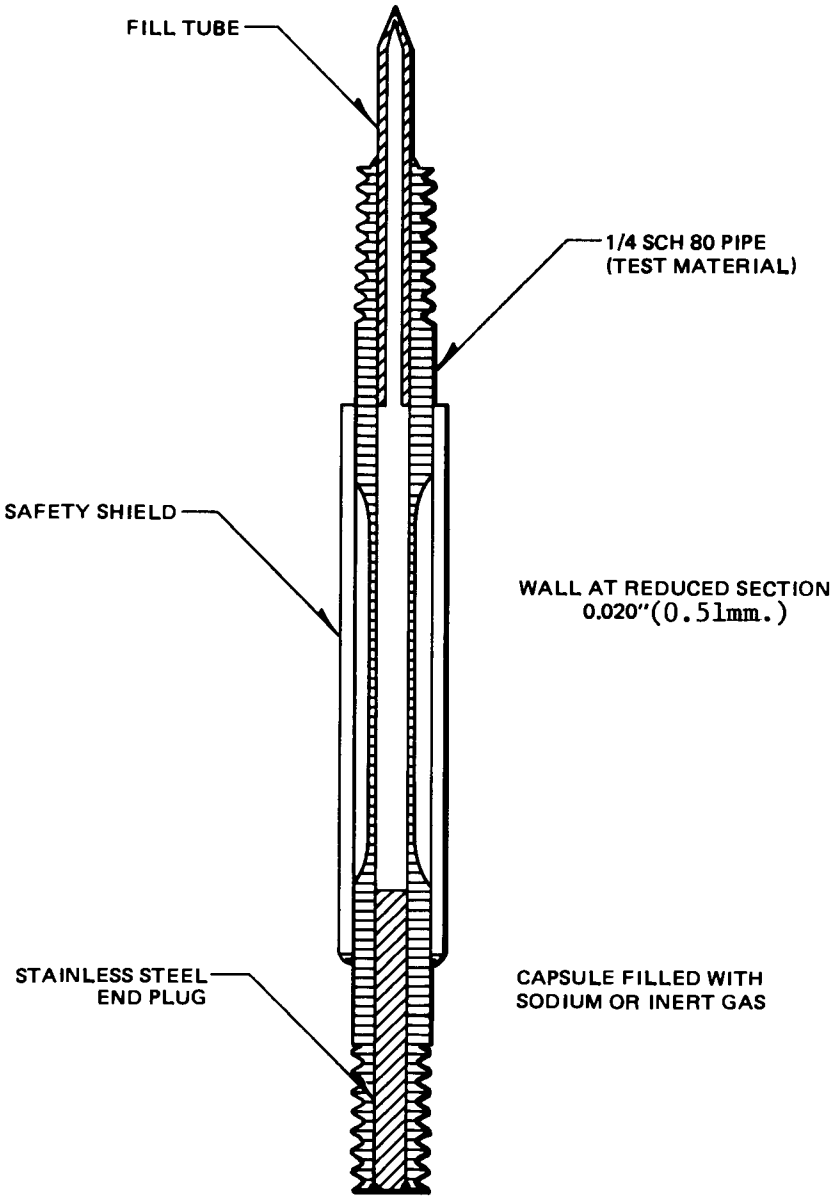

Figure 8.1 Uniaxial Creep/Fatigue Specimen

Table 8.3 Uniaxial Creep-Fatigue Test Parameters

Environment	-	C saturated Na and argon (air on outside) - in situ
Temperature	-	510°C (950°F)
Material	-	Annealed Type 316 stainless steel
Loading Modes	-	Constant load for creep Periodic load increase of 69MPa (10ksi.) for creep-fatigue
Load Increase Frequency	-	1 cycle per hr.
Hold Time at Peak Load	-	Zero and 30 min.

Table 8.4 Fatigue Crack Growth Test Parameters

Environment	-	C saturated Na and air (in situ)
Temperature	-	510°C (950°F)
Material	-	Annealed Type 316 stainless steel
Frequency	-	0.5 and 0.05 cycles/min.
Hold Time	-	zero and one min.
Load Ratio (R)	-	0.05
Range of ΔK_{eff}	-	About 11 to 44 $MPam^{\frac{1}{2}}$ (10 to 40 ksi. $in.^{\frac{1}{2}}$)
Load Wave Form	-	Sawtooth

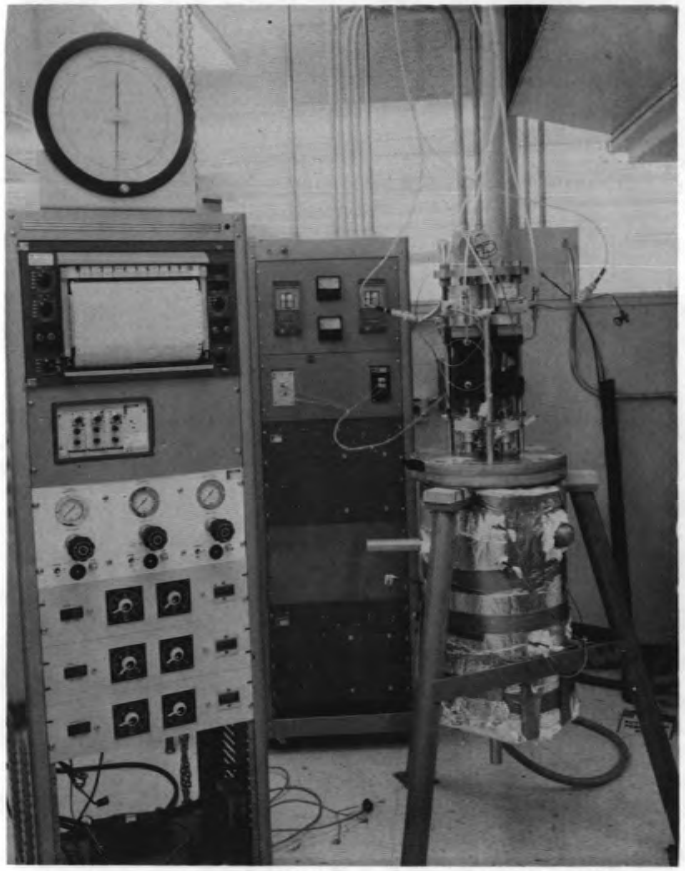

Figure 8.2 Fatigue Crack Growth Test Facility for Control Tests in Air at 510°C (950°F)

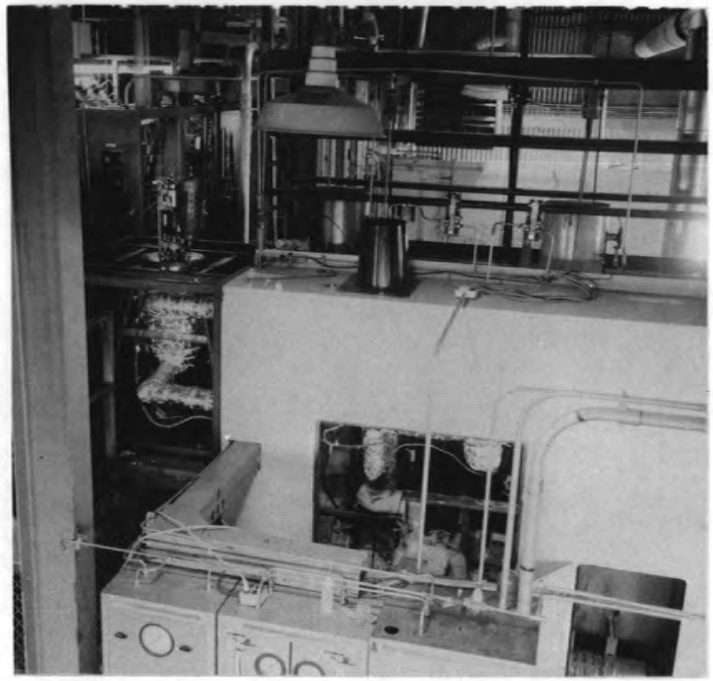

Figure 8.3 Fatigue Crack Growth Test Facility (Left, in Foil) For Tests in Loop A Sodium at 510°C (950°F)

8.2.2 Current Progress

8.2.2.1 Creep/Fatigue of Carburized Stainless Steel

Creep rupture results from the initial fourteen specimens are given in Table 8.5. Twelve specimens have ruptured, and minimum creep rates were computed from eleven tests. The loading strains (at cycle peak load) and failure strains are also tabulated; the tabulation for these specimens should be completed next quarter. A characteristic of the carburized, sodium and carbon-filled specimens is failure prior to the occurrence of tertiary creep. Thus, the failure strains are just above the corresponding loading strains and are somewhat low. No rupture times on control specimens have been determined, although minimum creep rates have been evaluated for two argon tests.

The rupture time data is plotted in Figure 8.4. For these initial results, there appears to be no significant effect of cycling or hold time when plotted in this manner. When more data becomes available a more complete analysis of creep-fatigue interaction for these environments will be possible. All results are for tests pre-exposed to Na/C at 510°C (950°F) for 1000 hr. and exposed to Na/C during the creep rupture test. These data fall just at, and slightly above, the ASME Code Case 1592 minimum expected value curve for Type 316 tests in air. When rupture time information is obtained from the argon-filled control tests, the environmental effect (if any) will be shown.

The minimum creep rate results are plotted in Figure 8.5. Although only two control test results are shown, an effect of environment seems evident. The creep rates for the Na/C tests are about twice those of the control tests. Several lower stress Na/C tests will be performed to extend this curve to lower creep rates and more accurately determine the stress dependency (slope of the curve). Additional control tests will also be performed to verify this initial trend. Hold time effects should also become more obvious with the generation of more data.

Broken test specimens were examined metallographically for evidence of carburization and surface (specimen inside diameter) cracking. Figures 8.6 and 8.7 show unetched thickness cross-sections of a Na/C specimen tested

Table 8.5 Interim Creep Rupture Results at 510°C (950°F) for Annealed Type 316 Stainless Steel, Pre-exposed at 510°C (950°F) for 1000 hr.

Specimen No.	Load Range, ksi.	(MPa)	Peak Load Hold Time (min.)	Test Environment (I.D.)	Test Time (hr.)	Peak Loading Strain (%)	Failure Strain (%)	Min. Creep Rate (%/hr.)
C - 7	65	(448)	-	Na/C	428.3*	13.4	14.0	0.0013
C - 9	59	(407)	-	Na/C	916.7*	9.5	10.6	0.0008
C - 6	55	(379)	-	Na/C	679.7*	7.2	7.9	0.0007
C - 10	49	(338)	-	Na/C	2429.6*	4.3	-	0.00036
C - 22	52.5/62.5	(362/431)	0	Argon	2151.4	7.4	-	0.000047
C - 1	44/54	(303/372)	0	Argon	960.0	21.95	-	0.00025
C - 13	60/70	(414/483)	0	Na/C	1585.0*	21.2	26.1	0.0046
C - 16	54/65	(372/448)	0	Na/C	4.6*	-	15.5	-
C - 18	54/65	(372/448)	0	Na/C	1860.2*	10.3	-	-
C - 15	54/65	(372/448)	0	Na/C	832.2*	10.9	14.2	0.00092
C - 11	49/59	(338/407)	0	Na/C	2107.8*	9.8	10.5	0.00031
C - 14	55/65	(379/448)	30	Na/C	422.5*	12.3	13.2	0.00127
C - 12	49/59	(338/407)	30	Na/C	903.4*	12.3	13.3	0.00088
C - 19	54/65	(372/448)	30	Na/C	2321.5*	-	-	-

*Rupture Time

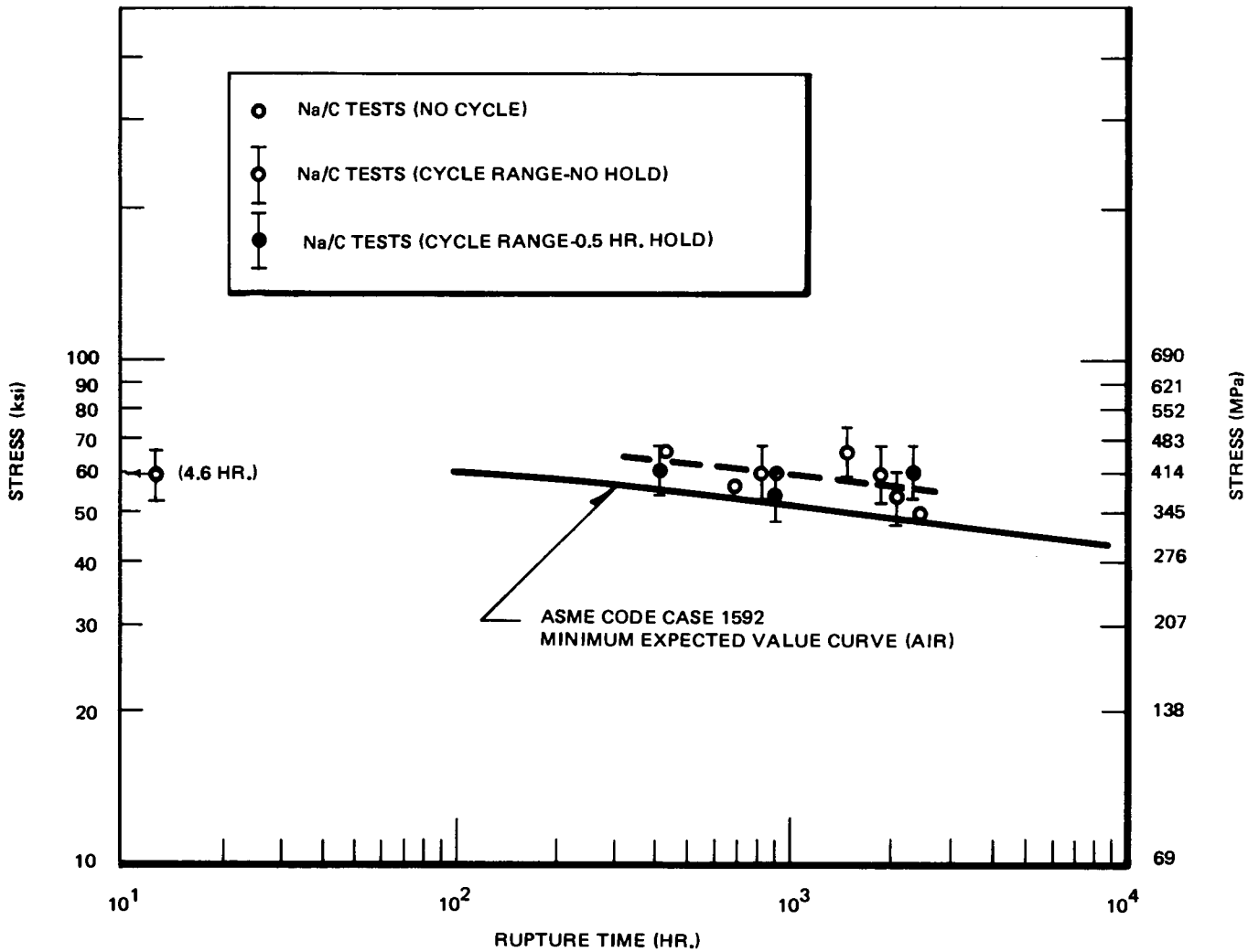

Figure 8.4. Creep and Creep-Fatigue Rupture Time Results for Annealed Type 316 Stainless Steel Pipe at 510°C (950°F), Exposed to Carbon-Saturated Sodium Before and During Test, 1000 Hr. Pre-Exposure at 510°C (950°F).

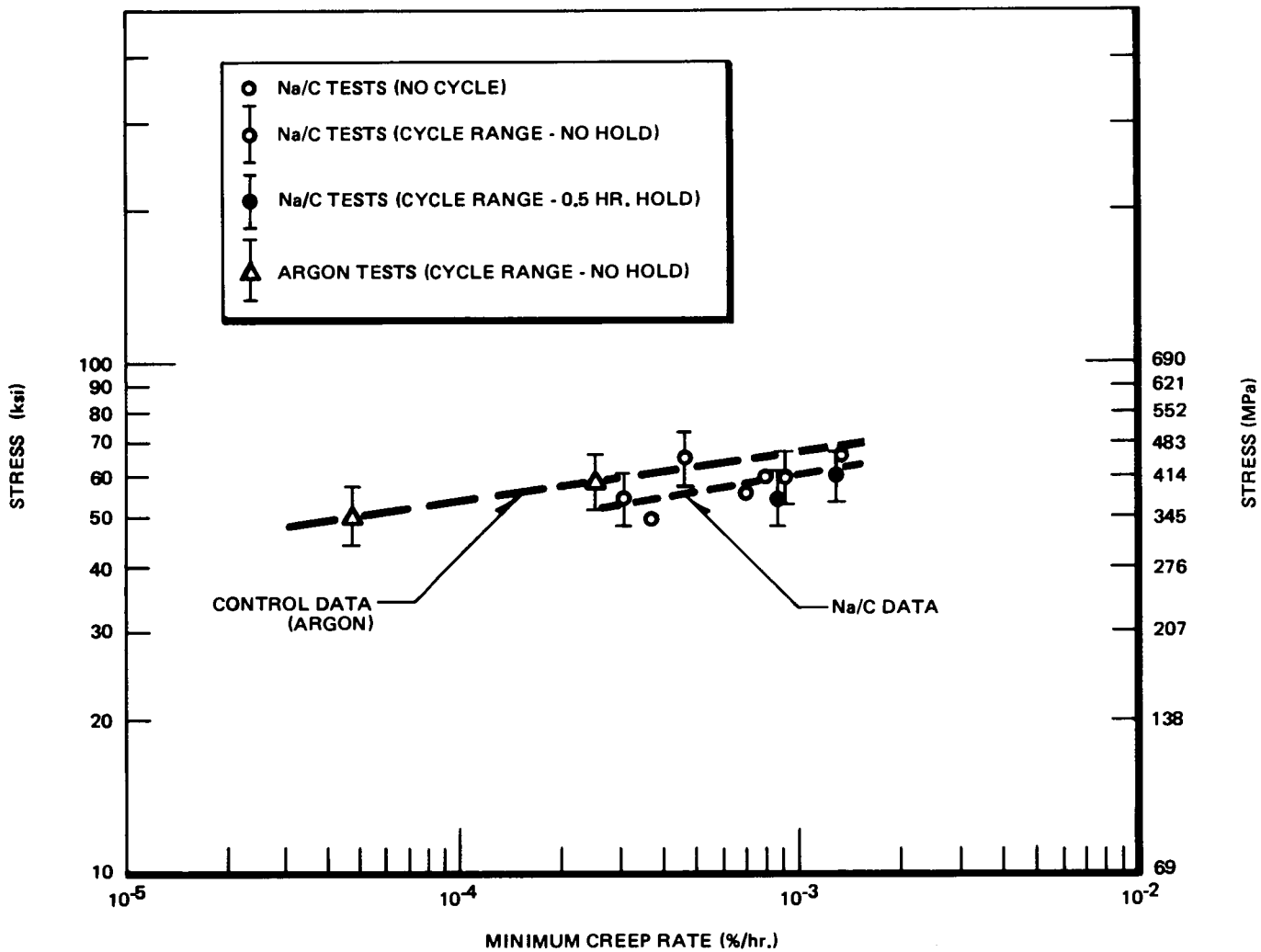

Figure 8.5. Creep and Creep-Fatigue Minimum Creep Rate Results for Annealed Type 316 Stainless Steel Pipe at 510°C (950°F). Exposed on Interior to Carbon-Saturated Sodium or Argon Before and During Test. 1000 Hr. Pre-Exposure and Thermal Aging at 510 °C (950 °F).

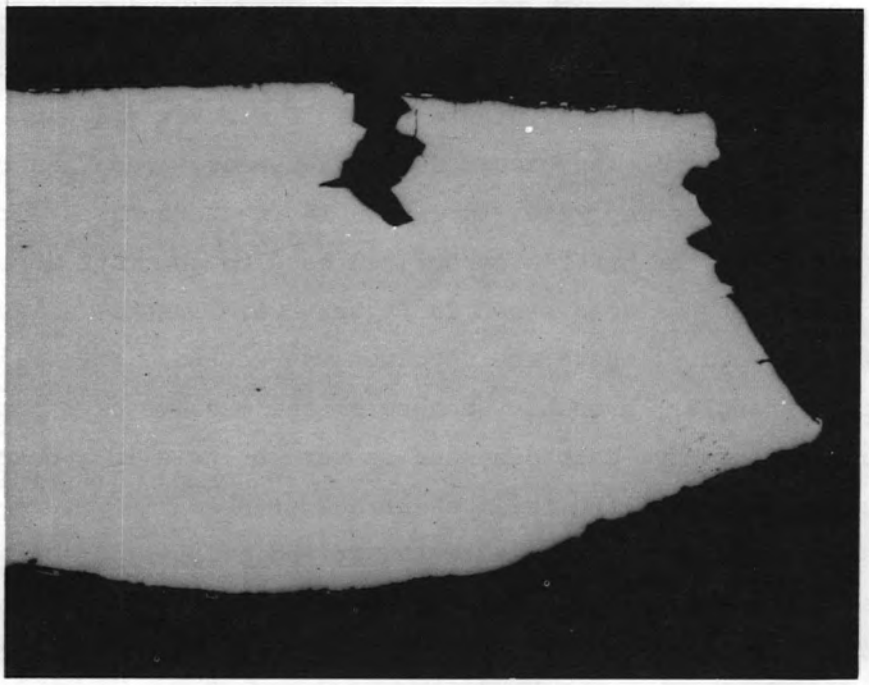

125 X

Figure 8.6 C-6, Na/C, 510°C (950°F), t_r = 680 HR.
σ = 379MPa. (55 ksi.), Tp. 316, .51mm. (20 MIL)
WALL, BULK C = 0.252 WT.%.

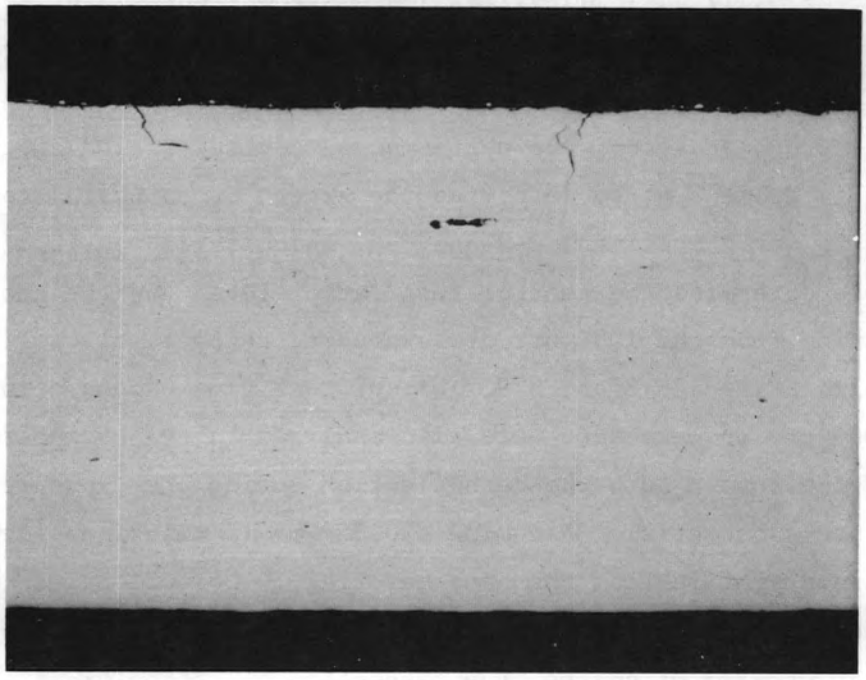

125 X

Figure 8.7 Same Conditions as Figure 8.6

at 379 MPa (55 ksi.) with no load cycling. The rupture time (t_r) was 680 hr. Surface cracks are apparent, both near the fracture and away from it. Deformation data printouts (every 6 minutes for each test) indicate that some cracking occurs during secondary creep, and, thus, causes an increased creep rate. A change in fracture appearance, as the fracture runs from the brittle carburized case to the more ductile material underneath is also shown in Figure 8.6. This is illustrated more clearly in Figure 8.8, where the specimen was etched. The failure of the case is intergranular, probably because of the massive precipitation of grain boundary chromium carbides, and is very brittle in appearance. A surface crack away from the failure surface is shown in Figure 8.9, for another specimen. This crack initiated at the carburized surface, propagated intergranularly through the case, and was blunted and arrested by the more ductile, uncarburized stainless steel beneath the case. This crack seems to have occurred just prior to failure since there is no evidence of subsequent carburization at the blunted crack tip. The carburized layer in these specimens is about 25% of the specimen wall thickness, or 0.127 mm (5mils), as judged from Figures 8.6, 8.8 and 8.9. Therefore, this is a severe test since the carburized layer comprises a large percentage of the test specimen cross-section.

Bulk carbon analyses were performed on several failed specimens, as indicated in Table 8.6, to determine the extent of carburization in a more quantitative way. Specimens C-2 and C-8, which failed on loading, were analysed to determine the control test carbon level and the amount of carburization from the 1000 hr. pre-exposure, respectively. Two tests which failed after 428.3 and 679.7 hr. of test time exposure in addition to the 1000 hr. pre-exposure were also analysed to evaluate carbon pick-up during the test. Both the carburization during pre-exposure and during the test are substantial. Assuming a 0.127 mm (5 mils) case depth and a linear carbon profile from the base material (0.061 wt. %) to the surface, the surface carbon content for specimen C-8 is 1.08 wt. % and for C-7 and C-6 is 1.60 wt. %. Of course, the assumption of carbon profile linearity is not strictly valid. However, as shown by Figure 8.10 (microprobe results on a bend specimen pre-exposed in Loop A for 1000 hr. at 510°C (950°F), in carbon-saturated sodium), these surface carbon concentrations

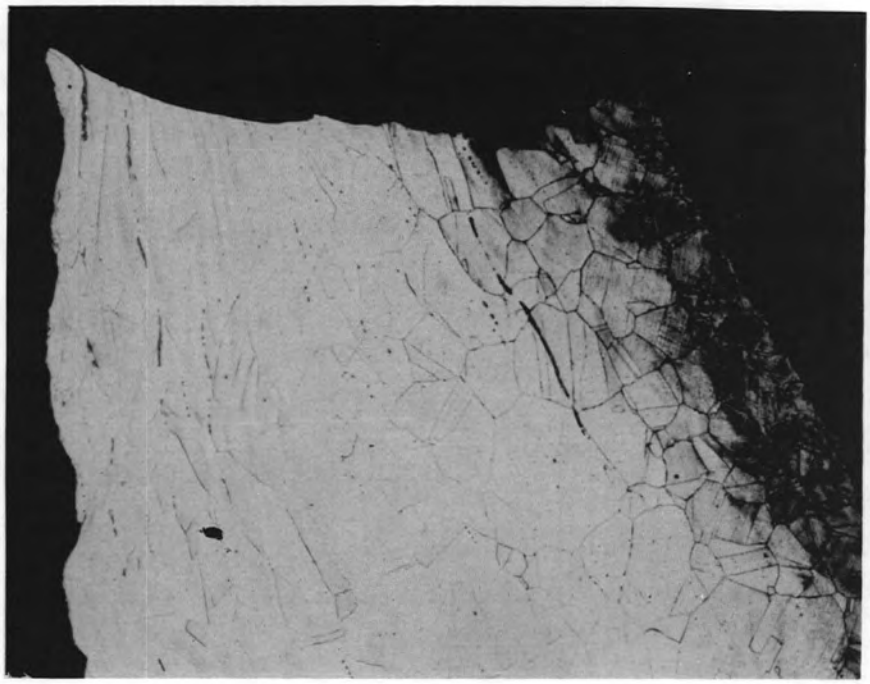

250 X

Figure 8.8 C-7, Na/C, 510°C (950°F), t_r = 428 HR.
σ = 448MPa. (65 ksi.), Tp. 316, .51mm. (20 MIL)
WALL, BULK C = 0.252 WT.%.

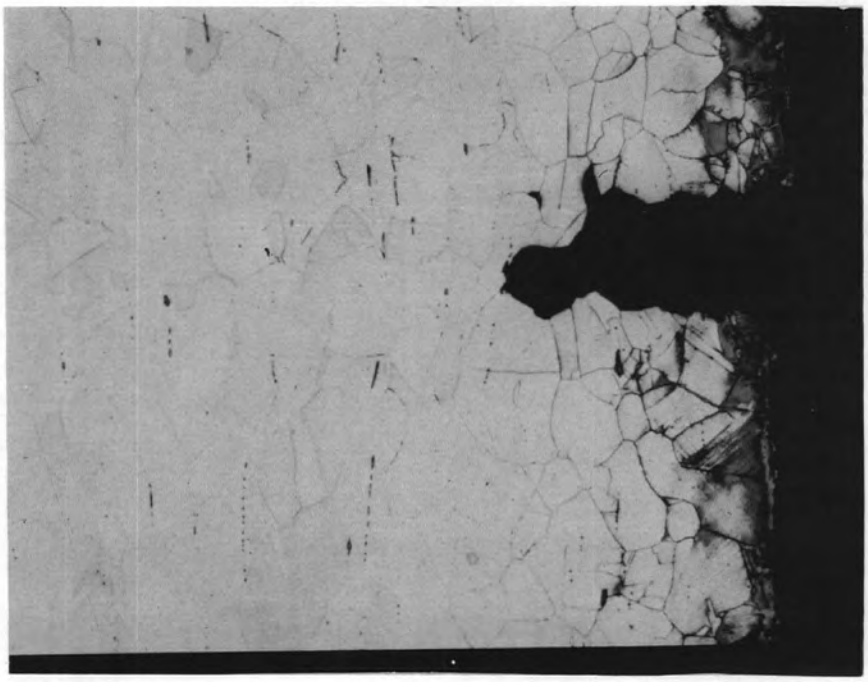

250 X

Figure 8.9 C-6, Na/C, 510°C (950°F), t_r = 680 HR.
σ = 379MPa. (55 ksi.), Tp. 316, .51mm. (20 MIL)
WALL, BULK C = 0.252 WT.%.

Table 8.6 Bulk Carbon Content Increase of Creep Specimens (20 mil [0.51 mm.] Wall) During Pre-Exposure and Testing (1095 Carbon Steel Source)

Specimen No.	510°C (950°F) Age Time (Hr.)	510°C (950°F) Test Time (Hr.)	0.51 mm. (20 Mil) Wall Bulk Carbon (Wt.%)
C-2	1000 (Argon)	< 1	0.061
C-8	1000 (Na/C)	< 1	0.187
C-7	1000 (Na/C)	428.3	0.252
C-6	1000 (Na/C)	679.7	0.252

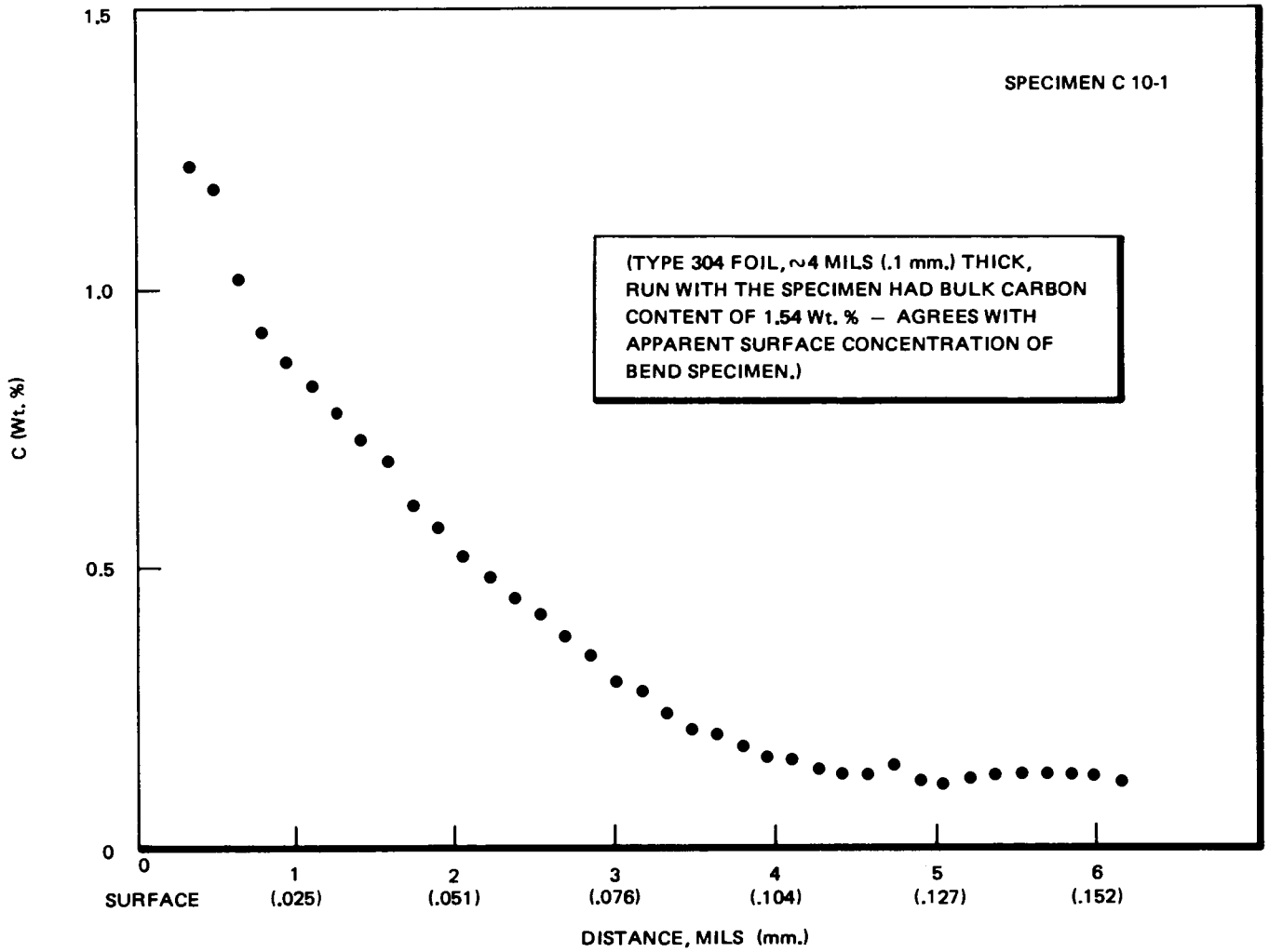

Figure 8.10. Carbon Profile (Electron Microprobe) on Annealed Type 316 0.5 in. (12.7 mm.) Bend Specimen Aged in Loop A for 1000 Hr. at 950°F (510°C). 1050 Carbon Steel Source (Carbon – Saturated Sodium).

appear to be reasonable estimates. It should be mentioned that carbon analysis below about 0.10 wt.% and analysis within approximately 5μm of the surface is difficult with present electron microprobe technology. Therefore, some extrapolation for surface carbon content is necessary, even with microprobe analysis.

Further creep and creep-fatigue testing of this type will be performed for control data, completion of current curves, and weldment studies.

8.2.2.2 Fatigue Crack Growth Studies of Carburized Stainless Steel

During the last quarter, the fatigue crack growth facility for control testing in air at 510°C (950°F) was completed. A test verification plan and a subsequent shakedown run were performed. Results were satisfactory with regard to load cycle and temperature stability. An initial test run at 510°C (950°F) was performed for three specimens, each tested at an average ΔK of about 38.5 MPa$\sqrt{m}$ (35 ksi $\sqrt{in.}$) with a cyclic frequency of .5 CPM. The load range and ΔK are related by Equation 8.1 where,

$$\Delta K = \frac{\Delta PS}{BW^{3/2}} \left[2.9\left(\frac{a}{W}\right)^{1/2} - 4.6\left(\frac{a}{W}\right)^{3/2} + 21.8\left(\frac{a}{W}\right)^{5/2} - 37.6\left(\frac{a}{W}\right)^{7/2} + 38.7\left(\frac{a}{W}\right)^{9/2}\right] \qquad \text{Eqn. 8.1}$$

ΔP is the load range, S is the span between lower specimen support points, B is specimen thickness, W is specimen width, and a is the crack length. Initial crack lengths, after fatigue precracking, were approximately 11.5 mm (.452 in.). The test plan is to grow the cracks to about 12.7 mm. (.50 in.) under test conditions. It is important to maintain elastic loading conditions (absence of gross yielding) in the specimens during the test. This may be checked by computing the plastic zone size at the crack tip. The plastic zone size for the plane strain stress state is given by Equation 8.2,

$$r_p = \frac{1}{6\pi}\left(\frac{\Delta K}{\sigma_{ys}}\right)^2 \qquad \text{Eqn. 8.2}$$

where r_p is the radius of the plastic zone centered at the crack tip, ΔK is the stress intensity factor range (zero to K max.), and σ_{ys} is the yield strength at temperature. For a ΔK value of 38.5 MPa$\sqrt{m}$ (35 ksi$\sqrt{in.}$), the plastic zone radius is only 2.72mm (0.107in.). Thus, the remaining, uncracked, ligament should realize essentially elastic loading, as desired, even at this relatively high ΔK level. These initial crack growth rate tests gave consistent crack growth rates which are in general agreement with the results of other investigations at 482°C (900°F)[7] and 538°C (1000°F).[8] The crack growth rates were determined by withdrawing the specimens after the desired number of cycles, checking the crack extension on the specimen sides, and then breaking open the specimen for a more exact measure of crack growth.

A second test run in air at 510°C (950°F) has been initiated for specimens loaded at ΔK values of 33 MPa$\sqrt{m}$ (30 ksi$\sqrt{in.}$), 22 MPa$\sqrt{m}$ (20 ksi$\sqrt{in.}$), and 11 MPa$\sqrt{m}$ (10 ksi$\sqrt{in.}$). Twenty one additional test specimens are currently being precracked and will be pre-exposed to sodium and aged during the next quarter. The test facility for fatigue crack growth tests in flowing sodium has been installed. The loading mechanism has been proven satisfactory, and after a vessel leak check and a shakedown run, testing will start. Results showing the effects of high carbon sodium will be available at the end of the next quarter.

8.3 DECARBURIZATION KINETICS AND DESIGN METHODS VERIFICATION TESTING

L. V. Hampton/J. L. Krankota

8.3.1 Background

The selection of 2¼Cr-1Mo steel as the reference alloy for sodium-heated steam generators was based primarily upon its immunity to stress corrosion cracking in chloride or caustic contaminated environments and its proven fabricability.[9] One of the major concerns with the use of this material for sodium applications is its susceptibility to decarburization during service. Early analyses assumed that relatively thin sections, such as steam generator tubing, would completely decarburize during the LMFBR lifetime, with concomitant severe design stress penalties necessarily

imposed.[10] In addition to the assumed carbon losses, the potential for severe carburization of stainless steel components in the loop was also recognized as a potential difficulty.

In the absence of an acceptable theoretical model for decarburization of 2¼Cr-1Mo steel, an approach introduced by Armijo and Krankota[11] was used to analyze the results obtained from many different experiments.[12-30] This technique treats carbon loss data as if it were corrosion data; that is, the loss of carbon per unit area is described as a function of time. A parabolic time dependence has been observed which suggests that the decarburization process is diffusion controlled. The decarburization rate constants, K*, from all available data were fit to an Arrhenius type expression for design use. Figure 8.11 shows the results of this analysis. The "data class" and the weighting applied to each class are defined in the NSM Handbook entry for decarburization of 2¼Cr-1Mo steel.[31] Based upon the upper limit curve given in Figure 8.11, estimates of carbon loss and associated design stress penalties can be made for steam generator components. These predictions of decarburization kinetics indicate that steam generator tubes would not be expected to lose more than 300 ppm carbon in the design life of the CRBRP. Only a small design stress penalty (<10%) is associated with this loss. While the handbook approach suggests that decarburization kinetics are too slow to yield a carbon loss at end-of-life of greater than 300 ppm for CRBRP steam generator tubing,** WARD experiments, utilizing thin foils, imply that the "equilibrium" carbon content of 2¼Cr-1Mo in 950°F sodium will be approximately 700-900 ppm.[15] The design stress penalty associated with these predictions of carbon loss can be accomodated.

---

*Where K is defined by:

$$K = \frac{gm^c}{cm^2 - sec^{\frac{1}{2}}}$$

$$M \quad \left(\frac{gm^c}{cm^2}\right) = Kt^{\frac{1}{2}}$$

**Tubing specification sets initial carbon levels of 700-1100 ppm.

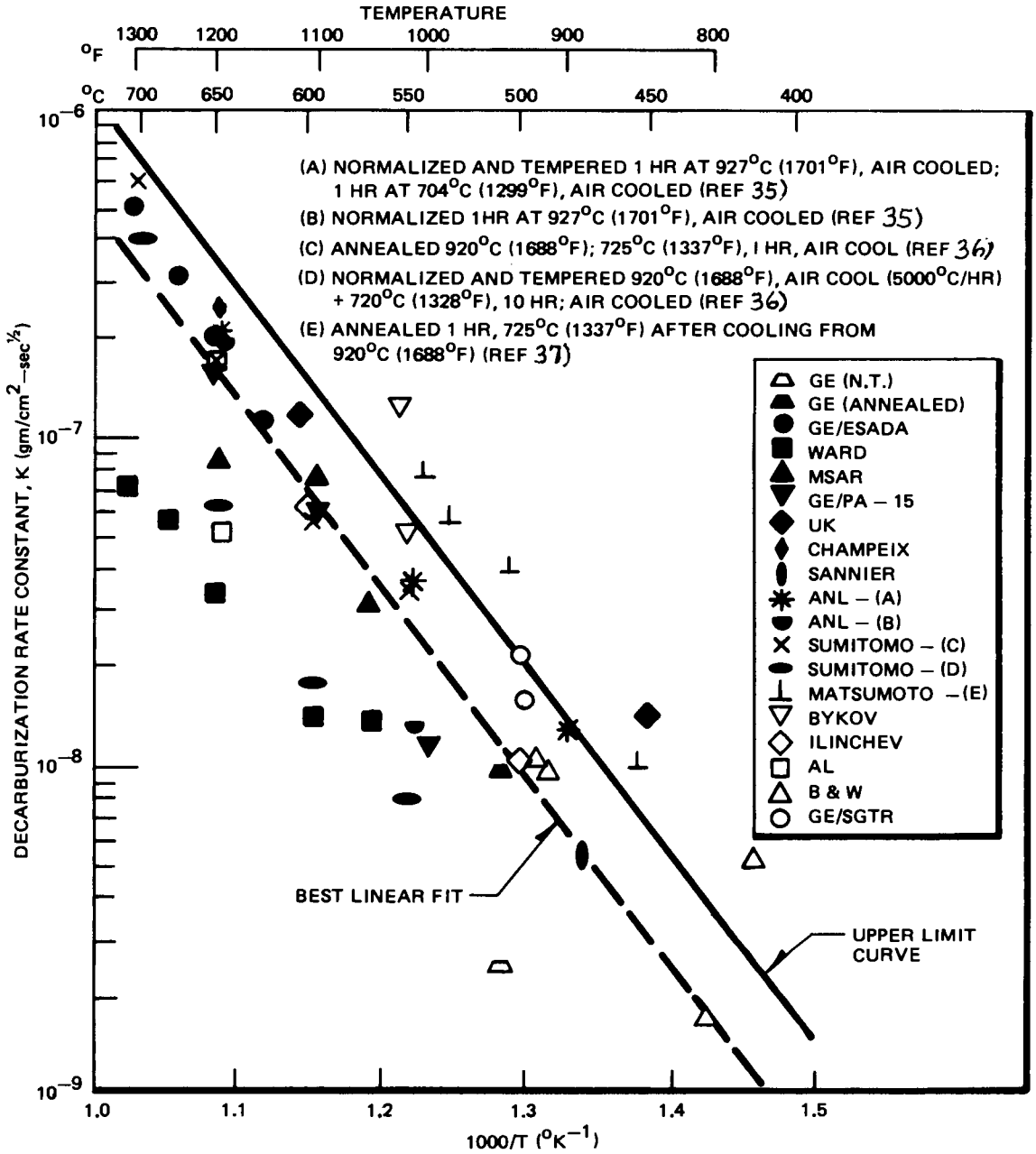

Figure 8.11. Decarburization Rate Constants for All Investigations

Design analysis for high temperature components requires a consideration of creep/fatigue interaction to accomodate the effects of transient loading. A recent study has provided creep/fatigue interaction information for 2¼Cr-1Mo[32] under conditions of uniform microstructure (i.e. no decarburized surface layer) with no ratcheting strains permitted. Steam generator tubes will experience cyclic loading with the potential to accumulate ratcheting strains, due to a weaker surface layer, as compared to the bulk metal. Interrupted creep tests on 2¼Cr-1Mo pipe, tubing, and weld metal are being undertaken to assess the effects of such loading on partially decarburized material. Uniaxial tests will be performed on sodium-filled and inert gas-filled pipe samples in order to characterize the effect of stress cycling on creep strains. Tubing and all-weld-metal tubes will be internally pressurized in sodium and argon environments to assess the effects of creep/fatigue on rupture life in a decarburizing environment. Description of the samples, test facilities, and test matrix is included in earlier reports.[33,34]

8.3.2 Current Progress

Testing to characterize the decarburization behavior of 2¼Cr-1Mo base and weld metal is currently being conducted. With the conclusion of the last decarburization run, DP-7, data for the decarburization of 2¼Cr-1Mo base metal for 10,000 hours in 510°C (950°F) titanium gettered sodium was obtained along with 4,500 hour weld metal data. The results of this and other investigations[35,36,37] are expressed in terms of the decarburization rate constant, K, and plotted in Figure 8.11. In all cases, the data indicate that decarburization rates are strongly dependent on the metallurgical structure of the carbides, i.e., the more stable the initial carbide, the slower are the decarburization kinetics for the material.

Heat treatments utilized in this study are shown in Table 8.7. The data indicate that the rate of carbon loss for the annealed material is nearly four times the rate for the normalized and tempered material at 10,000 hours. Decarburization rate constant measurements made earlier in this program (4,100 hours) indicated that the annealed material was decarburizing at a rate of 12×10^{-9} gr/cm^2-sec$^{\frac{1}{2}}$ while the normalized and

Table 8.7 Decarburization Rate Constants for 2¼Cr-1Mo Exposed to Static Sodium, 950°F (titanium-gettered)

		$K(gm/cm^2 - sec^{\frac{1}{2}})$	
		10,000 hrs.	4100 hrs.
Annealed*	½hr. - 1695°F (924°C) fce. cool to RT	$9.4X10^{-9}$	$12X10^{-9}$
Normalized & Tempered	½hr. 1695°F (924°C) AC to RT 1hr. 1250°F (677°C) Ac to RT	$2.5X10^{-9}$	$3.5X10^{-9}$

*Both treatments recieved a final stress relief anneal 1hr. @ 1350°F (732°C) with subsequent air cooling to room temperature.

tempered material had a K vaue of $3.5X10^{-9}$ gr/cm^2 - $sec^{\frac{1}{2}}$. The 10,000 hour data represents rate changes of 22 and 30% respectively. The normalized and tempered steel is achieving a lower limit K value at a faster rate than is the annealed material.

Differences in decarburization rates between various material heat treatments is becoming a well documented phenomenon (see Figure 8.11). Work conducted at Sumitomo[36] revealed consistent differences in the decarburization rates of annealed versus normalized and tempered material between 550°C(1022°F) and 700°C(1292°F) with the decarburization rate for annealed always higher. Studies made at ANL[35] also showed rate constant differences between material in the normalized and normalized/tempered conditions.

Currently, tests are being conducted to further refine the decarburization rate constant of 2¼Cr-1Mo (+ >10,000 hours) and also to characterize the kinetics of 2¼Cr-1Mo weld metal. Results will be reported at the next quarter. Plans to determine the decarburization rate constant for the heat affected zone of weldments will be implemented next quarter.

The first stage of uniaxial creep/fatigue interaction testing of 2¼Cr-1Mo pipe at 950°F (510°C) is nearing completion. The results obtained to date are shown in Table 8.8. The planned test matrix called for uniaxial creep testing at stresses as low as 25 ksi (172.35 MPa). It was found that under this loading condition, specimens were strained to only 0.1% in 1000 hours. Subsequent testing will be performed at 30 ksi (206.82 MPa) instead of 25 ksi in order to obtain shorter rupture times.

Several creep/fatigue tests have been completed or are nearing completion. These specimens are continuously stressed at 30 or 35 ksi (241.29 MPa) and peak-stressed to 45 ksi (310.23 MPa) once every 24 hours (zero hold time). Although the data have not yet been completely analyzed, results indicate that each time specimens are peak stressed to 45 ksi, as much as 0.6% plastic strain is added to the strain already accumulated during the test. This result is not totally unexpected when analyzing the stress-strain characteristics of this pipe material at 900°F. The curve indicates that as much as 1% plastic strain can be added to the material by loading to 45 ksi.

Uniaxial tests are continuing. Examination of the fracture surfaces and microprobe examination of those specimens filled with sodium will be reported in the next quarterly.

Table 8.8 Uniaxial Creep/Fatigue Tests 950°F (510°C)

Specimen	ENV	Stress MPa	Stress ksi	Stress Peak MPa	Stress Peak ksi	Rupture Time (hrs.)	Strain (%)
A02	Helium	310.23	45	-		39.9	9.1
A04	Helium	241.29	35	-		229.6	14.6
A05[a]	Helium	172.35	25	-		-	-
A05[a]	Helium	206.82	30	-		110.6	13.0
A13	Na+Ti	241.29	35	310.23	45	248.5	13.5
A14	Na+Ti	241.29	35	-		1021.6	12.5
A15	Na+Ti	241.29	35	-		397.3	13.4
A03	Helium	206.82	30	310.23	45	(b)	-
A08	Helium	206.82	30	310.23	45	(b)	-

(a) loading on specimen A05 was changed from 172.35 MPa (25 ksi) to 206.82 MPa (30 ksi).

(b) these specimens are still on test.

The preliminary stage of biaxial creep/fatigue interaction testing has been completed on 2¼Cr-1Mo base and weld metal and although the rupture time data fall generally above the minima set by the ASME Code Case 1592, there is considerable scatter in the results (Table 8.9). Base metal failures in the pressurization tests were characterized by an axial rupture in the specimen (the type of failure mode to be expected in this type of test). Weld metal specimens failed either by axial tearing or by pinhole perforations of the specimen tube. These perforation were related to voids in the specimen as a result of the initial welding operation. All weld samples will be radiographed in the future to avoid this problem.

Unstressed biaxial specimens (weld and base metal) have accumulated nearly 800 hours exposure time to static 950°F titanium-gettered sodium. Some of these specimens will be continuously pressurized to 32.4 and 36.5 ksi to assess the effects of decarburization on rupture life. Other specimens will be cyclically pressurized to a 45 ksi stress level.

8.4 METALLURGICAL CHARACTERIZATION OF VAR AND ESR 2¼Cr-1Mo ALLOY STEEL

H. P. Offer

8.4.1 Background

Steam generator integrity is a primary design criterion for the CRBRP. The existence of porosity in tube-tubesheet welds, attributed to the presence of impurities and nonmetallic inclusions, has been shown to lead to leaking welds in LMFBR steam generator using 2¼Cr-1Mo steel. Vacuum Arc Remelt (VAR) and Electroslag Remelt (ESR) processing produces very low levels of impurities and nonmetallic inclusions compared to non-remelted material. In order to use the processing techniques which will provide ultra-clean material in the critical tube-tubesheet weld region, the mechanical properties resulting from these processing techniques must be shown to meet the applicable Code and RDT Standards, which are based on non-remelted material.

The objective of this activity is to generate preliminary mechanical property data and microstructural characterization for consumable remelted 2¼Cr-1Mo alloy steel. This data will be used to compare the mechanical behavior of this steel to that developed by the Oak Ridge National Laboratory for air melted 2¼Cr-1Mo.

Table 8.9 Biaxial Creep/Fatigue Testing 950°F

Specimen	Env.	Stress MPa	Stress ksi	Rupture Time (hrs.)
B40-07	Helium	223.37	32.4	248.2
B40-08	Sodium	223.37	32.4	98.2
B45-07	Helium	251.63	36.5	116.2
B45-08	Sodium	251.63	36.5	168.5
B40-01	Helium	275.76	40.0	4.0
B40-02	Sodium	275.75	40.0	1.3
B45-01	Helium	310.23	45	0.5
B45-02	Sodium	310.23	45	0.4
W40-07	Helium	223.37	32.4	200.0
W40-08	Sodium	223.37	32.4	116.2
W45-07	Helium	251.63	36.5	172.5
W45-08	Sodium	251.63	36.5	108.0
W40-01	Helium	275.76	40.0	0.1
W40-02	Sodium	275.76	40.0	0.9
W45-01	Helium	310.23	45.0	0.3

B = base metal

W = weld metal

An investigation is being made to determine the effect of the vacuum-arc remelt (VAR) and electroslag remelt (ESR) processes on steam generator component material properties and structure, relative to non-remelted material. Emphasis is placed on the fracture toughness and creep properties produced by these processes. The mechanical properties will be determined for these remelt techniques for use in component design and performance prediction. The resulting microstructures will be determined to provide a basis for extrapolating data from the accelerated mechanical property tests to longer times at lower temperatures and/or stresses.

8.4.2 Current Progress

The series of mechanical property tests that are being conducted for the VAR and ESR processes include:

1. Uniaxial tensile tests at ambient and high temperatures up to the maximum service temperature.
2. Creep-rupture tests at several stress levels and at several temperatures spanning the service temperature range.
3. Charpy V-Notch impact toughness tests both below and above the nil-ductility transition temperature.
4. Drop-weight impact toughness tests near the nil-ductility transition temperature.

The series of microstructural examinations and chemical analyses that are being conducted for both alloy remelt techniques, include:

1. Determining the microscopic inclusion count.
2. Determining the grain size (ferrite and prior austenite).
3. Determining the hardness.
4. Determining the chemical composition.
5. Determining the microstructure for various heat treatments.

The mechanical property tests, microstructural examinations, and chemical analyses are being performed for various heat treatments including those proposed for the steam generator tubing and tubesheet forging. This activity will provide material property data based on the proposed processing techniques in order to determine compliance with RDT Standards M3-33 (tubing), and M2-19 (tubesheet forging).

8.4.2.1 Chemical Composition

A check chemical analysis was performed on each of the heats tested, and the results are presented in Table 8.10. Table 8.11 lists the results of the micro-inclusion content determination as a function of position in the ingot for VAR heats 56067 and 55262, and ESR heat R0110. The maximum permissible inclusion ratings permitted by RDT Standards M3-33 and M2-19 are also given. All three heats have inclusion ratings within the maximum permitted.

8.4.2.2 Heat Treatment

The five heat treatments considered in the metallurgical characterization are listed in Table 8.12. The specimens were packed in a box of iron chips approximately 6" X 12" X 18" (152mm X 304mm X 457mm) in order to simulate the cooling rate in the midsection of a tubesheet forging approximately 10" (254mm) thick. Specimen temperature was monitored by a thermocouple embedded in the iron chips. The major effect of this procedure was to reduce the air cooling rate between 1700°F (927°C) and 800°F (427°C) to 900°F per hour, (0.138°C/sec), resulting in only a limited amount of transformation to bainite. The microstructures corresponding to all of these heat treatments for VAR 55262 and corresponding to heat treatments B and D for heats VAR 56067 and ESR R0110 are shown in Figures 8.12 and 8.13. Heat ESR R0110 has an ASTM ferrite grain size of 10, whereas the VAR heats range in grain size from 6 to 9, as shown in Table 8.13 along with the corresponding values of Rockwell B Scale Hardness. The fine grain size of the electroslag remelted material is attributed to an increased aluminum content obtained from the high aluminum content slag used during remelting, rather than to fine grain practice during melting. The similar hardness resulting from the anneal and normalize/temper heat treatments is due to the relatively slow air cooling rate of the normalize/temper treatment.

8.4.2.3 Tensile Tests

Room temperature uniaxial tensile tests have been conducted at a nominal strain rate of 6.67×10^{-4}/sec for VAR heat 55262 and ESR heat R0110. The results of these tests are summarized in Table 8.14 along

Table 8.10 Chemical Analysis of 2¼Cr-1Mo Steel

	VAR 55262 Check Chemical Analysis (Anamet)	VAR 56067 Check Chemical Analysis (Anamet)	ESR R0110 Check Chemical Analysis (Anamet)	RDT M2-19 RDT M3-33	
				Minimum	Maximum
Aluminum	<0.005%	0.005%	0.027%****		
Antimony	<0.002%	<0.002%	<0.002%		
Arsenic	0.008%	0.006%	0.010%		
Carbon	0.099%*	0.098%**	0.100%***	0.070%	0.110%
Chromium	2.26%	2.31%	2.26%	1.90%	2.60%
Cobalt	<0.002%	<0.002%	<0.002%		
Copper	0.09%	0.08%	0.10%		0.35%
Hydrogen	0.0006%	0.0007%	0.0005%		
Manganese	0.50%	0.42%	0.50%	0.30%	0.60%
Molybdenum	1.00%	0.99%	0.99%	0.87%	1.13%
Nickel	0.15%	0.17%	0.15%		0.25%
Nitrogen	0.008%	0.006%	0.008%		
Oxygen	<0.001%	<0.001%	<0.001%		
Phosphorus	0.013%	0.010%	0.013%		0.015%
Silicon	0.07%	0.28%	0.09%	0.20%	0.40%
Sulfur	0.016%	0.007%	0.015%		0.015%
Tin	0.004%	<0.002%	<0.002%		
Titanium	<0.002%	0.002%	<0.002%		0.03%
Vanadium	0.013%	0.006%	0.013%		0.03%

* Average of 0.093%, 0.090%, 0.115%
** Average of 0.095%, 0.105%, 0.095%
*** Average of 0.113%, 0.103%, 0.086%
**** Average of 0.034%, 0.025%, 0.023%

Table 8.11 Inclusion Content Determination by ASTM E45-D

Position	Inclusion Type			
	A	B	C	D
VAR Heat # 56067				
Edge				
Thin	---	---	---	---
Heavy	---	---	---	1½
Midsection				
Thin	---	---	---	---
Heavy	---	---	---	1½
Center				
Thin	---	---	---	---
Heavy	---	---	---	1½
VAR Heat # 55262				
Edge				
Thin	½	---	---	---
Heavy	---	---	---	---
Midsection				
Thin	½	---	---	---
Heavy	---	---	---	---
Center				
Thin	½	---	---	---
Heavy	---	---	---	---
ESR Heat # R0110				
Edge				
Thin	---	---	---	---
Heavy	---	---	---	1½
Midsection				
Thin	---	---	---	---
Heavy	---	---	---	1
Center				
Thin	---	---	---	1
Heavy	---	---	---	---
RDT M3-33 and M2-19				
Thin	1½	1½	1½	1½
Heavy	1	1	1	1

A = Sulfide Type
B = Alumina Type
C = Silicate Type
D = Globular Type Oxides

Table 8.12 Heat Treatments* for 2¼Cr-1Mo Steel

A.	Isothermal Anneal:	1750°F (954°C) for ½ hr.
		Furnace Cool to 1310°F (710°C) for 2½hr.
		Air Cool to RT
	Postweld:	1340°F (727°C) for 4 hr.
		Air Cool to RT
B.	Anneal:	1680°F (916°C) for 1¼ hr.
		Furnace Cool (@ 50 to 100°F/hr.) (@ 27.7 - 55.6°C) to 600°F (316°C)
		Air Cool to RT
	Postweld:	1340°F (727°C) for 4 hr.
		Air Cool to RT
C.	Normalize and Temper:	1700°F (954°C) for 1 hr.
		Air Cool to RT
		1340°F (727°C) for 1 3/4 hr.
		Air Cool to RT
	Postweld:	1340°F (727°C) for 4 hr.
		Air Cool to RT
D.	(Same as B without Postweld)	
E.	(Same as A without Postweld)	

*Monitored according to specimen surface temperature.

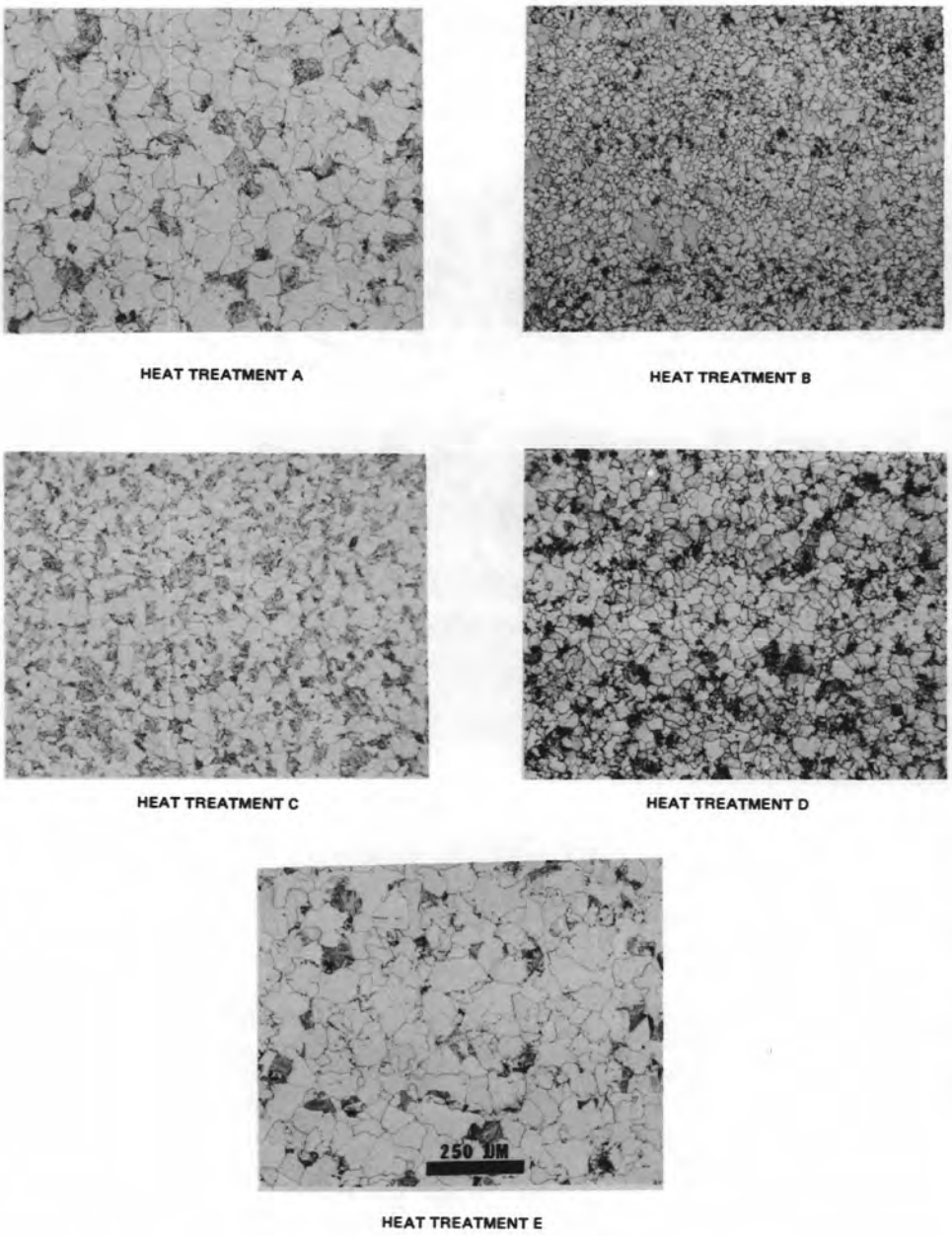

Figure 8.12. Microstructure of 2¼Cr-1Mo Steel, Heat VAR 55262

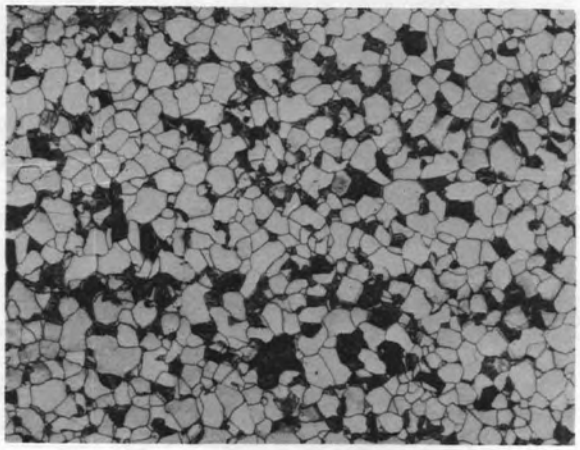

a) HEAT VAR 56067

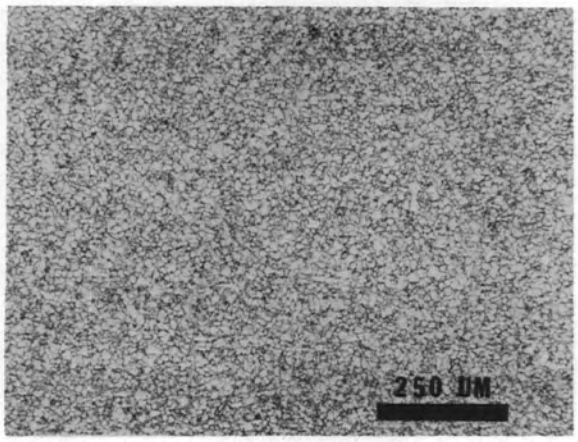

b) HEAT ESR R0110

Figure 8.13. Microstructures of 2¼Cr-1Mo Steel After Heat Treatment B, Full Anneal Plus Post Weld Heat Treatment

Table 8.13 Hardness, Ferrite, and Prior Austenite Grain Size of 2¼Cr-1Mo Steel

Heat No.	Treatment	Hardness R_B*	Ferrite Grain Size ASTM No.	Austenite Grain Size ASTM No.**
VAR 55262	A	66	6	4 - 5
VAR 55262	B	71	9	4 - 5
VAR 55262	C	72	7½	4 - 5
VAR 55262	D	73	7½	4 - 5
VAR 55262	E	70	6	4 - 5
VAR 56067	B	82	6½	4 - 5
VAR 56067	D	78	7	4 - 5
ESR R0110	B	72	10	8 - 9
ESR R0110	D	72	10	8 - 9
RDT M2-19	D	85	-	3 - 5

* Average of three readings

** McQuaid-Ehn

Table 8.14 Tensile Properties of VAR and ESR 2¼Cr-1Mo Steel*

Temperature °C	Temperature (°F)	Strength, MPa (ksi) Yield 0.2% Offset	Strength, MPa (ksi) Ultimate	Total Elongation, (%)	Reduction in Area, (%)
Heat Treatment A - Isothermal Anneal with PWHT** Longitudinal Orientation					
21	(70)	221 (32.0)	465 (67.5)	29.5	72.9
204	(400)	216 (31.3)	406 (58.9)	27.6	65.2
371	(700)	190 (27.6)	491 (71.2)	26.0	64.2
454	(850)	165 (24.0)	405 (58.8)	26.2	62.4
510	(950)	165 (23.9)	379 (54.9)	26.6	73.0
566	(1050)	157 (22.8)	317 (46.0)	32.2	81.6
Heat Treatment B - Full Anneal with PWHT. Longitudinal Orientation					
21	(70)	241 (34.9)	441 (63.9)	32.1	65.4
204	(400)	216 (31.3)	384 (55.7)	30.1	65.2
371	(700)	208 (30.2)	444 (64.4)	23.7	60.7
454	(850)	179 (25.9)	423 (61.4)	27.1	68.3
510	(950)	187 (27.1)	396 (57.4)	27.2	75.2
566	(1050)	168 (24.4)	352 (51.1)	33.2	74.7
Heat Treatment D - Full Anneal without PWHT. Longitudinal Orientation					
21	(70)	243 (35.2)	472 (68.5)	33.1	66.4
204	(400)	213 (30.9)	410 (59.5)	29.7	66.4
371	(700)	215 (31.2)	452 (65.6)	22.9	60.7
454	(850)	214 (31.0)	449 (65.2)	26.1	61.9
510	(950)	204 (29.6)	429 (62.2)	24.6	64.8
566	(1050)	200 (29.0)	372 (54.0)	30.0	72.4

* Strain Rate - 6.67×10^{-4}/sec

** PWHT - Post Weld Heat Treatment

Table 8.14 Tensile Properties of VAR and ESR 2¼Cr-1Mo Steel* (Cont'd.)

Temperature °C	Temperature (°F)	Strength, MPa (ksi) Yield 0.2% Offset	Strength, MPa (ksi) Ultimate	Total Elongation, (%)	Reduction in Area, (%)
Heat Treatment B - Full Anneal with PWHT. Longitudinal Orientation					
21	(70)	225 (37.0)	480 (69.6)	36.1	74.4
204	(400)	- -	- -	-	-
371	(700)	192 (27.9)	421 (61.0)	29.4	66.4
454	(850)	146 (21.2)	378 (54.8)	24.8	71.9
510	(950)	149 (21.6)	360 (52.2)	39.3	73.3
566	(1050)	144 (20.9)	301 (43.7)	42.1	80.8
Heat Treatment B - Full Anneal with PWHT. Transverse Orientation					
21	(70)	296 (43.0)	483 (70.0)	37.5	73.4
204	(400)	242 (35.1)	405 (58.7)	33.7	72.5
371	(700)	209 (30.3)	402 (58.3)	27.1	68.1
454	(850)	177 (25.7)	399 (57.8)	30.2	68.9
510	(950)	174 (25.3)	370 (53.7)	33.4	69.2
566	(1050)	145 (21.1)	305 (44.2)	40.3	79.9
Heat Treatment D - Full Anneal without PWHT. Longitudinal Orientation					
21	(70)	268 (38.9)	472 (68.5)	40.6	72.8
204	(400)	226 (32.8)	403 (58.4)	27.6	74.2
371	(700)	192 (27.9)	413 (59.9)	28.3	67.7
454	(850)	160 (23.2)	399 (57.9)	28.9	68.0
510	(950)	148 (21.4)	360 (52.2)	34.5	73.9
566	(1050)	150 (21.7)	314 (45.5)	38.3	77.5

* Strain Rate - 6.67×10^{-4}/sec

Table 8.14 Tensile Properties of VAR and ESR 2¼Cr-1Mo Steel* (Cont'd.)

Temperature °C	Temperature (°F)	Strength, MPa (ksi) Yield 0.2% Offset	Strength, MPa (ksi) Ultimate	Total Elongation, (%)	Reduction in Area, (%)
Heat Treatment D - Full Anneal without PWHT. Transverse Orientation					
21	(70)	299 (43.4)	487 (70.6)	37.5	72.1
204	(400)	226 (32.8)	401 (58.2)	34.0	67.7
371	(700)	195 (28.3)	459 (66.5)	25.1	65.3
454	(850)	168 (24.3)	403 (58.5)	27.6	65.6
510	(950)	154 (22.4)	378 (54.8)	31.8	70.1
566	(1050)	155 (22.5)	321 (46.5)	37.8	75.8
Requirements of RDT M3-33 (Tubing)					
21	(70)	206 (30)min.	414 (60) to 586 (85)	30 min.	--
Requirements of RDT M2-19 (Tubesheet Forging)					
21	(70)	206 (30)min.	414 (60) to 586 (85)	20 min.	--

* Strain Rate - 6.67×10^{-4}/sec

with the minimum strength and ductility values required for the tubing (RDT M3-33) and the tubesheet forging (RDT M2-19). Both the VAR and the ESR heats meet the minimum requirements for yield stress, tensile stress, elongation, and reduction in area specified for the tubing and tubesheet forging.

Testing was performed on VAR heat 55262 with heat treatments A, B, and C in the longitudinal orientation (relative to the rolling direction before heat treatment), and on ESR heat R0110 with heat treatments B and D in the longitudinal and transverse directions. Tensile tests are also reported for 400, 700, 850, 950, and 1050°F (204, 371, 454, 510, and 566°C) for the same heat treatments and orientations. The variation of yield strength with temperature for these conditions is shown in Figures 8.14 and 8.15. Properties for heat treatment C will be reported later.

8.4.2.4 Charpy Impact Tests and Drop-Weight Tests

The variation of energy absorbed in a Charpy V-Notch impact test with test temperature was determined for VAR heats 55262 and 56067, and ESR heat R0110 for various heat treatments and specimen orientations. A summary of the results of these tests is given in Table 8.15. The effect of specimen orientation relative to the hot rolling direction before heat treatment is evident for VAR heat 55262 in the fully annealed condition (B), but is not evident for ESR heat R0110 which has a finer ferrite grain size. Post weld heat treatment reduced the NDT 5°F (2.78°C) for the VAR heat and 10°F (5.56°C) for the ESR heat. These NDT values have been established as reference values according to NB-2300, which requires that the Charpy V-Notch test show 50 ft.-lb. (67.79J) and 35 mils (0.889 mm) lateral expansion at a temperature not less than NDT + 60°F (33.3°C). Based on the lowest temperatures where 50 ft.-lb. (67.79J) energy and 35 mils (0.889 mm) lateral expansion were obtained in the Charpy tests, the full anneal with post weld heat treatment provides the best protection against nonductile failure for the VAR or ESR heats tests.

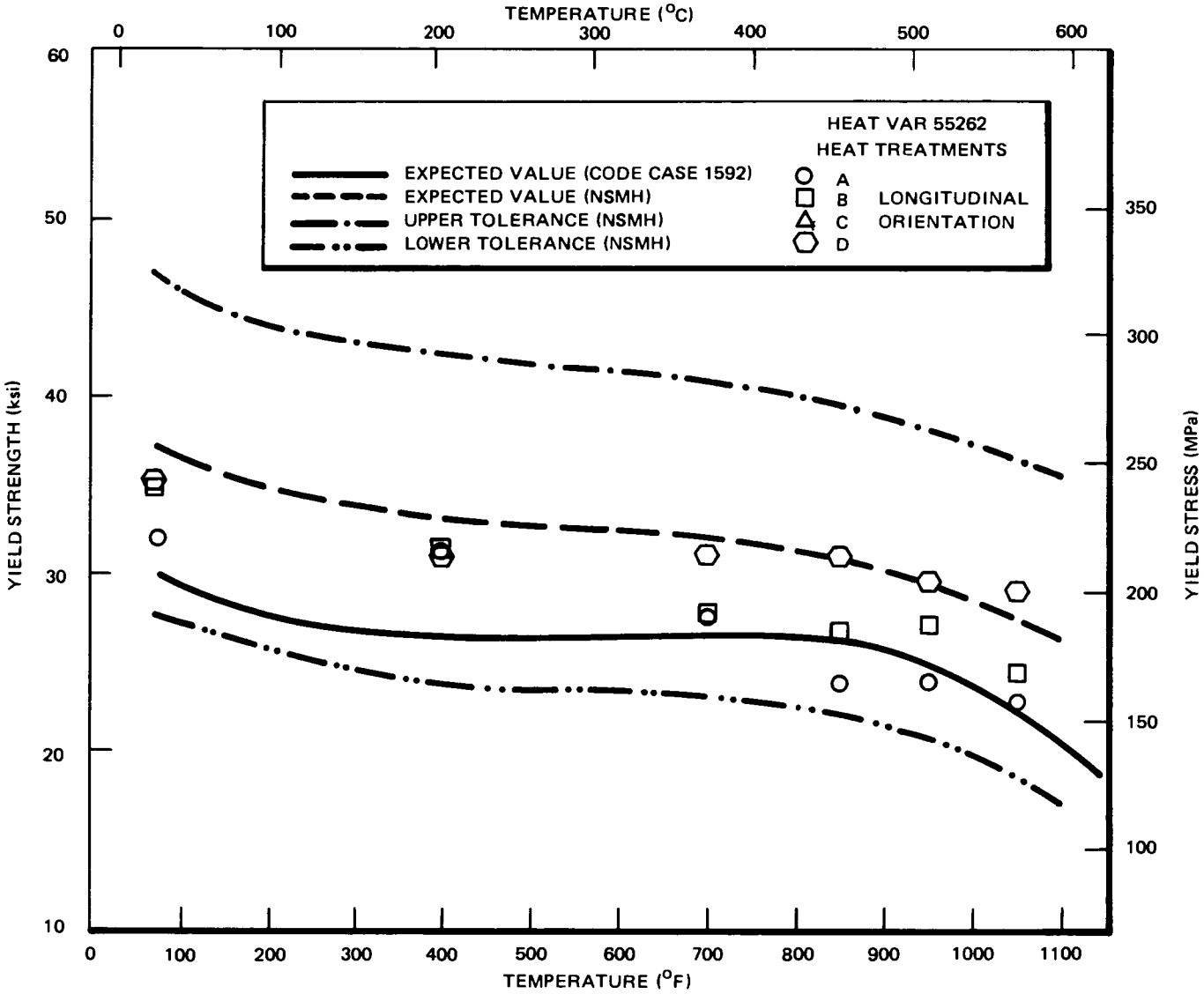

Figure 8.14. Relationship Between Yield Strength and Temperature for 0.10%C, VAR 2¼ Cr- 1 Mo Steel

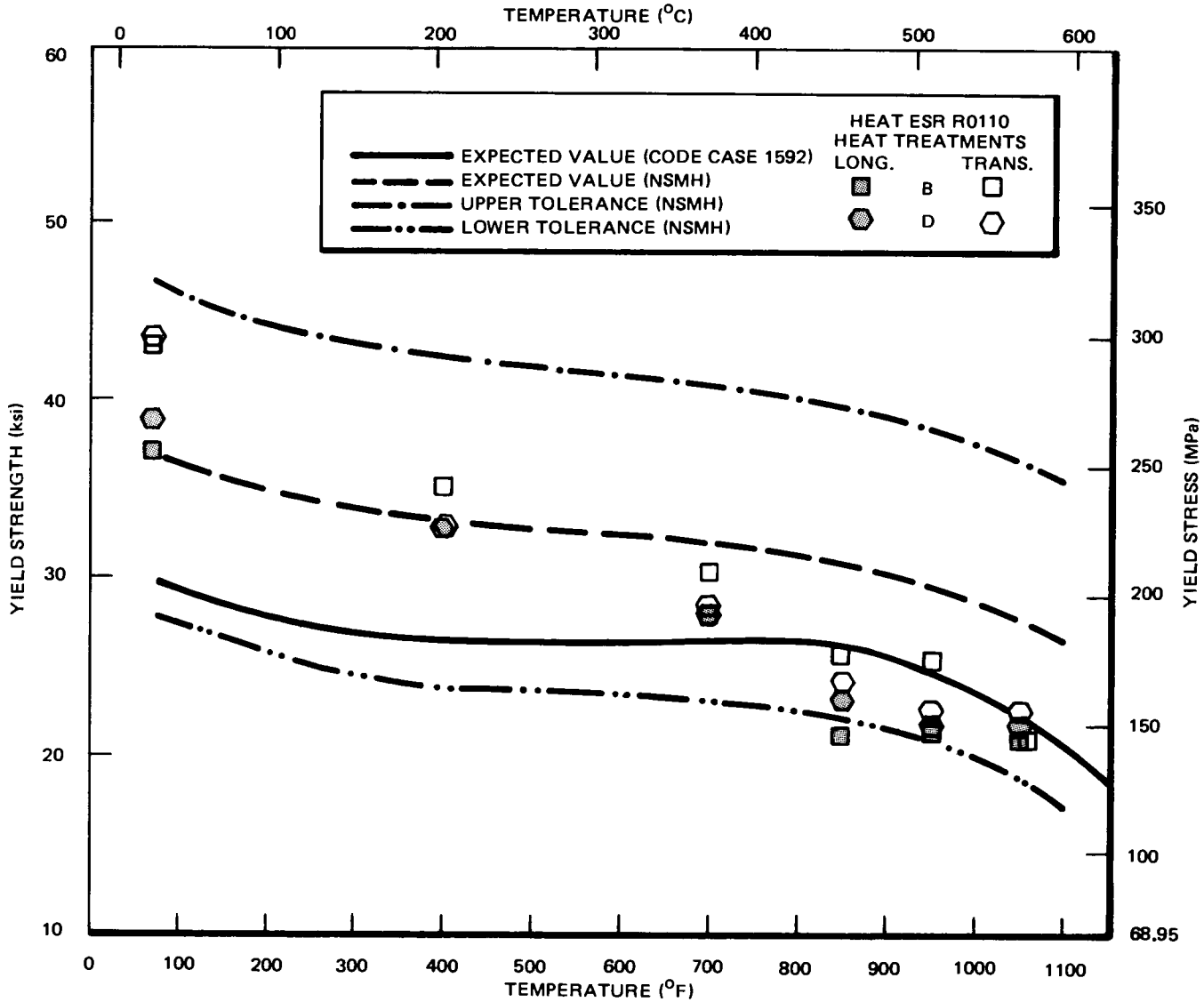

Figure 8.15. Relationship Between Yield Strength and Temperature for 0.10%C, ESR 2¼ Cr-1 Mo Steel

Table 8.15 Summary of Charpy Impact Test Data for 2¼Cr-1Mo Steel

ASTM Standard E23-72

Heat No.	Heat Treat-ment	Orien-tation	50ft.-lb. Energy Temp. °F (°C)	35 mils Lateral Expan-sion Temp. °F (°C)	50% Shear Fracture Temp. °F (°C)	Nil Ductility Temp., **(NDT) °F (°C)	Reference NDT*** °F (°C)	Upper Shelf Energy ft.-lb.(J)
VAR 55262	B	Long.	-30(-34.4)	-30(-34.4)	-25(-31.7)	20(-6.67)	20(-6.67)	>240(>325)
VAR 55262	A	Trans.	95(35)	85(29.4)	125(51.7)	--	--	103(140)
VAR 55262	B	Trans.	35(1.67)	25(-3.89)	85(29.4)	20(-6.67)	20(-6.67)	92(125)
VAR 55262	C	Trans.	55(12.8)	35(1.67)	125(51.7)	--	--	87(118)
VAR 55262	D	Trans.	50(10)	35(1.67)	110(43.3)	25(-3.89)	25(-3.89)	87(118)
VAR 55262	E	Trans.	120(48.9)	95(35)	130(54.4)	--	--	86(117)
VAR 56067	B	Trans.	165(73.9)	120(48.9)	175(79.4)	--	--	87(118)
VAR 56067	D	Trans.	165(73.9)	120(48.9)	175(79.4)	--	--	86(117)
ESR R0110	B	Long.	-45(-42.8)	-50(-45.6)	-45(-42.8)	-50(-45.6)	-50(-45.6)	>240(>325)
ESR R0110	D	Long.	-20(-28.9)	-25(-31.7)	0(-17.8)	-40(-40)	-40(-40)	>240(>325)
ESR R0110	B	Trans.	-45*(-42.8)	-50*(-45.6)	-45*(-42.8)	-50(-45.6)	-50(-45.6)	>240(>325)
ESR R0110	D	Trans.	-20*(-28.9)	-25*(-31.7)	0*(-17.8)	-40(-40)	-40(-40)	>240(>325)

* Approximate temperatures - insufficient data to determine precise values.
** Determined from Drop-Weight Tests.
*** Determined according to NB-2300.

8.4.2.5 Creep-Rupture Tests

A series of creep-rupture tests have been initiated on VAR heat 55262 and ESR heat R0110 at 850, 950, and 1050°F (454, 510 and 566°C). The stresses at each temperature have been adjusted to yield rupture times ranging from approximately 50 to 10,000 hours.

The minimum creep rate for all tests completed or in progress on VAR 55262 have been plotted versus stress in Figure 8.16 to 8.18. At 850°F (454°C) all heat treatments resulted in similar minimum creep rates at corresponding stress levels. For the VAR heat at 950°F (510°C) and 1050°F (566°C) the full anneal with post weld heat treatment (B) showed an improvement over the isothermal anneal with post weld heat treatment (A), and the normalize and temper with post weld heat treatment (C). Only limited data are available to date for the ESR heat, however, the data show higher minimum creep rates than the corresponding VAR values. At all three temperatures the experimental data show lower creep rates than the upper tolerance curve at the 0.95 confidence level, 60 ksi (413.7 MPa) ultimate tensile strength level, generated for the Nuclear Systems Materials Handbook (see Figures 8.16 to 8.18). The post weld heat treatment significantly increases the minimum creep rate for the fully annealed ESR material, and this effect apparently increases with decreasing test temperature.

The effect of prolonged exposure at elevated temperature on the microstructure for these materials has not been determined to date.

8.5 FRACTURE TOUGHNESS OF LMFBR STEAM GENERATOR MATERIALS

J. F. Copeland

8.5.1 Background

The objective of this program is to determine fracture toughness values (K_{Ic}) at 21°C (70°F), and higher temperatures, for potential steel plate and tubesheet materials. These results will be combined with Charpy V-notch and drop-weight test values (RT_{NDT} determinations) and tensile test results to evaluate resistance to fracture. The essence of this approach to prevent fracture is set forth in the K_{IR} curve of Apprendix G to Section III of the ASME Boiler and Pressure Vessel Code. No toughness data on 2¼Cr-1Mo

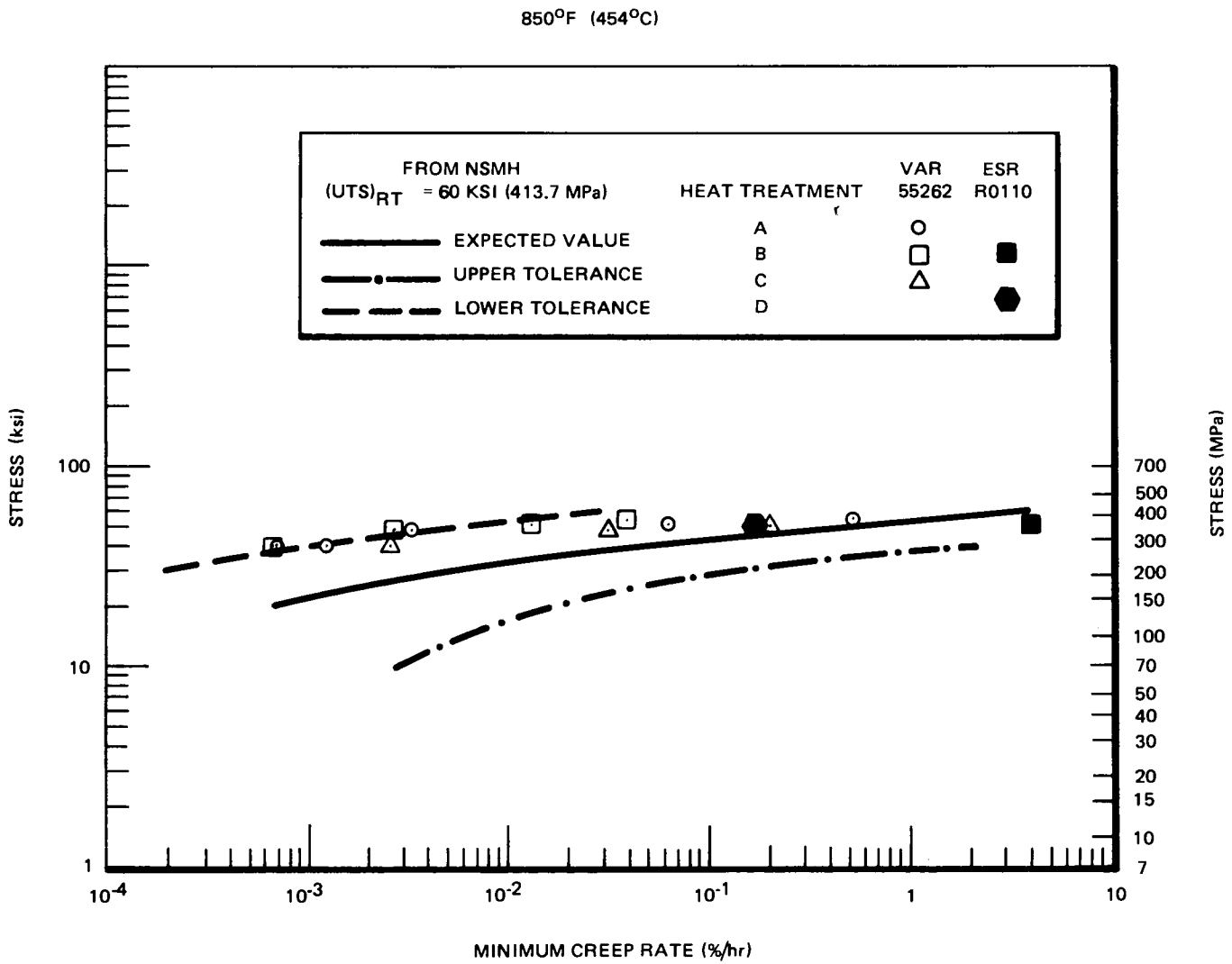

Figure 8.16. Relationship Between Stress and Minimum Creep Rate for 0.10%C, 2¼ Cr-1 Mo Steel at 850°F (454°C)

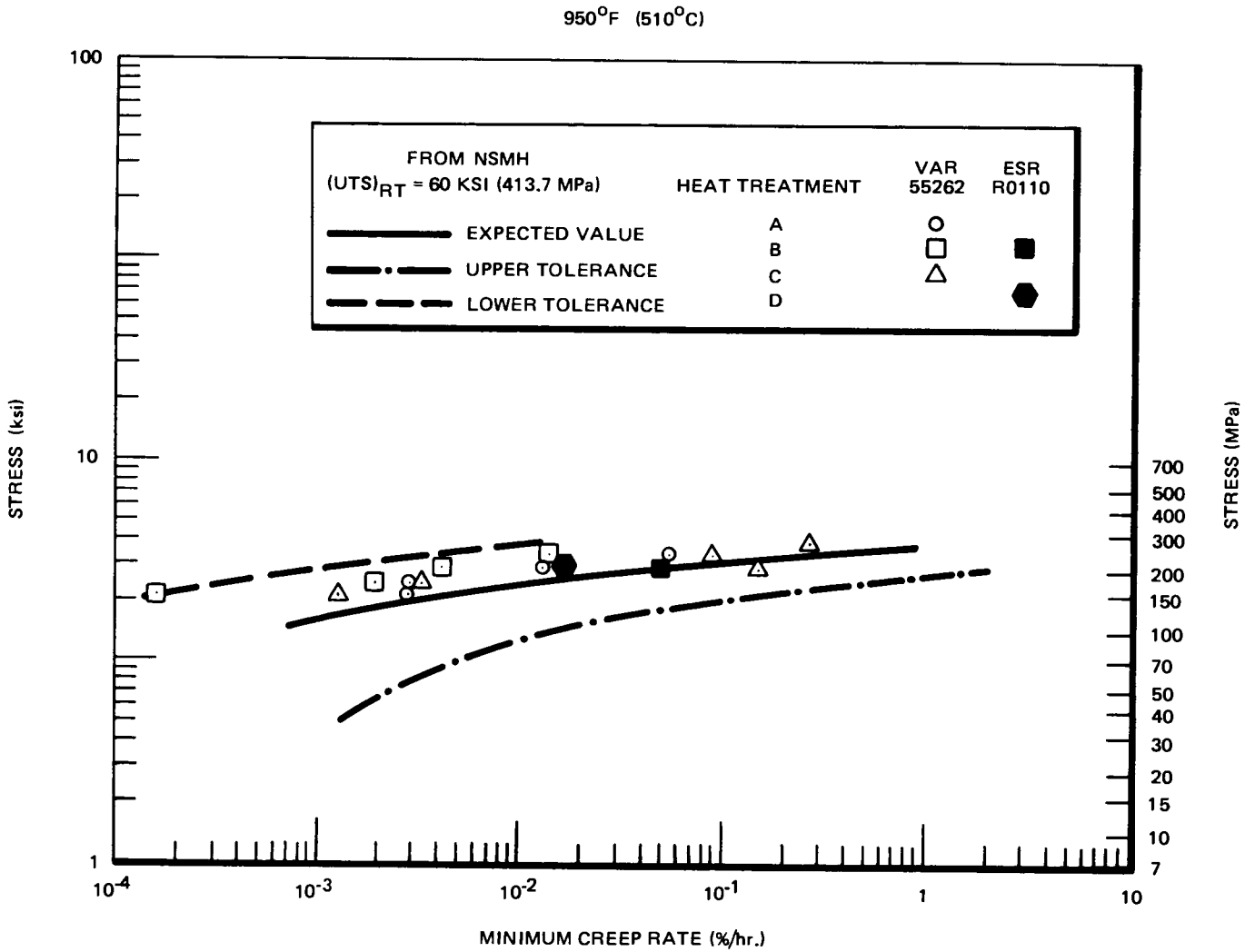

Figure 8.17. Relationship Between Stress and Minimum Creep Rate for 0.10%C, 2¼ Cr-1 Mo Steel at 950°F (510°C)

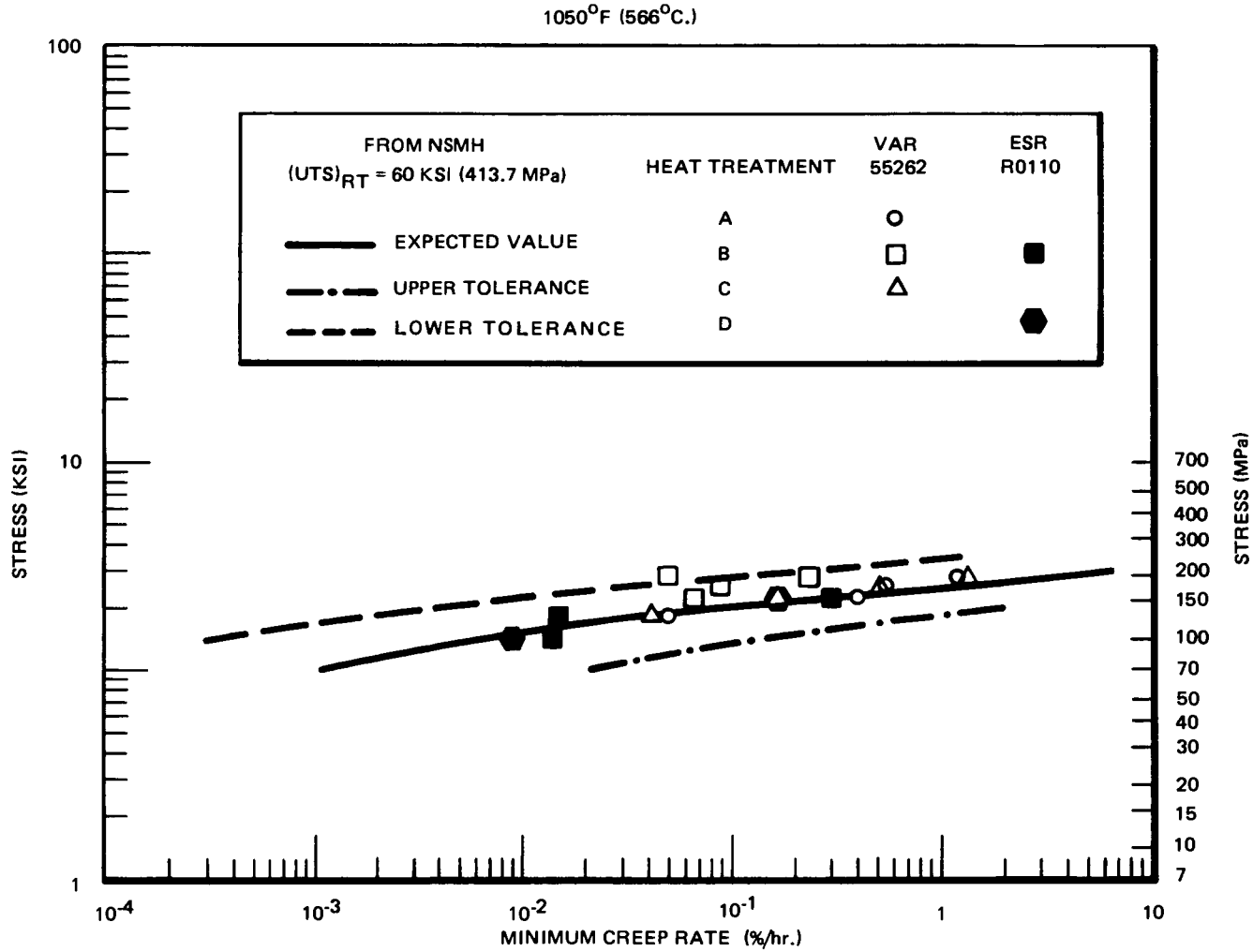

Figure 8.18. Relationship Between Stress and Minimum Creep Rate for 0.10%C, 2¼ Cr-1 Mo Steel at 1050°F (566°C)

steel was included in the derivation of the Code K_{IR} curve. The initial use of the results will be to predict any propensity to fracture during the hydrostatic testing of the component at approximately RT_{NDT} + 33°C (60°F), about 21°C (70°F). Heat treating and melting practices are to be studied for their effects on fracture toughness. Elastic-plastic fracture toughness testing methods (such as the J-Integral, Equivalent Energy, and COD approaches) will be employed to evaluate the fracture toughness of 2¼Cr-1Mo steel with 50.8 mm (2 in.) thick compact tension specimens.

The compact tension specimens will be fatigue precracked prior to testing. These specimens will then be instrumented with displacement gages to determine load versus load pin displacement curves for each specimen during loading with an MTS machine. Several techniques[38,39] will be employed to evaluate the point of crack growth initiation for each specimen. The area (A) under the load versus load pin displacement curve, up to the point of crack growth initiation will be measured and used to compute the J-Integral value (J_{Ic}) from

$$J_{Ic} = \frac{2A}{Bb} \qquad \text{Eqn. 8.3}$$

where B is the specimen thickness and b is the depth of the remaining ligament.[39] When certain specimen size requirements are met,[38]

$$B \geq 25\frac{J_{Ic}}{\sigma ys}, \qquad \text{Eqn. 8.4}$$

where σys is the yield strength, then J_{Ic} is valid and may be used to compute K_{Ic}, the plane strain fracture toughness. The equation employed[40] is

$$J_{Ic} = \frac{K_{Ic}^{2}\,(1 - \nu^{2})}{E} \qquad \text{Eqn. 8.5}$$

where ν is Poisson's ratio and E is Young's modulus. Equivalent Energy and COD computations of fracture toughness will also be made as a cross-check.[38] Post-test fracture surface and microstructure evaluation will be performed.

8.5.2 Current Progress

Air Melted (AM) and Vacuum Arc Remelted (VAR) 2¼Cr-1Mo steel plates were procured. These plates are 89 mm (3.5 in.) and 50.8 mm (2 in.) thick, respectively. The chemical compositions are presented in Table 8.16. The hot rolling ratios of these plates were approximately unity. The heat treatments given, using at least 305 mm (12 in.) square full thickness pieces, are shown in Table 8.17.

The microstructures resulting from these heat treatments, for the air melted plate, are shown in Figures 8.19, 8.20 and 8.21. The microstructures appear very similar for all heat treatments, even for the normalize and temper treatment, and consist principally of polygonal ferrite, with pearlite and some bainite. These microstructures represent the quarter thickness location in an 89 mm (3.5 in.) thick plate, and thus, the cooling rate, even for air cooling, is slow. For a heavy gage plate with the composition toward the low end of the ordinary specification range, it is not unusual for annealed and normalized and tempered microstructures to be similar.

For each heat treatment shown in Table 8.17, three 50.8 mm (2 in.) thick compact tension specimens, two 6.4 mm (0.252 in.) diameter tensile specimens, five P-3 drop-weight NDT specimens, and twelve Chapry V-notch specimens have been machined. Room temperature tensile test results for heat treatments A, B and E are given in Table 8.18. As would be anticipated from the microstructures, the strength levels for all heat treatments are very similar and meet ASME specification requirements. Tension test specimens for heat treatment D have been machined and will be tested within the next month. Charpy V-notch impact test transition curves, as shown in Figures 8.22, 8.23 and 8.24, were also generated for material with heat treatments A, B and E. The 68 J (50 ft.-lb.) transition temperatures for heat treatments A, B and E are, respectively, 29°C (84°F), -10°C (14°F) and 13°C (56°F). The 0.89 mm (35 mil) lateral expansion transition temperatures are, respectively, 11°C (52°F), -14°C (6°F) and 8°C (46°F). Charpy specimens with heat treatment D will be tested within the next month. Also, drop weight tests to determine the NDTT's are currently being performed for treatments A, B, D and E.

Table 8.16 Chemical Compositions of 2¼Cr-1Mo Steel Plates for Fracture Toughness Testing (wt. %)

Melting Process	Heat No.		C	Mn	P	S	Si	Cr	Ni	Mo	Al	As	Sb	Sn
AM	86693	Melt	0.11	0.45	0.009	0.028	0.20	2.01	--	1.04	--	--	--	--
		Check	0.11	0.41	0.014	0.026	0.19	2.00	0.12	1.00	<0.005	0.013	0.007	0.012
VAR	55262	Melt	0.09	0.52	0.016	0.014	0.08	2.22	--	0.01	--	--	--	--
		Check	0.10	0.50	0.013	0.016	0.07	2.26	0.15	1.00	<0.005	0.008	<0.002	0.004

Table 8.17 Heat Treatment of 2¼Cr-1Mo Steel Plates for Fracture Toughness Testing

A. Anneal (AM)

927°C (1700°F) for 3 hr., furnace cool at max. rate of 55.5°C (100°F) per hr. to room temperature

B. Anneal + Temper (AM)

927°C (1700°F) for 3 hr., furnace cool at max. rate of 55.5°C (100°F) per hr. to room temperature

C. Anneal + Temper (VAR)

927°C (1700°F) for 3 hr., furnace cool at max. rate of 55.5°C (100°F) per hr. to room temperature

+

727°C (1340°F) for 4 hr., air cool

D. Anneal + Temper + Embrittlement Treatment (AM)

927°C (1700°F) for 3 hr., furnace cool at max. rate of 55.5°C (100°F) per hr. to room temperature

+

727°C (1340°F) for 4 hr., air cool

+

510°C (950°F) for 1000 hr., air cool

E. Normalize + Temper (AM)

927°C (1700°F) for 3 hr., air cool

+

727°C (1340°F) for 4 hr., air cool

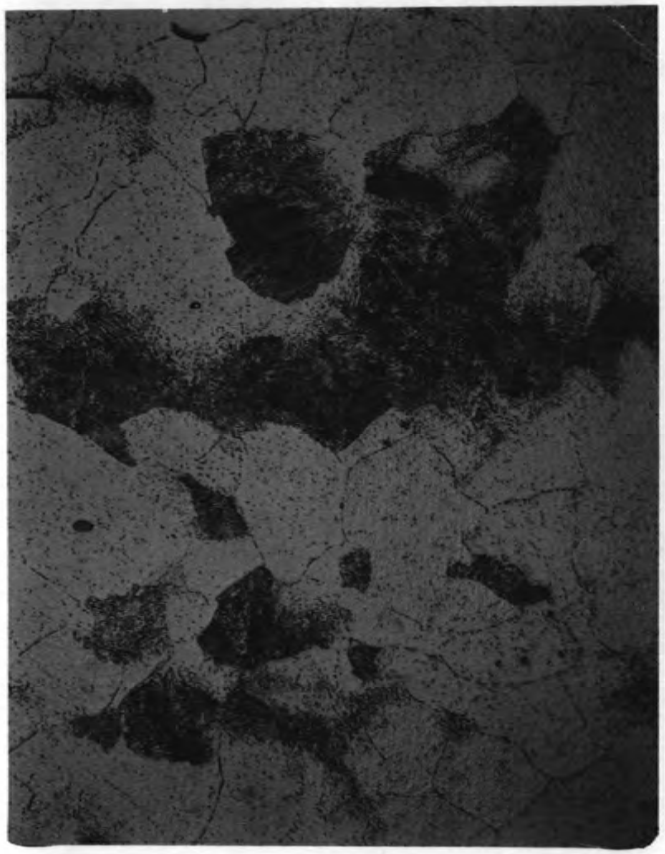

Figure 8.19. Heat Treatment A, Quarter Thickness of 89mm. (3.5 in.) 2¼Cr-1Mo Plate, 500 X.

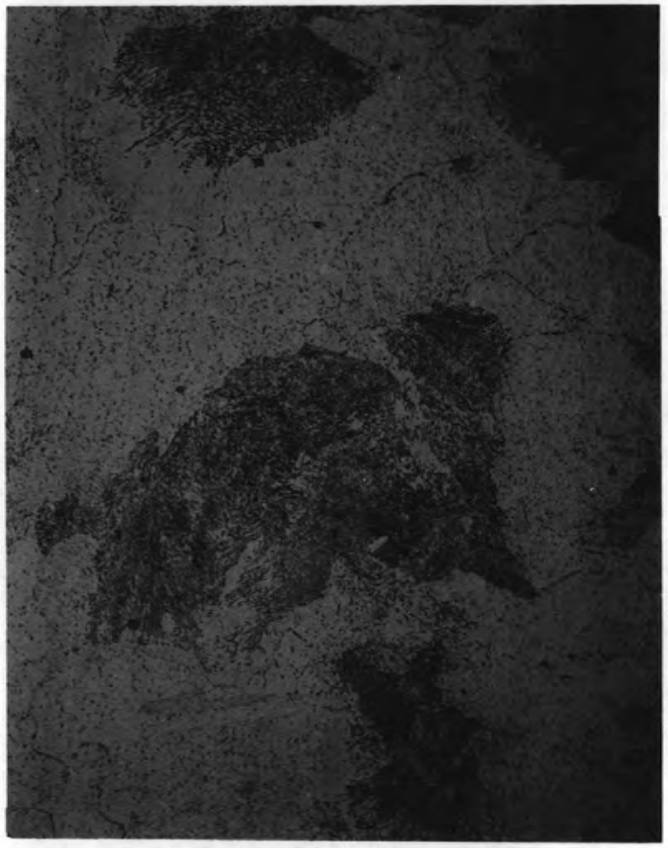

Figure 8.20. Heat Treatment B, Quarter Thickness of 89mm. (3.5 in.) 2¼Cr-1Mo Plate, 500 X.

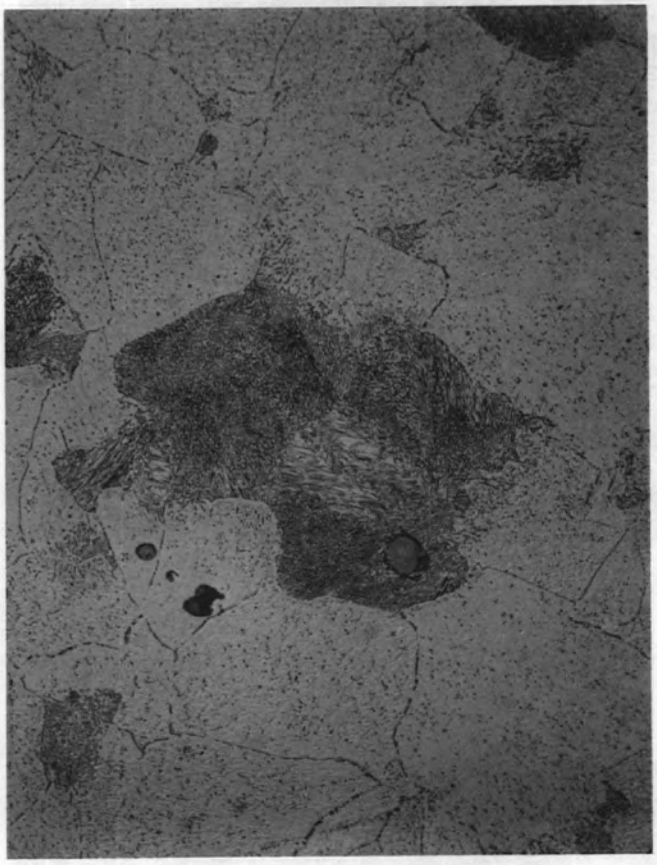

Figure 8.21. Heat Treatment E, Quarter Thickness of 89mm. (3.5 in.) 2¼Cr-1Mo Plate, 500 X.

Table 8.18 Tension Test Properties at 75°F (24°C) for 2¼Cr-1Mo Heat 86693. Air Melt, 3.5 in. (89 mm.) Thick Plate, Properties at ¼ T Location

Strain Rate = 0.04 $min.^{-1}$

	Y.P.	0.2% Y.S.	U.T.S. ksi, (MPa)	% El. (1")	% R.A.
Heat Treatment A	43.2(298)	41.4(285)	67.0(462)	38.4	68.7
	41.4(285)	38.3(264)	66.7(460)	40.0	68.8
Heat Treatment B	39.2(270)	35.2(243)	68.5(472)	39.6	65.3
	38.0(262)	35.2(243)	67.6(466)	38.2	66.1
Heat Treatment E	42.8(295)	37.9(261)	67.6(466)	33.3	65.9
	43.1(297)	38.7(267)	67.7(467)	34.6	65.1

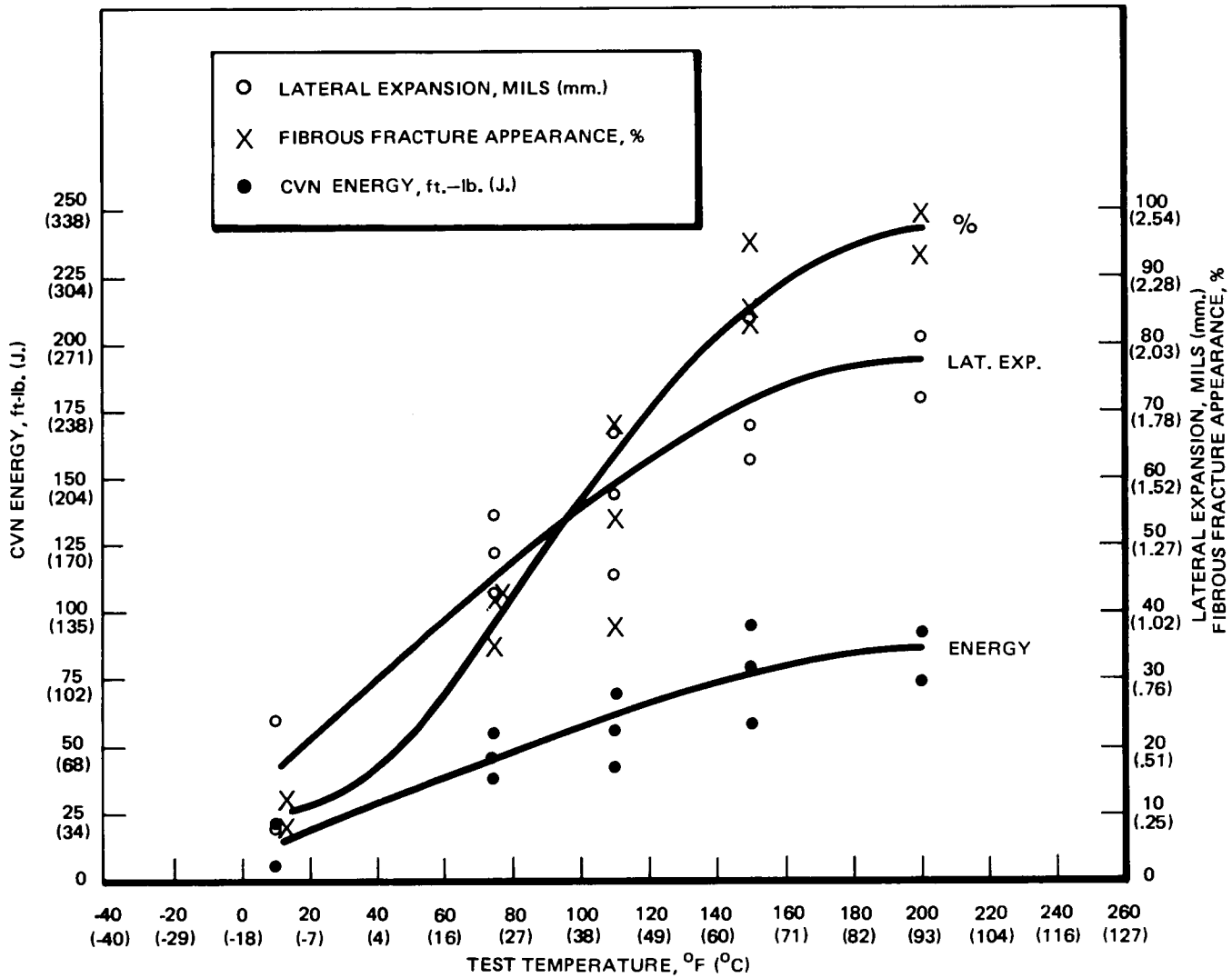

Figure 8.22. *Charpy V-Notch Transition Curves for 2¼ Cr-1 Mo Heat 86693, Air Melt, 3.5 in. (89 mm.) Thick Plate, Properties at Quarter Thickness, Rolling Ratio = 1.0, Heat Treatment A.*

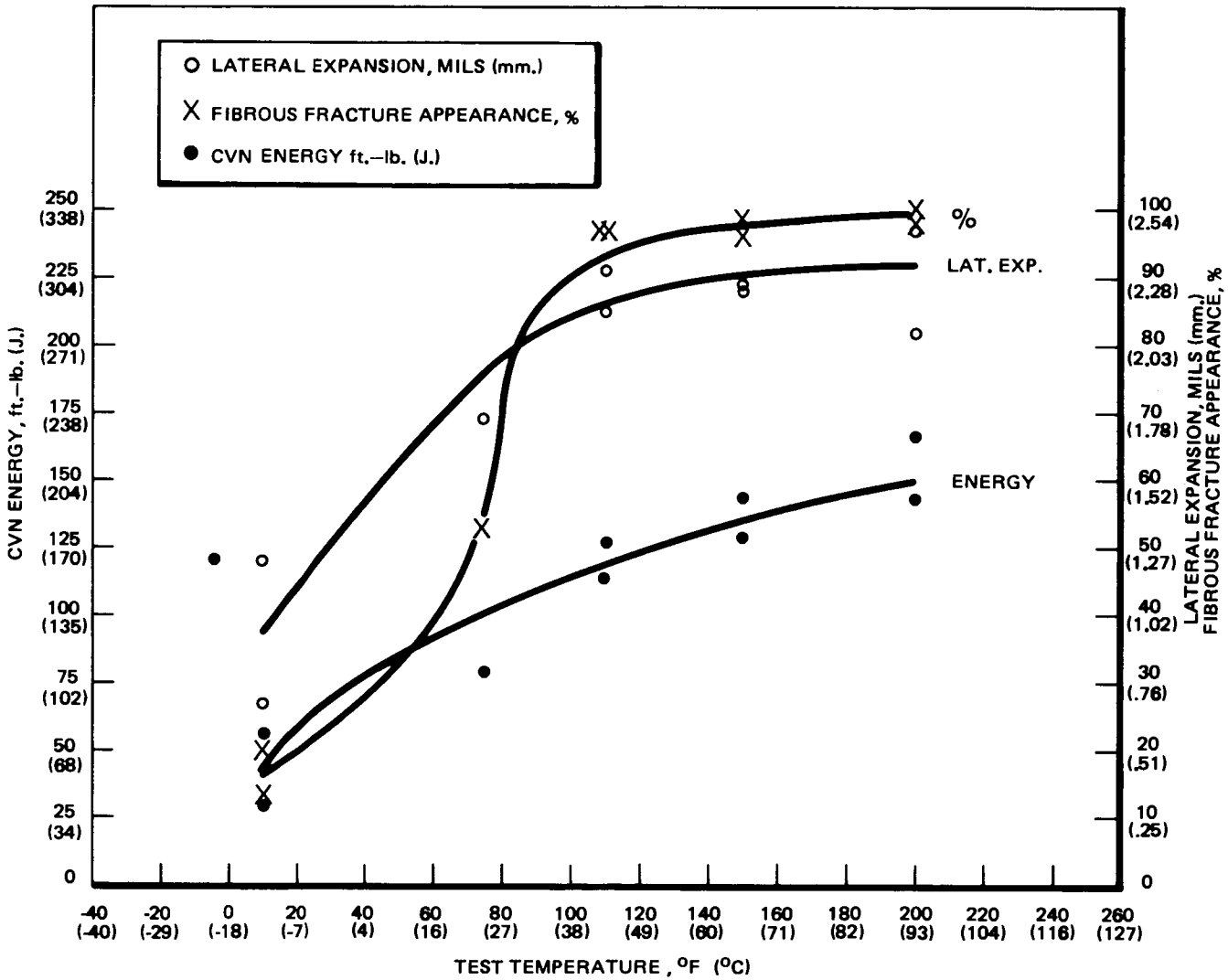

Figure 8.23. *Charpy V-Notch Transition Curves for 2¼ Cr-1 Mo Heat 86693, Air Melt, 3.5 in. (89 mm.) Thick Plate, Properties at Quarter Thickness, Rolling Ratio = 1.0, Heat Treatment B.*

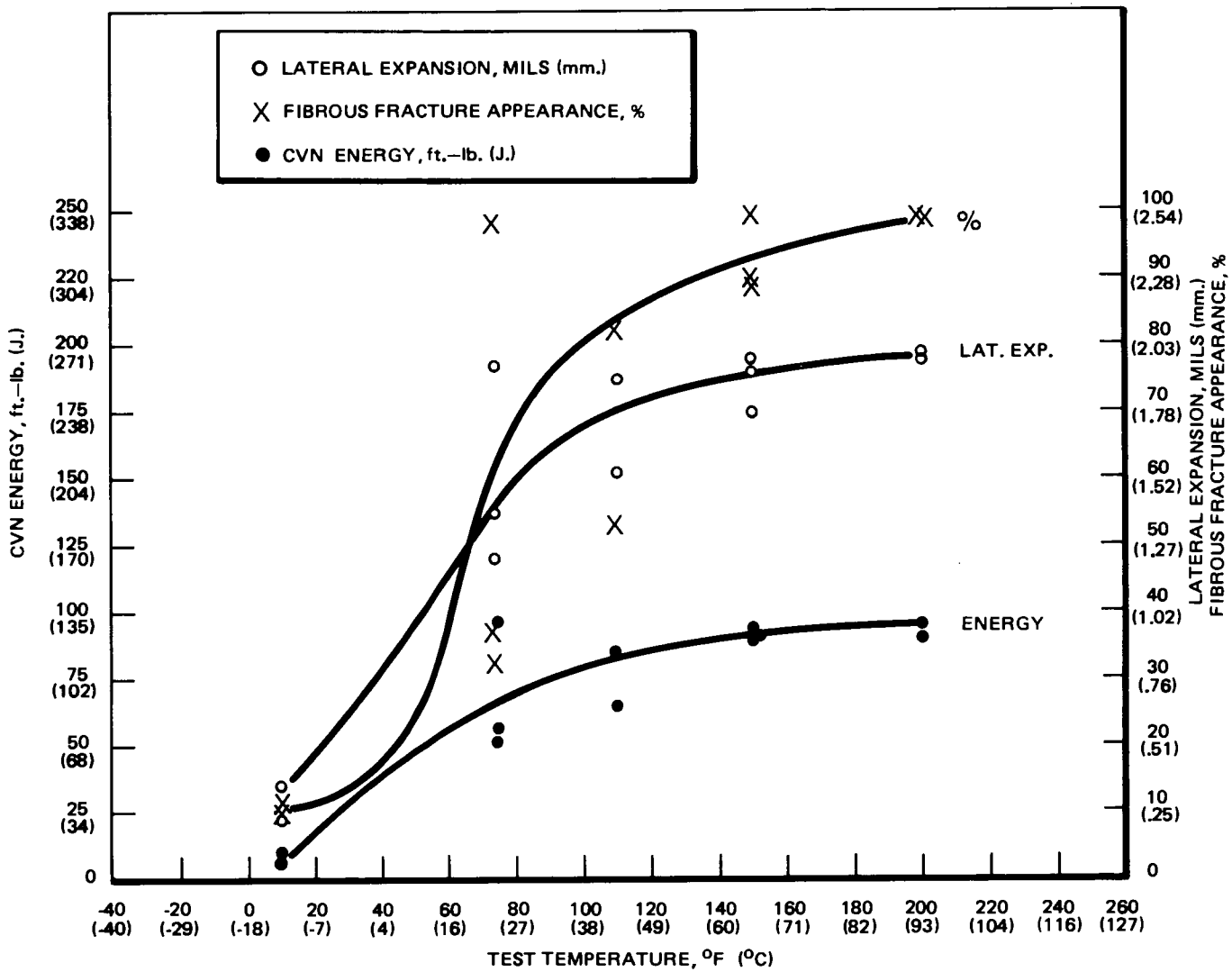

Figure 8.24. *Charpy V-Notch Transition Curves for 2¼ Cr-1 Mo Heat 86693, Air Melt, 3.5 in. (89 mm.) Thick Plate, Properties at Quarter Thickness, Rolling Ratio = 1.0, Heat Treatment E.*

Compact tension specimens for all heat treatments have been prepared. Three 50.8 mm (2 in.) thick compact tension specimens (CTS') were tested at 24°C (75°F) to evaluate the fracture toughness of the material with heat treatment A (full annealed). J-Integral theory was employed to compute K_{Ic} values. A multiple specimen analysis[39] gave a K_{Ic} value of 214 MPa $\sqrt{m}$ (194 ksi $\sqrt{in}$). In this method, the J values for each specimen at unloading are plotted against the total crack extensions. The intersection of a line through these data points and a line representing crack opening stretch is then taken as J_{Ic}, and K_{Ic} is computed from Equation 8.5. The crack extension from a typical specimen is shown in Figure 8.25. It is the dark, crescent-shaped region just after the fatigue precrack area. One specimen from heat treatment B has also been tested, but an exact analysis has not yet been performed for this condition. This testing should be completed in the next month, and the emphasis will shift to elevated temperature tests and the preparation of a weldment for tests.

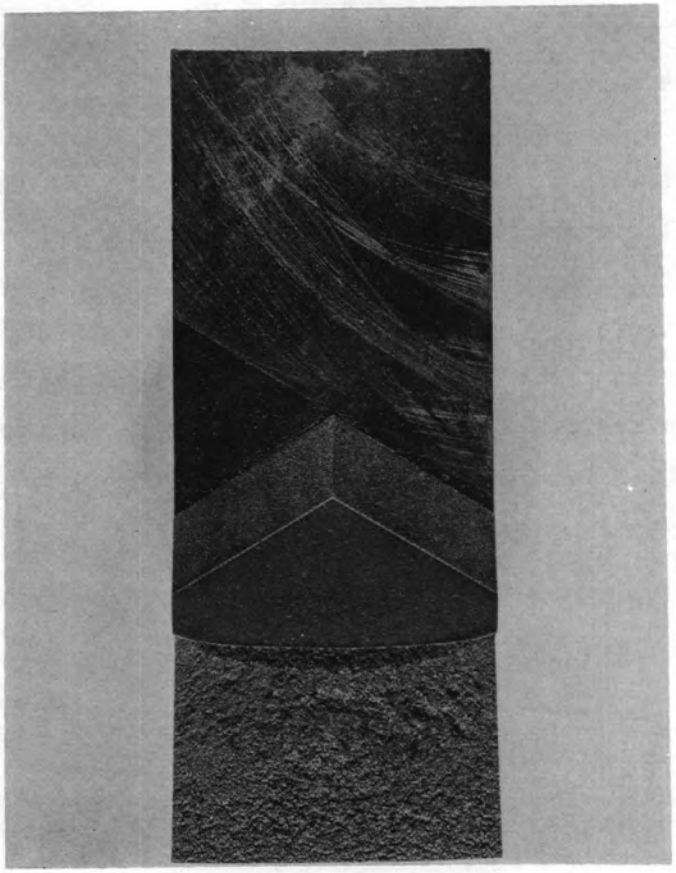

Figure 8.25. Typical 50.8 mm. (2 in.) Thick Compact Tension Specimen Fracture Surface After J_{Ic} Test, Heat Treatment A, 24°C (75°F), Shows (From Top) Machined Chevron Notch, Fatigue Precrack, Crack Extension During Test (Dark Crescent), and Brittle Separation Fracture (-196°C [-320°F] for Convenience)

8.6 REFERENCES

1. "LMFBR Heat Exchanger Materials Development Program". Second Quarterly Report, Sept.-Nov. 1972, GEAP-13919-2, AEC Contract AT(04-3)-189 Proj. Agree. 60, Dec. 1972.
2. R. B. Snyder, K. Natesan, and T. F. Kassner, "A Generalized Method of Computing Carbon-Diffusion Profiles in Austenitic Stainless Steels Exposed to a Sodium Environment", ANL-8015, AEC Contract W-31-109-Eng-38, (June 1973).
3. J. L. Krankota, "Carburization of Stainless Steel Rupture Discs in SGTR," GE letter report, August 1, 1974.
4. M. C. Rowland and D. E. Plumlee, "Sodium Mass Transfer: XXII - Metallurgical Examination of the Test Loops," GEAP-4838, October 1965.
5. Summary Report - Sodium Mass Transfer Program: "Effects of Sodium Exposure on the Corrosion and Strength of Stainless Steel", GEAP-10394, August 1971.
6. D. W. Koch and P. J. Kovach, "Materials Examination of a Model Sodium Heated Steam Generator", BAW-1280-37, June 1966.
7. P. Skahinian et.al., "Fatigue Crack Growth in Type 316 Stainless Steel at High Temperature", Trans. ASME, Nov. 1971, pp. 976-980.
8. L. A. James, "Effect of Thermal Aging Upon the Fatigue - Crack Propagation of Austenitic Stainless Steels", Met. Trans., Vol. 5, Apr. 1974, pp. 831-838.
9. G. J. Licina and J. F. Copeland, "A Review of 2¼Cr-1Mo Steel for Steam Generator Applications in the Clinch River Breeder Reactor," GEAP-20589 (August 1974).
10. "Task VI Final Report, Vol. 4, Steam Generator Development," NEDC-13655 (Oct. 1970).
11. J. L. Krankota and J. S. Armijo, "Decarburization Kinetics of Low Alloy Ferritic Steels in Sodium," Met Trans., 3, pp. 2515-2523, (Sept., 1972).
12. M. C. Rowland and D. E. Plumlee, "Sodium Mass Transfer: XXII - Metallurgical Examination of the Test Loops," GEAP-4838 (Oct. 1965).
13. J. M. Scott, et. al., "Sodium Heated Steam Generator Model Tests at SGTR: Volume 1," GEAP-10580-1, (June 1972).

14. J. L. Krankota and J. S. Armijo, "The Kinetics of Decarburization of 2¼%Cr-1%Mo Steel in Sodium," Nuc Tech., 24 (November 1974).

15. "Sodium Technology Program - Component Materials Compatibility," WARD-NA-3045-11 (August 1974).

16. D. E. Plumlee, R. W. Lockhart, and L. E. Pohl, "Sodium Mass Transfer: XVIII - Studies of Carbon Movement in Pumped Sodium Test Loops," GEAP-4834 (June 1965).

17. M. C. Rowland, et. al., "Sodium Mass Transfer: XIX - Long-Term Exposure Effects in a Bimetallic Type 316 Stainless Steel - 2¼Cr Test Loop," GEAP 4835 (April 1965).

18. L. H. Kirschler, R. H. Hiltz, and S. J. Rodgers, MSAR 64-81 (July 1964).

19. L. H. Kirschler, R. H. Hiltz, and S. J. Rodgers, MSAR 69-42 (April 1969).

20. L. H. Kirschler, R. H. Hiltz, and S. J. Rodgers, MSAR 69-207 (October 1969).

21. L. Champeix and O. Konovaltschikoff, Proceedings of the International Conference on Sodium Technology, pp. 93-103, ANL-USAEC Report ANL-7520-Part 1, (Nov. 1968).

22. J. Sannier, et al., Report on BNES Conference on Corrosion and Effects of Environment on Materials Properties in Nuclear Systems, pp. 137-147, London (July 1971).

23. G. Ilinchev, CEMA Symposium of Atomic Power Stations with Fast Reactors - Volume I (Obninsk), pp. 462-477, Joint Publications Research Service, Washington, D. C. (July 1969).

24. W. J. Anderson, G. J. Sheffield, and J. Birkle, NAA-SR-7544 (Nov. 1963).

25. L. H. Kirschler, R. H. Hiltz, and S. J. Rodgers, MSAR 72-286, (December 1972).

26. V. N. Bykov, et al., "The Problems of Corrosion Resistance of Structural Materials In Sodium," CEMA Symposium of Atomic Power Stations with Fast Reactors (Obninsk) Volume I, pp. 426-461 (July 1969).

27. A. Thorley, B. Longson, and J. Prescott, "Effect of Exposure to Sodium on the Mechanical Properties and Structure of Some Ferritic, Austenitic and High Nickel Alloys," TRG Report 1909 C (1969).

28. D. W. Koch, P. J. Kovach, BAW-1280-37 (June, 1966).

29. S. Ohta, "2¼Cr-1Mo-Nb Steel: A New Steel for Steam Generator Tubes of Sodium Cooled Fast Breeder Reactors," Central Research Lab Kobe Steel. Ltd. (in Reactor Steels Studies in Japan UCLA-34 pp. 177-179).

30. J. Motz, Zeit. Fur Metallkunde, Vol. 55, pp. 489-494, (1964).

31. Nuclear Systems Materials Handbook, Decarburization of 2¼Cr-1Mo Steel (January 1975).

32. R. M. Curran and B. M. Wundt, "A Study of Low-Cycle Fatigue and Creep Interactions in Steels at Elevated Temperatures," to be published.

33. Steam Generator Materials Engineering - First Quarterly Report, GEAP 14029-1 (Oct. 1971).

34. Steam Generator Materials Engineering - Second Quarterly Report, GEAP 14029-2.

35. K. Natesan, et. al., (ANL), Compatibility of Fe-2¼Cr-1Mo steel in Sodium Environment. To be published in Nuclear Technology.

36. T. Yukitoshi, et. al., (Sumitomo, Ltd.), Comparison of Various Chromium-Molybdenum Low Alloy Steels for LMFBR Steam Generators. To be published in Nuclear Technology.

37. K. Matsumoto, et. al., Carbon Transfer Behavior of Materials for LMFBR Steam Generators. To be published in Nuclear Technology.

38. J. F. Copeland, "Influence of Sulfur Content on the Fracture Toughness Properties of 2¼Cr-1Mo Steel", presented at ASME Second National Congress on Pressure Vessels and Piping Technology, San Francisco, June 23 - 27, 1975.

39. J. D. Landes and J. A. Begley, "Test Results from J-Integral Studies: An Attempt to Establish a J_{Ic} Testing Procedure", Fracture Analysis, ASTM STP 560, ASTM, 1974, pp. 170-186.

40. J. G. Merkle, "Analytical Applications of the J-Integral", Progress in Flaw Growth and Fracture Toughness Testing, ASTM STP 536, ASTM, 1973, pp. 264-280.

INDEX

Test	Material	Page
Creep Test Data		
Base-Line		
	type 304 SS bar	185—191; 236
	type 304 SS plate	17—19; 226
	type 304 SS tube	240
	type 304 SS welded plate	236
	type 304 SS welded bar	238
	type 308 SS weld metal	111—114; 127—134
	type 308 CRE weld metal	112—126
	type 316 SS plate	45—46
	type 316 SS tube	240; 296—313
	type 316 SS weld metal	111—113
	16-8-2 SS weld metal	111—115
	2 1/4 Cr-1 Mo weld metal	313—320
	2 1/4 Cr-1 Mo steel	320—333
Correlations		
	type 304 SS	65—84
	type 316 SS	65—93
	alloy 718	65—84
	2 1/4 Cr-1 Mo	65—84
Effect of Cycling		
	type 316 SS tube	296—313
	2 1/4 Cr-1 Mo	184—185
	2 1/4 Cr-1 Mo tube, weld metal	313—320
Effect of Environment		
	Hastelloy X	194—196
	2 1/4 Cr-1 Mo	194—196
	9 Cr-1 Mo	194—196

Test	Material	Page
Creep Test Data (Continued)		
Effect of Heat Treatment		
	type 304 SS	171–176
	2 1/4 Cr-1 Mo	141–154
Effect of Hold Time		
	type 316 SS	296–313
Effect on Microstructure		
	type 304 SS	265–269
Effect of Sodium Environment		
	type 316 SS tube (carburizing)	296–313
	2 1/4 Cr-1 Mo weld metal	313–320
Heat-to-Heat Variation		
	type 304 SS	61–66
Influence of Stress Change		
	type 304 SS	269–275
Multiaxial Tests		
	type 304 SS bar	190–193
Product Form Variation		
	type 304 SS	171–172
Elastic Constants		
Correlations		
	2 1/4 Cr-1 Mo	97–100
Distribution in Weld Metal		
	type 308 SS	101–109
Static Measurements		
	2 1/4 Cr-1 Mo	161
Fatigue Test Data		
Crack Growth Rate Data		
	type 304 SS	289–294
	2 1/4 Cr-1 Mo	196–203
Base-Line Data		
	type 316 SS plate	296–313

Test	Material	Page
Fatigue Test Data (Continued)		
Effect of Frequency		
	type 316 SS plate	296–313
Effect of Heat Treatment		
	Inconel 718	216–222
Effect of Hold Time		
	type 316 SS plate	296–313
Effect of Sodium Environment		
	Inconel 718	216
Effect of Stress Intensity Factor		
	type 316 SS	296–313
Effect of Stress Ratio		
	Inconel 718	216
Effect of Temperature		
	Inconel 718, A-286	216–223
Weldments		
	Inconel 718	216, 219, 220
Data Analysis		
	type 304 SS	176–182
	2 1/4 Cr-1 Mo	154–171
Dislocation Microstructure		
	Incoloy 800	275–286
Effect of Aging Hold-Time		
	alloy 718 plate	256
Effect of Sodium Environment		
	type 316 SS	12–15
	type 316 SS plate	246
Effect of Surface Finish		
	type 304 SS	2–12

Test	Material	Page
Hardness Data		
Effect of Aging		
	type 304 SS	30
Effect of Fabrication		
	type 316 SS	42—45
Effect of Prior Creep		
	type 304 SS	30
Variation in Weldment		
	type 304—308 SS	116—117; 127—129
Microstructure		
	type 304 SS, creep tested	18—35; 265—269
	Incoloy 800, fatigue tested	275—286
Fracture Surfaces		
	type 304—308 SS weldments	135—140
	16-8-2 SS weld metal	134—137
Relaxation Data		
	2 1/4 Cr-1 Mo	182—184
Tensile Test Data		
Base-Line Data		
	2 1/4 Cr-1 Mo	161; 320—351
	type 316 SS	34—42
	type 308 CRE SS weld metal	112—126
Effect of Aging		
	type 304 SS	18—34
Effect of Heat Treatment		
	type 304 SS	171—173
Effect of Prior Creep		
	type 304 SS	18—34

Test	Material	Page
Tensile Test Data (Continued)		
Heat-to-Heat Variation		
	type 304 SS	47–61
Pipe Seam Weld Metal		
	type 308 SS	127–134
Toughness		
Charpy V-Notch		
	2 1/4 Cr-1 Mo	320–351
J-Integral		
	2 1/4 Cr-1 Mo	320–351
Drop Weight NDT		
	2 1/4 Cr-1 Mo	320–351

ORNL-5107
UC-79b, -h, -k
(Liquid Metal Fast
Breeder Reactors)

INTERNAL DISTRIBUTION

1–2. Central Research Library
3. Document Reference Section
4–8. Laboratory Records Department
9. Laboratory Records, ORNL RC
10. ORNL Patent Office
11. R. J. Beaver
12. R. G. Berggren
13. J. J. Blass
14. M. K. Booker
15. C. R. Brinkman
16. D. A. Canonico
17. J. Corum
18. W. R. Corwin
19. F. L. Culler
20. J. E. Cunningham
21. J. H. DeVan
22. D. P. Edmonds
23. G. Fee
24. M. H. Fotana
25. W. R. Gall
26. B. L. Greenstreet
27. J. C. Griess, Jr.
28. J. P. Hammond
29. W. O. Harms
30. R. L. Heestand
31–35. M. R. Hill
36. D. O. Hobson
37. H. Inouye
38. P. R. Kasten
39. J. F. King
40. R. T. King
41. R. L. Klueh
42. K. C. Liu
43. C. T. Liu
44. A. L. Lotts
45–66. W. R. Martin
67. W. J. McAfee
68. H. E. McCoy
69. H. C. McCurdy
70. C. J. McHargue
71. J. Merkle
72. P. Patriarca
73. S. Peterson
74. H. Postma
75. C. E. Pugh
76. P. L. Rittenhouse
77. D. N. Robinson
78. T. Roche
79. J. L. Scott
80. Myrtleen Sheldon
81. V. K. Sikka
82. G. M. Slaughter
83. W. J. Stelzman
84. J. P. Strizak
85. R. W. Swindeman
86. D. B. Trauger
87. T. N. Washburn
88. J. R. Weir, Jr.
89. G. D. Whitman
90. T. Yahr
91. W. C. Leslie (consultant)
92. John Moteff (consultant)
93. Hayne Palmour III (consultant)
94. J. W. Prados (consultant)
95. G. V. Smith (consultant)
96. D. F. Stein (consultant)

EXTERNAL DISTRIBUTION

97—98. USERDA DIVISION OF REACTOR RESEARCH AND DEVELOPMENT, Washington, DC 20545

(2) Director

98—100. USERDA OAK RIDGE OPERATIONS OFFICE, P.O. Box E, Oak Ridge, TN 37830

Research and Technical Support Division
Director, Reactor Division

101—376. USERDA TECHNICAL INFORMATION CENTER, Office of Information Services, P.O. Box 62, Oak Ridge, TN 37830

For distribution as shown in TID-4500 Distribution Category, UC-79b (Fuels and Materials Engineering Development); UC-79h (Structural Materials Design Engineering); UC-79k (Components)

☆ U.S. GOVERNMENT PRINTING OFFICE: 1975-748-189/169